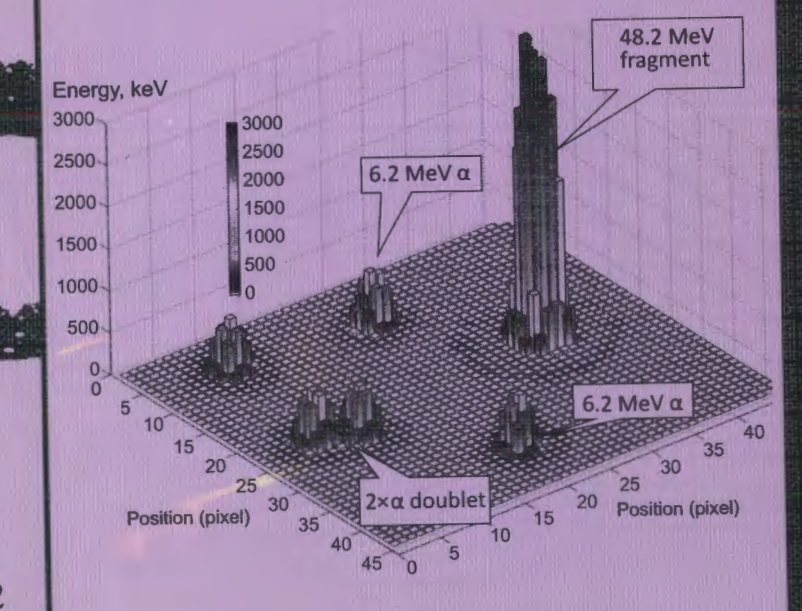
ISINN-19

Neutron Spectroscopy, Nuclear Structure, Related Topics

C 3435(04) N-50

Energy per pixel (keV)



Dubna 2012

• Экз.чит.зала

Joint Institute for Nuclear Research

<u> 63435/0</u> N-50

NEUTRON SPECTROSCOPY, NUCLEAR STRUCTURE, RELATED TOPICS

XIX International Seminar on Interaction of Neutrons with Nuclei

Dubna, May 25-28, 2011

Proceedings of the Seminar

of C)

бъединенный институт дер Пообрассе Дед Сваний БИБЛИОТЕКА УДК 539.125.5(042) ББК 22.383.2я431+22.383.5я431+22.383.25я431 N48

Organizing Committee

W. I. Furman (co-chairman), V. N. Shvetsov (co-chairman),
Yu. N. Kopatch (scientific secretary), T. S. Donskova,
M. V. Frontasyeva, S. V. Kozenkov, P. V. Sedyshev,
A. M. Sukhovoj, L. V. Mitsyna

Secretariat: N. A. Malysheva, I. N. Guseva, T. L. Pikelner, S. F. Yarovikov

The contributions are reproduced directly from the originals presented by the Organizing Committee.

Neutron Spectroscopy, Nuclear Structure, Related Topics: Proceedings N48 of the XIX International Seminar on Interaction of Neutrons with Nuclei (Dubna, May 25–28, 2011). — Dubna: JINR, 2012. — 402 p.

ISBN 978-5-9530-0320-9

This collection of papers reflects the current status of neutron-aided investigations of the properties of the nucleus, including fundamental symmetries, properties of the neutron itself, neutron-excited reactions, and the parameters of the nucleus that determine the reaction cross section, as well as the latest theoretical development of all these problems. The works on experimental investigations in the physics of nuclear fission by neutrons of various energies are presented in great detail. The state of the art of experiments on the physics of ultracold neutrons and facilities to obtain them is described at length. The status achieved by now of the most up-to-date (from the viewpoint of technique) experiments and environment studies are covered as well.

Нейтронная спектроскопия, структура ядра и связанные вопросы: Труды XIX Международного семинара по взаимодействию нейтронов с ядрами (Дубна, 25–28 мая 2011 г.). — Дубна: ОИЯИ, 2012. — 402 с. ISBN 978-5-9530-0320-9

В сборнике отражено современное состояние исследований свойств ядра с помощью нейтронов: фундаментальных симметрий и свойств самого нейтрона, возбуждаемых им реакций и параметров ядра, определяющих их сечения, а также последние теоретические разработки всех этих вопросов. Очень детально представлены работы по всем аспектам, связанным с экспериментальными исследованиями физики деления ядра нейтронами различных энергий. Достаточно полно описано современное состояние экспериментов по физике ультрахолодных нейтронов и установок для их получения, а также достигнутый к настоящему времени статус методически новейших экспериментов и результаты экологических исследований.

УДК 539.125.5(042) ББК 22.383.2я431+22.383.5я431+22.383.25я431

белиценций тастицы "Применействий БиБИНОТИКА

© Joint Institute for Nuclear Research, 2012

Surgidenting for the compact CONTENTS for the content of the first of the content of the content

| Preface9 |
|----------------------------------------------------------------------------------------------------------------------------------------------------------------------------------------------------------------------------------------------------------------------------------------|
| Fission |
| T-Odd Angular Correlations in the Emission of Prompt Neutrons in ²³⁵ U Fission Induced by Polarized Neutrons Danilyan G.V., Klenke J., Krakhotin V.A., Kopatch Yu.N., Novitsky V.V., Pavlov V.S., Shatalov P.B. 11 |
| Fractional Yields of Delayed Neutron Precursors from Fission of ²³⁸ U by Relativistic Protons Egorov A.S., Piksaikin V.M., Roshchenko V.A., Mitrofanov K.V., Myakishev G.A., Samylin B.F., Goverdovski A.A., Vaishnene L.A., Morozov F.A., Vorobyev A.S., Shcherbakov O.A. |
| T-Odd Asymmetry Effects of the Light Particles Emission in the Heavy Nucleus Ternary Fission by the Cold Polarised Neutrons Gagarski A.M., Gonnenwein F., Guseva I.S., Zavarukhina T.A., Kopatch Yu.N., Kuzmina T.E., Mutterer M., Nesvizhevsky V., Petrov G.A., Soldner T., Tiurin G |
| Online Coincidence Detection of Fission Fragments and Light Charged Particles Granja C., Kraus V., Kopatch Yu., Pospisil S., Telezhnikov S.A |
| Investigation of the Sub-Threshold Fission Cross Section for ²³² Th and ²³⁸ U |
| Grigoriev Yu.V., Khlustin D.V., Mezentseva Zh. V., Ryabov Yu.V44 |
| Collinear Cluster Tri-Partition: Current Status of Studies Kamanin D.V., Pyatkov Yu.V., Alexandrov A.A., Alexandrova I.A., Jakobs N., Kondratyev N.A., Kuznetsova E.A., Malaza V., Strekalovsky O.V., Zhuchko V.E |
| Study of Rare Modes of "Collinear Cluster Tri-Partition" of ²⁵² Cf(sf) Kamanin D.V., Pyatkov Yu.V., Malaza V.D., Alexandrov A.A., Alexandrova I.A., Jacobs N., Kondratyev N.A., Kuznetsova E.A., Strekalovsky O.V., Strekalovsky A.O., Zhuchko V.E |

| Relative Yields of Delayed Neutrons and Half-Lives of their Precursors from Fission of ²⁴¹ Am by Neutrons in the Energy Range 1–5 MeV | Nuclear Structure Physics with MonA-LISA Stephenson S.L., Brown J.A., De Young P.A., Finck J.E., Frank N.H., Hinnefeld J.D., |
|--------------------------------------------------------------------------------------------------------------------------------------------------------------------------------------|-----------------------------------------------------------------------------------------------------------------------------------------------------------------------|
| Piksaikin V.M., Mitrofanov K.V., Egorov A.S., Goverdovski A.A | Kaye R.A., Luther B.A., Peaslee G.F., Meyer D.A., Rogers W.F and the MoNA Collaboration |
| Are there Physical Spectators of the CCT Process? Pyatkov Yu.V., Kamanin D.V., Alexandrov A.A., Alexandrova I.A., Kondratyev N.A., Kuznetsova E.A., Strekalovsky O.V., Zhuchko V.E | Reactions with Neutrons, Charged Particles Cross-Section of γ-Ray Production by Fast Neutrons on Cadmium |
| Investigations of the Neutron Cross-Talk Effect in DEMON Detectors Telezhnikov S.A., Kopatch Yu.N., Mezentseva Zh., Stuttge L., Goennenwein F., | Bondar B.M., Bondar V.M., Gorbachenko O.M., Kadenko I.M., Leshchenko B.Yu., Onishchuk Yu.M., Plujko V.A |
| Mutterer M., Chernysheva E., Dorvaux O., Hanappe F., Hambsch FJ | The Experimental Investigation of 10 B(n, α_0) to 10 B(n, α_1) Branching Ratio for Neutron Energy Region from 4 to 7 MeV |
| Digital Pulse Processing Ionization Chamber Pulses Zeynalov Sh., Zeynalova O., Nazarenko M., Hambsch FJ., Oberstedt S | Bondarenko I.P., Khryachkov V.A., Kuzminov B. D., Semenova N.N., Sergachev A.I |
| Fundamental Properties of the Neutron, UCN | Excitation Function ¹⁴ N(n,t) ¹² C in Fast Neutrons Energy Region Ivanova T.A., Khryachkov V.A., Bondarenko I.P., Kuzminov B.D., Semenova N.N., |
| Interaction of Waves with Ordinary and Birefringent Media Moving with | Sergachev A.I |
| Acceleration Frank A.I., Geltenbort P., Jentschel M., Kulin G.V., Kustov D.V., Strepetov A.N | Investigation of ⁵⁰ Cr(n,α) ⁴⁷ Ti Reaction Cross Section for Neutron Energy Less than 7.2 MeV |
| New Spectrometer for Test of Equivalence Principle with UCN | Khryachkov V.A., Bondarenko I.P., Grudzevich O.T., Ivanova T.A., Kuzminov B.D., Semenova N.N., Sergachev A.I |
| Frank A.I., Geltenbort P., Goryunov S.V., Jentschel M., Kulin G.V., Kustov D.V., Strepetov A.N. 98 | Statistical Model Analysis of (n,a) Cross Sections Averaged over the Fission Neutron Spectrum |
| Measurement Methodology for the Main Characteristic of Radiative | Khuukhenkhuu G., Gledenov Yu.M., Sedysheva M.V., Odsuren M |
| Neutron Decay Khafizov R.U., Kolesnikov I.A., Nikolaenko M.V., Tarnovitsky S.A., Tolokonnikov S.V., Torokhov V.D., Solovei V.A., Kolhidashvili M.R., Konorov I.V., | Mixing of the s-Wave and p-Wave Resonances and P-Odd Asymmetry of γ-Quantum Emission in the Radiative Capture of a Slow Polarized Neutron by a Spinless Nucleus |
| Plonka-Spehr C | Lyuboshitz V.L., Lyuboshitz V.V |
| Calculation of Corrections for Precise Obtaining the n,e-Scattering Length from the Angular Anisotropy of Slow Neutrons Scattered by Noble Gases | Differential Cross Section Evaluation in (n,α) Reaction with Fast Neutrons Using Hauser – Feshbach Formalism |
| Mitsyna L.V., Popov A.B. | Oprea A., Oprea C., Gledenov Yu.M., Sedyshev P.V., Sedysheva M.V183 |
| Study of the Neutron Laue Diffraction in Large Silicon Crystal for the Bragg Angles Close to $\pi/2$ | Parity-Violating Gamma Asymmetry in np-Capture |
| Vezhlev E.O., Voronin V.V., Kusnetsov I.A., Semenikhin S.Yu., Fedorov V.V | Sharapov E.I., Alarcon R., Balascuta S., Barrón-Palos L., Bowman J.D., Carlini R.D., Chen W., Chupp T.E., Crawford C., Covrig S., Dabaghyan M., Fomin N., |
| | Freedman S.J., Gentile T.R., Gericke M.T., Gillis R.C., Greene G.L., Hersman F.W., Ino T., Jones G.L., Lauss B., Leuschner M., Lozowski W.R., Mahurin R., Masuda Y., |
| Nuclear Structure, Model Calculations | Mei J., Mitchell G.S., Muto S., Nann H., Page S.A., Penttilä S.I., Ramsay W.D., |
| Prospects of Using the Complicated ("Flaky") Neutron-Optical Potential Alexandrov Yu., Anikin G., Anikin V | Salas-Bacci A., Santra S., Sharma M., Seo PN., Smith T.B., Snow W.M., Wilburn W.S., Yuan V |
| ALCAUMIUV II., AMMII U., AMMII I. | |

| Modified Model of Neutron Resonances Width Distribution. Results of Neutron Reduced Neutron Widths Approximation for Mass Region 35≤A≤249 |
|--------------------------------------------------------------------------------------------------------------------------------------------------------------------------------------------------------------------------------------------------------------------------------------------------------------------------------------------------------------------------------------------------------------------------------------------------------------------------------------------------------------------------------------------------------------------------------------------------------------------------------------------------------------------------------------------------------------------------------------------------------------------------------------------------------------------------------------------------------------------------------------------------------------------------------------------------------------------------------------------------------------------------------------------------------------------------------------------------------------------------------------------------------------------------------------------------------------------------------------------------------------------------------------------------------------------------------------------------------------------------------------------------------------------------------------------------------------------------------------------------------------------------------------------------------------------------------------------------------------------------------------------------------------------------------------------------------------------------------------------------------------------------------------------------------------------------------------------------------------------------------------------------------------------------------------------------------------------------------------------------------------------------------------------------------------------------------------------------------------------------------|
| Sukhovoj A.M., Khitrov V.A |
| Modified Model of Neutron Resonances Width Distribution. Estimation of the Quality of Results and Interpretation of Available Physics Information Sukhovoj A.M., Furman W.I., Khitrov V.A |
| Modified Model of Neutron Resonances Width Distribution. Results of Total Gamma-Widths Approximation Sukhovoj A.M., Khitrov V.A |
| Nuclear Data, Methodical Aspects, Applied Physics |
| TOTAL CONTRACTOR CONTR |
| Micropixel Avalanche Photodiode as Alpha Particle Detector Ahmadov F., Ahmadov G., Madatov R., Sadygov Z., Tiutiunnikov S., Zhezher V |
| |
| Measurements of Characteristics of the Pulse Neutron Sources RADEX and IN-06 of the Moscow Meson Factory (INR RAS, Troitsk) Grigoriev Yu.V., Khlustin D.V., Mezentseva Zh. V., Vasiliev I.A., Ryabov Yu.V |
| Measurements of Neutron Total and Capture Cross Sections at the TOF Spectrometers of the Moscow Meson Factory Grigoriev Yu.V., Khlustin D.V., Mezentseva Zh. V., Ryabov Yu.V |
| A Multi-Section Frisch-Gridded Ionization Chamber for Studies of Neutron-Induced Fission at the GNEIS Facility Kovalev N.V., Ryzhov I.V., Tutin G.A., Shcherbakov O.A., Vorobyev A.S., Vaishnene L.A |
| Status of Pulsed Neutron Facility in Korea Kim G., Lee M., Kim K.S., Yang S., Kim E., Shvetsov V., Skoy V., Cho MH., Namkung W |
| Coincidence Module for Spectral- and Time-Correlated Multi-Particle Detection with Four Pixel Detectors Timepix Kraus V., Granja C |
| On the Possibility to Increase a Neutron Beam Flux of IREN Mitsyna L.V., Popov A.B., Song Zhaohui |
| and the first of the second of the second of the production of the first of the second |

| Multiinput Encoder for Recording Spectra of Scattered Neutrons Using Time-of-Flight Method Shvetsov V.N., Alpatov S.V., Astahova N.V., Gundorin N.A., Enik T.L., Mitsyna L.V., Pikelner L.B., Popov A.B., Salamatin I.M., Salamatin K.M., Samosvat G.S., Sedyshev P.V., Sirotin A.P. |
|--------------------------------------------------------------------------------------------------------------------------------------------------------------------------------------------------------------------------------------------------------------------------------------|
| Compilation of Nuclear Excited States CRF Sukhoruchkin S.I., Soroko Z.N., Sukhoruchkin D.S |
| Compilation of Nuclear Binding Energies MDF Sukhoruchkin S.I., Sukhoruchkin D.S |
| Study of Nonstatistical Effects due to Tensor Forces Sukhoruchkin S.I., Sukhoruchkina M.S |
| Nuclear Analytical Methods in the Life Sciences |
| Study of Heavy Metal Contents in Soil, River Water, Snow, Needles and Mosses of Ivanovo Region Dunaev A.M., Latukhina K.S., Abdalla A.A., Rumyantsev I.V., Nikiforov A.Yu. 320 |
| Determination of Magnesium, Aluminum and Silicon Content in Water Samples by Gamma-Activation and Neutron-Activation Analyses Using the MT-25 Microtron Maslov O.D., Gustova M.V., Belov A.G., Drobina T.P |
| Radioecological Investigation at the Construction of "BELENE" NPP Khristov Hr.G., Marinova S.G., Gustova M.V., Maslov O.D |
| Temporal Variations of ¹³⁷ Cs in Surface Air in Bratislava, Slovakia, over 33 Years Sykora I., Povinec P., Brest'akova L., Florek M., Holý K., Masarik J., Frontasyeva M.V., Steinnes E |
| Neutron Activation Analysis of Ca, Cl, Mg, Na, and P Contents in the Human Osteogenic Sarcoma Zaichick S., Zaichick V |
| Relationship between Ca, Cl, K, Mg, Mn, Na, P, and Sr Contents in the Human Rib Bone Investigated by Neutron Activation Analysis Zaichick S., Zaichick V |

| The Effect of Age on the Zinc Content in Prostate of Healthy Men Investigated by INAA and ICP-MS |
|--------------------------------------------------------------------------------------------------------------------------------------------------------------------|
| Zaichick S., Zaichick V., Karandashev V., Nosenko C |
| Papers received after deadline |
| Time Differential Perturbed Angular Correlation Study of Vegetable Oils Oprea C., Velichkov A., Oprea I.A., Filosofov D.V., Szalanski P.J |
| Evaluation of Parity Violation Effects for Thermal Neutrons Scattering on ²⁰⁴ Pb Nucleus |
| Oprea A., Oprea C., Gledenov Yu.M., Sedyshev P.V |
| Trace Heavy Metal Uptake by Crop Roots Oprea C., Gustova M.V., Oprea I.A |
| Air Filters Components Activity Measurements with HpGe Gamma Spectrometer |
| Shvetsov V., Bang J.H., Byun Y.C., Cho MH., Lee M., Kim E.A |
| Measurement of P-Odd Effect in Radiative Cross Section on Natural Lead Vesna V.A., Gledenov Yu.M., Lazebnik I.M., Nesvizhevsky V.V., Sedyshev P.V., Shulgina E.V |
| Nuclear Analytical Methods as Interface of Environmental and |

Oprea C., Gustova M.V., Maslov O.D., Belov A.G., Oprea I.A., Mihul A. 396

PREFACE

gradus to the second of the second of the second of the second

The 19th International Seminar on Interaction of Neutrons with Nuclei: "Fundamental Interactions & Neutrons, Nuclear Structure, Ultracold Neutrons, Related Topics" (ISINN-19), was traditionally organized by the Frank Laboratory of Neutron Physics (FLNP) of the Joint Institute for Nuclear Research (Dubna, Russia). The Seminar continues the series of annual conferences in the field of neutron physics.

ISINN-19 was held in Dubna from May 24 to 28, 2011. More than 100 participants attended the Seminar representing leading nuclear centers of Belarus, Czech Republic, France, Germany, Korea, Republic of South Africa, Romania, Russia, Serbia, Ukraine, and the USA. A numerous and representative delegation from JINR included participants from the FLNP, Flerov Laboratory of Nuclear Reactions, Veksler-Baldin Laboratory of High Energy Physics and Dzhelepov Laboratory of Nuclear Problems. More than 80 oral and poster reports were presented at the Seminar.

The Seminar started from discussion of ultracold neutron (UCN) physics and fundamental properties of the neutron. As usual, very interesting new results, obtained at one of the best research facility in the world – research reactor ILL, were presented. UCN optics and gravity resonances were discussed. Important progress in study of fundamental properties of the neutron by the method of Laue diffraction in large silicon crystal was presented. Preliminary results of large international collaboration on investigation of space parity violation in $(np,d\gamma)$ -reaction were reported and generated debates.

Many talks in the second day of the Seminar were devoted to different aspects of neutron induced reactions. The focus was on experimental and theoretical study of the (n,α) -reaction. The important for application results were presented by a group from Institute of Physics and Power Engineering (IPPE), Obninsk, Russia and from FLNP. There were also discussed the new approaches for description of photon strength function and statistical properties of neutron and gamma widths of compound states as well as P-odd effects in (n,γ) -reaction. Information on the new basic facility of FLNP IREN and coordination of its scientific program with that of a similar pulsed neutron source in Pohang, Korea was met with interest.

Third day was full of interesting reports devoted to nuclear fission. Experiments with slow polarized neutrons provide important information on basic mechanism of the fission process. The results of last measurements done at ILL and Hahn-Meitner Institute discovered new properties of binary and ternary fission. The report on study of nuclear tripartition in collinear geometry aroused great interest. Such experimental approach permits to discover the new phenomenon — cluster decay of strongly deformed fission products. The important new results were presented also for study of delayed neutrons and for development of new experimental technique related to coincidence detection of fission products. The day ended with a very informative poster session.

The final day of the Seminar includes two parallel sessions. One was devoted to various methodical aspects. It includes in particular a series of talks summarizing recent successes in application of micropixel detector systems for multidimensional experiments. Beside that the progress in development of neutron pulsed source at Institute of Nuclear Research, Troitsk, Russia was reported. The different applications of Neutron Analytical Methods were discussed in the parallel session. The environmental pollutions and human health problems were in the center of discussion.

We would like to acknowledge the traditional support of the Seminar by the Russian Foundation for Basic Research (grant № 11-02-06044-r). This allowed many young scientists to take part in the Seminar and made it possible to publish the Seminar Proceedings.

ISINN-19 Co-chairmen

W.I.Furman V.N.Shvetsov

T-ODD ANGULAR CORRELATIONS IN THE EMISSION OF PROMPT NEUTRONS IN ²³⁵U FISSION INDUCED BY POLARIZED NEUTRONS

Danilyan G.V.¹, Klenke J.², <u>Krakhotin V.A.¹</u>, Kopatch Yu.N.³, Novitsky V.V.³, Pavlov V.S.¹, Shatalov P.B.¹

 Institute for Theoretical and Experimental Physics, Moscow, Russia
 Forschungs-Neutronenquelle Heinz Meier-Leibnitz (FRM II), Garching, Germany

³ Frank Laboratory of Neutron Physics, JINR, Dubna, Russia

In 1998, the collaboration of Russian and German institutes performed at the high-flux reactor of the Institut Laue-Langevin (ILL) an experiment on search for the T-odd three-vector correlation in ternary fission of ²³³U by cold polarized neutrons. The investigated angular correlation can be represented by expression

$$W = 1 + D_{\alpha} \left(\vec{p}_{\alpha} \cdot [\vec{\sigma}_{n} \times \vec{p}_{LF}] \right). \tag{1}$$

Here D_{α} is the correlation coefficient; $\vec{\sigma}_n$ is the spin of the neutron captured by ²³³U; and \vec{p}_{α} and \vec{p}_{LF} are the momenta of the α particle emitted in ternary fission and of the light fission fragment, respectively. All the vectors are normalized.

Such an experiment to test the time reversal invariance of nuclear forces had been proposed earlier in [1]. But the violation of time reversal invariance in the inelastic nuclear reaction cannot be observed due to unavoidable final states interaction, which can imitate the T-odd correlations. So, unexpectedly large magnitude of the coefficient D_{α} (10⁻³) [2] was very surprising. It can result from interference effect in strong and/or electromagnetic interactions of α particle with fragments in final states. The most simple theoretical model explained the observed correlation by the Coriolis mechanism [3].

Later, a detailed study of the correlation (1) showed that the angular distribution of α particles relative to the fission axis is shifted when inversing the polarization direction of neutrons inducing fission [4]. The direction of shifting is determined by the direction of neutron beam polarization. Being unable to find any systematic effects which could explain the observed phenomenon, the authors concluded that the effect is caused by the rotation of polarized fissioning nucleus before it splits into the fragments,

and called it ROT effect. Analysis showed that it is not the shift of the angular distribution of α particles, which is formed with respect to the axis of deformation of the fissioning nucleus, but the rotation of the fission axis by a small angle with respect to which the angular distribution of α particles is measured. This axis deviates from the original direction of the deformation axis due to the composition of radial and tangential velocities of the fragments. The trajectory of the fragments, instead of linear in the absence of rotation, becomes hyperbolic. The polarization of the neutron beam determines the direction of polarization of the fissioning nucleus and sets the direction of its rotation; this determines the direction of the deviation of the fragment trajectory. Such a correlation of light charged particles emission directions with the direction of neutron beam polarization can also be formally represented by a T-odd function (five-vector correlation):

$$W = 1 + R \left(\vec{\sigma}_n \cdot \left[\vec{k}_{\gamma} \times \vec{p}_{LF} \right] \right) \left(\vec{k}_{\gamma} \cdot \vec{p}_{LF} \right). \tag{2}$$

In contrast to the correlation (1), the momentum of the fragment is squared in (2), and therefore, the effect has the same sign for both light and heavy fragments. The correlation coefficient R is proportional to the rotation angle of the fission axis during the acceleration of the fragments due to Coulomb repulsion and to the derivative of the angular distribution of the α particles, detected at an angle ϑ to the fission axis.

From the above semiclassical description of the ROT effect, it follows that a similar phenomenon can be found in the angular distribution of any other particles accompanying fission of the nucleus into two fragments. Therefore, once data were published in [4], an experiment has been set up at the beam of polarized cold neutrons of the BER-II reactor of HMI in Berlin in order to measure the ROT effect in the emission of prompt γ rays in binary fission of ²³⁵U by polarized cold neutrons [5, 6]. The sought effect was found, but about an order of magnitude smaller than for α particles. The angular distribution of γ rays emitted by fragments is anisotropic with respect to the direction of the momentum of the fragment. and this experimental fact was explained by Strutinsky [7] as a consequence of the spin alignment of the fragments during breakup of the nucleus in a plane orthogonal to the deformation axis of the fissioning nucleus. So γ rays emitted by the fragments are anisotropic with respect to the axis of the fissioning nucleus deformation. And although they are emitted not at the moment of scission, however, they may demonstrate the ROT effect.

Similar effect can be expected in the emission of prompt fission neutrons, assuming that the angular distribution of prompt neutrons in the rest frame of the fragments is anisotropic.

We have performed such an experiment at a beam of cold polarized neutrons MEPHISTO at the FRM II reactor of the Technical University of Munich [8]. The threefold and fivefold correlations in the emission of prompt neutrons from fission of $^{235}\mathrm{U}$ were measured simultaneously. The neutrons were detected by plastic scintillators placed at angles $90^{\circ} \pm 22.5^{\circ}$ and $270^{\circ} \pm 22.5^{\circ}$ to the fission axis in coincidence with light and heavy fragments. The detectors recorded γ rays and neutrons being separated from γ rays by time of flight from the target to the detector. To control the operation of the equipment, threefold and fivefold correlation in the emission of γ rays were measured. ROT effect in the emission of γ rays has been confirmed with high precision, but other effects were not found within the experimental errors of the order of $(2-3)\times 10^{-5}$. Since the desired effects were measured only at an angle of 67° to the fission axis, the setup was slightly modified and measurements were continued.

Collimated beam of cold polarized neutrons passes through a system of controlling the direction of the longitudinal polarization and, being guided by leading magnetic field, enters into a fission chamber filled with isobutane to a pressure of 8 mbar. It hits the target, which is a 1-mm-thick zirconium plate, covered by a layer of oxide-protoxide of 235U with a thickness of $500 \,\mu\text{g/cm}^2$. The start and stop multiwire proportional counters are placed parallel to the target plane at a distance of 2.5 and 12.5 cm from the target, respectively. Start-stop technique allows identifying the mass of the detected fragment, i.e., separating the light and heavy fragment groups (Fig. 1). Eight neutron detectors, which are plastic scintillators with a diameter of 70 mm and a length of 120 mm, supplied with a photomultiplier EMI 9839A, are placed outside the chamber at a distance of 25 cm from the target center. Neutron detectors are located at angles of ±22.5°, ±67.5°, ±112.5°, ±157.5° relative to the direction of registration of the fragments. Centers of neutron detectors and detectors of the fragments are located in the plane orthogonal to the direction of the neutron beam passing through the center of the target. Neutron detectors allow for the registration of γ rays as well. Separation of neutron and γ rays could be done using time-offlight technique (Fig. 2). Every event matching coincidence of the signals from the neutron and fragment detectors is digitized by multichannel TDC CAEN V775N and stored together with the information about the direction

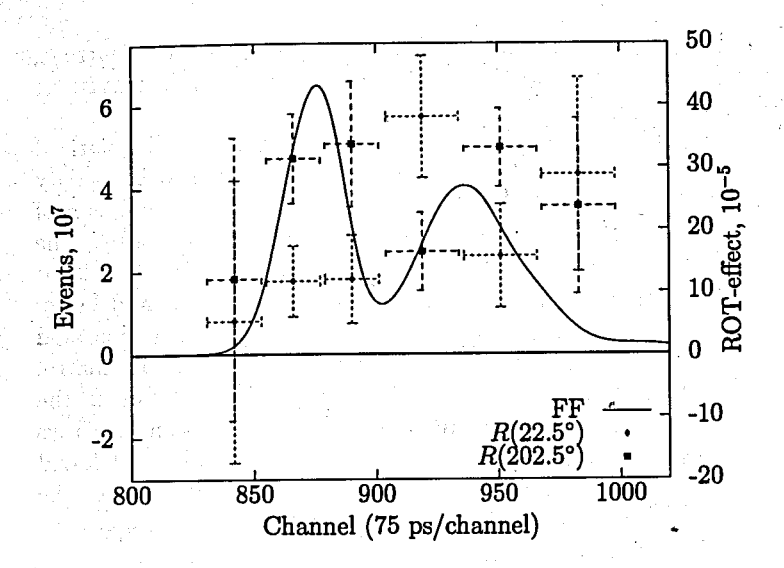


Figure 1: ROT effect for different groups of fission fragments. FF – time-of-flight spectrum of 235 U fission fragments at 10 cm base; $R(\vartheta)$ – ROT effect at angle of ϑ relative to the direction of the fragment's motion.

of polarization of the neutron beam. Reverse of polarization occurs at a frequency of 1 Hz, the input of the TDC being inhibited by the time of the neutron spin flip. At the same time, for the on-line control of the installation, the coincidence count rates of neutrons/ γ rays and the light/heavy fragments were recorded by counters, which were read out every 5 min for each detector. The values of asymmetries, calculated by the formula $R = \frac{N^+ - N^-}{N^+ + N^-}$, were constantly monitored. Here N^+ and N^- are the coincidence count rates for opposite directions of neutron polarization. Simultaneously, the asymmetry of the fragment count rates was measured and controlled.

Table 1 shows the values of ROT effect in the angular distribution of prompt neutrons and γ rays from fission, obtained in this study, [5] and [8]. Figure 2 shows the results of measurements of ROT effect in separate intervals of the TOF spectrum of coincidences of the signals from neutron/ γ

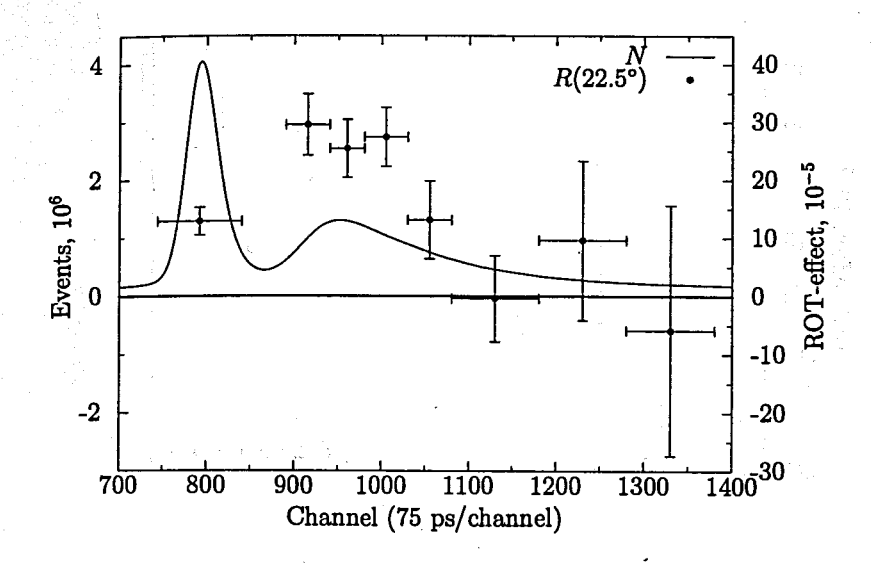


Figure 2: TOF spectrum of neutrons and γ rays, ROT effect in fission of ²³⁵U for different intervals of the time-of-flight spectrum. Left – the prompt γ ray peak; right – the peak of prompt fission neutrons:

Left – the prompt γ ray peak; right – the peak of prompt fission neutrons; $R(\vartheta)$ – ROT effect at angle of ϑ relative to the direction of the fragment's motion.

Table 1: ROT effect R for different angles relative to the fission axis in $^{235}\mathrm{U}$ fission

| Ð | R_n , 10^{-5} | $R_{\gamma}, 10^{-5}$ |
|-------|-------------------|-----------------------|
| | 21.2 ± 2.5 | |
| 22.5° | 10 ± 5 | |
| 55° | 0±6 | 23 ± 4 |
| 67.5° | -0.3 ± 2.2 | 20.0 ± 1.8 |

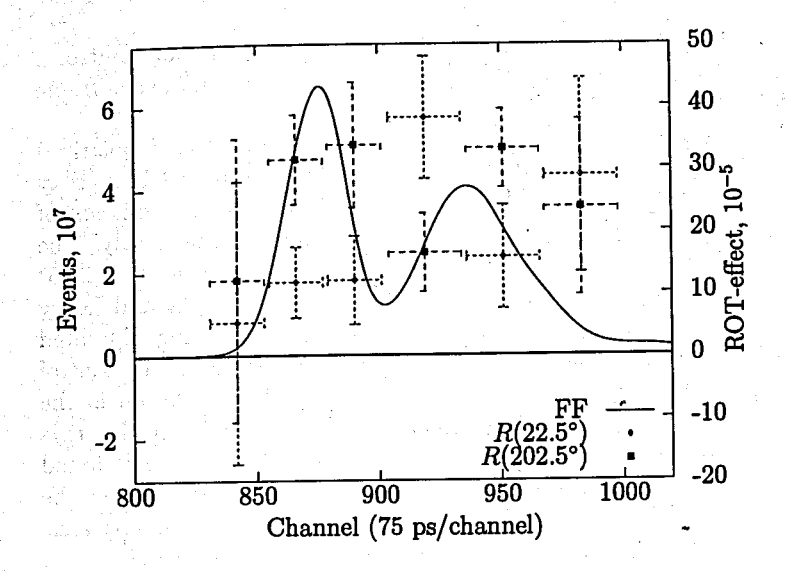


Figure 1: ROT effect for different groups of fission fragments. FF – time-of-flight spectrum of 235 U fission fragments at 10 cm base; $R(\vartheta)$ – ROT effect at angle of ϑ relative to the direction of the fragment's motion.

of polarization of the neutron beam. Reverse of polarization occurs at a frequency of 1 Hz, the input of the TDC being inhibited by the time of the neutron spin flip. At the same time, for the on-line control of the installation, the coincidence count rates of neutrons/ γ rays and the light/heavy fragments were recorded by counters, which were read out every 5 min for each detector. The values of asymmetries, calculated by the formula $R = \frac{N^+ - N^-}{N^+ + N^-}$, were constantly monitored. Here N^+ and N^- are the coincidence count rates for opposite directions of neutron polarization. Simultaneously, the asymmetry of the fragment count rates was measured and controlled.

Table 1 shows the values of ROT effect in the angular distribution of prompt neutrons and γ rays from fission, obtained in this study, [5] and [8]. Figure 2 shows the results of measurements of ROT effect in separate intervals of the TOF spectrum of coincidences of the signals from neutron/ γ

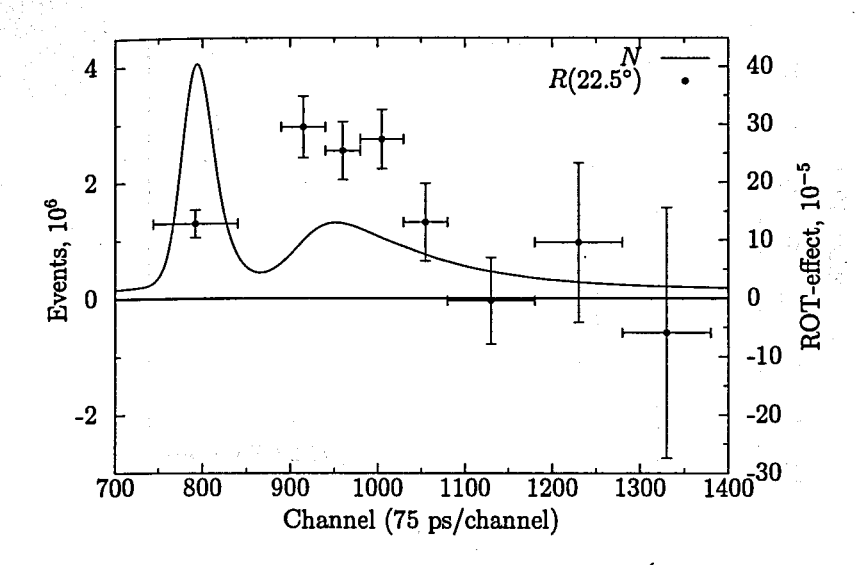


Figure 2: TOF spectrum of neutrons and γ rays, ROT effect in fission of 235 U for different intervals of the time-of-flight spectrum.

Left – the prompt γ ray peak; right – the peak of prompt fission neutrons; $R(\vartheta)$ – ROT effect at angle of ϑ relative to the direction of the fragment's motion.

Table 1: ROT effect R for different angles relative to the fission axis in $^{235}\mathrm{U}$ fission

| 9 | R_n , 10^{-5} | R_{γ} , 10^{-5} |
|----------|-------------------|--------------------------|
| 22.5° | 21.2 ± 2.5 | 12.9 ± 2.4 |
| 35° | 10 ± 5 | 15 ± 4 |
| 55° | 0 ± 6 | 23 ± 4 |
| 67.5° | -0.3 ± 2.2 | 20.0 ± 1.8 |

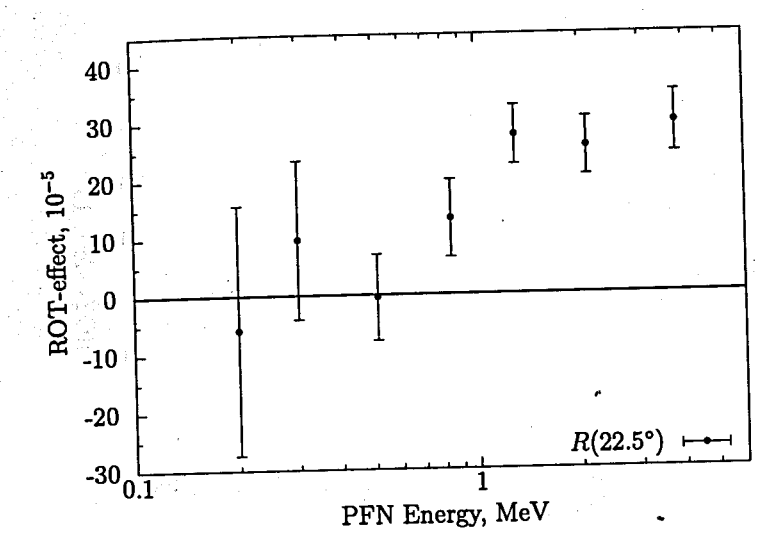


Figure 3: Energy dependence of ROT effect in ²³⁵U fission

ray detectors and the fragments. The effects in the maximum of neutron peak are about two time larger than the effect in the γ peak, which can be explained by a larger anisotropy of the neutron emission in the rest frame of the fragment, compared to that of the γ rays. The ROT effect is showing for prompt fission neutrons of 1 MeV and higher (see Fig. 3).

Since the setup allowed us to distinguish between light and heavy fission fragments, we were able to compare values of ROT effect at angles of 22.5° relative to the direction of light and heavy fragments motion. One can see in Fig. 4 that magnitude of ROT effect is higher at angle of 22.5° relative to the direction of heavy fragment motion. We tried to obtain more detailed dependence of ROT effect on fragment's mass, and the result is shown in Fig. 1. Higher statistics and better mass resolution are necessary to make up any conclusion.

TRI effect in the emission of prompt fission neutrons at angle of 67.5° relative to fission axis $D_n^*(67.5^\circ) = (-0.7 \pm 2.3) \times 10^{-5}$, so the correlation coefficient D_n in formula

$$W = 1 + D_n \left(\vec{p}_n \cdot [\vec{\sigma} \times \vec{p}_{LF}] \right)$$

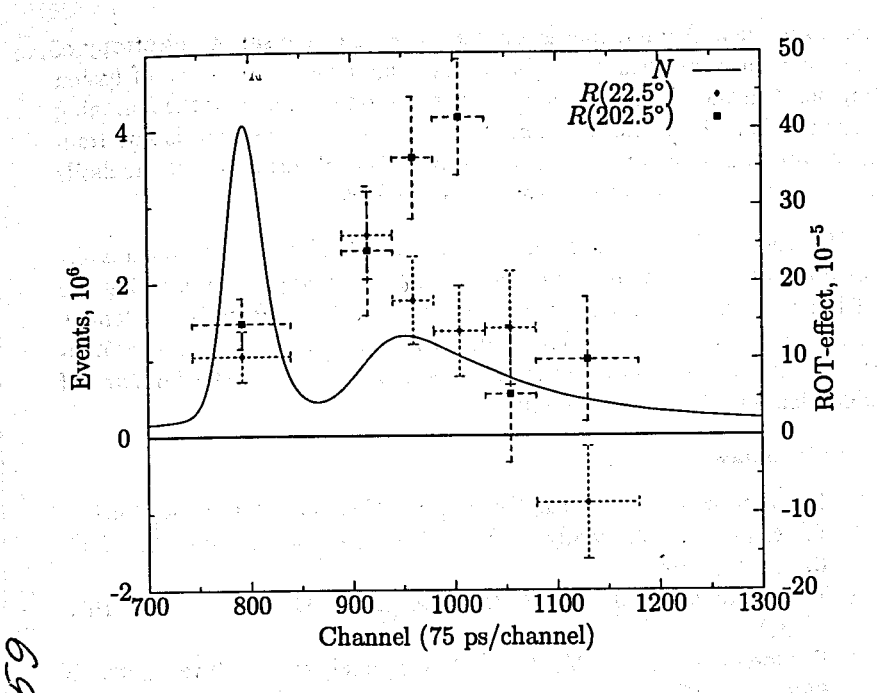


Figure 4: TOF spectrum of neutrons and γ rays, ROT effect in fission of ^{235}U for different intervals of the time-of-flight spectrum for light and heavy fragments separately. $R(\vartheta)$ – ROT effect at angle of ϑ relative to the direction of the light fragment's motion.

$$D_n = (-0.8 \pm 2.5) \times 10^{-5}$$
.

O?

Main result of this work is observation of the ROT asymmetry in the emission of prompt fission neutrons. There is significant asymmetry at angle 22.5° relative to fission axis, while the effect at angle 67.5° has not been observed. ROT effect increases with increase of the energy of prompt fission neutrons. It is higher in the direction of heavy fragment's motion.

In a first approximation, the results are consistent with the calculations of the effects at angles of 22.5° and 67.5°, represented in the work of Guseva [9]. Calculations were performed under the assumption that the angular distribution of fission neutrons in the rest frame of the fragment is anisotropic. Mechanism for the appearance of anisotropy in neutron emis-

)бъединенный институт ядерных ₁ысследований БИБЛИОТЕКА sion from excited fragments is similar to the mechanism of anisotropy of prompt γ rays and can be explained by alignment of the spins of fission fragments in the plane orthogonal to the deformation axis of the fissioning nucleus. Thus, both the emission of neutrons and γ rays from fission fragments are anisotropic with respect to the axis of deformation of the fissile nucleus, which leads to the observed ROT effects.

We are grateful to Yu.A. Belov and A.S. Zhokhov for technical assistance in carrying out the experiment, Prof. W. Petry for supporting the setting up of the experiment at the reactor FRM II, and Prof. M.V. Danilov for his interest in this work. This work was supported by the Russian Foundation for Basic Research (grant no. 10-02-00350-a) and the Ministry of Education and Science of the RF.

References

- 1. K. Schreckenbach, Intern. ILL Report 88SCO9T (Grenoble, 1988).
- P. Jesinger, G. V. Danilyan, A. M. Gagarski, et al., Phys. At. Nucl. 62, 1608 (1999).
- V. E. Bunakov and S. G. Kadmenskii, Izv. RAN, Ser. Fiz. 68, 1090 (2004).
- 4. F. Goennenwein, M. Mutterer, A. Gagarski, et al., Phys. Lett. B 652, 13 (2007).
- 5. G.V.Danilyan, P.Granz, V.A.Krakhotin, et al., Phys. Lett. B 679, 25 (2009).
- G. V. Danilyan, J. Klenke, V. A. Krakhotin, et al., Phys. At. Nucl. 72, 1812 (2009).
- 7. V. M. Strutinskii, Zh. Eksp. Teor. Fiz. 37, 861 (1959) [Sov. Phys. JETP 10, 613 (1959)].
- 8. G. V. Danilyan, J. Klenke, V. A. Krakhotin, et al., Phys. At. Nucl. 73, 1116 (2010).
- 9. I. S. Guseva, in Proceedings of the XVIII International Seminar on Interactions of Neutrons with Nuclei, Dubna, Russia, 2010, p. 84.

Fractional yields of delayed neutron precursors from fission of 238U by relativistic protons

Egorov A.S., Piksaikin V.M., Roshchenko V.A., Mitrofanov V.F., Myakishev G.A., Samylin B.F., Goverdovski A.A.

State Scientific Center of Russian Federation Institute of Physics and Power Engineering, Obninsk, Russia

Vaishnene L.A., Morozov F.A., Vorobyev A.S., Shcherbakov O.A.

Petersburg Nuclear Physics Institute, Gatchina, Russia

Abstracts

In present paper the method and set-up for measurements of delayed neutron characteristics in interaction of heavy nuclei with relativistic protons are described. On the basis of this method the time dependence of delayed neutron activity has been measured from interaction of ²³⁸U sample with 1 GeV pulsed proton beam of the synchrocyclotron of the Petersburg Institute of Nuclear Physics, Gatchina. The measured data was analyzed in frame of 8-group precursor's model with a consistent set of half-lives. Obtained results on the fractional yields of delayed neutron precursors are compared with an appropriate data from the fast neutron induced fission of ²³⁸U and systematics developed on the basis of these data. It was shown that there is strong redistribution of fission products in the case of fission of ²³⁸U by relativistic protons in respect of the neutron induced fission.

Experimental method and set-up

The measurements of delayed neutron decay from the fission of ²³⁸U induced by relativistic protons were carried out on the set-up installed at the synchrocyclotron of the Petersburg Institute of Nuclear Physics, Gatchina. The synchrocyclotron is a pulsed accelerator with a 1 GeV proton beam intensity of about 10¹⁰ protons/cm²·s in the location of sample. The width of proton pulses in the ²³⁸U experiment was 0.008 s with the repetition time of 0.02 s. Time profile of proton beam measured by neutron detector with the help of prompt neutrons from secondary (p,xn) is presented on Fig.1. The targets in these measurements were the water enriched by isotopes ¹⁸O and polytetrafluoroethylene.

The experimental method employed in the measurements of delayed neutron decay curves is based on cyclic irradiations of the ²³⁸U samples by protons followed by the registration of the time dependence of accumulated delayed neutron activity.

តែការស្រែក មានកំពង់ស្រួន ដែលប្រជា

A MORNING HIS

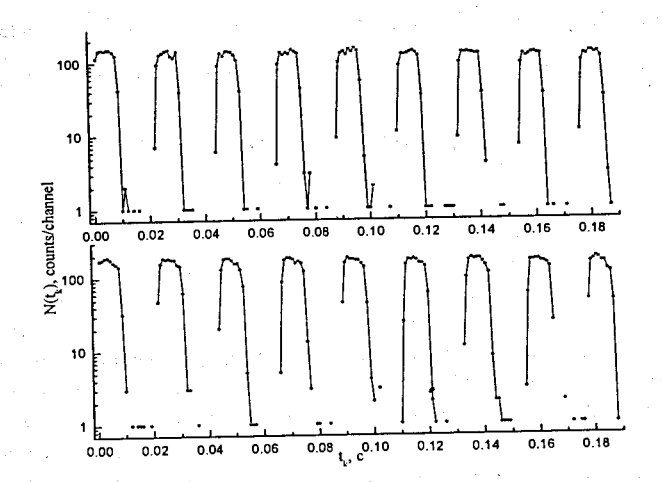


Fig.1. Time profile of proton beam measured by registration of prompt neutrons from secondary (p,xn) reactions. Upper picture—target is a water sample enreached in isotope ¹⁸O; lower picture—target is polytetrafluoroethylene. Time-channel width-0.001s.

Block diagram of the experimental set-up is presented on figure 2.

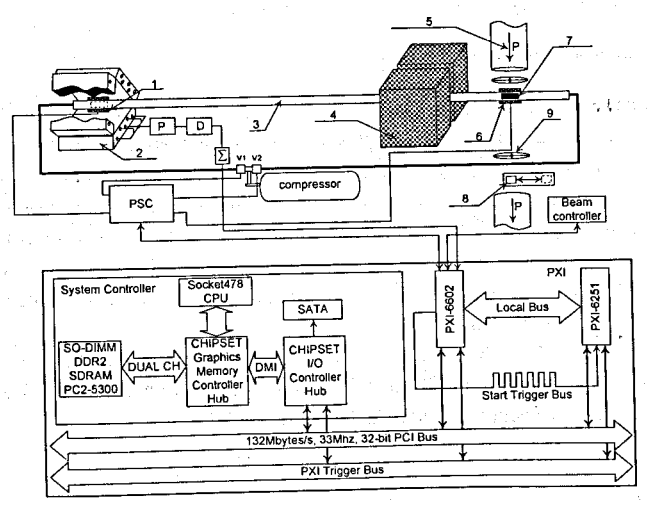


Fig. 2. Block diagram of the experimental set-up: 1,6-sample position detector; 2-neutron detector; 3-pneumatic transfer system; 4-neutron detector shield; 5-beam line; 7-sample of ²³⁸U; 8,9 Laser positioning device; (P) preamplifier, (D) pulse discriminator; (Σ) summator; (PSC) Pneumatic System Controller; In the bottom of the figure the Data Acquisition system based on the National Instruments modules and the Labview programs is presented.

The boron counter of SNM-11 type at the operational potential of 650 V in the proportional mode of operation was chosen as the main detector counting unit. Radiator in this counter is a 1 mg/sm² thick layer of boron enriched by isotope ¹⁰B up to 95%. The counter is filled by the gas mixture of ⁴He (97%) and Ar (3%). The SNM-11 counter is one of the best one in respect to balance of neutron and gamma ray detection efficiency. The pulse amplitudes from the compton electrons originated from gamma rays are significantly smaller than amplitudes from neutrons. The test of the neutron detector showed that the detector is insensitive to gamma rays from ²³⁷Np sample of 2 grams. The manufactured detector is an assembly of 15 boron counters distributed in three separate blocks of polyethylene moderator. The detector is shielded against the neutron background by borated polyethylene and cadmium sheets. The amplifier (A) and pulse discriminator (D) were used for two sets of counters – outer and inner as related to incident neutrons. The output signals from these electronic channels are fed to a mixing module (Σ) coupled with DAQ electronic system. The dead time of neutron detector is 2.3±0.2 μs.

The pneumatic transfer system is capable to transport the sample for the time short enough to measure the delayed neutron yields with the shortest half-lives. Two electromagnetic valves are responsible for the sample transportation route. The stainless steel tube with inner diameter of 12 mm and wall thickness of 1 mm serves as a pneumatic flight guide (3). The positions of the sample in the neutron detector and irradiation location are fixed by the plugs with adjustable central hole which provides the excessive pressure in front of the moving sample and smoothes the contact between the sample and the plug. The information on the sample location is obtained from sample position detector (6). Time of flight of the sample is about 150 ms.

Data acquisition system (DAQ) is based on the National Instruments modules [2]. The system is comprised of controller PXI-8104, multifunctional high speed module M – PXI-6251 and time counter PXI-6602. Controller PXI-8104 is made on the bases of processor Intel Celeron M 440 with frequency 1.86 MHz and dual memory DDR2 with frequency 533 MHz. All modules are installed in special chassis equipped with PXI/PC1 bus that allows to integrate all modules in single platform. Counter/timer PXI-6602 was used for registration of the time dependence of delayed neutron intensity. The PXI-6602 unit contains 8 counter/timer channels each of which has size 32 bite. Three of them can be used simultaneously in high-speed pulse counting in the buffered operation mode with direct access memory (DMA) and the rest 5 counters can be run with interrupts procedure. Counter/timer PXI-6602 is fully integrated in DAQ system with the help of RTSI real-time bus that enables its synchronization with other modules of the system.

Measurement procedure

²³⁸U sample was made of metallic uranium. It was installed in a hermetic container made of stainless steel. The container with the ²³⁸U sample was enclosed in thin metallic can which transported by the pneumatic system. The start of the measurement was initiated by TTL DAQ signal which was used as a command to open the proton beam. The same signal was generated at the end of irradiation with the purpose to shut down the proton beam. Timebase stability of the DAQ system was determined by a crystal oscillator and was equal to 50 ppm (parts per million). Background was measured with the help of a sample unit with the same construction parameters but without ²³⁸U.

where $N(t_k)$ - the number of counts in the time-channel t_k with time-channel width Δt_k , registered in N cycles of irradiation, v_d - the total delayed neutron yield per one fission, B- the intensity of neutron background, λ_i is a_i - the decay constant and the relative abundance of i -th group of delayed neutron precursors, n- number of proton pulses in one cycle of irradiation, m- the number of delayed neutron groups, T - the duration of one cycle of measurements, which includes the irradiation and delayed neutron counting time, t_{ir} - width of proton pulse, ε_n - efficiency of neutron detector, φ - the proton flux, σ_f - the fission cross section, N_f - the number of atoms in a sample under investigation.

The accumulated decay curves were analyzed in the 8-group model approximation [4] with the help of the iterative least-squares method [5]. The relative abundances for ²³⁸U were obtained on the basis of experimental data which were measured with different irradiation times. In the analysis of the delayed neutron time-dependence the data with irradiation time of 180 s were used to obtain the group constants for the first, second and third group of delayed neutrons. Group constants for the fourth to the eighth groups were obtained from the data measured in the experiment with the irradiation time of 15 s. The group constants obtained from the long time irradiation data were fixed in the analysis of short time irradiation data. In the course of data processing two additional groups of delayed neutron precursors were introduced to take into consideration decay ¹⁶C and ¹⁷N with half-life 0.747 и 4.17 s respectively. These nuclides are produced in interaction of 1 GeV proton with ²³⁸U with high probability [6]. It is allowed to take into account a contribution of the fragmentation channel in the composite delayed neutron decay curve. Thus the obtained fractional yields of delayed neutron precursors are corresponding mainly to the fission channel of the investigated interaction. The average half-life of delayed neutron precursors was obtained on the basis of the relative abundances and half-lives of their precursors according to formula $< T > = \sum T_j a_j$ (j=1-8). Obtained results on the fractional yields of delayed neutron precursors and their average half-life calculated on the basis of these data are presented in table I.

Table I. Fractional yields of delayed neutron precursors and their average half-life from fission of ²³⁸U by 1 GeV protons.

| - | Group | number, I | nalf-life a | nd predom | ninant prec | ursors of | delayed ne | utrons | Average hal |
|-----------------------------|---------------------------------|-----------------|---------------------|---------------------------------------------------------------------------|------------------------------------------------------------------------------------------------|--------------------------------------------------------|-------------------------------------------------------|-----------------------------|----------------------------------------|
| Target, proton energy | 1 55.6 c ⁸⁷ Br | 2 24.5 c | 3 16.3 c 88Br | 4 5.21 c ¹³⁸ I, ⁹³ Rb, ⁸⁹ Br | 5 2.37 c ⁹⁴ Rb, ¹³⁹ I, ⁸⁵ As, ^{98m} Y | 6 1.04 c ⁹³ Kr, ¹⁴⁴ Cs, | 7 0.424 c ⁹¹ Rb, ⁹⁵ Rb | 8 0.195 c %Rb, %Rb | life, s $< T >= \sum_{j=1}^{x} T_{j}.$ |
| ²³⁸ U | 0.025 ±0.001 | 0.090 ±0.003 | 0.068 ±0.003 | 0.289 ±0.005 | 0.313 ±0.010 | 0.157 ±0.006 | 0.033 ±0.005 | 0.025 ±0.002 | 7.13 ±0.12 |

It was shown in [7] that the average half-life of delayed neutron precursors obtained in the fast neutron induced fission of all isotopes of heavy nuclides can be approximated by the exponential expression $\langle T \rangle = a \exp[-b \cdot (A_c/Z) \cdot 92)]$, where A_c and Z — the mass number and

Results and discussion

Composite decay curves which were measured in interaction of 1 GeV pulsed beam of protons with ²³⁸U with irradiation times 15 and 180 s is presented on fig.3. The original scale of protons with ²³⁸U with irradiation times 15 and 180 s is presented on fig.3. The original scale of protons with ²³⁸U with irradiation times 15 and 180 s is presented on fig.3. The original scale of 0.1 s/channel. The obtained data time analyzer (0.0001 s/channel) was transformed in scale of 0.1 s/channel. The obtained data were also corrected for the degradation effect of counting response of neutron detector placed in a high intensity field of neutrons and gamma rays during irradiation time [3].

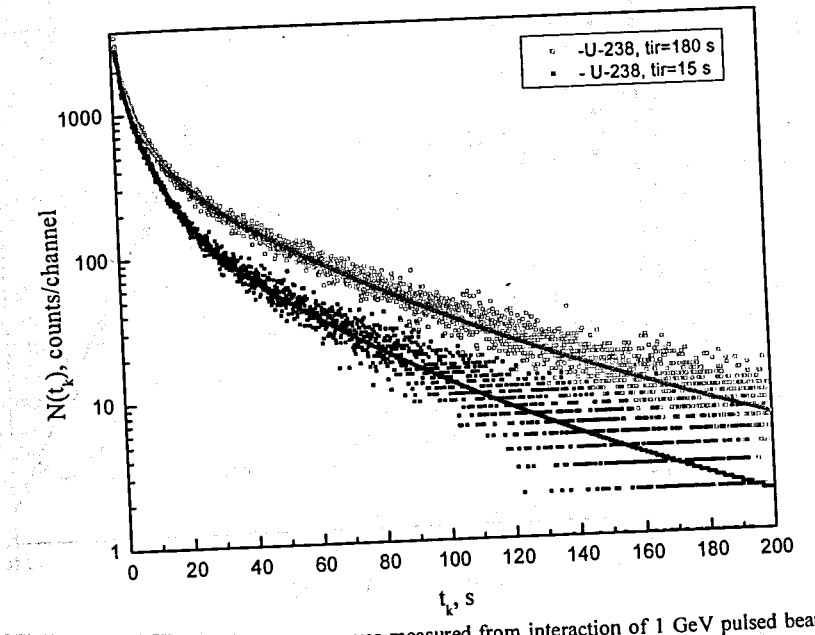


Fig. 3. Composite delayed neutrons curves measured from interaction of 1 GeV pulsed beam of protons with 238 U with irradiation times 15 and 180 s. Solid lines – results of delayed neutron parameters estimation. Time-channel width – 0.1 s.

The general equation for the determination of the temporary delayed neutron characteristics (a_i, λ_i) on the basis of measured values in case of cyclic irradiation with pulsed proton beam can be represented by the following expression

$$\begin{split} N(t_{k}) &= A \cdot \sum_{i=1}^{m} T_{i} \cdot \frac{a_{i}}{\lambda_{i}} \cdot (1 - e^{-\lambda_{i} \cdot \Delta t_{k}}) \cdot e^{-\lambda_{i} \cdot t_{k}} + B \cdot \Delta t_{k}, \\ T_{i} &= (1 - e^{-\lambda_{i} \cdot t_{m}}) \cdot \frac{(1 - e^{-m \cdot \lambda_{i} \cdot t})}{(1 - e^{-\lambda_{i} \cdot t})} \cdot \left(\frac{N}{1 - e^{-\lambda_{i} \cdot T}} - e^{-\lambda_{i} \cdot T} \cdot \left(\frac{1 - e^{-N \cdot \lambda_{i} \cdot T}}{(1 - e^{-\lambda_{i} \cdot T})^{2}} \right) \right), \\ A &= \varepsilon_{n} \sigma_{f} \varphi N_{f} V_{d}, \end{split}$$

atomic number of compound nucleus respectively. As compared with $(A_c-3\cdot Z)\cdot A_c/Z$ systematic [8], which is valid for isotopes of one element, systematic $(A_c/Z)\cdot 92$ allows to predict the average half-life of isotopes of all elements with the only set of parameters a and b. On fig.4 the evaluated values of average half-life obtained on the basis of experimental data for the fast neutron induced fission of U, Pu, Am, Np and Th isotopes are shown by separate points. Solid line is an approximation of these data by the dependence $< T >= a \cdot \exp[-b \cdot (A_c/Z)\cdot 92)]$.

(๑) ประการสำนักสารประจาชน์ เพลาะสนุญ ซึ่งสิ่ง โดยบารที่ระดีวิ

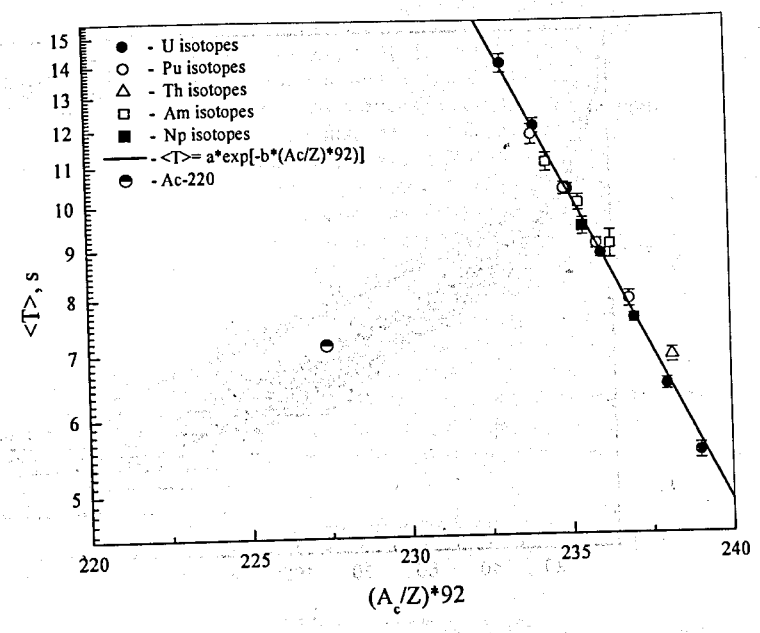


Fig.4. Systematics of the average half-life of delayed neutron precursors < T > from fast neutron induced fission. The < T > values evaluated on the basis of experimental data for neutron induced fission of heavy nuclei are shown by separate points. An approximation by expression $< T >= a \exp[-b \cdot (A/Z) \cdot 92)]$ is shown by solid line. The < T > values for 1 GeV proton induced fission of 238 U is shown by semi-filled circle.

In order to compare the systematic $(A_c/Z)\cdot 92$ obtained for the < T> data obtained from the fast neutron induced fission with the average half life < T> of delayed neutron precursors from 1 GeV proton induced fission of ^{238}U we need information about nucleon composition of fissioning system. The parameter $(A_c/Z)\cdot 92$ was estimated on the basis of the data on the cross sections and the ratio of the average number of neutrons to number of protons obtained for products from the inverse kinematics reaction $^{238}U(1 + \Gamma) = [9]$ presented on fig. 5. The data on the prompt neutron emission from fission fragments were taken into account.

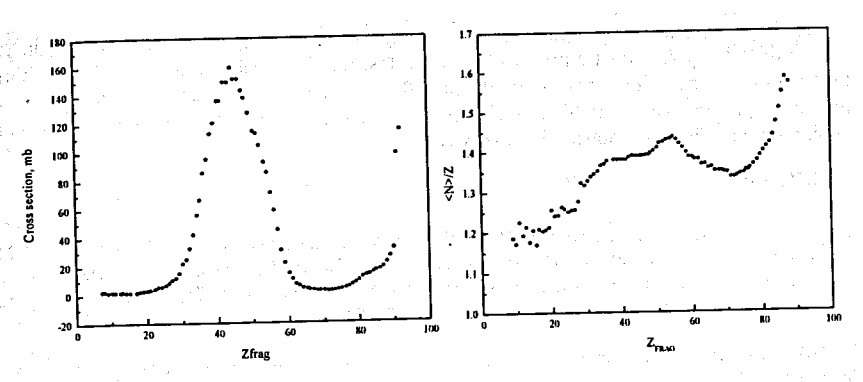


Fig. 5. Left side: the production cross section of products formed in interaction 238 U (1 A Γ_{3} B)+p as a function of charge [9]. Gauss-like distribution in the middle of picture is related to fission products. Right side: the ratio of the average number of neutrons to number of protons as a function of product charge.

Obtained data are shown on fig.4 by semi-filled circle. It is seen that the average half life of delayed neutron precursors from relativistic proton induced fission of 238 U is significantly different from the appropriate data related to the fast neutron induced fission. For more detailed picture of distinctive features of low and high energy fission of 238 U the ratio of fractional yields of 8 groups of fission products from 1 GeV proton and 4.7 MeV neutron induced fission was calculated. The results are presented on fig.6. This ratio is closely related to the ratio of cumulative yields of appropriate fission products inasmuch as the emission probability of delayed neutrons P_n in both cases is the same.

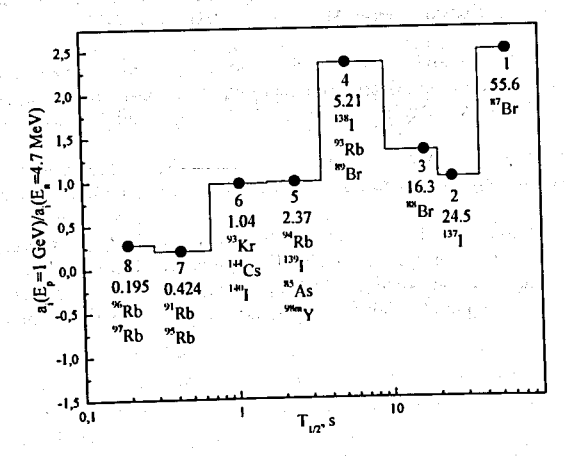


Fig.6. The fractional yield ratio of 8-fission product groups from 1 GeV proton and 4.7 MeV neutron induced fission of ²³⁸U. First line under points are the group number; second - average half-life, s; the rest – dominant precursors of the group.

It is seen from fig.6 that there is strong redistribution of fission products in case of fission of ²³⁸U by relativistic protons. One can observe a decrease of contribution of short lived precursors groups with half-life 0.195 and 0.424 s and an increase of contribution of the precursor groups with half-lives 5.21 and 55.6 s in the composite delayed neutron curve as compared with the fast neutron induced fission.

Literature

- V. M. Piksaikin, N. N. Semenova, V. I. Mil'shin, V. A. Roshchenko and G. G. Korolev. "A Method and Setup for Studying the Energy Dependence of Delayed Neutron Characteristics in Nuclear Fission Induced By Neutrons From the T(p,N), D(d,N), and T(d,N) Reactions". Nuclear Experimental Technique 49, No. 6 (2006), pp. 765-777.
- 2. "Measurements and Automation", device catalog http://www.ni.com/dataacquisition/ National Instruments, 2010.
- 3. V. A. Roshchenko, V. M. Piksaikin, L. E. Kazakov and G. G. Korolev "Relative yield of delayed neutrons and half-life of their precursor nuclei with fissioning of ²³⁹Pu by 14.2–17.9 MeV neutrons" Atomic Energy Vol. 101, Number 6(2006), p. 897-900.4. G.D. Spriggs, J.M. Campbell, and V.M. Piksaikin. "An 8-Group Delayed Neutron Model Based on a Consistent Set of Half-Lives". Progress in Nuclear Energy Vol. 41, no. 1-4 (2002), pp. 223-251.

kritteres arbeit 1987, ar telas 🖰 er elle ellerette på delle et freienter strikete, forme elle en elle eller

- 5. I. Dostrovsky, R. Davis, Jr., A. M. Poskanzer, and P. L. Reeder "Cross Sections for the Production of Li, I6C, and 17N in Irradiations with GeV-Energy Protons". Phys. Rev. 139, (1965), pp. B1513-B1524.
- 6. V.M.Piksaikin, L.E. Kazakov, S.G. Isaev, M.Z. Tarasko, V.A. Roshchenko, R.G. Tertytchnyi, G.D. Spriggs, and J.M. Campbell. "Energy Dependence of Relative Abundances and Periods of Delayed Neutrons From Neutron-Induced Fission of U-235, U-238, Pu-239 in 6- and 8-Group Model Representation". Progress in Nuclear Energy 41, no. 1-4 (2002), pp. 203-222.
- 7. V. A. Roshchenko, V. M. Piksaikin, G. G. Korolev, and A. S. Egorov "Time Features of Delayed Neutrons and Partial Emissive-Fission Cross Sections for the Neutron-Induced Fission of ²³²Th Nuclei in the Energy Range 3.2–17.9 MeV". Physics of Atomic Nuclei, 2010, Vol. 73, No. 6, pp. 913–921.
- 8. V.M.Piksaikin, S.G. Isaev, and A.A. Goverdovski. "Characteristics of Delayed Neutrons: Systematics and Correlation Properties". Progress in Nuclear Energy Vol. 41, no. 1-4 (2002), pp. 361-384.
- 9. M. V. Ricciardi, P. Armbruster, J. Benlliure, M. Bernas, A. Boudard, S. Czajkowski, T. Enqvist, A. Keliæ, S. Leray, R. Legrain, B. Mustapha, J. Pereira, F. Rejmund, K.-H. Schmidt, C. Stephan, L. Tassan-Got, C. Volant, O. Yordano. "Light Nuclides Produced in the Proton-Induced Spallation of ²³⁸U at 1 GeV". GS1 Report 2005, 6 September 2005, Gesellschaft für Schwerionenforschung mbH, Darmstadt, Germany.

T-ODD ASYMMETRY EFFECTS OF THE LIGHT PARTICLES EMISSION IN THE HEAVY NUCLEUS TERNARY FISSION BY THE COLD POLARISED NEUTRONS

A.M. Gagarski¹, F. Gonnenwein², I.S. Guseva¹, T.A. Zavarukhina¹, Yu.N. Kopatch³, T.E. Kuzmina⁴, M. Mutterer⁵, V. Nesvizhevsky⁶, G.A. Petrov¹, T. Soldner⁶, and G. Tiurin⁴

¹ FSBE "Petersburg Nuclear Physics Institute named B.P. Konstantinov", 188300 Leningrad region, Gatchina, Orlova Roscha, Russia

²Universitat Tubingen, Physicalisches Institut, D 72976 Tubingen Germany

³ Joint Institute for Nuclear Researches, 141980 Moscow region, Dubna, Russia

⁴ Radium Institute named V.G. Khlopin, 194021 Skt. Petersburg, Russia

⁵ Technische Universitat Darmstadt, D 64289 Germany

⁶Laue-Langevin Institute, BR156, 38042 Grenoble, France

1. Introduction

The new physical effect of the T-odd asymmetry of the light charged particle (LCP) emission relative to the light fission fragment direction (with the unit momenta p_{α} and p_f) in the ²³³U ternary fission induced by the cold polarized neutrons (with polarization σ_n) was observed for the first time by the wide international collaboration at the end of 90-th at the ILL High Flux Reactor in Grenoble /1,2/. It was named "TRI-effect" because of formal similarity to the well known effect of Time Reversal Invariance in β -decay /3/.

$$W_{TRI} = 1 + D_{TRI} \sigma_n [p_i \times p_\alpha]$$
 (1)

No essential dependence of the T-odd asymmetry coefficient D_{TRI} on the angle between the vectors \mathbf{p}_{I} and \mathbf{p}_{α} was observed in the first experiments. But with further investigations of the similar effect in the ²³⁵U ternary fission and with the increasing of experimental accuracy in the ²³³U ternary fission the definite and specific dependence of such coefficients has been established /4,5,6/. The observed second type of the T-odd asymmetry effect named "ROT-effect" could be described by the following vector-scalar product:

$$W_{ROT} = 1 + D_{ROT} \cdot \sigma_n \cdot [\mathbf{p_f} \times \mathbf{p_\alpha}] \cdot (\mathbf{p_f} \cdot \mathbf{p_\alpha})$$
 (2)

In this equation (2) the coefficient D_{ROT} represents the angle of the LCP angular distribution shift.

To account for these effects the quasi-classical model of the polarized fissioning system rotation about its polarization direction has been proposed by the authors for the first time, /5,6,7,8/. Such a model seems to be rather natural if one takes into account that the even-even compound fissioning system formed after the cold polarized neutron capture has mainly collective types of excitations above the barrier top (including rotation ones). The directions of such rotation and the start velocity have to be completely defined by the compound state spins and their projections on the system symmetry axis. With the assumption that this symmetry axis is conserved along whole way of the system decent from the barrier top to the rupture point, the rotation speed has to be progressively reduced as the inertia momentum is increased with the nucleus elongation up to the rupture.

As a result of the system rotation the trajectories of the resulting charged fission products will be affected in the motion in its relative Coulomb field. In its turn such trajectory changing after fissioning system rupture may give rise to a small turn (or shift) of the LCP angular distribution, compared to the angular distribution without the system rotation. In a general sense the ROT-effect can be considered as a first direct exhibition of the polarized nucleus rotation.

The second section of the adjust the condi-

าง ราคคาร 2 ใช้ เอาสาราชาช**ร**รฐ และสมัยสาราชาวิท

By now detailed investigations of both T-odd asymmetry effects have been performed only for the ^{233,235}U, ²³⁹Pu and partly for the ²⁴⁵Cm ternary fission induced by the cold polarized neutrons. Therewith, all obtained experimental results for the TRI and ROT-effects are successfully described in the frameworks of our semi-classical model of rotation /8/.

In principle, since the T-odd asymmetry effects discovery for the LCP it was evident that similar effects can exist for the neutrons and γ -rays emitted near the rupture time. Nevertheless, the first experiments in the 233,235 U binary fission did not lead to these effects observation /9.10/.

However, already collected information allowed to conclude that the new T-odd asymmetry effects are closely connected with low energy fission dynamics and its further investigations may open absolutely new ways for the studies of the fission dynamics.

After discovery of the TRI and ROT-effects of the LCP emission asymmetry and its first detailed investigations a number of theoretical publications appeared with the attempts to find acceptable explanations of these two effects in low energy fission. First of all it was done in the framework of the statistical model /11/, then within pure quantum mechanical approach /12/ and, recently, in the approach of spin-orbital interaction /13/. In two first cases the authors left room for possibility to use quasi-classical model for the T-odd asymmetry effect explanation but underlined the necessity to take into account different interference effects between neighbouring nuclear levels. The author of the third publication doesn't need any rotation of the system to explain the T-odd asymmetry effects. However, neither of the three theoretical works gives any ways to perform numerical analysis of the experimental data and the more so to get any estimations of expected values of parameters of new planned experiments.

2. The main experimental results of the TRI and ROT-effects investigations in ternary fission

All results of the TRI and ROT-effects investigations were obtained with the use of the same experimental set-up. Being placed at the polarized neutron beam of ILL High Flux Reactor this set-up makes possible to measure simultaneously energies and angular distributions of the LCPs and fission fragments emitted from the thin targets of fissile nuclei.

Normalized differences of the LCP emission probabilities for two mutually opposite directions of the cold neutron polarizations as a function of the angle between LCP and the light fragments emission directions (ROT-effect) are presented in the Figs 1,2 and 3.

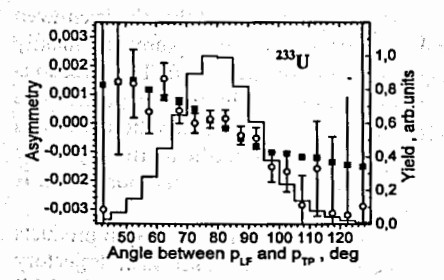


Fig.1. ROT-effect in ²³³U ternary fission

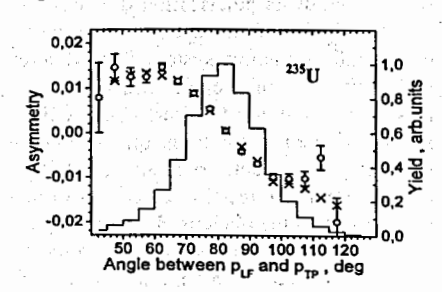


Fig.2. ROT effect in ²³⁵Pu ternary fission

| 11421 | | _ |
|----------|----------------------------------------------------------------------------------------------|-------|
| 0,002 | | 1.0 |
| O,001 | | 0.8 ई |
| 0,000 | ^ݞ ֡֡֡֓֞֡֓֞֡֓֞֞֞֞֞֞֞֞֓֞֡֓֞֡֓֞֡֞֡֓֓֡֡֞֡֓֞֡֞֓֓֓֡֡֡֡֓֓֓֡֡֡֡֡֓֓֓֡֡֡֓֓֡֡֡֡֡֓֡֡֡֡֓֓֡֡֡֡֡ | 0,6 ਵ |
| e -0,001 | ▎ [ੵ] ▗▘ [*] ┋┋╩ _┪ ┋ | 0.4 등 |
| -0,002 | 7.7 | 0,0 |
| | 50 60 70 80 90 100 110 120 Angle between p _{LF} and p _{TP} , deg | |

| | | | | •• | | |
|----------|---------------------------------------------------------------------------------------------------------------|-----------|-------------------|-----------|----------|--|
| | Arteria de la composição | | 220_ | | - | |
| Tr! - '3 | DOT | effect in | $\omega_{p_{11}}$ | ternary | ticcion | |
| H103 | . KUI- | | ı u | terriar y | 11001011 | |

| Target | spin | ROT ⁰ | TRI 10 ⁻³ |
|-------------------|--------|------------------|----------------------|
| ²³³ U | 2+, 3+ | 0.03(1) | -3.9(1) |
| ²³⁵ U | 3,4 | 0.215(5) | 1.7(2) |
| ²³⁹ Pu | 0+, 1+ | 0.020(3) | 0.023(9) |
| ²⁴⁵ Cm | 3+,4+ | , · · · . | 1.2(1)* |

Table I. TRI and ROT effects values for all investigated fissile heavy nuclei

In these cases the part of information that has no angular dependence (TRI-effect) has been subtracted. The LCP angular distributions are shown as the histograms, the points with the error bars are experimental asymmetries of the LCP emission and the calculated asymmetry values are shown by the crosses. The deviations of the experimental and calculated points from the smooth behavior (especially for the case of ²³⁹Pu fission) in the region (90° + 120°) may be connected with registration of some admixture of the heavy mass fragments because of relatively bad experimental mass resolution.

Separate values of the TRI and ROT-effects for the ^{233,235}U and ²³⁹Pu ternary fission are presented in the Table I. In the case of the ²⁴⁵Cm ternary fission only the sum of both T-odd asymmetry effects has been measured up to now.

3. Comparison of the results of model calculations with the experimental data

The rotation model analyses of the TRI and ROT effects are based on the trajectory calculations of the LCP emission with taking into account the rotation of the polarized fissioning system about the polarization axis. To estimate the influence of the system rotation on the fragments and LCP trajectories in the Coulomb field one needs to know the angular velocity of the system and the start position of the charged fission products just near the rupture point. The angular velocity of a strongly deformed fissioning system just near the rupture point is obtained with the following main assumptions:

- 1. After the cold polarized neutron absorption the resulting excited compound nucleus is brought above the fission barrier with the spins of the transition states $J^{\pm} = (I \pm \frac{1}{2})$. The ratio of these states occupancies $s = \sigma(I \frac{1}{2})/\sigma(I + \frac{1}{2})$ can be obtained from the nuclear data analysis.
- The resulting polarization of these transition states is conserved up to the fissioning system rupture and is defined by the following equations:
 - $P(J^+)=(2I+3)/[3(2I+1)]\cdot p_n$ for $J^+=(I+1/2)$ and $P(J^-)=-1/3\cdot p_n$ for $J^-=(I-1/2)$ (3) where p_n is the cold neutron polarization. The resulting polarized compound nucleus will undergo rotation around the polarization axis with the angular velocity ω :

$$\omega_{+/-}(J,K) = \begin{cases} \frac{J(J+1) - K^2}{J} \cdot \frac{\hbar}{2\Im} \cdot p_n & \text{for } J = I + 1/2 \\ -\frac{J(J+1) - K^2}{(J+1)} \cdot \frac{\hbar}{2\Im} \cdot p_n & \text{for } J = I - 1/2 \end{cases}$$
(4)

where K is J projection on the fission symmetry axis, which is conserved the whole fission process, and \mathcal{I} is the moment of inertia, which constantly increases during the descent from the fission barrier to the rupture point.

If the fission process is going through several transition states, then to obtain the effective angular velocity one needs to perform the following summation:

$$\omega(J) = \sum_{K} \left| a_{K}^{J} \right|^{2} \omega(J, K). \tag{5}$$

where $|a_K'|^2$ - probability of the (J, K) state existence.

3. Fissioning system configuration just before the rupture time was chosen in such a way that all energy and angular distributions of fission products well known from experiments would be well described. /7/

With such assumptions the first estimates of the LCP angular distribution shifts were obtained /8/.

In contrast to the ROT-effects of T-odd asymmetry the TRI-effect has no such a visual interpretation. In principle some factors may have an influence on the probability of the LCP-emission relative to the plane of fission fragments and LCP emission direction such as: a character of vibration excitations on the way to the rupture and the peculiarities of the fissioning system rupture into the fragments and LCP. As a result, it is evident that some supplementary forces may have an effect on the LCPs in addition to the Coulomb and nuclear ones, as for example: Coriolis, centrifugal, and inertial (catapult) forces, connected with successive decreasing of the rotation velocity. It is important to note here that these forces depend on the rotation velocity, starting positions, and linear velocities of the fission fragments and LCPs:

$$F_{\text{Cori}} = -2m \left[\mathbf{v} \times \mathbf{\omega} \right]$$
 $F_{\text{centr}} = m\mathbf{\omega} \times \left[\mathbf{r} \times \mathbf{\omega} \right]$ $F_{\text{catap}} = m \left[\mathbf{r} \times d\mathbf{\omega} / dt \right]$ (6)

As both T-odd asymmetry effects appear together and are closely connected with fissioning system rotation it seemed to be reasonable to try to find the way of their joined description in the frameworks of our model. To do so both observed T-odd asymmetry effects were presented as the following sum:

$$D_{ROT}^{TRI} = D_{ROT} + D_{TRI} = A \cdot \left[\omega^{+} \frac{1}{1+s} + \omega^{-} \frac{s}{1+s} \right] + B \cdot \left[K^{+} \omega^{+} \frac{1}{1+s} + K^{-} \omega^{-} \frac{s}{1+s} \right]$$
(7)

where $s = \sigma(J^{+})/\sigma(J^{-})$ is the ratio of fission probabilities through the transition states with the spins J^{\pm} , ω^{\pm} - the proper angular velocities, calculated with the formulas (4), and A, B - the constants. These constants were found from the fit of expression (7) to the experimental data for the TRI and ROT-effects in the ²³⁵U ternary fission, where the measurements were performed with the best accuracy.

The empirical expression obtained in such a way was used then for the calculations of the T-odd asymmetry effects in the ²³³U and ²³⁹Pu ternary fission. Tables II - IV show the calculated T-odd effects for different combinations of the K₊ and K₋ values with the s-values (ratio of J+

and J- cross sections) and the experimental values of D_{exp} shown in table captions. The value which is the closest to the experimental one is shown in **bold**.

Tables II, III, IV. Calculated values of the ROT-effects (left side) and TRI-effects (right side) in the ternary fission of ^{233,235}U and ²³⁹Pu

| | ²³⁵ U ROT (°). $\sigma(J=3)/\sigma(J=4)=0.57/15/$ D _{exp} = 0.215(1) ⁰ | | | | | | |
|---|----------------------------------------------------------------------------------------------------------|---------------|-------------------|-------------------|-------------------|--|--|
| ı | <u> </u> | $K_{\perp}=0$ | K ₊ =1 | K ₊ =2 | K ₊ =3 | | |
| | | 0.183 | | | 0.058 | | |
| | K=1 | 0.191 | 0.177 | 0.135 | 0.066 | | |
| | | 0.215 | | 0.159 | 0.090 | | |

 ^{233}II ROT (°). $\sigma(J=2)/\sigma(J=3)=0.79/14/$

239
Pu ROT (°). σ =0/ σ (J=1)=2.09/15/
 $D_{exp} = 0.020(3)$ °
 K_{+} =0 K_{+} =1
 K_{-} 0 0.057 0.028

²³⁵U TRI-эффект (х 10⁻³)

| $D_{exp} = 1.7 \cdot 10^{-3}$ | | | | | | | | |
|-------------------------------|------|-----------|------|-------------------|--|--|--|--|
| | K+=0 | $K_{+}=1$ | K+=2 | K ₊ =3 | | | | |
| K.=0 | 0 | -3.5 | -6.0 | -6.1 | | | | |
| K.=1 | 1.2 | -2.4 | -4.8 | -5.0 | | | | |
| K_=2 | 1.7 | -1.8 | -4.3 | -4.4 | | | | |
| | | | | 1 | | | | |

 $\begin{array}{c|c} ^{239}\text{Pu TRI-эффект (x 10$^{-3}$)} \\ D_{\text{exp}} = -0.23 \cdot 10$^{-3} \\ \hline K_{+} = 0 & K_{+} = 1 \\ \hline K_{-} = 0 & 0 & -0.38 \\ \end{array}$

As one can see, it is possible to explain successfully all experimental data using equation (7) both in values and in signs. Moreover, the most probable calculated values of the TRI and ROT-effects in the ²³³U and ²³⁹Pu ternary fission very well coincide with experimental ones. This fact, on the one hand corroborates the main assumptions of our semi-classical model and on the other hand permits to predict the expected T-odd asymmetry effects in the new planned experiments in the ²⁴¹Pu and ²⁴⁵Cm ternary fission.

It is well known that the transition state spins of the ²⁴²Pu* and ²⁴⁶Cm* formed after cold neutron capture coincide in values with the corresponding spins of ²³⁴U* and ²³⁶U*. Then, if one assumes that the TRI and ROT effects in the ²⁴²Pu* and ²⁴⁶Cm* ternary fission exist at the similar J,K combination as in the ²³⁴U* and ²³⁶U* one can expect their signs and values given in the bold type (see Tables V and VI).

Tables V and VI. Expected values of ROT and TRI-effects in the 245Cm and 241Pu fission

| 245Cm | ROT (0 |). σ(J=3)/ | σ(J=4)= | 5,7 /15/ | ,, |
|-------|--------|------------|---------|----------|----|
| | N+=0 : | l K.+=1 | I K=2 ′ | I K.+=3 | - |
| K.=0 | -0.156 | -0.159 | -0.169 | -0.185 | П |
| K=1 | -0.138 | -0.141 | -0.150 | -0.166 | |
| K=2 | -0.083 | -0.086 | -0.095 | -0.111 | |
| [K_=3 | 0.009 | 0.006 | -0.004 | -0.020 | |

| | ²⁴¹ Pu | ROT (° |). σ(J=2) | /σ(J=3)= | 0.15 /15/ |
|---|-------------------|--------|-----------|----------|-----------|
| ı | $\overline{}$ | K =0 | V -1 | I V -2 | V -2 |

| | K ₊ =0 | K.=1 | K.=2 | K.=3 |
|-----|-------------------|-------|-------|-------|
| K=0 | 0.277 | 0.252 | 0.177 | 0.052 |
| K=1 | 0.280 | 0.255 | 0.181 | 0.056 |
| K=2 | 0.292 | 0.267 | 0.192 | 0.067 |

²⁴⁵Cm TRI (x 10⁻³)

| | | _ | | | |
|-----|-------------------|--------|-------------------|-------------------|--|
| | K ₊ =0 | K.+=1 | K ₊ =2 | K ₊ =3 | |
| K=0 | 0 | -0.829 | -1.396 | -1.440 | |
| K=1 | 2.751 | 1.923 | 1.355 | 1.312 | |
| K=2 | 4.002 | 3.173 | 2.606 | 2.562 | |
| K=3 | 2.251 | 1.422 | 0.855 | 0.812 | |

²⁴¹Pu TRI-эффект (х 10⁻³)

| | K₊=0 | K,=1 | K ₊ =2 | K.+=3 |
|------|-------|--------|-------------------|--------|
| K_=0 | 0 | -3.746 | 5.448 | -3.065 |
| K.=1 | 0.256 | -3.490 | -5.193 | -2.809 |
| K.=2 | 0.205 | -3.541 | -5.244 | -2.860 |

The simultaneous description of both, TRI and ROT effects by the same combination of the K+/K- values for each measured nucleus, including the predicted ones for ²⁴²Pu* and ²⁴⁶Cm*, will be very convincing argument in the support of our rotation model of the T-odd asymmetry effects of the LCP-emission in the ternary fission of heavy polarized nuclei.

4. Main results of the search for T-odd asymmetry effects of the γ-rays and neutron emission in the binary fission of polarized nuclei

As it was pointed out in introduction, just after the first observation of TRI-effect of the LCP emission in ternary fission it was evident that similar effects should exist in the processes of the neutrons and γ -quanta radiation if they are emitted near the rupture point. But these effects in the ^{233,235}U binary fission have not been observed in the first experiments /9, 10/ up to the level of accuracy about $5\cdot10^{-5}$. And only in 2009 in the work /16/ the ROT-effect of T-odd asymmetry was observed for the γ -quanta radiation in the ²³⁵U binary fission and was considered by the authors as an evidence of the prompt γ -quanta emitted near the rupture time. Our subsequent work /17/ corroborated this observation. However, quite different explanation of the observed effect has been proposed. Following the work of Strutinsky /18/ and the mention of Novitsky /16/ we are convinced that this effect is the direct consequence of the appearance in the rupture process of a strongly deformed fissioning system of large angular momenta of the fission fragments. These momenta, which are normally oriented relative to the fission fragment axis of symmetry, are conserved up to the time of the γ -quanta emission ($\geq 10^{-14}$ sec) and lead to the well known angular anisotropy of the γ -quanta emission and the T-odd asymmetry effects:

$$W(\theta') = 1 + A \cdot \cos^2 \theta' + D_{ROT}(\theta') \cdot \left(\sigma_n \left[\mathbf{p}^f \mathbf{p}^{\mathsf{T}} \right] \right)$$
 (8)

This expression after some simple transformations will lead to the following formula for the T-odd asymmetry coefficient value:

$$D^{\exp}_{ROT} \cong -A \cdot \delta \cdot \sin(2\theta^{\prime}) / [1 + A \cdot \cos^{2}(\theta^{\prime})]$$
(9)

where δ is the shift of the γ -quanta angular distribution, θ – the angle of the γ -quanta emission, and A – angular anisotropy value. The value of δ obtained in our work /17/ was equal to 0.103^0 , which is not too far from the angle of the LCP angular distribution shift in the ternary fission of the same nucleus ²³⁵U.

It is necessary to point out that in spite of relatively simple and quite understandable mechanism of the γ -quanta ROT-effect appearance in the binary fission it is undoubtfully closely connected with fissioning system rotation. Namely because of these circumstances the future investigations of this effect in comparison with similar effect for the LCP in ternary fission may be very fruitful for the fission dynamics study at the low excitation energies.

The question about existence of the ROT-effect for the fission neutrons and its energy dependence has been theoretically investigated in details in the work /19/. The main results of this work together with the recent results of its experimental investigations /20/ are shown in Figure 4.

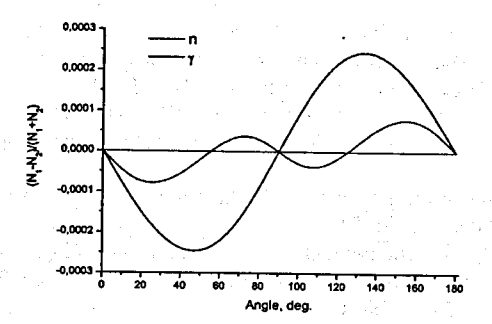


Fig.4. Experimental ROT-effects for neutrons /20/ (black squares) in comparison with theoretical angular dependence of the ROT effects for neutrons and γ -quanta /19/

With regard to the first observation of the ROT-effect of the neutron emission asymmetry the following remarks have to be pointed out. First of all the definite physical effect evidently exists in the ²³⁵U binary fission induced by the cold polarized neutrons. However the sign and value of the observed effect turn out to be in the contrast with the theoretical predictions /19/.

But if the difference in signs may be explained by another choice of the vectors order in the formula (2), it is difficult to find the reason for the two times larger size of the effect. It suggests an idea to propose that some instrumental asymmetry could exist during the measurements or the experimental result presented in the Fig.4 includes some value of the TRI-effect of the T-odd asymmetry of neutron emission. In principle TRI-effect value about 1.5·10⁻⁴ would not contradict to the upper limit of this effect existence (< 6·10⁻⁵) obtained by the same authors in the work /9/.

On the other side complete absence of the TRI-effect for the neutron emission or its relatively small magnitude gives evidence of absolutely different mechanism of neutron emission in fission, as compared to the LCP. The angular distribution of so called "scission" neutrons has to be much less pronounced compared to the LCP one. In addition, the yield of "scission" neutrons accompanied the ²³⁵U binary fission is not higher than (3+5)·10⁻²/21/, which is much smaller than the average of 2.5 prompt neutrons emitted from the excited fission fragments.

All aforesaid supports the necessity of new more detailed investigations of the TRI and ROT-effects of T-odd asymmetry for neutrons and γ-quanta radiation in comparison with similar effects in ternary fission with the LCP-emission.

References

- 1. P.Jesinger, G. Daninyan, A. Gagarski et al. Phys. Atom. Nucl.v. 62, (1999)1608.
- 2. P. Jesinger, A. Kotzle, A. Gagarski, F. Goennenwein et al. NIM A440, 2000, p. 618.
- 3. K. Schreckenbach et al. In "Time Invariance and Parity Violation in Neutron Reactions" Singapore, World Scientific, 1994, p. 187.
- 4. A. Gagarski, G. Petrov, F. Goenenwein et al. Proc. Inter. Sem. ISINN-12, JINR 2004, p. 255.

- 5. A. Gagarski, I. Guseva, F. Goennenwein, G. Petrov et al, Proc. Inter. Sem. ISINN-14, JINR, 2007, p. 93.
- 6. F. Goennenwein, M. Mutterer, A. Gagarski, I. Guseva, Phys. Lett. B 652, (2007) 13.
- 7. I. Guseva and Yu. Gusev. Proc. Intern. Sem. ISINN-14, JINR, 2007, p.101.
- 8. A. Gagarski, F. Goennenwein, I. Guseva et al. Proc. Int. Sem. ISINN-17, JINR, 2010, p.17.
- 9. G. Danilyan, V. Krakhotin, V. Pavlov et al. JETP Pis'ma v. 72 (2000)859.
- 10. V. Sokolov, A, Gagarski, G, Petrov et al. Proc. Inter. Sem. ISINN-12, JINR 2004, p. 25.
- 11. V. Bunakov and G. Petrov. Proc. Intern. Sem. ISINN-8, JINR, 2000, p.100.
- 12. V. Bunakov and S. Kadmensky. Proc. Intern. Sem. ISINN-15, JINR, 2008, p.256.
- 13. A. Barabanov. Proc. Intern. Sem. ISINN-19, JINR, 2011 (to be published). Abstracts p. 20.
- 14. Yu. Kopath, A. Popov, V.Furman et al. Phys. At, Nucl, v.62, 1999, 840.
- 15. V. Maslov et al. JENDL, ENDF/B6
- 16. G. Danilyan, I. Klenke, V. Krakhotin et al. Nucl. Phys. (rus) v.72 (2009)1872.
- 17. G. Val'ski, A. Gagarski, I. Guseva et al. Izv. RAS (ser. fiz.) v.74 (2010)793.
- 18. V. Strutinsky. JETF v.37 (1959)861.
- 19. I. Guseva. Proc. Intern. Sem. ISINN-18, JINR, 2010, p.84.
- 20. G. Danilyan, I. Klenke, V. Krakhotin et al. Nucl. Phys. (rus)v.73 (2010) p.1155. Abstracts of Intern. Sem. ISINN-19, JINR, 2011, p.24.
- 21. G. Petrov, A. Vorobiev, V. Sokolov et al. Proc. of 4-th Inter. Workshop on Nuclear Fission and Fission Product spectroscopy. AIP, New York, v. 1175, 2009, p. 289.

ONLINE COINCIDENCE DETECTION OF FISSION FRAGMENTS AND LIGHT CHARGED PARTICLES

Carlos Granja¹, Vaclav Kraus¹, Yuri Kopatch², Stanislav Pospisil¹, Sergei A. Telezhnikov²

¹Institute of Experimental and Applied Physics, Czech Technical University in Prague, Czech Republic

²Frank Laboratory of Neutron Physics, Joint Institute for Nuclear Research JINR, Dubna, Russia

Abstract

With the goal to study angular correlations of rare fission decay, charged-particle spatial- and time-correlated measurements of fission fragments are being investigated with a modular multi-parameter coincidence system based on several pixel detectors Timepix. In addition to high granularity, wide dynamic range and per pixel threshold, Timepix provides energy and time sensitivity capability per pixel. The detector is operated with the integrated USB 2.0-based readout interface FITPix and the data acquisition software tool Pixelman. A number of coincidence setups and techniques were investigated. Triggered measurements are performed with an integrated spectrometric module with embedded analogue signal chain electronics. Demonstration of the technique is presented with a spontaneous fission source.

Motivation

Charged-particle coincidence studies such as angular correlations between ternary particles and main fission fragments provide so far only partial information such as energy cutoff, poor spatial resolution and narrow range of studied ion Z numbers. Many of these drawbacks which arise from the standard detectors used so far can be solved by highly segmented quantum counting pixel detectors. Desired tasks include measuring the angular distributions of light charged particles (LCP) and resolving different modes of rare fission decay (see Fig. 1).

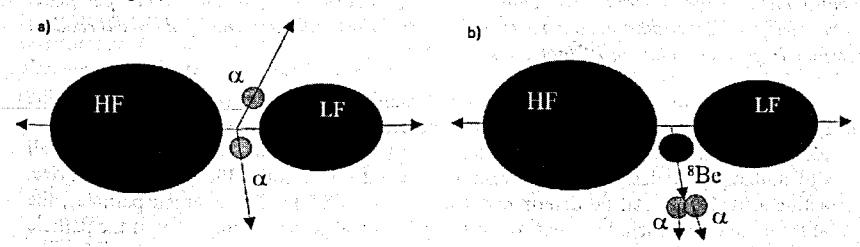


Figure 1: Two modes of quaternary fission: (a) true and (b) pseudo quaternary fission. Spatial information of the emitted light charged particles detected in coincidence gives the signature.

Rare fission decay with the emission of one (ternary fission) or two (quaternary fission) LCPs is a unique tool to explore the dynamics and structure of atomic nuclei by probing the fissioning system near the scission point and observing fissioning reaction and decay mechanisms [1]. Detailed spectroscopy of fission products is the necessary input for the understanding of fission configurations and dynamics of reaction mechanisms. Observables such as the angular momenta of LCPs correlated with the binary fragments are closely related to the dynamics of the fissioning system in its final stages [1–3].

Pixel Detector Timepix + FITPix Readout Interface + Pixelman Control/DAQ

The hybrid semiconductor pixel detector of the Medipix type [4] consists of a radiation sensitive sensor bump bonded to an ASIC readout chip with integrated electronics per pixel (see Fig. 2a). The chip is divided into an array of 256 × 256 pixels of 55 µm pitch with full sensor size 14 × 14 mm². Hybrid technology allows using sensors of different materials (Si, GaAs, CdTe) and thickness (300, 700, 1000 µm). Per-pixel pulse processing electronics provides fast and noise free images.

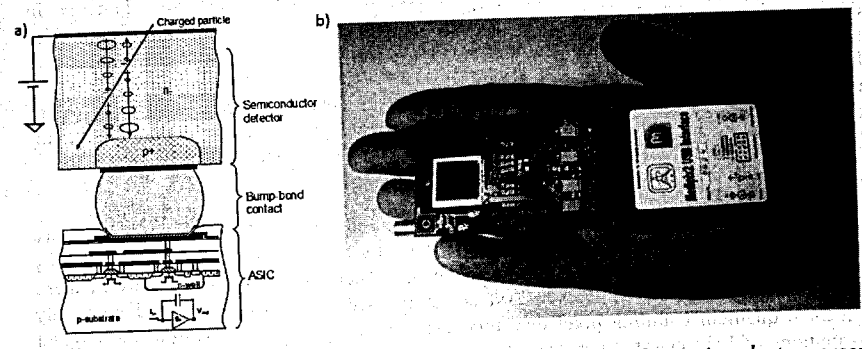


Figure 2: Left: Principle of the hybrid pixel detector Medipix with the semiconductor sensor bump-bonded to the readout ASIC chip containing integrated signal electronics per pixel. Right: Medipix/USB radiation camera assembled from the chipboard and USB-based readout interface (right). Data link to PC/notebook via USB port.

In addition to high granularity, wide dynamic range and per pixel threshold the Timepix device [5] provides energy and time sensitivity capability per pixel. The detector provides more complete information (position, energy, time, stopping power) for basically all types of ionizing particles. Per-pixel threshold is about 4 keV for a 300 μ m silicon device. Interaction/arrival time can be determined with a step of 25 ns. For charged particles, the spatial resolution can reach, by event-by-event analysis and pattern recognition of the particle track, sub-pixel resolution down to few μ m.

The pixel detector is operated with integrated USB-based readout interfaces such as the USB 1.0 [6] and FITPix [7] devices (see Fig. 2b) which provide control, power and DAQ. Operation and online visualization are enabled by the software package Pixelman [8,9]. The assembled system serves as an online radiation camera [10] for table-top and vacuum operation, portability and configurability of different measurements and setups.

Online Detection of Fission Fragments

The response of the Medipix2 detector to fission fragments were demonstrated [11]. The resolving power of the Timepix device to an alpha and spontaneous fission source (252Cf) is shown in Fig. 3. Timepix allows applying timing and spectral correlated techniques in the same sensor for enhanced background suppression and unambiguous event-by-event detection. We have developed a variety of instrumental configurations, trigger architectures and multi-detector setups. These features combined with pattern recognition and event track analysis provide enhanced signal to noise ratio with marked suppression of background and unwanted events. As Fig. 3 shows, the spatial information can be correlated to the spectral information in order to distinguish desired events and suppress unwanted background.

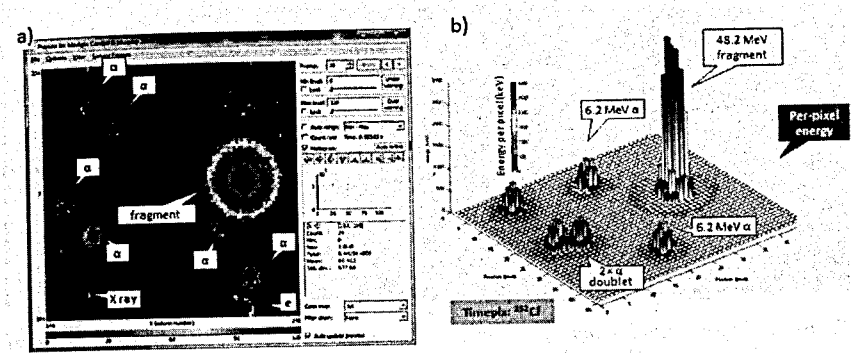


Figure 3: Left: Online visualization window of the Pixelman software showing the response to a 252 Cf source of the Timepix detector operated in energy (TOT) mode. Sensor region shown of about 80×80 pixels. Right: Detail of detection of a fission fragment and several a particles. Sensor region shown of about 45×45 pixels. In addition to the spatial 2D information the energy per pixel is recorded and can be displayed as a third axis by the vertical bar in color. Unwanted events such as α -decay particles, pile-ups, X-rays and electrons are clearly resolved by the spatial- and spectral-analysis (particle tracking and pattern recognition).

Coincidence Detection of Fission Fragments

In order to detect particles in coincidence, such as the two binary fission fragments or a LCP correlated to the binary fragments, we carried out measurements with two and also with four pixel detectors. The experimental layout with four detectors and a spontaneous fission source (252Cf) carried out at the JINR Dubna is shown in Fig. 4. Description of the instrumentation is given in Ref. [12]. In addition to the trigger implementation, an integrated master module has been newly built [12] in order to validate the operation and synchronize the data readout when two and more detectors are connected. This synchronizing module provides fully correlated data readout among all detectors maximizing data taking and suppressing dead time but also significantly easing the offline data evaluation.

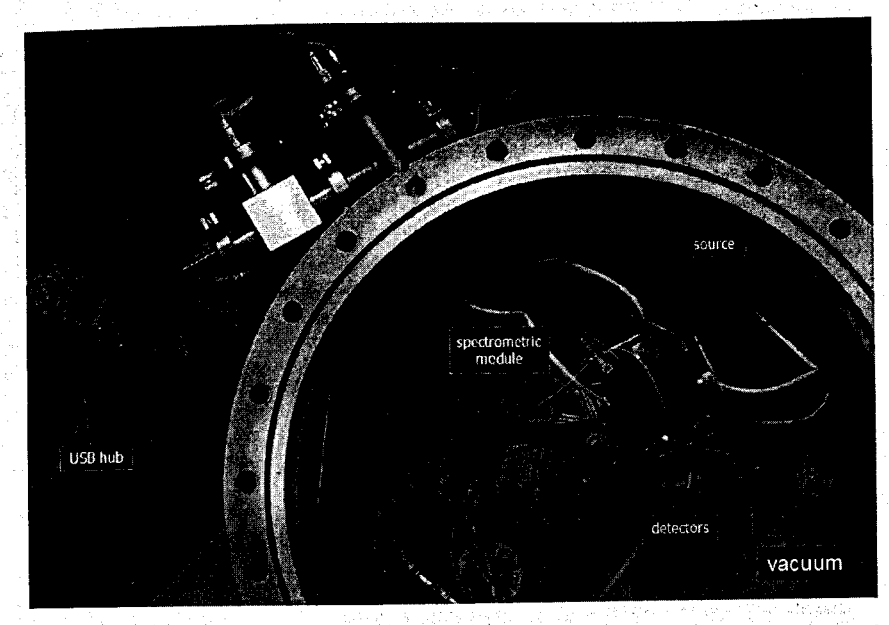


Figure 4: Experimental setup of coincidence detection of fission fragments with 4 pixel detectors in vacuum. The analog signal from one detector is processed by an integrated spectrometric module which triggers itself and all other detectors.

Several hardware techniques have been implemented and tested on various setups with a spontaneous fission source (252Cf):

a) Software Trigger + Low Threshold + Short Exposure Time

In this approach, the detectors start simultaneously by trigger generated arbitrarily and sequentially by the readout interface of one of the detectors. The detectors are run with low per-pixel threshold and collect data in short exposure time (Fig. 5). Data shown were collected in Time mode in which the time of interaction (time stamp) of every event is registered and can coincidence events can be correlated among different detectors. In these measurements one detector acts as master and sequentially generates the trigger to all other detectors. This technique is useful when it is desired to register all types of radiation including low energy particles. The data count rate is limited by the dead time of the readout interfaces which is about 15 ms and also the USB 2.0 speed capacity and the performance of the PC. Up to about 10 and 20 fps per device can be collected with four and two detectors, respectively. Thus up to 10 and 20 sets of coincidence events can be recorded per second.

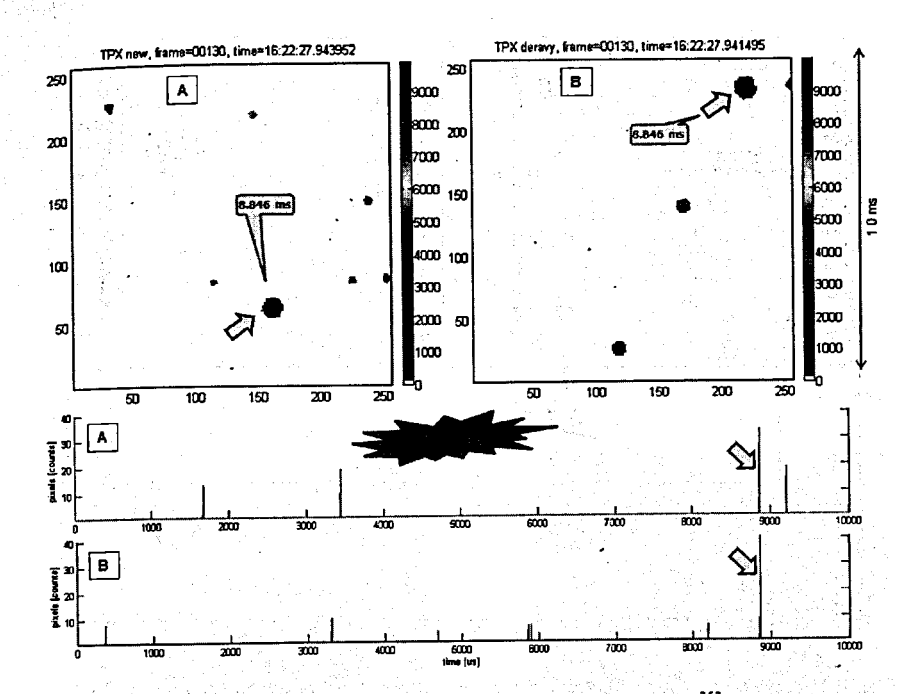


Figure 5: Detection in coincidence of two fission fragments from a 252 Cf source by two Timepix detectors in <u>low pixel threshold</u>. Data taken in time mode and short exposure time (10 ms). The spatial information (top) correlates to the timestamp (bottom spectra). The time scale is displayed in color by the vertical scale in μs . The large clusters correspond to two binary fragments (appear in red at 8.846 ms). The small clusters are a particles from a decay of 252 Cf. The frames correspond to the full sensor area (256 × 256 pixels = 14×14 mm²) of two Timepix detectors equipped with a 300 μm thick silicon sensor.

b) Software Trigger + High Threshold + Long Exposure Time

In another approach, the per-pixel thresholds are raised in order to suppress unwanted events (Fig. 6) also allowing measuring for long exposure times. In this approach, only the fission fragments are registered. Unwanted events such as α -decay particles and electrons from interaction of γ rays in the sensor are fully suppressed and produce no signal. This approach thus maximizes the signal to noise ratio and count rate minimizing dead time. The count rate of desired events (correlated pairs of fragments) can be thus increased by a factor 10–100 compared to the technique above (a). This factor can be even higher with a higher activity source and/or closer target geometry.

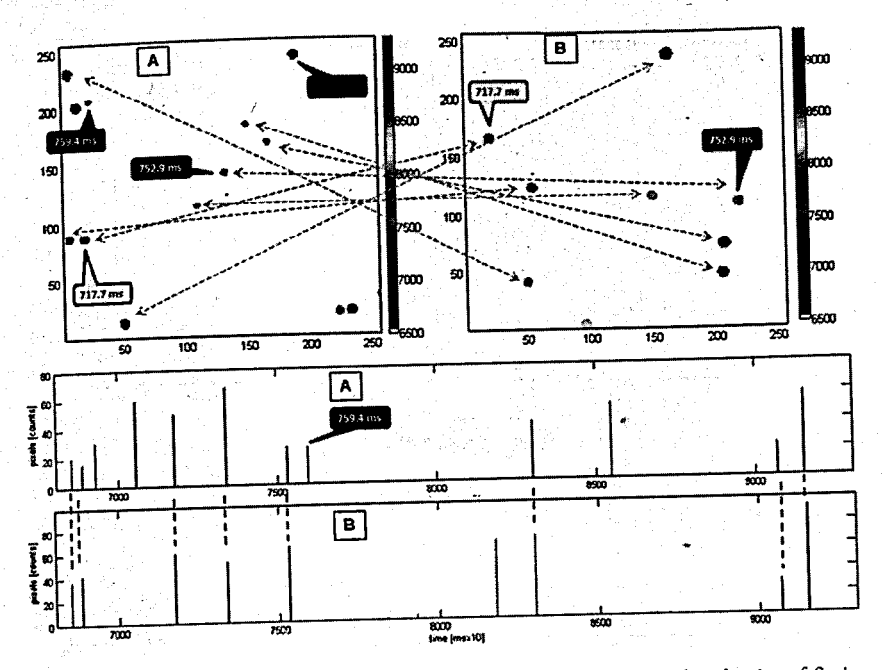


Figure 6: Spatial- and time-correlated detection in coincidence of correlated pairs of fission fragments by two Timepix detectors operated in high pixel threshold and long exposure time (300 ms). The spatial information is correlated to the time information (bottom). The pixels were operated in time mode registering the events interaction time. Correlated events are linked by straight dash arrows for illustration. The high threshold suppresses and effectively removes unwanted events such as a particles from a decay which allows for long exposure times.

c) Hardware Trigger + Integrated Spectrometric Module

Another technique implemented for online detection of fission fragments [13] makes use of the analogue signal of the common sensor of the pixel detector (called back-side-pulse) which can be used as an independent tool to control the start or end time of detector acquisition. With devoted spectrometric signal chain electronics and processing, this signal can be, like for standard p-i-n diodes, used to tag desired ions and provide a fast trigger. We employed a devoted spectrometric module built on an integrated and miniaturized chipboard which can be embedded into the USB 1.0 readout interface. This module is operated with a Windows running plugin application which loads and controls the sensor bias, sets the threshold level and displays and stores the module's MCA. The triggered detection of three fragments in coincidence is shown in Fig. 7. The data shown were collected in energy TOT mode. The short exposure times provide unambiguous identification of coincidence event and straightforward analysis.

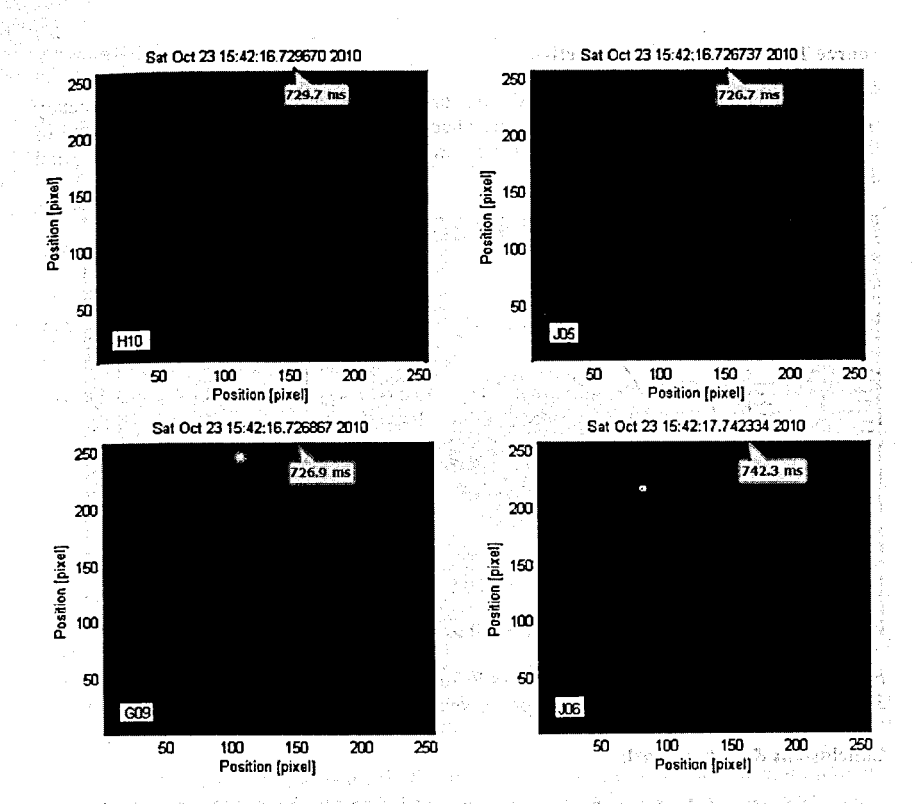


Figure 7: Detection of three fragments in coincidence using a setup of four pixel detectors (shown in Fig. 4) consisting of two Timepix devices (bottom) and two Medipix2 devices (top). Events measured in trigger mode (trigger signal generated by detector TPX J06) and short exposure time (1 ms). The timestamp of data transfer and storage at the measuring PC for each frame is indicated.

The time registry of transfer storage of the given frame in the measuring PC is included. The time shift between the triggering detector (master) and the triggered detectors (slave) is about $1-2~\mu s$ (trigger generation in the USB 1.0 interface) plus few tens of ns (processing time of trigger in the slave detectors). The data packages are then sent and stored at the measuring PC at yet greater different times (due to the data transfer and the data storage at the PC introduce further shifts) which can reach few tens of ms. During this interval the next trigger can be generated which means some of the detectors may not be ready to collect a new frame. This results in unsynchronized and incomplete sets of correlated data frames at the PC. Thus the need arises for a coincidence veto module [12] which can validate the status and synchronize the data readout of all detectors.

Source Target Image Reconstruction

The spatial information obtained from the coincidence detection of the main binary fragments can be used further – e.g. to visualize the distribution and determined density of source material in the target. The target used and its reconstructed image with the material density are shown in Fig. 8.

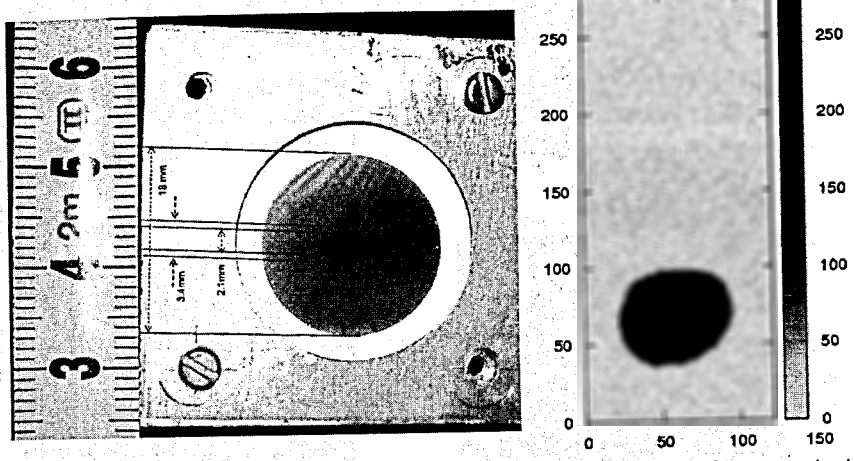


Figure 8: ²⁵²Cf source target used (left) and its reconstructed image (right). The source size is 3.4 mm. The material distribution and spatial density are shown in color by the vertical bar.

Conclusions & Future work

The setup and operation of up to four pixel detectors have been implemented for spatial and time coincidence detection of correlated particles for spatially directional studies of rare fission decay. Several techniques have been constructed and demonstrated under a number of particular detector and experiment conditions such as trigger implementation, perpixel threshold, sensor bias, and measurement exposure time. Fully synchronized data acquisition and readout require a devoted coincidence module to sever as arbiter for ready/busy/veto device monitoring. Analysis of angular distributions/correlations and data evaluation of ternary fission are underway. Long term measurements are planned for studies of low yield rate such as quaternary fission.

Acknowledgements

This work was supported by a Research Grant from the Committee of the Czech Republic for Cooperation with JINR Dubna and by the Research Program MSM6840770029 Fundamental Experiments for the Physics of the Microworld of the Ministry of Education, Health and Sports of the Czech Republic. Research performed in frame of the Medipix Collaboration.

References

- [1] C. Wagemans, The nuclear fission process, CRC Press, USA (1991)
 M.Mutterer, and J.Theobald, Nuclear Decay Modes, ed. D.N. Poenaru, IOP, UK (1996)
- [2] F. Gonnenwein, A. Moller, M. Croni, et al., Nuovo Cimento A 110 Nuclei particles and fields (1997) 1089-1095.
- [3] L. Nowicki, E. Piasecki, J. Sobolewski, et al., Nuclear Physics A 375 (1982) 187-216.
- [4] X. Llopart, M. Campbell, R. Dinapoli, D. San Segundo, E., Pernigotti, Medipix2—a 64 k pixel readout chip with 55 mm square elements working in single photon counting mode, IEEE Trans. Nucl. Sci. NS-49 (2002) 2279.
- [5] X. Llopart, R. Ballabriga, M. Campbell, and W. Wong, Timepix, A 65 k programmable pixel readout chip for arrival time, energy and/or photon counting measurements, Nucl. Inst. and Meth. A 585 (2007) 106-108.
- [6] Z. Vykydal, J. Jakubek, M. Platkevic, S. Pospisil, USB Interface for Medipix2 Enabling Energy and Position Detection of Heavy Charged Particles, Nucl. Instr. and Meth. A 563 (2006) 112-115.
- [7] V. Kraus, M. Holik, J. Jakubek, M. Kroupa, P. Soukup, Z. Vykydal, FITPix Fast Interface for Timepix Pixel Detectors, Journal of Instrumentation 6 (2011) C01079.
- [8] T. Holy, J. Jakubek, S. Pospisil, J. Uher, D. Vavrik, Z. Vykydal, Data acquisition and processing software package for Medipix-2 device, Nucl. Instr. and Meth. A 563 (2006) 254-258.
- [9] D. Tureček, T. Holý, J. Jakůbek, S. Pospíšil, Z. Vykydal, Pixelman: a multi-platform data acquisition and processing software package for Medipix2, Timepix and Medipix3 detectors, Journal of Instrumentation 6 (2011) C01046.
- [10] Z. Vykydal, J. Jakubek, T. Holy, S. Pospisil, A portable pixel detector operating as an active nuclear emulsion and its application for X-ray and neutron tomography, 9th ICATPP 2005 Conf. Proc. (2006) 779-784; doi:10.1142/9789812773678_0123
- [11] C. Granja, J. Jakůbek, S. Pospíšil, Z. Vykydal, Y. Kopatch, S. Telezhnikov, Position-sensitive spectroscopy of ²⁵²Cf fission fragments, Nucl. Instr. and Meth. A 574 (2007) 472-478.
- [12] V. Kraus, C. Granja, Coincidence module for spectral and time correlated multi-particle detection with four pixel detectors Timepix, in these Proceedings.
- [13] C. Granja, V. Kraus, J. Jakubek, S. Pospisil, P. Masek, Z. Vykydal, M. Platkevic, Z. Kohout, Y. Kopatch, S.A. Telezhnikov, Spatially Correlated and Coincidence Detection of Fission Fragments with the Pixel Detector Timepix, Nuclear Science Symposium IEEE NSS/MIC, Knoxville, Conf. Record (2010) 1578-1584.

ه کې د د د کوه کې د د د هغور کوه د د د د دره تو د خاران پروستان کې څا سوست پر د د د د د د وير دخ د ده. د خوې د څو د د څخه د د وهغور کوه د د خاران وتو د خاران پروستان کې څا سوست پر د د د د د د وير دخ د ده.

Investigation of the Sub-threshold Fission Cross Section for 232 Th and 238 U

Yu.V. Grigoriev^{1,2}, D.V. Khlustin¹, Zh.V. Mezentseva², Yu.V. Ryabov¹

¹Institute for Nuclear Research RAN, Troitsk, Russia ²Joint Institute for Nuclear Research, Dubna, Russia

Abstract Time-of-flight spectra from 1^{st} to 15^{th} gamma-rays multiplicity coincidence of 232 Th and 238 U were measured on the 121.65 m flight path of the IBR-30 using the 16-section liquid (n, γ)-detector "PARUS" [1]. Two plates of metallic thorium and a U_3O_8 powder with 99.9 % of 238 U were used as the radiator-samples. The U_3O_8 powder was packed in the aluminium tank. The spectra from 1^{st} to 7^{th} multiplicities coincidence of γ -rays and their averaged multiplicities $<K>=\Sigma P_k*K$ (K - multiplicity number, P_k - part of multiplicity) were used to obtain the resonance and group capture cross-sections at the energy range from 1 eV to 4.65 keV. The spectra from 9^{st} to 15^{th} multiplicities coincidence of γ -rays were served to determine, the sub-threshold fission cross-section of 15^{th} and 15^{th} 0. The normalization of the sub-threshold fission cross-sections at the energy range from 1 eV to 4.65 keV was done using the fission cross-sections for 15^{th} 1 and 15^{th} 2 u at the energy range from 2.5 MeV to 4 MeV.

We have carried out measurements of the TOF-spectra from 1st to 15th multiplicity coincidences of gamma-rays of ²³²Th and ²³⁸U to determine the radiation capture cross-sections at the energy range from 1 eV to 4.65 keV. These measurements have been performed on the 121 m neutron flight path of the IBR-30 (W = 10 kW, f = 100 Hz, τ = 4 μ s) with the 16-section liquid detector "PARUS" [2] with a total volume of 80 l. The general view of this detector is given in Fig.1.

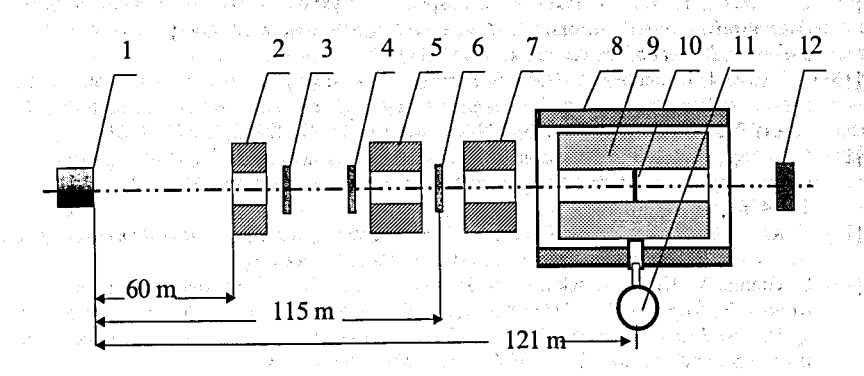


Fig. 1 The general view of the experiment: 1 – the IBR-30 fuel core moderator; 2, 5, 7 – collimators; 3 – resonance filter; 4 – monitor; 6 – sample-filter; 8 – lead shielding of the (n, γ)- detector; 9 – liquid detector; 10 – radiator-sample; 11 - HPGe - detector; 12 - neutron detector

The intensity level of the neutron source was controlled by two boron counters SNM-12. The neutron flux on the sample was determined by the following expression:

$$\varphi(E) = \frac{400}{E^{0.9}} [n/cm^2 s eV] (1)$$

Two plates of metallic 232 Th (99.4%, 4 g) with a total thickness of 0.2 mm and with an area of S = 4.5 x 4.5 cm² were used as the radiator-samples. The U₃O₈ powder with 238 U (99.999%) and 3.86 g of a weight, packed in the aluminium tank, was served as standard radiator-sample as well.

To determine background components in time-of-flight spectra were used the resonance filters from Al, Mn, Na, Cd and B₄C, which were fixed in the neutron beam. The background components were subtracted and measured spectra were brought to a general monitor coefficient.

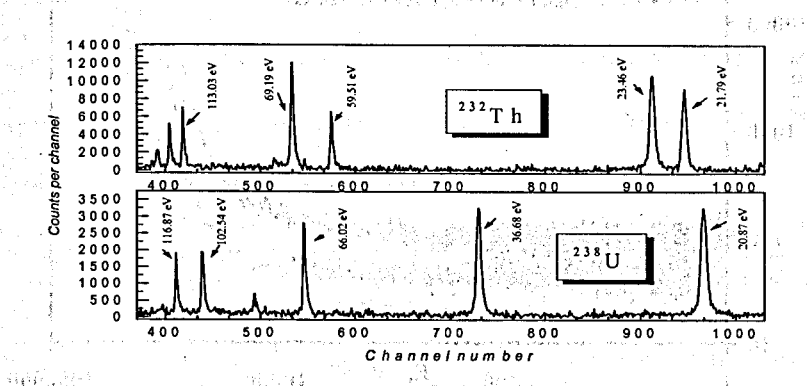


Fig. 2. The measured time-of-flight spectra of ²³²Th and ²³⁸U after background subtraction.

The integral counts within the energy groups are connected with ²³²Th and ²³⁸U capture cross-sections by the following expression:

$$\sigma_c(Th) = \sigma_c(U) \frac{M^U S^U n^U N_c^{Th}}{M^{Th} S^{Th} n^T N_c^{U}}$$
(2)

where: $\langle \sigma_c \rangle^{Th}$ and $\langle \sigma_c \rangle^U$ - capture cross-sections, M^U and M^{Th} - monitor coefficients for the U and Th samples, n^U and n^{Th} - thicknesses of radiator-samples, S^U and S^{Th} - areas of radiator-samples.

We assume that the registration efficiency of γ - rays for the U and Th samples is the same. Then to determine capture cross-sections of ²³²Th one can use the expression (2), knowing capture cross-sections of ²³⁸U.

Since an influence of scattered neutrons is observed in the first three multuplicities, the summation from the 4th multiplicity to the 7th one was performed to obtain capture cross-

section. The experimental errors of capture cross sections are about 7%.

Also the radioactive capture cross-sections were calculated by the GRUKON code [3] on

the base of the estimated data of various libraries.

To determine the ²³⁸U and ²³²Th radioactive capture cross-sections were carried out several campaigns of measurements to obtain a good statistical accuracy in counts per / channel in every multiplicity. It was also allowed to observe a weak resonance effect of the sub-threshold fission. To achieve the statistical accuracy in the fission cross-section the measured TOF spectra from 8th to 15th multiplicities were used in the broad energy region. These spectra are shown in Fig.3.

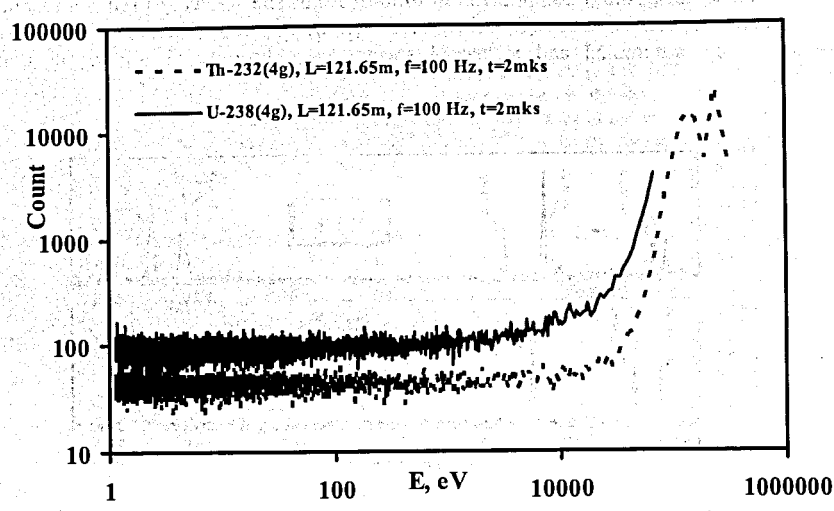


Fig. 3. Sum of the time of-flight spectra of ²³²Th and ²³⁸U from 8th to 15th multiplicities without background subtraction.

As one can see, that any resonance structure of the sub-threshold fission cross sections was not observed in the energy region from 1 eV to 10 keV. The accuracy of determination of sub-threshold fission cross sections for Th and ²³⁸U was done by comparison the fission cross sections in the energy range 1 eV - 4.65 keV with one $<\sigma_{i}>^{HE}$ = 0.13 barn of 232 Th and $<\sigma_c>^{HE}$ = 0.58 barn of ²³⁸U in energy range from 2.5 MeV to 4 MeV by the following expression:

$$\begin{split} N_f^{HE} &= \phi^{HE} < \sigma_f >^{HE} MSn \\ N_f^{LE} &= \phi^{LE} < \sigma_f >^{LE} MSn \\ &< \sigma_f >^{LE} = \frac{N_f^{LE} \phi^{HE}}{N_f^{HE} \phi^{LE}} \end{split} \tag{3}$$

where: $\langle \sigma_i \rangle^{HE}$ and $\langle \sigma_i \rangle^{LE}$ - fission cross-sections at the HE - high energy and at the LE - low

one, M - a monitor coefficient, n -a thickness of the radiator-sample: S- an area of radiatorsample, N_f^{LE} , N_f^{HE} - counts within the energy groups, Φ^{LE} , Φ^{HE} - neutron fluxes within the energy groups.

It should be stressed that the background components in the measured spectra was practically coincide with the own background of the "PARUS" setup, consisting of the electronic noise and cosmic radiation.

In future, we are planning to continue this investigation in order to determine the subthreshold fission cross-sections by this method at better background conditions at the setup IREN-1 (FLNP JINR, Dubna). [4]

References

1. Yu.V.Grigoriev, V.Ya. Kitaev, V.V.Sinitsa, H.Faikov-Stanczyk, Hyon Sung Ho. Measurements of the gamma-ray multiplicity spectra of U-235 and Pu-239 with 16-

liquid scintillation detector, ISINN-6 on Neutron Spectroscopy, Nuclear Structure, Related

Topics, Dubna, May 13-16, 1998, p.250-259; Yu.V.Grigoriev, V.Ya..Kitaev, G.P.Georgiev.

Preprint FEI № 2391.- Obninsk: FEI,1994

- 2. W.Y. Baek, G.N. Kim, M.H. Cho, I.S. Ko, W. Namkung, Yu.V. Grigoriev, H. Faikov-Stanczyk, V.N.Shwtshoy, W.I. Furman. Investigation of multiplicity spectra and neutron capture cross-sections of ²³² Th in the energy region 21.5-215 eV. Nuclear Instruments and Methods in Physics Research B 168 (2000) 453-461
- 3. V.V.Sinitsa, Program for Calculating the Group Constants Using the Library of Evaluated Neutron Data, VANT, ser. Nuclear Constants, 1984, v.5 (59), p. 34.
- 4. Belikov O V et al. Physical start-up of the first stage of IREN facility, 2010 J. Phys.: Conf.

Ser. 205 012053

COLLINEAR CLUSTER TRI-PARTITION: CURRENT STATUS OF STUDIES

D.V. Kamanin¹, Yu.V. Pyatkov^{1,2}, A.A. Alexandrov¹, I.A. Alexandrova¹, N. Jacobs³, N.A. Kondratyev¹, E.A. Kuznetsova¹, V. Malaza³, O.V. Strekalovsky¹, V.E. Zhuchko¹

¹Joint Institute for Nuclear Research, Dubna, Russia ²Moscow Engineering Physics Institute, Moscow, Russia ³University of Stellenbosch, Faculty of Military Science, Military Academy, Saldanha 7395, South Africa

"Ni"-BUMP AND ITS INTERNAL STRUCTURE

In our recent publications [1] we have presented experimental evidences of existing of a new type of ternary decay of heavy low excited nuclei called by us collinear cluster tripartition (CCT). The results were obtained in the frame of the "missing mass" approach. It means that only two from at least three decay partners were actually detected whereas a total mass of these fragments being less the mass of mother system serves a signature of multibody decay. Evidently direct detection of all CCT products proves to be a most convincing experimental approach but much complicated one because mosaic detection systems must be used to achieve the goal.

COMETA (Correlation Mosaic E-T Array) setup aimed at studying of rare multibody decays was put into operation recently in the Flerov Laboratory of the JINR. It is a double arm time-of-flight spectrometer which includes micro-channel plate (MCP) based "start" detector with the ²⁵²Cf source inside, two mosaics of eight PIN diodes each and a "neutron belt" comprises 28 ³He filled neutron counters. Below we discuss some results obtained at the COMETA setup.

LIGHT CHARGE PARTICLES ACCOMPANIED CCT: SPECTATORS OR PARTNERS OF THE DECAY?

We report here some results of three different experiments (marked Ex1, Ex2, Ex3 below) devoted to the search for collinear cluster tri-partition of 252 Cf (sf). The TOF-E (time-of-flight vs. energy) method for the measurements of two FF masses in coincidence with detectors placed at 180 degrees was used in all three experiments. In this method, the fragment velocities V, obtained by means of TOF and the energy E are measured for each detected fragment individually. Only two fragments were actually detected in each fission event (in two detectors, at 180°) and their total mass, the sum M_{τ} will serve as a sign of a multi-body decay, if it is significantly smaller than the mass of the initial system ("missing mass" method).

The most pronounced manifestation of the CCT as a missing mass event is a bump (fig. 1) in the two dimensional of the mass-mass correlation plot [1]. In this distribution of the fission fragment masses the bump occurs in one of the spectrometer arms with dispersive media (M_1) , whereas it is absent in the analogues variable for the second arm (M_2) . The bump is marked by the arrow in fig. 1a. We see two great bumps due to binary fission; the pronounced vertical and horizontal intensities are due to binary fission fragments scattered from the entrance support grid for the windows of the gas detectors. The FF mass correlation plot similar to that

obtained in Ex1 (fig. 1a) is shown in fig. 2a. Projections of this distribution both on the M_1 axis and on the M_2 = const directions are presented in fig. 2b, and c, respectively. They are compared with the analogous spectra from the experiments Ex1 including the result from the 235 U(n_{th} , f) reaction [1]. The bump in the projected FF mass correlation data in fig. 2b is centered on mass (68÷70) amu, associated with magic isotopes of Ni. This bump will be called below as the "Ni"-bump. The bump marked by the arrow in fig. 2a looks less pronounced as compared to that obtained in Ex1 (fig. 1a). This can be partially explained by a worse mass resolution due to the wide-aperture avalanche counter used as "start" detectors in Ex2, instead of the MCP based detector in Ex1. Projections for Ex2 are shown in the "difference" version, i.e. as a difference of the tail regions in arm1 and in arm2, respectively. Overall a good agreement is observed in the position of the peaks in fig. 2b, and c for all three experiments. The shift of the peak for the 235 U(n_{th} , f) reaction in fig. 2c has already been discussed in ref. [1].

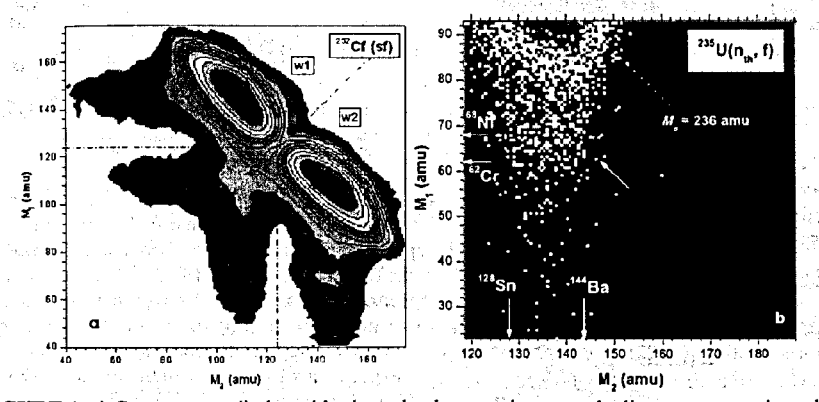
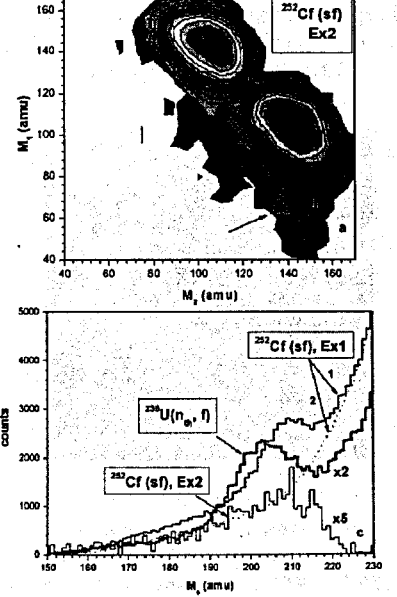


FIGURE 1. a) Contour map (in logarithmic scale, the steps between the lines are approximately a factor 2.5) of the mass-mass distribution of the collinear fragments of 252 Cf (sf), detected in coincidence in the two opposite arms of the FOBOS spectrometer. The specific bump in arml is indicated by an arrow. Two large windows w1 and w2 are used in the later analysis (section 4). b) The region of the mass distribution for the FFs from the reaction 235 U(n_{th}, f) around the bump. The bump is bounded by magic clusters (marked by corresponding symbols near the axes). The tilted arrow shows a valley between the ridges $M_1 + M_2 = 210$ amu of $M_s = \text{const. See}$ text for details.

The methodically quite different experiment Ex3 shows results, which confirm our previous results concerning the structures in the missing mass distributions. In this case there is no tail due to scattering from material in front of the E-detectors. Fig. 3 shows the region of the mass distribution for the FFs from 252 Cf (sf) around the "Ni"-bump ($M_1 = 68 \div 80$ amu, $M_2 = 128 \div 150$ amu). The structures are seen in the spectrometer arm facing the source backing only. No additional selection of the fission events has been applied in this case; the experiment has no background from scattered FFs. A rectangular-like structure below the locus of binary fission is bounded by magic nuclei (their masses are marked by the numbered arrows) namely 128 Sn (1), 68 Ni (2), 12 Ni (3). Two tilted diagonal lines with $M_3 = 196$ amu and $M_3 = 202$ amu (marked by number 4) start from the partitions 68/128 and 68/134, respectively. In experiment Ex1 [1], Figure 6, similar sub-structures have been seen for masses $M_3 = 204$, 208, 212, 214 amu where they were revealed indirectly by the applying of

the second derivative filter, but in the absolutely statistically reliable distribution ("Ni"-bump) processed. Bearing in mind essential difference in the geometry of blocking mediums in Ex1 and Ex3 to be decisive for the relative experimental yields of the CCT modes with different angular distributions between the fragments forming the fork flying in the same direction the preference of lighter partitions standing behind the tilted ridges in Ex3 is not strange. Positions of the points in the lower part of fig. 3 do not contradict to possible existence of all the ridges revealed in Ex1 if the following magic partitions are assigned to their beginnings: 70/134, 68/140, 68/144, 70/144.



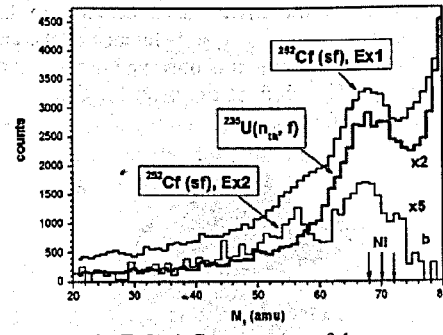


FIGURE 2. Ex2. a) Contour map of the mass-mass distribution (logarithmic scale, with lines approximately a factor 1.5) from a coincidence in the two opposite arms of Ex2. The bump in the spectrometer arm (arml) facing the backing of the Cf source is marked by the arrow. b) Projections onto the M_1 axis for comparison with the experiments Ex1, and with the results of the 235 U(n_{th} , f) reaction (fig. 1b) [1]. c) Projections onto the direction $M_s = M_2 + M_1$. Ex1 is presented by two curves marked by the arrows 1 and 2 (dotted) for the arml and arm2, respectively.

Thus, comparison of Ex1 and Ex3 which are absolutely different both by the detectors and mass calculation procedures used as well as the statistics collected delivers strong confirmation of the existence of tilted ridges M_r = const linked with magic partitions. As can be inferred from fig. 3, the yield of the FFs with the mass 128 amu, which is extremely low in conventional binary fission, is clearly seen. It means that scattered binary fragments in any case cannot give rise to this structure. A part of the plot just below the locus of the binary FFs is shown in a larger scale in the insert. The structure is bounded by the magic nuclei of 80 Ge, 78 Ni, 132 Sn, 144 Ba (their masses are marked by the arrows 5, 6, 7, 8, respectively). The observations presented point to the fact that the CCT decay occurs in a variety of modes (mass combinations), which could not be distinguished in Ex1 without additional gating due to the large background from scattered FFs. Likely due to the difference in the parameters of the blocking mediums the yield of the "Ni"-bump in Ex3 does not exceed 10^{-3} per binary fission i.e. much less then inEx1 and Ex2. At the same time with the absence of scattered FFs in Ex3, allowed the observation of the internal structure, without any additional cleaning of the FF mass distribution.

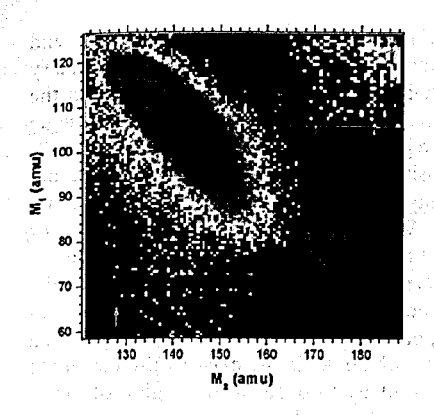


FIGURE 3. Results of Ex3: The region of the massmass distribution for the FFs from ²⁵²Cf (sf) around the CCT bump (figs. 1a and 2a). No additional gates were applied. An internal structure of the bump as the straight lines (marked by the arrows) is seen in fig. 2c, as a projection. A part of the plot just below the locus of binary FFs produces the rectangular structure seen before. It is shown in the insert in a larger scale.

SOMETHING NEW IN "BUMPOLOGY"

Above we have discussed the "Ni"-bump, which is vividly seen in the FFs mass-mass correlation plot without any processing (fig. 1), because it is located below the loci of binary fission. As was stressed in ref. [1] the bump shows internal structure consisting of two different sequences of ridges namely $M_s = M_1 + M_2 = \text{const}$ (tilted ridges) and $M_1 = \text{const}$ (where M_1 is the lighter fragment among two detected). In the neutron gating data obtained at the modified FOBOS and COMETA spectrometers [2] we have observed rectangular structures bounded by magic clusters not only spherical (Ni, Ge) but also deformed ones (98Sr, 108Mo). This observation gave hints that in the data of Ex1 deformed light clusters could manifest themselves as well. In order to peruse this idea we have reanalyzed the data of Ex1, namely the M_1-M_2 distribution (fig. 1a), in this figure we choose two large windows w1 and w2. The corresponding projections of the distributions onto the coordinate axis in the "clean" arm2 (box w1) and those facing to the source backing, arm1 (box w2), are compared in Figure 4a. The spectra were normalized to the same number of counts. The difference spectrum is shown in fig. 4b). Some statistically significant peaks are seen. The first one from the left is the projection of the "Ni"-bump onto the M₁ axis. Further structures follow: a wide peak bounded by magic nuclei of 82Ge and 94Kr (deformed), and peaks centering, respectively, at ⁹⁸Sr and ¹⁰⁸Mo isotopes (both to be magic and deformed). The origin of the peaks becomes clear from following consideration illustrated by fig. 5. Let us focus our attention on the peak in the vicinity of mass 70 amu (Ni) in the difference spectrum (right part of the "Ni"-bump, fig. 4b). The fact that the "Ni"-bump is observed only in one of the spectrometer arms facing the source backing was treated above as being due to a stopping in the entrance mesh of the ionization chamber of the third light fragment directed in the same arm as the Ni cluster. In contrast, the same pair of fragments directed at the "clean" arm2 predominantly (due to a low angular divergence) gives overlapping energy signals in the "stop" detector and time-of-flight signals corresponding to the faster of them. As a result the calculated mass will be incorrect but registered as an "almost normal" binary decay within the experimental mass dispersion. Such events from arm2 play a role of "donors" for the bump events in arm1. In other words the events being actually ternary should move from the locus defined as binary in arm2 to the "Ni"-bump in arm1 (illustration in the upper part of fig. 4d). As a result the difference spectrum Y(w2)-Y(w1) (low part of fig. 4d) must have the peak of positive counts and corresponding negative counting tail for the "donors" fragments in the region of binary fission. Evidently the yields of the bump and the "tail" must be equal to each other. In the experiment one observes a superposition of partial contributions from different magic clusters. For instance, the gross central peak in fig. 4b lies on the negative "background" (tail) provided by all less massive magic clusters. The position of the local peaks in fig. 4b could depend from a possible shift in the centers of the spectra in fig. 4a due to independent mass calibrations in the opposite arms of the spectrometer. We have two independent evidences for the required quality of the calibrations. The maximal mass of the light fragment in the massasymmetric fission mode cannot exceed 120 amu due to the known extreme stability of the complimentary heavy fragment (double magic ¹³²Sn nucleus). This is just the feature observed in fig. 4b: the negative yield in the difference spectrum vanishes for the mass partition 120/132 amu. The negative minimum at $M_c/2$ (fig. 4b where M_c is the mass of the fissioning nucleus of 252Cf, shows, that ternary fragmentation is likely to occur in the region of masssymmetric fission as well. Another argument for the quality of the mass calibrations can be inferred from fig. 4c. The figure shows the second derivative of the mass spectrum linked with the box w2 of the data from Ex1 this shows similar peaks as the difference spectrum in fig. 4b. Thus fig. 4b can be treated as a manifestation of a whole sequence of bumps, based on magic spherical and deformed clusters of ^{68,70}Ni, ⁸²Ge, ⁹⁴Kr, ⁹⁸Sr, ¹⁰²Zr, ¹⁰⁸Mo, ¹¹¹Tc. The yield of the most populated "Mo"-bump (A = 106 (111) is about 8×10^{-3} per binary fission, i.e. twice as high as the corresponding value for the "Ni"-bump directly seen in the mass correlation plot (fig. 1a).

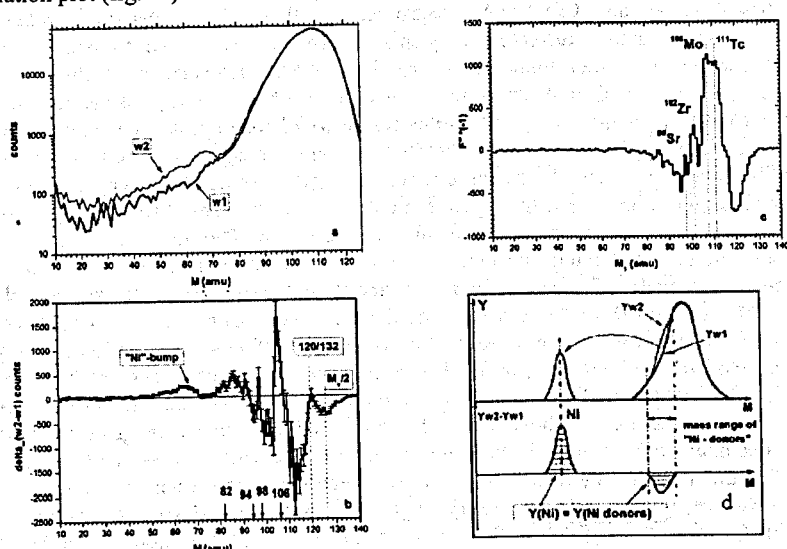


FIGURE 4. a) Projections of the events from box w1 and box w2 (Ex1, shown in fig. 1a onto M_2 and M_1 axes, respectively; b) difference between these projections and, c) the second derivative of the spectrum being the projection of the events from box w2 onto M_1 axis, d) schematic representation of fig. 4) (upper part of the figure) for illustrating a reason of forming a negative tail of the "Ni"-bump in the difference spectrum of yields Y(w2)-Y(w1) (lower part).

RESULTS ON TRUE TERNARY COINCIDENCES

In this section ternary events observed at the COMETA setup will be analyzed. It means that three fragments were really detected in coincidence in each event. The FFs from such events are labeled as m_1 , m_2 , m_3 in an order of decreasing masses in each ternary event. Mass correlation plot for the masses m_1 , m_2 is shown in fig. 5. It is observed only for the events where the fork of two fragments was detected in the spectrometer arm faced to the source backing.

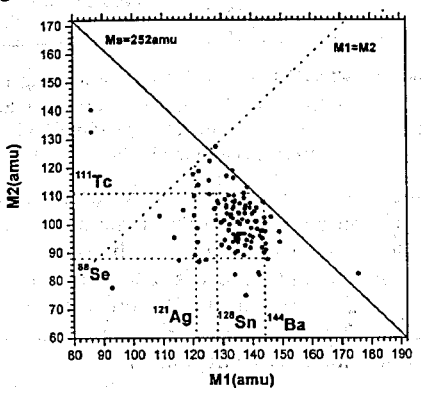


FIGURE 5. Correlation mass plot for two heavy partners of ternary decay. Rectangular structure in its center is bounded by the magic nuclei.

Rectangular structure bounded by the magic nuclei is seen in the center of the plot. Missing masses are ranged from 4 (alpha particle) up to 48 amu. Another distribution (fig. 6) is convenient for testing mass conservation law in ternary decays. Normally experimental points must lie on the line $M_s = 252$ amu (where M_s is a total mass of all three decay partners i.e. $M_s = m_1 + m_2 + m_3$) within mass resolution of the spectrometer. It is not so for the bulk of the points presented in the typical $M_{s12}-m_3$ distribution in fig. 6. It seems they form some families of events which met the condition $m_1 + m_2 = \text{const}$ what corresponds to the fixed mass of the third fragment. But only part of this fragment was actually detected almost in all the events presented. For instance, presumable configuration for the events marked by the circle is shown in the insert of Figure 6. Likely the middle fragment of the initially three body chain was clusterized into two lighter fragments in the scission point and only one of them (14 C) was detected.

The following alternative scenario could give rise to the peculiarity mentioned (fig. 7). After first rupture, for instance, in the configuration shown in the insert of fig. 6, ¹³²Sn nucleus and di-nuclear system Ge/S become free. Then a break-up of the molecule appears to occur due to inelastic scattering in the backing of the source. As a result the scattered Ge nucleus and knocked out ion of ²⁷Al or ¹⁶O can be detected in the corresponding spectrometer arm while the ⁴⁰S nucleus flies in the opposite direction following ¹³²Sn nucleus. Similar process with even larger energy is known as Coulomb fission [3]. The yield of such process is strongly dependent from the binding energy of the molecule and scattering angle. If the scenario under discussion is really realized a knocked out ion can be regarded as a specific spectator of the CCT process.

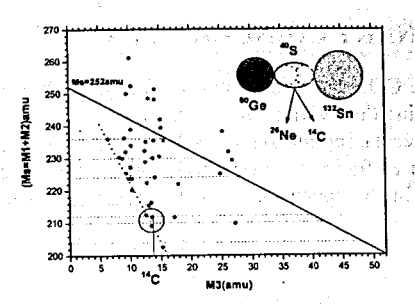


FIGURE 6. Typical distribution $M_{s12} = m_1 + m_2$ vs. m_3 . Presumable pre-scission configuration for the events underlined by the circle is presented in the insert. See text for details.

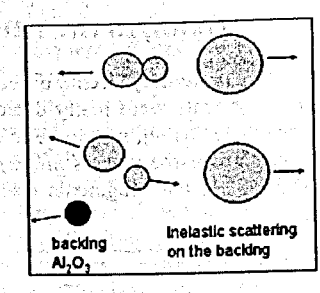


FIGURE 7. Possible way of forming a fork of two fragments flying in the same direction due to a breakup of the di-nuclear molecule in an inelastic scattering in the source backing.

Summing up, the results obtained at the COMETA setup on direct detecting of three partners of at least ternary decay of 252 Cf (sf) can be treated in the frame of two following hypothesis. The first one is that the light detected fragment (m_3) can be some part of the middle clusterized fragment of the three-body chain-like pre-scission configuration in the CCT channel. The second hypothesis treats m_3 as a mass of the ion knocked out from the source backing. The same inelastic scattering gives rise to the break-up of the di-nuclear molecule formed after first rupture of the pre-scission CCT configuration.

TO A UNIFIED MODEL OF TERNARY DECAYS OF LOW EXCITED NUCLEI

For the moment three different types of ternary decays of low excited nuclei are known, namely, conventional ternary fission, polar emission and CCT. It seems there is a deep link between the polar emission and CCT, at least with the CCT accompanied by a light charged particle [4]. It would be extremely interesting to compare all three ternary decays in the frame of the unified experimental approach. We are planning to do this by means of step by step increasing of the aperture of the COMETA spectrometer and the first step has been already done. Recently COMETA-2 set up (fig. 8) was put into operation at the FLNR of the JINR.

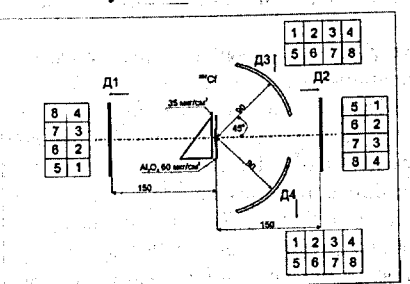




FIGURE 8. COMETA-2 setup. The scheme of the FFs detectors (left side) and their photo (right side).

It complains four mosaics of Si semiconductor detectors of eight diodes each and the micro channel plates based "start" detector with the ²⁵²Cfi inside. The FFs detectors are surrounded by the "neutron belt" which was used previously at the COMETA spectrometer. Processing of the data of the test run is in progress.

CONCLUSIONS

- New evidences were obtained in favor of conclusion that the CCT is due to the
 preformation of at least two magic clusters, deformed as well. The CCT modes based
 on these combinations are more preferable.
- New experimental information obtained gives evidence of a nontrivial scenario of the collinear cluster tri-partition process and structure of the lightest decay partner especially.
- 3. Additional efforts are needed for studying of all known ternary decays in the frame of the unified experimental approach.

REFERENCES

- 1. Yu.V. Pyatkov et al. Eur. Phys. J. A 45 (2010) 29.
- 2. Yu.V. Pyatkov et al., submitted in Eur. Phys. J. A, (2011).
- 3. L. Wilets et al., Phys. Rev. 156 (1967) 1349
- 4. Yu.V. Pyatkov et al., Bulletin of the Russian Academy of Sciences. Physics, v. 75, (2011) 949.

If the second of the second of

STUDY OF RARE MODES OF "COLLINEAR CLUSTER TRI-PARTITION" OF ²⁵²Cf (SF)

D.V. Kamanin¹, Yu.V. Pyatkov^{1,2}, <u>V.D. Malaza³</u>, A.A. Alexandrov¹, I.A. Alexandrova¹, N. Jacobs³, N.A. Kondratyev¹, E.A. Kuznetsova¹, O.V. Strekalovsky¹, A.O. Strekalovsky¹, V.E. Zhuchko¹

¹Joint Institute for Nuclear Research, Dubna, Russia ²Moscow Engineering Physics Institute, Moscow, Russia ³University of Stellenbosch, Faculty of Military Science, Military Academy, Saldanha 7395, South Africa

INTRODUCTION

In our experiments devoted to the study of a new ternary decay of low excited heavy nuclei called "collinear cluster tri-partition" (CCT) [1–3], a specific CCT mode was observed based on the double magic ¹³²Sn cluster. Mass-mass distribution for the events selected by velocities and energies is shown in fig. 1. Tilted red lines correspond to missing magic clusters of ¹³²Sn and ¹⁴⁴Ba. They are vividly seen as well in the mass spectrum (fig. 2) which is the projection along these lines.

Pre-scission configuration which presumably gives rise to the mode under discussion is shown in fig. 3. Sn cluster can "move" as a whole along the cylinder like configuration which consists of residual nucleons. Two light fragments marked by symbols M1 and M2 were actually detected in previous experiment. The mass M2 changes in the range {0÷(252–132–95)} amu while M1 cannot be less 95 amu (deformed magic ⁹⁵Rb nucleus).

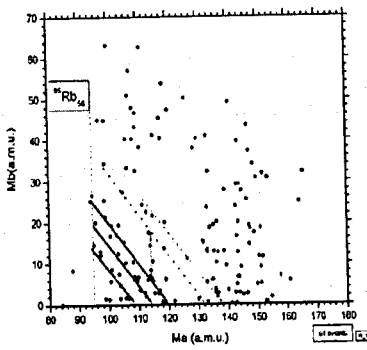


FIGURE 1. Mass-mass distribution of fragments selected by velocities and energies.

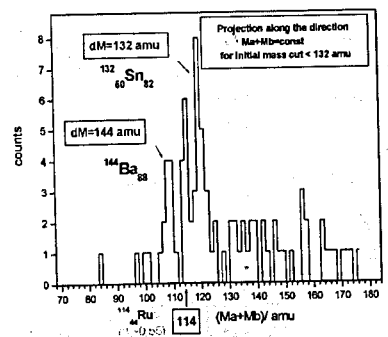


FIGURE 2. Mass spectrum for the structures marked by red in fig. 1. Missing magic clusters of ¹³²Sn and ¹⁴⁴Ba are vividly seen.

MOTIVATION

The question arises whether ¹³²Sn can be changed by also double magic ²⁰⁸Pb? Theoretical indication on such mode was obtained in [4] (fig. 4). It would be a new type of lead radioactivity. Searching for such mode is one of the goals of our forthcoming experiment.

We need as well better statistics to be collected and more precise measurement of time-offlights for studying of the CCT modes observed earlier.

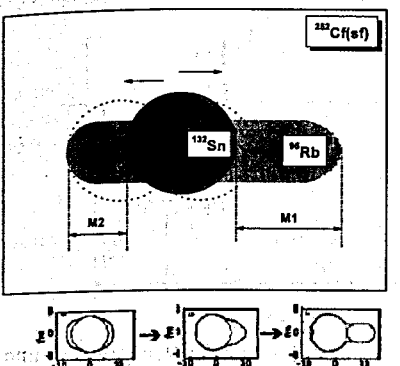


FIGURE 3. Schematic pre-scission configuration of the CCT mode based on the double magic ¹³²Sn cluster.

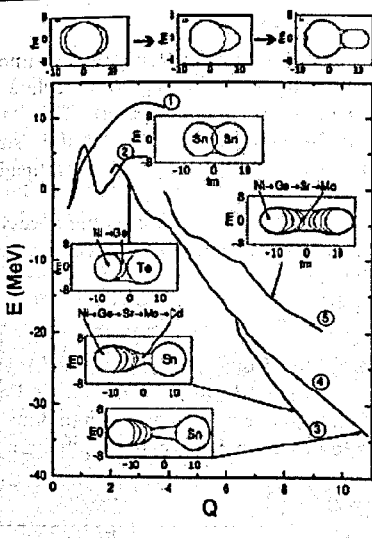
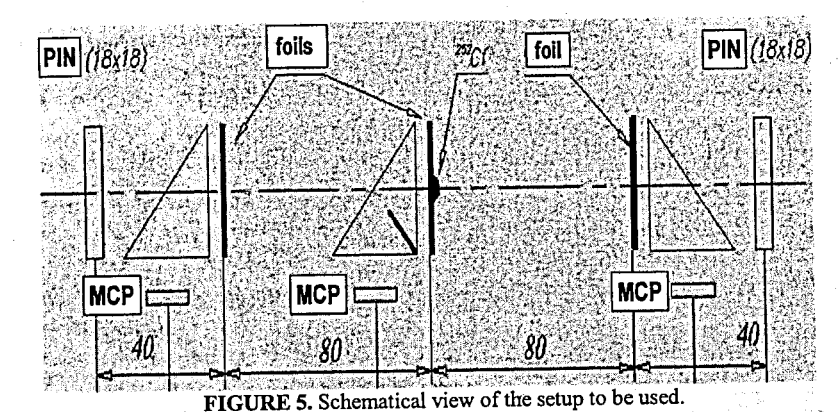


FIGURE 4. The bottoms of the fission valleys as a function of parameter Q (proportional to the quadruple moment) for ²⁵²Cf nucleus. The panels depict the shapes of the fissioning system at the points marked by arrows. Valley 1 in the figure is due to preformation of double magic ²⁰⁸Pb. Evolution of the nuclear shape in this mode is presented above the figure.

EXPERIMENTAL PROBLEMS

As can be referred from fig. 1 the masses of fragments defining the modes under investigation differ radically, namely one of them is very light while the second one is very heavy. Therefore we have a problem involving the method of measuring the correct energy and time-of-flight of heavy ions in the wide range of energies and masses using PIN diodes as "stop" detectors. In order to exclude negative influence of the known "plasma delay" effect for timing of the fragments, three micro-channel based timing detectors will be used (fig. 5).

Also well known "pulse height defect" in silicon semiconductor detectors will be taken into account using special procedure worked out by us earlier [5]. In our previous experiments first approximation approach was used for this purpose (fig. 6).



The "first approximation" is based on the simple transformation of energy and time in channels to MeV and nanoseconds (ns), respectively. Using these values we calculate the mass of the heavy and light fission fragment in atomic mass units (amu). This "first approximation" approach neglects the energy lost in the entrance window of the "start" detector and the source backing, while the PHD is estimated rather roughly. We also neglect the so called "plasma delay" in the time signal.

The "first approximation" comprises of reading the raw data and performs the necessary transformations into the required units. The energy in channels E [ch] is converted according to the following equation to the energy in MeV, E [MeV]:

$$E_i[\text{MeV}] = C \cdot \exp(-\frac{E_i[\text{ch}]}{D}) + E_0$$
 (1)

The values of C, D, and E_0 are determined by using the known positions for the energy peak of light and heavy fragment and the natural alpha peak from ²⁵²Cf with $E\alpha = 6.118$ MeV. The subscript *i* in equation (1–2) shows that each event is processed individually.

The time in channels T [ch] is converted according to the following equation to the time in nanoseconds T [ns]:

$$T[ns] = A \cdot T_i[ch] + B \tag{2}$$

The values of A and B are determined by using the known velocities $V_{L,H}^{ref}$ of light and heavy fragment from literature. The experimental expected time-of-flight in nanoseconds of the light and heavy fragment is calculated as follows:

$$T_{L,H} = \frac{L_{TOF}}{V_{L,H}^{ef}},\tag{3}$$

where L_{TOF} is the flight path of fission fragments. Knowing the values of $T_{L,H}$ from equation (3) we calculate the value of A as follows:

$$A = \frac{T_H[ns] - T_L[ns]}{T_H[ch] - T_L[ch]} \tag{4}$$

Therefore the value of B is calculated as follows:

$$B_{H,L} = T_{H,L}[ns] - A \cdot T_{H,L}[ch]$$
(5)

In principle the value of B obtained from the heavy fragment and the value of B obtained from the light fragment has a significantly small difference from each other, so the average between the two values is used and is given by the following:

$$B = \frac{B_H + B_L}{2} \tag{6}$$

Once we have obtained the values of A and B we apply equation (2) to our raw data to calculate the time in nanoseconds. We then use the time from equation (2) to calculate the velocity in centimeters per nanoseconds as follows:

$$V_i[cm/ns] = \frac{L_{TOF}}{T_i[ns]} \tag{7}$$

Equation (1) and (7) allows us to calculate the mass as follows:

$$M_{i}[amu] = \frac{1.9297E_{i}[MeV]}{(V_{i}[cm/ns])^{2}}$$
 (8)

After processing an amount of data, a mass spectrum is obtained. The process of the "First Approximation" approach is illustrated in fig. 6.

The improved version of code for calculating of fragment mass is presented in fig. 7. The true energy calibration and reconstruction of FF masses is quiet a complicated task do due to the influence of pulse-height defect (PHD). The channel number of energy in which we register the fission fragment depends on the energy of the fission fragment as well as on the PHD. But on the other hand, the PHD depends on the mass and the kinetic energy of the registered fragment. To combine together the calculation of true energy and reconstruction of fission fragments masses we use a specially designed procedure presented in [7–8].

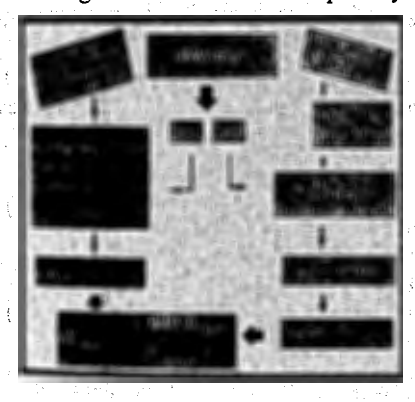


FIGURE 6. "First approximation" approach for calculation of fragment mass.

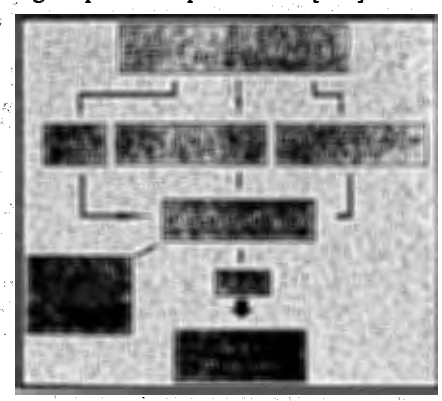


FIGURE 7. Processing of velocity- energy data for calculation of fragment mass. Code is based on parameterization [6] of pulse height defect in PIN diodes.

The main idea of the procedure is to calculate the FF mass spectrum $Y_{ex}(M_{TE})$ depending on current values of parameters and compare this spectrum with a known one from the literature [9]. This procedure is applied to every single detector. The energy E in MeV, of the

registered fission fragment is defined as the sum of the detected energy E_{det} and the pulse-height defect denoted by R(M,E):

 $E = E_{\text{det}} + R(M, E), \tag{9}$

where the detected energy of fission fragments is given by:

$$E_{\text{det}}[\text{MeV}] = E[\text{ch}] \cdot dE / dk + E_0, \tag{10}$$

where dE/dk and E₀ are calibration parameters. These parameters are calculated experimentally by using a high precision pulse generator (in our case we use ORTEC 448 Research Calibrator) and the natural alphas from ²⁵²Cf source. The expression for the pulse-height defect in equation (9) was proposed by Mulgin and his colleagues [6] as the following empirical expression:

 $R(M,E) = \frac{\lambda \cdot E}{1 + \phi \cdot \frac{E}{M^2}} + \alpha \cdot ME + \beta \cdot E, \qquad (11)$

where $\{\lambda, \varphi, \alpha, \beta\}$ are parameters for the true calibration. In addition we know that:

$$E = \frac{M \cdot V^2}{1.9297} , {12}$$

where E is the energy of the FF in MeV, M is the mass of the FF in amu and V is the velocity of the FF in cm/ns. The velocity, for this purpose is calculated using the parameters obtained from time calibration. From the above equations, we can calculate the mass of the fission fragment provided the parameters $\{\lambda, \phi, \alpha, \beta\}$ are known. It is worth noting that the numerical values for the parameters $\{\lambda, \phi, \alpha, \beta\}$ proposed in [6] make it impossible to reconstruct the mass M_{TE} for the FF.

In order to find the correct values of the parameters $\{\lambda, \phi, \alpha, \beta\}$ a special iteration procedure has been designed. This procedure consists in obtaining the solution of the following equation analytically:

$$G(\{\lambda, \phi, \alpha, \beta\}, M) = 0 \tag{13}$$

To obtain the solution of equation (13) above, we combine equation (9), (11), and (12) as follows:

$$\frac{MV^2}{k} = E_{\text{det}} + \frac{\lambda \cdot \frac{MV^2}{k}}{1 + \phi \cdot \frac{V^2}{Mk}} + \alpha \cdot \frac{M^2V^2}{k} + \beta \cdot \frac{MV^2}{k} , \qquad (14)$$

where k = 1.9297. The above equation can be written as follows:

$$M^3 + aM^2 + bM + c = 0, (15)$$

where

$$a = \frac{\phi V^2}{k} + \frac{\beta + \lambda - 1}{\alpha}$$

$$b = \frac{kE_{\text{det}}}{\alpha V^2} + \frac{\phi V^2}{\alpha k} (\beta - 1)$$

$$c = \frac{\phi E_{\text{det}}}{\alpha}$$
(16)

As we can see equation (15) is a third order equation, which means its solution consists of three roots. To select the roots that must be used from the three possible roots, we must take

note of the fact that the mass cannot be negative, so any root that is negative we neglect it. We also neglect the complex roots. In case of three real roots which are greater than zero, we compare them with the value of the mass obtained from "first approximation", i.e. we take the root that is closest to the value of the mass obtained from first approximation. A special program for this purpose was designed using FOTRAN-99 codes.

Using the above procedure we process each event individually based on the current values of $\{\lambda, \phi, \alpha, \beta\}$ and calculate the mass of the fission fragment. The mass is calculated under the condition that $M_{TE} \in [1 \text{ amu}, 252 \text{ amu}]$. After processing an amount of data a mass spectrum is obtained.

The procedure uses the MINUIT package [MIN] to minimize the following criterion function by changing the parameters $\{\lambda, \phi, \alpha, \beta\}$:

$$F = [(\langle ML_{T} \rangle - \langle ML \rangle)^{2} + (\langle MH_{T} \rangle - \langle MH \rangle)^{2}] + \mu \sum_{M_{T}} \frac{(Y(M_{TE}) - Y_{T}(M_{TE}))^{2}}{Y(M_{TE})}$$
(17)

where μ is a free parameter that is chosen by the user and it is used as an input parameter to the MUNUIT minimization procedure. This parameter plays a role of specific relative weight of the second term in the criterion function F. The values <ML> and <MH> are average masses of light and heavy fragments calculated from the experimental mass spectrum Y(M_{TE}). In the above equation the known values from literature are denote by "T". It is worth noting that the first square bracket term in equation (17) is sensitive to the difference between the centers of the mass peaks for the fission fragments while the second term is responsible for the agreement in shapes between the experimental mass spectrum Y(M_{TE}) and the mass spectrum from literature $Y_T(M_{TE})$.

REFERENCES

- 1. Yu.V. Pyatkov et al., Romanian Reports in Physics 59 (2007) 388.
- 2. D.V. Kamanin et al., Int. Journal of Modern Physics E 17 (2008) 2250.
- 3. Yu.V. Pyatkov et al., Eur. Phys. J. A 45 (2010) 29.
- 4. V. Pashkevich et al., Int. J. Mod. Phys. E18 (2009) 907.
- 5. Yu.V. Pyatkov et al., Proc. ISINN-14, Dubna, May 24-27, 2006. Dubna 2007, p. 134.
- 6. S. Mulgin et al., NIM A 388 (1997) 254.
- Yu.V. Pyatkov et al., Proc. ISINN-14, May 24-27, 2006, Dubna, Russia. Dubna (2007), 134.
- Yu.V. Pyatkov et al., Proc. Int. Symposium on Exotic Nuclei (EXON-2006), July 17-24, 2006, Khanty-Mansiysk, Russia, AIP Conference Proceedings, 912 (2007) 144.
- 9. C. Wahl, Atomic data and nuclear data tables 39 (1988) 60.

Relative yields of delayed neutrons and half-lives of their precursors from fission of ²⁴¹Am by neutrons in the energy range 1-5 MeV

Piksaikin V.M., Mitrofanov K.V., Egorov A.S., Goverdovski A.A.

State Scientific Center of Russian Federation Institute of Physics and Power Engineering, Obninsk, Russia

Management of radioactive waste is one of the key issues encountered in considering the prospects for nuclear power. The special place in this issue is paid to the development of concepts and technologies of high-level nuclear waste disposal based on the fundamental possibility of a significant reduction of their lifetime by their transmutation during which the minor actinides and long lived fission products are dangerous. The main source of long-lived components of radioactive nuclear wastes is obtained by the extraction of uranium and plutonium isotopes from spent fuel are minor actinides (MA) - isotopes of neptunium, americium and curium. Several physical processes are currently considering that could form the basis for technology of transmutation radionuclides. Among them the most promising are the processes associated with the use of nuclear reactors and sub-critical systems with high neutron flux generated by particle accelerators.

Delayed neutrons play an important role in the safe management of nuclear power plants and its kinetics. Therefore the development of any of the above concepts of nuclear waste transmutation requires information about the nuclear physical characteristics of delayed neutrons for MA in the reactor energy range of primary neutrons. ²⁴¹Am is one of the "candidates" for transmutation by fission in nuclear reactors of new generation. These reactors will have a harder neutron energy spectrum. Therefore the availability of reliable information about the characteristics of delayed neutrons from fission of ²⁴¹Am by neutrons with corresponding energies is essential for safe operation of the reactor in which such transmutation would be.

The purpose of this study was to measure the energy dependence of the relative yields of delayed neutrons and half-lives of their precursors from fission ²⁴¹Am in the neutron energy range 1-5 MeV.

Experiment

The measurements were made with beams of protons and deuterons of the cascade generator KG-2.5 (FSUE "SSC RF – IPPE"). Generation of neutron beam was carried out by nuclear reaction T(p,n) and D(d,n). The basic experimental method employed in these experiments is based on cyclic irradiations of the ²⁴¹Am samples in a well defined neutron flux followed by the measurement of the time dependence of delayed neutron activity [2]. The variation of the sample irradiation times and the registration time of delayed neutrons can enhance the contribution of certain groups of delayed neutrons in the composite decay curve of the neutron activity. This circumstance makes possible to obtain more reliable information about the characteristics of individual groups of delayed neutrons. In the experiment we used a pneumatic transport system for transferring the sample from the irradiation position to the neutron detector. Two electromagnetic valves are responsible for the sample transportation route. The information on the sample location is obtained from two photodiodes and light sources installed on a flight tube at the sample irradiation position and the central point of the

neutron detector. The time of sample transportation from the irradiation position to the neutron detector was approximately 150 ms that allowed to obtain information about the most short-lived groups of delayed neutrons.

The Faraday cup served as a device for switching on the ion beam to the accelerator target to start the irradiation of a fissionable sample and switching off the ion beam from the target at the beginning of the delayed neutron counting.

The boron counter of SNM-11 type at the operational potential of 650 V in the proportional mode of operation was chosen as the main detector counting unit. In general the neutron detector is an assembly of 30 boron counters distributed in polyethylene moderator along three concentric circles with diameters of 106, 160 and 220 mm. The outer diameter of moderator is 400 mm, its length is 300 mm. In the centre of the detector there is a through hole with diameter of 36 mm to install the sample flight tube. The detector is shielded against the neutron background by borated polyethylene, boron carbide powder and cadmium sheets. The main difficulty in carrying out of the experiment and processing the data was that the sample of 241 Am made of americium dioxide along with a large gamma-ray activity is a source of neutrons produced by the reaction $O(\alpha,n)$. Gamma rays were suppressed by lead cylindrical screen installed in the center of the neutron detector. Neutron background due to the reaction $O(\alpha,n)$ significantly exceeded the background of the experimental hall of the accelerator (the hall plus a sample) and was about 130 counts per second. This is more than two or three order times larger than the value of background that took place, for example, when the characteristics of delayed neutrons on 232 Th, 233 U were measured (see Table 1).

Table 1. Comparison of the background conditions of the experiment with nuclides 232 Th, 233 U and 241 Am. (t – delayed neutron counting interval (s), b – intensity of neutron background (neutron/s), $\Sigma(Nd)$ – number of counts in appropriate time interval (724.5 or 224.5 s))

| | 232 | Th | 23 | ³U | | ²⁴¹ Am | |
|--------------------------------|-------------|-------------|-------|-------|-------|-------------------|-------------|
| t, s | 724.5 | 224.5 | 724.5 | 224.5 | 229.5 | 224.5 | 100 |
| $\Sigma(b)*t / \Sigma(N_d),$ % | 1.10 - 1.84 | 0.35 - 0.58 | 5.95 | 2.69 | 95.2 | 95.1 | 41.5 |
| b, 1/s | 0. | 16 | 0 | .73 | * .: | 129.9 | Tage, Maria |

For obtaining the more information from experiment as possible the optimization of experimental parameters was carried out - such as the time of irradiation, the registration of induced neutron activity, the measurement time of neutron background, the width and the number of channels of a multichannel analyzer designed for measuring the temporal distribution of the intensity of delayed neutrons. As a result the delayed neutron decay curves were obtained from which a statistically significant number of events related to "pure" effect of delayed neutrons was extracted. In Figure 1 you can see an example obtained in one run of measurements of the time dependence of the neutron activity which consists of the induced activity of delayed neutrons and neutrons from the reaction $O(\alpha n)$ in a sample of 241 Am. The dashed line shows separately the contribution of the background from the reaction $O(\alpha n)$ to the total measured activity. Solid line shows the curve obtained by the estimation of parameters of delayed neutrons using an iterative least squares method [3].

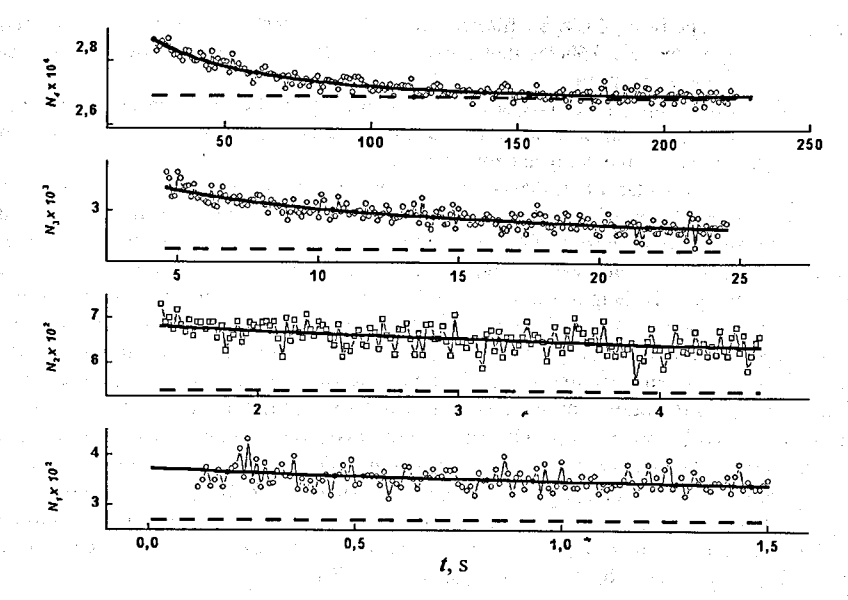


Figure 1. Time dependence of neutron activity caused by the induced activity of delayed neutrons and neutrons from the reaction $O(\alpha n)$ in a sample of ²⁴¹Am. Dashed line - the neutrons from the reaction $O(\alpha n)$. Solid curve - the time dependence obtained in the process of estimating the parameters.

Results

As a result of the measurements a 6-group data on the relative yields of delayed neutrons and half-lives of their precursors were obtained from fission ²⁴¹Am by neutrons at energies of primary neutrons 0.75 - 5 MeV (see Table 2).

Table 2. The energy dependence of the relative abundances and half-lives of their precursors from fission of ²⁴¹Am.

| E_n | | | G | roup numi | oer | | | -m |
|-------------|----------------|--------------------|------------------|------------------|------------------|------------------|--------------------|-----------------|
| MeV | i . | 1 | 2 | 3 | 4 | 5 | 6 | < <i>T</i> >, s |
| 0.62 ± 0.06 | a _i | 0.0434 ± 0.001 | 0.264 ± 0.008 | 0.201 ± 0.006 | 0.317 ± 0.009 | 0.152 ± 0.005 | 0.0229 ±0.0007 | 10.16 + 0.07 |
| 0.02 ± 0.06 | T_i | 54.3 ± 1.6 | 21.94 ± 0.66 | 6.08 ± 0.18 | 2.24 ± 0.07 | 0.496 ± 0.015 | 0.179 ± 0.005 | 10.16 ± 0.27 |
| 0.86 ± 0.06 | ai | 0.0432 ± 0.0005 | 0.271 ± 0.003 | 0.199 ± 0.002 | 0.314 ± 0.004 | 0.151 ± 0.002 | 0.0228 ± 0.0003 | 10.45 + 0.11 |
| 0.80 ± 0.00 | T_i | 53.97 ± 0.61 | 22.61 ± 0.25 | 6.08 ± 0.07 | 2.24 ± 0.03 | 0.498 ± 0.006 | 0.179 ± 0.002 | 10.45 ± 0.11 |

| | | | | | | | | The state of the s |
|-----------------|---------|----------|---------|---------|---------|---------|----------|--------------------------------------------------------------------------------------------------------------------------------------------------------------------------------------------------------------------------------------------------------------------------------------------------------------------------------------------------------------------------------------------------------------------------------------------------------------------------------------------------------------------------------------------------------------------------------------------------------------------------------------------------------------------------------------------------------------------------------------------------------------------------------------------------------------------------------------------------------------------------------------------------------------------------------------------------------------------------------------------------------------------------------------------------------------------------------------------------------------------------------------------------------------------------------------------------------------------------------------------------------------------------------------------------------------------------------------------------------------------------------------------------------------------------------------------------------------------------------------------------------------------------------------------------------------------------------------------------------------------------------------------------------------------------------------------------------------------------------------------------------------------------------------------------------------------------------------------------------------------------------------------------------------------------------------------------------------------------------------------------------------------------------------------------------------------------------------------------------------------------------|
| 1 | ai | 0.0436 | 0.284 | 0.199 | 0.302 | 0.148 | 0.0229 | |
| 0.96 ± 0.06 | | ± 0.0007 | ± 0.005 | ± 0.003 | ± 0.005 | ± 0.003 | ± 0.0004 | |
| 1 | T_{i} | 53.99 | 23.51 | 6.27 | 2.279 | 0,494 | 0.179 | 11.04 ± 0.17 |
| | | ± 0.93 | ± 0.39 | ± 0.11 | ± 0.039 | ± 0.009 | ± 0.003 | |
| 1 | ai | 0.0436 | 0.276 | 0.202 | 0.308 | 0.148 | 0.0228 | |
| 1.06 ± 0.06 | | ± 0.0009 | ± 0.006 | ± 0.004 | ± 0.006 | ± 0.003 | ± 0.0005 | |
| 1.00 = 0.00 | T_i | 54.0 | 23.92 | 6.13 | 2.31 | 0.49 | 0.179 | 10.98 ± 0.21 |
| | | ± 1.1 | ± 0.45 | ± 0.12 | ± 0.05 | ± 0.01 | ± 0.004 | |
| 1 : | a_i | 0.0434 | 0.272 | 0.199 | 0.312 | 0.150 | 0.0229 | |
| 3.27 ± 0.14 | | ± 0.0009 | ± 0.006 | ± 0.004 | ± 0.007 | ± 0.003 | ± 0.0005 | 10 == |
| 1 | T_i | 54.5 | 23.47 | 6.10 | 2.26 | 0.496 | 0.179 | 10.75 ± 0.21 |
| | | ± 1.1 | ± 0.49 | ± 0.13 | ± 0.05 | ± 0.011 | ± 0.004 | |
| | a_i | 0.0433 | 0.251 | 0.201 | 0.329 | 0.153 | 0.0228 | |
| 3.81 ± 0.11 | , | ± 0.0007 | ± 0.004 | ± 0.003 | ± 0.005 | ± 0.003 | ± 0.0004 | 71-2- |
| 2.01 - 1.11 | T_{I} | 54.47 | 21.28 | 5.85 | 2.23 | 0.503 | 0.179 | 9.69 ± 0.13 |
| | | ± 0.93 | ± 0.31 | ± 0.09 | ± 0.04 | ± 0.009 | ± 0.003 | |
| 1 | a_i | 0.0433 | 0.266 | 0.202 | 0.317 | 0.149 | 0.0228 | · · · · · · · · · · · · · · · · · · · |
| 4.27 ± 0.11 | | ± 0.0009 | ± 0.006 | ± 0.004 | ± 0.006 | ± 0.003 | ± 0.0005 | 1016.0 |
| | T_i | 54.4 | 21.75 | 5.99 | 2.30 | 0.49 | 0.179 | 10.16 ± 0.19 |
| | | ± 1.2 | ± 0.41 | ± 0.12 | ± 0.05 | ± 0.01 | ± 0.004 | |
| | a_i | 0.043 | 0.237 | 0.202 | 0.336 | 0.159 | 0.0229 | |
| 4.97 ± 0.13 | | ± 0.001 | ± 0.007 | ± 0.006 | ± 0.008 | ± 0.005 | ± 0.0007 | |
| | T_i | 56.5 | 22.19 | 5.69 | 2.18 | 0.502 | 0.180 | 9.65 ± 0.21 |
| | | ± 1.7 | ± 0.39 | ± 0.15 | ± 0.05 | ± 0.015 | ± 0.005 | |
| | | | | | | | | |

Comparison of parameters (a_i, T_i) -obtained in this work with the relevant data from other authors was carried out in terms of the average half-life of delayed neutron precursors $< T>=\Sigma a_iT_i$ [4]. A similar approach was used for analysis of the behavior of the energy dependence of relative yields and periods of individual groups of delayed neutrons. Figure 2 presents the energy dependence of the average half-life delayed neutrons precursors from fission 24 Am by neutrons calculated and data from other authors.

However, it should be noted that the data of other authors are described as obtained from fission ²⁴¹Am by fast neutrons. It means that these data are representing the averaged values over a finite energy interval that does not allow a correct comparison of these data with the appropriate data of the present work. Figure 2 shows that the present results averaged in the range of 0.6-1 MeV within the limits of their uncertainties agree with the data from the papers [5, 6].

Figure 2 shows that the behavior of the average half-life of delayed neutron precursors in fission ²⁴¹Am in the range of 1-5 MeV is similar to the behavior of this quantity in fission of other nuclei (²³⁸U, ²³⁹Pu, ²³³U, etc.) – average half-life <T> decreases with increasing excitation energy of fissioning nucleus. A specific feature of the energy dependence of the temporal parameters of delayed neutrons in fission ²⁴¹Am is a sharp increase in the average half-life of delayed neutron precursors near the threshold of fission reaction (0.5-1 MeV) up to a maximum value of 11 at the first plateau of fission cross-section. The effect of increasing <T> at the threshold of fission cross section found in fission ²⁴¹Am is not observed in case of other threshold nuclides. Moreover, in case of ²³⁷Np one can observe the opposite effect - the increase of the average half-life of delayed neutron precursors with decreasing excitation energy of compound nucleus [7].

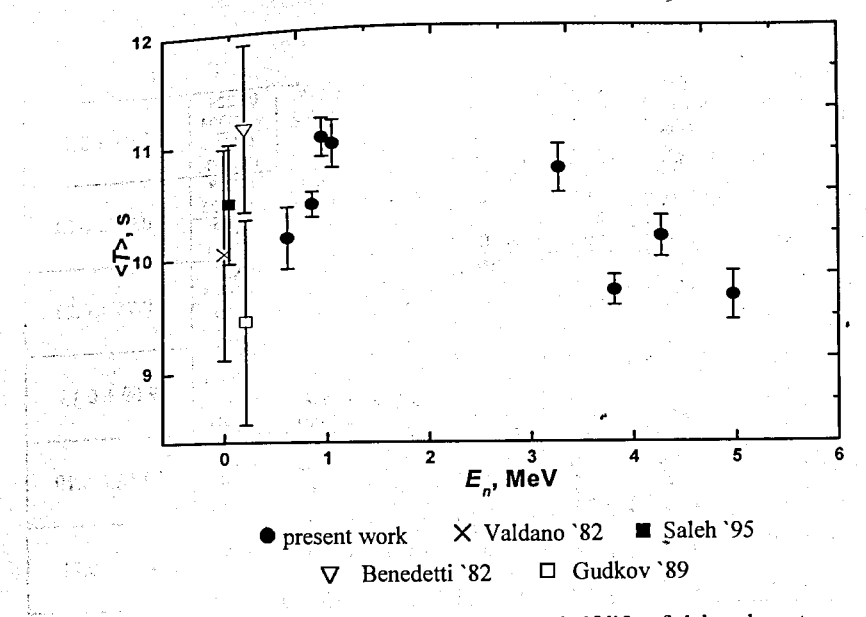


Figure 2. Energy dependence of the average half-life of delayed neutron precursors from fission ²⁴¹Am in a 6-group representation (parameters are taken from the compilation of Spriggs and Campbell [8])

It is well known that the average half-life of delayed neutron precursors for isotopes of one element exponentially depends on the parameters related to nucleon content of compound nucleus $-(A_c-3Z)$ or close to it Z^2/A_c , where A_c – mass number and Z – atomic number of compound nucleus [4]. Estimated value obtained under the systematics of the delayed neutrons characteristics is shown in Figure 3 by dotted line.

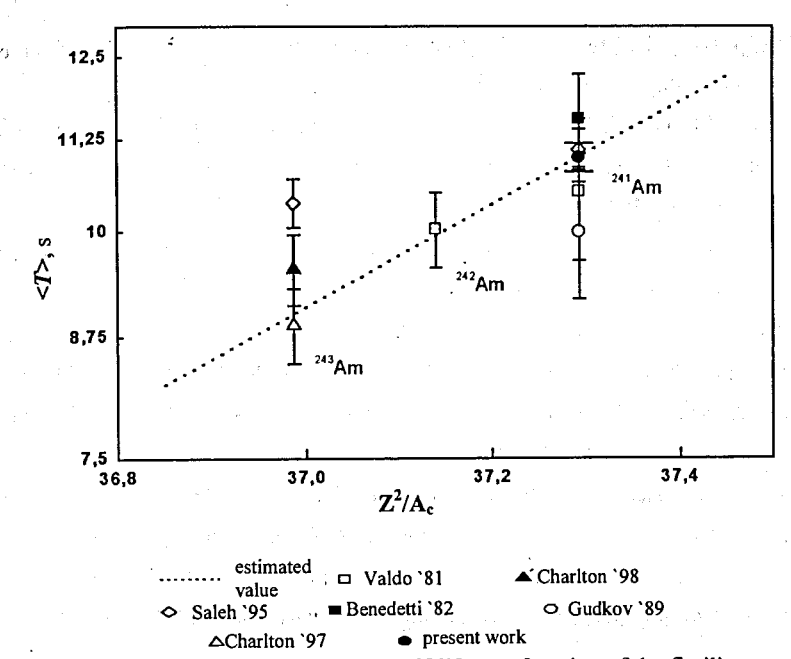


Figure 3. Systematics of the average half-life as a function of the fissility parameter for americium isotopes [4] (values are taken from the compilation of Spriggs and Campbell (1999)).

As it is seen from Figure 3 the data obtained in this study for the relative yield of delayed neutrons and half-lives of their precursors in fission of ²⁴¹Am by neutrons expressed in terms of the average half-life agrees with the estimates made with the help of the systematics of the delayed neutrons time parameters [4].

Literature

- K.Fujimura et al. // Enhancement of Transmutation Characteristics of the Minor Actinide Burning Fast Reactor Core Concept. // J. of Nuclear Science and Technology -2001 - v.38 - No.10 - pp.879-886.
- Piksaikin V. M., Semenova N. N., Mil'shin V. I., Roshchenko V. A., Korolev G. G. //
 Method and setup for studying the energy dependence of delayed neutron
 characteristics in nuclear fission induced by neutrons from the T(p, n), D(d, n), and T(d,
 n) reactions. // Nuclear Experimental Technique. 2006. vol.49. №6. p.765–777.
 http://dx.doi.org/10.1134/S0020441206060030.

- 3. Linnik Yu.V. // Least-squares method and basis of the theory of reduction of observations. // Phys.-Math. Lit. 1958 p334.
- Piksaikin V.M., Isaev S.G., Goverdovski A.A. // Characteristics of Delayed Neutrons: Systematics and Correlation Properties. // Progress in Nuclear Energy – 2002 – v. 41 – No.1-4 – pp. 361 – 384.
- Saleh H. H., Parish T. A., Raman S., Shinohara N. // «Measurements of Delayed-Neutron Decay Constants and Fission Yields from ²³⁵U, ²³⁷Np, ²⁴¹Am and ²⁴³Am» // Nucl. Sci. Eng. – 1995 – vol.125 – p.51.
- 6. Benedetti G., Cesana A., Sangiust V., Terrani M. // Delayed Neutron Yields from Fission of Uranium-233, Neptunium-237, Plutonium-238, -240, -241, and Americium-241 // Nucl. Sci. Eng. 1982. vol.80. p.379.
- Piksaikin V.M., Isaev S.G., Balaksheev Yu.F., Korolev G. G., Semenova N. N., Sergachev A.I., Tarasko M.Z. // Measurements of the relative yields of delayed neutrons and half-lives of their predecessors in fission ²³⁷Np by fast neutrons // Questions of Atomic Science and Technology. – Nuclear Constants. – 1997– №1-2. – p.18.
- 8. Spriggs G.D., Campbell J.M. // A Summary of Measured Delayed Neutron Group
 Parameters // LANL report LA-UR-98-918 1999 Rev.3.

ARE THERE PHYSICAL SPECTATORS OF THE CCT PROCESS?

Yu. V. Pyatkov^{1,2}, D.V. Kamanin¹, A.A. Alexandrov¹, I.A. Alexandrova¹, N.A. Kondratyev¹, E.A. Kuznetsova¹, O.V. Strekalovsky¹, V.E. Zhuchko¹

¹Joint Institute for Nuclear Research, Dubna, Russia ²Moscow Engineering Physics Institute, Moscow, Russia

INTRODUCTION

In our recent publications [1] we have presented experimental evidences of existing of a new type of ternary decay of heavy low excited nuclei called by us collinear cluster tripartition (CCT). The results were obtained in the frame of the "missing mass" approach. It means that only two from at least three decay partners were actually detected whereas a total mass of these fragments being less the mass of mother system serves a signature of multibody decay. Evidently direct detection of all CCT products proves to be a most convincing experimental approach but much complicated one because mosaic detection systems must be used to achieve the goal.

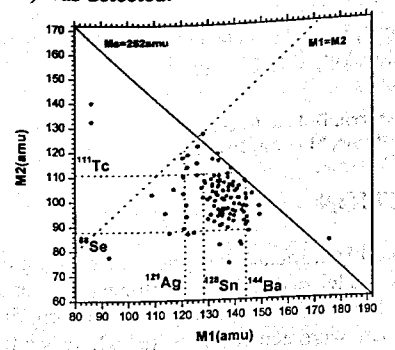
COMETA (Correlation Mosaic E-T Array) setup aimed at studying of rare multibody decays was put into operation recently in the Flerov Laboratory of the JINR. It is a double arm time-of-flight spectrometer which includes micro-channel plate (MCP) based "start" detector with the ²⁵²Cf source inside, two mosaics of eight PIN diodes each and a "neutron belt" comprises 28 ³He filled neutron counters. Below we discuss some results obtained at the COMETA setup.

LIGHT CHARGE PARTICLES ACCOMPANIED CCT: SPECTATORS OR PARTNERS OF THE DECAY?

In this section ternary events observed at the COMETA setup will be analyzed. It means that three fragments were really detected in coincidence in each event. The fission fragments (FFs) from such events are labeled as m_1 , m_2 , m_3 in an order of decreasing masses in each ternary event. Mass correlation plot for the masses m_1 , m_2 is shown in fig. 1. It is observed only for the events where the fork of two fragments was detected in the spectrometer arm faced to the source backing.

Rectangular structure bounded by the magic nuclei is seen in the center of the plot. Missing masses are ranged from 4 (alpha particle) up to 48 amu. Another distribution (fig. 2) is convenient for testing mass conservation law in ternary decays. Normally experimental points must lie on the line Ms = 252 amu (where Ms is a total mass of all three decay partners i.e. $Ms = m_1 + m_2 + m_3$) within mass resolution of the spectrometer. It is not so for the bulk of the points presented in the typical Ms_{12} - m_3 distribution in fig. 2. It seems they form some families of events which met the condition $m_1 + m_2 = const$ what corresponds to the fixed mass of the third fragment. But only part of this fragment was actually detected almost in all the events presented. For instance, presumable configuration for the events marked by the circle is shown in the insert of fig. 2. Likely the middle fragment of the initially three body

chain was clusterized into two lighter fragments in the scission point and only one of them (14C) was detected.



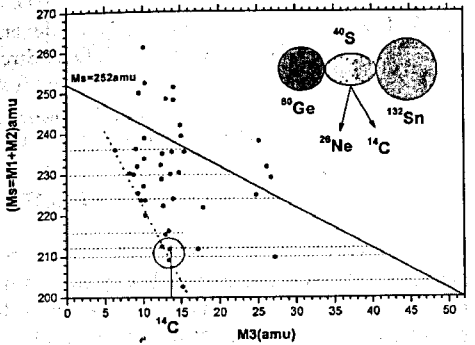


FIGURE 1. Correlation mass plot for two heavy partners of ternary decay. Rectangular structure in its center is bounded by the magic nuclei.

FIGURE 2. Typical distribution $Ms_{12} = m_1 + m_2$ vs. m_3 . Presumable pre-scission configuration for the events underlined by the circle is presented in the insert. See text for details.

The following alternative scenario could give rise to the peculiarity mentioned (fig. 3).

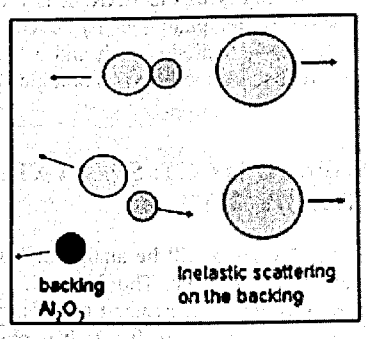


FIGURE 3. Possible way of forming a fork of two fragments flying in the same direction due to a breakup of the di-nuclear molecule in an inelastic scattering in the source backing.

After first rupture, for instance, in the configuration shown in the insert of fig. 2, ¹³²Sn nucleus and di-nuclear system Ge/S become free. Then a break- up of the molecule appears to occur due to inelastic scattering in the backing of the source. As a result the scattered Ge nucleus and knocked out ion of ²⁷Al or ¹⁶O can be detected in the corresponding spectrometer arm while the ⁴⁰S nucleus flies in the opposite direction following ¹³²Sn nucleus. Similar process with even larger energy transfer is known as Coulomb fission [2]. The yield of such process is strongly dependent from the binding energy of the molecule and scattering angle. If the scenario under discussion is really realized a knocked out ion can be regarded as a specific spectator of the CCT process.

Summing up, the results obtained at the COMETA setup on direct detecting of three partners of at least ternary decay of ²⁵²Cf (sf) can be treated in the frame of two following hypothesis. The first one is that the light detected fragment (m₃) can be some part of the middle clusterized fragment of the three-body chain-like pre-scission configuration in the

CCT channel. The second hypothesis treats m₃ as a mass of the ion knocked out from the source backing. The same inelastic scattering gives rise to the break-up of the di-nuclear molecule formed after first rupture of the pre-scission CCT configuration. In the latter case lightest detected fragment plays a role of the CCT spectator.

UNIDENTIFIED CCT SPECTATORS

Analysis of the data obtained at the COMETA setup let us to suppose that sometimes we have the "start" signals provided by the MCP based detector to be shifted as compared to the "normal" ones delivered by the accelerated electrons (mode_1 of the detector operation) (fig. 4). In order to test this hypothesis a series of dedicated experiments were carried out. In one of them the external accelerated greed of the electrostatic mirror was switched off (mode_2).

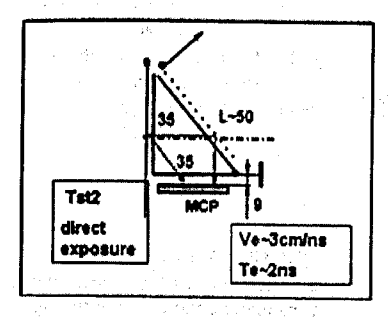
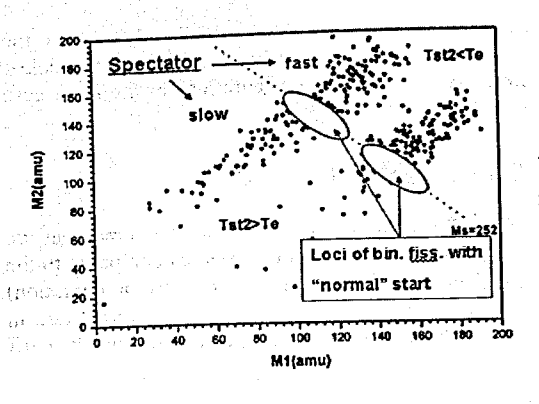


FIGURE 4. MCP based "start" detector. The MCP can be hit by the accelerated electrons produced by the ion passing through the detector or directly by some CCT spectator.

and the second

Nevertheless there were signals from the detector resulted from the direct exposure of the MCP by an unknown ionizing substance. Time-of-flight channel was previously calibrated at the usual operation of the timing detector (the mirror is switched in, mode_1). Typical time-of-flight (Te) of the path "emitting foil-MCP" and corresponding velocity of the electrons are marked in fig. 4. For a spectator time-of-flight of the direct path from the foil to the MCP is designated Tst2. FFs correlation mass-mass distribution obtained under condition that the "start" detector was operated in mode_2 is presented in fig. 5. The position of the loci of conventional binary fission known due to the calibration is marked by the ovals. As can be inferred from the figure direct hitting of the MCP can appear to occur by the CCT spectator which could be both faster (Tst2 < Te) or slower (Tst2 > Te) the accelerated electrons provided the signal in mode_1.

In the next experiments two "start" detectors were simultaneously used operated in mode_1 and mode_2 respectively. In this case Tst2 parameter was used for selecting of fission events. Mass-mass distribution of fission events under condition that slow spectator gave a signal in MCP 2 is presented in fig. 6. Rectangular structure bounded by magic nuclei is seen in the center of the plot. The upper boundary of the rectangle coincides with the line M1 + M2 = const (missing ¹⁸O nucleus). Similar line but starting from its low left corner (marked by the arrow) corresponds to the missing ³⁴A1 nucleus. The structure was never observed before at another gating.



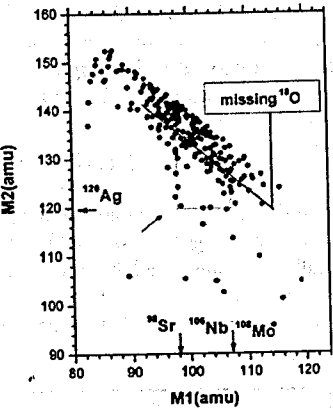
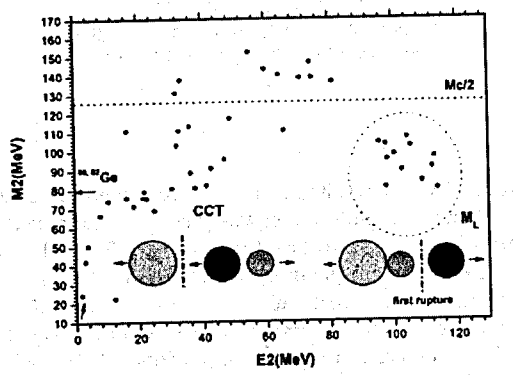


FIGURE 5. Correlation plot of the masses of fragments detected in coincidence in the opposite arms of the COMETA setup. See text for details.

FIGURE 6. Mass-mass distribution of the fission events registered in coincidence with slow spectator. See - text for details.



distribution in one of the spectrometer arms under condition that timing detector operated in mode 2 was heated by some spectator and total mass of two detected fragments is less than 252 amu. See text for details.

Mass-energy distribution of fission events which met the conditions that total mass of two detected fragments is less than 252 amu and some spectator heated the timing detector operated in mode 2 is shown in fig. 7. Two groups of events below the line Mc/2 where Mc is a mass of the decaying system are seen. They radically differ by the energy. The group of events inside the circle shows masses and energies typical for the fragments of the light mass peak of conventional binary fission. At the same time the fragments with similar masses can have the energies approximately 70 MeV lower. Keeping in mind that in fact according to the gating all the events presented in fig. 7 are ternary ones two different pre-scission configurations shown in the bottom of the plot give rise to the corresponding groups of the decay events under discussion. An interesting peculiarity of the low energy group of events should be stressed. There is a specific shoulder at the mass ~80amu associated with magic Ge nucleus. While pre-scission elongation of the decaying system increases due to Coulomb forces the mass of the light fragment (Ge) stays unchanged in some range of elongations and

only then destroying of the Ge cluster appears to occur with the transfer of the nucleons to the heavy fragment.

In the frame of the experiments discussed in this section we cannot identify spectators used for the gating of fission events. Nevertheless, gated data contain original manifestations of different CCT modes. Thus it is promising way of revealing the CCT events to be developed in forthcoming experiments.

CONCLUSIONS

- Experimental approaches additional to the missing mass method confirm the existence of the CCT decay channel.
- New experimental information obtained gives evidence of a nontrivial scenario of the collinear cluster tri-partition process and structure of the lightest decay partner especially.
- 3. Further studying of the process stays an actual task.

REFERENCES

- 1. Yu.V. Pyatkov et al., Eur. Phys. J. A 45 (2010) 29.
- 2. L. Wilets et al., Phys. Rev. 156 (1967) 1349.

INVESTIGATIONS OF THE NEUTRON CROSS-TALK EFFECT IN DEMON DETECTORS

Telezhnikov S.A.*, Kopatch Yu.N.*, Mezentseva Zh.*, Stuttge L.°, Goennenwein F.d, Mutterer M.*, Chernysheva E.b, Dorvaux O.°, Hanappe F.f, and Hambsch F.-J.*

*Frank Laboratory of Neutron Physics, JINR, 141980 Dubna, Russia

b Flerov Laboratory of Nuclear Reactions, JINR, 141980 Dubna, Russia

c Institut de Recherches Subatomiques, F-67037 Strasbourg Cedex, France

d Physikalisches Institut der Universität, D-72076 Tübingen, Germany

f Institut für Kernphysik, Technische Universitt, D-64289 Darmstadt, Germany

f Universite Libre de Bruxelles, 1050 Bruxelles, Belgium

EC-JRC-Institute for Reference Materials and Measurements, Retieseweg 111, B-2440

Geel, Belgium

1. Introduction

The experiment on fragment-neutron angular correlations, aimed at the investigation of the influence of fragment angular momentum (spin) on the neutron emission process is performed at Strasbourg (France) [1] using the CORA setup, which consists of the double ionization chamber CODIS [2] for measuring the fission fragments and a set of DEMON neutron detectors [3]. It is well established that the prompt neutrons evaporated from the fragments of nuclear fission are emitted anisotropically with respect to the fission axis, main source of the anisotropy being the kinematic focusing of the neutrons, emitted from the moving fragments [4, 5]. However, various attempts to analyze the experimental data on neutron emission anisotropy lead to a conclusion that the anisotropy cannot be fully described only by the kinematic focusing, but an additional component of the neutron emission should exist, which is either isotropic (or close to isotropic) in the laboratory system – so called scission neutrons, or anisotropic in the center-of-mass system of the fission fragments [6], which leads to a slight change in the neutron emission anisotropy in the laboratory system, observed experimentally.

In the CORA experiment triple fragment-neutron-neutron angular correlations in the spontaneous fission of ^{252}Cf are analyzed, which are supposed to be sensitive to the anisotropy of the neutron emission with respect to the fragment spin direction. The preliminary analysis of the experimental data showed that one of the most important sources of the background is the so called cross talk effect – scattering of neutrons between neighboring DEMON detectors. The main aim of the present work is to obtain quantitative characteristics of the cross-talk effect in the DEMON detectors.

In order to investigate the cross talk effect and its influence on the main experiment two dedicated measurements have been performed. In both of them an Am-Be neutron source was used, which emits only one neutron at a time, thus any measured neutron-neutron coincidence in two or more neutron detectors should be due the cross talk effect. In the first experiment two separate DEMON detectors were placed at a distance to the Am-Be neutron source, approximately corresponding to the geometry of the main experiment. Neutron-neutron coincidences were measured as a function of the distance between the two DEMON detectors. In the second experiment the same Am-Be neutron source was

placed at the position of the ²⁵²Cf source and neutron-neutron coincidences were measured with the full set of DEMON detectors.

The main parameter of the cross talk effect, which can be measured, is its probability. If a neutron is registered in detector a, then scattered and registered in detector b, the probability of such a process in terms of measurable values can be defined as

$$P_{ab} = N_{ab}/N_a \tag{1}$$

where N_a is the number of neutrons registered in detector a and N_{ab} is the number of neutrons which were scattered from detector a and registered in both detectors a and b in coincidence. It can be shown that the probability of cross talk observation, defined in such a way, is equal to

$$P_{ab}(E_n) = p_{ab}(E_n) \times \epsilon_b(E'_n) \tag{2}$$

where p_{ab} is the probability of neutron scattering from detector a to detector b, E_n and E'_n - energies of the incident and scattered neutron, and ϵ_b is the detection efficiency of detector b.

2. Experiment with two detectors

In this experiment one DEMON detector was placed at a fixed position at a distance 75 cm from the source to the front side of the detector. The second detector was placed at six different positions with distances between the centers of the two detectors: 27.5, 33.5, 40.0, 46.0, 53.0 and 59.0 cm; and distances from the front side of the second detector to the source: 77.0, 75.0, 75.0, 74.0, 75.0 and 82.0 cm, respectively. In addition, a BaF₂ detector was placed near the source and was used as a trigger by gamma-rays, emitted in coincidence with neutrons. For each DEMON detector the time-of-flight was measured with respect to the BaF₂ signal, as well as the standard Q_{total} and Q_{slow} values – total and slow parts of the collected charge, allowing for the n-gamma discrimination.

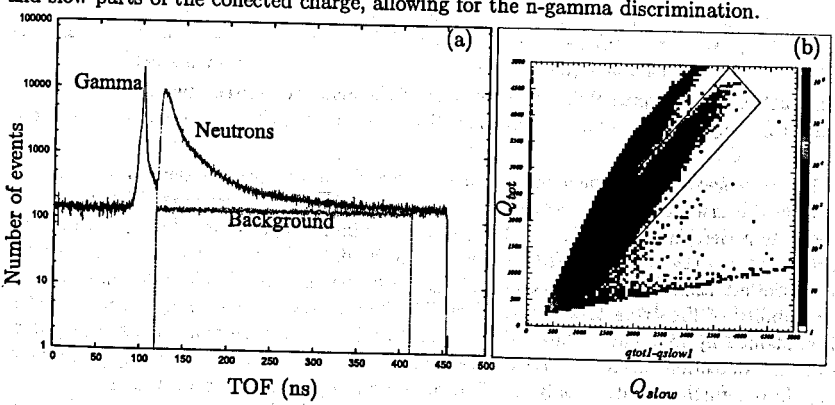


Figure 1: (a) TOF spectrum from detector 1. (b) Neutron-gamma separation plot.

The TOF spectrum from detector 1 is shown in Fig.1 (a). At this distance the time-of-flight parameter could be effectively used for neutron-gamma separation. The background

was assumed to be constant in time, it was determined from the region on the left side from the gamma peak and extrapolated to the full spectrum. The time of appearance of the coincident signals in detectors 1 and 2 relative to the start signal from BaF_2 was used for the identification of the primary and scattered neutrons – the earlier signal was always interpreted as the primary event. Those events which appeared in both detectors within a coincidence window of 10 nsec were assumed to be neutron-gamma cross talk events (most probably due to the $(n, n'\gamma)$ process) and were excluded from the analysis.

Another method of neutron-gamma separation is provided by the pulse-shape analysis of DEMON signals. Figure 1 (b) shows the Q_{total}/Q_{slow} plot with neutron events selected by a polygon. As one can see from the TOF spectrum, the admixture of gamma-ray events in the neutron part is rather small, thus the time-of-flight method could be used alone for the n-gamma separation. The Q_{total}/Q_{slow} method is less accurate, especially in the region of small amplitudes where neutrons and gamma-rays practically overlap, so it was used only as extra more strict criterion in addition to the time-of-flight separation.

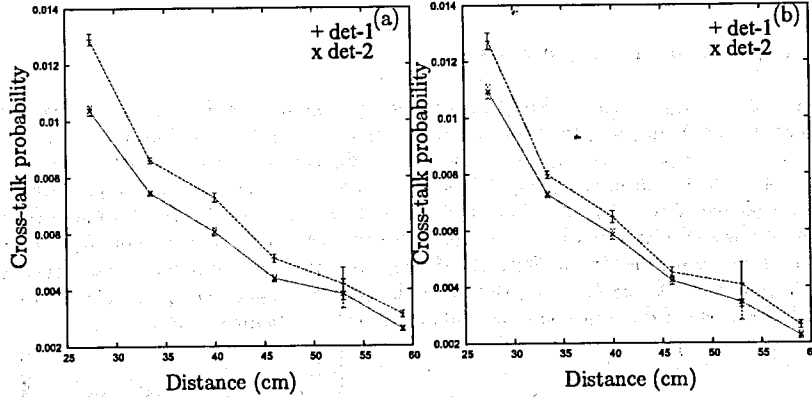


Figure 2: Cross talk probability as a function of the distance between two DEMON detectors. (a): only TOF n-gamma separation; (b): TOF + Q_{total}/Q_{slow} n-gamma separation.

Figure 2 shows the dependence of the cross talk probability, as defined by formula (1), on the distance between the centers of two DEMON detectors with TOF n-gamma separation (left) and with TOF + Q_{total}/Q_{slow} n-gamma separation (right). Two curves correspond to the scattering from detector 1 to detector 2 and vice versa. One can see that the addition of more strict Q_{total}/Q_{slow} criterion practically doesn't influence the probability of the cross talk effect. The difference of the effects for detectors 1 and 2 is explained by different settings of the electronic detection threshold, which resulted in different detection efficiency and different cross talk probabilities according to formula (2). In our further analysis only the TOF n-gamma separation method was used.

The dependence of the cross talk effect on the energy of incident neutrons has been also analyzed. Neutron energy was determined by the time-of-flight method, and the cross talk probability as a function of distance was plotted for several intervals of incident (primary) neutron energy. It is shown in Fig. 3 (left) for the neutrons scattered from

detector 1 to detector 2. The cross talk probability slightly increases with the increase of the neutron energy. Such an increase is indeed expected according to formula (2). It turns out that the most important parameter, responsible for the magnitude of the cross talk effect, is the efficiency of detector b, which is mainly governed by the setting of the energy detection threshold. For the DEMON detectors this threshold is typically between 500 keV and 1 MeV. For low energy incident neutrons, hitting detector a, there will be always relatively large number of scattered neutrons, which fall below the detection threshold in detector b. Such events will not be registered in the experiment and will not contribute to the observable cross talk effect. With an increase of the neutron energy the number of those neutrons which fall below the threshold will decrease, thus increasing the detection efficiency and, in turn, the observable cross talk effect.

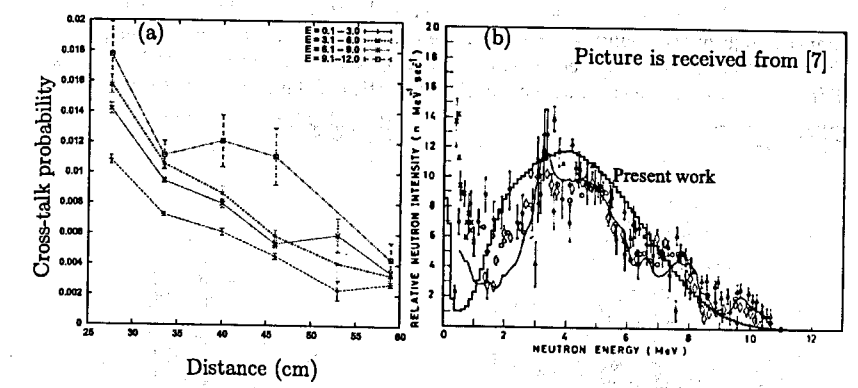


Figure 3: Left: Cross talk probability as a function of the distance between two DEMON detectors for different incident neutron energies, from bottom to top: 0.1-3 MeV; 3.1-6 MeV; 6.1-9 MeV; 9.1-12 MeV. Right: Energy spectrum of neutrons from the Am-Be source, reconstructed using the time-of-flight method and compared to literature data.

An attempt to obtain spectrum of neutron energies from Am-Be source by TOF method was made. As the length of the detector (20 cm) is comparable with the distance to the source, there is rather large uncertainty in the neutron flight paths as long as information about a place of interaction of neutrons in detector is absent. In order to account for this uncertainty in the process of conversion from TOF to neutron energy the interaction point of each event was randomly distributed along the full length of the sensitive part of the detector. The resulting neutron energy spectrum appeared to be smoothed. It is plotted as thick line in Fig. 3 (right) in comparison with results of other experiments and calculated curve from [7].

2. Experiment with sixty detectors

Sixty DEMON detectors, which were installed for the CORA experiment, were used in the second part of the present work. The geomentry of the experiment, as well as the electronics remained basically the same as in the main experiment with only minor

modification. The DEMON detectors were placed in nearly spherical geometry around the source. Two types of mechanical support, each holding 5 DEMON detectors were used (see Fig. 4). Ten such supports (five of each type) were placed in a circle around the source in alternating order. Thus, there were 5 horizontal rings of 10 DEMON detectors each, and two rings (top and bottom) of 5 DEMON detectors. The distance from the source to the front side of the detectors in the middle ring was 60 cm. Schematically top view of the positions of all detectors is shown in Fig. 5.

In this test measurement an additional BaF_2 detector was used in the same way as in the experiment with two DEMON detectors. It was placed in the lower part of the installation in such a way that the Am-Be source could be placed on it, being in the geometrical center of the set-up, e.g. in the position of the ^{252}Cf fission source. The lower hemisphere of the full installation was partially shaded by the BaF_2 detector. This changed slightly the counting rates of the detectors located in the lower hemisphere and the energy spectrum of the neutrons, registered by those detectors, but we believe that it didn't have any significant influence on the properties of the cross talk effect.

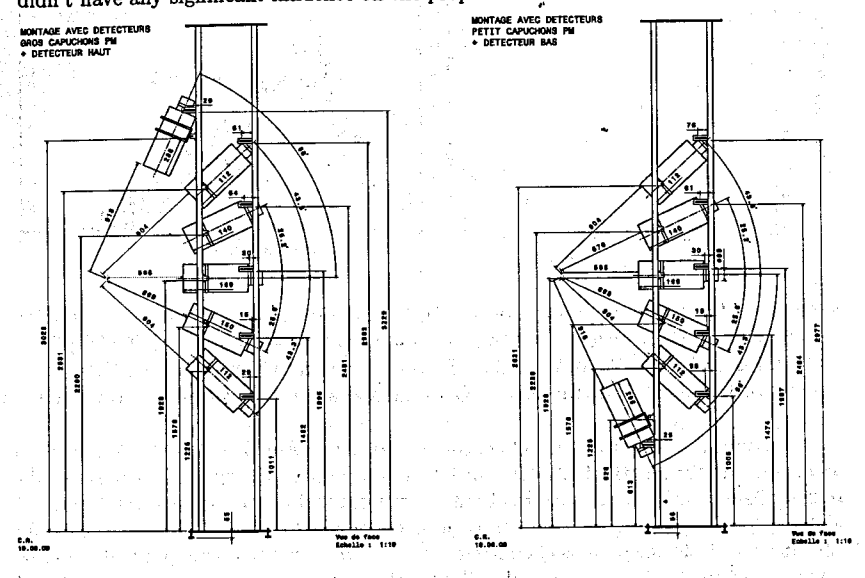


Figure 4: Two types of DEMON supporting structures used in the experiment

As in the experiment with two detectors, BaF_2 was used as a start for the time-of-flight measurement, and for each DEMON detector the TOF, Q_{total} and Q_{slow} parameters were recorded. A coincidence between the BaF_2 and any of the DEMON detectors was used as a trigger. Those events which occurred simultaneously in any pair of DEMON detectors within a given coincidence time window and which were identified as neutron events were assumed to be the cross talk events. The background due to random coincidences was determined for each DEMON detector in the same way as in the first part of the

present work. For simplicity reasons neutrons and gamma-rays were separated using only the time-of-flight method, keeping in mind the result from the first experiment which demonstrated that the more strict Q_{total}/Q_{slow} n-gamma separation doesn't change the measured probability of the effect. As in the experiment with two detectors, the event, which arrived first after the start signal from BaF₂, was assumed to be the primary neutron event, all subsequent events were assumed to be scattered ones. Those events which occurred within a time window of 10 nsec after the primary event were counted as neutron-gamma cross talk and were excluded from the analysis.

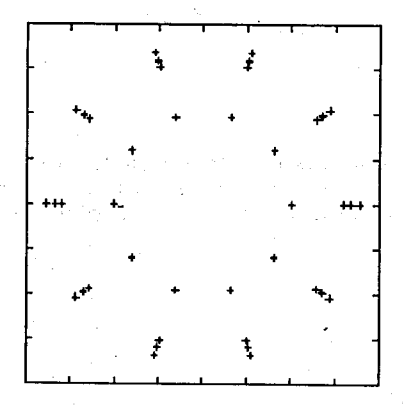


Figure 5: Top view of positions of detectors

During the experiment more than 128 millions events were collected. Only two-fold coincidences between any pair of DEMON detectors were analyzed as cross-talk events. Higher multiplicities give only minor contribution to the effect.

Figure 6 (left) shows the normalized total number of events collected by seven horizontal rings of DEMON detectors. The rings are numbered from top to bottom. The total number of counts in each ring is divided by the number of detectors in the ring (five detectors in rings 1 and 7 and ten detectors in rings 2-6). In addition, it is weighted by the squared inverse distance to the corresponding ring to compensate for the differences in solid angle. In the right side of Fig. 6 the mean number of double coincidences in the same rings is plotted, normalized to the corresponding number of single coincidences. In both plots all measured events were summed up, without separation of neutrons and gammarays. The first figure demonstrates the differences in efficiencies of the DEMON detectors. It predictably drops for those detectors, which are located in the lower hemisphere, as they are partially shaded by the BaF2 detector. The second plot, which shows the ratio of multiplicities 1 and 2 for each ring, indicates the differences of the cross talk probability for each ring, albeit both, for neutrons and gamma-rays. One can see that the presence of the BaF2 detector has almost no influence on it (except for the slight difference at ring 7). The increase of the cross talk for the central rings is easily explained by the closer distance between neighboring detectors in these rings.

on the control lights with a first executing dis-

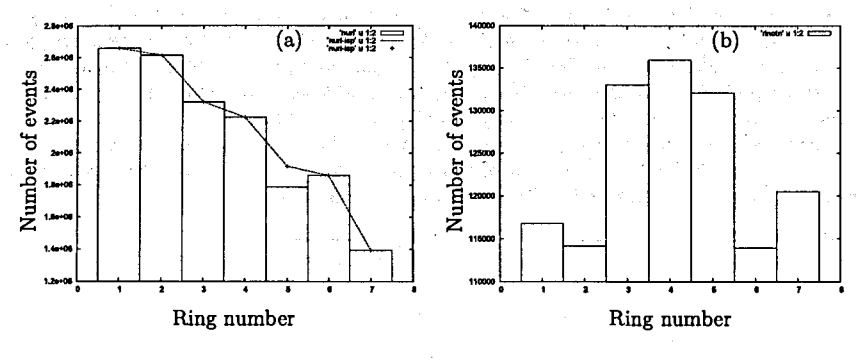


Figure 6: Left: Mean number of events with multiplicity 1 registered in in each ring of detectors. Right: Mean number of events with multiplicity 2, normalized to multiplicity 1, registered in each ring of detectors. Rings are numbered from top to bottom.

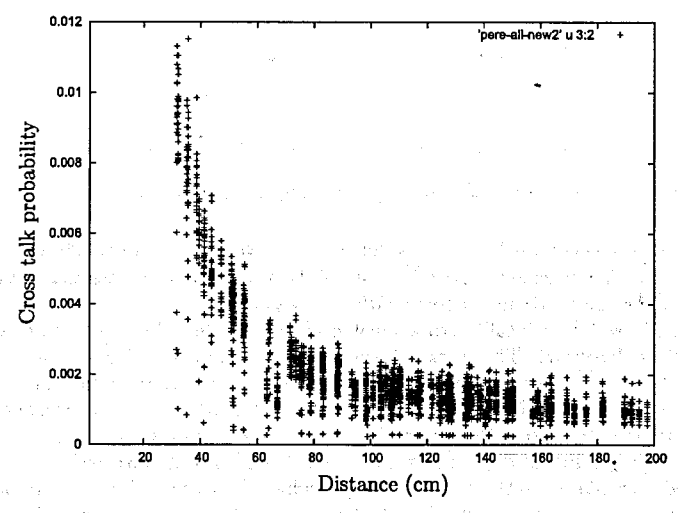


Figure 7: Cross talk probability as a function of distance between two detectors for all possible pairs of detectors.

From all obtained statistics the events with multiplicity 2 for all 60 detectors were analyzed in the following steps:

- 1. Neutrons were separated from gamma-rays using time-of-flight spectra, as in Fig. 1(a).
- The primary neutron event was assumed to be the one having smaller TOF value with respect to the start signal from the BaF₂ detector. The second event was assumed to be scattered one.

- 3. If value tof(2) tof(1) was smaller than 10 ns, such an event was supposed to be neutron-gamma scattering and was excluded from the analysis.
- 4. For all pairs of detectors total number of neutron-neutron coincidences N_{ab} and N_{ba} (see formula 1) was determined. At the same time, number of single neutron events in each detector was counted.
- 5. The cross talk probability was determined for each pair of detectors as the ratio between the number of coincident and single events, as defined by formula 1.

The resulting cross talk probability is plotted in Fig. 7 as a function of the distance between two detectors for all possible pairs of DEMON detectors.

3. Conclusions

The dedicated experiments on cross talk with two DEMON detectors and with sixty detectors in the same arrangement as the main experiment demonstrated that the probability of its registration is about 1% when the distance between the centers of the detectors is about 30 cm. It drops by a factor of 5 when the distance increases by a factor of 2 to 60 cm. More strict $n-\gamma$ separation using Q_{total}/Q_{slow} plots doesn't change the probability of the cross talk observation. The main factor which has large influence on the measured cross talk effect is the neutron detection efficiency of the second detector (the one which measures scattered neutrons). A possible way to reduce the cross talk effect in an experiment would be to increase the registration threshold of all detectors. Application of a special filter for cross talk rejection, as it was proposed in [8] and tested in [9] is even more efficient way for reducing the background in the experimental data, caused by the cross talk effect. The final plot (Fig. 7) shows large fluctuations in cross talk detection probabilities between different pairs of detectors even at the similar distances between them. The reason for these discrepancies is most probably the above mentioned differences in the detection efficiency, which is caused by different settings of electronic thresholds or different amplification of the signals in individual detectors.

References:

- [1] L. Stuttge et al, Proc. Int. Seminar on Fission, Gent, Belgium, 2010, p. 181
- [2] Yu.N. Kopach et al, Phys. Rev. Lett. 82, (1999), p. 303
- [3] Tilquin I. et al, NIM A 365 (1995) p 466.
- [4] H.R.Bowman et al: Phys. Rev.126(1962)2120
- [5] K.Skarsvag and K.Bergheim: Nucl. Phys. 45(1969)72
- [6] V.E.Bunakov et al, Proc. Int. Sem. ISINN-13, Dubna 2005, p 293
- [7] A. D. Vijaya and Arun Kumar, NIM A 111 (1973) pp 435-440.
- [8] F.M. Marques et al: NIM A 450 (2000) 109
- [9] E. Prokhorova et al: Int. Seminar ISINN-14, Dubna, Russia, 2006, p. 128

Digital pulse processing ionization chamber pulses

Sh. Zeynalov^a, O. Zeynalova^{ab}, M. Nazarenko^b, F.-J. Hambsch^c, S. Oberstedt^c

^aJINR-Joint Institute for Nuclear Research, Dubna, Moscow region, Russia ^bMoscow State Institute of Radioengineering and Automation, 78 Vernadski Avenue, 119454 Moscow, Russia

^cEC-JRC Institute for Reference Materials and Measurements, Retieseweg 111, 2440 Geel, Belgium

Abstract. The purpose of the present paper was to report the recent results, obtained in development of digital pulse processing mathematics for prompt fission neutron (PFN) investigation using twin ionization chamber (TIC) along with fast neutron time-of-flight detector (ND). Due to well known ambiguities in literature (see refs. [4, 6, 9 and 11]), concerning a pulse induction on TIC electrodes by FF ionization, we first presented detailed mathematical analysis of fission fragment (FF) signal formation on TIC anode. The analysis was done using Ramo-Shockley theorem, which gives relation between charged particle motion between TIC electrodes and so called weighting potential. Weighting potential was calculated by direct numerical solution of Laplace equation (neglecting space charge) for the TIC geometry and ionization, caused by FF. Formulae for grid inefficiency (GI) correction and digital pulse processing algorithms for PFN time-of-flight measurements and pulse shape analysis are presented and discussed.

Keywords: Grid Inefficiency, ²⁵²Cf(sf), Ionization chambers, Fission. PACS: 29.30.Hs, 29.40.Cs, 29.40.Mc, 29.85.Fj, 25.85.Ca

INTRODUCTION

Nuclear fission model and prompt fission neutron emission (PFN) was first considered in classic paper of N. Bohr and J. Wheeler [1], where nuclei considered as a drop of charged liquid, which surface constantly distorted in competition between attractive nuclear and repulsive Coulomb forces. Rarely large distortion brought the nuclear into the configuration, where repulsion could not be compensated by nuclear force and the system split, sometimes after neutron emission. In this case the neutrons, called scission neutrons in order to distinguish them from the PFN, which are emitted from the fully accelerated fission fragments. First investigation of PFN emission was done in experiments [2, 3] in 1960-ies concluded that about 5 to 15% of fission neutrons were emitted before the fissile system split. Development of experimental technique and birth of commercial nuclear electronics allowed measurement of fission fragment (FF) and fission neutron kinematic parameters in a single fission event. In new experimental approach developed in ref. [4] authors investigated PFN emission in spontaneous fission of ²⁵²Cf using twin Frish-grid ionization chamber (TIC) for FF kinetic energies and PFN emission angle along with PFN velocity measurement with help of liquid scintillator (NE213) based neutron detector (ND). Despite the authors demonstrated a power and high capacity of the new approach, some of their results (for example, dependence of average PFN multiplicity on total kinetic energy of FF) contained obvious contradictions with simple energy balance in fission. In present work we described further development of the experiment using modern digital pulse processing (DPP), implemented

with the detector signals along with in depth analysis of a signal induction on TIC electrodes by FF.

SIGNAL FORMATION ON TWIN IONIZATION CHAMBER ANODE

A sketch of the experimental setup with digital pulse processing electronics is shown in Fig. 1. A TIC was used for fission fragment mass-TKE and PFN emission angle (②) measurement. A target with fissile material, deposited on thin organic foil located on the common cathode of the chamber. Fission fragments were decelerated inside sensitive volume of two independent chambers spending their kinetic energy for free electron creation. Free electrons drifted inside the chamber to respective anodes. The electric charge, induced on two anodes and common cathode were proportional to fission fragments kinetic energy, are measured by three synchronized waveform digitizers (WFD). Approximately 0.15% of fission fragment detection coincided with neutron detection by ND, which signal was digitized using fourth WFD. The common time base was achieved due to all four digitizer was

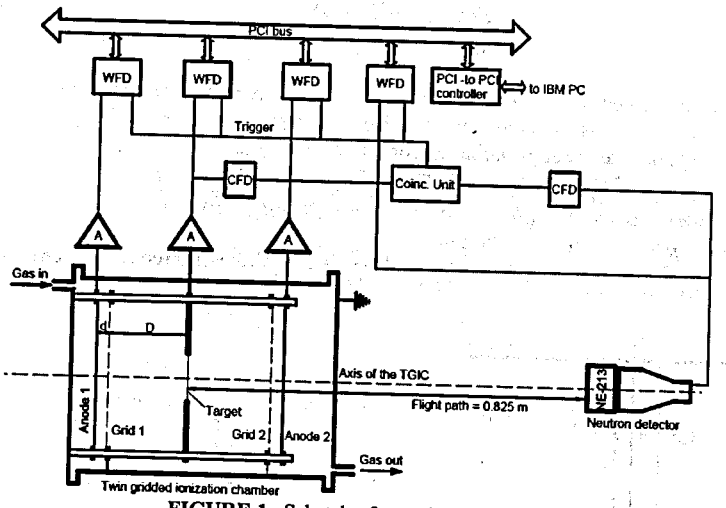


FIGURE 1. Scketch of experimental setup

sampling detector pulses synchronously and the common cathode pulse was considered as an indication of a fission event. The common cathode pulse was used as a "T-zero" signal for PFN time-of-flight measurement and as one of the input pulses of coincidence unit. A neutron, detected inside the time interval of 200 ns duration after "T-zero" was considered as PFN. In such a way two types of fission events were recorded in given experiment: with and without coincidence with ND pulse. Apparently, the intensity of fission events with coincidence with ND was proportional to conditional probability of neutron emission in a detected fission event. In given experiment the following parameters of fission event were required to be measured: kinetic energies of correlated FF, their angle in respect to the TIC axis, PFN time-of-flight and the angle between FF and PFN (thanks to allocation of ND on the TIC axis). The information about listed parameters was retrieved from the sampled TIC and ND pulses using DPP algorithms. The waveform of the anode signal, being preprocessed

by charge-sensitive preamplifier, was step-like pulse with height proportional to total charge of the electrons released during FF deceleration. The FF angle information can be obtained from the anode pulse rise time, which is proportional to the electron drift time from the point of origin to the respective anode. Relation between chamber geometry and the charge induction on the anode of TIC is given by the Ramo-Shockley theorem [5, 6]. According to the theorem a full charge, induced on the electrode by a moving charge can be calculated using a weighting electric field potential, calculated for all electrodes grounded except the considered one, which potential is raised to 1 V. In present work the calculation was done for a single cell with periodical boundary conditions in respect to x-axis of two dimensional Cartesian coordinates chosen as schematically shown in Fig. 2, where D and d are cathodegrid and grid-anode distances respectively. Dirichlet boundary conditions for this case required us to specify the potential along the boundaries: anode potential set to 1, cathode and grids both grounded, potential along the dotted lines set to linear rising function of y coordinate from the zero at the cathode to 1 at the anode.

The electric potential can be found as the solution of Laplace equation

$$\frac{\partial^2 F(x,y)}{\partial x^2} + \frac{\partial^2 F(x,y)}{\partial y^2} = 0 \tag{1}$$

satisfying to described above boundary conditions. To solve eq. 1 numerically the inside of the rectangular cell was covered with a uniform computational grid with pitch h and the following finite difference approximation formulae were used:

$$\frac{\partial^2 F}{\partial x^2} = \frac{2F_v}{v(v+q)} + \frac{2F_q}{q(q+v)} - \frac{2F_o}{qv}, \quad \frac{\partial^2 F}{\partial y^2} = \frac{2F_p}{p(p+u)} + \frac{2F_u}{u(p+u)} - \frac{2F_o}{pu}$$

$$\frac{F_v}{v(v+q)} + \frac{F_q}{q(v+q)} + \frac{F_p}{p(p+u)} + \frac{F_u}{u(p+u)} = \frac{pu+qv}{puqv}F_o - \text{finite difference Laplace equation}$$
(2)

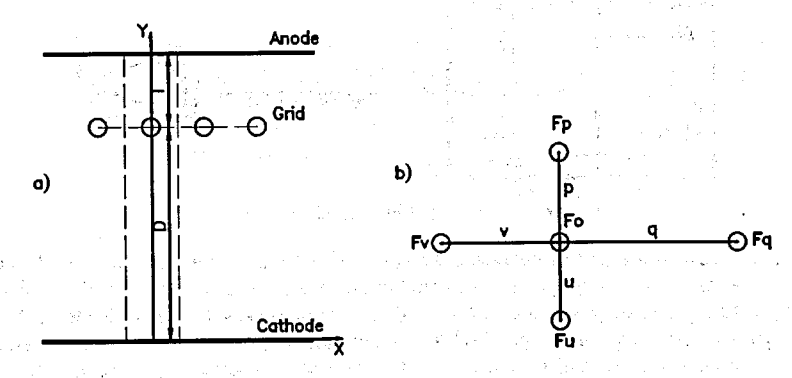


FIGURE 2 a) Area, confined by dashed lines, where the Laplace equation solved with periodical Dirichlet boundary conditions. b) generalized finite difference scheme demonstrating how the second order derivatives were calculated at the grid node F_0 using adjacent nodes F_q , F_p , F_p and F_v .

When the point F_0 was far enough from the grid the distances p,q,u and v were supposed to be equal to the chosen pitch h. When at least one point crossed the grid boundary, then the

corresponding distance was set to the distance between F_0 and the boundary. The obtained solution F(x,y) was integrated over x-coordinate and plotted in Fig. 3a as $F_1(y)$.

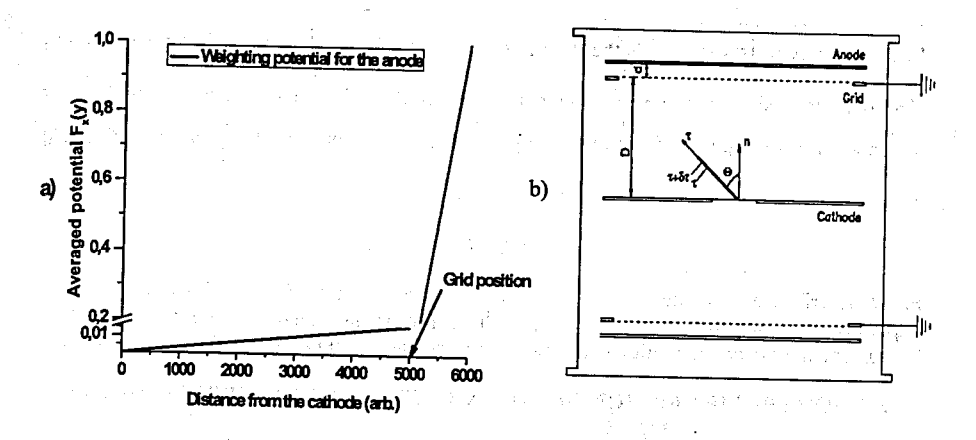


FIGURE 3. a) Weighting potential for the anode b) Illustration of the free electron drift in TIC.

Charge induced on the anode when free electrons with total charge q are drifting from the point of origin τ (we suppose that the τ -axis aligned along the FF motion direction) to a point with potential $F_x(y)$ can be calculated using the following formula:

$$Q(y) = (F_x(y) - F_x(y = \tau \times \cos(\Theta)) \times q$$
(3),

where subscript x in $F_x(y)$ denotes averaging of calculated weighting potential F(x,y) in respect to x. The following dependence of averaged weighting on y was obtained and plotted in Fig. 3a:

$$F_{\mathbf{x}}(\mathbf{y}) = \begin{cases} \sigma \frac{\mathbf{y}}{D} & \text{for } 0 \le \mathbf{y} < D \\ (1 - \sigma) \frac{\mathbf{y} - D}{l} + \sigma & \text{for } D \le \mathbf{y} \le D + 1 \end{cases}$$
(4)

The parameter σ – is a grid inefficiency factor [6] and eq. 3 gives charge $q = \rho(\tau)d\tau$, induced by the electrons in the interval $(\tau, \tau + d\tau)$ when they drifted from the point of origin to the point, having potential $F_x(y)$, the induced charge dQ(y) can be expressed as

$$dQ(y) = ((1-\sigma) \times \frac{y-D}{l} + \sigma - \sigma \times \frac{\tau \times \cos(\Theta)}{D}) \rho(\tau) d\tau$$
 (5)

BOOK TO A TO A WOOD AND THE STEAM OF A WAY OF A

Assuming all FF decelerated inside the cathode-grid area and integrating eq. 5 over τ gives the charge Q, induced by whole electrons along a FF deceleration path, when they collected on the anode as:

$$Q(D+d) = \int_{0}^{L} e \times \rho(\tau) \times (1 - \sigma \times \frac{\tau \times \cos(\Theta)}{D}) d\tau = N \times e \times (1 - \sigma \frac{\hat{X} \times \cos(\Theta)}{D})$$
 (6)

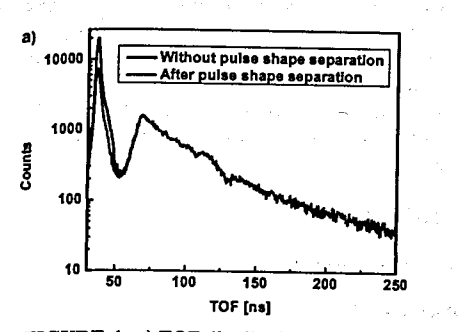
In eq. 6 the $\hat{X} = \int_0^L \tau \times \rho(\tau) d\tau$ is the "centre of charge" and $N = \int_0^L \rho(x) dx$ is a total number of electrons, created during the FF deceleration. Drift time T of the "charge centre" of FF ionization from the point of origin to the point with coordinate $y = D + \frac{l}{2}$ can be calculated as:

$$T = \frac{D}{W} \left(1 + \frac{l}{2D} - \frac{\hat{X}}{D} \cos(\Theta) \right) \tag{7}$$

Eq. 7 describes dependence of drift time T on $cos(\Theta)$. The DPP algorithms and practical implementation of pulse height and angle evaluation were described in previous papers [7-9]. In next chapter we are providing some new results related to PFN time-of-flight spectroscopy.

DPP FOR PROMPT FISSION NEUTRON TIME-OF-FLIGHT SPECTROSCOPY

Measurement of PFN time-of-flight in present experiment we used cathode pulse of TIC as a "T-zero" signal and the ND signal as "Stop" signal. Time difference between these two signals was considered as the PFN time-of-flight (TOF). Narrow bandwidth (100 MHz sampling) available in our measurements and wide pulse height range (~100) of ND pulses, made data analysis more complicated due to some surprising effects was not foreseen beforehand. ND, used in experiment, was sensitive to prompt fission gamma radiation and this fact became helpful to overcome the limitation of narrow bandwidth of the apparatus. The bandwidth of ND pulse can be evaluated from the pulse rise time, which was found to be ~100 MHz for ~4 ns rise time. Because of 100 MHz sampling frequency and taking into account Shannon sampling theorem the signal bandwidth was limited with help of antialiasing filter of 4-th order (Bessel filter with 45 MHz cutoff frequency). Before data analysis ND waveform passed additional 4-th order digital Butterworth filter, constructed using algorithm described in ref. [7]. Constant fraction time triggering (CFTT) was implemented digitally to measure the time difference between TIC cathode and ND pulse. It is well known that CFTT works well when it is implemented to pulses, having identical rise times. In present measurement scheme the identity of ND pulses was guaranteed by filters, applied to ND signals as was described above. Constant fraction value was selected 0.2 of pulse height and parabolic interpolation was implemented between successive samples. Resulting TOF distribution measured using considered approach and pulse shape separation of neutrons from gamma radiation presented in Fig.4a. In order to demonstrate the effects, distorting the shape of the TOF plot from Fig. 4a, two-dimensional plot in coordinates TOF - ND total light output was plotted in Fig. 4b. The points on the Fig. 4b, corresponding to gamma-radiation, demonstrate obvious dependence on the total light output (proportional to ND pulse height). We explained that dependence by the filters, introduced additional phase delay for ND pulses. To correct those phase delays we first parameterized gamma radiation shift on the ND pulse height using linear approximation. Then the shift corrected for both neutron and gamma radiation pulses in similar way during data analysis. Result after correction presented on Fig. 5 and looks more reasonable in comparison with Maxwell distribution with parameters taken from ref. [4]. It should be noticed that problems related to phase delays are quite complicated for investigation using pure theoretical approach and should be combined with experimental methods.



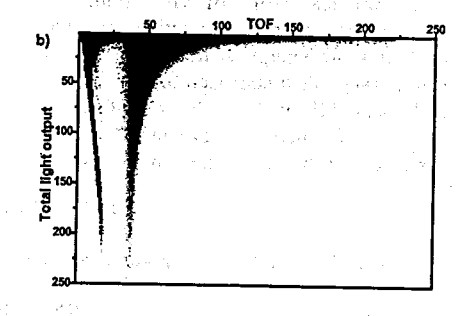
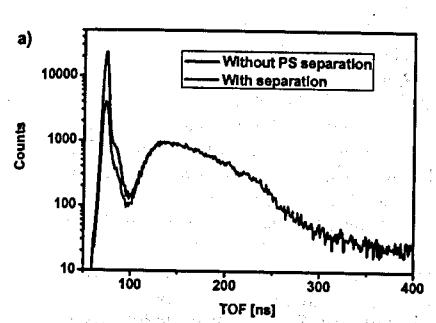


FIGURE 4. a) TOF distribution obtained using digital CFTT method. b) Two-dimensional plot in coordinates TOF-ND total light output.



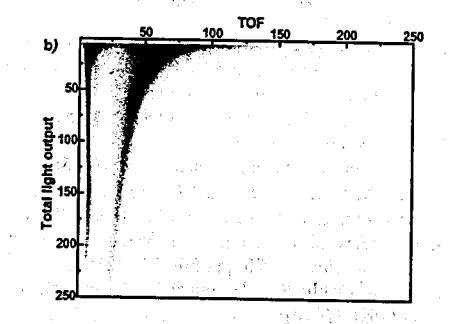


FIGURE 5. Application of mathematical analysis of signal formation in TIC and developed DPP algorithms for prompt fission neutron TOF spectroscopy allowed us to avoid some uncertainties and correct the final results of PFN emission. a) time-of-flight distribution after correction for pulse height dependence and pulse shape analysis, b) Two-dimensional TOF-ND plot after correction.

DISCUSSION

Our result concerning grid inefficiency (GI) correction factor, deducted from eq. 6, is in very good agreement with paper from ref. [6] and early result published in ref. [10]. It should be noticed that in recent years there was another point of view to GI factor correction published in ref. [11], where experimental method of GI factor determination with help of digitized anode signal waveform was provided. Eq. 6 in present work was deducted from classic electrodynamics (see ref. [5]) and reflects the electrostatic induction of charges, moving in the electrostatic field, created by the electrodes of TIC (Fig. 3a). Both authors of ref. [10] and ref. [11] used correction of eq. 6 in order to eliminate effect of angular dependence. In case of ref. [10] the goal was achieved by addition to eq. 6 of the

term $Ne\sigma \frac{\hat{X}\cos(\Theta)}{D}$, and subtraction of the term $Ne\sigma(1-\frac{\hat{X}\cos(\Theta)}{D})$ in case of ref. [11].

From practical point of view both approaches bring to correct results, when proper spectrometer energy calibration procedure was implemented. For example, when one calibrates the energy scale of spectrometer with alpha particles with extrapolation to FF energy range then approach of ref. [10] would be more precise, because it does not introduce additional shift of $Ne\sigma$. In case of the energy scale calibration using known average heavy and light FF kinetic energy values both approaches will bring to the same results because any systematic shift is eliminated in the energy calibrating.

ACKNOWLEDGMENTS

This work partially was supported by RFBR grant 10-07-00541a.

REFERENCES

- 1. N. Bohr, J.A. Wheeler, Physical Review, 56, pp. 426-450 (1939)
- H. R. Bowman, S. G. Thompson, J. C. D. Milton, W. J. Swiatecki, *Physical Review*, 126, pp. 2120-2136, (1962)
- 3. K. Skarsvag, K. Bergheim, Nucl. Phys., 45, pp. 72-97, (1963).
- 4. C. Budtz-Jørgensen and H.-H. Knitter, Nucl. Phys., A490, 307-328 (1988).
- 5. W. Shockley, Journal of Applied Physics, 9, pp. 635-636 (1938).
- 6. A. Göök, F.-J. Hambsch, A. Oberstedt and S. Oberstedt, submitted to Nucl. Instr. Meth. A.
- O. Zeynalova, Sh. Zeynalov, F.-J. Hambsch and S. Oberstedt, "DSP Algorithms for Fission Fragment and Prompt Fission Neutron Spectroscopy in Application of Mathematics in Technical and Natural Sciences-2010, edited by M. D. Todorov and C. I. Christov, AIP Conference Proceedings 1301, American Institute of Physics, Melville, NY, 2010, pp. 430-439.
- 8. O.V. Zeynalova, Sh.S. Zeynalov, F.-J. Hambsch, S. Oberstedt, Bulletin of Russian Academy of Science: Physics, 73, pp. 506-514 (2009).
- A. Al-Adili, F.-J. Hambsch, S. Oberstedt, S. Pomp, Sh. Zeynalov, Nucl. Instr. Meth. A624, pp. 684-690 (2010).
- C. Budtz-Jorgensen, H. H. Knitter, Ch Straede, F. J. Hambsch, R. Vogt, Nuclear Instruments and Methods in Physics Research Section A, 258, pp. 209-220 (1987).
- 11. V.A. Khriachkov, et al., Nuclear Instruments and Methods in Physics Research Section A, 394, pp. 261-265, (1997).

Interaction of waves with ordinary and birefringent media moving with acceleration

A.I.Frank¹, P.Geltenbort², M.Jentschel², G.V.Kulin¹, D.V.Kustov^{1,3} and A.N.Strepetov⁴

Frank Laboratory of Neutron Physics, Joint Institute for Nuclear Research, Dubna, Russia

²Institut LaueLangevin, Grenoble, France ³Institute for Nuclear Research, Kiev, Ukraine

National Research Centre "Kurchatov Institute", Moscow, Russia

Abstract

Already at the end of the last century theory predicted that the wave number and frequency of any wave will change when passing through an accelerating refractive medium. The effect was calculated both for electromagnetic and neutron waves. As a refractive index may be introduced for waves of any nature one can speak about a very general Accelerating Medium Effect. As far as we know this effect has not yet been observed for light. Here we report on a neutron-optics experiments performed with ultra-cold neutrons where this effect has been demonstrated for the first time ever. The maximum energy transform in the experiment was \pm (2÷6) ×10⁻¹⁰ eV, which agrees with theory within less than 10%. Possibilities for future investigations of the Accelerating Medium effect will be discussed.

1. Introduction

The investigations of light propagation through a moving matter are continuing, starting from the historical paper of Fizeau [1] and up to the nowadays. In the 1970's the similar line of investigation has appeared also in the neutron optics [2-9]. By analogy with the light optics, the neutron experiments with moving matter are called Fizeau neutron experiments. Some results of the light and neutron optical investigations were reviewed and compared in [10]. In most of the mentioned papers, authors were mainly interested in the phase shift of a wave transmitted through a moving sample. Less attention was paid to the question of wave frequency in matter.

However, if a layer of some matter and its boundaries moving as a single whole, the wave frequency in matter measured in the laboratory frame will be different from that in vacuum. This is the case both in light [11] and neutron optics [2,12], where the frequency shift is caused by the Doppler effect and is determined by the following relation $\Delta\omega = (n-1)k_0\nu$, where n is the index of refraction in the moving coordinate frame with matter at rest, k_0 is the wave number of the incoming wave, and ν is the speed of the moving matter.

In the case of uniform motion of a material layer the Doppler shift resulting from passage of the wave through two boundaries are equal in magnitude but opposite in sign. The total effect is zero and the frequency of the wave transmitted through the moving matter does not change. For a long time the role of uniform velocity has been underestimated, although it is a decisive one. In the case of arbitrary motion frequency shifts on the sample boundaries do not cancel each other and the frequency of the transmitted wave is not equal to the incoming one. This was first shown by Tanaka [13] who solved the problem of electromagnetic wave transmission through a linearly accelerated dielectric matter on the basis of a covariant generalization of the Maxwell equations. As far as we know, the corresponding light optics

randra de la composición del composición de la composición del composición de la com

experiment has not been carried out till now, although the possibility of doing that has been discussed [14].

The problem of neutron transmission through a layer of matter moving with linear acceleration was considered by Kowalski [15] in the context of a new type of experiment to verify the equivalence principle. The author comes to the conclusion that the energy of neutrons transmitted through such a layer must change. Later, the same result was obtained by Nosov and Frank [16] who calculated the velocity of the neutron transmitted through the accelerated boundaries of the sample.

The first brief note of experimental observation of neutron energy change on transmission through accelerated matter can be found in [17]. A more detailed investigation of the accelerated medium effect (AME) is given in [18]. Recently, acceleration and slowing down of neutrons on transmission through an oscillating sample was observed by a peculiar time-of-flight method [19]. The detected energy change was in a good agreement with the theory.

In the next sections we shall present rather briefly the main results of the experiments [18,19]. Then we discuss some new aspects of the neutron AME for the birefringent media.

2. Observation of the accelerating matter effect in experiments with ultracold neutrons.

2.1 Spectroscopy with UCN

The equation determining energy change due to AME was obtained by the different methods in [15,16] in the form

$$\Delta E \cong mwd\left(\frac{1}{n}-1\right) \tag{1}$$

1、1864、高磁压^{量的}"30"的"6"。1875年的1876年。

Where m is the neutron mass, d - thickness of the sample, n - refraction index and w - sample acceleration. As shown in [18] eq. (1) can be obtained with good approximation from the equivalence principle without any detailed calculation. It was tested with reasonable accuracy in spectroscopic experiment with ultracold neutrons (UCN) [18].

The change of energy by transmission through an accelerating sample was firstly measured several years ago in experiments with ultracold neutrons. Neutrons passed through a silicon sample, which oscillates. Accordingly the energy change of the quasi-monochromatic neutrons is given as

$$\Delta E \cong -mA\Omega^2 d \frac{1-n}{n} \sin \Omega t, \quad \Omega \ll \frac{v_i}{d},$$
 (2)

where A and Ω – denote the oscillation amplitude and frequency of the sample and v_i – their velocity inside the sample material. The layout of the experimental setup, a modified spectrometer of [15,16], is shown in Figure 1.

Ultra-cold neutrons enter the top part of the spectrometer horizontally before falling through an annular corridor. At the lower end of the corridor, a monochromator (1) is placed. It is a neutron interference filter and acts as a kind of Fabry-Perrot interferometer (FPI). It transmits only UCN with a narrow spectrum of vertical velocities. The sample (2), silicon plates of 0.6 and 1.85 mm thickness respectively, are located just below the monochromator. It can be harmonically moved up and down by means of a special driver (3). The sample was oscillating with 40 or 60 Hz. The maximal tunable acceleration of the sample was 90m/s².

Passing the monochromator and sample, neutrons arrive at a vertical mirror neutron guide, where the second FPI, analyzer 4, is located and whose position can be varied in height. A

scintillation detector for UCNs 5 is placed below the analyzer. The transmission line maxima of the monochromator and analyzer correspond to 107 and 127neV, respectively. The dependence of the count rate on the distance between the filters is qualitatively presented in Figure 2. The sign-alternating change in the neutron energy caused by passage through a sample moving with variable acceleration leads to the periodic variation in the count rate, as shown by the dashed straight lines in Figure 2.

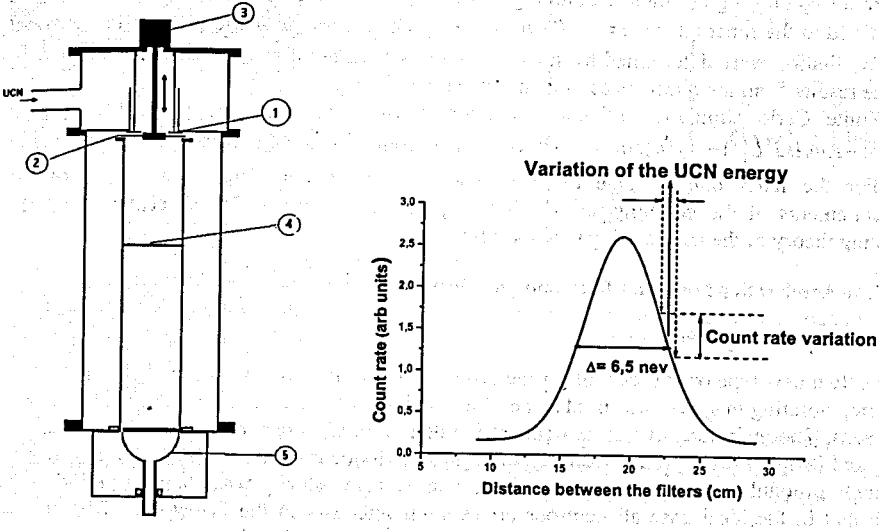


Figure 1. Layout of the experimental

Figure 2. Count rate vs. the distance between the filters (scanning curve) and the detection principle of periodical variation of energy

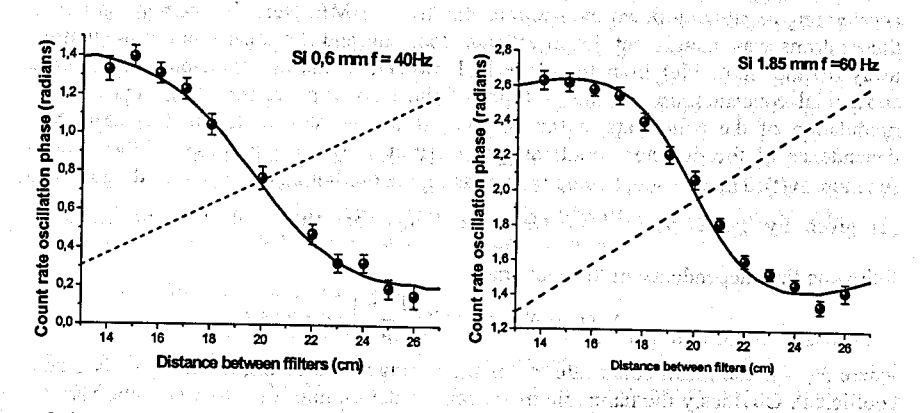


Figure 3. Measured phase of the counting-rate oscillation versus the analyzer position. Solid (red) curve – Monte-Carlo simulation. Dashed (blue) line – theoretical prediction for the phase in the absence of the Accelerating medium effect

The first the shall be be still the vertical like it in the significant with a significant contract of

The maximum change in the energy of UCNs, which is determined by Eq. (6), reaches

approximately 0.6neV.

The phase and amplitude of the count rate modulation were measured in the experiment for various positions of the analyzer filter. The time dependence of the count rate was determined in a time interval equal to the oscillation period. The origin of the scale was specified by a generator controlling the sample motion. The data were normalized to the averaged count rate and fitted to the function $f(t)=1+B\sin(\Omega t-\varphi)$. The amplitude B and phase φ of the count rate oscillation were determined by such a way in each value of the position of the analyzer. Some results from the phase measurements are shown in Figure 3.

Monte Carlo simulation of the oscillation phases were repeated using the relation $\Delta E = -KmA\Omega^2 L[(1-n)/n] \sin \Omega t$ which differs from equation (2) by the correction factor K. For the latter one a value of $K = 0.94 \pm 0.06$ was found. Thus, the results of the measurements of the counting-rate oscillation phase are in reasonable agreement with the existing theory of the accelerating medium effect.

2.2. The Accelerating Medium Effect and time focusing of neutrons.

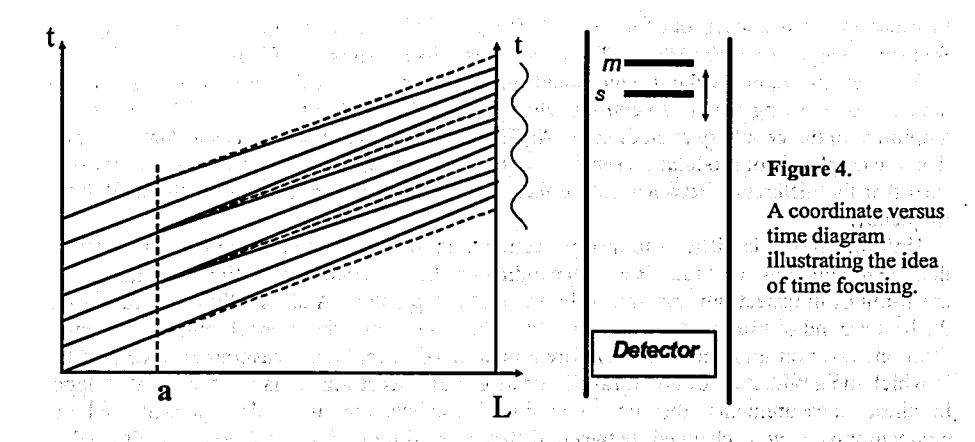
2.2.1. Experimental Principle

Recently a new type of experiment for the observation of the AME was carried out [19]. Here a plate, vibrating in space, was used as periodic modulator to change the velocity of ultra-cold neutrons. The main idea of this experiment is rather similar to experiments on time focusing [20] and its main principle is illustrated in Figure 4. Monochromatic neutrons are transmitted through a modulator - acting as a time lens. The neutron velocity was changed periodically such that in the ideal case all neutrons arrive simultaneously in the detector L. The lens is working in a cyclic regime and time focuses those neutrons passing through it in one cycle. In reference [20] an aperiodic diffraction grating moving across the neutron beam was used as a lens. In the current experiment we used a plate of silicon oscillating along the propagation direction of the ultra-cold neutron beam. Moving with periodic acceleration it was periodically accelerating or slowing down the neutrons due to the AME. Here the momentum transfer to the neutrons was insufficient for an efficient focusing and the focal plane was significantly away (to the right side) from the plane L. However, in the detection plane there occurs a substantial concentration in time of flight of the incoming neutrons. This leads to a time modulation of the count rate at the detector. It can be shown that in this case the time dependence of the detector count rate is determined by the derivative of the modulation function $\Delta v(t)$. The change of velocity by passing the oscillating plate is according to equation (2) given by $\Delta v_n = -A\Omega^2 \frac{d}{v_0} \left(\frac{1-n}{n}\right) \sin \Omega t$ and therefore the weak focusing leads to the

following time dependence of the count rate

$$N_a(t) = N_0 + C_a A \Omega^3 \left(\frac{1-n}{n}\right) \cos \Omega(t+\tau)$$
 (3)

where N_0 - is the mean count rate, τ - is the average time of flight and C_a - is a constant coefficient. Obviously the harmonic movement of the sample leads to a periodic variation of the neutron velocity with respect to the sample. As the dependence of all absorbing processes in the case of ultra-cold neutrons is proportional to 1/v the transmission of the sample is also changing accordingly. Therefore, additionally to the AME given by equation (8) there is another systematic effect described by the following equation $N_{\nu}(t) = N_0 + C_{\nu}A\Omega\cos(t+\tau)$.



As both effects are synchronous, the harmonic modulation of the count rate is obtained by summing the amplitudes of both

$$\Delta N(\Omega) = A\Omega^2 \left(C_a \Omega + \frac{C_v}{\Omega} \right) \tag{4}$$

Expression (4) is written such, that it underlines the main principle of the given experiment: the measurement is carried out such that the quantity $A\Omega^2$ stays constant and the AME is growing proportionally while the systematic velocity effect if inversely proportional to the frequency of modulation.

The systematic velocity effect was encountered in former experiments [17,18]. In these measurements it was already found that if the monochromatisation happens after transmission through the sample the AME is excluded. All experimentally observed modulations are due to the systematic velocity effect. This finding has been explored for the current measurement.

The experimental strategy consisted in the measurement of the modulation amplitude of the ultra-cold neutron count rate transmitted through an oscillating sample for a large set of frequencies Ω and fixed values of $A\Omega^2$. The measurement was carried out in two geometries. In the first case the monochromatic neutrons were transmitted through the sample and the amplitude modulation was given by equation (4). In the second case the neutrons were transmitted through the oscillating sample and only after through the mononchromator. In the second case the modulation amplitude is defined by the systematic velocity effect only. The frequency dependence of the difference of both effects is defined exclusively by the AME and should depend linearly on the frequency of modulation.

2.2.2. Experimental realisation and results

For the experiment the same spectrometer as in reference [18] was used. A schematic illustration is given in Figure 1. The only difference consists in the absence of the analyzer 4. As in earlier works we used a Fabri-Perot interferometer as monochromator. It transmits a single wave length at about 107 neV with a relative width of $\Delta E/E \approx 0.04$. As a sample we used a wafer with 1.85 mm thickness, which was put into oscillation by the same driving stage as in [18]. The time depending acceleration was permanently measured by a piezoelectric sensor, the sinusoidal signal of which was also used for the stabilization of the amplitude of the driving stage. This allowed to stabilize the quantity $w_{max} = A\Omega^2$ on the level of 2%. The

measurement was carried out for two values $w_{max} = 57 \text{ m/s}^2$ and $w_{max} = 72 \text{ m/s}^2$ and for a frequency range of f = 20 + 100Hz. The obtained results are shown in Figure 5.

The results show without any doubt the presence of weak time focusing, i.e. the acceleration/slowing down of neutrons when passing the oscillating sample. The modulation amplitude in the geometry excluding the AME effect (lower blue points) is substantially lower than the amplitude of modulation sensitive to both effects (upper red points). Further, it can be seen that the difference between both effects is growing with an increase of the modulation frequency.

Unfortunately it is difficult to directly compare these data with calculations. The reason is that the modulation amplitude is also depending on the dispersion of the time of flight, i.e. on the width of the spectrum transmitted by the monochromator. Additionally it turned out that the background of the spectrometer is slightly changing, when the monochromator is changed from one position into another. Therefore a number of calibration measurements were added, in which the modulation of the ultra-cold neutron flux was realized via a mechanical chopper. In these measurements the non moving silicon sample was also present and the monochromator was changed between different positions. Such calibrations allowed to normalize the data of Figure 6. The difference of the two curves should be a straight line, corresponding to the first term of equation (4). These results are shown in Figure 6 and it is possible to compare them directly to theoretical calculations. The main parameter here is the inclination angle of the straight line. The calculations were done by assuming several origins of the background. The dispersion of the calculated background values was included into a systematic error.

The error of the linear fit of the data in Figure 6 was considered to be the statistical error. From the obtained results it was possible to estimate the agreement of the calculated velocity change when neutrons are transmitted through an oscillating refractive sample.

For the factor $K = \Delta v_{exp}/\Delta v_{exp}$ and values of $w_{max} = A\Omega^2$ as mentioned above the agreement of experiment and calculation was: $K_1 = 0.95 \pm 0.10_{stat} \pm 0.05_{syst}$ and $K_2 = 0.95 \pm 0.05_{stat} \pm 0.05_{syst}$

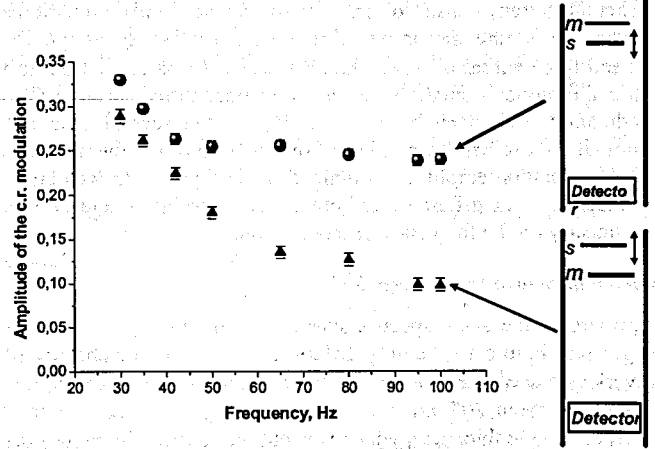


Figure 5. The count rate oscillation amplitude as a function of frequency for a fixed value of $w_{max} = A\Omega^2 = 72 \text{m/s}^2$. The measurements were done in two geometries, which symbolically are indicated on the right. Here M – is the monochromator and S – is the sample.

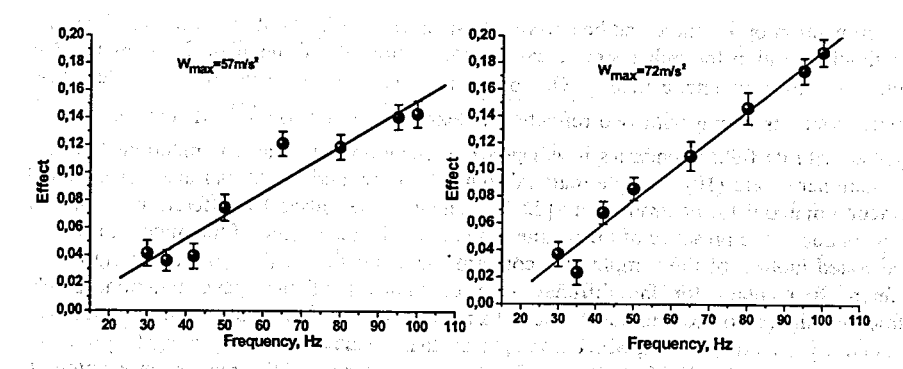


Figure 6. The difference between normalized amplitudes of the count rate oscillation versus frequency. The value $w_{max} = A\Omega^2$ was fixed. On the left $w_{max} = 57 \text{m/s}^2$, on the right $w_{max} = 72 \text{m/s}^2$.

3. The Accelerating Matter Effect in the case of double refraction

In the present works concerning the AME the polarization of waves was not considered so far. In order to partially fill this gap we will consider briefly the case of matter with double refraction, which is characterized by two indices of refraction n_{\pm} , according to two polarizations of the incoming wave.

In neutron optics the quantities n_{\pm} correspond to two different projection of the neutron spin on a physical axis. Accordingly we will rewrite equation (1) as

$$\Delta E_{\pm} \cong mwd(1-n_{\pm})/n_{\pm}$$
, $\Delta \omega_{\pm} = \Delta E_{\pm}/\hbar$.

After transmission through an accelerated birefringent sample the two spin components of the neutron wave function differ by a frequency and form a non-stationary superposition. In the case of an arbitrary polarization of the original wave function $\Psi_0(x,t)$ the final state will have the form

$$\Psi(x,t) = A_{+} \exp\left[-i\left(\Delta k_{+} x + \Delta \omega_{+} t + \chi_{+}\right)\right] \left|\uparrow\right\rangle + A_{-} \exp\left[-i\left(\Delta k_{-} x + \Delta \omega_{-} t + \chi_{-}\right)\right] \left|\downarrow\right\rangle$$
 (5)

where $\Delta k_{\pm} = (m/\hbar^2)(\Delta E_{\pm}/k_0)$ and t is the time counting from the moment when the wave escapes the matter. The constant phase angles, χ_{\pm} , that are irrelevant to what follows, determine spin directions on transmission through a moving sample [21]. The wave function in equation (5) describes the state with spin precession. The precession angle is obtained from the difference between the phase angles of two spin components:

$$\varphi(x,t) = (\Delta k_+ - \Delta k_-)x - (\Delta \omega_+ - \Delta \omega_-)t + \chi_+ - \chi_+$$

Assuming here the simplifying condition $\Delta E_{\star}/E <<1$ it is possible to write that $(\Delta k_{+} - \Delta k_{-})x = (\Delta \omega_{+} - \Delta \omega_{-})x/v$, from which follows that in the reference system moving with the velocity of the neutron the direction of the spin vector is unchanged. However, in a fixed point of observation, x=L, the spin direction changes periodically in time with the frequency $\Omega = \Delta \omega_{+} - \Delta \omega_{-}$. This periodic change of the polarization direction can be measured. The beat frequency Ω and respective energy transfers $\hbar \Omega$ can be quite small.

In neutron optics there can be several physical reasons for double refraction. First of all one should mention the rather simple case of interaction of the magnetic momentum of the neutron μ with a magnetic field B. Obviously any space in which the magnetic field has a nonzero value is acting with two refraction indexes $n_{\pm} = (1 \mp \mu B/E)^{1/2}$. If this space moves together with its field boundaries it will generate according to what was mentioned above a non-stationary state (10). Sample material, put into a magnetic field can also act as double refracting material for neutron waves [22,23]. This will be caused by different neutron wave numbers due to the presence of the magnetic field and the dispersion of the material itself. An accelerated motion of the sample in a constant magnetic field will also lead to states with different frequencies for the different spin components of the wave function. Double refraction might also occur in the absence of a magnetic field. First of all one might focus here on nuclear pseudomagnetism, which takes place when a neutron wave is propagating in matter with polarized nuclei. [24,25]. Due to the spin dependence of the nuclear interaction the coherent scattering length b_{\pm} is different for the two values of the total spin. As a result, the medium has two refractive indices.

Finally, double refraction might be caused by parity violation in neutron-nucleon interaction. The forward scatter length and consequently the refractive index will be depending on the neutron spin orientation [26,27]

4. Conclusion

It was shown, that the Accelerating Medium Effect is closely related to the equivalence principle (EP). Consequently, the equations which describe the frequency change after their passage through accelerated refractive samples, may be derived not only from first principles but from the EP too. This can be interpreted as additional evidence for the general nature of this effect which exists for waves and particles of different nature. Two experiments detecting the AME in neutron optics were described. The measured energy variations were equal or less than 5×10^{-10} eV while the velocities changed by about 1 cm/s. The measurements agree with theoretical predictions better than 10%. New possibilities for the detection and for applications of the AME may be possible by the use of birefringent material.

This work is partly supported by the Russian Foundation for Basic research (project 11-02-00271).

References

- 1. Fizeau H. L., Acad. Sci. Ser. B, 33 (1851) 349; Ann. Chim. Phys., 57 (1859) 385.
- 2. Horn M. A. and Zeilinger A., Neutron Interferometry, edited by U. Bonse and H. Rauch, Vol. 9 (Clarendon, Oxford) 1979, p. 350.
- 3. Klein A. G. et al., Phys. Rev. Lett., 46 (1981) 1551.
- 4. Home M. A., Zeilinger A., Klein A. G. and Opat G. I., Phys. Rev. A, 28 (1983) 1.
- 5. Sears V. F., Phys. Rev. A, 32 (1985) 2524.
- 6. Arif M. et al., Phys. Rev. A, 31 (1985) 1203.
- 7. Bonse U. and Rump A., Phys. Rev. Lett., 56 (1986) 2411.
- 8. Arif M. et al., Phys. Rev. A, 39 (1989) 931.
- 9. Bonse U. and Rump A., Phys. Rev. A, 37 (1989) 1059.
- 10. Neutz R. J., Stedman G. E. and Bilger H. R., J. Opt. Soc. Am., 13 (1996) 2065.
- 11. Yeh J., J. Appl. Phys., 36 (1965) 3513.

- 12. Peres A., Am. J. Phys., 51 (1983) 947.
- 13. Tanaka K., Phys. Rev. A, 25 (1982) 385.
- 14. Neutze R. and Stedman G. E., Phys. Rev. A, 58 (1998) 82.
- 15. Kowalski F. V., Phys. Lett. A, 182 (1993) 335.
- 16. Nosov V. G. and Frank A. I., Yad. Fiz., 61 (1998) 686 [Phys. Atom. Nucl., 61 (1998) 613].
- 17. Frank A. I. et al., Pisma Zh. Eksp. Teor. Fiz., 84 (2006) 131 [JETP Lett., 84 (2006) 363]
- 18. Frank A. I. et al., Yad. Fiz., 71 (2008) 1686 [Phys. Atom. Nucl., 71 (2008) 1656].
- Frank A. I. et al., Pisma Zh. Eksp. Teor. Fiz., 93 (2011) 403 [JETP Lett., 93 (2011) 361].
- 20. Frank A I, Geltenbort P, Kulin G V and Strepetov A N JETP Letters 78 (2003) 188
- 21. Littrell K. C., Werner S. A. and Allman B. E., J. Phys. Soc. Jap. Suppl., 65A (1996) 98.
- 22. Baryshevskii V G, Cherepitsa S V and Frank A I 1991 Phys. Lett. A 153 299
- 23. Frank A I, Bondarenko I V, Kozlov A V, Høghøj P and Ehlers G 2001 Physica B 297 307
- 24. Baryshevkii V G, Podgoretsky M I 1964 JETP 47 1050
- Abragam A, Bacchella G L, Glätti H, Meriel P, Pinot M, and Piesvaux J 1973 Phys. Rev. Lett 31 776
- Forte M, Heckel B R, Ramsey N F, Green K, Greene G L, Byrne J and Pendlebury J M 1980 Phys. Rev. Lett. 45 2088

the wantiger of the company of the control of the c

The state of the s

en kalander i de de mente de en profesion formalis en la tradició de la filosoficia de la comencia de la comen La comencia de la co

क्रिकेट कुछ । तीम अपने किलाने में देखां का कुछ । यह करिएकि क्रिकेट क्रिकेट

and the property of the territories of the contract of the con

The second section of the second second second second

The second of th

大型 (1985年 - 1985年 - 1

The second of the second secon

and a supplied to the problem of the supplier of the supplier

the above with a regard of the following with year the prime to be

27. Sushkov O P and Flambaum V V 1982 Sov. Phys. Usp. 25 1

New spectrometer for test of equivalence principle with UCN

A.I. Frank¹, P. Geltenbort², S.V. Goryunov¹, M. Jentschel², G.V. Kulin¹, D.V. Kustov^{1,3} and A.N. Strepetov⁴

Frank Laboratory of Neutron Physics, Joint Institute for Nuclear Research, Dubna, Russia

²Institut Laue Langevin, Grenoble, France

Institute for Nuclear Research, Kiev, Ukraine

⁴National Research Centre "Kurchatov Institute", Moscow, Russia

Abstract:

We propose a next generation experiment to test the equivalence principle for neutrons. For this purpose a new spectrometer has been build. The main modification is the measurement of a modulation phase instead of the absolute count rate. By this reason it is expected to overcome former limitations due to background fluctuations and to improve the sensitivity by one order of magnitude. First tests of the new spectrometer were performed.

In our experiment [1] the change in the energy of the ultracold neutrons falling in the Earth's gravitational field (mgH) was compensated by the quantum of energy transferred to the neutron $(h\Omega)$ in the nonstationary interaction with a moving phase grating. The results of that experiment confirm the validity of the equivalence principle within $2x10^{-3}$. One of the major limitations of this experiment was a time dependence of the background count rate. Later we found [2] that the precision of the experiment of this type may be improved at least by one order of magnitude using the same UCN source.

The controlled variation of the neutron energy in a planned new experiment on verification of the weak equivalence principle will be measured by a peculiar time-of-flight method. For this purpose the neutron flux will be modulated by a chopper and the detector will measure the corresponding oscillation of the count rate. The count rate oscillation phase $\Phi = 2\pi F \tau$, where F is the frequency of the chopper, is proportional to the time of flight τ .

For these purposes a time-of-flight gravitational spectrometer with neutron interference filters has been built (fig. 1). At the end of 2010 first tests of the new spectrometer were performed. The main part of this device was the chopper-modulator of the UCN beam (fig.2). Two aluminum disks with 3 opened sectors might be rotated in opposite directions with the help of high vacuum PHYTRON stepper-motors and toothed belts. The rotation frequency and relative phase of discs rotation were controlled by a computer.

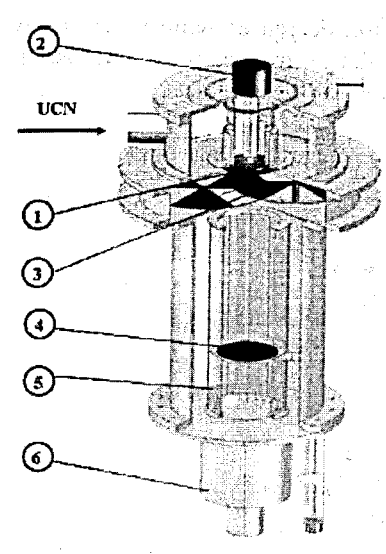


Figure 1. New spectrometer. 1 – monochromator, 2 – motor for the grating spinning, 3 – chopper-modulator, 4 – analyzer (can be moved in vertical direction), 5 – glass neutron guide, 6 – detector.



Figure 2. Chopper-modulator was a finance as a contract of the same and the same of the sa

Two test experiments were performed. In the first one quasi-monochromatic neutron beam, prepared by transmission of UCN through Fabry – Perrot monochromator, was modulated by the chopper. The amplitude and phase of the count rate oscillation were measured for different modulation frequencies. It was

found that the amplitude of count rate oscillation decreases with increasing of frequency relatively slowly (see fig.3) and modulation frequency around 100 Hz may be used in the experiment without serious loss of the contrast.

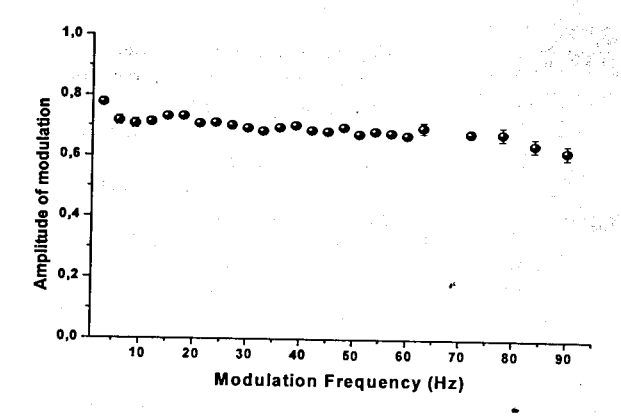


Fig.3 Amplitude of the count rate oscillation measured at different modulation frequencies

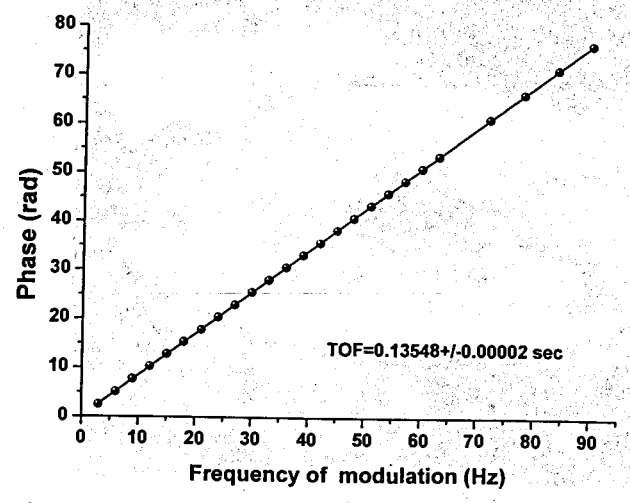


Fig.4 Phase of the count rate oscillation measured at different modulation frequencies

From the measurement of the dependence of count rate oscillation phases on frequency it was possible to obtain the value of UCN time of flight. It was found as $t = 0.13548 \pm 0.00002$ sec.

The second test experiment was to measure the dependence of the count oscillation on the position of monochromator at a fixed frequency. In this experiment UCNs of a wide energy spectrum passed through modulator and only after that through Fabry – Perrot monochromator located below modulator. The position of the last one was possible to vary in height. This test experiment was important, because such experiment will be a part of experimental procedure of the planning test of the equivalence principle. Results are presented in fig. 5.

It was shown experimentally that new spectrometer with Fabry-Perrot monochromator and fast modulation of UCN flux might be used for real measurements.

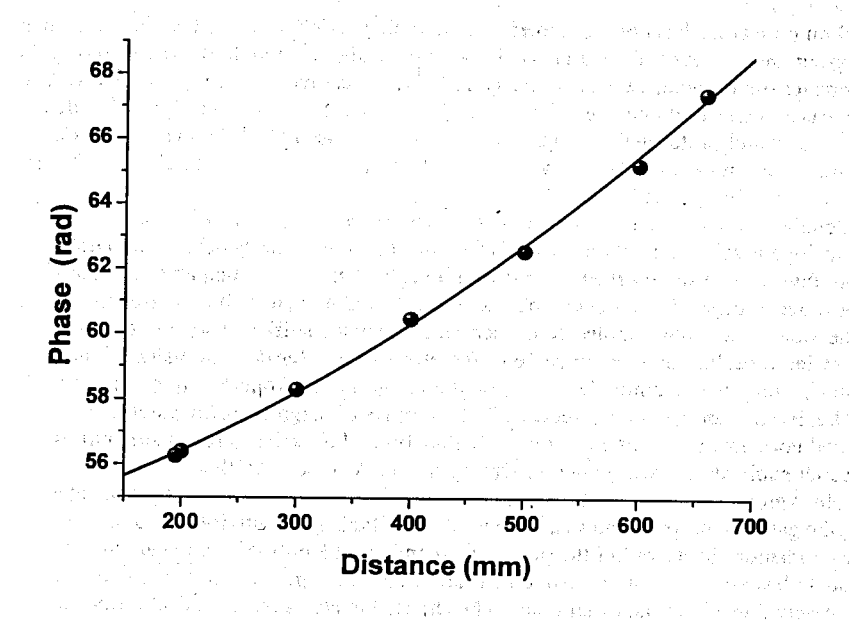


Figure.4 Phase of count rate oscillation measured at 60Hz of modulation frequency, at different position of the analyser

This work was partly supported by Russian Foundation for Basic research (RFBR projects 09-02-00117-a and 11-02-00271-a)

References

- 1. A.I. Frank, P. Geltenbort, M. Jentschel, et al. JETP Letters, 86, 225 (2007)
- 2. A.I. Frank, P. Geltenbort, M. Jentschel et al. Nucl. Instrum. Methods A 611, 314 (2009)

Measurement methodology for the main characteristic of radiative neutron decay

Khafizov R.U. a, Kolesnikov I.A. a, Nikolaenko M.V., Tarnovitsky S.A., Tolokonnikov S.V. a, Torokhov V.D. a, Solovei V.A. b, Kolhidashvili M.R. b, Konorov I.V. c, Plonka-Spehr C.d

^aRNC "Kurchatov Institute", Moscow, Russia

^bPetersburg Nuclear Physics Institute, Gatchina, Russia

^cTechnical University of Munich, Munich, Germany

^dUniversity Mainz, Germany

Ta One.

Annotation

Based on critical analysis of our experiment on radiative decay, as well as the experiment of emit group and work conducted at NIST, we present the methodology for measuring the main characteristic of radiative neutron decay, namely, its relative intensity (B.R.). Relying on spectra measurements of double beta-electron and proton coincidences and triple coincidences of beta-electron and proton with the gamma quantum, we discovered the events of radiative neutron decay and measured its relative intensity B.R.=(3.2±1.6)10⁻³ (with C.L.=99.7% and gamma quantum energy over 35 kev).

The double coincidences spectrum we measured corresponds in all of its characteristics with an analogous spectrum obtained by emiT group studying ordinary beta neutron decay. In particular, this group also observed a significant ionic background, comparable with the value of the beta-decay peak. From Avogardo's law it follows that even with a very deep vacuum inside the vacuum chamber, molecule concentration remains sufficient for the creation of a significant ionic background, comparable to the effect itself. Besides, the value of the ionic background is only very slightly dependent on the vacuum: it is proportional to the cubic root of pressure. Even if the pressure is reduced by two orders of magnitude, the value of the ionic background goes down only by a few times. The analysis of ionic background structure shows that research publication presents not a narrow beta-decay peak but rather a wide ionic peak. Gamma background must also be considered when measuring the triple coincidences. Besides, the gamma spectrum shows a wide peak of artificial radioactivity due to the presence of intense radiation. In its width, the peak corresponds to the only gamma peak measured at NIST and so has no relation to radiative neutron decay. Our spectrum of triple coincidences shows not only this wide peak of artificial radioactivity but also a narrow peak, formed by the events of radiative neutron decay. However, our spectra also show additional background response peaks, arising from the response of our electronic system to the registration of betaelectrons and protons. The only solution to the situation where backgrounds cannot be ignored is precisely measuring the time spectra of double and triple coincidences and clearly distinguishing both the ionic and the gamma backgrounds from these spectra. For our new experiment on precise BR measurements we created a new electronic system, which significantly overcomes the response and which allows to obtain a BR value with 1% precision by measuring the time spectra of double and triple coincidences.

PACS numbers: 13.30.Ce; 13.40.Hq; 14.20.Dh

Introduction. Among the many branches of elementary decay with charged particles in the final state, the radiative branch, where the decay occurs with the creation of an additional particle – the gamma quantum, is usually the most intensive, as the relative intensity (or branching ratio B.R.) of this mode is determined by the fine structure constant α of 10^{-2} order of magnitude. This decay branch is well established and has been investigated for almost all elementary particles. However, the radiative decay of the free neutron

$$n
ightarrow p + e + \overline{\nu} + \gamma$$
 . The stable was taken in the source mass γ

has not been discovered, and all the experiments were aimed at the study of the ordinary neutron decay branch.

The main characteristic of any rare mode of elementary particle decay is its relative intensity, branching ratio (BR). By definition, BR is equal to the ratio between the intensity of the rare decay mode to the intensity of the ordinary mode. In the case of neutron, this intensity ratio can be reduced to the ratio between the number of triple coincidences between the registration of beta-electrons, radiative gamma-quantum and the delayed proton N_T to the number of double coincidences between the registration of the ordinary decay products, beta electron and recoil proton N_D:

 $BR = I(radiative\ decay) / I(ordinary\ decay) = N(e,p,\gamma) / N(e,p) = N_T / N_D$ These two values can be determined only from the analysis of temporary spectra of double and triple coincidences, which form corresponding peaks. Identifying these peaks and distinguishing them from the significant background is the central problem in the methodology of BR measurements.

Further, this experimental BR value needs to be compared with the theoretical value, estimated within the framework of the electroweak model. Any difference between these two values would mean that we are observing a deviation from the electroweak interaction theory.

Our group calculated the neutron radiative spectrum in the framework of standard electroweak theory about ten years ago [1-4]. The calculated branching ratio for this decay mode as a function of the gamma energy threshold was published in these papers. This value for the energy region over 35 keV was calculated to be about $2 \cdot 10^{-3}$.

In 2002 we conducted the first experiment on the discovery of this rare neutron decay branch on the intensive cold neutron beams at ILL (Grenoble, France), where we received a limit for the relative intensity: B.R. < 6.9*10⁻³ (90% C.L.) [5]. This value exceeds the theoretical value we calculated and published by only a few orders of magnitude. This, in turn, means that in our experiment of 2002 we came very close to discovering the radiative mode of neutron decay. For reasons outside of our control we did not receive beam time on intensive cold neutron beam at ILL for a number of years and were able to continue our experiment only in 2005, after we received beam time at the newly opened FRMII reactor in Munchen. In the 2005 experiment we identified the events of radiative neutron decay and measured its relative intensity B.R.=(3.2±1.6) 10-3 with C.L.=99.7% and gamma quanta energy over 35 kev [6]. A year after our discovery of the radiative neutron decay, a NIST experimental group published the results of their experiment on the study of the radiative neutron decay [7] in Nature, with their own value of B.R. = (3.13±0.34)·10⁻³ with C.L.=68% and gamma quanta energy from 15 to 340 kev. Here it is also important to note the work of the emiT group, where the team researched the asymmetry of electron departure in ordinary neutron decay and measured the time spectrum of double coincidences between beta-electron and the delayed proton.

We will formulate the optimal conditions for our future experiment on radiative neutron decay based on a comparison between the experimental spectra of double and triple coincidences, obtained in the experiments of these three groups.

Comparison of double coincidences spectra. We have published the diagram of our experimental equipment on numerous occasions [5-6, 8]. Here we will simply note that in its parameters our equipment is comparable to the equipment used by the two other groups and the distance between the observed decay mode and the proton detector in our equipment is about 0.5m. The accelerating potential of the electric field is also approximately the same in all three equipment sets, so all three experiments should lead to similarly shaped spectra of double and triple coincidences spectra.

Fig. 1 demonstrates the summary statistics on double e-p coincidences (coincidences of electron with delayed proton). Fig. 1 clearly shows two major peaks: one peak with a maximum in channels 99-100, which is the peak of zero or prompt coincidences [6, 8]. The position of this peak marks the zero time count, namely the time when the electron detector registered the electron. This peak is not physical in its nature. Instead, it is a reaction of the detectors and the electronic system to the registration of the beta electron. It is namely the pulse from the electron channel that opens the time windows on spectra Fig. 1 for 2.5 µs forward and backwards. The next peak visible on Fig. 1 has a maximum in channel 120 and is the peak of e-p coincidences of electron with delayed proton.

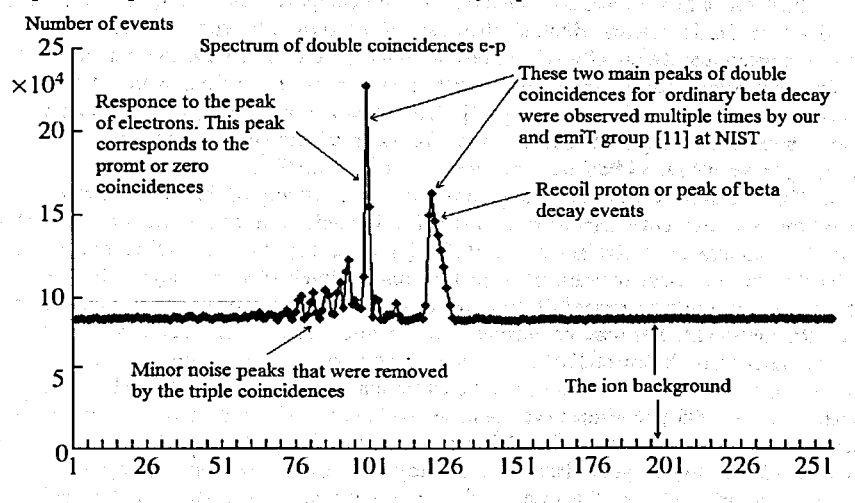


Fig. 1. Timing spectrum for e-p coincidences. Each channel corresponds to 25 ns. The peak at channel 99-100 corresponds to the prompt (or zero) coincidences. The coincidences between the decay electrons and delayed recoil protons (e-p coincidences) are contained in the large peak centered at channel 120.

An analogous situation was observed in experiments on the measurement of the correlation coefficients by two independent groups at ILL [10] and emiT group at NIST [11], and it was also mentioned at [12]. We would especially like to emphasize the correspondence of our spectrum of double coincidences with an analogous spectrum from the result obtained by the emiT group from NIST [11]. On Fig. 2 we present their spectrum and diagram for the registration of the beta electron and the recoil proton. A comparison of our results with the results of the emiT group shows their unquestionable similarity. Moreover, the position of the second proton peak in Fig. 2 (emiT group), like in Fig. 1 (our result), corresponds well to the simple estimate obtained by dividing the length of a proton trajectory by its average speed.

Here we will also note the presence of a significant homogenous ionic background in Fig. 1 and Fig. 2. However, in both cases this background allows to easily distinguish the neutron decay peak. As we will shortly demonstrate, this ionic background will play a dominant role in the presence of a strong magnetic field and it will become impossible to distinguish events of ordinary neutron decay against it.

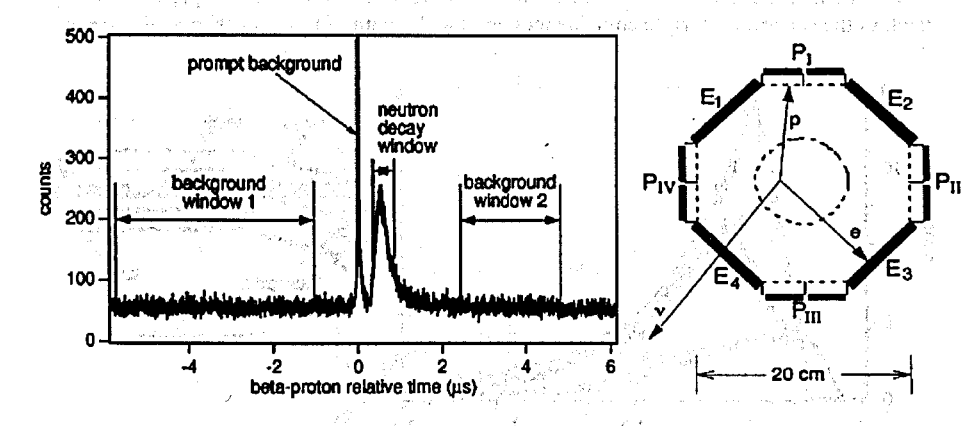


Fig. 2 Spectrum of double electron-proton coincidences obtained by emiT Group [11] with two peaks and ion background value comparable to the neutron decay peak; emiT group scheme for registering beta electron and recoil proton.

Fig. 1 shows that the total number of events in e-p coincidences peak in our experiment equals N_D =3.75·10⁵. This value exceeds the value we obtained in our previous experiment conducted on beam PF1 at ILL by two orders of magnitude. It was precisely because of the low statistics volume that we could not identify the events of radiative neutron decay in that experiment and instead defined only the upper B.R. limit [5]. It is very important to note that the peak of double coincidences between electron and the delayed proton is observed against a non-homogenous background: besides the homogenous ionic background, which has a value comparable to the value of the e-p coincidences peak, there is an obvious peak in channels 99-100. In essence, this peak is a response peak to the time spectrum of electron registration, which contains just one peak in channels 99-100, signifying the time when the electron detector registered the electron. We will shortly see that the radiative peak

of triple coincidences appears against a non-homogenous background with not one, but two response peaks.

The remaining peaks on Fig. 1 are small, with just seven peaks distinct from the statistical fluctuations. These occurred because of the noise in the electric circuits of the FRMII neutron guide hall. There are no other physics-related reasons for their occurrence. These peaks appeared and disappeared depending on the time of day, reaching their maxima during the work day and disappearing over the weekends. Such behavior was observed throughout the experiment as we collected statistics. Since the nature of these seven small peaks is in no way related to radiative and ordinary decay, we did not emphasize them in our article.

The comparison conducted demonstrates that our results on the spectra of double coincidences completely correspond with the results obtained by the emiT group. Now we will compare these two spectra with the spectrum of double coincidences obtained by the third group. Unfortunately, the authors did not publish the spectrum of double coincidences in their original Nature article, instead it was only published this year in paper [13]. Fig 3 displays the spectrum of triple coincidences and the diagram of their experimental equipment.

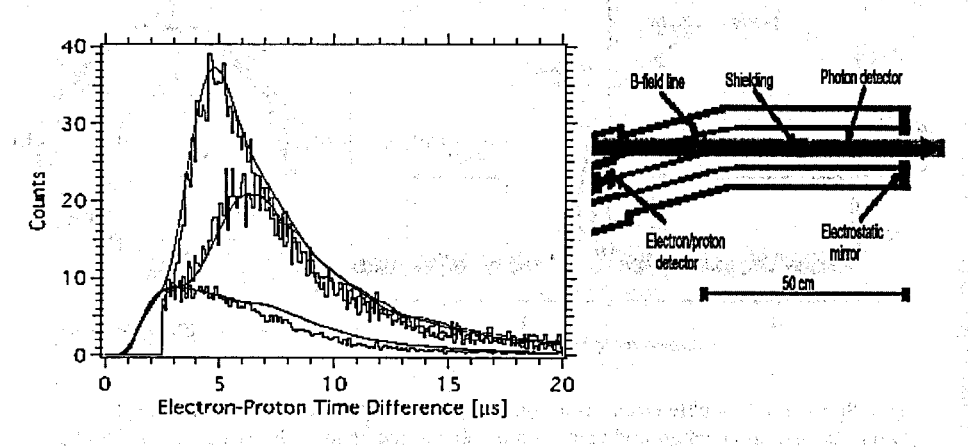


Fig. 3 Equipment diagram and the single peak of "electron-proton" coincidences, published in (lower, middle and upper curves subsequently for 0, 300, 500 volts on electrostatic mirror [13]. The location of the peak's maximum and its significant width differ from our and the emiT results subsequently by one and two orders of magnitude. The location and the width of the peak also deviate by one and two orders of magnitude from the elementary estimates of delay times (see below).

The significant deviation obtained is explained by the fact that the peak in the NIST experiment consists not of beta-decay protons, but rather of ions. The density of gas molecules inside the equipment is proportional to pressure and according to the Avogadro's Law is at the order of 10⁷ mol/cm³ even at the pressure of 10⁸ – 10⁻⁹ mbar. This is a very significant number, which quite enough for creation the large ionic background in the presence of ionizing radiation. The energy of beta-electrons significantly exceeds the energy of ionization. Besides, the probability of ion creation by electrons is proportional not to

volume taken up by one molecule but to the average distance between molecules. It is precisely due to this reason that the ionic background falls proportionally to the cubic root of the pressure and not proportionally to pressure. In our experiment the pressure was 10-6 mbar, while the emiT group it was the same as in the NIST experiment, i.e. several hundred times lower. However, the values of the ionic background differ by only 5-6 times of magnitude. The light ions, together with the beta protons, should have a delay time comparable to 1 µs. The pulses from these particles are simply not visible in the spectrum due to the NIST group's use of combined electron-proton detector (see Figure 4 with the shape of electron and ion pulses). The maximum of the proton peak in the NIST experiment, according to the delay times estimations (delay time is proportional to square root of ion mass), falls exactly to the air ions 4-6 µs.

Fig 4 presents the impulse forms on the electron-proton detector. As was pointed out above, the significantly delayed impulses of low amplitude correspond to ion impulses, and the impulses from protons are simply invisible due to a presence of a wide electron impulse of high amplitude. Namely this fact explains the dead zone around zero on the spectrum of electron-ion coincidences on Fig. 3.

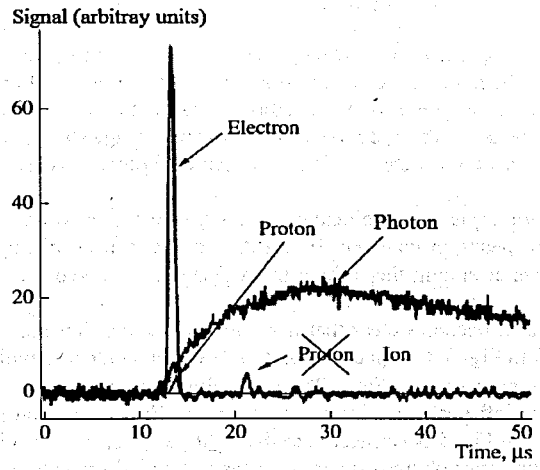
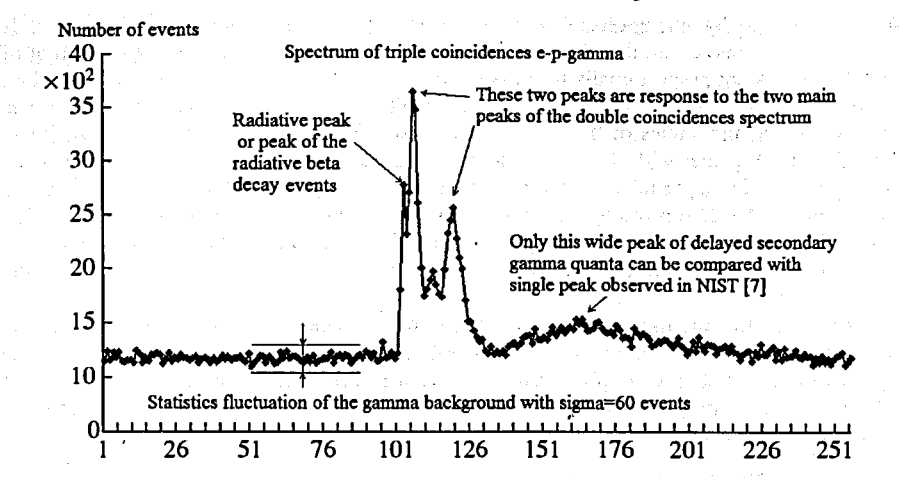


Fig. 4. The signal from the decay proton has to be delayed by less than one microsecond, which is why it is located at the base of the electron pulse (see line number 2) and so cannot be registered by the combined electron-proton detector. The pulses that are delayed by longer than 1 microsecond are pulses not from decay protons, as it was indicated in ref. [7], but rather from ions, formed in the decay zone. The line number 1 shows the shape of pulses from the gamma detector

Comparison of triple coincidences spectra. In paper [11] the emiT group researched only the ordinary decay mode, thus this comparison is limited to our spectrum of triple coincidences, presented in Fig 5, and the only peak published by the NIST authors in Nature [7], presented on Fig 6. Analysing the double coincidences spectra obtained by our and the emiT groups (both of which present two main peaks) shows that in the spectrum of triple coincidences we should observe not two but three peaks. Namely, along with the sought after

The Bally is recard that I believe held



radiative peak, the triple e-p-gamma coincidences spectrum should show two response peaks to the registration of beta-electrons and the registration of protons. Fig. 5 of triple coincidences clearly shows three peaks, and the leftmost peak with the maximum in channel 103 is connected to the peak of the radiative gamma-quanta in question, as this gamma-quantum is registered by the gamma detectors in our equipment before the electron.

Fig. 5 Timing spectrum for triple e-p-g coincidences. Each channel corresponds to 25 ns. In this spectrum, three main peaks in channels 103, 106 and 120 can be distinguished. The leftmost peak in 103 channel among these three main peaks is connected with the peak of radiative decay events.

Comparing Fig. 1 and 5, it becomes clear that if we ignore the first leftmost peak with the maximum in channel 103 in Fig. 5, the spectrum of double e-p coincidences will resemble the spectrum of triple e-p- γ coincidences on Fig. 1. The peak with the maximum in channel 106 on Fig. 5 is connected to the left peak of false coincidences on Fig. 1, and the peak with the maximum in channel 120 on Fig. 5 is connected to the right peak of e-p coincidences on Fig. 1. The emerging picture becomes obvious when one uses a standard procedure, introducing a response function for gamma channel $R_{\gamma}(t,t')$ [6], which is also necessary for calculating the number of triple radiative coincidences N_T in radiative peak. Using the method of response function, one can confidently define our double-humped background: the narrow peak with the maximum in channel 106 on Fig. 5 is the response to the narrow peak of zero coincidences (by other words this peak is response to beta-electron registration) in channels 99-100 on Fig. 1, and the second peak in this double-humped background on Fig. 5 is the response to the peak in channels 117-127 on Fig. 1 (or this peak is response to proton registration).

When discussing the similarities between the spectra on Fig. 1 and Fig. 5, it is important to note that the response peak on Fig. 5 with a maximum in channel 106 is shifted to the right or delayed in comparison to the peak responding to electron registration in channel 100 on Fig 1. This is due to the fact that in our electron diagram we used a constant fraction discriminator (CFD). CFD has its own delay line and the location of the time-pickoff signal it generates is determined by the method of comparing the fraction of the original signal to the delayed (CFD method [14]). Thus, there is a shift in the first response peak with a maximum in

channel 106 on Fig 5 versus the first peak on Fig 1 with the maximum in channel 100. The value of this delay is equal to the length of the gamma quantum impulse signal front and is on average 150 ns. The CFD method obviously also shifts the radiative peak, but it should be located to the left of the response peak, as is observed on Fig 5.

As for the wide, almost indistinguishable peak in channel 165 on Fig. 5, its influence on radiative peak in channel 103 is negligible. Its nature is in no way related to the researched phenomenon, so we do not discuss it in our article. This peak is created by the radioactive gamma quanta delayed on average by 1.25 µs and emitted by the radioactive medium within our experimental equipment. The medium is activated by registered beta-electrons. This event of artificial, induced radioactivity has been known for over 100 years and does not have anything in common with the new event of radiative neutron decay which is the subject of current research. As we will demonstrate below, only this 1 microsecond peak and delayed from the registration time by about the same time can be compared to the peak observed by the authors of paper [7] at NIST (see Fig. 6). Thus, the authors of this experiment observed not the events of radiative decay but rather the event of artificial radioactivity, already well known in the time of Joliot-Curie.

After analyzing the spectra with the help of the non-local response function we finalize the average value for the number of radiative neutron decays N_T =360 with a statistics fluctuation of 60 events. B.R. can be expressed as a ratio of N_T to N_D as BR = k (N_T / N_D), where coefficient k=3.3 is the geometrical factor that we can calculate by using not isotropic emission of radiative gamma-quanta Fig. 3. With the number of observed double e-p coincidences N_D = 3.75·10⁵ and triple e-p- γ coincidences N_T = 360, one can deduce the value for radiative decay branching ratio of (3.2 ± 1.6) · 10⁻³ (99.7 % C.L.) with the threshold gamma energy ω =35 keV. The average B.R. value we obtained deviates from the standard model, but because of the presence of a significant error (50%) we cannot make any definite conclusions. The measurements must be made with greater precision. According to our estimates, in our future experiment we will be able to make more definite conclusions about deviation from the standard electroweak theory with experimental error less than 10%.

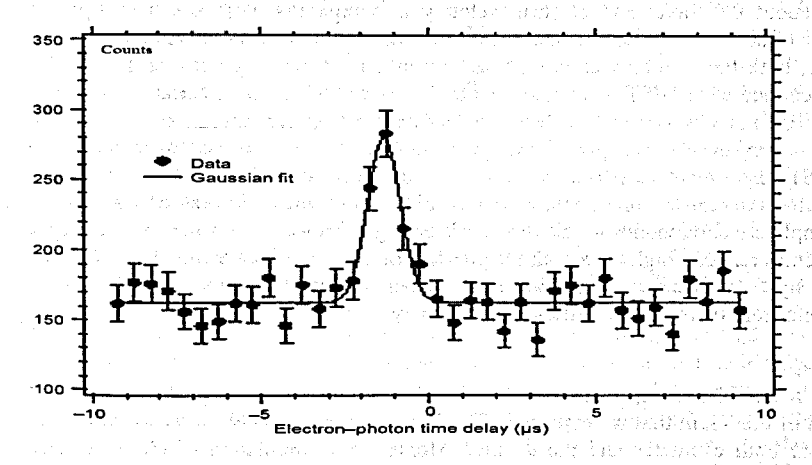


Fig. 6 Only peak of "electron-photon" coincidences, shifted to the left of 0 – the time of betaelectron registration – by 1.25 microseconds, published in [7].

The difference between the NIST experiment and our experiment becomes immediately apparent. First and foremost, it is the time scale: in our spectra, the scale is measured in nanoseconds, while in the other experiment the scale is in microseconds. Besides, we used three types of detectors, each of which registered its own particle: one detector for the electrons, one for the protons, and six identical detectors for the radiative gamma-quanta (see [6]). The duration of the front pulse from the electron and proton detectors is 10 nanoseconds in our experiment and 100 times greater than that in the NIST experiment, in the order of 1 μs. The rise time of gamma signal from our gamma-detectors is on average 150 ns, and from avalanche diode on the NIST equipment greater than 10 µs, besides that the diode pulse arrives with significant noise, which makes the thickness of the front pulse line equal to more than 0.5 µs (see the photon line on Fig. 7 from [7]). All of this leads to our factual time resolution being two orders of magnitude better than the resolution achieved in the NIST experiment. However, as the two experiments used equipment which was practically the same in size and smaller than 1 meter, the choice of the time scale is a matter of principle. Given this geometry, it is impossible to get microsecond signal delays from all of the registered charged particles, i.e. electrons and protons. In this light, it is surprising that the peak identified by the authors of the NIST report [7] as the peak of radiative gamma-quanta. is shifted by 1.25 microseconds to the left. The expectation that magnetic fields of several tesla in magnitude delay all electrons and protons, are absolutely ungrounded.

Indeed, the magnetic field cannot change the speed of charged particles. It can only twist a line trajectory into a spiral. The length l of this spiral depends on angle θ between particle velocity and magnetic field direction. In beta decay, electrons can fly out under any angle θ , therefore the magnetic field can increase the time of delay by several orders of magnitude only for a negligible portion of the charged particles. Even this negligible number of particles that flew out at an almost 90 degree angle to the direction of the magnetic field that coincides with the direction of the narrow neutron guide (see Fig. 3) will most likely end up on the walls of the neutron guide rather than reach and hit the detector due to the presence of the strong electrostatic field. Because the distance between the point of decay and the detector is about 0.5 meter and electron velocity is comparable with speed of light, the electron time of delay should be less than a microsecond by two orders of magnitude.

Thus, both the 1 microsecond shift and the width of the only peak on Fig 6 in the experiment conducted at NIST, is in sharp contradiction to elementary estimates. We, on the other hand, did not observe any wide peaks before electron registration and our gamma background is very even in this part of the spectrum (see Fig 5). However, when we assume that the NIST experiment authors observed the wide peak, shifted by 1 microsecond, not before, but after the registration of beta-electrons. In that case, the wide peak on our spectrum in Fig 5 completely corresponds to the wide peak on Fig 6. However, as noted above, density of gas molecules remains high even with the pressure of 10^{-8} - 10^{-9} mbar and this atmosphere is activated by beta-electrons. The wide peak in our spectrum is formed by the delayed gamma quanta from this induced artificial radioactivity.

Conclusions.

The main result of our experiment is the discovery of the radiative peak namely in the location and of the width that we expected. The location and the width of the radiative peak correspond to both estimates and the detailed Monte Carlo simulation of the experiment. Thus, we can identify the events of radiative neutron decay and measure its relative intensity,

which was found to be equal B.R. = $(3.2\pm1.6)\ 10^{-3}$ (with C.L.=99.7% and gamma quanta energy over 35 keV).

At the same time, the average experimental B.R. value exceeds the theoretical value by 1.5 times. However, due to a significant error we cannot use this result to assert that we observe a deviation from the standard model. Therefore, our most immediate goal is to increase experiment precision, which we can improve by several percents according to estimates.

For last two years we were preparing this new experiment and conducted number of tests for our new electronics. We constructed multi channel generator what can generate the pulses with the same forms as our electron, proton and gamma detectors. During these tests we got the same responses as during our last experiment on real neutron beams at FRMII. It means that all additional peaks on our spectra have no any physics reasons and It proves once more that we were absolute correct when applied the response function method for explaining these peaks as response ones and for developing our experimental spectra.

We created and tested our new electronic system for obtaining experimental spectra. By using this new programmable electronics we can significantly reduce the influence of response peaks on peak with radiative decay events. Now we can get this peak almost isolated from responses. On our estimations all these allow us to reach accuracy for our new experiment about 1% So, on the base of our new electronics we can confirm or refuse the deviation of our average experimental value of BR from the standard model one.

As concerning the comparison of our experimental results with others we can make the following two main conclusions. The main parameters of our spectrum of double electron-proton coincidences identifying the events of ordinary neutron decay fully coincide with an analogous spectrum published by emiT group in [11].

Unfortunately we cannot say same for another experiment measuring the radiative neutron decay published in [7]. Particularly vexing is the authors' unsubstantiated assertion that they observe their only wide peak of gamma quanta before the registration of beta-electrons. Both the position and the width of this peak are located in sharp contradiction to both the elementary estimates, and the results of our experiment. In the course of our entire experiment we did not observe such a wide peak in the triple coincidences spectrum, located before the arrival of electrons at a huge distance of 1.25 μ s. However, it is possible to reconcile our spectra of triple coincidences with the one isolated peak observed at NIST if we assume that at NIST, the gamma-quanta were registered after the beta electrons. Only in this case does the NIST peak almost completely coincide with the peak we observed in the spectra of triple coincidences with the maximum in channel 165, both in terms of the huge delay of 1.25 μ s and in terms of its huge width. This peak is created by the delayed secondary radioactive gamma-quanta, arising from the activation by beta electrons of the media inside experimental chamber, which was the real object of the NIST experimentalists' observation.

Despite the recent disagreements [15], which we consider to be subjective in nature [16], we acknowledge the contribution of our Western colleagues Profs. N. Severijns, O. Zimmer and Drs. H.-F. Wirth, D. Rich to our experiment conducted in 2005. Here it is important to note that the authors of the article published in Nature [7] consciously misled first our Western colleagues and then the physics community at large by insisting that their only wide peak is removed by 1.25 microseconds to the left from the time of electron registration, when in reality this peak was formed by delayed gamma-quanta, emitted by the activated medium inside the experimental equipment, and corresponds to our wide peak with the maximum in channel 165 (refer to Fig. 6) [15, 16]. The authors would like to thank Profs. D. Dubbers and Drs. T. Soldner, G. Petzoldt and S. Mironov for valuable remarks and discussions. We are

also grateful to the administration of the FRMII, especially Profs. K. Schreckenbach and W. Petry for organizing our work. We would especially like to thank RRC President Academician E.P. Velikhov and Prof. V.P. Martem'yanov for their support, without which we would not have been able to conduct this experiment. Financial support for this work was obtained from RFBR (Project N 07-02-00170).

References

- [1] Gaponov Yu.V., Khafizov R.U. Phys. Lett. B 379 (1996) 7-12
- [2] Radiative neutron beta-decay and experimental neutron anomaly problem. By Yu.V. Gaponov, R.U. Khafizov. Weak and electromagnetic interactions in nuclei (WEIN '95): proceedings. Edited by H. Ejiri, T. Kishimoto, T. Sato. River Edge, NJ, World Scientific, 1995. 745p.
- [3] About the possibility of conducting an experiment on radiative neutron beta decay R.U. Khafizov, N. Severijns Proceedings of VIII International Seminar on Interaction of Neutrons with Nuclei (ISINN-8) Dubna, May 17-20, 2000 (E3-2000-192), 185-195
- [4] Khafizov R.U. Physics of Particles and Nuclei, Letters 108 (2001) 45-53
- [5] M. Beck, J. Byrne, R.U. Khafizov, et al., JETP Letters 76, 2002, p. 332
- [6] R.U. Khafizov, N. Severijns, O. Zimmer et al. JETP Letters 83 (2006) p. 5
- [7] J.S. Nico, et al. Nature, v. 444 (2006) p. 1059-1062
- [8] Discovery of the neutron radiative decay R.U. Khafizov, N. Severijns et al. Proceedings of XIV International Seminar on Interaction of Neutrons with Nuclei (ISINN-14) Dubna, May 24-25, 2006
- [9] B. G. Yerozolimsky, Yu. A. Mostovoi, V P. Fedunin, et al., Yad. Fiz. 28, 98 (1978) [Sov. J. Nucl. Phys. 28, 48 (1978)].
- [10] I.A. Kuznetsov, A. P. Serebrov, I. V. Stepanenko, et al., Phys.Rev.Lett., 75 (1995) 794.
- [11] L.J. Lising, S.R. Hwang, J.M. Adams, et al., Phys. Rev. C. v.6, 2000, p. 055501
- [12] J.Byrne, R.U. Khafizov, Yu.A. Mostovoi, et al., J. Res. Natl. Inst. Stand. Technol. 110, p.415, (2005).
- [13] R.L. Cooper, T. E. Chupp, M. S. Dewey, et al, Phys. Rev. C 81, 035503 (2010)
- [14] T.J. Paulus, IEEE Transactions on Nuclear Science, v.NS-32, no.3, June, p.1242, 1985.
- [15] N. Severijns, et al., e-print arXiv:nucl-ex/0607023; J. Nico, private communication.
- [16] R.U. Khafizov, V.A. Solovei, e-print arXiv:nucl-ex/0608038.

CALCULATION OF CORRECTIONS FOR PRECISE OBTAINING THE n,e-SCATTERING LENGTH FROM THE ANGULAR ANISOTROPY OF SLOW NEUTRONS SCATTERED BY NOBLE GASES

L.V.Mitsyna, A.B.Popov

Frank Laboratory of Neutron Physics Joint Institute for Nuclear Research, 141980 Dubna, Moscow region Russia

For the precise measuring the angular anisotropy of neutrons scattered by noble gases in energy region from a few meV up to 1 eV with use of time-of-flight method it is necessary to know all corrections with the accuracy not worse than of 10^{-4} . Only in this case one can assure obtaining the n,e-scattering length $b_{\rm ne}$ with the accuracy 2-3%. The corrections for efficiency difference of detectors, which register slow neutrons scattered forward or backward, with taking into account the thermal motion of Ar is calculating by Monte Carlo method in real geometry.

1. Introduction

As we noted more than once (see, for example [1]), a necessity of measuring the n,e-scattering length is still kept, as a dispersal of a number of obtained by this time b_{ne} values is several times more than their uncertainties. Thus, an accuracy of corrections in precision experiments is open to question. From the point of view of corrections clarity the experiment with measuring the angular anisotropy of slow neutrons scattered by noble gases is the most easily understood. The b_{ne} value extraction from a neutron scattering anisotropy, when neutrons elastically scattered by noble gases forward and backward, was done by Krohn and Ringo a long time ago [2]. But as these experiments were carried out at the reactor using thermal neutron beam, the authors had to average all energy dependent corrections and atom form-factor over whole neutron spectrum. Application of the time-of-flight method [3] allows exact corrections introducing at certain neutron energies.

The success of b_{ne} value extraction is determined by the accuracy of obtained intensities ratio at neutrons scattering forward ($\theta_1 \sim 45^{\circ}$) and backward ($\theta_2 \sim 135^{\circ}$). Of course, the correction for the thermal motion of gas atoms is the largest one in this experiment, but it must be calculated in case of noble gas sample absolutely correctly for each certain neutron energy [4]. Seemingly, the main difficulty in this experiment is the correct calculation of the energy loss at scattering of a neutron: it is necessary to know the counters efficiencies ratio with the accuracy $\sim 10^{-4}$ in order to obtain b_{ne} value with systematic uncertainty notably less than statistical one.

2. Setting of experiment and geometry for calculations

The experimental installation represents the turn-table and fixed on it the chamber with gas Ar and four ³He-counters (with gas pressure 8 at and sizes Ø3×18 cm). Neutron counters are placed at the angles 45° and 135° relative to the beam axis at the distance 30 cm from the center of working volume, where neutrons are scattered. The scattering volume is confined by cadmium (or boron polyethylene) collimators, which also restrict the scattering angles

range. Using the Monte Carlo method the calculations of the neutron scattering anisotropy were carried out taking into account thermal motion of gas atoms for argon in geometry, which is shown in Fig.1.

The chamber, in which neutrons are scattered, is a double cross of collimators. They form neutron beam and windows in the directions of detectors. Four collimators with detectors at the ends (in the boron polyethylene shielding), where neutrons come after scattering, and collimators for neutron beam passing before scattering are disposed crosswise. Turning at 45° the turn-table allows to use for measurements all possible positions of each detector with respect to neutron beam.

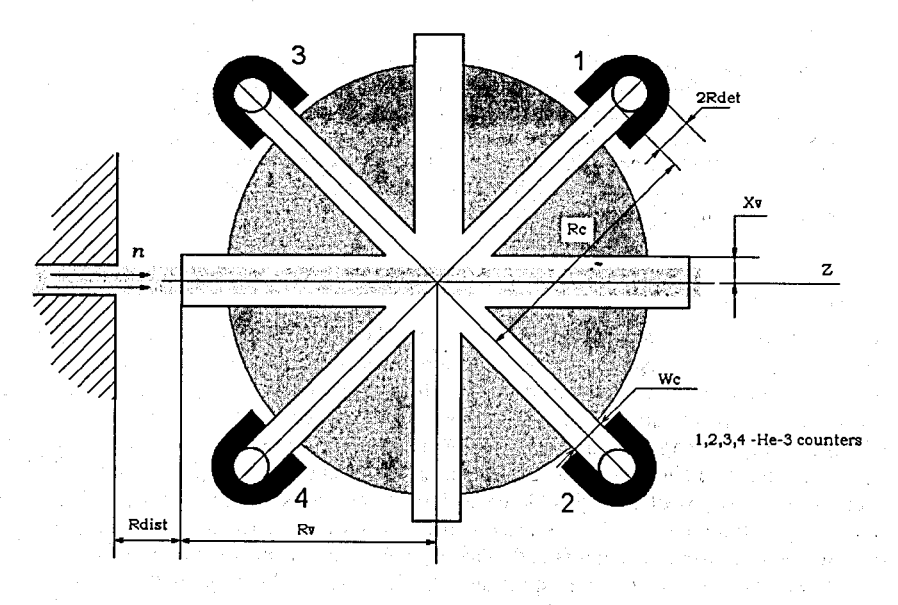


Fig.1. Scheme of the installation for calculating the neutron scattering (view from above). 1, 2, 3, 4 – detectors in shielding at the ends of collimators on the tern-table.

Width of collimators slit before detector Wc and diameter of the detector $2R_{det}$ are equal to 3 cm, height of counters inlets is 18 cm, and the height of collimators slits and neutron beam is the same. Width of collimators for neutron beam is 2Xv=3 cm, their length is Rv=30 cm, length of collimators from the centre of installation to the slit is Rc=30 cm.

For each of four counters a measuring anisotropy of neutrons scattered at angles θ_1 and θ_2 is determined as a ratio of scattering intensities $I(E,\theta)$:

$$R(E) = \frac{\sigma(E, \theta_1)}{\sigma(E, \theta_2)} = \frac{I(E, \theta_1)}{I(E, \theta_2)}C(E),$$

where $I(E,\theta)$ are the scattering intensities of neutrons. The correction coefficient $C(E) = \varepsilon(\theta_2)/\varepsilon(\theta_1)$ for efficiency variation of neutron registration at different angles is indispensable to extract the b_{ne} value. The motion of turn-table changes positions of detectors, and intensities ratio is obtained from the ratio of counts of neutrons scattered forward $(\theta_1 \sim 45^0)$

and backward ($\theta_2 \sim 135^{\circ}$), which are measured alternately at turning the installation relative to the beam axis. This ratio is calculated by the formula of the geometrical mean

$$R = \left(\frac{N_{1f}N_{2f}N_{3f}N_{4f}}{N_{3b}N_{4b}N_{1b}N_{2b}}\right)^{1/4},$$

where N are corrected counts, numbers determine counters, and counters positions (at forward or backward scattering) are indicated by letters f and b.

3. Results of calculations

The ratio of counter efficiencies for neutrons scattered backward and forward is dependent on energy of incident neutron and real scattering angular distributions, which are complicated by thermal motion of gas atoms. It must be calculated carefully to have a possibility to correct experimental results at each point of investigated energy range. For that the Monte Carlo calculations were carried out at initial energy of neutrons from 0.001 eV to 1 eV for argon pressure 10 at. The capture cross section was presumed to be zero to reduce a counting time. Addition individual calculations showed that influence of capture can be neglected for argon. These calculations in above-mentioned geometry allowed to obtain the angular distributions of neutrons scattered into forward and backward detectors and efficiencies of their registration with taking into account thermal motion of gas atoms.

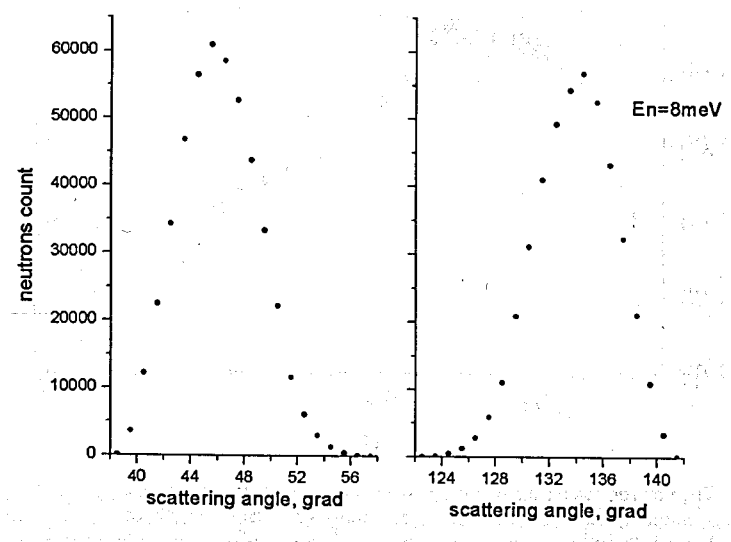


Fig.2. The calculated angular distributions of neutrons with initial energy 8 meV scattered by argon forward (left picture) and backward (right picture) taking into account registration efficiency of counters (one run for ~10¹¹ neutrons falling into the target)

With the purpose to determine the correction coefficient C(E) with the adequate accuracy it is necessary to carried out a multiple calculations for each energy point (the higher neutron energy the more statistics of events is required). Gradual "rise of statistics" is

realized by averaging-out of independent calculations, which imitate separate measurements, with computation of random uncertainty of their arithmetic mean. Bit by bit this uncertainty is made more exact.

The angular distributions of neutrons with initial energy 8 meV for one of the calculations are shown in Fig.2. The statistics was 6×10^{10} of incident neutrons into scattered volume. As Fig.2 illustrated the limited by detectors slits dispersions of angles in given geometry after forward and backward scattering are $38^0 \div 58^0$ and $122^0 \div 142^0$, correspondingly.

The scattering anisotropy dependence on neutron energy R(E) for argon is shown in Fig.3. Here the results of calculating the R(E) without taking into account of the efficiencies of neutrons registration and after introducing of these corrections are shown by the black and open points, correspondingly. In all calculations the effect of n,e- scattering was taken into account, and it was of opinion that $b_{ne} = -1.32 \cdot 10^{-3}$ fm. Effect induced by n,e-scattering is apparent in the Fig.3 as a evident depression of revised (open) points relative to R(E)=1.07 what must be at $b_{ne}=0$ in the concerned neutron energy region.

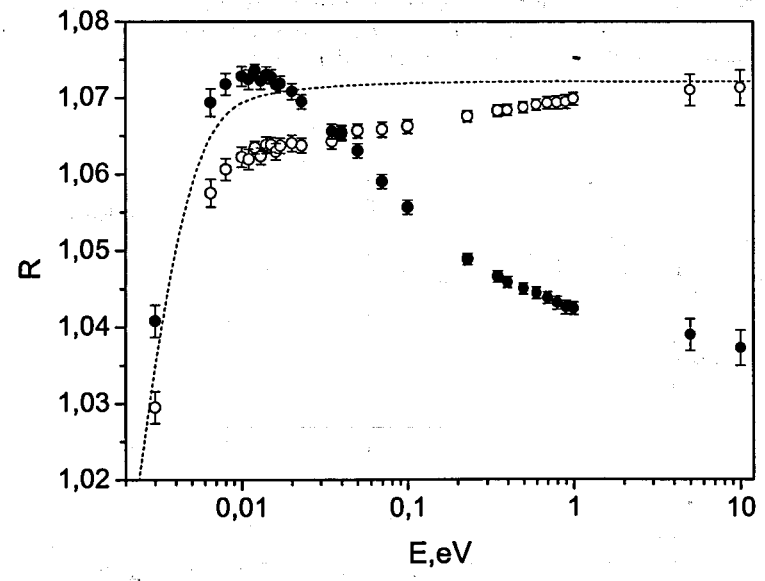


Fig. 3. The neutron scattering anisotropy dependence on their incident energy with taking into account thermal motion of argon atoms (scattering length of n,e-interaction is $b_{\rm ne}=-1,32\cdot10^{-3}$ fm): open circles are calculations with correction for efficiency, black circles are the calculations without these correction. Dashed curve is anisotropy calculation without taking into account n,e-scattering.

At last, the calculations of the energy dependence for correction coefficient C(E) is shown in Fig.4. For comparison a rough count of C(E) without taking into account thermal motion of argon atoms is illustrated by a dashed curve. In this case a counter efficiency was calculated as multiple integral by working scattering volume and by volume of counter, and

the energy losses for neutrons scattered forward and backward were determined exactly at the angles 45^0 and 135^0 (without angular dispersal), i.e. the neutron energy E_{ns} after scattering was found from a simple expression $E_{ns} = E_n (40 + \cos \theta)^2 / (40 + 1)^2$, where θ is a scattering angle, and E_n is the initial neutron energy. Taking into account the thermal motion the energy distributions of neutrons scattered backward shifts towards smaller energies at $E_n > 0.025$ eV and towards bigger energies at $E_n < 0.025$ eV. The efficiency of ³He-counter with gas pressure 8 at slumps with neutron energy increasing (from almost 100% at the neutron energies \sim meV up to somewhat more 15% at 10 eV), and hence at $E_n > 0.025$ eV the counter efficiency of registration for neutrons scattered backward become higher. And vice versa, the counter efficiency for these neutron energies below 1. The energy distributions of neutrons scattered forward shifts incidentally, and the efficiency of registration for neutrons scattered backward becomes slightly higher than for neutrons scattered forward at the energies more than 0.05 eV. As it is shown in our papers, to ensure an accuracy of the b_{ne} value 2 - 3% the energy region more than 0.1 eV is very important.

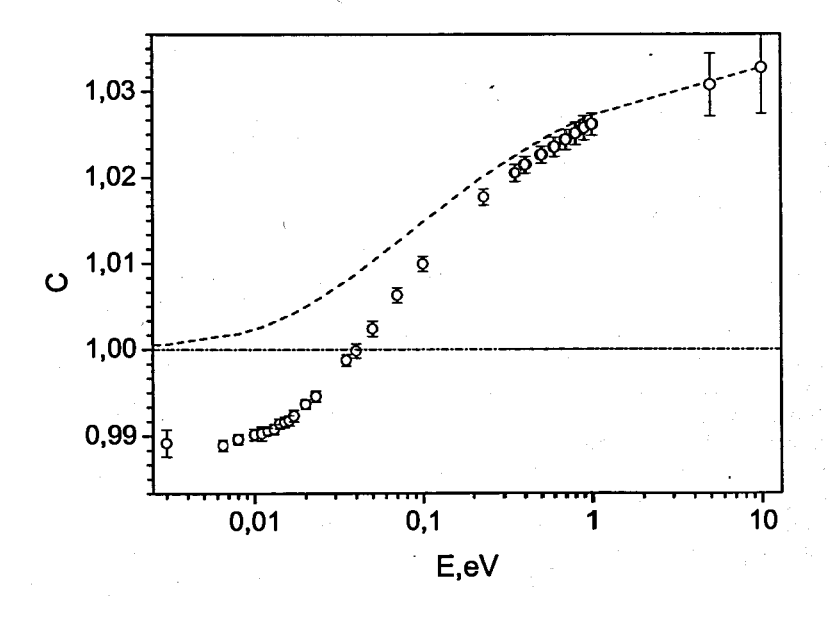


Fig.4. The corrections $C(E)=\varepsilon(135^{\circ})/\varepsilon(45^{\circ})$ obtained from Monte Carlo calculations for intensities of neutrons scattered forward and backward by argon. Dashed curve is raw count of C(E) without taking into account thermal motion of gas atoms.

Calculations showed that the introducing of corrections for efficiency variation is necessary in principle, if we use 3 He-counter with gas pressure 8 at as a detector. Parameterization of C(E) values calculated in certain energy points by curve with adequate accuracy will allow correcting the desired quantity of R(E) at any neutron energy. In order to improve an accuracy of these corrections calculations are still continued.

Conclusion

The bulky calculations in real geometry with taking into account the thermal motion of gas is urgent to reduce the uncertainty of correction coefficient C(E) to required magnitude. Just accurate taking into account of these corrections allows obtaining the R(E) values in the neutron energy region more than 0.1 eV.

References

- Mitsyna L.V., Nikolenko V.G., Parzhitski S.S., Popov A.B., Samosvat G.S., in XVI International Seminar on Interaction of Neutrons with Nuclei, Dubna, June 11-14, 2008, JINR, E3-2009-33 (Dubna, 2009), p.9.
- 2. Krohn V.E., Ringo G.R., Phys.Rev., 148, 1303(1966); Phys.Rev., D8(1973)1305.
- Bunatian G.G., Nikolenko V.G., Popov A.B., Samosvat G.S., Tretyakova T.Yu., Z.Phys., A359(1997)337.
- 4. Nikolenko V.G., Popov A.B., Eur. Phys.J. A34, 443-446 (2007).

STUDY OF THE NEUTRON LAUE DIFFRACTION IN LARGE SILICON CRYSTAL FOR THE BRAGG ANGLES CLOSE TO $\pi/2$

E.O. Vezhlev, V. V. Voronin, I.A. Kuznetsov, S. Yu. Semenikhin, V.V. Fedorov Petersburg Nuclear Physics Institute, Gatchina, Russia

Abstract

The Laue diffraction on (220) plane of large (\sim 200 mm) silicon crystal was investigated for the Bragg angles close to $\pi/2$. It was demonstrated that the effective neutron absorption length for the low-absorbed Bloch wave can reach about 3 m instead of 40 cm for the non-diffracted neutrons. Therefore, we saw reasonable reflected neutron beam intensity for the Bragg angles about 88^0 and it was possible to observe specific dynamical diffraction effects for Laue neutron diffraction with such Bragg angles in the extremely thick crystal. Experimental results are in good agreement with theoretical predictions for both one-crystal scheme and for two-crystal scheme of setup.

Introduction

The crystal-diffraction experiment to test weak equivalence principle for the neutron was recently proposed [1, 2]. It is based on the essential magnification of external affect on the neutron diffracting under Laue for the Bragg angles close to the right one. Recently we observed an additional enhancement factor of small effects exerting influence on a neutron undergoing Laue diffraction at such Bragg angles [3]. This factor arises due to the time of diffracted neutron delay inside the crystal and is proportional to $tan^2(\theta_B)$. Its value can reach 10^3 . In the aggregate with diffraction enhancement factor, which is also known as decreasing of diffracting neutron effective mass [4], the total diffraction enhancement factor may be as large as 10^9 . So, it becomes interesting to try to utilize this enhancement phenomenon for investigation of external affects acting on a diffracting neutron.

In the experiment we were working with two-crystal scheme of Laue diffraction in large $\oslash 150 \times 220 \text{ mm}^3$ silicon crystal. The working crystalographic plane is (220). Experimental setup is based on direct neutron beam collimation with system of slits which allows us to observe neutron beam shift on the exit surface of the crystal. In this consideration specific dynamical diffraction effects become very significant. First of all, effect of anomalous transmission or Borrmann effect [5] should be taken into account. This effect gives different absorption lengths for different types of Bloch waves excited in crystal (in fact for low-absorbed wave absorption length is by one order of magnitude higher than for non-diffracted neutrons). Borrmann effect was investigated for x-rays more than fifty years ago and its detailed description can be found in [5]. Theoretical consideration of this effect for neutrons can be found in [6] and also in [7, 8].

1. Neutron Laue diffraction in perfect crystals

Here we consider the symmetrical Laue diffraction scheme in a transparent crystal with the system of crystallographic planes described by the reciprocal lattice vector g normal to the planes (see Fig. 1), $g=2\pi/d$, d is the interplanar distance. In this case, the neutron wave function in a crystal will be a superposition of Bloch waves

$$\psi^{j}(\mathbf{r}) = a_{j}(\mathbf{r}) e^{(i\mathbf{k}_{j}\mathbf{r})}. \tag{1}$$

In two-beam approximation (1) becomes a superposition of two Bloch waves $\psi^{(1)}$ and $\psi^{(2)}$ corresponding to two branches of the dispersion surface [6]

$$\psi^{1,2} = \psi_0^{1,2} + \psi_\alpha^{1,2},\tag{2}$$

where ψ_0 – is the wave function of direct beam and ψ_g – is the wave function of reflected beam. In the plane wave approximation neutron currents directions (Fig. 1) in crystal can be defined for each Bloch wave field separately and, neglecting the fast oscillating interference terms, are given by

 $\mathbf{j}_{1,2} = \frac{\hbar |\mathbf{k}|}{m} \left(\mathbf{n}_0 |\psi_0^{1,2}|^2 + \mathbf{n}_g |\psi_g^{1,2}|^2 \right), \tag{3}$

where \mathbf{n}_0 and $\mathbf{n}_{\mathbf{g}}$ – are the unit wave vectors corresponded to direct and reflected directions.

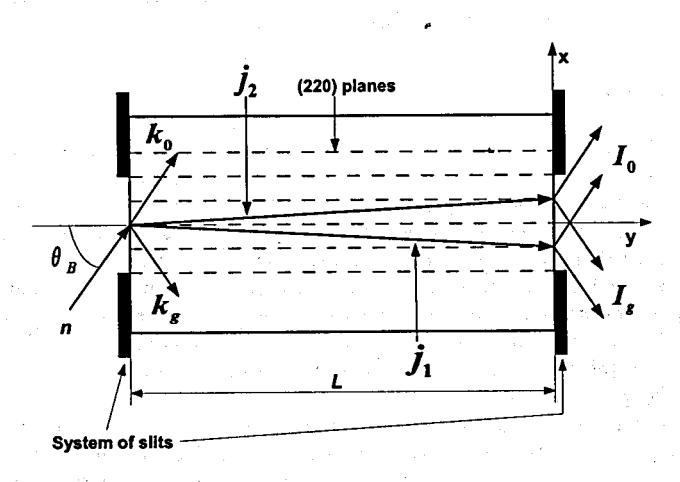


Figure 1: Laue diffraction in single crystal. j_1 and j_2 - directions of neutron currents.

Neutron currents in crystal are bounded by the size of so-called "Borrmann fan". It's convenient to describe distribution of "Borrmann fan" by using the parameter of deviation from exact Bragg condition

 $\Gamma = \frac{tg(\theta)}{tg(\theta_B)} = \frac{x}{2Ltg(\theta_B)}.$ (4)

Under this term "Borrmann fan" lies between $-1 < \Gamma < 1$. One can also describe the wave amplitudes inside the crystals by the terms of Γ . They are given by the following expressions:

$$a_0^{1,2}(\Gamma) = \frac{1-\Gamma}{2(1+\Gamma)\sqrt{1-\Gamma^2}},$$
 (5)

$$a_{\mathbf{g}}^{1,2}(\Gamma) = \frac{1}{2\sqrt{1-\Gamma^2}}.$$
 (6)

Finally without taking interference effects into account one obtains the intensity profile on the exit surface of crystal [6]

$$R_{0,\mathbf{g}}(\Gamma) = \left[(a_0^{1,2}(\Gamma))^2 + (a_{\mathbf{g}}^{1,2}(\Gamma))^2 \right] \frac{1}{(1 - \Gamma^2)\sqrt{1 - \Gamma^2}}.$$
 (7)

The intensity profile (7) shows increase of the intensity on the margins of the "Borrmann fan" (when $|\Gamma| \to 1$). This effect in neutron diffraction was first observed in [9] and explained in [10].

2. Influence of absorption

For the case of non zero absorption the amplitudes of diffracted in Bragg direction waves are given by [6]:

 $a_{\mathbf{g}}^{1,2}(\Gamma) = \frac{e^{-\Sigma_0 L_{eff}}}{\sqrt{2}(1-\Gamma^2)^{1/4}} \times \left(\sin^2\left(\frac{A}{\sqrt{1-\Gamma^2}}\right) + \sinh^2\left(\Sigma_{\mathbf{g}} L_{eff}\sqrt{1-\Gamma^2}\right)\right)^{1/2},$ (8)

where $\Sigma_0 = \frac{1}{V} \sum_{i} \sigma_i^I$ and $\Sigma_{\mathbf{g}} = \frac{1}{V} \sum_{i} \exp{(-i\mathbf{g}\mathbf{r}_i)} \sigma_i^I$ – zero and g-harmonic of absorption (σ_i^I – is total cross-section of absorption and incoherent scattering); $L_{eff} = L/\cos{\theta_B}$ – effective crystal length; $A = (\pi L)/\xi_{\mathbf{g}}$, where $\xi_{\mathbf{g}}$ – is so called extinction length which describes the period of "Pendellosung" oscillations [6].

With increasing of crystal length and consequently the $(\pi L)/\xi_g$ value one can average the amplitudes over "Pendellosung" oscillation period. Therefore (8) can be simplified:

$$a_{\mathbf{g}}^{1,2}(\Gamma) = \frac{e^{-\Sigma_0 L_{eff}}}{2(1 - \Gamma^2)^{1/4}} \left(\pm \cosh 2 \left(\Sigma_{\mathbf{g}} L_{eff} \sqrt{1 - \Gamma^2} \right) \right). \tag{9}$$

In case of diffraction in thick crystal when $\Sigma_{\bf g} L_{eff} >> 1$ what gives us $\exp(-\Sigma_{\bf g} L_{eff}) << 1$, the amplitudes (9) become:

$$a_{\mathbf{g}}^{1,2}\left(\Gamma\right) = \frac{\exp\left(-L_{eff}\left(\Sigma_{0} \pm \Sigma_{\vec{g}}\sqrt{1-\Gamma^{2}}\right)\right)}{4(1-\Gamma^{2})^{1/4}}.$$
 (10)

The amplitudes value for transmitted wave can be obtained similar to (10)

$$a_0^{1,2}\left(\Gamma\right) = \frac{\exp\left(-L_{eff}\left(\Sigma_0 \pm \Sigma_{\mathbf{g}}\sqrt{1-\Gamma^2}\right)\right)}{4(1-\Gamma^2)^{1/4}}\sqrt{\frac{1-\Gamma}{1+\Gamma}}.$$
 (11)

The intensity profile at the exit surface of the crystal after averaging over interference term will be:

$$R_0 = (a_0^1)^2 + (a_0^2)^2, R_g = (a_g^1)^2 + (a_g^2)^2.$$
(12)

From equations (10, 11) one can see that for the second type of two Bloch waves $(\psi_{0,g}^1,\psi_{0,g}^2)$ absorption will be much more weaker than for the first one. In fact this is the direct consequence of anomalous transmission or Borrmann effect. This effect gives an opportunity for the diffracting neutrons to pass through extremely large (we worked with 220 mm of silicon) crystals without considerable losses of intensity.

3. Experimental observation of Borrmann effect

Experimental studies were done at WWR-M research reactor (PNPI, Gatchina). Neutron Laue diffraction with Bragg angles close to $\pi/2$ was investigated both for one-crystal (Fig. 1) and for two-crystal (Fig. 2) schemes on (220) crystallographic planes of large ($\oslash 150 \times 220 \text{ mm}^3$) silicon crystal with interplanar distance $d=1,92\cdot 10^{-8}$ cm. Silicon crystal was mounted in thermostat for minimization of thermal deformation effect in crystalline medium. The necessary high collimation of the neutron beam was provided by the first crystal with slits placed on entrance and exit faces.

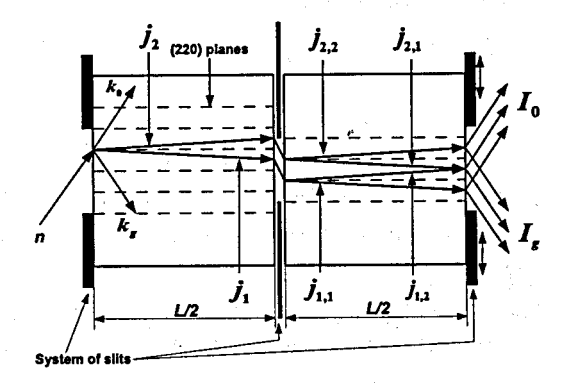


Figure 2: Two-crystal scheme of Laue diffraction. Collimating slits are mounted at the entrance and exit surfaces of the crystal. $\mathbf{j_1}$ and $\mathbf{j_2}$ – directions of neutron currents in the first crystal; $\mathbf{j_i}$, (i, j = 1, 2) – directions of neutron currents in the second crystal.

In the experiment we took the intensity dependences for one- and two-crystal schemes of Laue diffraction on a Bragg angle value (Fig. 3). Bragg angle value reached 88° . On the Fig. 3 one can also see effective crystal length value $L_{eff} = L/\cos\theta_B$ that reaches 6 meteres for 88° . Theoretical calculations were made for silicon absorption length $L_{abs} = 40$ cm. The g-harmonic of the linear absorption coefficient can be presented by the following formula

$$\Sigma_{\mathbf{g}} = \Sigma_0 \left(1 - \delta_{\mathbf{g}} \right) \tag{13}$$

where $\delta_{\bf g}$ – is a free parameter. The best agreement with experiment had been obtained for $\delta_{\bf g}=0,012$. In this case the linear absorption coefficient value for the first Bloch wave type is

$$\Sigma_1 = \Sigma_0 (2 - \delta_{\mathbf{g}}) = 0,05 \text{ cm}^{-1}$$

and for the second Bloch wave type is

$$\Sigma_2 = \Sigma_0 \delta_{\mathbf{g}} = 0,003 \text{ cm}^{-1}.$$

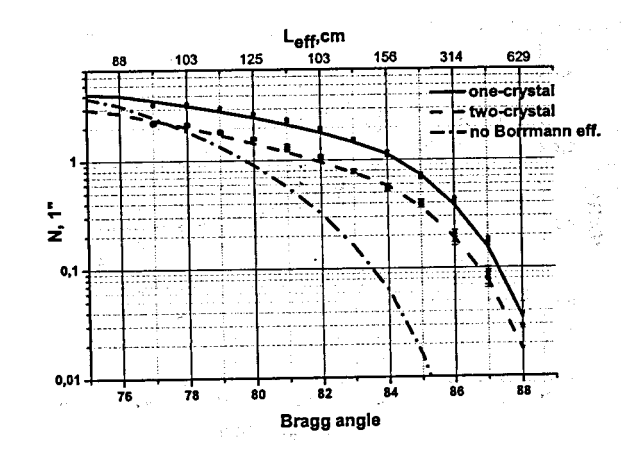


Figure 3: Intensity dependence on a Bragg angle value for one- and two-crystal schemes of the setup for silicon crystal. Crystallographic plane (220). Crystal thickness L=220 mm. Dots stand for the experimental data and lines for theoretical predictions.

For the two-crystal scheme of Laue diffraction the intensity profile for tramsmitted beam (Fig. 2) can be derived from

$$R_0 = \frac{1}{2} R_0 (L/2) R_0 (L/2) = \dots$$

$$\dots = \frac{1}{2} \left[\left(a_0^1 (L/2) \right)^2 + \left(a_0^2 (L/2) \right)^2 \right]^2.$$
 (14)

Dependence of intensities values ratio on a Bragg angle for one- and two-crystal schemes is shown on the Fig. 4. Taking diffraction focusing [11] and Borrmann effects into account theory predicts increasing of intensity for the two-crystal scheme in comparison with one-crystal scheme when diffraction is going with normal Bragg angles. But when Bragg angles are tending to $\pi/2$ the intensity in two-crystal scheme becomes lower than for one-crystal scheme. This fact coincides with our experimental setup geometry and also corroborates results of plane wave approximation for Laue diffraction case.

AND AND A SECURITION OF A SECU

and the second transaction of the second second

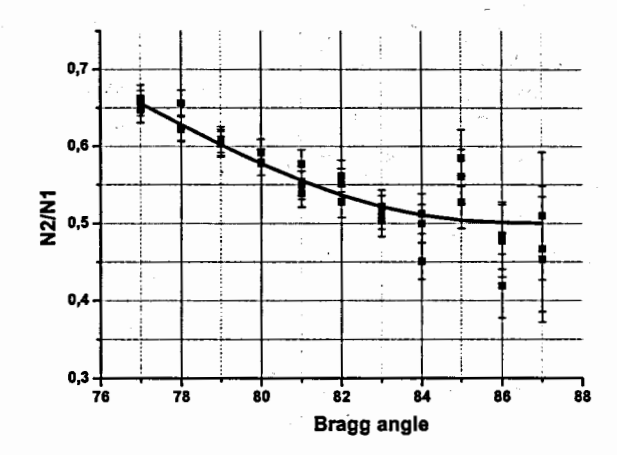


Figure 4: Dependence of intensities values ratio on a Bragg angle for one- and two-crystal schemes of the setup for silicon crystal. Solid line is a theoretical curve.

4. Influence of an external force on a Laue diffracting neutron

For the neutron Laue diffraction in deformed crystals special theory was developed [10]. In this theory effective "Kato force" f_k is imposed. This force describes diffracting neutron propagation inside weakly deformed crystal [12]. In terms of the "Kato force" neutron current's behaviour in deformed crystal is determined by the equation

$$\frac{\partial^2 x}{\partial y^2} = \pm \frac{c}{m_0} f_k(y, x),\tag{15}$$

where $c \equiv \tan \theta_{\rm B}$ and $m_0 \equiv 2F_{\rm g}d/V$ is the so called "Kato mass" with $F_{\rm g}$ – the neutron structure amplitude and V – the unit cell volume. The sign \pm in equation (15) corresponds to different Bloch waves.

In (15) the "Kato force" depends on the spatial coordinates X and Y (see Fig. 1). It can be easily demonstrated that putting an undeformed perfect crystal in a force field affecting the neutron along the reciprocal lattice vector g, we will have the same result as for a deformed crystal. So, the theory which was developed for weakly deformed crystals also works well in the presence of any external field affecting the diffracting neutron in undeformed crystal. An external field affecting a diffracting neutron was considered in [13].

It is also easy to show that an external force \mathbf{F}_n acting on a neutron along vector \mathbf{g} (X axis, see Fig. 1) is equivalent to a gradient of interplanar distance with the value

$$\xi_{\rm f} = \frac{F_{\rm n}}{2E_{\rm n}}, \tag{16}$$

where E_n is the neutron energy.

Therefore the neutron trajectory equation (15) in the crystal in the presence of an external field will have the form

$$\frac{\partial^2 z}{\partial y^2} = \pm \frac{c^2 g}{2m_0} \frac{F_{\rm n}}{2E_{\rm n}}.\tag{17}$$

Let's compare this equation for the "Kato trajectory" with that for a usual trajectory of a neutron under the same external field in free space. The last one is described by standard Newtonian equation which has the form

$$\frac{\partial^2 z}{\partial u^2} = \frac{F_{\rm n}}{2E_{\rm n}}.$$
 (18)

As it follows from (17) and (18) the "curvature" of the diffracting neutron trajectory in the crystal is magnified by the factor

$$K_{\rm e} = \pm \frac{c^2 g}{2m_0}. (19)$$

This factor depends on the Bragg angle as $c^2 \equiv \tan^2 \theta_{\rm B}$, so for Bragg angles $\theta_{\rm B} \approx (84-88)^0$ influence of deformation can be intensified by a factor $\sim 100-1000$ as compared with a Bragg angle of $\sim 45^0$.

The numerical calculation of the factor K_e for (220) silicon crystallographic planes gives

$$K_e^{(220)} = \pm 0.85 \cdot 10^8, \tag{20}$$

for a Bragg angle $\theta_{\rm B}=87^{\rm o}$ (c=20).

Therefore, a 10 cm long crystal is equivalent to ~ 1 km of free flight. The diffraction enhancement of the angular deflection of a neutron trajectory inside a crystal is well known, see for instance [14], but we have to note that such an effect can be considerably magnified by an additional gain factor proportional to $\tan^2\theta_{\rm B}$ for Bragg angles close to $\pi/2$ [15]. The observed effects give us a chance to build a device with unprecedented sensitivity to external force acting on a neutron.

5. Possible application of two-crystal diffraction scheme. m_i/m_G experiment with neutron

Principle scheme of the setup is based on two-crystal scheme of diffraction as it was shown in Fig. 2. The necessary high collimation of the beam was provided by the first crystal with slits placed on entrance and exit surfaces, for details see [14]. An external force which is parallel to the reciprocal lattice vector curves the neutron trajectories inside the crystals. This results in a shift of the neutron beam along the exit surface of the second crystal:

$$\Delta_{\mathbf{F}}^{1}(1,2) = \pm \frac{\pi c^{2}L^{2}}{m_{0}d E_{\mathbf{n}}} F_{\mathbf{n}} \equiv \pm \Delta_{\mathbf{F}}^{1},$$
 (21)

where \pm corresponds to the two type of Bloch waves excited in a crystal.

After averaging over "Pendellosung" oscillations which arise due to the interference of $\psi(1)$ and $\psi(2)$ and in case of large crystal (see section 2) we get the shift of the neutron beam along the second crystal exit surface

$$\Delta_{\rm S} = \Delta_{\rm F}^{1} = \frac{\pi \ c^{2} L^{2}}{m_{0} d \ E_{\rm n}} F_{\rm n}. \tag{22}$$

The resolution of the external force, i.e. magnitude of force when the neutron beam shift Δ_S is equal to the slit size δ_{s_1} is equal to:

$$F_{\rm W} = \frac{m_0 d E_{\rm n}}{\pi c^2 L^2} \delta_s \tag{23}$$

One of the applications can be connected with the measurement of inertial to gravitational neutron mass ratio. Our Earth is moving at a stationary orbit around the Sun, it means that the gravitational force which is proportional to the gravitational mass is in balance with the centrifugal force which is proportional to the inertial mass. If this is not so for free neutrons, then in the coordinate system connected with the Earth a free neutron will feel a non zero force¹

$$F_{\rm m} = \frac{(m_i - m_G) \cdot GM_S}{R_c^2} \approx \Delta_{G_i} \cdot 6 \cdot 10^{-4} m_G g \tag{24}$$

where m_G and m_i are the neutron gravitational and inertial masses, G is the gravitational constant, M_S is the mass of the Sun, R_S is the distance to the Sun, $\Delta_{\rm Gi} \equiv (m_i - m_G)/m_G$. Moreover, this force will oscillate in the laboratory coordinate system with one day period due to the Earth spinning motion, see Fig. 5.

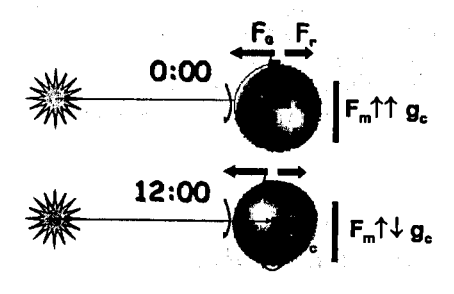


Figure 5: Position of the setup relatively to the Sun. gc is the setup orientation.

Conclusions

The good agreement of experimental results with theoretical predictions based on specific dynamical diffraction speculations was shown. With taking Borrmann effect into account absorption

length for low-absorbed Bloch wave for (220) silicon plane is by one order of magnitude higher compared to non-diffracted neutron.

Observed dynamical diffraction effects discussed in this paper give a chance to measure any small external force acting on a neutron with unprecedented sensitivity. Preliminary estimations and test experiments [1, 17] showed us that the possible sensitivity to external force can reach the magnitude

$$\sigma(F_{ext}) \cong 10^{-17} \text{ eV/cm}$$

which provides us for instance measuring m_i/m_G ratio with the accuracy $\sigma(m_i/m_G) \sim 10^{-5}$ for the available silicon crystal and cold neutron beam flux. This is more than one order of magnitude better than the best modern result [18].

This work was supported by RFBR (grants 11-02-00188 and 11-02-12161-ofi-m-2011) and program of Russian Ministry of Sciense and Education (grant 2.1.1/12359).

References

- [1] V.V. Voronin, I.A. Kuznetsov, E.G. Lapin, S.Yu. Semenikhin, V.V. Fedorov, Physics of Atomic Nuclei, 72, 3, 470 (2009)
- [2] V.V. Voronin, V.V. Fedorov, I.A. Kuznetsov, E.G. Lapin, S.Yu. Semenikhin, Yu.P. Braginetz, E.O. Vezhlev, Physics Procedia, 17, 2011, P. 232–238.
- [3] V.V. Voronin, I.A. Kuznetsov, E.G. Lapin, V.V. Fedorov, JETP Lett., 71, 76 (2000).
- [4] A. Zeilinger, C.G. Shull, M.A. Horne and K.G. Finkelstein, Phys. Rev. Lett., 57, 3089 (1986).
- [5] G. Borrmann, Z.Physik, 42, 157 (1941).
- [6] H. Rauch and D. Petrachek, In Neutron diffraction/ed. by H. Duchs, Berlin:Springer, 1978, P. 303-351.
- [7] Yu. Kagan, A.M. Afanasiev, JETP, 49, 1504 (1965).
- [8] Yu. Kagan, A.M. Afanasiev, JETP, 59, 271 (1966).
- [9] J.W. Knowles, Acta Cryst. 9, 61 (1956).
- [10] N. Kato, Acta Cryst. 13, 349 (1960).
- [11] V.I. Indenbom, I.Sh. Slobodetsky, K.G. Truni, JETP, 66, 1110 (1974).
- [12] V.L. Alexeev, E.G. Lapin, E.K. Leushkin, V.L. Rumiantsev, O.I. Sumbaev, V.V. Fedorov, JETP 94, 371 (1988)
- [13] S.A. Werner, Phys. Rev. B 21, 1774 (1980)
- [14] A. Zeilinger, C.G. Shull, M.A. Horne, K.G. Finkelstein, Phys. Rev. Lett. 57, 3089 (1986)
- [15] V.V. Fedorov, I.A. Kuznetsov, E.G. Lapin, S.Yu. Semenikhin, V.V. Voronin, JETP Lett. 85, 82 (2007)

¹The idea of this experiment is an analogue to the well known Eōtvõs experiment for the equivalence principle checking [16]

- [16] R.V. Eotvos, D. Pekar, and E. Fekete, Ann. Phys. (Leipzig) 68, 11 (1922)
- [17] V. V. Voronin, Yu. P. Braginetz, E. O. Vezhlev, I. A. Kuznetsov, E. G. Lapin, S. Yu. Semenikhin, V. V. Fedorov, PNPI Preprint-2849. Gatchina, 2010.
- [18] J. Schmiedmayer, Nucl. Instr. Meth. A 284, 59 (1989)

Prospects of Using the Complicated ('flaky') Neutron-Optical Potential

Yu. Alexandrov¹, G. Anikin², V. Anikin²

¹FLNP, JINR, Dubna, Russia, e-mail: alex@nf.jinr.ru
²Instuitute of Physics and Power Engineering, Obninsk, Russia

Abstract: The big work on research of thin structure of neutron-optical potential for heavy nuclei has been done.

Motivation of this research is connected with necessity of an explanation of following phenomena:

1. Presence enough sharp fluctuation of parameters of potential by studying of their power dependence which at neutron energies more than 0.5 MeV appear to be very close, for example, for lead and uranium nuclei.

2. Correlation of structures in energy dependence of any characteristics of interaction of neutrons with nuclei: full cross sections, cross sections of fission, kinetic energy of products of fission and etc.

3. Equidistant arrangement of correlating structure similar under the form not in scale of energies but in a scale of lengths of waves of neutrons.

4. Small-angle neutron scattering of MeV neutrons by heavy nuclei.

The assumption of possibility to explain the observable phenomena by diffraction of neutron waves on spatially divided structures of a nucleus with inevitability has raised the question about existence of correlations in cross sections for various radiations, for example, neutrons and gamma beams, at coincidence of their lengths of waves. The first attempts to find such correlations have crowned success and are the most difficulty refutable proof of existence of spatially divided nuclear structures.

Figure 1 shows two variants of the optical potential real part, obtained in the work [1] in result of a detailed search, where at every integration step of Schrodinger equation the ordinate of the potential is considered to be a free parameter. At that, an apprehension can arise that in such search procedure a risk exists of the terms values of potential departing into the physically unreal area of the parametric space.

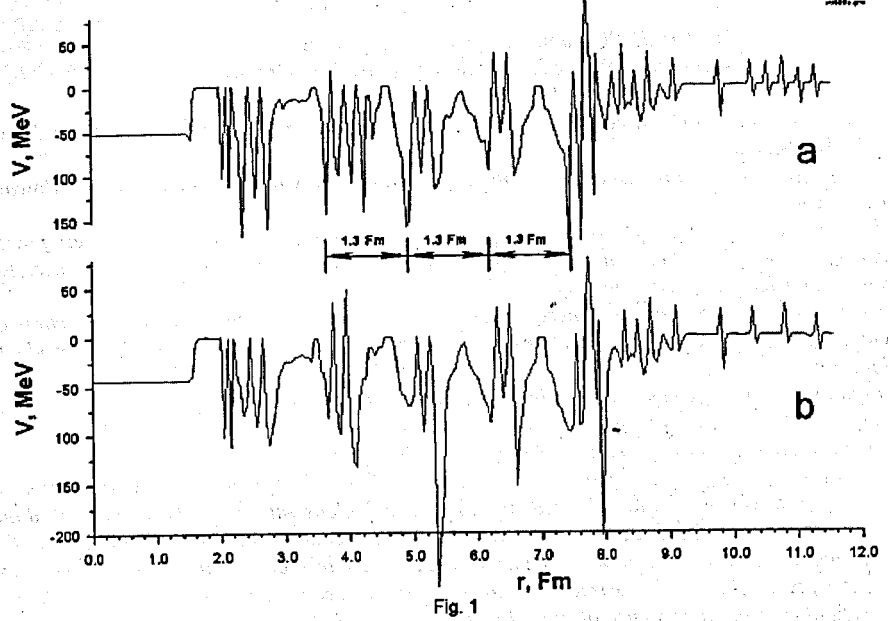
Nevertheless, this risk might be brought to a minimum: firstly, the ordinates of the potential should be announced as free only after the approximation of the experimental data had been obtained using it (i.e. the squared search functional is in the minimum, and the optimal value of the volume integral of a required potential had been acquired). Secondly, radical methods of search should not be applied, e.g., random search, when the random number generator can 'throw' the parameter set to the physically unreal area of the parametric space.

A more time consuming but a more dependable method of cyclic enumeration of parameters with their small increments at each search step was used in the work [1]. In this case, a departure from already found minimum of the quadratic search functional is practically impossible.

The work [1] emphasizes that at the initial stage of the search, the experimental material was used for full cross-sections and differential cross-sections of neutron scattering by lead to large and small angles [2]. In the aftermath, small-angle scattering was excluded from the consideration. Thus, further, to evaluate the neutron electric polarizability with a new potential the verification of its peripheral part is to be carried out.

It can be said that the search of the nuclear potential was performed as a search for its more complicated form. The idea of heavy nuclei 'neutron coat', for instance, compelled the authors of the work [2] to use the real part of the potential in the form of two Woods-Saxon

terms. The investigation of the nuclear charge density distribution by way of research of high energy electrons scattering ($E_e \sim 120 \div 180$ MeV) by Hofstadter et al [3,4] lead to the conclusion of a possibility to reduce protons density in the center of the nucleus. This result



The real part of the nuclear-optical potential from the work [1] (see the text).

was more surely registered for gold nuclei, and was not marked for lead-208.

With account of these results, the work [5] on the possibility of scattering very high energy protons $(E_p \sim 1 \text{ GeV})$ by nuclei also comes to the conclusion of a possibility to reduce protons density in the center of the nucleus. The work [6] considered the possibility to introduce analytically the decrease of a potential hole assuming of the real part of the potential in the 'bottle bottom' form.

The authors of the work [7] realized this idea using the real part of the potential as the sum of three members:

$$-V = \sum_{i=1}^{3} V_i/(1 + \exp((r-r_i)/a_i))$$
.

The initial values of the parameters V_3 and r_3 were: $V_3 = 0$, $r_3 = 3$ Fm

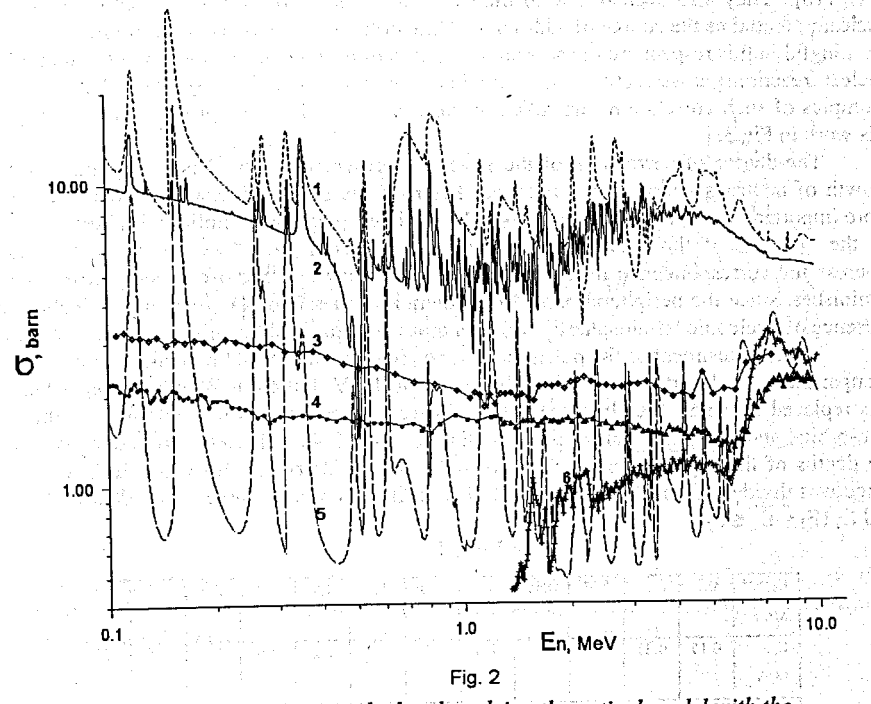
In the automatic search process these parameters acquired the values: $V_3 = -4.45$ MeV, $r_3 = 2.75$ Fm (for uranium) and $V_3 = 3.25$ MeV, $r_3 = 2.56$ Fm (for lead) which provided the decrease of a potential's pit depth in the central area of the nucleus by the range of about 4 MeV. This decrease disappears very rapidly with the growth of the distance from the nucleus center (parameter $a_3 = 0.1$ Fm).

It is marked in the work that the increase of a_3 parameter up to 0.2 Fermi doubles the squared search functional for angular distributions of neutrons with a wave length of $2 \div 3$ Fm. This suggested the idea of existing of structural elements with rapidly changing with radius in the nuclear potential and served a stimulus for conducting a detailed research of the optical potential radial dependence [1]. One of the found variants of the real part of the potential is presented in the work [8].

It turned out that the potential possesses a 'flaky' (almost periodical) structure, the elements of which do not have an over high 'hardness'. The work [1] shows that each of these elements can deform at coincidence of its radial address with the indicated wave length $\lambda/2\pi$ of the oncoming neutron.

In view of the above, it can be possibly noted that the most suitable instrument for the nuclear structure investigation could have been a detailed examination of cross-sections of neutrons scattering with not so high energy (e.g. $0.05 \text{ MeV} \leq E_n \leq 25 \text{ MeV}$). At using very high energy particles, as it is correctly noted in the work [5], we can obtain the picture of localization of individual nucleons in the kernel, but the structures being the result of their interaction will be scarcely evaluated accurately. Most probably, they will be deformed or even destructed.

Reviewing the prospect of a more precise determination of neutron electric polarizability, it needs to assess – if all the possibilities had been used in already completed works. There, the correlation is marked of deviations from the theory of the experimental small angle cross-sections with energy dependence of the real part of the nuclear amplitude [9]. That indicated the interferential nature of the deviations which were maximal at neutrons energy of $1 \div 2$ MeV. It is not surprising that propositions were expressed to repeat the measurements of differential cross-sections namely at these neutrons energies [10].



Comparison of the cross-sections calculated applying the optical model with the 'flaky' potential (dotted curves) with experimental data for heavy nuclei (see the text).

At the assessment of neutron polarizability, the analysis of cross-sections takes place, which cross-sections are averaged in a certain energy interval. But, as was noted in the works [11, 12], the elements of the full cross-section resonant structure should be also taken into account

For assessing the resonant structures in the cross-sections the complicated ('flaky') potential of the optical model could be used, as shown in Fig. 1. Its possibilities are illustrated in Fig. 2, where the results are shown of the adjustment of the potential to describe the full cross-sections massive measured in Los-Alamos [13]. The massive contained 11 thousand values of σ_t in the range of neutron energy from 0.1 to 12 MeV. In the result of the averaging procedure it was reduced to 300 values (it is represented in the figure by continuous curve with number 2). The dotted curve under number 1 is the result of calculations of full cross-sections with 'flaky' potential [1]. It is worth to note a considerable consent in the behavior of the averaged σ_t with the calculated cross-sections values. Moreover in the energies range of about 0.5—1 MeV the calculation also reproduce separate narrow resonances.

Curves 3 and 4 represent the cross-sections of fissions of Cm-247 [14] and U-235 [15,16], correspondingly. On the curve 6 the cross-sections of fission of Th-232 [17] are shown, elevated by an order, for a better compactness of the figure. Curve 5 is the cross-section of the compound nucleus formation, normalized in such way that its resonances allowed to track the structures correlation in the calculated and experimental cross sections in a better way, and also the structure correlation of experimental cross sections for various heavy elements with the structures in lead o₁. These correlations are discussed in detail in the work [18]. They also became one of the stimulus of the search for spatial structures in the nuclear potential as the source of additional diffraction effects in the cross sections. Especially meaningful in this respect are the correlation of structures in neutron cross sections and photonuclear reactions cross-sections at coincidence of neutron and γ ray wave lengths. The examples of such correlations are given in the works [1, 18]. We reproduce one of them in this work in Fig.3.

The degree of correlation of the structures presented in Fig. 2 is increasing with the growth of neutrons energy since for these neutrons the role of diffraction effects becomes more important in the inner nucleus 'layers', which are practically similar with heavy nuclei. At the decrease of the energy the correlation for fission cross-sections remains notable, whereas the correspondence in the positions of resonances with those in lead cross section diminishes, since the peripheral part of the potential comes into play, perhaps, reflecting the presence of nucleonic 'stratosphere', which is more poor for lead than for other heavy nuclei.

At the adjustment of the potential its terms [curve a) in Fig. 1] was taken with a certain change: the central part with the depth of about 50 MeV, left from Woods-Saxon potential, was replaced by small (nearly zero) values. Energy dependence is tracked anew of the real spin-orbital and imaginary part of the potential, K_{re} , K_{so} , K_{IM} coefficients are found, by which the depths of these parts were multiplied in 12 energy intervals, into which all the energy range was divided (from 0.1 to 12 MeV). The interval limits in Table 1 are identified as E_1 and E_2 ($E_1 < E_n \le E_2$).

Table 1

| E _I , MeV | 0.1, | 0.15 | 0.31 | 0.51 | 0.8 | 1.0 | 1.3 | 1.7 | 2.2 | 2.9 | 3.5 | 5.5 |
|-------------------------|------|------|------|------|------|------|------|------|------|------|------|------|
| E ₂ , MeV | 0.15 | 0.31 | 0.51 | 0.80 | 1.0 | 1.3 | 1.7 | 2.2 | 2.9 | 3.5 | 5.5 | 12 |
| K _R | 0.60 | 0.30 | 0.23 | 0.34 | 0.40 | 0.39 | 0.40 | 0.44 | 0.49 | 0.49 | 0.10 | 0.10 |
| Ksı | 0.5 | 0.5 | 0.5 | 0.5 | 0.5 | 0.5 | 0.5 | 0.5 | 0.5 | 0.5 | 0.2 | 0.1 |
| K _{S2} | 2.17 | 6.16 | 6.18 | 0.6 | 0.6 | 0.6 | 0.6 | 0.6 | 0.6 | 0.6 | 0.0 | 0.0 |

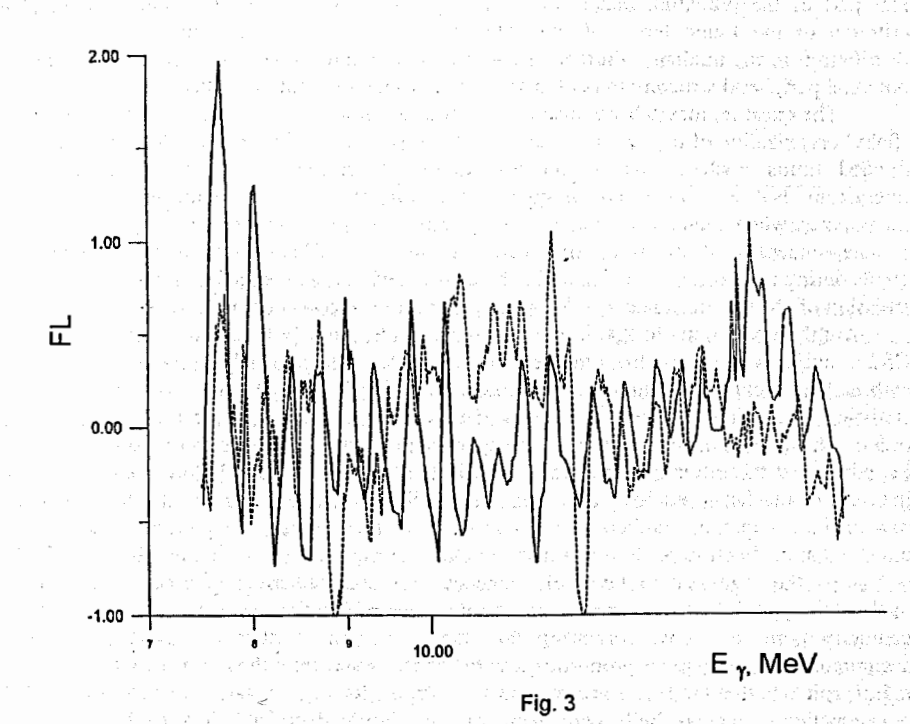
The said multipliers were calculated by the table data as $K_{RE}=K_RE_n$, $K_{SO}=K_{S1}E_n+K_{S2}$, E_n is neutron energy. What concerns the imaginary part, its energy dependence rate is approximated analytically by the formula:

$$K_{1M} = 0.0031/E_n^{1/2} + \sum_{l=1}^{3} K_{1ml} \cdot E_n \cdot \exp(B_l)/(1 + \exp(B_l))^2$$

Here $B_l = |E_n - E_l|/A_l$, and the rate of attenuation of exponents A_l was changing its values at threshold values of E_l : $A_l = A_n$ at $E_n < E_l$ and $A_l = A_n$ at $E_n \ge E_l$.

The parameters of this formula are specified in Table 2.

er 🖅 👫 Jing a Host sak francosa estra-



Comparison of fluctuations of U^{235} fission cross-section by neutrons with the energy of ≈ 0.08 MeV [29] (dotted curve) and the cross-section of the interaction of gamma-rays with lead σ in the gigantic resonance area [30] (continuous curve).

It is worth noting that some juxtaposition of full cross-section structures of neutrons interaction with lead and 'flaky' potential structures had been already presented in the said work [8].

| | | | • |
|----------------------|-------|-------|------|
| E | 1 | 2 | 3 |
| K _{lml} | 0.037 | 0.09 | 0.24 |
| E _l , MeV | 0.27 | 1.40 | 7.0 |
| A _{II} , Fm | 0.004 | 0.215 | 0.4 |
| A ₁₂ , Fm | 0.48 | 1.0 | 2.0 |

It was stressed in the work [11] that the sensibility to the change of the positions ('addresses') of resonances acquired in the calculation of the energy scale, first of all, of the real part of the potential, makes the reproduction of these 'addresses' the most reliable criterion of the found terms of the potential real part (and hence, the nucleon density distribution in the nucleus). Further, it could be reasonable to work on detailing the 'flaky' potential peripheral structure to get the assessment of neutron polarizability.

The question inevitably is also raised about the atomic nucleus structure in view of the 'flaky' organization of the optical potential. Of course, we can further consider that within the divided limits nucleons go on moving almost independently, with a little 'residual' interaction. But we can accept another radical variant – cluster organization of nucleon membranes, when nucleons are tied similar to carbon nuclei in fullerenes.

The concept of cluster in atomic nuclei was introduce Blokhinsev still in the middle of 1950s during his work in Obninsk and published in 1958 [19] in connection with discovery of emission of clusters from nuclei at high energies protons incident upon them.

Are there any hints to that in the experiment? The work [20] reviews a triple fission of Cf-252 nuclei with escape from the neck of the fissile nucleus of light nuclei from tritium to carbon. The yield of a major part of masses (H-3, He-6, He-8, Li, Be, B) corresponds its statistical evaluations, whereas the output of He-4 and C-12 excess these evaluations by two orders. The authors of the work make the conclusion of the cluster nature of the yield excess, i.e. admit that these two nuclei already exist in the form of a cluster before the escape from the neck of the fissile nucleus. But when we recall that numbers 2 and 6 are the first in the row of the occupation numbers of nucleon shells of the nucleus, it would be reasonable to assume that ready clusters also exist in the nucleus for the next occupation numbers.

As the argument in favor of existence of spatial spherical nucleon 'flaky' in the nucleus the possibility can serve to get the numbers occupation sequence, clearly from the geometry point of view. Assuming that the maximum number of nucleons that can accommodate in the layer is proportional to the sphere space with the radius equal to the layer radius, and also that the layers are positioned in the nucleus equidistantly, the following table of occupation of nuclear shells by nucleons can be compiled (see Table 3, V.Anikin).

In the cluster variant, the number of nucleons in the shells is proportional to the square of its radius R_n . Non-dimensional values B in the table, giving the correct occupation numbers by the formula $N = B^2 - 0.25$ can be selected at any length measuring unit, though the right distances $(R_n - R_{nl} \sim 1.3 \text{ Fermi})$ between the shells found at the adjustment of the optical potential are obtained at applying the length units of 1.3 Fermi.

It is shown in the table that the 'magical' numbers, if referred to the nuclei with occupied shells, can be obtained only with the omission of certain shells. It is, perhaps, related to proton shells of the heavy nuclei, and is connected with the necessity of the nuclear attraction and Coulomb repulsion forces balance.

| | | - 40.0. | 7 | | | | | |
|--------------------------|-----|----------|--------------|-----------------------------------------|------------------------------|----------|-------------------------|---------|
| Shell number N | I | 2 | - 3 · · | 411 457 g | 5 | 6 | 7 | 8 |
| $B=R_n$ / Length unit | 1.5 | 2.5 6 | 3.5 | 4.5 | 5.5 30 | 6.5 | 7.5 56 | 8.5 |
| Fill number $N=B^2-0.25$ | | | | | | | | 72 |
| | | • | | | 30.740 | | | 1 |
| Magic numbers: | | 1 | | 4 4 4 4 4 4 5 1 5 1 5 1 5 1 5 1 5 1 5 1 | e de gras Latergras | restori | .afs.354 | , š., . |
| 2 | 2 | | | 3.62 | n kuru en 1 ana - Digital | | | à ac |
| 8 | 2 | 6 | and dish | 54. j.t | 8 46 A 3 18 | 674 F | est, pitc | |
| 20 | 2 | 6 | : - 12 - | 33.4.8 | | 424.131 | 100 37 27 | gNorth |
| 28 | 2 | 6 | - | 20 | Blog : | 4,700 | af _{ra Dire} f | Pariti |
| 50 | 2 | - 6 | 12 | ruik 5 | 30 | yang d | r terselijk | 20.0 |
| 1. 82 | 2 | 6 | 12 | 20 | - Sept 1 | 42 | 11/25-11 | Marin. |
| 126 | 1 | 6 | 12 | 20 | 20 | Acres Se | | 13000 |
| 120 | 2 | U | . 12 | 20 | 30 | ANGER | - 56 | 100 |

Then, taking into account that the nucleus sometimes is decomposed mainly to deuterons or alpha-particles in the reaction with energetic particle, a temptation emerges to create the alpha-particle or deuteron model of the nucleus. At the same time it would be reasonable to assume that the nucleons positioned in the nucleus shell in the 'chessman' order are capable to form various clusters depending on lengths of the waves excited on the nucleus shell by the incoming particle.

Of course, while accepting the cluster structures, it would be necessary to change the approaches to solving a lot of problems concerning the nucleus structure: distances between nucleons inside the nucleus, calculation of the nucleus level density, where the cluster component should have been sharply raised. Some works have already indicated the necessity of accounting the influence of clusters on the atomic nucleus features, in particular, on the nuclear level density (see e.g. [21-24]).

In addition as show the analysis [25] in the determination of the polarizability of the fast neutron scattering by heavy nuclei one should consider the impact of nuclear charge form factors. Such consideration should be especially actual in the case of 'flacy' potential. Must also bear in mind that in [12] was shown that the polarizability of the electron shell of a heavy atom may give appreciable contribution to the anomalous scattering of neutrons at energies of several MeV. For the neutron polarizability obtained in this case the order of 10^{-42} cm³. This means that the electric polarizability of the neutron was observed in experiments on neutron scattering at small angles in heavy nuclei already in 1957 (first job [26]) i.e. one-two years after the hypothesis of it and sooner than the polarizability of the proton in the experiments on the γ p-scattering [27], conducted in 1960. Detection of polarizability (i.e. deformation) of the nucleon (as well as first (1953-1957) Hofstadter's experiments) was direct evidence of the spatial expansion of the nucleon.

It should be noted that W-type structures of the 'flaky' potential can be considered as zero approximation of assessments of potentials (n, p)-interaction (external part of the structure, more distant from the nucleus center) and (n, n)-interaction (internal part of the W-structure).

Such conception could be justified if to consider that the protons and neutrons form a single shell where the protons are offset by Coulomb forces to the nuclear periphery. Both the potentials (n, p) and (n, n) have limited height repulsive kerns in the center.

Conclusion

The fact of existing of correlating resonant structures in the cross-sections for various radiations (e.g. neutrons and gamma-rays), at coincidence of their wavelengths and not energies, indicates that the atomic nucleus has space-divided nucleons complexes. Such correlation can hardly be explained by anything but the waves diffraction on the same nucleon structures. The examples of similar correlations are given in the works [1], [18] and in this work (see Fig. 3). Some correlation effects in resonance structure of different nuclides are considered for instance in [28] and other publication of these authors.

A detailed adjustment for the experiment of the optical potential gives the picture of nucleon density distribution in the nucleus only in a first approximation.

At the same time, as Fig. 2 of this work shows, the approximation turns out to be acceptable since it allows replicating not only the general nature of the averaged resonance structures, but also some narrow resonances in the full cross-sections. The necessity of future work is evident to ascertain the details of the potential and their physical interpretation. A substantial contribution in such ascertaining could be made by the description of precisely measured angular distribution of scattered neutrons. It might be noted that such measurements can be accomplished, e.g., in the Institute for Physics and Power Engineering in Obninsk where the accelerators are available, which are able to provide neutron currents from kiloelectronvolt single units to 15 MeV.

The authors are grateful for the discussion of the above matters to O.D. Kazachkovskiy, B.D. Kuzminov, P.P. Dyachenko and B.I. Fursov, and also to A.V. Gulevich – for the attention and the interest to the work.

References

- 1. Anikin.G.V., AnikinV.G. Preprint IPPE-3031, Obninsk—2004.
- 2. Anikin G.V., KotukhovI.I.|| Yad.Fiz. 49, 1989, p.101.
- 3..Hofstadter R.|| Rev.Mod.Phys., 28, 1956, 214.
- 4. Hahn B., Ravenhall D.G., Hofstadter R. Phys. Rev., 101, 1956, 1131.
- 5. Alkhasov G.D.|| Electromagnetic interactions of nuclei at the small and middle energy. Proc. of the 5-th seminar, Moscow, 15-17 June 1981, p.15.
- 6. Wong C.Y. Phys. Lett. 41B, 1972, p.446.
- 7. Anikin G.V., Kotukhovl.I.|| VANT, ser.: Yad. Const., 1989, iss.4, p.58.
- 8. Alexandrov Yu.A., Anikin G.V. || ISINN-16, Dubna, June 11—14, 2008. E3-2009-33, Dubna 2009, p.29.
- 9. Anikin G.V., KotukhovI.I. VANT, ser.: Yad. Const., 1986, iss.1, p.20.
- 10. Sawada T.|| Nihon University, NUP-A-2000-7. Tokyo, 2000
- 11. Anikin V.G., Anikin G.V., Kolesov V.E.|| In Proc. of Conf. Moscow Inst. of Calc. Matem. RAN, 2000, vol. II-M.
- 12. Alexandrov Yu.A.|| Part. Nucl. 32, 2001, Iss.6, p. 1405.
- 13. Carlton R.F., Winters R.R., Harvey J.A. at al. || Bull of Am. Phys., 36, 1991, p.1349.
- 14. Dabbs J.W.T.|| Nucl.Sci.Eng., 89, 1985, p.293.
- 15. Wasson O., Meier M., Duvall K.|| Nucl.Sci.Eng., <u>81</u>, 1982, N2, p.196-212; EXFOR 10595.
- 16. Cierjacks | Sig(n,f) U-235 Proc.conf. on Fast Neutron Fission Cross Sections at ANL, June 1976. (R, ANL-76-90).
- 17. Shcherbakov O.A., Donets A.Y., Evdokimov A.V. et al. || ISINN-9, Dubna, Nov 23-26, 2001. E3-2001-192, Dubna 2001, p.257.
- 18. Anikin G.V., Anikin V.G. | Atom. Energ. 94, 2003, iss.4, p.309.

- 19. Blokhinsev D.I.|| JETP, 33, 1957, p.1295.
- 20..Mutterer M., Singer P., Kopach Yu.N. et al. || ISINN-5, Dubna, May 14-17, E2-97-213, 1997, p.331.
- 21. Solov'ev V.G.|| Electromagnetic interactions of nuclei at a small and a middle energies Proc. of a 5-th sem., Moscow, 1981, p.144.
- 22. Khitrov V.A., Sukhovoj A.M. at al.||ISINN-5, Dubna, May14-17, E2-97-213, 1997,p.207.
- 23. Khitrov V.A., Sukhovoj A.M. ||ISINN-16, Dubna, June11-14, 2008, E3-2009-33, Dubna 2009, p.203
- 24. Potupa A.S., Tretjakov V.N. || Izv. AN BSSR, 1, 1970, p.87.
- Alexandrov Yu., Nikolenko V.|| ISINN-17, Dubna, May 27-29, 2009, E3-2010-Dubna, 2010, p.353
- 26. Alexandrov Yu. JETP, 33, 1957, p.294
- 27. Goldansky V. et al. | JETP, 8, 1960, p. 1695
- Soroko Z.N., Sukhoruchkin S.I., Sukhoruchkin D.S.|| ISINN-16, Dubna, June11-14, 2008, E3-2009-33, Dubna 2009, p.139.
- 29. Migneco E. et al.|| The fission cross section of U-235 with neutron energy 0,7 Kev-1,1 Mev. In Proc. of Conf. Wash., 1975, p.607.
- 30. Ishkhanov B.S., Kapitonov I.M., Lazutin E.V. et al. Yad.Fiz., 12, 1970, p.682.

$\begin{array}{c} {\rm NUCLEAR} \,\, {\rm STRUCTURE} \,\, {\rm PHYSICS} \,\, {\rm WITH} \\ {\rm MoNA-LISA} \end{array}$

S. L. Stephenson, J. A. Brown, P. A. DeYoung, J. E. Finck, N. H. Frank, J. D. Hinnefeld, R. A. Kaye, B. A. Luther, G. F. Peaslee, D. A. Meyer, W. F. Rogers and the Mona Collaboration

¹Gettysburg College, Gettysburg Pennsylvania 17325, USA
 ²Wabash College, Crawfordsville Indiana 47933, USA
 ³Hope College, Holland Michigan 49423, USA
 ⁴Central Michigan University, Mount Pleasant Michigan 48859, USA
 ⁵Augustana College, Rock Island Illinois 61201, USA
 ⁶Indiana University South Bend, South Bend Indiana 46634, USA
 ⁷Ohio Wesleyan University, Delaware Ohio 43015, USA
 ⁸Concordia College, Moorhead Minnesota 56562, USA
 ⁹Rhodes College, Memphis Tennessee 38112, USA and
 ¹⁰Westmont College, Santa Barbara California 93108, USA

Abstract

Interesting nuclear structure physics exists near the neutron dripline; extremely neutron-rich nuclei can even have different magic numbers than their more stable peers. Studies of these exotic nuclei at the National Superconducting Cyclotron Laboratory (NSCL) at Michigan State University demand knowledge of the complete reaction kinematics and require high detector efficiency as well as the capability for multiple neutron detection and discrimination. The Modular Neutron Array (MoNA) [1] has been successful at meeting these demands and has led to furthering our understanding of the nuclear structure for a number of exotic nuclei such as ¹²Li [2], ¹⁵Be, ²⁸F, and ¹⁸B [3]. The first decay energy spectrum for neutron unbound states in ²⁴O was observed by this array, and data suggest ²⁴O is a doubly magic nucleus [4]. This year MoNA will be used with LISA (Large multi-Institutional Scintillator Array) for a higher-resolution measurement of the first two excited states of ²⁴O with possible confirmation of a newly found excited state at 7.5 MeV. A MoNA-LISA study of ²⁰C in an effort to better understand how the *sd* shell evolves with neutron number is also in preparation.

Introduction

One only has to look at the experimental facilities being upgraded to see that studies of exotic nuclei at the neutron dripline play a key role in the international nuclear physics program. While the European Union continues to support CERN's ISOLDE (on-Line Isotope Mass Separator), Canada is upgrading the Isotope Separator and Accelerator (ISAC) to ISAC-II. In addition, France is upgrading the Systme de Production d'Ions Radioactifs en Ligne en Legne (SPIRAL) to SPRIRAL2 and Germany is upgrading their Heavy Ion Synchrotoron (SIS) to the Facility for Antiproton and Ion Research (FAIR) [5]. Japan

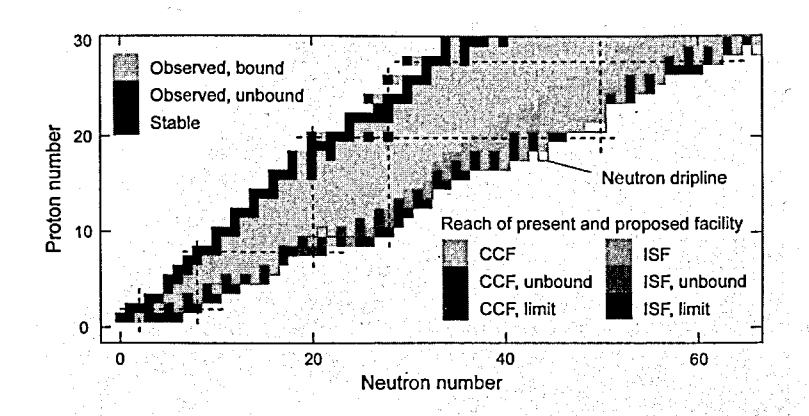


Figure 1: Expected reach of the FRIB and the present NSCL CCF (Coupled Cyclotron Facility) for light neutron-rich nuclei. Lightly shaded fields indicate nuclei predicted to be found and in reach of the CCF and FRIB (previously called the ISF). Darker fields show unbound nuclei where spectroscopy has been performed or can be done. The darkest fields at the dripline represent isotopes beyond the dripline which can be confirmed to be unbound with the FRIB, respectively [6].

plans to upgrade the RIKEN Accelerator Research Facility (RARF) to the Rare-Isotope Beam Factory (RIBF), and in the US the Facility for Rare Isotope Beams is currently under construction, supporting the US campaigns at both the Holifield Radioactive Ion Beam Facility and NSCL. This paper focuses on the current neutron dripline physics program supported by two detector arrays, the Modular Neutron Array (MoNA) and the Large multi-Institutional Scintillator Array (LISA), both currently in use at NSCL. MoNA-LISA has the appropriate energy resolution and efficiency for use at FRIB, and plans are underway to use the combined detector system at that facility.

Physics at the neutron dripline takes place on short time scales – the lifetimes of extremely neutron-rich nuclei beyond the dripline are on the order of 10^{-21} s. Bound nuclei close to the dripline usually lack bound excited states; γ -ray spectroscopy is therefore not feasible. Instead, these short-lived nuclei are studied indirectly by inferring structure based on their detected decay products (the neutrons and the charged-particle fragments are measured in coincidence). Both a highly efficient, position sensitive neutron detector array like the MoNA-LISA detector system, as well as a set of charged particle detectors, are necessary. For the experiments performed at the NSCL, the charged particles are "swept" out of the neutrons' flightpath by a large bending magnet, the "Sweeper."

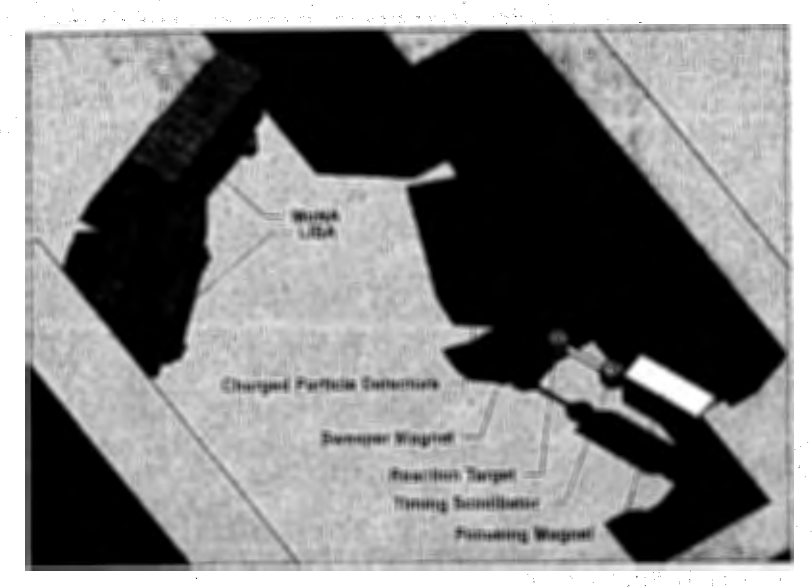


Figure 2: Typical layout of the MoNA-LISA in at the NSCL. The beam enters the vault from the bottom right.

Nuclear structure measurements with MoNA-LISA and the Sweeper

To create neutron-unbound states of oxygen, for example, as was previously done by the MoNA Collaboration [7], a beam of ²⁶F from the NSCL A1900 spectrometer was incident on a ⁹Be target to create neutron-unbound excited states of ²⁴O as well as the ground state of ²⁵O. All charged fragments (including non-reacted beam) were deflected with a rigidity up to 4 Tm through the Sweeper [8, 9, 10, 11]. Neutrons are not deflected and a gap in the Sweeper magnet allows transmission of these neutrons; MoNA or LISA can therefore be at zero degrees relative to the ²⁶F beam. MoNA and now also LISA record both the neutron's position and time signature (with multiple-hit capability). The neutron energy is determined based on its time-of-flight (TOF) and the neutron position along each scintillator bar found from the time difference between photomultiplier signals at either end of each scintillator. The TOF spectra and the position of the neutron yield the neutron's momentum vector [1]. LISA was built and benchmarked in 2010 and installed in the N2 vault of the NSCL in the spring of 2011. Like MoNA, LISA consists of 144 plastic scintillators, each 2 m x 10 cm x 10 cm. A typical configuration of MoNA, LISA and the Sweeper with necessary charged particle detectors is shown in Figure 2.

All isotopes are identified by a set of charged-particle detectors that determine each frag-

ment's energy loss, position, time of flight, and total kinetic energy. Position information comes from cathode-readout drift chambers. The energy deposited for a particular fragment in an ion chamber and also in a thin plastic scintillator in conjunction with a measurement of the remaining kinetic energy with a thick plastic scintillator yields the proton number for each fragment since energy loss per unit thickness is proportional to the proton number Z. See the work by Frank et al. for more details about the charged particle detection system [12].

For isotope identification, however, we need not only Z but also A. Typically the resolution on the energy-loss information is not high enough to resolve specific isotopes. The MoNA collaboration uses TOF information that must be carefully analyzed in order to resolve isotopes. The t_{zero} for such a technique comes from a timing detector located immediately upstream from the reaction target (in this example of creating neutron-unbound states of oxygen, the reaction target is ${}^9\mathrm{Be}$). Raw TOF data is insufficient since the charged fragments are sensitive to the non-uniformities of the Sweeper magnet's field. Fragment energy and emission angle at the reaction target are determined using COSY INFINITY [13], based on an inverse transformation of the fragment's trajectory at the charged particle detectors using the measured Sweeper magnetic field map.

Once isotopes are correctly identified, then the decay energy for a particular isotope can be found via the invariant mass method, where the relativistic four-momentum vectors of the fragment and the neutron are determined from detector information and calculated at the point of the neutron-fragment state's breakup:

$$E_{decay} = \sqrt{m_{frag}^2 + m_n^2 + 2(E_{frag} \cdot E_n - p_{frag} \cdot p_n \cdot \cos(\theta))} - m_{frag} - m_n, \tag{1}$$

where E_{decay} is the decay energy of the state, θ is the angle between the neutron and the fragment in the laboratory frame, E_{frag} is the fragment's total energy, m_{frag} is the fragment's rest mass, m_n is the neutron's rest mass, E_n is the neutron's total energy, p_{frag} is the fragment's momentum, and p_n is the neutron's momentum.

The structure of ²⁴O

An exotic nucleus of special interest, due to the strong possibility that it may be doubly magic, is ²⁴O [4]. In June of 2011 a commissioning experiment for LISA will remeasure the neutron-unbound excited states of ²⁴O. In the work by Hoffman et al. [7], the first two excited states of ²⁴O were measured at 4.7 and 5.3 MeV but with limited energy resolution. The June experiment will use a thinner ⁹Be target to increase the energy resolution of the previous measurement and higher beam current for better statistics. See Figures 3 and 4.

Previous experiment shows that 24 O has an excited state at 7.5 MeV, beyond the S_{2n} level of 6.8 MeV [14, 15]. Analysis by Hoffman et al. [16] suggests a cascade through a resonance at 0.6 MeV with neutron decay to the unbound first excited state of 23 O and

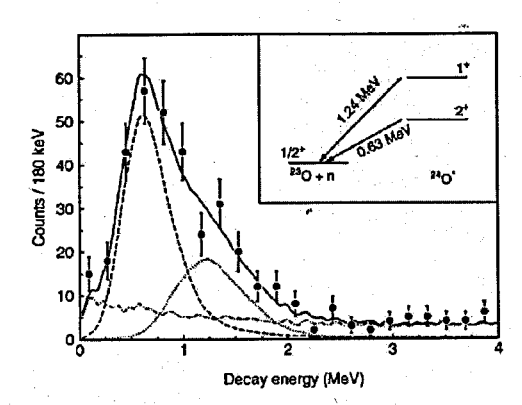


Figure 3: Decay energy spectrum for two excited states in ²⁴O [4]. Note that the states are not well resolved due to the thickness of the ⁹Be target.

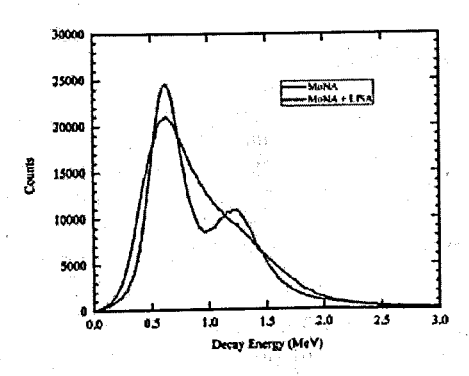


Figure 4: Simulated decay energy spectra for ²⁴O excited states. The single peak reproduces previous experimental data [4]. The two-peaked spectrum simulates a thinner ⁹Be target (by a factor of two) but with increased beam current and the addition of LISA to MoNA.

then a 0.045 MeV resonance with neturon decay to the ground state of ²²O. An analysis technique called two-neutron coincidence spectroscopy is noteworthy, demonstrating where spectroscopy techniques can be used for highly excited unbound states.

The June commissioning experiment will also study the unbound excited state of 23 O, previously measured to be 4.0 MeV. This nucleus is of special interest to shell model theorists. Data suggest it has two sizable subshell gaps at N=14 and N=16 [17]. The shell model predicts this state to be a $\nu d_{3/2}$ single particle state [18]. A previous experiment used a (d,p) reaction to create the unbound excited state of 23 O. The June 2011 commissioning experiment will populate the unbound excited state of 23 O using the 26 F on a 9 Be reaction target through proton knockout followed by two-neutron decay.

Previous data suggests that ²⁴O has more to tell; excited states higher than the 7.5 MeV state may well exist. These possible states would likely decay through the 4.0 MeV neutron-unbound excited state of ²³O to the ²²O ground state. With both LISA and MoNA used together for the June 2011 experiment, the greater effective solid angle allows a better search for these higher energy excited states in ²⁴O.

The structure of 20 C

²⁰C is one of a number of heavy carbon isotopes of special interest to nuclear structure physics. Halo nuclei, deemed "one of the most spectacular phenomena that nuclear structure physicists have observed," include ²²C as the heaviest example to date [19]. And yet, it seems that ²⁰C is not a halo nucleus based on data and theory [20]. How the core nucleus couples to valence neutrons, in the nomenclature of halo nuclei, can be used to further our understanding of shell structure far from stability.

The N=14 magic number was first identified from a study of 22 O [21], and it raises questions about how the sd shell evolves with neutron (and proton) number. The MoNA Collaboration is preparing a study of 20 C in an effort to better understand how the sd shell evolves with neutron number. The proposed experiment will take place at the NSCL and use both MoNA and LISA as well as the Sweeper and charged particle detectors. 20 C will be created via (d, p) on 19 C using a deuterium target.

This campaign has two experimental differences from the oxygen campaign. Previous experiments to study oxygen, for example, have either used a ²⁶Ne beam on a ⁹Be target (to produce neutron-unbound excited states in ²⁴O and ²³O) or a ²⁶F beam on a ⁹Be target to produce neutron-unbound excited states of ²⁴O as well as the ground state of ²⁵O. The charged fragments of interest in the oxygen measurements can be differentiated from unreacted beam. However, in the ²⁰C measurement the unreacted beam of ¹⁹C beam must be distinguished from the ¹⁹C fragments. A new hodoscope, currently under development by Nathan Frank of Augustana College, will improve the kinetic energy resolution to the level where the beam can be distinguished from the ¹⁹C fragments.

The second experimental difference from the oxygen campaign is the possible existence of neutron-bound excited states in ¹⁹C, and therefore, gamma-ray spectroscopy should be utilized. The MoNA Collaboration proposes to use CEASAR (CAESium iodide ARray), a set of 192 CsI(Na) scintillators for in-beam gamma-ray spectroscopy [22].

Conclusion

The era of exotic beam facilities marks an exciting time in nuclear structure physics; improvements in beam development techniques, analysis, and magnetic spectrometer technology push measurements further up the neutron dripline. Experiments at the NSCL and future FRIB using neutron detector systems like MoNA-LISA will continue to inform our knowledge of nuclear structure. Halo nuclei and studies of nuclei like $^{24}\mathrm{O}$ and $^{20}\mathrm{C}$ demonstrate the high sensitivity nuclear structure has with regard to neutron (and proton) number.

Acknowledgments

This work was supported in part by US National Science Foundation Awards 0922409, 0922446, 0922462, 0922473, 0922537, 0922559, 0922622, 0922794 and 0922335.

References

- [1] T.Baumann et al., Nucl. Instr. and Meth. A 543, 517 (2005).
- [2] C. Hall et al., Phys. Rev. C 81 (2010) 021302(R).
- [3] A. Spyrou et al., Phys. Lett. B 683, 129 (2010).
- [4] C.R. Hoffman et al., Phys. Lett. B672 (2009) 17.
- [5] National Research Council of the National Academies, Rare-Isotope Science Assessment Committee, Scientific Opportunities with a Rare-Isotope Facility in the United States, National Academies Press, (2007) pp. 122 124.
- [6] Isotope Science Facility at Michigan State University, MSUCL-1345, November 2006.
- [7] C. R. Hoffman et al., Phys. Rev. Lett. 100, 152502 (2008).
- [8] S. Prestemon et al., IEEE Trans. Appl. Supercond. 11, 1721 (2001).
- [9] J. Toth et al., IEEE Trans. Appl. Supercond. 12, 341 (2002).
- [10] M. B. Bird et al., IEEE Trans. Appl. Supercond. 15, 1252 (2005).
- [11] M. B. Bird et al., IEEE Trans. Appl. Supercond. 14, 564 (2004).
- [12] N. Frank et al., Nucl. Instr. and Meth. A 580, 1478 (2007).
- [13] K. Makino and M. Berz, Nucl. Instr. and Meth. A 427, 338 (1999).
- [14] G. Audi et al., Nucl. Phys. A 729, 3 (2003).
- [15] B. Jurado et al., Phys. Lett. B 649, 43 (2007).
- [16] C. R. Hoffman et al., Phys. Rev C, 031303(R) (2011).
- [17] A. Schiller et al., Phys. Rev. Lett. 99, 112501 (2007).
- [18] Z. Elekes et al., Phys. Rev. Lett. 98 102502 (2007).
- [19] K. W. Kemper and P. D. Cottle, Physics 3, 13 (2010).
- [20] M. Petri et al., Phys. Rev. Lett. 107, 102501 (2011).
- [21] M. Stanoiu et al., Phys. Rev. C 69, 034312 (2004).
- [22] D. Weisshaar et al., Nucl. Instr. and Meth. A 624, 615 (2010).

CROSS-SECTION OF Y-RAY PRODUCTION BY FAST NEUTRONS ON CADMIUM

B.M. Bondar, V. M. Bondar, O. M. Gorbachenko, I. M. Kadenko, B. Yu. Leshchenko, Yu. M. Onishchuk, V. A. Plujko

Nuclear Physics Department, Taras Shevchenko National University, Kiev, Ukraine

Abstract On title the instruction of the sequence of the seque

Measurements of prompt γ -ray yield produced by the interaction of 14 MeV neutrons with cadmium have been performed. Time-of-flight method based on pulse neutron generator was applied. Differential cross sections of ^{nat}Cd (n, xy) reactions were unfolded from amplitude spectra and cross section uncertainties were estimated. Experimental results are compared with theoretical calculations performed by the use of EMPIRE and TALYS codes. Sensitivity of the calculations to characteristics of nuclear excited states was analyzed.

1. Introduction

Determination of the cross sections of $(n, x\gamma)$ reactions induced by interaction of fast neutrons with nuclei of the reactor constructive materials is of special importance for the calculations of the γ -ray fields in the active zone of the reactors. These cases are important for estimation of energy release and γ -ray radiation shielding. The cross sections values are also needed for investigation of different nuclear reaction mechanisms in the neutron induced reactions as well as characteristics of nuclear excited states and their decay.

Despite of numerous experimental measurements performed by neutrons with 14 MeV energy, data on γ -spectra in full energy range (up to excitation energy of the nucleus) in the same experiment are absent. In this contribution we present results of the γ -spectra measurements from $(n, x\gamma)$ reactions on ^{nat}Cd within the energy interval from 2 to 18 MeV. Measurement results are compared with theoretical calculations allowing gamma-emission from compound nucleus states and preequilibrium states.

2. Experimental measurements and data analysis

The measurements of γ -spectra are performed using the scintillation γ -spectrometer based on 15x10 cm NaI(Tl) detector. The geometry of the experiment is presented on Fig. 1.

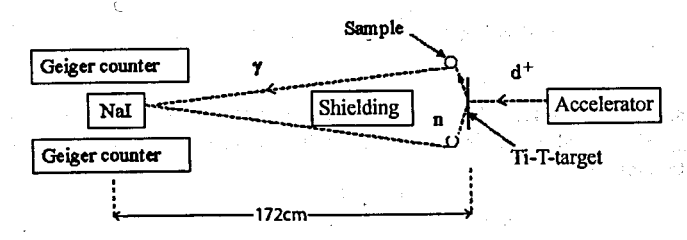


Fig. 1. Geometry of the experiment.

in the second of the

Time-of-flight method based on pulse neutron generator was applied for separation of prompt γ -rays from source neutrons, background and rescattered γ -rays. Reaction $T(d, n)^4$ He in Ti-T target was used as neutron source. Deuterons were accelerating by low-voltage accelerator with klystron bunching of deuteron beam and finally deuteron energy was 130 keV. Pulse generation frequency was equal to 7.25 MHz, average neutron intensity $\sim 10^7 \, \mathrm{s^{-1}}$. Measurements were performed with neutrons of energy 14.0 ± 0.2 MeV which corresponds to the angle 90 ° on deuteron beam. Neutron source was placed in the centre of ring sample of cadmium with radius 16 cm. The Geiger counters were used in anticoincidence with spectrometer signals in order to reduce the influence of cosmic rays. The flight path between the neutron source and NaI(Tl) detector was equal to 172 cm which provides reliable separation of prompt γ -rays from neutron and γ -ray background (Fig.2). More details concerning experiment can be found in Refs. [1-3].

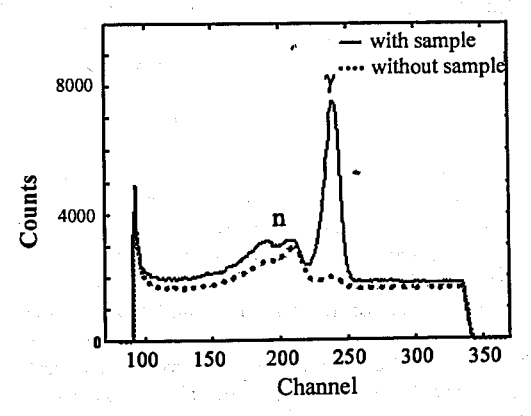


Fig. 2. Time separation of the prompt γ -rays and background neutrons: solid curve — spectrum, obtained with sample, dashed curve — without sample.

Relation between amplitude spectra $A(V, \Delta V, \theta_{\gamma})$ and differential cross section $\sigma_{\gamma}(E_{\gamma}, \theta_{\gamma}) \equiv d^2 \sigma(E_{\gamma}, \theta_{\gamma}) / dE_{\gamma} d\Omega_{\gamma}$ is given by the expression

$$A(V, \Delta V, \theta_{\gamma}) = \int_{0}^{E_{\text{max}}} R(V, E_{\gamma}) \cdot \sigma_{\gamma}(E_{\gamma}, \theta_{\gamma}) dE_{\gamma}, \tag{1}$$

where V is signal amplitude; ΔV is signal amplitude width; θ_r is scattering angle; E_r is γ -ray energy; $E_{max} = E_n + S_n$, where E_n is energy of incident neutron, S_n is neutron separation energy of composite nucleus;

$$R(V, E_{\gamma}) = \int_{V-\Delta V/2}^{V+\Delta V/2} G\alpha_{\gamma}(E_{\gamma})e(V, E_{\gamma})dV.$$
 (2)

Here, G is geometry factor; $\alpha(E_{\gamma})$ is energy-depended coefficient of the γ -ray self-absorption by sample detector; $\epsilon(V, E_{\gamma})$ is detector response function. The expression for the detector

response function $\varepsilon(V, E_{\gamma})$ was taken from Ref. [4]. It is based on analytical approximation of the bremsstrahlung experiment with correction on Monte Carlo simulations as well as on detection of 4.43 MeV γ -rays from neutron inelastic scattering on carbon.

Amplitude spectrum have been measured at $\theta_{\gamma} = 90^{\circ}$; which gives cross sections $\sigma_{\gamma}(E_{\gamma}, \theta_{\gamma} = 90^{\circ})$. Because of weak angular dependence of the differential cross sections the quantity $4\pi\sigma_{\gamma}(E_{\gamma}, \theta_{\gamma} = 90^{\circ})$ can be considered as angle-integrated energy spectrum

$$\frac{d\sigma(E_{\gamma})}{dE_{\gamma}} = \sigma(E_{\gamma}) = 4\pi \cdot \sigma_{\gamma}(E_{\gamma}, \theta_{\gamma} = 90^{\circ}). \tag{3}$$

We use this expression for determination of experimental data on angle-integrated γ-spectrum.

Eq. (1) is Fredholm integral equation of the first kind. There are problems in its solving due to instability of unfolded spectra to the experimental data uncertainties (so called ill-posed). Algorithm on the compact set of limited variations with set of monotonically decreasing functions [5] was used to find cross sections. Uncertainties of the cross sections were estimated in assumption that the amplitude spectrum is distributed with Gauss distributions due to the large number of external factors; then additional unfolding procedures were used [3]. Sensitivity of the unfolded cross sections to variation of detector response functions was also analyzed. It was obtained that variation of response function within interval of 10-15% leads to changes of cross sections values not more then 5-7%.

Experimental values of the unfolded differential cross sections and their uncertainties are shown on Fig. 3.

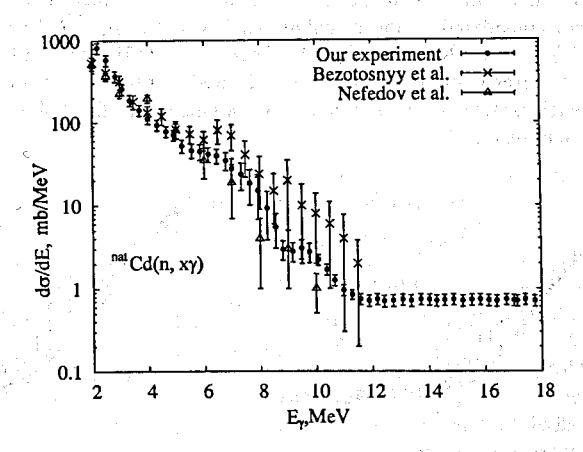


Fig. 3. Differential cross sections of the reactions nat Cd(n, xy) obtained using regularization algorithm on the compact set of limited variations: points – results of our experiment, crosses – experimental data from [6], triangles – [7].

Rather good agreement of measured cross sections with results from Ref. [6, 7] is obtained.

3. Results of the theoretical calculations

Experimental results were compared with theoretical calculations of inclusive γ spectrum which corresponds to the sum of spectra for all possible reactions with incident
neutron:

$$\frac{d\sigma(n,x\gamma)}{dE_{\gamma}} = \frac{d\sigma(n,\gamma)}{dE_{\gamma}} + \sum_{J} \frac{d\sigma(n,jb,\gamma)}{dE_{\gamma}} + \sum_{k} \frac{d\sigma(n,\gamma,kc)}{dE_{\gamma}} + \dots, \tag{4}$$

where j and k are the numbers of emitted particles b, c of different kind (b, c = n, p, d, t, α) determined by conservation laws.

Theoretical calculations performed using EMPIRE (version 3.0) [8] and TALYS (version 1.2) [9] codes with allowing emissions from compound nucleus and preequilibrium nuclear states. The Hauser-Feshbach model was used in the calculations of emission from compound nuclei and the exciton model was applied from calculations of preequilibrium emission. the following input parameters are required for cross section calculations[10]: nuclear level density, optical potential and radiative strength function (RSF).

Fig. 4 shows experimental differential cross sections of the reactions ^{nat}Cd(n, xγ) in comparison with theoretical calculations. In case of EMPIRE code, the following input parameters were used in the calculations [12]: dipole electric RSF (E1 RSF) within model of modified Loretzian (MLO) and Enhanced Generalized Super-Fluid Model (EGSM) for the nuclear level densities. In TALYS code E1 RSF was calculated within Enhanced Generalized Loretzian (EGLO) with Gilbert-Cameron approach for nuclear level densities. These set of parameters are used in corresponding codes as default ones. The following isotopes of cadmium were considered in the calculations: ¹⁰⁶Cd (12 %), ¹⁰⁸Cd (0,9 %), ¹¹⁰Cd (12,4 %), ¹¹¹Cd (12,8 %), ¹¹²Cd (24 %), ¹¹³Cd (12,3 %), ¹¹⁴Cd (28,8 %) and ¹¹⁶Cd (7,6 %) where abundances of corresponding isotopes are indicated in brackets. Calculated values of cross sections for each isotope were summed in accordance with their abundances to obtain cross sections of reactions on ^{nat}Cd.

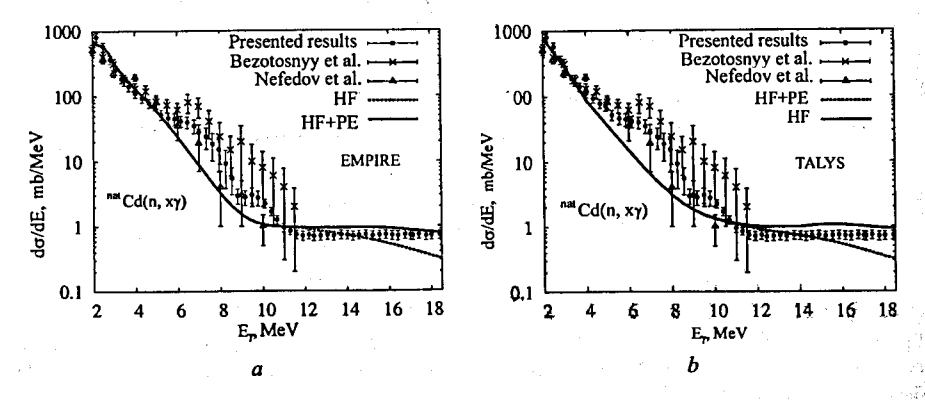


Fig. 4. Differential cross sections of the reactions ^{nat} Cd(n, xy) performed using EMPIRE (a) and TALYS (b) codes: points – our experimental results, solid curve – calculations within Hauser - Feshbach model, dashed curve – calculations within Hauser - Feshbach model with taking into account preequilibrium emission (PE).

As one can see from Fig.4, rather satisfactory agreement of the theoretical calculations with experimental data is obtained for the $^{nat}Cd(n, xy)$ reactions almost in all energy range accept interval from 6 MeV to 11 MeV, where experimental results exceed theoretical ones. It is also can be concluded that taking into account preequilibrium processes gives the better agreement of experimental data and theoretical calculations for the energy range above 12 MeV. Calculations within EMPIRE and TALYS codes are in rather good agreement.

Sensitivity of the calculated cross sections to input parameters mentioned above was analyzed. Calculations were performed with using EMPIRE code. Fig. 5 demonstrates the cross sections obtained by the use of different optical potentials taken from [11-13]. It can be seen from Fig. 5 that theoretical results obtained using all potentials gives rather same agreement of theoretical calculations with experimental results.

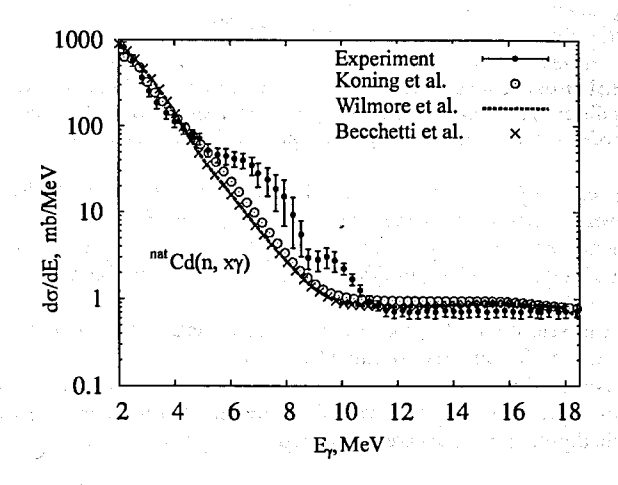


Fig. 5. Differential cross section of the reactions $^{nat}Cd(n, xy)$ calculated with EMPIRE code using different optical potentials: points – our experimental results, circles – Koning potential [11], dashed curve – Wilmore potential [12], crosses – Becchetti potential [13].

To check sensitivity of the cross sections to the different approaches for nuclear level densities the following models were used: Enhanced Generalized Super-Fluid Model (EGSM), Back-Shifted-Fermi-Gas Model (BSFG) and Gilbert-Cameron approach (GC). More detailed description of all the models mentioned above can be found in Ref. [10]. Fig. 6 demonstrates the example of the dependence of nat Cd(n, xy) reaction cross sections on nuclear level density.

It can be seen from Fig. 6 that theoretical results obtained using both EGSM and BSFG models gives rather same agreement of theoretical calculations with experimental results.

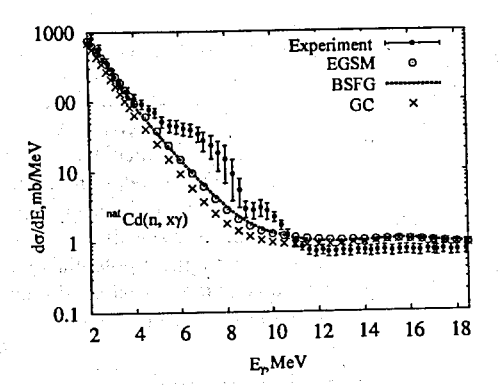


Fig. 6. Differential cross sections of the nat Cd(n, xy) reactions calculated with EMPIRE code using different models different models for the nuclear level densities: open circles – EGSM model, dashed curve – BSFG model, crosses – Gilbert-Cameron approach. Experimental results are shown by points.

We also checked sensitivity of the calculations to the shape of electric dipole RSF. Calculations were performed using the following models: Standart Loretzian (SLO), Enhanced Generalized Loretzian (EGLO), modified Loretzian (MLO), Generalized Fermi liquid (GFL) model [11, 14-16]. EGSM model was used for the nuclear level densities. Results of the calculations are shown on Fig. 7.

As one can see, the best agreement with the experiment is obtained in case of using SLO and MLO models for radiative strength function.

It was also checked that calculated cross sections are insensitive to the high values of the γ -ray transition multipolarity. It is caused by the fact that number of the nuclear levels is large and electric dipole transitions are dominated.

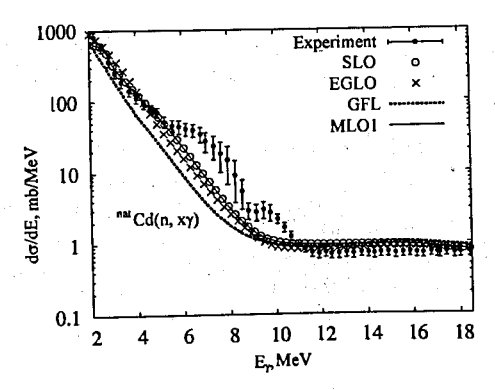


Fig. 7. Differential cross sections of the ^{nat} Cd(n, xy) reactions calculated with EMPIRE code using different models for the RSF: open circles – SLO model, crosses – EGLO, dashed curve – GFL, solid line – MLO. Experimental results are shown by points.

From the results presented on Figs. 5-7, one can conclude that good agreement of the theoretical calculations with experimental results can be obtained in the case of simultaneous changes of the models both the nuclear level density and E1 radiative strength function.

4. Conclusions

Differential cross sections of $^{nat}Cd(n, x\gamma)$ reactions were measured using time-of-flight technique. The algorithm on the compact set of limited variations was used in order to obtain the cross sections values and their uncertainty estimations.

The experimental results are compared with theoretical calculations performed with allowing emission of γ -rays and particles from equilibrium and preequilibrium nuclear states. It was demonstrated that taking into account preequilibrium processes gives the best agreement of experimental data and theoretical calculations. Results of the calculations are rather in good agreement with experimental data except energy region from 6 to 11 MeV. Disagreement within this interval can be caused by some effect of nuclear structure on the input parameters, especially on nuclear level density.

In order to obtain the best agreement of calculated cross sections with experimental results, the optimal set of models for nuclear level densities, potential and RSF should be used. According to our analysis, cross sections of $^{nat}Cd(n, x)$ reactions calculated by the use SLO and MLO models for radiative strength functions and with EGSM for the nuclear level densities lead to the best agreement with experimental results.

Acknowledgments. O.M. Gorbachenko expresses his deep gratitude to the Organizing Committee of the Conference for financial support and warm welcome.

REFERENCES

- V. M. Bondar, I. M. Kadenko, B. Yu. Leshchenko et al., Reactor Dosimetry State Of The Art 2008: Proc. 13th Int. Symp. (25-30 May, 2008, Alkmaar, Netherlands), (2009) 516.
- 2. V. M. Bondar, I. M. Kadenko, B. Yu. Leshchenko et al., Bull. Russian Acad. Sciences: Physics, 73(11) (2009) 1511.
- 3. B. M. Bondar, V. M. Bondar, O.M. Gorbachenko et al., Nuclear Physics and Atomic Energy, 12(2) (2011) 129.
- 4. G. M. Gurevich, V. M. Mazur, G. V. Solodukhov, Instr. Exp. Techn., 2 (1975) 59.
- 5. A. N. Tikhonov, A. V. Goncharsky, V. V. Stepanov et al., Numerical methods for the solution of ill-posed problems, Moscow, 1990 (in Russian).
- 6. V. M. Bezotosnyi, V. M.Gorbachev, M. A. Efimova et al, Atomic Energy, 4 (1980) 239.
- 7. Yu.Ya. Nefedov, V.I.Nagornyy, V.I.Semenov et al., Vop. At.Nauki i Tekhn., Ser. Yadernye Konstanty, 1 (2000) 7.
- 8. M. Herman, R.Capote, B.V. Carlson et al., Nucl. Data Sheets, 108 (2007) 2655.

- 9. A. J. Koning, S. Hilaire, M. C. Duijvestijn, In Proc. of the International Conference on Nuclear Data for Science and Technology, ND2007 (April 22 - 27, 2007, Nice, France), 1 (2007) 211.
- 10. R. Capote, M. Herman, M. Oblozinsky et al, Nucl. Data Sheets, 110 (2009) 3107.
- 11. A.J. Koning, J.P. Delaroche, Nucl. Phys. A713 (2003) 231.
- 12. D. Wilmore, P. E. Hodgson, Nucl. Phys., 55 (1964) 673.
- 13. F. D. Becchetti, G. W. Greenlees, Phys. Rev., 182 (2000) 1190.
- 14. V. A. Plujko, I. M. Kadenko, O. M. Gorbachenko et al., Int. J. Mod. Phys. E., 17 (2008) 240.
- 15. V.A. Plujko, R. Capote, O.M. Gorbachenko, At. Nucl. Data Tables, 97 (2011) 567.
- 16, V.A. Pluiko, O.M. Gorbachenko, V.M. Bondar et al., Journal of Korean Physical Society, 59(2) (2011) 1514.

The experimental investigation of $^{10}B(n, \alpha_0)$ to $^{10}B(n, \alpha_1)$ branching ratio for neutron energy region from 4 to 7 MeV and the property of the control of the second of the control of th

I.P.Bondarenko, V.A.Khryachkov, B.D.Kuzminov, N.N.Semenova, A.I.Sergachev

FSUE "SSC RF - IPPE", Obninsk, Russia

Abstract

The method of branching ratio ${}^{10}B(n,\alpha_0)$ to ${}^{10}B(n,\alpha_1)$ experimental investigation is described in this work The ionization chamber with Frisch grid, filled up with gas mixture of 95% Kr and 5% BF3, was used in these experiments. Using of fast neutron beam profiling method allied with digital signal processing allowed us to select particles, appearing in fixed volume of working gas. This method of branching ratio measurement is almost free from systematical uncertainties, which is typical for experiment, where the solid target is used. The branching ratio $^{10}B(n,\alpha_0)$ to $^{10}B(n,\alpha_1)$ measurement results for neutron region from 4 to 7 MeV are presented in this work. A second of the seco

The second of the second of the street of the following second

Introduction

n de la companya de l ¹⁰B (n,α)⁷Li reaction is related to standard nuclear reaction and is of great importance for criticality control of any reactor type due to usage of boron as neutron absorber. In addition, this reaction is very important for dosimetric (neutron detectors, individual dosimetry) and radiobiological (neutron capturing therapy) applications.

All modern national and regional bases of evaluated nuclear data are represented by experimental cross section data related to ¹⁰B(n,a) reaction, caused by neutrons from 4 till 7 MeV energy region, obtained by Bonner's group in 1961 [1]. In that experiment considerable mistakes could be caused by side effect that relates from angular distribution of α - particles. This distribution is undefined and may vary from one neutron energy to another.

A new method based on gaseous target usage and digital signal processing was used in present work. The usage of this method allowed us to decrease parasitic reaction influence significantly and to rectify many systematical uncertainties that are so typical for classical spectrometers. In current work The branching ratio ${}^{10}B(n,\alpha_0)$ to ${}^{10}B(n,\alpha_1)$ measurement results for neutron region from 4 to 7 MeV are presented in this work. Typical uncertainty of data obtained is approximately 5 %. The second results are second as the second results are second results.

Experimental method

Pulse ionization chambers with solid targets set on the cathode are widely used for direct measurement that based on number of appearing α-particles estimation. This method allows us to get double-differential cross-section, though it has a few drawbacks: 1) number of investigating isotope nuclei number, that could be set as a solid target, is relatively small due to α-particles energy loss in the target and their full absorption in it; 2) the determination of accurate nuclei number of target is a very complicated problem especially in case of the stable element; 3) in case of working with high energy neutrons the detector itself (chamber electrodes, target backing, chamber working gas) becomes a powerful source of background

the large and control of the control of the large three largest with public to

from α -particles, protons, γ -rays and so on, 4) chamber response function, especially in case of light nuclei as emitters, becomes complicated – observable α -particles energy depends on emission angle due to in-target energy loss and kinematics. The emission of both reaction products inside the sensitive volume of the chamber (particles leakage) becomes kinematically possible. Amendments (on kinematics, energy loss in layer) are different for events taking place in solid target and working gas components. Still classical method (of working with analog signals) does not allow us to separate signals that makes obtained spectrum analysis much more complicated, 5) all measurements should be carried out twice to get full cross section – for direct (α -particles is emitted in neutron movement direction) and back (α -particles is emitted in opposite to neutron movement direction) geometry, α -particles is emitted in opposite to neutron movement direction)

It is known from literature [1], that BF₃ (enriched with 10 B isotope) was used as the target and injected in work gas (Ar). This allowed to increase target nuclei number in 100 times approximately and to make simple analysis of one dimensional spectra for events number determination. Really, both α -particle and residual nucleus contributed to anode signal amplitude for the event took place on work gas components. In this case summarized energy (E_{Sum}) doesn't depend on emission angle and will be:

$$E_{Sum}=E\alpha+E_R=En+Q$$
, /1/

where $\text{E}\alpha$ - α -particles energy, E_R - residual nucleus energy, Q - reaction energy. Besides, anode specter is discreet and every peak can be associated with exact channel of the reaction, that takes place on such and such isotope. In the described works the whole chamber was irradiated by fast neutron beam. Big uncertainty in number of investigating isotope nuclei estimating ought to be limitation of these methods. Especially due to great contribution that events on these nuclei make to complete absorption peak. Side effect is related from chamber geometry and reaction products angle distribution and can't be dtermined with adequate accuracy. Significant background that prevents events number determination is caused by events distorted with side effect, events take place on construction elements, and events from protons appearing in working gas.

That is why it was decided to use neutron collimator and digital processing methods for separating fixed gas sell in the working volume. This sell was chosen so that particles produced in it could not reach chamber electrodes or escape from sensitive volume of the chamber. Collimator is forming a truncated cone sell inside working gas, which height is set by developed digital signal processing method. Finally, effective number of engaged in the reaction boron atoms could be estimated from comparison of three factors: sell volume, working gas pressure, concentration of investigating atoms in working gas. But for α_0/α_1 branching ratio determination it is not necessary to know the number of atoms. It is only enough to provide number of atoms equality. Meaning the atoms forming peaks correspond to investigating reactions.

Digital spectrometer based on ionization chamber with Frisch grid was created for solving this problem. Detector construction scheme is on Fig. 1.

Krypton Kr(95%) and boron trifluoride BF3(5%) gas mixture with pressure of 3 atmospheres (absolute pressure) was used as working a gas. This gas mixture was made with high accuracy (9.10±0.27% BF3, other – Kr) by Linde AG, Linde Gas Deutschland.

Presenting in working gas boron was also the target where investigating reaction (n,α) took place. Falling neutron beam was coincide with chamber symmetry axis. The beam itself was formed by copper collimator. Experimental setup scheme is on Fig. 2.

Cathode and anode signals from main chamber was amplified and get to the wave form digitizer input to be converted into digital view. The described process was ruled by

standard signal gathered from cathode signal. Using of such signals converting scheme allows us to keep digitized information about experimental events on PC hard drive for further digital signal processing analysis [2].

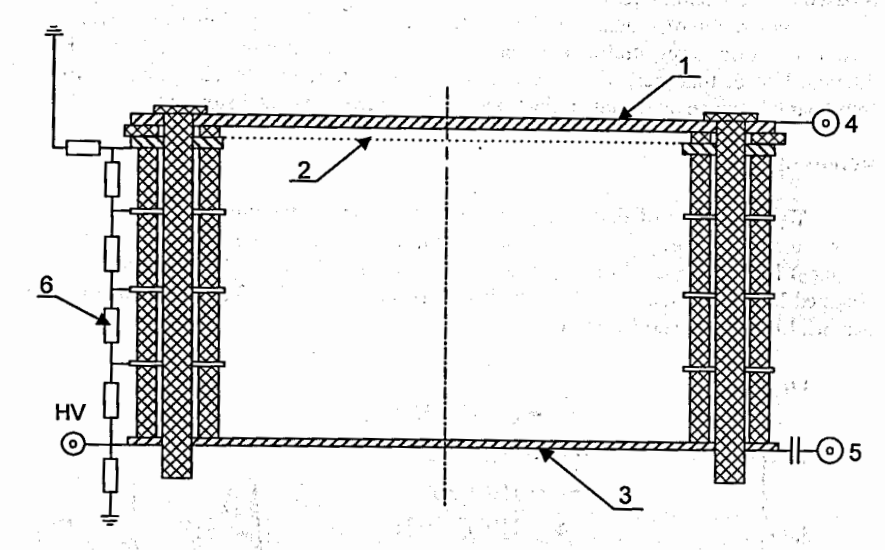


Figure 1. 1 – anode, 2 – Frisch grid, 3 – cathode, 4 – anode pin, 5 – cathode pin, 6 – voltage divider, 7 – guard electrodes

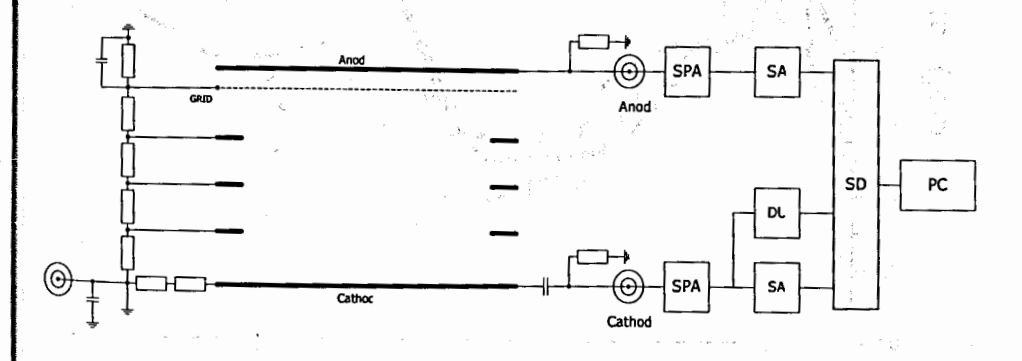


Figure 2. SPA – signal preamplifier, SA – signal amplifier, DU – delay unit, SD – signal digitizer, PC – personal computer.

There are a few main parameters that we use: anode and cathode amplitudes, maximal electron drift time (that are the most distant from anode – the only beginning and the end of the track) TD=(TEA-TSC), and anode signal rising time (while anode collects electrons) TR=(TEA-TSA). Maximal drift time can be easily converted to distance between cathode and

track beginning (ending) at most distant from anode. Measurement of anode signal rising time allowed us to get the length of track projection on chamber axis. All further digital processing is based on these parameters.

Digitization of signals and their further digital processing allow us to develop superior method of particles registration and determination of their birth place in cathode – Frisch grid interval. Use of this method makes it possible to separate events take place in working gas from that take place on chamber electrodes and also from events distorted by side effect.

Results obtained

There are lots of data on (n, α_1) reaction channel determined by γ -rays. In case we know α_0/α_1 branching ratio, we can determine as α_0 cross section as full cross section. $^{10}B(n,\alpha_0)^7Li$ to $^{10}B(n,\alpha_0)^7Li$ branching ratio was obtained for 4 to 7 MeV neutrons. The data obtained both with nuclear data from ENDF/B-VII.0, JENDL 3.3, and also Bonner[1] and Sealock [3] data are shown on Fig. 3.

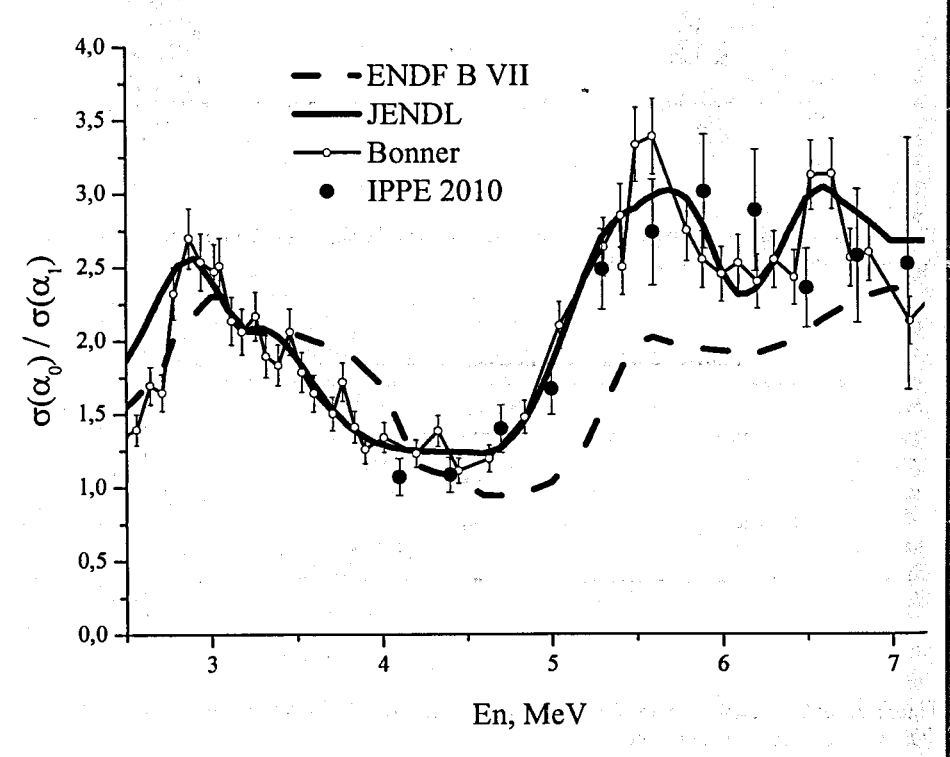


Figure 3. 10 B $(n,\alpha_0)^7$ Li to 10 B $(n,\alpha_1)^7$ Li branching ratio.

Conclusion

New method that makes it possible to use toxic and mordant gas BF₃ as working one was developed. This method is based on signal wave form digitizing allied with usage of ionization chamber working gas as a target. The fixed gas cell separation inside the sensitive volume of ionization chamber was used. The method allowed us to compensate electron loss due to their broad capture by very electronegative gas (BF₃). The energy resolution that permit us to separate α_0 and α_1 channels of reaction $^{10}B(n, \alpha)^7Li$ was obtained. The developed method of determining branching ratio of different reaction channels is almost free from statistical uncertainties. The branching ratio for neutron energy region from 4 to 7 MeV were obtained in this work. The obtained data is in a close fit with Bonner data and JENDL 3.3 estimation, but seriously (up to 30%) differs from ENDF B VII estimation.

All experimental and theoretical data that is obtained in this work can be used in different nuclear data libraries.

This work was carried out with RFFI and Kaluga region administration support (grant № 11–02–97523).

References

1. E. A. Davis, F. Gabbard, T. W. Bonner and R. Bass, The disintegration of ¹⁰B and ¹⁹F by fast neutrons, Nuclear Physics 27, p.448,1961.

Control of the careful of the second

- 2. V. A. Khryachkov, I. P. Bondarenko, B. D. Kuzminov, Study of (n, α) reaction cross section on a set of light nuclei. Proc. Of XVIII Int. Seminar on Interaction of Neutrons with Nuclei, ISINN-18.
- 3. R. M. Sealock, J. C. Overley, 10B(n, α)⁷Li, Li* differential cross section measurements between 0.2 and 1.25 MeV, Physical Review 13, p. 2149, 1976.

් වෙන නිව්වා විසින් වෙන නිව්වා සිට ප්රදේශයින් වෙන අතුරු වැනි අතුරුවන් විසින් වෙන අතුරු වැනි අතුරුවන් විසින් වෙන අතුරුවන් වෙන වෙන අතුරුවන් අතුරුවන් අතුරුවන් අතුරුවන් වෙන අතුරුවන් අතුරුවන් අතුරුවන් අතුරුවන් අතුරුවන් වෙන අතුර අතුරුවන් අතුරුවන් අතුරුවන් අතුරුවන් වෙන අතුරුවන් අතුරුවන් අතුරුවන් අතුරුවන් අතුරුවන් අතුරුවන් අතුරුවන් අතුරුවන Excitation function ¹⁴N(n,t)¹²C in fast neutrons energy region

T.A.Ivanova², V.A.Khryachkov¹, I.P.Bondarenko¹, B.D.Kuzminov¹, N.N.Semenova¹, A.I.Sergachev¹

¹FSUE "SSC RF – IPPE" Obninsk, Russia.

²National Research Nuclear University MEPhI, Obninsk Institute for Nuclear Power Engineering of NRNU MEPhI

Abstract

In this work experimental investigation of ¹⁴N(n,t)¹²C reaction is described. The ionizing chamber with Frisch greed was used for reaction products spectroscopy. Working gas of the ionizing chamber contained ~3% of nitrogen. This gas we used as target where investigated reaction took place. Using of digital signal processing methods allows us to select the signals correspond to (n,t) reaction from large number of background events. ¹⁴N(n,t)¹²C reaction cross section experimental data for is presented in this work.

Introduction

One of the possible fuel types for advanced nuclear reactors is nitride fuel. This kind of fuel has a lot of advantages - nitride fuel is high-density, has good heat conductivity that provides rather low temperature of fuel elements at operation and it, in turn, has positive effect for safety. Nevertheless there is a big problem which connected with an additional tritium source from ¹⁴N (n, t) ¹²C reaction.

Tritium leaks in the environment because it has a high mobility and easily penetrate through constructional materials. Tritium is dangerous for personnel of nuclear stations because it can easily replace light hydrogen isotope in human body and it can create inner radiation source.

The set of experimental data for ¹⁴N (n, t) ¹²C reaction available from the literature as well as different theoretical estimations show big discrepancy. In this condition only new experimental research of ¹⁴N(n, t) ¹²C reaction cross section based on modern techniques can provide sufficient precision for this value.

Experimental method

In present work measurement of section of $^{14}N(n, t)^{12}C$ reaction were executed on accelerator EG-1 of IPPE. Neutrons were generated in D (d, n) reaction on a firm titanic target, which thickness is 1 mg/cm². Measurements were executed for 37 various neutron energies in an interval from 5.1 to 7.0 MeV.

Cross section research was carried out using doubled ionizing chamber with a common cathode. The main ionization chamber with Frisch grid was used as detector of the events of neutron interaction with nuclei of nitrogen. A parallel plate chamber which contains a thin solid ²³⁸U layer was used as neutron flux monitor (fig. 1).

Signals from various electrodes of the chamber were amplified and then were digitized with the help the wave form digitizer – LeCroy 2262. The further processing of signals was made by means of programs. The information on amplitudes of anode and cathode signals, and also the moments of the beginning and the ending of these signals was taken during

processing. Joint analysis of this information allowed us to define charged particle energy, place of event occurrence in the interelectrode space and charge collecting time (charge is formed by a particle).

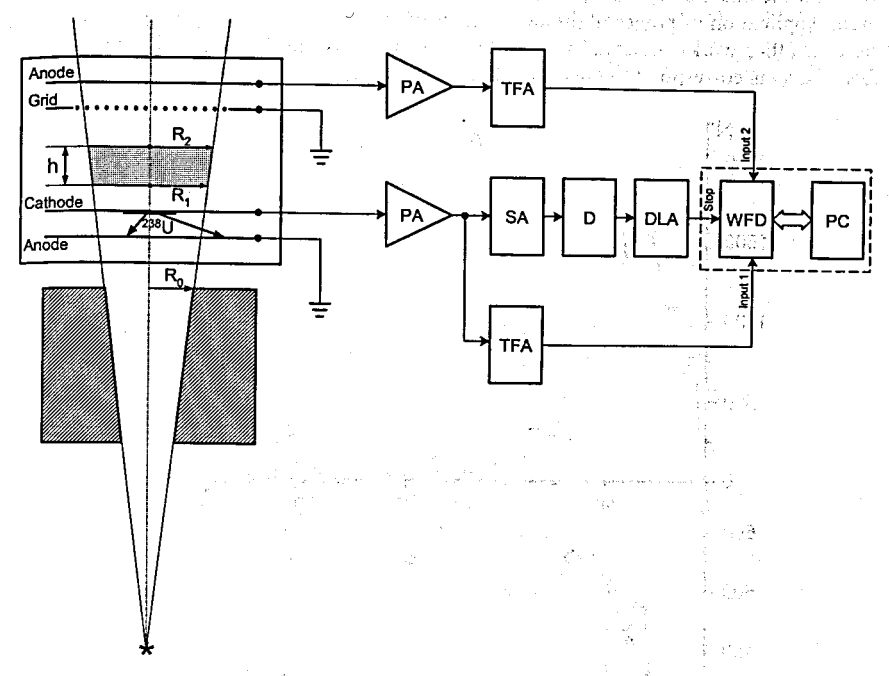


Figure 1. Block diagramme of experimental setup. DA – preamplifier, TFA – timing filter amplifier, D – discriminator, SA – spectroscopy amplifier, DLA – delay line amplifier, WFD – waveform digitizer, DC – personal computer.

Chambers were filled by 97%Kr + 3%N₂ gas mixture. The nitrogen contained in working gas was a target for neutron interactions. Gas target use has allowed us to considerably increase nuclei number in the investigated sample and hence, to reduce time of measurements. Use of fast neutron collimation together with signal digital processing methods has allowed us to allocate a certain gas cell in the sensitive volume of the chamber. So we can take in consideration events that happen in the cell only. One of the main advantages of such approach is that accurate choice of the gas cell size and position makes it possible to suppress wall effect practically. Number of nitrogen atoms in can be easily calculated for fixed gas cell using simple gas laws.

It should be noted especially that the increase time of anode signal bears in itself type of the registered particle information. For example, free path and time of charge collecting for proton appears much more than for α-particles of the same energy. In this work it was possible to use this principle for particles division on type and to reduce a background arising from parasitic reactions in working gas and on detector electrodes. In Fig. 2 the spectrum of anode signals received from the detector (top part of figure). In the bottom part of figure 2 the

same spectrum after suppression of a background is given. Really, only after background suppression it is possible to observe a number of lines related to α_2 , α_3 channels of ¹⁴N (n, α) reaction and the channel of reaction with tritium emission which is the subject of the current research. Application of powerful digital methods of suppression of the background, which is not used in other works, essentially has allowed to improve the situation with definition of number of events correspond to the channel of reaction (n, t).

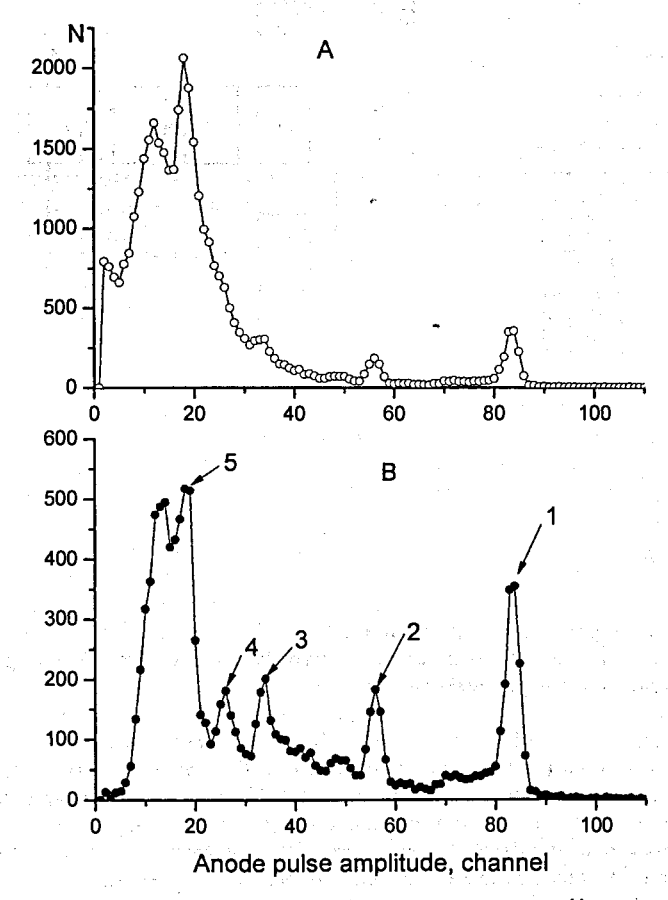


Figure 2. Energy spectrum for: A – all events; B – after selection. $1^{-14}N(n,\alpha_0)$, $2^{-14}N(n,\alpha_1)$, $3^{-14}N(n,t)$, $4^{-14}N(n,\alpha_2)$, $5^{-14}N(n,\alpha_3)$.

Experimental results

14N (n, t) reaction cross sections data that is obtained in this work are shown in fig. 3 and fig. 4. On the fig.3 new data and experimental data available from the literature [1-4] are shown. On the fig.4 our experimental data is plotted together with different libraries estimations

(ENDF/B VII, BROND, and JENDL). In average, for neuron energy range 5.6-7 MeV our cross section data level in 2-3 times less then other authors' one. For low neutron energy range (5.25-5.6 MeV) value of cross section significantly higher then Bonner group data [1].

Additionally our energy dependence of 14N (n, t) reaction cross section is different from other authors' one. In our data set we don't observe the well shaped resonances in (n, t) reaction cross section for energy 5.66, 6.05 and 6.7 MeV predicted by ENDF/B VII library (see fig.4).

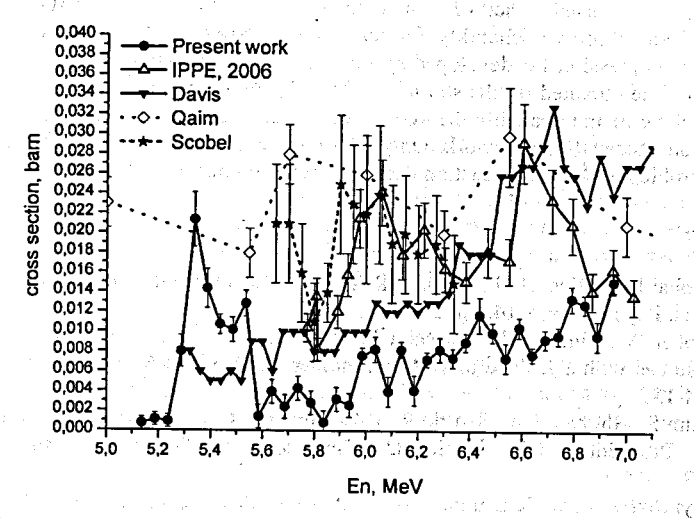


Figure 3. ¹⁴N(n,t)¹²C reaction cross section in comparison with experimental data of other authors.

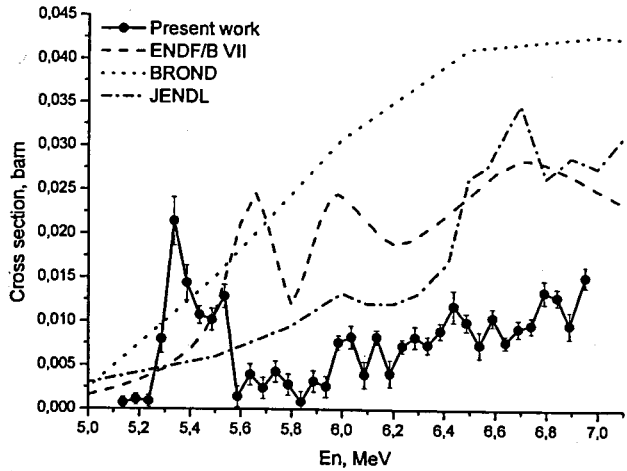


Figure 4. ¹⁴N(n,t)¹²C reaction evaluated cross section in comparison with experimental data.

At the same time in our cross section data we have clean peak for energy 5.4 MeV which is not presented in available estimations. The same structure we can see in tendency of data, predicted by ENDF/B VII library, but a peak position on a energy scale essentially differs (250 keV).

Conclusion

In this work was used a set of new methods which allows us significantly reduce a background and improve reliability for number of $^{14}N(n,t)$ events definition. As effect – background suppression for developed spectrometer is much better than for the others were used before. The obtained results strongly differ from other authors' data accessible from the literature. None of the available theoretical estimations can describe energy dependence for cross section obtained in this work. Only additional experimental and theoretical effort can solve the problem of $^{14}N(n,t)$ reaction excitation function behavior.

References

- Gabbard F., Bichsel H., Bonner T. The disintegration of nitrogen by fast neutron. -Nucl. Phys., 1959, v.14, pp. 277-294.
- 2. Scobel W., Fink R.W., Bormann M. The reaction ¹⁴N (n, α) ¹¹B and ¹⁴N (n, t) ¹²C observed with a gridded ionization chamber. Zeitschrift für Physik, 1966, v. 197, pp. 124-135.
- Qaim S., Shuhaimi A., Wolfle R. Measurement of (n, t) cross sections on light nuclei.
 In: Proc. Intern. Conf. Nuclear Data for Science and Tecnology. Mito, 1988, pp. 225-228.
- Kryachkov V.A., Kuzminov B.D., Dunaev I.V., Semenova N.N., Sergachev A.I.
 ¹⁴N(n,α)¹¹B and ¹⁴N(n,t)¹²C reaction cross section measurement for neutrons in 5.45 7.2 MeV energy range. Atomic energy, 2006, v. 101, issue 4, p.307.

Investigation of 50 Cr $(n,\alpha)^{47}$ Ti reaction cross section for neutron energy less than 7.2 MeV

V.A.Khryachkov¹, I.P.Bondarenko¹, O.T.Grudzevich², T.A.Ivanova², B.D.Kuzminov¹, N.N.Semenova¹, A.I.Sergachev¹

¹Institute for Physics and Power Engineering (IPPE), Obninsk, 249020, Russia, ²Obninsk Institute for Nuclear Power Engineering, Obninsk, Russia

Abstract

 50 Cr(n, α) 47 reaction cross section experimental investigation results is presented in this work. An ionization chamber with Frisch grid allied with wave form digitizer was used for this investigation. The developed investigation method of information accumulation and processing allowed significantly decrease background from parasitic reactions and select signals from investigating reaction. The 50 Cr(n, α) 47 Ti cross section measurements for 4.7 – 7.2 MeV neutron energy region is presented in this work.

Introduction

Construction materials radiation resistance is considerably defined by gaseous products (such as helium or hidrigen) of (n_{fast},α) nuclear reactions. The carried out analysis made it clear the lack of experimental data for a few elements (though of their great practical importance), for example, chromium is investigated for 14 MeV only [1-3]. And even these data differ from author to author in tens of percents (fig.1). There is total data absence for neutrons from reactor energy region. The consequence of such situation is wide dispersion in theoretical estimations of $^{50}\text{Cr}(n,\alpha)^{47}$ reaction cross section, shown also on Fig. 1. Comparison of ENDF/B VII to JENDL 3 $^{50}\text{Cr}(n,\alpha)^{47}$ Ti reaction cross section data is shown on Fig. 2. The difference between them raise up to 27 times for low energy neutrons! This difference can only be solved by appearance of new experimental data.

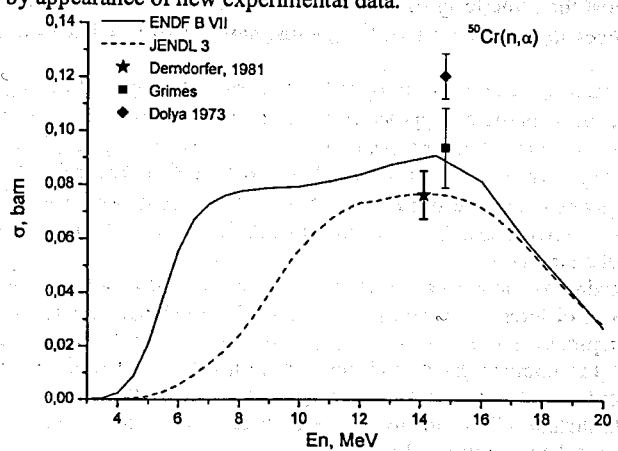


Figure 1. ⁵⁰Cr(n,α)⁴⁷Ti cross section experimental data and theoretical estimations known for today.

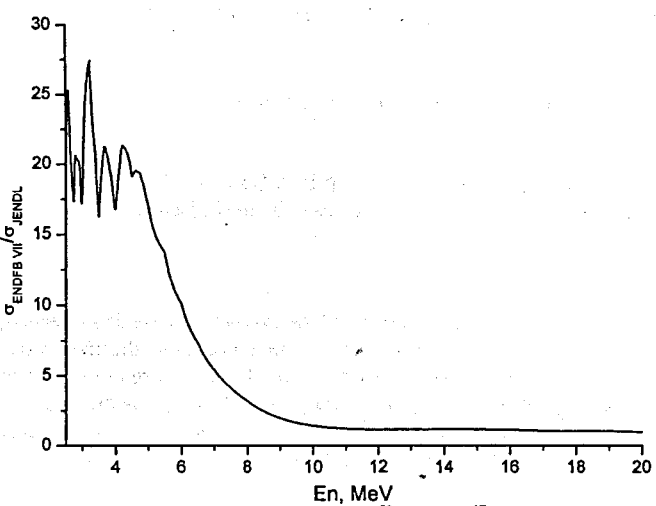


Figure 2. Comparison of ENDF/B VII to JENDL 3 ⁵⁰Cr(n,α) ⁴⁷Ti reaction cross section data.

Experimental method

The solid cromium target with 96,8% of 50 Cr isotop was used in this work. The other isotopes were: 52 Cr (2.98%), 53 Cr (0.18%), and 54 Cr (0.04%). Target's full mass is 5.15 mg. The target was spread on golg foil with 84 mg/sm² thickness. The target was plased in ionization chamber with Frsch grid filled up with 97%Kr+3%CH₄ gas mixture wich pressure was 3 atmospheres. Great background to investigation effect arise from recoil protons registration that appears due to usage of hydrogen reach methane. Still, an attempt to use carbon dioxide has brought almost the same level of background, this time from oxygen. We found out that signal digital processing is easier for working with recoil protons background than oxygen α -particles.

First attempt of placing the target on the cathode showed that its material components became intensive source of α -particles appearing from (n, α) reaction. The authors have great experience of (n, α) reaction investigation in case of gaseous targets [4-5]. So, using this experience, the target was placed in the cathode – Frisch grid interval (Fig. 3). This approach allowed us to separate α -particle signals of different origin: from target surface, from cathode or that appeared in working gas. It is important that such a detailed analysis can be made with signal digital processing only.

Signals from anode and cathode were digitized separately, resulting numerical matrix with their amplitudes in different moments of time. This digitized signals were kept on PC hard drive for further processing. So we could get amplitudes of signals and their start and end time moments. Information joint analysis for each event allowed us to get detailed information about registered particle — energy, place of birth and her type. Every of determining parameters allow to reduce background and so, to increase number of investigating events determination reliability.

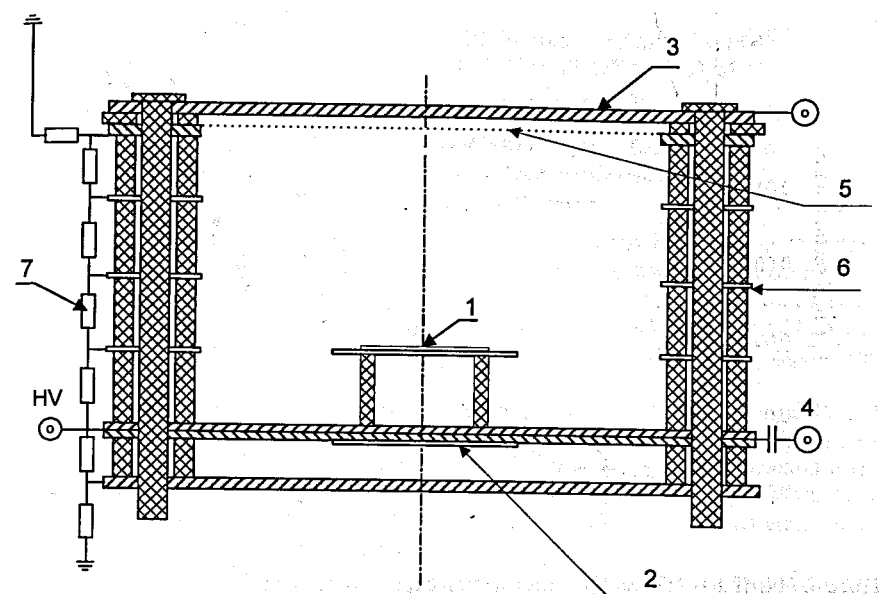


Figure 3. Detector construction scheme. $1 - {}^{50}$ Cr target; $2 - {}^{238}$ U target; 3 - IIC Anode; 4 - common cathode; 5 - Frisch grid; 6 - guard electrodes; 7 - divider.

All described investigations were carried out on EG-1 accelerator of IPPE. Neutrons were get from D(d,n) reaction on solid titanium target wich thickness is 1 mg/sm². Investigations is made for 4,7 to 7.2 MeV neutron energy region.

Flat double ionization chamber was used in our investigations. The second, made in back-to-back geometry, ionization chamber with 238 U target (99,99% enrichment) was used as α -particle source for neutron flux monitoring. Uranium target is 4,60 mg (determined by mass-spectrography). The describing methode allowed us to make the same dead time for both reaction channels – in main and monitor chambers. So we can record signals from common cathode not depending what sterted it – event from main or monitor chamber (fission fragments and α -partiles of 238 U).

Results obtained

Results of our investigatins are shown on Fig. 4. Совершенно очевидно что результаты наших измерений полностью противоречат оценке даваемой ENDF/B VII. В ряде точек отношение сечения даваемого ENDF/B VII к эксперименту достигает 50. В заметно лучшем согласии экспериментальные данные находятся с предсказаниями даваемыми библиотекой JENDL. Однако и в этом случае можно отметить, что в целом полученное экспериментально сечение систематически находится ниже оценки. Кроме того в экспериментальных данных отчетливо прослеживается некоторая структура в области энергии нейтронов ~ 6 МэВ которая отсутствует в оценке даваемой JENDL.

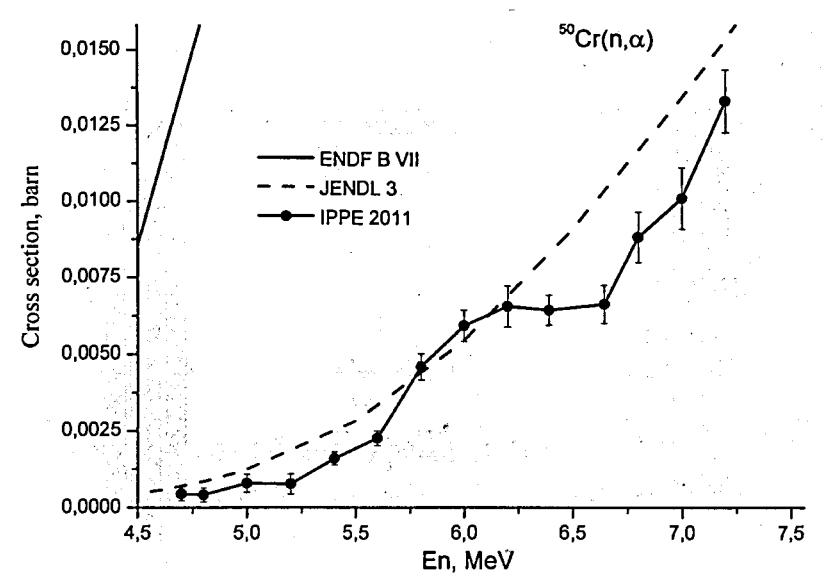


Figure 4. 50Cr(n,α)47Ti reaction cross section experimental data.

Conclusion

New digital spectrometer with a solid target for (n,α) reaction cross section investigation was developed. Its reliability of working in heavy parasitic reactions background was proved. Digital algorithms for background suppression was found. $^{50}Cr(n,\alpha)^{47}Ti$ reaction cross section in neutron energy region from 4,7 to 7,2 MeV was measured. Big discrepancy (up to 400%) with ENDF/B VII was found. Though JENDL data is much closer to experimental data, its average cross section and its excitation function tendency is not match with experimental data.

References

- C. Derndorfer, R. Fischer, P. Hille, H. Vonach and P. Maier-Komor. Investigation of the 50Cr(n,α)47Ti reaction at En=14.1 MeV Zeitschrift für Physik A Hadrons and Nuclei Volume 301, Number 4, 327-334.
- 2. Dolja G.D. et al. 1973, Kiev conf, v.3, 131 (1973).
- 3. Grimes S.M., et al; Phys.Rev. C19, 2127 (1979).
- G.Giorginis, V.Khryachkov et al. The cross section of the 16O(n,α)13C reaction in the MeV energy range. In Proc. Of Int. Conf. NDST 2007 conference. Nice, 2007, pp.525-528.
- Khryachkov V.A., Bondarenko I.P., Kuzminov B.D., Study of (n,α) reaction cross section on a set of light nuclei. Proc. Of XVIII Int. Seminar on Interaction of Neutrons with Nuclei, ISINN-18.

STATISTICAL MODEL ANALYSIS OF (n,\alpha) CROSS SECTIONS AVERAGED OVER THE FISSION NEUTRON SPECTRUM

G.Khuukhenkhuu¹, Yu.M.Gledenov², M.V.Sedysheva² and M.Odsuren¹

¹Nuclear Research Center, National University of Mongolia, Ulaanbaatar, Mongolia ²Frank laboratory of Neutron Physics, JINR, Dubna, Russia

1. INTRODUCTION

The study of (n,α) reaction cross section for fast neutrons is important to estimate radiation damage due to helium production, nuclear heating and transmutations in the structural materials of fission and fusion reactors. On the other hand, systematical analysis of neutron cross sections is of interest to study nuclear reaction mechanisms. In addition, it is often necessary, in practice, to evaluate the neutron cross sections of the nuclides, for which no experimental data are available.

Analysis of the experimental (n,α) cross sections was carried out in 1973 by Levkovskii [1] and a systematic dependence of the (n,α) cross sections on the relative neutron excess parameter (N-Z)/A of the target isotopes was observed for 14-15 MeV neutron energy. This systematic behavior of the cross sections is termed in the literature as isotopic effect. Several formulae were proposed to describe the isotopic effect for the (n,p) and (n,α) cross sections around the neutron energy of 14-15 MeV [1-7], only.

In 1994 we observed a similar dependence for the (n,α) cross sections in the neutron energy range of 8 to 16 MeV [8]. Moreover, the statistical model was suggested [9] to explain the isotopic dependence of the (n,α) cross sections for wide energy range of neutrons.

In this work we have used the statistical model based on the Weisskopf and Ewing theory [10] to carry out a systematical analysis of known experimental (n,α) cross sections [11-14] averaged over the ²³⁵U fission neutron spectrum produced by thermal neutrons.

2. STATISTICAL MODEL FORMULAE

The direct and pre-equilibrium mechanisms are neglected for fission neutrons and the compound mechanism can be considered, only. Then, the (n,x) reaction cross section in the framework of the compound mechanism can be written as follows:

$$\sigma(n,x) = \sigma_c(n)G(x) \tag{1}$$

where $\sigma_c(n) = \pi (R + \lambda/2\pi)^2$ is the compound nucleus formation cross section; $R = r_0 A^{1/3}$ is the target nucleus radius; A is the mass number of the target nucleus; λ is the wave length of the incident neutrons. The decay probability of the compound nucleus into channel x (x=p, n, α ...) is expressed as

$$G(x) = \frac{\Gamma_x}{\Gamma} = \frac{\Gamma_x}{\sum_{i} \Gamma_i} \quad , \tag{2}$$

where Γ_x and Γ are the partial and total level widths, respectively.

The decay width of the compound nucleus can be written as follows using the Weisskopf-Ewing evaporation model and detailed balancing principle [14]:

$$\Gamma_{x} = \frac{2S_{x} + 1}{\pi^{2}h^{2}\rho_{c}(E_{c})} M_{x} \int_{V_{c}}^{\varepsilon_{x}^{\text{max}}} \varepsilon_{x} \sigma_{c}(E_{c}) \rho_{y}(U_{x}) d\varepsilon_{x}$$
(3)

where S_x , M_x , ε_x and V_x are the spin, mass, energy and Coulomb potential for the outgoing particle x, respectively; $\rho_c(E_c)$ and $\rho_y(U_x)$ are the compound nucleus and residual nucleus level densities, respectively; $\sigma_c(E_c)$ is the inverse reaction cross section.

Then, the partial level width can be determined using the constant nuclear temperature approximation [15] and the semi-classical formula for the inverse reaction cross section:

$$\Gamma_{x} = \frac{2S_{x} + 1}{\pi h^{2}} M_{x} R^{2} \int_{V_{x}}^{\varepsilon_{x}^{max}} \varepsilon_{x} \left(1 - \frac{V_{x}}{\varepsilon_{x}}\right) e^{\frac{B_{x} + \delta_{x} + \varepsilon_{x}}{\Theta}} d\varepsilon_{x}$$
(4)

Here: B_x and δ_x are the binding energy and odd-even effect parameter for the x-particle, respectively; Θ =kT is the nuclear thermodynamic temperature; k is the Boltzmann constant. We can neglect the γ -emission, use the Weizsacker's formula [16] for binding energy and carry out the integration of (4). Then, a formula for fast neutron induced (n,α) reaction cross section can be obtained from (1), (2) and (4):

$$\sigma(\eta,\alpha) = C\pi(R+\lambda)^2 e^{-\frac{R^2 - 2 + a5}{A}}, \tag{5}$$

where
$$C = 2 \exp \sqrt{\frac{A}{13.5 (E_n + Q_{n\alpha})}} \left[-3\alpha + \gamma \frac{4Z}{A^{1/3}} + \varepsilon_{\alpha} - 2.058 \frac{Z}{A^{1/3}} \right]$$
 (6)

and

$$K = 2\xi \sqrt{\frac{A}{13.5 (E_0 + Q_{out})}}$$
 (7)

Here: N and Z are the neutron and proton numbers in the target nuclei; α , γ and ξ are the Weizsaker's formula constants; \mathcal{E}_{α} is the internal binding energy of α -particle; $Q_{n\alpha}$ is the reaction energy; E_n is the neutron energy.

The parameters K and C in formula (5) can be determined by two methods. First, they can be fitted as constant parameters at each energy point for all isotopes. Second, the K and C parameters can be immediately obtained from the formulae (6) and (7). We will use here the first method.

3. SYSTEMATICAL ANALYSIS OF THE (n, a) CROSS SECTIONS

The values of C and K, as fitting parameters, were obtained by using the formula (5) from the systematical analysis of known experimental (n,α) cross sections averaged over the fission neutron spectrum. The result of such an analysis for 35 isotopes of ²³Na to ¹⁸⁴W is displayed in Fig. 1.

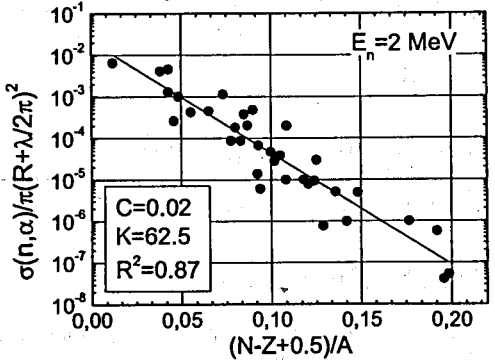


Fig.1. The dependence of the reduced (n,α) cross sections on the relative neutron excess parameter at E_n=2 MeV.

Here, black points are the recommended by Calamand data [11,12] and line is the theoretical one with fitted parameters C=0.02 and K=62.5 for the formula (5).

The light isotopes, such as ^{7}Be , ^{11}B and ^{19}F were not considered in this systematic because the (n,α) cross sections for these nuclei have resonance structure and essential deviations from one energy point to other one. Also, ^{50}Ti and ^{118}Sn were not included in the analysis in connection with visible deviation from the systematical behaviour of the (n,α) cross sections which is well described by the formula (5).

4. THE EFFECTIVE NEUTRON ENERGY

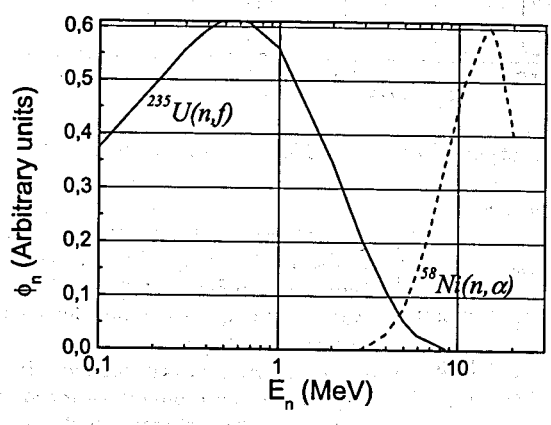


Fig. 2. Fission neutron spectrum of ^{235}U [17] and cross section curve of the $^{58}Ni(n,\alpha)^{55}Fe$ reaction [18]

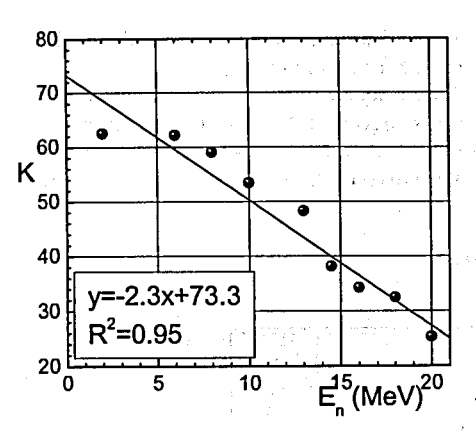
The effective neutron energy is important for theoretical analysis of averaged neutron cross sections. Average energy for fission neutron spectrum is, usually, around 2 MeV [17]. At the same time, the threshold energy of (n,α) reaction for most of isotopes lies in the region of $E_h\approx 3-6$ MeV [18]. So, the effective average energy of the incident neutrons for fission spectrum in the case of (n,α) reaction should be different from 2 MeV. To clarify this statement the excitation function of the 58 Ni $(n,\alpha)^{55}$ Fe reaction [18] is shown in Fig.2, as example. Fission neutron spectrum of 235 U [17] is, also, displayed in Fig.2. It is seen that an average (n,α) cross section is determined by overlap of two curves for neutron energy spectrum and excitation function. Almost the same pictures can be drawn for other isotopes given in [11,12].

Therefore, the weighted average (n,α) cross section is expressed as follows:

$$\langle \sigma(n,\alpha) \rangle = \frac{\int \sigma_{n\alpha} (E_n) \phi(E_n) dE_n}{\int \phi(E_n) dE_n}, \tag{11}$$

where $\phi(E_n)$ is the neutron spectrum.

In order to determine the average neutron energy of fission spectrum for the (n,α) cross sections we should take into account the systematical regularity of parameter K [19]. Values of the fitted parameters K and C were obtained by using formula (5) at neutron energies of 6 to 20 MeV [19]. These values of the K and C parameters are given in Table 1.



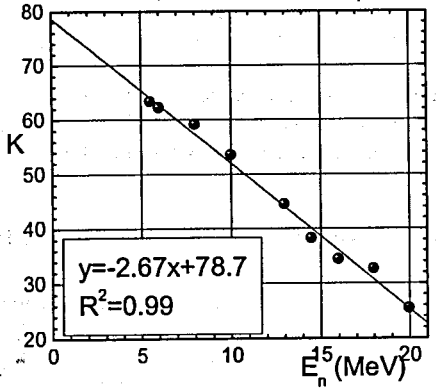


Fig.3. Energy dependence of parameter K

Fig.4. The same as in Fig.3, K=63.1, $E_n\approx5.5$ MeV

Table 1. The K and C Parameters

| E _n (MeV) | K | С | |
|----------------------|------|------|--|
| 6 | 62.1 | 0.41 | |
| 8 | 59.0 | 1.10 | |
| 10 | 53.4 | 1.46 | |
| 13 | 48.3 | 1.80 | |
| 14.5 | 38.2 | 1.02 | |
| 16 | 34.3 | 0.55 | |
| 18 | 32.5 | 0.48 | |
| 20 | 25.3 | 0.17 | |
| | | | |

It is seen that the parameter K depends linearly on the neutron energy. But, our value K=62.5 at $E_n=2$ MeV given in Fig.1 is not placed on the line which was drawn through all points for each energy of neutrons (see Fig.3).

As a result, we can find the value of parameter K for fission spectrum by variation of the effective average neutron energy. In this case the value of parameter K was found to be 63.1 for $E_n\approx 5.5$ MeV. This result shows that the average effective energy of fission neutrons for (n,α) reactions is to be $\langle E_n \rangle \approx 5.5$ MeV which is in good agreement with linear dependence of K on neutron energy (see Fig.4).

5. EXPERIMENTAL AND THEORETICAL CROSS SECTIONS

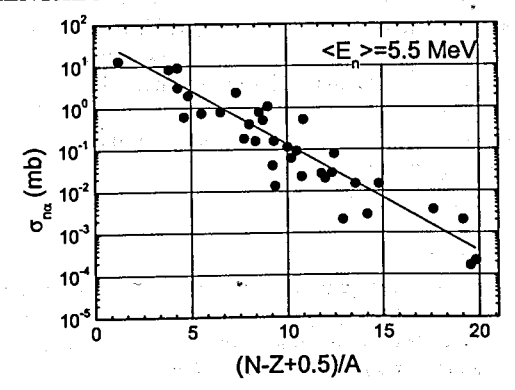


Fig.5. Calculated (n,α) cross section (solid line) and experimental data (black points)

Result of the theoretical calculation for the (n,α) cross section using the formula (5) with parameters K=63.1 and C=0.03 is compared in Fig.5 with experimental data taken from [12]. It can be seen that theoretical line is in good agreement with the experimental data in the case of average effective neutron energy <En><5.5 MeV for (n,α) reactions.

6. CONCLUSION

1. Known experimental (n,α) cross sections for fission neutron spectrum of ²³⁵U were analyzed using the statistical model based on the Weisskopf-Ewing theory and certain systematical behaviour was observed.

- The average effective energy of fission neutrons of the ²³⁵U was found to be around 5.5 MeV for (n,α) reactions.
- 3. It was shown that the experimental data of (n,α) cross sections for fission neutrons is described by the statistical model.

REFERENCES

- 1. V.N. Levkovsky, Yadernaya Fizika. v.18, N4, 1973, p.705, (in Russian).
- 2. K.Gul. INDC (PAK)-009, IAEA, Vienna, 1995
- 3. A.Yu.Konobeyev et al., Nucl. Instr. Meth. B, v.108, 1996, p.233
- 4. A.D.Majdeddin et al., INDC(HUN)-031, IAEA, 1997, Vienna
- 5. Kh.T.Osman and F.Habbani, INDC (SUD)-003, IAEA, 1998, Vienna
- 6. F.I.Habbani and Kh.T.Osman, Appl. Rad. Isot. v.54, 2001, p.283
- 7. Junhua Luo et al., Nucl. Instr. Meth.B. v.266, 2008, p.4862
- 8. G.Khuukhenkhuu et al., Communication of the JINR. E3-94-316, Dubna. 1994
- G.Khuukhenkhuu et al., In book: "Proceedings of the International Seminar on Interaction of Neutrons with Nuclei", ISINN-XV, May 16-19, 2007, Dubna, 2008, p.157
- 10. V.F. Weisskopf and D.H. Ewing, Phys. Rev., v.57, 1940, p.472
- 11. A.Calamand, INDC(NDS)-55/L, IAEA, 1973
- A. Calamand, In book: "Handbook on Nuclear Activation Cross-Sections", IAEA, Technical Report: Ser. N156, 1974, Vienna, p.273
- 13. E.M.Gryntakis, J.Radioanal. Chem., v.52, 1979, p.219
- 14. V.M.Bychkov *et al.*, Cross Sections of the Threshold Reactions Induced by Neutrons, Energoizdat, 1982, Moskow (in Russian)
- J.M.Blatt, V.F.Weisskopf. Theoretical Nuclear Physics, John Wiley and Sons, New York, 1952.
- 16. C.F.v. Weizsacker, Z.Phys.A., v.96, 1935, p.431
- 17. B.I. Starostov *et al.*, Voprocy Atomnoi Nauki i Tekhniki, Ser. Yadernye Konstanty, v.2 (37), 1980, p.3 (in Russian)
- Handbook on Nuclear Activation Data. Technical Reports. Series N273, IAEA, 1987, Vienna.
- G.Khuukhenkhuu and M.Odsuren. Fast Neutron Induced Reaction Cross Sections.
 "Munkhiin Useg" Press, 2010, Ulaanbaatar (in Mongolian)

MIXING OF THE S-WAVE AND P-WAVE RESONANCES AND P-ODD ASYMMETRY OF γ-QUANTUM EMISSION IN THE RADIATIVE CAPTURE OF A SLOW POLARIZED NEUTRON BY A SPINLESS NUCLEUS

V. L. Lyuboshitz, V. V. Lyuboshitz *

Joint Institute for Nuclear Research, 141980 Dubna, Moscow Region, Russia

* E-mail: Valery.Lyuboshitz@jinr.ru

Abstract

Using the technique of helicity amplitudes, the theoretical consideration of the P-odd asymmetry of γ -quantum emission in the radiative capture of an S-wave polarized neutron by a nucleus with zero spin, which is conditioned by the mixing of S-wave and P-wave resonances with equal spins and opposite space parities on account of weak interaction, has been performed. It is shown that, under the parity nonconservation, the differential cross section of the radiative capture of a slow neutron by a spinless nucleus is anisotropic and has the following structure: $A + B(P, l_{\gamma})$, where the coefficients A and B depend on the neutron energy but do not depend upon the angle of γ -quantum emission, the coefficient A depends also on the parameters of the S-wave resonance, and the coefficient B depends upon the parameters of both the S-wave and P-wave resonances as well as upon the matrix element of mixing due to weak interaction, P is the neutron polarization vector and l_{γ} is the unit vector directed along the γ -quantum momentum.

1. Helicity amplitudes and differential cross sections of resonance binary processes

The helicity amplitude of a binary resonance process $a+b \rightarrow R \rightarrow c+d$ has the following structure:

$$f_{ab\to cd}(\lambda_a, \lambda_b; \lambda_c, \lambda_d) = \frac{2J_R + 1}{2\sqrt{k_{ab} k_{cd}}} \frac{A_b(\lambda_a, \lambda_b) d_{\Lambda'\Lambda}^{(J_R)}(\theta) e^{i\Lambda\phi} A_f(\lambda_c, \lambda_d)}{E_R - E - \frac{i}{2} \Gamma_R} . \tag{1}$$

Here J_R is the resonance spin, E_R is the resonance energy, Γ_R is the total resonance width, $\lambda_a, \lambda_b, \lambda_c, \lambda_d$ are helicities of the primary and final particles, $A_b(\lambda_a, \lambda_b)$ are the helicity amplitudes of resonance decay into the channel $R \to a + b$, $A_f(\lambda_c, \lambda_d)$ are the helicity amplitudes of resonance decay into the

channel $R \to c + d$, $d_{\Lambda'\Lambda}^{(J_R)}(\theta)$ are Wigner d-functions of the order J_R , θ is the angle between the momentum $\hbar \, \mathbf{k}_{ab}$ of the primary particle a and the momentum $\hbar \, \mathbf{k}_{cd}$ of the final particle c in the reaction c.m. frame, ϕ is the azimuthal angle, $k_{ab} = |\mathbf{k}_{ab}|$, $k_{cd} = |\mathbf{k}_{cd}|$,

$$\Lambda' = \lambda_c - \lambda_d, \quad \Lambda = \lambda_d - \lambda_b \tag{2}$$

are the differences of helicities for the final particles and primary particles, respectively, which satisfy the conditions:

$$\Lambda' \le J_R, \quad \Lambda' \le s_c + s_d; \quad \Lambda \le J_R, \quad \Lambda \le s_a + s_b$$
 (3)

where s_a, s_b, s_c, s_d are the spins of the primary and final particles.

In doing so, the sums

$$\sum_{\lambda,\lambda_b} |A_b(\lambda_a,\lambda_b)|^2 = \Gamma_{ab}^{(R)}, \qquad \sum_{\lambda,\lambda_d} |A_f(\lambda_c,\lambda_d)|^2 = \Gamma_{cd}^{(R)}$$
(4)

have the meaning of partial widths of the resonance decay into the channels $R \to a + b$ and $R \to c + d$, respectively. It is obvious that

$$\sum_{ab} \Gamma_{ab}^{(R)} = \sum_{cd} \Gamma_{cd}^{(R)} = \Gamma_R \qquad , \tag{5}$$

where Γ_R is the total resonance width included in Eq. (1).

The differential cross section of the resonance binary process, summed over the spin projections of the final particles c and d and averaged over the spin projections of the primary particles a and b, amounts to:

$$\frac{d\sigma_{a+b\to R\to c+d}}{d\Omega} (\lambda_a, \lambda_b; \lambda_c, \lambda_d) = \frac{k_{cd}}{k_{ab}} |f_{ab\to cd}(\lambda_a, \lambda_b; \lambda_c, \lambda_d)|^2 =
= \frac{(2J_R + 1)^2}{4k^2 (2s_a + 1)(2s_b + 1)} \frac{1}{(E_R - E)^2 + \frac{1}{4}\Gamma_R^2} \times$$
(6)

$$\times \sum_{\lambda_a \lambda_b} \sum_{\lambda_c \lambda_d} \left[(A_b(\lambda_a, \lambda_b))^2 (d_{\Lambda'\Lambda}^{(J_R)}(\theta))^2 (A_f(\lambda_c, \lambda_d))^2 \right]$$

(here $k \equiv k_{ab}$).

Taking into account the relation:

$$\int (d_{\Lambda'\Lambda}^{(J_R)}(\theta))^2 d\Omega = \frac{4\pi}{2J_R + 1} \tag{7}$$

which is true at any values of Λ' and Λ (integration is performed over the full solid angle), the integral cross section of the resonance binary reaction $a+b \to R \to c+d$ equals:

$$\sigma_{a+b\to R\to c+d} = \frac{2J_R + 1}{(2s_a + 1)(2s_b + 1)} \frac{\pi}{k^2} \frac{\Gamma_{ab}^{(R)} \Gamma_{cd}^{(R)}}{(E_R - E)^2 + \frac{1}{4} \Gamma_R^2}$$
(8)

(we have applied Eqs. (4)) .

Let us consider now the neutron radiative capture by a nucleus $n + a \rightarrow \gamma + c$. According to Eq. (8), the integral cross section of resonance radiative capture on an unpolarized nucleus is as follows:

$$\sigma_{n+a\to R\to\gamma+c} = \frac{2J_R + 1}{2(2s_a + 1)} \frac{\pi}{k^2} \frac{\Gamma_n \Gamma_{\gamma}}{(E_R - E)^2 + \frac{1}{4}\Gamma_R^2} , \qquad (9)$$

where Γ_n is the neutron width and Γ_{γ} is the radiative width.

If the nucleus a is spinless, then in case of the S-wave resonance $J_R = \frac{1}{2}$, $s_a = 0$, and Eq. (9) gives:

$$\sigma_{n+a\to R\to\gamma+c} = \frac{\pi}{k^2} \frac{\Gamma_n^{(s)} \Gamma_{\gamma}}{(E_R - E)^2 + \frac{1}{4} \Gamma_R^2} \tag{10}$$

It is easy to see that in this case the differential cross-section of radiative capture is isotropic and it does not depend upon the neutron polarization:

$$\frac{d\sigma_{n+a\to R\to\gamma+c}}{d\Omega} = \frac{1}{4k^2} \frac{\Gamma_n^{(s)} \Gamma_\gamma^{(s)}}{(E_R - E)^2 + \frac{1}{4}\Gamma_R^2}$$
(11)

2. Mixing of the S-wave and P-wave resonances with opposite space parities

Under the space parity nonconservation, the S-wave and P-wave resonances with equal spins are mixed by the weak interaction. The new quasistationary states with mixed parity have the form [1,2]:

$$|s'\rangle = |s\rangle + \varepsilon |p\rangle$$
, $|p'\rangle = |p\rangle - \varepsilon |s\rangle$, where ε is a sum of ε . (12)

where $|s\rangle$ and $|p\rangle$ are the S-wave and P-wave states with the positive and negative parity, respectively, ε is the mixing parameter. In the Born approximation, we have:

$$\varepsilon = \frac{W_{sp}}{E_s - E_p - \frac{i}{2}(\Gamma_s - \Gamma_p)}, \qquad (13)$$

where $W_{sp} = \langle p \mid W \mid s \rangle$ is the matrix element of weak interaction, E_s , E_p are energies of the S- and P-wave resonances being mixed, Γ_s , Γ_p are their widths. Due to hermiticity and T invariance, $W_{sp} = W_{ps}$, Im $W_{sp} = 0$. Obviously, $|\varepsilon| << 1$.

Taking into account the smallness of the mixing parameter, we have neglected the contribution of terms of the order of $|\varepsilon|^2$ into the normalizing multipliers for the states $|s'\rangle$ and $|p'\rangle$. In doing so, $E_{s'}\approx E_s$, $\Gamma_{s'}\approx \Gamma_s$, $E_{p'}\approx E_p$, $\Gamma_{p'}\approx \Gamma_p$.

According to relations (12), the states with definite space parity represent the superpositions of the quasistationary states $|s'\rangle$ and $|p'\rangle$:

$$|s\rangle = |s'\rangle - \varepsilon |p'\rangle$$
, $|p\rangle = |p'\rangle + \varepsilon |s'\rangle$. (14)

Since the slow neutron is captured by the nucleus a into the S-state ($|s\rangle$), the spins of the S-wave resonance and the P-wave resonance being admixed are equal to:

$$J_R^{(S)} = J_R^{(P)} = s_a \pm \frac{1}{2} \quad , \tag{15}$$

where s_a is the spin of the primary nucleus a.

3. Helicity amplitudes of resonance radiative capture of neutrons at the mixing of S-wave and P-wave resonances

Let us consider the *P*-odd asymmetry at the radiative capture of a polarized slow neutron by a nucleus with zero spin [2,3]. In this case, the neutron is captured into the *S*-state $|s\rangle = |s'\rangle - \varepsilon |p'\rangle$ with spin $J_R^{(S)} = J_R^{(P)} = \frac{1}{2}$.

At the electric and magnetic dipole radiation, the spins of the final nucleus c can take the values $s_c=\frac{1}{2}$ and $s_c=\frac{3}{2}$. To be definite, we will consider that $s_c=\frac{1}{2}$. The γ -quantum helicities can take the values $\lambda_{\gamma}=+1$ and $\lambda_{\gamma}=-1$, and the helicities of the final nucleus c with spin $\frac{1}{2}$: $\lambda_c=+\frac{1}{2}$ and $\lambda_c=-\frac{1}{2}$.

At the total angular momentum $J_R=\frac{1}{2}$, the nonzero helicity amplitudes of the decay into the γ quantum and the final nucleus are : $a_{\gamma}(1,-\frac{1}{2})$ and $a_{\gamma}(-1,+\frac{1}{2})$.

In doing so,

$$a_n^{(s)}(-\frac{1}{2}) = a_n^{(s)}(+\frac{1}{2}) , \quad a_{\gamma}^{(s)}(1,-\frac{1}{2}) = a_{\gamma}^{(s)}(-1,+\frac{1}{2}) ,$$
 (16)

$$a_{\gamma}^{(p)}(1,-\frac{1}{2}) = -a_{\gamma}^{(p)}(-1,+\frac{1}{2})$$
 (17)

Taking into account relations (1) and (12)-(14), the helicity amplitudes of the resonance process have the form:

$$\begin{split} &f_{n+a\to\gamma+c}(+\frac{1}{2};1,-\frac{1}{2}) = \\ &= \frac{a_n^{(s)}(+\frac{1}{2})}{\sqrt{k_nk_\gamma}} d_{2/2}^{(s)} \frac{\partial}{\partial z} \left[\frac{a_1^{(s)}(1,-\frac{1}{2}) + \epsilon a_1^{(p)}(1,-\frac{1}{2})}{E_s - E - \frac{i}{2}\Gamma_s} - \frac{\epsilon a_1^{(p)}(1,-\frac{1}{2})}{E_p - E - \frac{i}{2}\Gamma_p} \right] = \\ &= \frac{a_n^{(s)}(+\frac{1}{2})}{\sqrt{k_nk_\gamma}} d_{2/2}^{(s)} \frac{\partial}{\partial z} \left[\frac{a_1^{(s)}(1,-\frac{1}{2}) + W_{sp} a_1^{(p)}(1,-\frac{1}{2})}{E_s - E - \frac{i}{2}\Gamma_s} + \frac{W_{sp} a_1^{(p)}(1,-\frac{1}{2})}{(E_s - E - \frac{i}{2}\Gamma_s)(E_p - E - \frac{i}{2}\Gamma_p)} \right], \\ &f_{n+a\to\gamma+c}(+\frac{1}{2};-1,+\frac{1}{2}) = \\ &= \frac{a_n^{(s)}(+\frac{1}{2})}{\sqrt{k_nk_\gamma}} d_{-2/2}^{(s)} \frac{\partial}{\partial z} \left[\frac{a_1^{(s)}(-1,+\frac{1}{2})}{E_s - E - \frac{i}{2}\Gamma_s} + \frac{W_{sp} a_1^{(p)}(-1,+\frac{1}{2})}{(E_s - E - \frac{i}{2}\Gamma_s)(E_p - E - \frac{i}{2}\Gamma_p)} \right], \\ &f_{n+a\to\gamma+c}(-\frac{1}{2};1,-\frac{1}{2}) = \\ &= \frac{a_n^{(s)}(-\frac{1}{2})}{\sqrt{k_nk_\gamma}} d_{2/2}^{(s)} \frac{\partial}{\partial z} \frac{\partial$$

(19)

Here $k_n = |\mathbf{k}_n|$, $k_{\gamma} = |\mathbf{k}_{\gamma}|$, where $\hbar \mathbf{k}_n$ and $\hbar \mathbf{k}_{\gamma}$ are the respective momenta of the neutron and γ quantum in the c.m. frame of the resonance reaction $n + a \rightarrow \gamma + c$.

4. P-odd asymmetry at the radiative capture of slow polarized neutrons

Let us remark that, taking into account T invariance, all the helicity amplitudes of decay may be considered to be real, neglecting the electromagnetic final-state interaction.

In accordance with relations (16), we have:

$$\left(a_n^{(s)}(+\frac{1}{2})\right)^2 = \left(a_n^{(s)}(-\frac{1}{2})\right)^2, \quad \left(a_{\gamma}^{(s)}(1,-\frac{1}{2})\right)^2 = \left(a_{\gamma}^{(s)}(-1,+\frac{1}{2})\right)^2,$$

$$\left(a_{\gamma}^{(p)}(1,-\frac{1}{2})\right)^2 = \left(a_{\gamma}^{(p)}(-1,+\frac{1}{2})\right)^2,$$

$$a_{\gamma}^{(s)}(-1,+\frac{1}{2}) a_{\gamma}^{(p)}(-1,+\frac{1}{2}) = -a_{\gamma}^{(s)}(1,-\frac{1}{2}) a_{\gamma}^{(p)}(1,-\frac{1}{2}) .$$
(20)

Disregarding the second-order terms $\sim W_{sp}^2$, we obtain – taking into account equalities (20) – the following expressions for the differential cross section of radiative capture of slow neutrons with the helicities $(+\frac{1}{2})$ and $(-\frac{1}{2})$ by a spinless nucleus:

$$\frac{d\sigma}{d\Omega}(\frac{1}{2})\Big|_{n+a\to\gamma+c} = \frac{k_{\gamma}}{k_{n}} \left[\left| f_{n+a\to\gamma+c}(\frac{1}{2}; 1, \frac{1}{2}) \right|^{2} + \left| f_{n+a\to\gamma+c}(\frac{1}{2}; -1, \frac{1}{2}) \right|^{2} \right] = \frac{1}{k_{n}^{2}} \frac{|a_{n}^{(s)}(\frac{1}{2})|^{2} |a_{\gamma}^{(s)}(1, \frac{1}{2})|^{2}}{(E_{s}-E)^{2} + \frac{\Gamma_{s}^{2}}{4}} \left[\left(\frac{d_{\gamma_{s}}^{(\gamma)}}{d_{\gamma_{s}}^{(\rho)}(1, \frac{1}{2})} \right)^{2} + \left(\frac{d_{\gamma_{s}}^{(\gamma)}}{d_{\gamma_{s}}^{(\rho)}(1, \frac{1}{2})} \right)^{2} + \frac{2}{k_{n}^{2}} \frac{|a_{n}^{(s)}(\frac{1}{2})|^{2} |a_{\gamma}^{(s)}(1, \frac{1}{2}) W_{sp} a_{\gamma}^{(p)}(1, \frac{1}{2}) (E_{p}-E)}{\left[(E_{p}-E)^{2} + \frac{\Gamma_{p}^{2}}{4} \right]} \times \left[\left(\frac{d_{\gamma_{s}}^{(\gamma)}}{d_{\gamma_{s}}^{(\rho)}(1, \frac{1}{2})} \right)^{2} - \left(\frac{d_{\gamma_{s}}^{(\gamma)}}{d_{\gamma_{s}}^{(\rho)}(1, \frac{1}{2})} \right)^{2} \right],$$

$$(21)$$

$$\frac{d\sigma}{d\Omega}(-\frac{1}{2})\Big|_{n+a\to\gamma+c} = \frac{k_{\gamma}}{k_{n}} \left[\left| f_{n+a\to\gamma+c}(-\frac{1}{2}; 1, -\frac{1}{2}) \right|^{2} + \left| f_{n+a\to\gamma+c}(-\frac{1}{2}; -1, +\frac{1}{2}) \right|^{2} \right] = \frac{1}{k_{n}^{2}} \frac{|a_{n}^{(s)}(-\frac{1}{2})|^{2} |a_{\gamma}^{(s)}(1, -\frac{1}{2})|^{2}}{(E_{s}-E)^{2} + \frac{\Gamma_{s}^{2}}{4}} \left[\left(\frac{d_{\gamma_{s}}^{(\gamma)}}{d_{\gamma_{s}}^{(\rho)}(1, -\frac{1}{2})} (E_{p}-E)} \right)^{2} + \left(\frac{d_{\gamma_{s}}^{(\gamma)}}{d_{\gamma_{s}}^{(\rho)}(1, -\frac{1}{2})} \right)^{2} + \left(\frac{d_{\gamma_{s}}^{(\gamma)}}{d_{\gamma_{s}}^{(\gamma)}(1, -\frac{1}{2})} \right)^{2} + \left(\frac$$

As it is known, the d-functions corresponding to the angular momentum $\frac{1}{2}$ have the form:

$$d_{1/2,1/2}^{(1/2)}(\theta) = d_{-1/2,-1/2}^{(1/2)}(\theta) = \cos\frac{\theta}{2} , \quad d_{-1/2,1/2}^{(1/2)}(\theta) = -d_{1/2,-1/2}^{(1/2)}(\theta) = \sin\frac{\theta}{2} . \quad (23)$$

Without losing generality, the phases of states $|s\rangle$ and $|p\rangle$ may be chosen in such a way that:

$$|a_n^{(s)}(+\frac{1}{2})|^2 = \frac{\Gamma_n^{(s)}}{2} , \quad \left(a_\gamma^{(s)}(1, -\frac{1}{2})\right)^2 = \frac{\Gamma_\gamma^{(s)}}{2} , \quad \left(a_\gamma^{(p)}(1, -\frac{1}{2})\right)^2 = \frac{\Gamma_\gamma^{(p)}}{2} ,$$

$$a_\gamma^{(s)}(1, -\frac{1}{2}) \ a_\gamma^{(p)}(1, -\frac{1}{2}) = \frac{1}{2} \sqrt{\Gamma_\gamma^{(s)} \Gamma_\gamma^{(p)}} ,$$
(24)

where Γ_n is the neutron width of the S-wave resonance, $\Gamma_{\gamma}^{(s)}$ and $\Gamma_{\gamma}^{(p)}$ are the radiative widths of the S-wave and P-wave resonances, respectively.

Taking into account Eqs. (23) and (24), in the considered case of radiative capture of slow neutrons with helicities $(+\frac{1}{2})$ and $(-\frac{1}{2})$ the differential cross section has the following structure:

$$\frac{d\sigma}{d\Omega}(+\frac{1}{2})\Big|_{n+a\to\gamma+c} = A + B\cos\theta ,$$

$$\frac{d\sigma}{d\Omega}(-\frac{1}{2})\Big|_{n+a\to\gamma+c} = A - B\cos\theta ,$$
(25)

where

$$A = \frac{1}{4k_n^2} \frac{\Gamma_n^{(s)} \Gamma_{\gamma}^{(s)}}{(E_s - E)^2 + \frac{\Gamma_s^2}{4}} , \qquad (26)$$

$$B = \frac{1}{2k_n^2} \frac{\Gamma_n^{(s)} W_{sp} \sqrt{\Gamma_{\gamma}^{(s)} \Gamma_{\gamma}^{(p)}} (E_p - E)}{\left[(E_s - E)^2 + \frac{\Gamma_s^2}{4} \right] \left[(E_p - E)^2 + \frac{\Gamma_p^2}{4} \right]} , \qquad (27)$$

and θ has the meaning of the angle between the neutron and $\gamma\text{-quantum}$ momenta .

Let us note that, as follows from relations (18), (19) and equalities (16), (20), the products of helicity amplitudes of the reaction $n+a\to\gamma+c$, correspondding to the opposite primary helicities and equal final helicities, are expressed through the quantity B and the angles determining the direction of vector \mathbf{k}_{γ} :

$$\begin{split} \frac{k_{\gamma}}{k_{n}} \left[f_{n+a\to\gamma+c}^{*}(+\frac{1}{2}; 1, -\frac{1}{2}) f_{n+a\to\gamma+c}(-\frac{1}{2}; 1, -\frac{1}{2}) + \right. \\ \left. + f_{n+a\to\gamma+c}^{*}(+\frac{1}{2}; -1, +\frac{1}{2}) f_{n+a\to\gamma+c}(-\frac{1}{2}; -1, +\frac{1}{2}) \right] = \end{split}$$

$$= B \left[d_{\frac{1}{2},\frac{1}{2}}^{(\frac{1}{2})}(\theta) d_{\frac{1}{2},-\frac{1}{2}}^{(\frac{1}{2})}(\theta) e^{i\varphi} - d_{-\frac{1}{2},\frac{1}{2}}^{(\frac{1}{2})}(\theta) d_{-\frac{1}{2},-\frac{1}{2}}^{(\frac{1}{2})}(\theta) e^{-i\varphi} \right] = B \sin \theta \cos \varphi .$$

(28)

Thus, at the parity-violating mixing of the S-wave and P-wave resonances, the differential cross section of radiative capture of a slow neutron with an arbitrary vector of spin polarization P is as follows:

$$\frac{d\sigma}{d\Omega}\Big|_{n+a\to\gamma+c} = A + B\left(P_{\parallel}\cos\theta + P_{\perp}\sin\theta\cos\varphi\right) \quad , \tag{29}$$

where the quantities A and B are determined according to Eqs. (26), (27), P_{\parallel} is the degree of neutron longitudinal polarization, P_{\perp} is the degree of neutron transverse polarization, θ is the angle between the vectors \mathbf{k}_n , \mathbf{k}_{γ} ; φ is the angle between the neutron polarization plane $(\mathbf{P}, \mathbf{k}_n)$ and the reaction plane $(\mathbf{k}_{\gamma}, \mathbf{k}_n)$.

Formula (29) may be rewritten in the simple form:

$$\frac{d\sigma}{d\Omega}\Big|_{n+a\to\gamma+c} = A + B(\mathbf{P}, \mathbf{l}_{\gamma}) \quad , \tag{30}$$

where l_{γ} is the unit vector along the γ -quantum momentum.

References

- 1. O. P. Sushkov and V. V. Flambaum, Pis'ma v ZhETF 32, 377 (1980).
- 2. V. E. Bunakov and L. B. Pikelner, Progr. Part. Nucl. Phys. 39, 337 (1997).
- 3. J. Adrzejewski et al., Yad. Fiz. 67, 1254 (2004) .

Differential cross section evaluation in (n,α) reaction with fast neutrons using Hauser – Feshbach formalism

A. Oprea, C. Oprea, Yu. M. Gledenov, P.V. Sedyshev, M.V. Sedysheva 141980 Dubna, Moscow Region, Russian Federation Joint Institute for Nuclear Research (JINR) Frank Laboratory for Neutron Physics (FLNP)

Abstract. In this work we have analyzed the $^{64}Zn(n,\alpha)^{61}Ni$ reaction with fast neutrons. For incident neutrons energy from 1 MeV up to 8 MeV we have evaluated the cross section and differential cross sections using the computer codes Talys and his default parameters for mentioned reaction. The done evaluation established that the contribution to the cross sections are mainly due to the compound processes and direct processes can be neglected. For these reasons the cross sections were evaluated in the frame of Hauser – Feshbach formalism (HF).

The obtained results were compared with existing experimental data. These experimental data were in principal obtained at the electrostatic generators from JINR FLNP Dubna (EG-5) and from Institute of Heavy Ions Physics – Pekin University (China).

Theoretical and experimental data are in a satisfactory agreement but in the future it is necessary to try other parameters then Talys default to have a better agreement.

Introduction

Researches of the nuclear reactions induced by fast neutrons with emission of charged particles like protons and alpha particles are important from theoretical point of view as well as for applications in the field material science for construction of reactors.

Part in recent in new or did if at

In the conventional classification of the neutrons fast neutrons are considered from $0.5 \, MeV$ up to $20 \, MeV$ [1]. In this neutron energy interval are few experimental data that differ from one group to another. Cross sections for (n,p) and (n,α) reactions are of order of tens of milibarns or lower and difficult to measure or evaluate. The difficulties are coming from the background caused by many open channels. Further, in this energy interval, for incident neutrons usually together with compound processes are present other reaction mechanisms like direct or preequilibrium. Therefore it is of great interest for theory to establish the quote of each type of process (compound, direct, preequilibrium) to the cross sections. The experimental and theoretical evaluations are also important in the field of nuclear structure and astrophysics [2].

For practical purposes the knowledge of the cross sections induced by neutrons and emission of charged particles is of a great importance in material sciences field for nuclear reactors construction [2]. During the time takes place a process of accumulation of Hydrogen and Helium in the walls of reactor building, vessels and other object around the reactor ensemble. This accumulation leads to the changing of resistance parameters of these walls and in this light it is clear that the evaluation of accumulation process is direct related to the cross sections.

sections. We have evaluated the differential cross sections for $^{64}Zn(n,\alpha)^{61}Ni$ reaction for neutrons energy from 1~MeV up to 8~MeV using the Talys computer codes [3]. The incident neutrons energy interval was chosen in relation with our experimental possibilities because in fact the codes allow in principal to study the nuclear reaction up to 200~MeV including all necessary reaction mechanisms.

Talys codes can be very useful for theorist and experimenters in the field of nuclear reactions. In this software are implemented many nuclear reaction models, data basis for nuclear structure, density levels and others for quick and efficient analysis of nuclear reaction. Talys is an open project and many researchers may bring their contributions to the improvement of the codes [4].

Theoretical background

For the evaluation of the cross sections we used mainly the HF formalism [5]. This formalism is an efficient tool for cross section evaluation and first was developed in the '50 years of last century for binary reaction induced by neutrons with formation of an intermediate compound nucleus. For a binary reaction of type $\alpha+A\rightarrow C\rightarrow \beta+B$ (α incident particle, A – target nucleus, C – compound nucleus, β – emergent particle, B – residual nucleus) the cross section has the following form:

$$\sigma_{\alpha\beta} = \pi \hat{\mathcal{A}}_{\alpha}^2 \frac{T_{\alpha} T_{\beta}}{\sum T_c} W_{\alpha\beta} \tag{1}$$

 $T = \text{transmission coefficient}, W_{\alpha\beta} = \text{width fluctuation correction factor (WFC)}.$

As it can be seen an important factor in the cross section evaluation are the transmission (or penetrability) coefficients in the incident channel and emergent possible open channels. This coefficient represents the probability for a particle to penetrate a potential barrier and can be evaluated using the so called "semi classical" approach or more accurate in the frame of a quantum mechanical formalism described in [6]. The authors have evaluated the penetrability coefficients in the both approaches in [7], respectively [8].

First expression of relation (1) was without of WFC [9]. This factor shows the correlation between the incident channel and outgoing channels. With the increasing of the incident particle energy the correlation also is increasing. Quantitatively WFC is equal to unity when no correlation yield and slowly decrease with energy.

The differential cross section in the HF formalism has the expression (for simplicity without WFC factor):

$$\frac{d\sigma}{d\Omega} = \pi \mathcal{H}^2 (2l+1) T_l \sum_j \frac{A_j(l,j|l',j'|\theta)}{1 + \sum_{p,q,r} T_p(E_q)}$$
(2)

$$A_{J}(l,j|l',j'|\theta) = \sum_{m,m'} |(l,j;0m|l,j;Jm)|^{2} |(l',j';m'm-m'|l',j';Jm)|^{2} |Y_{l'm'}(\theta,\varphi)|^{2}$$
(3)

We also have evaluated the contribution of direct processes but their contribution can be neglected in the mentioned neutron energy interval and therefore we do not show here the main formulas for these processes.

Results

We used the default Talys parameters and first we have evaluated the cross section and from cross section has resulted that the dominant processes are the compound ones.

า ศัสมาชาติสาร เหมืองรูน โมวารมาการมูวสร้างปฏิวัติย

Arranguage efficiency or moistair in the

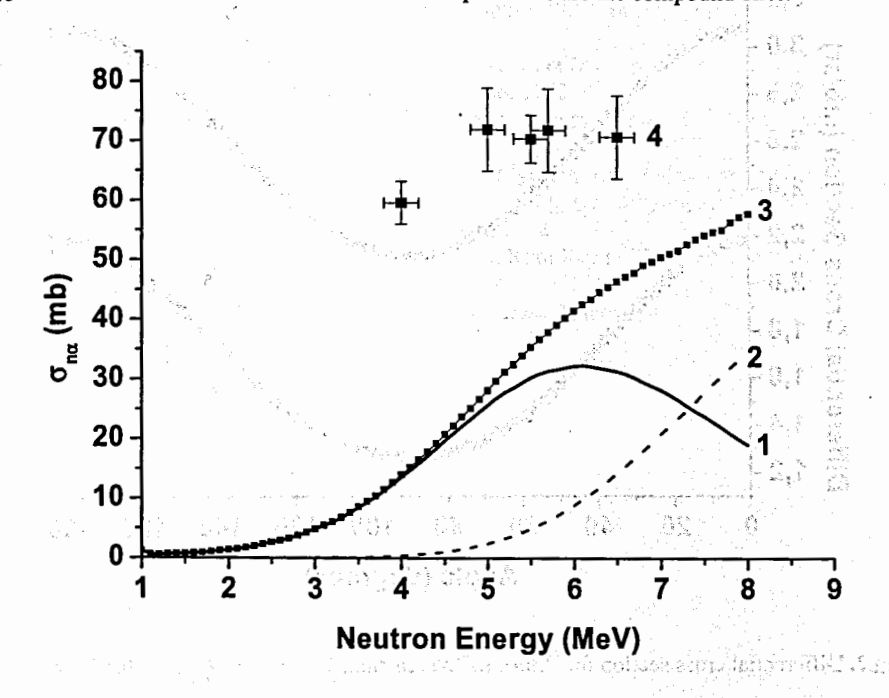


Fig.1. Cross section of $^{64}Zn(n,\alpha)^{61}Ni$ reaction. 1 – contribution of the compound processes on discrete states of residual nucleus (10 levels), 2 – contribution of the compound processes on continuum states of residual nucleus, 3 – contribution of all processes (inclusive neglected direct processes), 4 – experimental data.

In the beginning the compound processes on discrete states of residual nucleus are dominant but with the increasing of the energy they reach a maximum and after that they slowly decrease giving priority to the compound processes on continuum states (Fig.1). Here is not showed but higher than $8 \, MeV$ processes on continuum also reach a maximum followed by a slow decreasing, direct and multiples processes (like (n, 2n), (n, np) and others of such type) becoming dominant. Experimental data [10] (4 from Fig.1) are obtained mainly by our group using a double gridded ionization chamber and in the beginning can be considered in agreement with theoretical evaluation.

We have obtained the differential cross section for all energies but in Fig.2.are shown only the cases for $5.5 \, MeV$ and $8 \, MeV$. From Fig.1. it is expected that the differential cross section will be symmetric around 90^0 due to the contribution of the compound processes. For indicated neutrons energy interval in the evaluation were taken into account neutrons with orbital momentum greater than zero and as results the differential cross section has an

anisotropy (the presence of Legendre polynomials of second order or fourth, sixth, eight,..., orders for higher energies if is necessary).

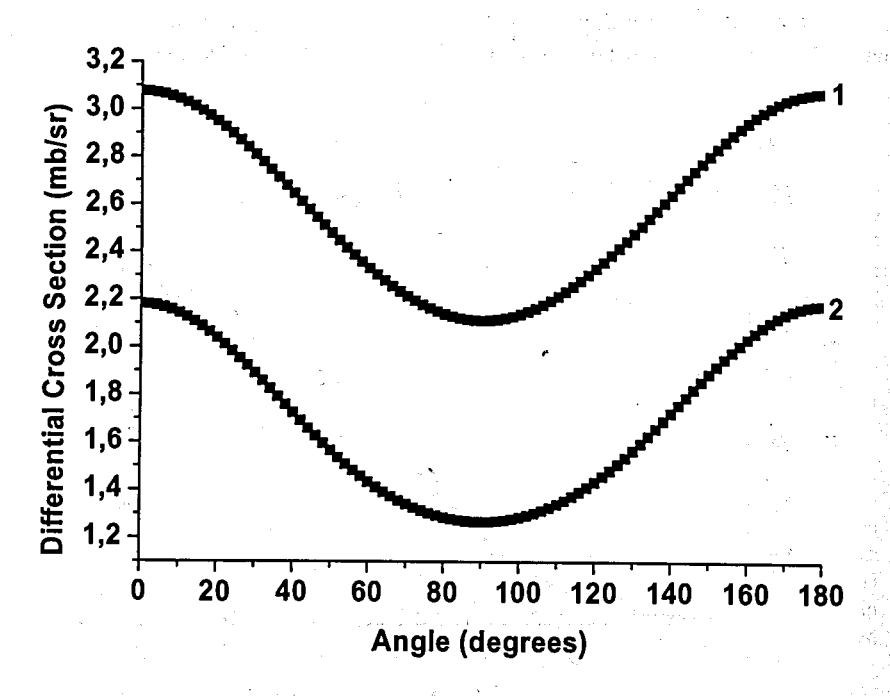


Fig.2. Differential cross section for $^{64}Zn(n,\alpha)^{61}Ni$ reaction. 1 – for 5.5 MeV, 2 – for 8 MeV

Discussion and Conclusions

ំពីទី ស្គីជំនាំ នាមស្នង៖ សម្រៀប មុខ ស

Theoretical evaluations presented in this work are not final. First, it is necessary to try other parameters than defaults suggested by Talys in order to describe better the experimental data. In future a set of experimental data in a large energy interval will be of a great help in the selection of necessary optimal parameters.

Also will be of great interest a set of experimental data for differential cross section for different energies to verify the presence of the anisotropy and / or the existence of a forward – backward asymmetry. This asymmetry will confirm or infirm our statement concerning the presence and the contribution of the direct processes.

The $^{64}Zn(n,\alpha)^{61}Ni$ reaction is a part of a research program for nuclear reactions induced by neutrons with emission of charged particles (protons, alpha particles) on medium and heavy nuclei developed at JINR FLNP Dubna for many years.

The work was supported partially by the Program of Collaboration between JINR and Romanian Research Institutes on 2010 and 2011 years under the coordination of Romanian Plenipotentiary Representative to JINR.

References

- [1] C. Oprea, Doctoral Thesis, Bucharest University Faculty of Physics, Bucharest, September 2002 (in Romanian)
- [2] Yu. Gledenov, Doctoral Thesis, JINR-FLNP Dubna, 2003 (in Russian)
- [3] Talys Code, http://www.talys.eu
- [4] A.J. Koning, S. Hilaire, M. Duijvestijn, Talys 1.2 User Manual, 2009
- [5] W. Hauser, H. Feshbach, Phys. Rev., v.87, p.366, 1952
- [6] Antonio Foderaro, The Neutron Interaction Theory, The MIT Press, Cambridge, Massachusetts and London, England, 1971
- [7] Yuri Gledenov, Milana Sedysheva, Pavel Sedyshev, Alexandru Oprea, Zemin Chen, Yingtang Chen, Jing Yuan, Guohui Zhang, Guoyou Tang, Gonchigdorj Khuukhenkhuu, Pavel Szalanski, J. Nucl. Sci. Techn., Suppl. 2, p.342-345, 2002
- [8] A. I. Oprea, C. Oprea, C. Pirvutoiu, D. Vladoiu. Rom Rep in Phys, v.63, №1, p.107, 2011

on the list has hit is write and a well to alk had see

die gedagteingswaptigen gescheiden in. Mystopatopiet waarde stiffe geschaal in.

the COME STOCK the endings the leavest consistings in group that the constraint stock to the state of the plane of the state in the con-

(4) A section of the contract of the first enemy projection of the contract of the contract

The to relative the second of the second

i di di e ode o besituatura

na dhean an cheann dhean air an Airean a Ta an Airean an an Airean an A

Same that because of their light in a large of

The second of the second of the second of the second

าร ค.ส. ค.ศ. เมื่อน วิธีสิร เกิดกา เพลิ เกิดเกา เมื่อ

- [9] P.A. Moldauer, Phys. Rev. B v.135, p.642, 1964
- [10] EXFOR Data ⁶⁴Zn(n, ct)⁶¹Ni reaction http://www-nds.iaea.org

Parity-Violating Gamma Asymmetry in np-Capture

E.I. Sharapov¹, R. Alarcon², S. Balascuta², L. Barrón-Palos³, J.D. Bowman⁴, R.D. Carlini⁵, W. Chen⁶, T.E. Chupp⁷, C. Crawford⁸, S. Covrig⁵, M. Dabaghyan⁹, N. Fomin¹⁰, S.J. Freedman¹¹, T.R. Gentile¹², M.T. Gericke¹³, R.C. Gillis⁶, G.L. Greene^{4,10}, F.W. Hersman¹⁴, T. Ino¹⁵, G.L. Jones¹⁶, B. Lauss¹⁷, M. Leuschner⁶, W.R. Lozowski⁶, R. Mahurin^{5,13}, Y. Masuda¹⁵, J. Mei⁶, G.S. Mitchell¹⁸, S. Muto¹⁵, H. Nann⁶, S.A. Page¹³, S.I. Penttilä⁴, W.D. Ramsay¹³, A. Salas-Bacci¹⁹, S. Santra⁶, M. Sharma⁷, P.-N. Seo²⁰, T.B. Smith²¹, W.M. Snow⁶, W.S. Wilburn¹⁹, V. Yuan¹⁹

¹Joint Institute for Nuclear Research, 141980 Dubna, Russia
 ²Arizona State University, Tempe, AZ 85287, USA
 ³Universidad Nacional Autónoma de México, C.P. 04510, D.F., Mexico
 ⁴Oak Ridge National Laboratory, Oak Ridge, TN 37831, USA
 ⁵Thomas Jefferson National Accelerator Facility, Newport News, VA 23606, USA
 ⁶Indiana University, Bloomington, IN 47405, USA
 ⁷University of Michigan, Ann Arbor, MI 48104, USA; ⁸University of Kentucky, 40506, USA
 ⁹University of New Hampshire, Durham, NH 03824, USA; ¹⁰University of Tennessee, Knoxville, TN 37996, USA; ¹¹University of California, Berkeley, CA 94720-7300, USA
 ¹²National Institute of Standards and Technology, Gaithersburg, MD 20899-0001, USA
 ¹³University of Manitoba, Winnipeg, MB, R3T 2N2, Canada
 ¹⁴University of New Hampshire, Durham, NH 03824, USA

¹⁵High Energy Accelerator Research Organization, Oho 1-1, Tsukuba-shi, 305-0801, Japan
 ¹⁶Hamilton College, Clinton, NY 13323, USA; ¹⁷Paul Scherrer Institut, CH-5232, Switzerland
 ¹⁸Department of Biomedical Engineering, University of California, Davis, CA 95616, USA
 ¹⁹Los Alamos National Laboratory, Los Alamos, NM 87545, USA
 ²⁰Department of Physics, North Carolina State University, Raleigh, NC 27695, USA
 ²¹University of Dayton, Dayton, OH 45469, USA

Abstract

The npdgamma Collaboration uses a pulsed polarized cold neutron beam, a parahydrogen target, and an array of 48 CsI scintillation detectors to measure, in n+p \rightarrow D + γ reaction, the parity-violating asymmetry A_{γ} of the photons emission along the neutron spin and opposite to it. The theory-predicted value is $A_{\gamma}\approx -0.5\times 10^{-7}$. Knowledge of A_{γ} and other parity-violating observables in few-body nuclear systems should provide constraints for a parameterized description of the parity-violating phenomena free from complications of nuclear structure. We report final results of the first phase of the experiment, which took place at the spallation neutron source of the Los Alamos Neutron Science Center: $A_{\gamma}=-(1.2\pm 2.1({\rm stat.})\pm 0.1({\rm sys.}))\times 10^{-7}$, and the parity allowed, left-right (LR) asymmetry $A_{\gamma}^{LR}=-(1.8\pm 1.9({\rm stat.})\pm 0.2({\rm sys.}))\times 10^{-7}$. Our A_{γ} value reproduces the previous upper limit from a measurement at the Grenoble ILL reactor facility, while the A_{γ}^{LR} value is obtained for the first time. The second phase of the experiment, aimed at a better statistical accuracy, is presently started by the npdgamma Collaboration at another source — the Spallation Neutron Source of the Oak Ridge National Laboratory.

Introduction

The observable of interest in the polarized cold neutron capture $\vec{n}+p\to D+\gamma$ (E₇=2.2 MeV) is the parity-violating (PV) asymmetry A_{γ} in the angular distribution of the 2.2-MeV photons with respect to the direction of the neutron polarization $\mathbf{P_n}$

$$\frac{d\omega}{d\Omega} \propto \frac{1}{4\pi} \left(1 + A_{\gamma} P_{n}(\mathbf{s_{n} \cdot k_{\gamma}}) \right). \tag{1}$$

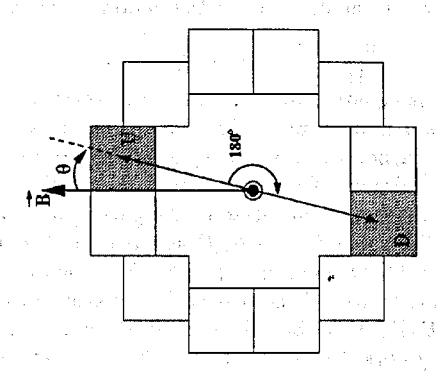
The scalar product in this equation reduces to $\pm\cos\theta$ where θ is the angle between the neutron spin s_n and gamma momentum k_γ (s_n and k_γ are unit vectors). In the absence of parity violation, $A_\gamma=0$. A nonzero asymmetry A_γ results from an interference between regular M1 and the PV admixed E1 gamma transitions. The M1 transition connects the parity conserving 1S_0 np scattering state to the parity conserving 3S_1 deuteron state (labeling of states is ${}^{2J+1}L_I$ with L=S, or P as the orbital momentum, I — the spin of the pair and J — the total momentum). The E1 transition can be, for example, from the 3S_1 np-scattering state to the PV admixed 3P_1 deuteron state. The matrix elements (${}^3S_1|\mathbf{M}1|^1S_0$) and (${}^3P_1|\mathbf{E}1|^3S_1$) can be calculated in theory, see for example [1, 2, 3]. In the meson-exchange framework, the result for A_γ , which is essentially the ratio of of these quantities, is

$$A_{\gamma} = -0.1069h_{\pi}^{1} - 0.0014h_{\rho}^{1} + 0.0044h_{\omega}^{1} \approx -0.11h_{\pi}^{1}, \tag{2}$$

where the h_{π}^1 , h_{ρ}^1 , h_{ω}^1 are weak meson-nucleon coupling constants. They have been calculated in Ref. [4] from the Standard Model using a valence quark model of QCD. In this meson exchange picture, the nucleon-nucleon weak interaction is modeled as a process in which the three lightest mesons $(\pi, \rho, \text{ and } \omega)$ couple to one nucleon via the weak interaction at one vertex and to the second nucleon via the strong interaction at the other vertex. In the latest decade the effective field theory approach to the weak interaction has been also developed, e.g. in Refs. [5, 6, 7],. It reformulated the problem in terms of the parameters of the parity violating Lagrangian. This new approach, which thought to be less model dependent, invigorated the present study of parity violation in the npd γ reaction and few body systems.

In particular, the value of the h_{π}^1 coupling constant is widely debated. With the 'best DDH' value of $h_{\pi}^1 = 4.6 \times 10^{-7}$ the predicted A_{γ} value is $\approx -5 \times 10^{-8}$. Such a value is really small and has not been yet experimentally proved, only an upper limit of $\sim 10^{-7}$ was obtained in the npd γ experiment at Grenoble [8, 9]. Measurements of the circular polarization of the gamma ray decay in ¹⁸F, e.g. [10], and of the parity-violating triton emission asymmetry in the ⁶Li(n, α)T reaction [11] have been interpreted to indicate a rather small value $h_{\pi}^1 \leq 1 \times 10^{-7}$ as compared to the theory expectation, while the anapole moment of ¹³³Cs from the parity violation in Cs atoms seem to favor a much larger value [12], $h_{\pi}^1 = (9.5 \pm 2.1) \times 10^{-7}$. So the h_{π}^1 remains to be proved experimentally.

The left-right asymmetry in the npd γ reaction is due to the parity-allowed interference of M1 and E1 capture amplitudes and is described by the form $A^{LR}\mathbf{s_n} \cdot [\mathbf{k_n} \times \mathbf{k_{\gamma}}] \propto 1 \pm A^{LR}P_n \sin\theta\sin\phi$. The angle ϕ is between $\mathbf{k_n}$ and $\mathbf{k_{\gamma}}$. The calculated value A^{LR} is 0.67 \times 10⁻⁸ at energy of 3-meV [13] and increases linearly with the neutron energy.



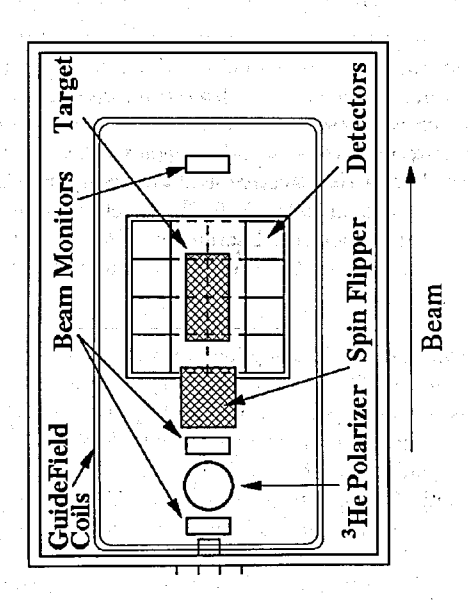


Figure 1: The experimental setup of the npDg experiment at LANSCE.

The apparatus and experiment

. '15

4187

1. 71

ded.

1003

134 %

1.

4: 1

36.3

The np \rightarrow D γ experiment has been performed at the spallation neutron source of the Los Alamos Neutron Science Center (LANSCE) [14]. The spallation neutrons, produced by 20 Hz 250 ns-long 800 MeV proton pulses on a tungsten target, are moderated by a 5 cm-thick liquid hydrogen moderator. The neutron flight path FP12 and the apparatus were developed by the Collaboration. The FP12 neutron supermirror guide ends at about 20 m from the moderator. Fig. 1 shows a schematic side view and the cross section of the apparatus. Not shown are magnetic field coils providing a vertical guide field. There are three beam monitors. The distance from M1 to M3 is about 1.7 m. Besides the guide, the flight path beam line consists of a shutter, and a beam chopper. The chopper is used to define the neutron time of flight region within the 50 msec time of flight frame set by the 20 Hz source frequency. This corresponds to energy range from 2 to 15 meV and prevents neutrons from different frames from mixing. For this energy range, the integrated neutron current at the end of the guide was measured to be 1.0×10^9 n/s s at an average proton current of $100~\mu$ A. An instantaneous intensity was about four order of magnitude higher, therefore the gamma-detector array, as well as monitors, were run in current mode [15].

The neutrons were vertically polarized by passing through a 12 cm diameter glass cell containing polarized 3 He [17, 18, and references there]. The 3 He polarization was monitored using NMR. The beam polarization was measured with the beam monitors using neutron transmission through the polarized and unpolarized 3 He target. The neutron energy averaged polarization was 55 ± 7 %. The beam polarization was reversed with each spallation pulse using a radio frequency (RF) spin rotator [16] — a solenoid positioned coaxially with the beam that operates by magnetic spin resonance. In this device, the neutron spin precesses in the presence of the static 10 G holding field and RF field of the solenoid. To make RF field proportional to the neutron velocity, the amplitude of the RF field was varied in time as 1/TOF, so that all neutrons within the measured time-of-flight (TOF) region were rotated by 180° while moving inside the solenoid.

The proton target was a 16-liter parahydrogen in a cryogenic vessel [19]. About 60% of the polarized neutrons that enter the target are captured on hydrogen. The parahydrogen is required to ensure that the neutrons are not depolarized in the liquid hydrogen before capture. Ortho- H_2 depolarizes cold and thermal neutrons, while in para- H_2 only thermal neutrons with energies greater than 16 meV are depolarized. The thermal equilibrium fraction of ortho- H_2 is known to be low at liquid hydrogen temperatures (≈ 17 K), however the rate of conversion is slow. In our experiment, the para- H_2 concentration higher than 99.9% was achieved and maintained by circulating the liquid hydrogen through a chamber of iron oxide catalyst.

The 2.2-MeV gamma rays were measured using the detector described in [20]. This is an array of 48 CsI(Tl) scintillator cubes, each with a 15-cm side length. It was designed to have sufficient spatial and angular resolution, high efficiency, and large solid angle coverage. There are four rings of detectors, arranged in a cylindrical fashion. Each ring has twelve detectors, as shown in the cross sectional view of Fig. 1. Current mode

detection is performed by converting the scintillation light from CsI(Tl) to current signals using vacuum photo diodes, and the photocurrents are converted to voltages and amplified by low-noise solid-state electronics [15].

Asymmetries were measured in TOF bins for 55 different neutron energies between 2 and 16 meV. The analysis of data was performed separately in this bins on each of the six detector pars in each ring. Geometry of pairs in one ring is shown in Fig. 1. The raw asymmetry A_{raw} for an Upper (U), Down (D) pair was defined by

$$A_{raw} = \frac{N_{U,\uparrow}(\theta) - N_{D,\uparrow}(\theta) - N_{U,\downarrow}(\theta) + N_{D,\downarrow}(\theta)}{N_{U,\uparrow}(\theta) + N_{D,\downarrow}(\theta) + N_{U,\downarrow}(\theta) + N_{D,\downarrow}(\theta)}$$
(3)

and the physics asymmetry A_{γ} was calculated from equation

$$A_{\gamma}P_{n}\cos\theta = A_{raw}. (4)$$

Here N is the detector signal. Symbols \uparrow and \downarrow refer to the direction of beam polarization. To suppress detector gain drifts, one such raw asymmetry was calculated (summed) over one eight step secuence $(\uparrow\downarrow\downarrow\uparrow\downarrow\uparrow\uparrow\downarrow)$ and raw asymmetries were formed from all 'valid sequences' in the run. Typical run lengths were $\simeq 8.3$ minutes and included 10000 beam pulses or 1250 eight step sequences. One successful week of measurements resulted in about 700 runs.

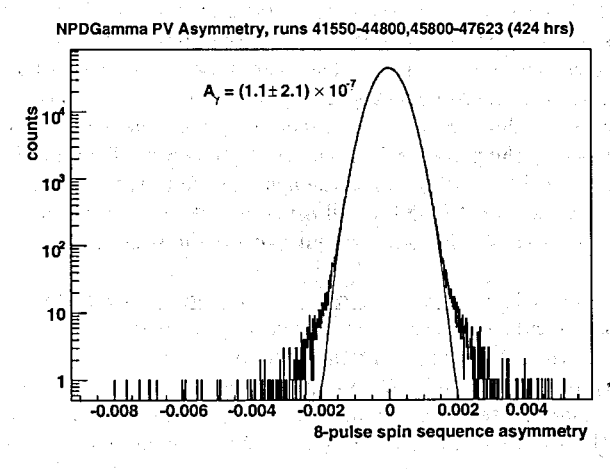


Figure 2: An example of measured row asymmetries for hydrogen.

The Results

Prior to the main experiment, the control measurements of the PV asymmetry in cold neutron capture on a 1-cm thick CCl₄ target have been performed. The obtained result

Table: PV asymetries results and their statistical uncertainties of

| Ring | ϵ | Direction | A_{raw} (ppm) | σ_{raw} (ppm) | A_{γ} (ppm) | σ_{γ} (ppm) |
|----------|------------|-----------|-----------------|----------------------|--------------------|-------------------------|
| 1 | 0.5 | UD LR | -0.27 -0.20 | 0.29 0.28 | -0.38 -0.20 | 0.49 0.49 |
| 2 | 0.4 | UD LR | -0.015 -0.29 | 0.24 0.24 | 0.01 -0.33 | 0.36 0.35 |
| 3 | 0.2 | UD LR | -0.17 -0.38 | 0.33 0.27 | -0.19 -0.42 | 0.40 0.33 |
| 4 | 0.12 | UD LR | -0.02 0.41 | 0.43 0.40 | -0.013 0.48 | 0.48 0.45 |
| Combined | | UD LR | -0.12 -0.23 | 0.15 0.14 | -0.12 -0.18 | 0.21 0.19 |

 $A_{\gamma}(Cl) = -(19.0 \pm 2.0) \times 10^{-6}$ is in an agreement with that of $-(21.2 \pm 1.7) \times 10^{-6}$ in Ref. [21]. The left-right asymmetry is much smaller and cannot be seen in this measurement.

An example of measured row asymmetries for hydrogen is shown in Fig. 2. Detailed results are presented in Table. They are statistically limited. The final statistical uncertainties are higher than the uncertainties for the raw asymmetries due to a $\simeq 30\%$ background. The main source of background were capture gamma rays from the aluminum wall of the cryogenic vessel. The quantity $\epsilon = Y_{bgr}/Y_p$ is the fractional background to hydrogen yield. The total asymmetry A_{γ} is a sum of a left-right parity-allowed term and an updown PV term which were extracted from a fit to the angular dependence of $A_{\gamma}(\theta) \equiv A_{\gamma}^{UD} cos\theta + A_{\gamma}^{LR} sin\theta$.

The uncertainties on the beam polarization and spin flip efficiency were measured to be 5% and 1% respectively. Possible systematic uncertainties are discussed elsewhere [22].

Summary

The final result for the parity-violating asymmetry $A_{\gamma}=-(1.2\pm2.1({\rm stat.})\pm0.1({\rm sys.}))\times 10^{-7}$ reproduces the previous upper limit from a measurement at the Grenoble ILL reactor facility. The result for the parity allowed left-right (LR) asymmetry $A_{\gamma}^{LR}=-(1.8\pm1.9({\rm stat.})\pm0.2({\rm sys.}))\times 10^{-7}$ is obtained for the first time. The second phase of the experiment, aimed at a better statistical accuracy, is presently under preparation at the Spallation Neutron Source (SNS) of the Oak Ridge National Laboratory. The beam line FNPB with a supermirror polarizer is built there. The installed npD γ apparatus is currently undergoing modifications for starting PV runs at FNPB. Both LANSCE and SNS are pulsed spallation sources, but SNS is expected to provide an average neutron intensity on the target of about 30 times greater than at LANSCE. A main modification is the change of the neutron polarizer from the ³He filter to a supermirror FeSi bender.

This work was supported in part by the U.S. Department of Energy (Office of Energy Research, under Contract W-7405-ENG-36), the National Science Foundation (Grants No. PHY-0457219, PHY-0758018, and PHY-0100348), the NSF Major Research Instrumentation program (NSF-0116146) for the procurement of the CsI crystals and neutron shielding, the Natural Sciences and Engineering Research Council of Canada (NSERC), and the Japanese Grant-in-Aid for Scientific Research A12304014.

References

- [1] E. G. Adelberger and W. C. Haxton, Ann. Rev. Nucl. Part. Sci. 35, 501 (1985).
- [2] B. Desplanques, Nucl. Phys. A 335, 147 (1980).
- [3] R. Schiavilla, J. Carlson, and M. Paris, Phys. Rev. C 70, 044007 (2004).
- [4] B. Desplanques, J.F. Donoghue, and B.R. Holstein, Annals of Physics 124, 449 (1980).
- [5] S. L. Zhu et al., Nuclear Physics A 748, 435 (2005).
- [6] C.-P. Liu, Phys. Rev. C 75, 065501 (2007).
- [7] M. R. Schindler and R. P.Springer, Nuclear Physics A 846, 51 (2010).
- [8] J. F. Cavaignac, B. Vignon and R. Wilson, Phys. Lett. B 67, 148 (1977).
- [9] J. Alberi et al., Can. J. Phys. 66, 542 (1988).
- [10] S. A. Page et al., Phys. Rev. C 35, 1119 (1987).
- [11] V. A. Vesna et al., Phys. Rev. C 77, 035501 (2008).
- [12] V. V. Flambaum and D. W. Murray, Phys. Rev. C 35, 1119 (1987).
- [13] A. Csótó, B. F. Gibson and G. L. Payne, Phys. Rev. C 56, 631 (1997).
- [14] P.W. Lisowski, C.D. Bowman, G.J. Russell, S.A. Wender, NSE 106 208, 1990.
- [15] W. S. Wilburn, J. D. Bowman, M. T. Gericke, and S. I. Penttilä, Nucl. Instr. Meth. A 540, 180 (2005).
- [16] P.-N. Seo et al., Phys. Rev. ST Accel. Beams. 11, 084701 (2008).
- [17] T. R. Gentile et al., J. Res. Natl. Inst. Stand. Technol. 110, 299 (2005).
- [18] T. E. Chupp et al., Nucl. Instr. Meth. A 574, 500 (2007).
- [19] S. Santra et al., Nucl. Instr. Meth. A 620, 421 (2010).
- [20] M. T. Gericke, et al., Nucl. Instr. Meth. A 540, 328 (2005).
- [21] M. Avenier, et al., Nuclear Physics A 436, 83 (1985).
- [22] M. T. Gericke, et al., Phys. Rev. C 83, 015505 (2011).

MODIFIED MODEL OF NEUTRON RESONANCES WIDTH DISTRIBUTION. RESULTS OF REDUCED NEUTRON WIDTHS APPROXIMATION FOR MASS REGION 35 ≤A ≤249

A.M. Sukhovoj, V.A. Khitrov

Joint Institute for Nuclear Research, Dubna, Russia

Abstract

The distributions of the reduced neutron widths of s-, p- and d-resonances of nuclei of any type from nuclear mass region $35 \le A \le 249$ were approximated with maximal precision by the model which presents experimental data set as a superposition of, maximum, four independent neutron amplitudes. Under the assumption that each of these amplitudes has the Gauss distribution with the unique maximum there were determined the most probable values of contribution of each amplitude in summary width distribution, their most probable mean values and dispersions. Comparison of the obtained χ^2 values with value χ^2 at description of the experimental data by one distribution of neutron amplitudes with best fitted parameters shows that all widths from more than 157 analyzed data sets can have few different types of their wave functions.

1. Introduction

Ç1.

Experimental investigation of super-fluidity of heated nuclei can give unique information on so fundamental physics process as interaction and intertransition between Fermi- and Bose-systems. The new of principle data as compared with the other objects of investigation can be obtained in this case owing to radical difference of parameters of macrosystems and nucleus.

The main parameter that characterizes the degree of super-fluidity of heated nucleus is entropy and determined by it density ρ of excited levels [1]. The special interest for its study is the region of nuclear excitation energy from doubled energy of nucleon paring Δ up to their binding energy B_n . Just here is developing the process of break up of Cooper pairs of nucleons onto the pairs of independent quasi-particles. Unfortunately, just in this region of excitations the ρ value is determined in the experiment with inevitable and, often, rather significant systematical errors. This conclusion follows from comparison of nuclear properties, obtained from interpretation of the one-step reactions data, (which determine ρ from the total gamma-spectra [2] or spectra of evaporation nucleons [3]) and two-step reaction $(n, 2\gamma)$.

Respectively, a nucleus can be presented as:

- (a) the system of non-interacting Fermi-particles,
- (b) the Bose-condensate (practically only below nucleon binding energy B_n) or
- (c) the mixture of increasing number of quasi-particles and some number of phonons, where occurs break-up of Cooper pair number n with interval of about $2\Delta_n$, which decreases with increase of nuclear excitation energy [4].

These principally incompatible conclusions [2-4] of nuclear properties point to presence of serious systematical errors in different experiments. The most probable and largest systematical error is caused by the use the model ideas of unknown [5] probability of the reaction product emission, corresponding to transition of nucleus between its excited levels and low sensitivity to variations of the desired parameters [6].

The noticeable problem can be and error in determination of the experimental density of neutron resonances $\rho_{\lambda} = D_{\lambda}^{-1}$ from the results of analysis of the experimental data with the use of the neutron time-of-flight method. This value is basic for any experiments where nuclear level density in the excitation region above some MeV is derived from the spectra of gamma-rays or evaporation nucleons. But, potentially high precision in determination of D_{λ}^{-1} can be realized, at least, by careful accounting and correction of all systematical errors of the experiment. This statement concerns, first of all, the model intended for description of distribution form of the obtained values of reduced neutron widths of resonances Γ_n^0 (or Γ_n^1 ...) for its following extrapolation below sensitivity threshold of the experiment. Of course, precision of this procedure is determined by degree of correspondence of theoretical ideas on distribution of Γ_n^0 to the experiment.

The not removable uncertainty D_{λ}^{-1} is caused by the fact that the independent variable of the analyzed distribution of the widths $X = \Gamma_n^0 / < \Gamma_n^0 >$ always contains unknown systematical error. This error is caused by impossibility of unambiguous determination of the mean value $<\Gamma_n^0>$ only from the set of the experimental values of widths. According to the theoretical analysis, the Γ_n^0 value for neutron resonances is determined by few-particle components of wave function, whose square contribution in normalizing is estimated [7] in nuclei of middle and large mass by the value of about $10^{-6}-10^{-9}$. It is generally accepted that the experimentalists use the Porter-Thomas hypothesis [8] for description of fluctuations of Γ_n^0 and parameters of its distribution. The smallness and chaotic character of items of neutron amplitudes of resonances are determined by strong fragmentation [9] of low-lying one- and two-quasi-particle states of a nucleus. Id est., it is confirmed by modern nuclear theory. Another obligatory condition of applicability of [8] - mathematical expectation of mean value of amplitude $A = \sqrt{\Gamma_n^0}$ must be equal to zero and its dispersion – to mean $<\Gamma_n^0>$. Both conditions:

M(A)=0, D(A)= $\langle \Gamma_n^0 \rangle$ (1) are not tested in modern analysis of experimental values Γ_n^0 . Id est., applicability of the

are not tested in modern analysis of experimental values $\Gamma_n^{\ \nu}$. Id est., applicability of the Porter-Thomas distribution is postulated, but ground conditions of its truth are not proved.

Experimental distribution of widths is not also tested for possibility of existence of superposition of several gamma-functions with different values M(A) and D(A). The latter situation can appear at presence of groups of neutron resonances with noticeably (or strongly) differing structure of wave functions and is trivial at presence of two and more spins of resonances. Approximation [4,10, 11] of level density below B_n , derived from intensities of two-step gamma-cascades, shows that the structure of any nucleus at increase of excitation energy undergoes cyclic change because of discrete character of break-up process of Cooper pairs of nucleons. Corresponding conclusion was obtained for different tested functional dependences of correlation function of two nucleons Δ_n on excitation energy of a nucleus for the set from \approx 40 nuclei from the mass region $40 \le A \le 200$. High reliability of establishment of this fact is conditioned by its obtaining in the frameworks of the only realized by now practically model-free method for determination of ρ - [12].

Cyclic change of structure of neutron resonances at increase of excitation energy of a nucleus must occur owing to appearance of nuclear states with increasing number of quasi-particles and with possible variation of number and type of phonons. Fragmentation of these complicating nuclear states inevitably changes coefficients of wave functions of neutron resonances (as it follows from the main notions of quasi-particle-phonon model of a nucleus). As a result, there is possible violation of the Porter-Thomas distribution in its existing today interpretation (1).

Distributions of the experimental Γ_n^0 values are usually approximated at analysis in different form of functional dependence [8]. But, experimental data contain fixed (and limited) quantity of information. Therefore, the accessible for its extraction maximally possible volume must not depend on analysis type. And choice of form of data presentation and algorithms of analysis are determined only by problems of obtaining of maximally precise values of the determined parameters at presence of random and systematical errors and, it is desirable, the best visualization of the obtained results.

The main problem of analysis of distribution of the measured neutron widths at presence of their registration threshold - absolute absence of the experimental data on value of it's portion which is really observed in experiment. In the other words, modern experiment cannot give the $\Gamma_n^0/<\Gamma_n^0>$ values. As a consequence, here arises the problem of the random value unit – it must not depend on presentation form for distribution. The most suitable form of the data presentation for the task under solution is cumulative sum of the experimental values $X = \Gamma_n^0/<\Gamma_n^0>$, which increases at increasing X. The main preference of such presentation is clearness of the presence of change in form of distribution and the lowest degree of its dependence on the error $<\Gamma_n^0>$ and revealing of the most strong misprints. The example of expected random cumulative sums for distribution [8] is shown in Fig. 1.

Corresponding analysis was performed for the obtained experimentally and included in known compilations (for example, in [13,14] or library ENDF/B-VII [15]) values of widths of neutron resonances.

3. The model and method for the suggested analysis

The sample average $\langle \Gamma_n^0 \rangle$ for the experimental cumulative sum was determined from this set without accounting for omitted resonances and their unresolved multiplets. This uncertainty does not tell on influence on of ratio of values χ^2 for different approximating functions – the shapes of experimental and approximating distributions and their relative difference for cumulative sum X do not depend on the units in which is determined the width Γ_n^0 .

The fitted object is the sum of k distributions of gamma-functions $\Gamma(X)$ for squares of normally distributed random amplitudes with independent variables X_k each. The desired parameters in compared variants are the most probable value b_k of amplitude A_k , its dispersion σ_k and the total contribution C_k of gamma-function number k for the variable $X_k = ((A_k - b_k)^2)/\sigma_k^2$ (2) in the full experimental cumulative sum of widths $S_{\text{exp}}(X)$. The maximum possible value of k

is determined by variation of its tested values at the beginning from k=1. Here can be also used fitted threshold of resonance parameters registration.

The number of distribution k and sign of amplitude A_k for given resonance are unknown. That is why, further was used only its positive value because (2) is invariant with respect to simultaneous change of sign of both A_k and b_k . But, everywhere is supposed that in considered distribution number k can exist the only desired value b_k . Id est., any distribution number k of widths has only one most probable value of amplitude. There is the main (and absolutely necessary) hypothesis of the performed below analysis of distributions of the reduced neutron widths of resonances. It should be noted in addition that the modules of values b_k and σ_k are strongly correlating variables, at least, for large enough values b_k .

Concrete value of function P(X) for variable (2) in the described analysis was obtained by compression and shifting of the generally known Euler gamma-function. The

obtained in this way value corresponds to the magnitude of this mention function for the variable $X=(A\cdot\sigma+b)^2$. At present the basis for this algorithm for setting of parameters of approximating function is excellent degree of description of all known experimental distributions of the widths.

It is obvious that the case: k=1, $b_k=0$ and $\sigma=1$ corresponds to distribution [8]. The case of arbitrary value b_k =const and $\sigma=0$ corresponds to the degenerate (caused) distribution of widths for corresponding value of amplitude. Any other values of approximation parameters correspond to any point of the spectrum of possible values of amplitudes for wave functions of concrete neutron resonances. According to the main axiom of mathematical statistics, their most probable values correspond to minimum of χ^2 . Naturally, the best values of k, b, σ and contribution of each from k partial distributions in the total sum are distorted by random fluctuations of widths in maximally possible extent. However, unlike usual approximations of distributions of neutron widths, the obtained values of the parameters contain maximally possible information on their real structure.

Analysis of the different spin of resonances data sets was approximated a distribution $g \Gamma_n^0$ (s-resonances of even-odd and A-odd target nuclei) or only Γ_n^0 for fixed (on basis of some information) spins of resonances. More correct methodically and physically is separate approximation of the data of the one and the same spin. But, it is true only for the case if they were determined for the all resonances with high enough precision. In principle, real analysis must take into account distortions of the experimental data so that the most probable parameters of the width distribution would be maximally reliable at presence of arbitrary systematical errors. By this reason it was performed in given work only for $g \Gamma_n^0$.

The region of approximation for distribution [8] must be great enough. In all the calculations adduced below it was corresponded to the interval from zero to the maximal experimental values $1.5X_{\text{max}}$. Cumulative sum in point X_{max} was normalized to the number of the experimentally determined widths. By this, the region $(0-1.5\ X_{\text{max}})$ in all cases contained more than M=1000 points, where was minimized the difference of the experimental cumulative sum S_{exp} and approximating it function S_{fit} . This is necessary because the approximating function is determined by numerical integration of width distribution.

In the region of neutron resonances, the experimental level density of nuclei from mass region $40 \le A \le 200$ obtained in Dubna (by model-free method of analysis of intensities of two-step cascades), according to [4,10, 11], is described by sum of four (sometimes three) partial level densities with different number of quasi-particles and phonons. Just from this follows that neutron resonances can, in principle, have several different types of wave functions. In practice, it is accepted by calculating problems that the experimentally observed resonances can in limited cases belong, maximum, to four different distributions of Γ_n^0 for even-even target nuclei. It is true for A-odd nuclei (and all p-resonances) at equality $< g \Gamma_n^0 >$ for resonances with different spins J. In the other case the results of approximation can be determined also by the possible spin dependence of the neutron strength functions.

Physically, from parameters of different variants of approximation of the total set of level density, obtained for 40 nuclei in Dubna, it is follow also to limit the maximal value k by magnitude k=4. In this case the system of corresponding non-linear equations will be badly stipulate and sometimes - degenerate. Last remark concerns only "partial" cumulative sums with number k, sum $S_{\rm fit}$ of which is the approximation of experimental value $S_{\rm exp}$. And instead of determination of their unique function parameters value, in this case is necessary and possibly to determine only limited region of A_k , b_k and σ_k variation, which corresponds to one and the same χ^2 minimum.

4. Practical approximation of the data

Relative smallness of set of the experimental values of widths and exponential functional dependence of probability of their observation at different $g \Gamma_n^0$ very strongly complicate the process of search of approximating function $S_{\rm fit}$, which provides the lowest value $\chi^2 = ((S_{\rm exp} - S_{\rm fit})/\sigma_{\rm cum})^2/M$. Therefore, it is worth while to realize this operation so that the algorithm for search of the minimum would admit stable approximation of $S_{\rm exp}$ at presence of two and more weakly differing by parameters b and σ distributions, sum of which is equal to $S_{\rm fit}$. Practical degeneration of the realized process makes difficult (but does not exclude) the use of the Gauss method for solution of systems of non-linear equations in form of existing library programs. But, the cases of appearance (as the most probable value) of near to zero values σ and corresponding to them "steps" in cumulative sums exclude possibility to use this method. Id est., some part of neutron widths sets contains, as the most probable, some quantity of non-random values.

In this situation the most simple way for fit of parameters of the width distribution is to use the Monte-Carlo method of solution of the systems of degenerate equations. Namely—combination of randomly choice of elements of correction vector of parameters for fitted function with maximum possible variation of their initial values. By the use of two and more sets of unknown parameters (2) for approximating curve it is very worth while to account strong anti-correlation of the total value of cumulative sums for different k for acceleration of convergence to zero the length of correction vector. The used (and decreasing with different speed) in this work their values for the beginning of random process were varied usually by 1 to 5 percents of initial values of b, σ and c. This provided achievement of local minimum of c after some tens of thousands of iterations. Obvious criterion of achievement of absolute minimum of c for such well regulated function as cumulative sums—equality of value of approximating function to the value c of the main part of the experimental data, but may be non-effective for the maximal values c in the parameters of the weight c of the maximal values c in the parameters of the width distribution is to use of the decreasing c of the width distribution is the value of the experimental data, but may be non-effective for the maximal values c of the value of the experimental data, but may be

In practice, the unsolvable problem is setting of dispersion σ_{cum} of each point of cumulative sum for arbitrary X value for calculation of unshifted value χ^2 . The regularity of the data set in cumulative sum sharply decreases fluctuations of form of the analyzed here data. By normalization of cumulative sum on the experimental number of resonances, σ_{cum} changes from zero to the some maximal value in region of magnitudes $X \approx 2$ -10 (see. Fig. 1) and then - up to zero. Dispersion of each element of cumulative sum consists from the experimental error of neutron width and unknown value of its fluctuations. Naturally, it must be one and the same in all variants of approximation for $1 \le k \le 4$.

Methodically, the problem has the simple solution: there are generated the large (minimum 10^6 random numbers) sets of cumulative sums of squares of normally distributed random values with given b and σ for each partial function. Then, by means of usual relations of mathematical statistics, from them is determined for each value of variable the dispersion of cumulative sum $\sigma_{\text{cum}}=f(X)$ in any point X. But, really this procedure requires unacceptable computer time. Therefore, possible change in value χ^2 for different expected densities of neutron resonances for realistic magnitudes of dispersions of cumulative sums was performed only for 232 Th, 233,235 U and 239 Pu and only in variant b=0 and $\sigma=1$. The main results of given here analysis keep and in the realized case $\sigma_{\text{cum}}=1$.

Besides, it must be taken into account that the practical search of parameters b and σ , which provide minimum of χ^2 in the used algorithm of analysis, cannot guarantee the best approximation of the experimental data in arbitrary variant of calculation. Only many times

เลยโด ว่า ได้เปลี่ยว ระได้เกี่ยว เรื่องจะไป โดยได้ เลยได้เลยได้

repeated variation of initial values and ways of random processes provides the sufficient for practical applications reliability and precision of determination of the lowest possible value χ^2 . The results of approximation of the experimental cumulative sums, as it is seen from the comparison of the data presented in figures 2-18 for each nucleus, depend on model notions and, first of all, on concrete value k. The analysis was limited by nuclei in which the set of sresonances had, with some exceptions, the value $N_r \approx 90$ and more.

5. On influence of experimental systematical errors to the approximation parameters

An attempt of objective estimation of the portion of resonances not observed in experiment with accounting of possible discrepancy of their real distribution to the Porter-Thomas distribution was realized in [16]. There was obtained, proceeding from independence of χ^2 on varied portion of omitted resonances, that this criterion of the maximum likelihood method can have the lowest and equal value in the interval corresponding to the portion of omitted resonances from zero to $\approx 90\%$. This result is truthful, at least, for actinides. Id est., the value of the most serious systematical error for density of neutron resonances (and, correspondingly, mean value of widths) cannot be objectively determined at present from the model approximations of the observed data and following extrapolation of the approximated distributions to their zero value.

Some notion on the value of the next by significance uncertainty of analysis can be obtained from the data [14] for 99 Tc. According to this compilation, there are at present two Γ_n^0 values sets [17, 18], which contain:

(a) 658 and

(b) 689 s- and p-resonances. Accordingly, the number of s-resonances for them is equal to 516 and 383. The results of approximation of these four sets are compared in Fig. 19. It is seen that the errors of determination of orbital momentum of resonances and/or their omission do not change principally the conclusion on possible difference of structure of neutron resonances and rather weakly change the form of cumulative sum for the case l=0. Twofold change of number of p-resonances noticeably distorts the form of cumulative sum in the region of the largest values of X. The sum of the χ^2 values for l=0 and l=1 in variant k=1 for the set (a) is 1.3 times more than for (b); for k=4 they practically coincide. Id est., examined systematical errors in determination of l and Γ_n^0 values bring distortions in the picture of the studied here nuclear properties, which are acceptable for reliability of conclusions obtained below.

6. Problems of interpretation the results of analysis

The key problems of analysis of the form of neutron widths distributions for the experimental data, as it can be seen from the data presented in Figures 2-18, are the determination of the number of possible types of their wave functions with maximally possible reliability and determination of $\langle g \Gamma_n^0 \rangle$ with the highest precision. The seriously problem here is the really unknown and not removable fluctuations of cumulative sums in function of parameter X. Id est., it is necessary to extract new information on properties of neutron resonances at presence of different nature significant deviations of the experimental data from their real value and not removable ambiguity of the used algorithm of analysis.

Parameters of approximation (Figs. 2-18) contain superposition of useful and wrong information and depend on:

- (a) portion of resonances with the widths which are less than the registration threshold,
- (b) structure of resonances under consideration,

(c) systematical error of determination of mean value $\langle g \Gamma_n^0 \rangle$,

(d) systematical errors of determination of parameters of the each existed resonance and

(e) magnitude of dispersion of their pure "nuclear" fluctuations.

This mixture can be decomposed onto components only with using of the additional experimental data. The existing and potentially possible nuclear models like [8] cannot provide acceptable for the present solution of such problem. The ground here can be only the hypothesis of the Gauss form of distribution of neutron amplitudes. But, the performed analysis also is not the more or less strong proof of last essumption — the lack of any facts which contradict any hypothesis cannot be its proof.

The attempt [16] of maximally correct approximation of the distribution parameters of the experimentally observed resonances for the following extrapolation of the distribution to Γ_n^0 =0 demonstrated that the accepted in [8] assumption about small portion of omitted resonances is not grounded. There is possible with non-zero probability the situation that the number of resonances below threshold of experiment can many times exceed the number of the observed resonances: analysis [16] showed that the maximally probable density of resonances can be 5-10 times larger than the accepted values. This conclusion was obtained in the frameworks of the only hypothesis of the Gaussian form of the distribution of neutron widths and does not require fixation of values k, b and σ .

Besides, this analysis allow also to estimate of the lowest number of resonances which permits one to determine realistically the presence/absence of noticeable variations of structure of wave functions of resonances. Any distribution from assumed superposition must contain much more resonances than the number of parameters (which equals three for every k). Both the proof of truth or mistakenness of possible very considerable error of determination of D_{λ}^{-1} , and fact of existence of groups of resonances with different structure of their wave functions require corresponding decrease of the observation threshold of weak resonances and precise enough determination of their parameters as compared with the achieved by now level of the experiment in formativeness.

In spite of this, the performed analysis of 157 sets of resonances allows one to make conclusion on high probability that in experiment is really observed superposition of levels whose wave functions concern two or more their types. Such result was obtained owing to revealed in [16] zero or very weak dependence of parameter χ^2 (i.e. form of general approximating curve) on number of omitted resonances in wide enough interval of their values.

In Fig. 20 is shown the histogram of values of ratio R of approximation parameters $\chi^2(k=4)$ to $\chi^2(k=1)$. From this distribution follows that the analyzed set of the data has value $\langle R \rangle = 0.33(19)$. This permits one to make the conclusion on high probability of existence of resonances with different structures for nuclei of different mass and orbital momentums $0 \le l \le 3$. Realistic estimation of reliability of this conclusion requires, most probably, analysis of the factors of distortions of the experimental data (b) – (d).

7. Conclusion

1. The results of the performed analysis do not contradict the notion of normal distribution of neutron amplitudes with the changing from nucleus to nucleus parameters b and σ , at least, for the main part of studied resonances. In this case, the mean value of amplitudes and their dispersion can depend on structure of wave function of levels excited by resonance neutrons and, in principle, on excitation energy of a nucleus.

- 2. A totality of the data on parameters σ and b and dynamics of their change with change of mass of a nucleus fully permits possibility of values $\sigma = 1$ and b = 0 in some energy intervals of neutron resonances. The width of corresponding interval and its location in scale of excitation energy of given nucleus cannot be, most probably, one and the same for different nuclei.
- 3. Precision of the approximated by model [8] neutron resonance widths distribution (in the generally accepted notions or with the varied values of parameters b and σ) is enough for any practical applications.
- 4. It is possible that for determination of the reliable properties of a nucleus there are necessary the estimation of required precision of parameters of the width distribution for concrete situation (experiment) and the use of the best data for parameters of the available sets of widths.
- 5. The presence of several neutron amplitudes with different mean values and dispersions is alternative to [8] notion on distribution $g\Gamma_n^0$ practically for all nuclei studied here. It is worth while to take into account this possibility in analysis of distributions of widths by use of the new experimental data for maximal reliability of the obtained conclusions.
- 6. The increase of precision of determination of any nuclear-physics parameters requires, most probably, to take into account the degree of influence of structure of the excited nuclear levels on their density and emission probability of the nuclear reaction products in wide excitation energy diapason. In particular in the region of neutron resonances.
- 7. The unique conclusion on this statement requires one to perform the experiment, in which the observables depend on structure of wave function of resonances. For example, there can be the experiment, where is measured the ratio of intensities of the primary gamma-transitions to the groups of levels with different number of the broken Cooper pairs. This conclusion was made in [19] on the basis of approximation of the radiative strength functions of the primary gamma- transitions in near to the neutron binding energy diapason.

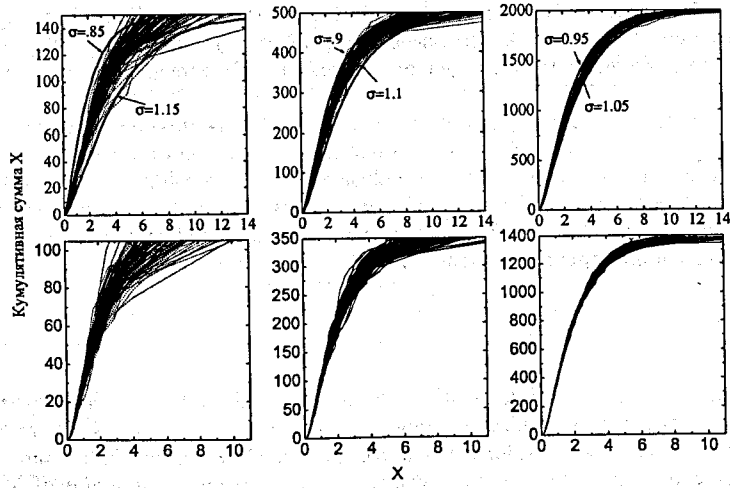


Fig. 1. Upper row – the example of cumulative sums for some tens of sets from 150, 500 and 2000 random X values. Lower row – cumulative sums for the same sets after exclusion of 30% of the lowest X values.

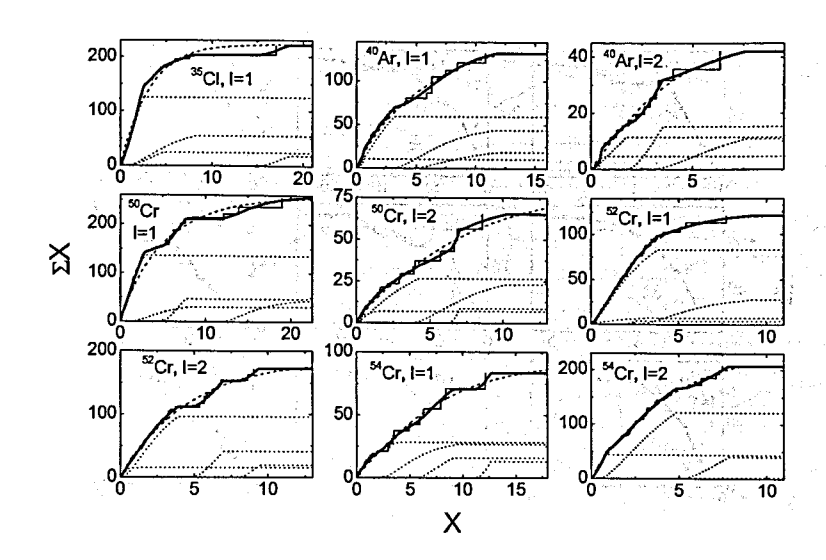


Fig. 2. The results of approximation of distribution of neutron widths for 35 Cl, 40 Ar and 50,52,54 Cr. Histogram – the experiment, dash line – approximation for k=1, thick line – k=4, dot lines – the variant of decomposition of experimental distribution over partial functions.

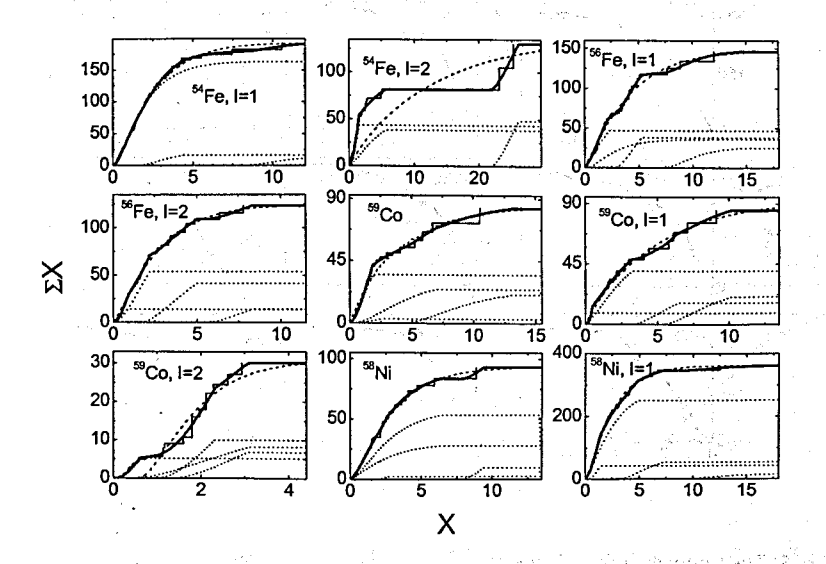


Fig. 3. The same, as in Fig. 2, for 54,56Fe, 59Co and 58Ni.

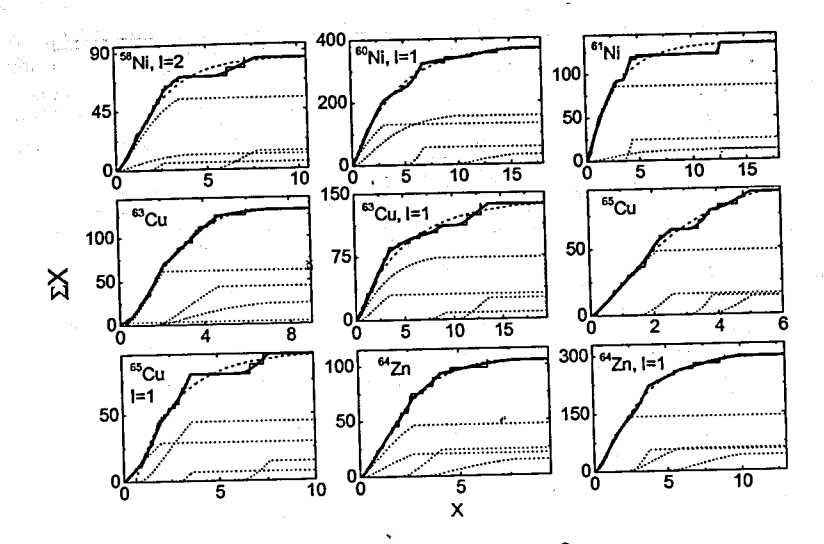


Fig. 4. The same, as in Fig. 2, for 58,60,61 Ni, 63,65 Cu and 64 Zn.

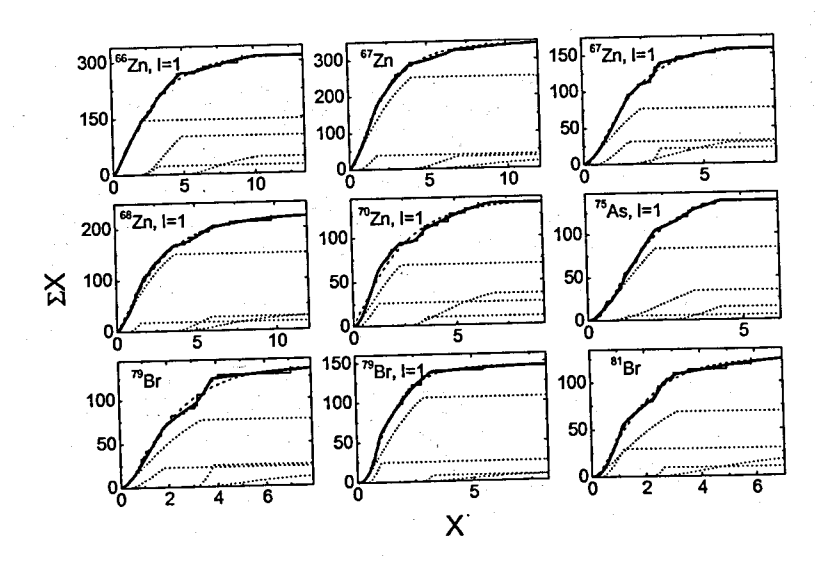


Fig. 5. The same, as in Fig. 2, for 66,67,68,70 Zn, 75 As and 79,81 Br.

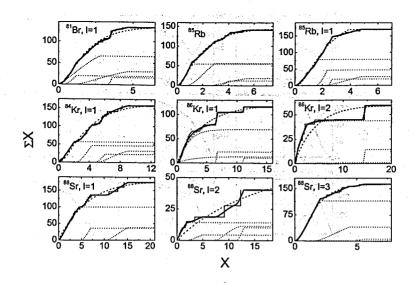


Fig. 6. The same as in Fig. 2, for ⁸¹Br, ⁸⁵Rb, ^{84,86}Kr and ⁸⁸Sr.

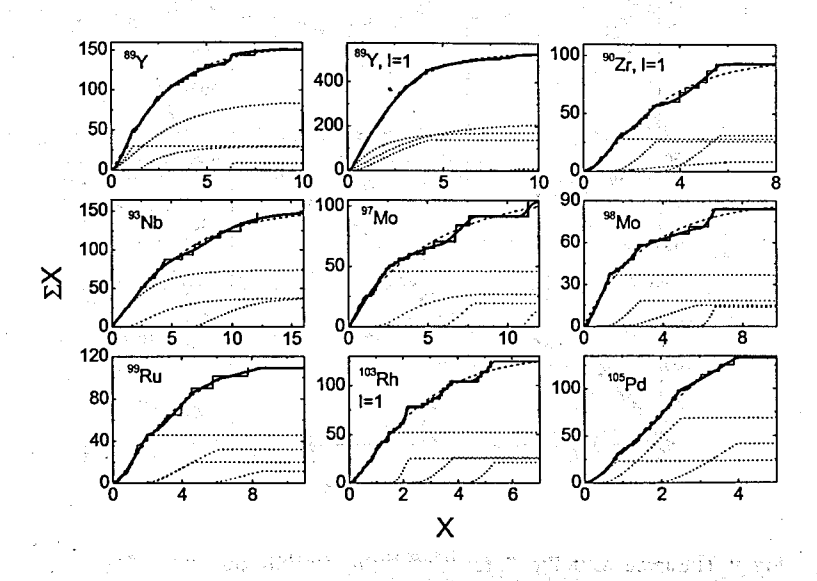


Fig. 7. The same, as in Fig. 2, for ⁸⁹Y, ⁹⁰Zr, ⁹³Nb, ^{97,98}Mo, ⁹⁹Ru, ¹⁰³Rh and ¹⁰⁵Pd.

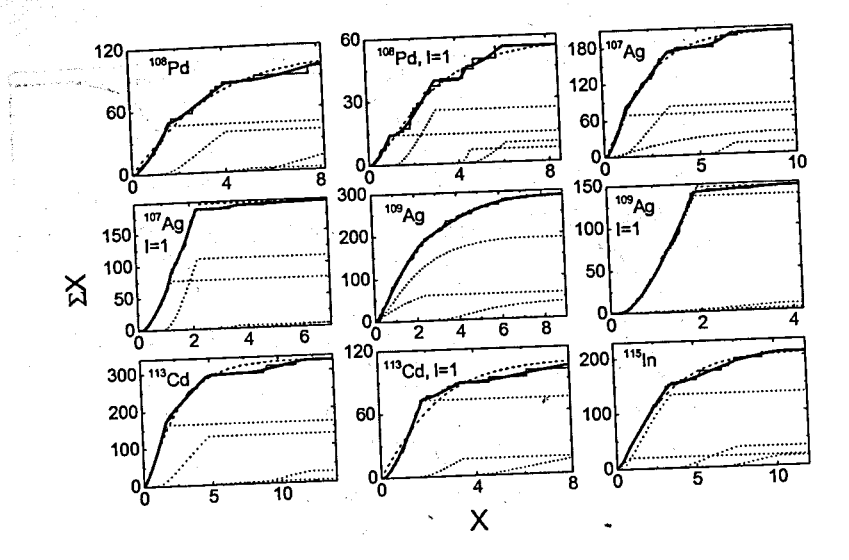


Fig. 8. The same, as in Fig. 2, for ¹⁰⁸Pd, ^{107,109}Ag, ¹¹³Cd and ¹¹⁵In.

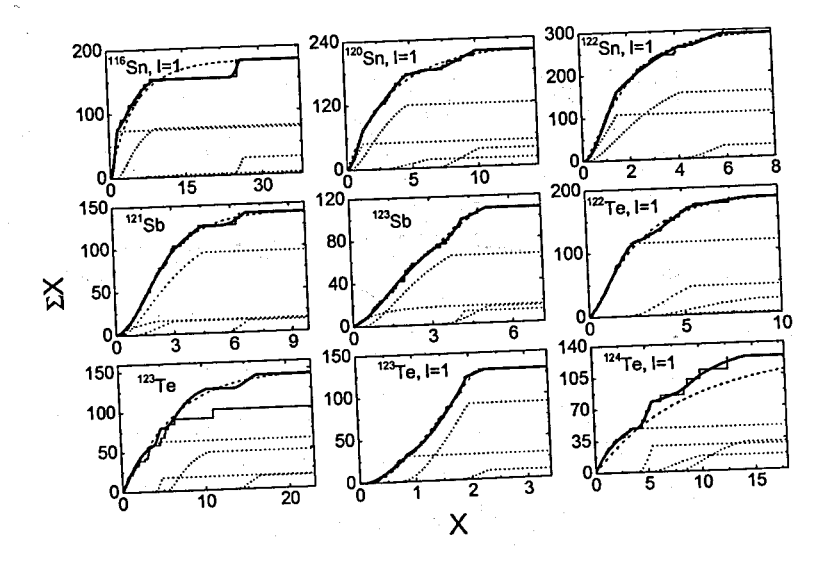


Fig. 9. The same, as in Fig. 2, for ^{116,120,122}Sn, ^{121,123}Sb and ^{122,123,124}Te.

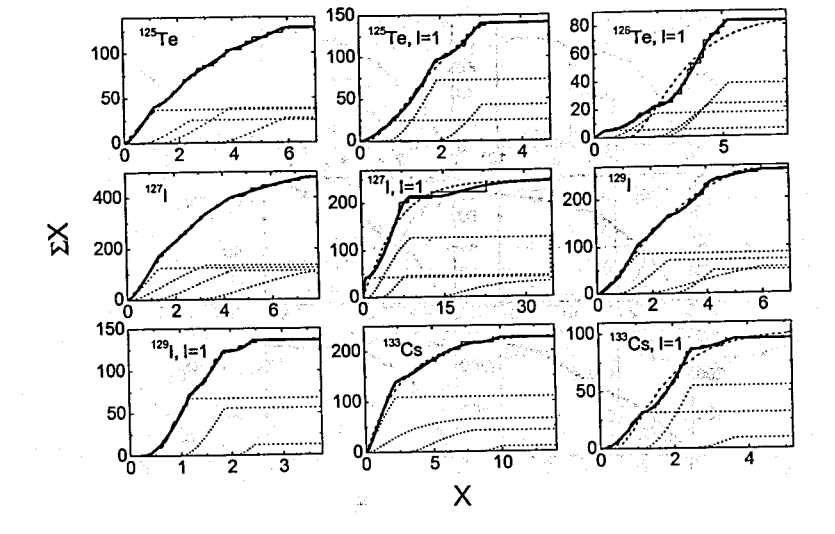


Fig. 10. The same, as in Fig. 2, for 125,126 Te, 127,129 I and 133 Cs.

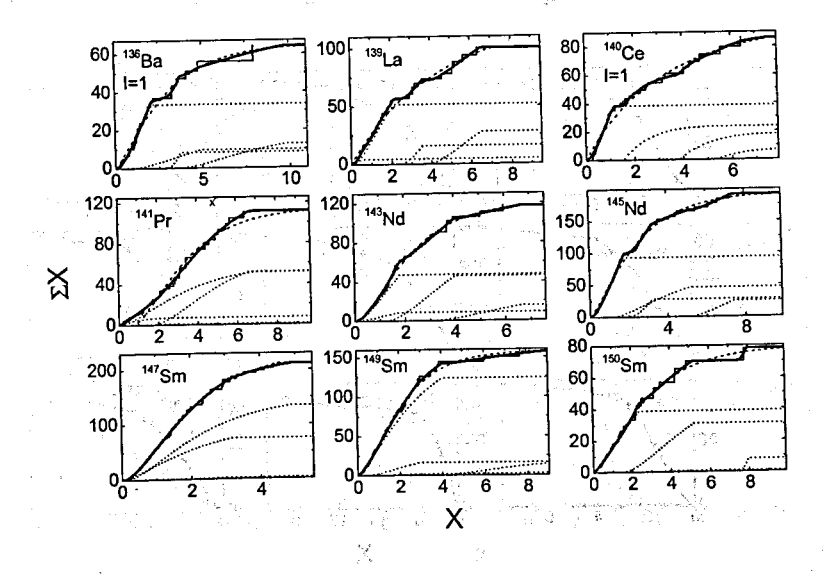


Fig. 11. The same, as in Fig. 2, for ¹³⁶Ba, ¹³⁹La, ¹⁴⁰Ce, ¹⁴¹Pr, ^{143,145}Nd and ^{147,149,150}Sm.

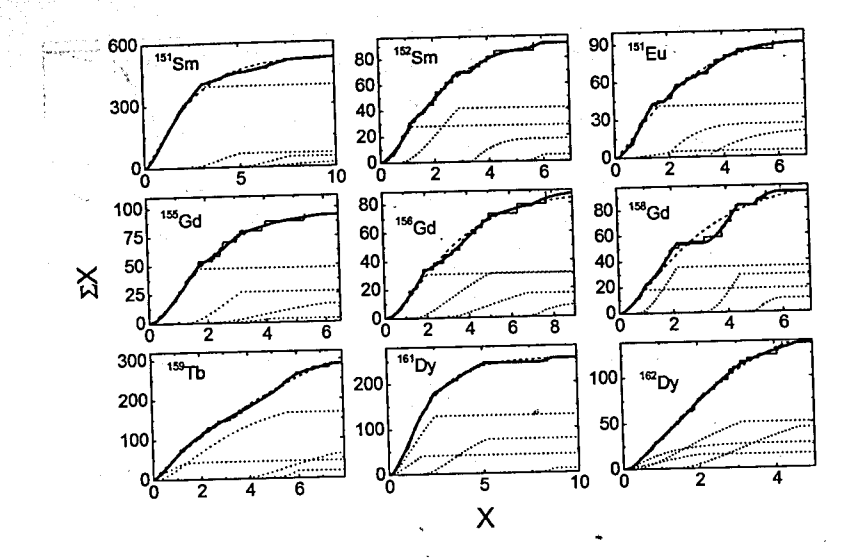


Fig. 12. The same, as in Fig. 2, for ^{151,152}Sm, ¹⁵¹Eu, ^{155,156,158}Gd, ¹⁵⁹Tb and ^{161,162}Dy.

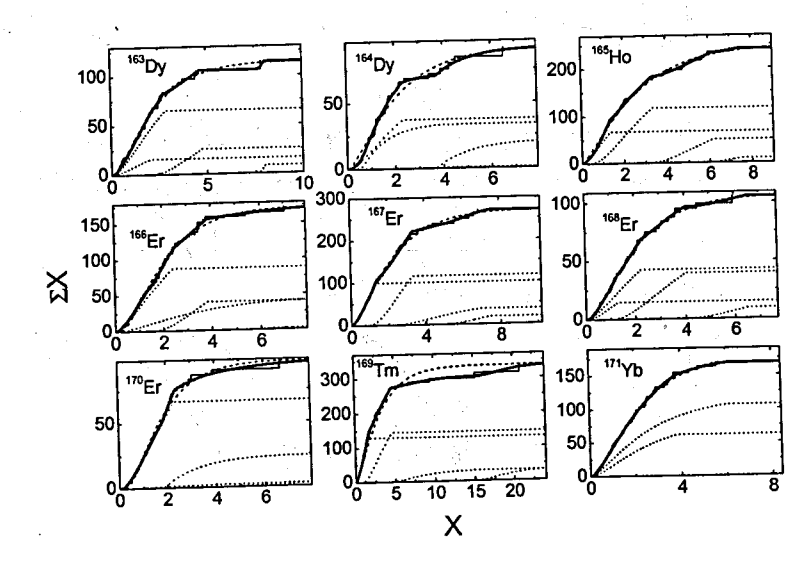


Fig. 13. The same, as in Fig. 2, for 163,164 Dy, 165 Ho, 166,167,168,170 Er, 169 Tm and 171 Yb.

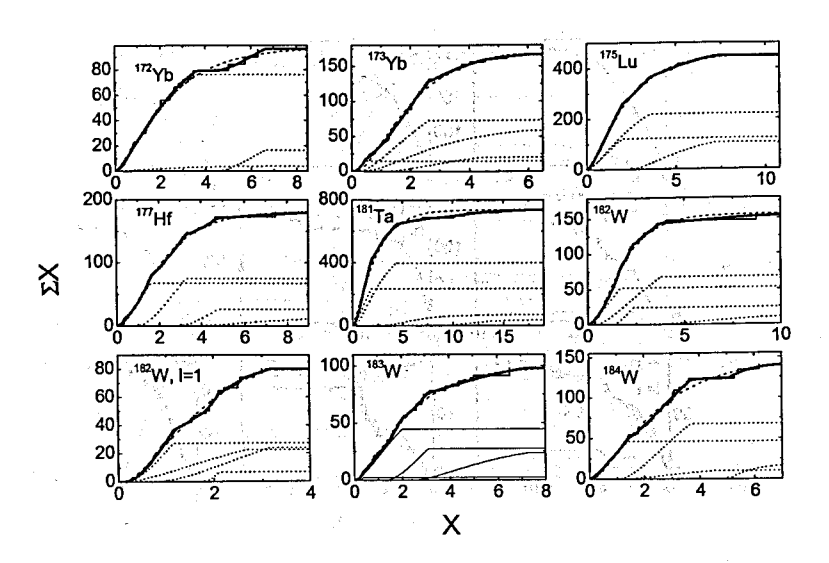


Fig. 14. The same, as in Fig. 2, for ^{172,173}Yb, ¹⁷⁵Lu, ¹⁷⁷Hf, ¹⁸¹Ta and ^{182,183,184}W.

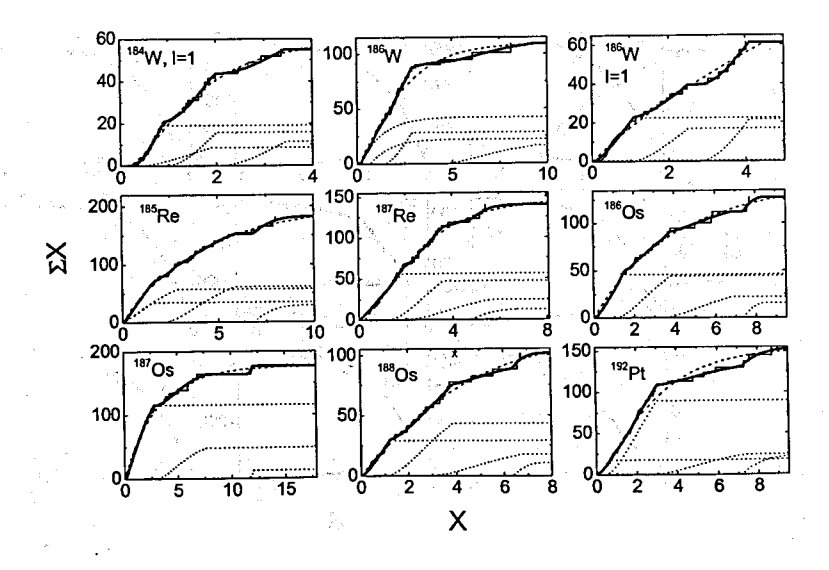


Fig. 15. The same, as in fig. 14, for ^{184,186}W, ^{185,187}Re, ^{186,187,188}Os and ¹⁹²Pt.

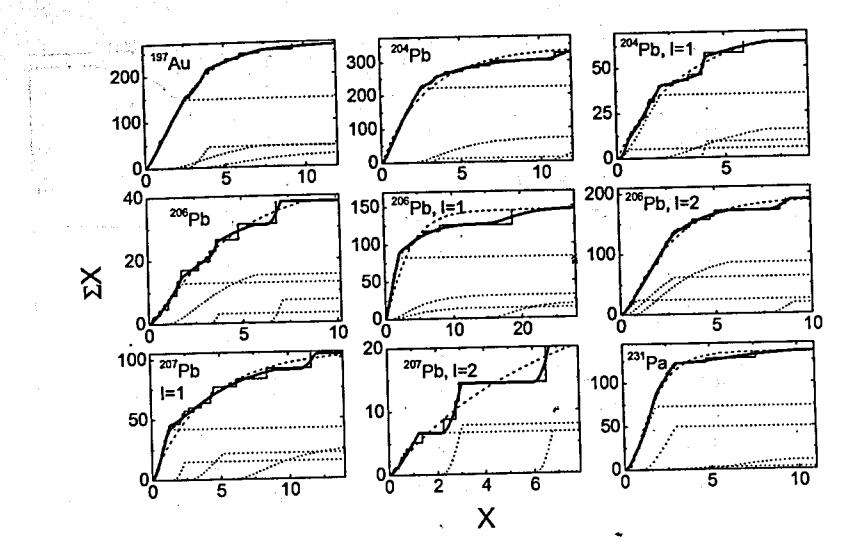


Fig. 16. The same, as in Fig. 2, for 197 Au, 204,206,207 Pb and 231 Pa.

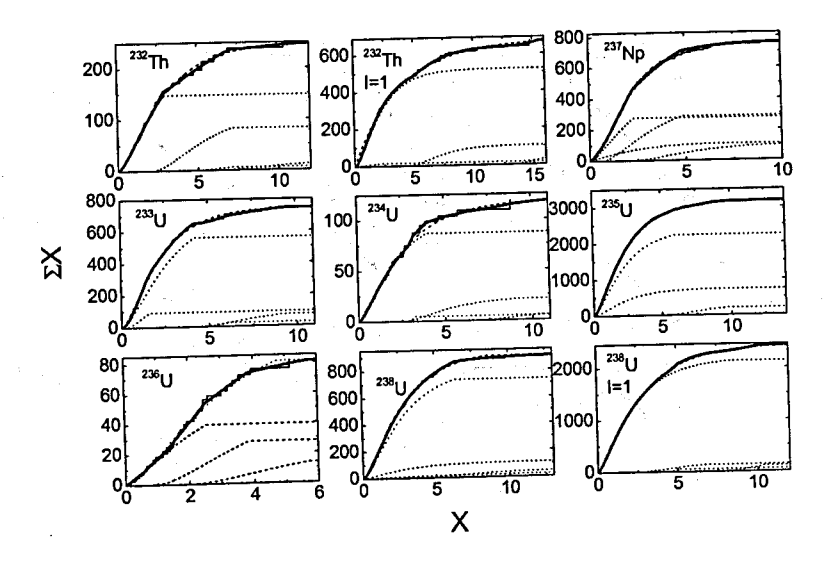


Fig. 17. The same, as in Fig. 2 for 232 Th, 237 Np and 233,234,235,236,238 U.

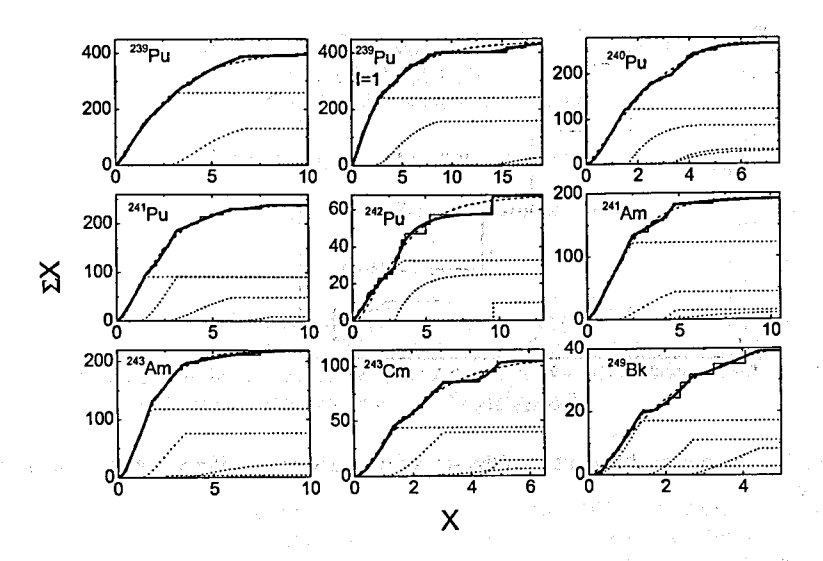


Fig. 18. The same, as in Fig. 2 for ^{239,240,241,242}Pu, ^{241,243}Am, ²⁴³Cm and ²⁴⁹Bk.

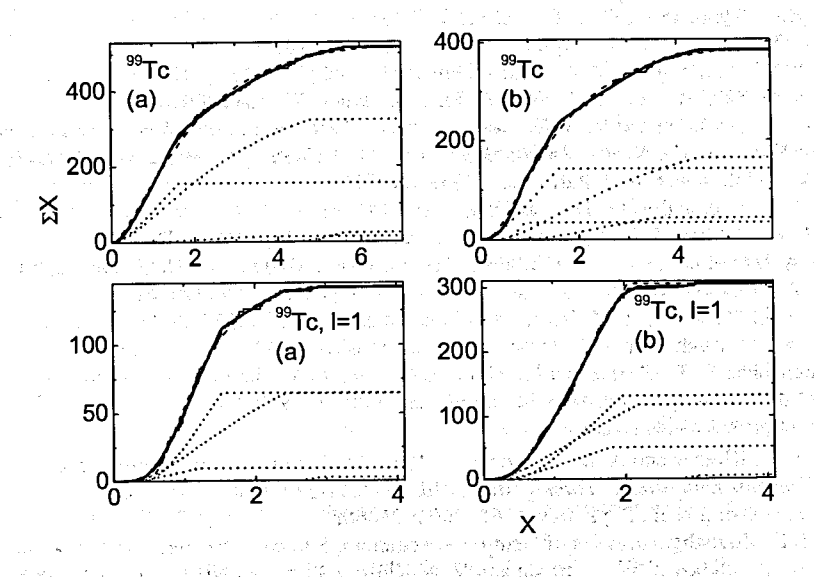


Fig. 19. Approximation of two sets of neutron widths of s- and p-resonances 99Tc.

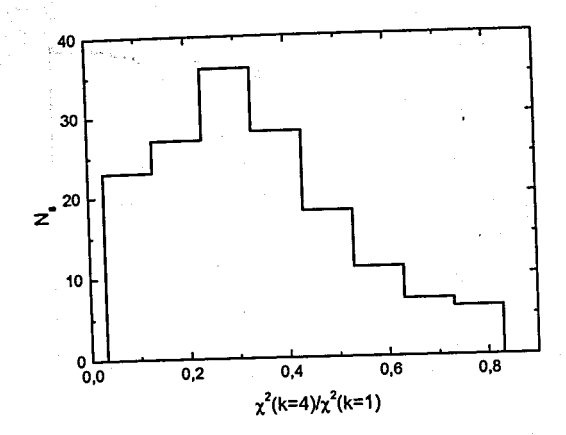


Fig. 20. Frequency distribution of the sets of resonances for different values $\chi^2(k=4)/\chi^2(k=1)$ ratio.

References

- 1. A. V. Ignatyuk, Report INDC-233(L), IAEA (Vienna, 1985).
- 2. H. T. Nyhus at al., Phys. Rev. C 81, 024325 (2010).
- 3. B. V. Zhuravlev et al., Phys. At. Nucl., 73, 1111 (2010).
- 4. A. M. Sukhovoj and V. A. Khitrov, Phys. At. Nucl., 73, 1507 (2010).
- 5. A. M. Sukhovoj and V. A. Khitrov, Phys. At. Nucl., 73, 1635 (2010).
- 6. A. M. Sukhovoj and V. A. Khitrov in: Proc. XVII International Seminar on Interaction of Neutrons with Nuclei, Dubna, May 2009, E3-2010-36, p. 268; nucl-ex/1009.4761.
- 7. V.G. Soloviev, Sov. J. Part. Nucl., 3, 390 (1972).
- 8, C. F. Porter and R. G. Thomas, Phys. Rev. 104, 483 (1956).
- 9. L. A. Malov and V. G. Soloviev, Sov. J. Nucl. Phys., 26, 384 (1977).
- 10. A. M. Sukhovoj and V. A. Khitrov, Preprint No. E3-2005-196, JINR (Dubna, 2005).
- 11. A. M. Sukhovoj and V. A. Khitrov, Phys. Part. Nucl., 37, 899 (2006).
- 12. A. M. Sukhovoj and V. A. Khitrov, Phys. Part. Nucl., 36, 359 (2005).
- 13. S.F. Mughabghab, Neutron Cross Sections BNL-325. V. 1. Parts B, edited by Mughabhab S. F., Divideenam M., Holden N.E., N.Y. Academic Press, (1984)
- 14. http://www.springermaterials.com/navigation/#l 1_197716
- 15. http://www-nds.iaea.org.
- 16. V. A. Khitrov and A. M. Sukhovoj, in Proc. XVIII International Seminar on Interaction of Neutrons with Nuclei, Dubna, May 2010, E3-2011-33 (Dubna, 2011), 216.
- 17. F. Gunsing et al., Phys. Rev. C 61 (2000) 054608.
- 18. S.F. Mughabghab, Atlas of Neutron Resonances, 5-th ed., Elsevier, The Netherland, 2006.
- 19. A. M. Sukhovoj, W.I. Furman and V. A. Khitrov, Phys. At. Nucl., 71, 982 (2008).

MODIFIED MODEL OF NEUTRON RESONANCES WIDTH DISTRIBUTION. ESTIMATION OF THE QUALITY OF RESULTS AND INTERPRETATION OF AVIALABLE PHYSICS INFORMATION

A.M. Sukhovoj, W.I. Furman, V.A. Khitrov

्राप्त कर्मा के का नाम की कार्यक्रम के अनुसार के किया है। इस माने के साम के किया है किया है कि किया है। किया क विकास कर्मा के किया की कार्यक्रम के अनुसार की किया की किया की किया की किया की की किया की किया की किया की किया

Joint Institute for Nuclear Research, Dubna, Russia - ละ - และสาราช และสาราช ซากับ ซากับ ซากับ เลือดสาราช เกิดเลือดสาราช เลือดสาราช เลือดสาราช เลือดสาราช เลือดสาร - สาราช เลือดสาราช ซากับ ซ

Abstract

ાના પુત્રા પ્રાપ્ય માનવાના તેવા હોય જેવા જાણી પ્રાપ્તિ પ્રાપ્તિ માનવાના છે. જે પ્રાપ્ય પ્રાપ્તિ માનવાના માનવાન In the work was performed analysis of parameters of approximation of 157 sets of resonances in the mass region of nuclei 35 \leq A \leq 249. It was shown that the experimental values of widths can correspond with high probability to superposition of several independent neutron widths with their non-zero mean values and non-unit dispersion. ्राचार के अने के हो। प्रोत्तर के किया की किया के किया के किया किया के किया की किया की किया की किया की किया की जान के अने के हो प्रोत्तर के किया की किया किया किया किया किया की किया की किया की किया की की किया की की की की क

1. Introduction

Extraction of any nuclear-physics information is impossible, at least, at present without the use of model ideas. These ideas are formed on the grounds of the limited by volume and distorted by errors of experiment information. Moreover, usually there is realized the analysis algorithm which provides objective unambiguity of the obtained conclusions on determined parameters of a nucleus. As a consequence, determined with unknown error of a and the state of the contract of the state of model.

One can bring as an obvious example the problem of determination of penetrability T for product emission of the used reaction and level density ρ of complicated nuclei in excitation region where the mean spacing between them $D=\rho^{-1}$ is less than resolution of spectrometer FWHM. The known methods for determination of this value [1] and [2] from one-step reactions (registration of reaction products without regime of coincidences) the use, for example, the not tested model notion on independence of the $T=f(E_{prod})$ values on excitation energy of final nucleus. Evident mistakenness of this hypothesis was revealed [3,4] by analysis of the experimental data of the two-step reaction $(n,2\gamma)$. This fact could be obtained more earlier. For this the authors of corresponding experiments had to perform analysis of obtained data in comparison of its results by means of different nuclear models. Here - of two long ago known, but principally different models of level density [5,6].

There is rather considerable and the other aspect of this problem: connection between the measured spectra (cross-sections) and determined parameters of reaction under study is nonlinear, and systems of corresponding equations are badly stipulated or degenerated. I. e., the desired data, at least in some cases, cannot be unambiguous even in principle. However, the interval of their possible values, corresponding to maximum of the likelihood function, can be final [3,4].

2. The problems of the use of new method for analysis of the neutron width distributions

This situation is observed and by analysis of the data on the reduced neutron widths of resolved resonances in frameworks of the modified model of their distribution (several independent neutron amplitudes with different mean values and dispersions can correspond to the existing set of the experimental Γ_n^0 values). There were used in the corresponding method [7] the model ideas which are equivalent to the widest set of the fitted functions (the Porter-Thomas distribution [8] -their only particular case) and selection of the most suitable one is performed by the criterion χ^2 . In this case, to the same minimum of χ^2 in variant of the best approximation usually correspond the functions with different values of the parameters. But only their superposition in any set from 157, presented in [7] results of analysis of the concrete Γ_n^0 values, was the only which reproduced cumulative sums of the experimental widths with a precision which is higher than that provided by model [8].

Just so was obtained the main conclusion of analysis [7] – neutron resonances of any nuclei with $A \ge 35$ for $0 \le l \le 3$, as a minimum, can have different structure of their wave functions. And number of probable groups of like by structure neutron resonances can achieve the value k=4. Unfortunately, at present this conclusion is not, as a minimum, absolute. As a consequence, it is necessary, first of all, to take into account and analyze a possibility that the interpretation of the experimental width distribution as a superposition of several identical functions with different values of parameters of their neutron amplitudes can be the result of random (first of all – nuclear) fluctuations of widths of resonances.

Although the number of the experimental values of neutron widths strongly exceeds the number of parameters of approximating curve (4 -for variant k=1, 13 - for k=4) for the main mass of nuclei by ≈ 80 and more units, the number of degrees of freedom decreases when X increases. This circumstance excludes any possibility of simple application of the criterions of mathematical statistics for estimation of probability of random appearance of small values of $R=\chi^2(k=4)/\chi^2$ (k=1). Just small volume of the data on the Γ_n^0 values does not allow one to make absolute conclusion on this account only from analysis of ratios χ^2 for competing notions.

Therefore, besides the analysis of the experimental data it is worth while in addition completely to model the algorithm of the method [7] for random values which correspond by their quantity to typical experimental sets. One variant must by parameters of distribution correspond to model [8], the other - to typical values [7].

3. Analysis of results of approximation of experimental data in modified model

The statement on reliability of the main results of approximation [7] requires, first of all, to proof their independence on mass of nuclei and number of resonances in the approximated sets. This can be done only by means of analysis of ratios $R = \chi^2(k=4)/\chi^2(k=1)$ as unitary set of random values. The data in Fig. 1 do not reveal evident dependence of the R values for nuclei with different parity of nucleons and orbital momentums of neutrons. Its maximal scattering for the lowest numbers of resonances N_r in any of 157 data sets has, most probably, clearly statistical nature. The mean value of R for s-resonances varies from 0.34(16) to 0.42(22) for nuclei with different parity of nucleons, and from 0.30(16) to 0.21(15) for their p- and d-resonances. (Discrepancy of this scale for different l is, most probably, caused by imperfection of the methods for determination of the momentum values of concrete resonances.)

In Fig. 2 are given the ratios R of parameters of approximation, averaged over several intervals of nucleus mass A and numbers of resonances N_r . Evident absence of dependence on both parameters and their considerably less than unity experimental and model values for big enough N_r quite correspond to preliminary conclusion [7] on existence in arbitrary nucleus of superposition of neutron resonances with different structure.

Relatively small random fluctuations of form of the width distribution at truth of the Porter-Thomas distribution [8] can be expected for the sets of resonances with their number $N\approx$ 400-500 and more. That is why, the approximate conservation of form of the analyzed cumulative sum of widths in different energy intervals of neutron resonances of large enough

width would be an additional argument in favor of hypothesis on superposition of neutron resonances of different structure in their experimentally obtained set.

Really such analysis (although with insufficient data set) can be performed only for s- and p-resonances of 235 U and 238 U respectively. Although in compilation [9] and library ENDF/B-VII [10] are given the data on of spins of resonances, but at absence of the quantitative data on reliability of their determination it is preferably to use in the testing analysis the values $g \Gamma_n$. Both sets contain resonances with two possible spins. Therefore, the possibility of difference between the mean values of $g \Gamma_n$ can bring to superposition of two distributions with the expected and practically constant relation of their contributions in the total function at any neutron energies E_n , but, in principle, with different parameters of their neutron amplitudes. (The evaluated data of 238 U for p-resonances contain "fictitious resonances" of small width, introduced by authors [11] for reproduction of the capture cross sections of neurons. But they, probably, increase the ratio R.)

The energy interval of the studied resonances E_n for the nuclei under consideration equals 2.26 and 20.0 keV, respectively. Cumulative sums of g Γ_n were obtained in two variants in the intervals of energy $\Delta E_n = 0.45$ and 4.0 keV for the data presented in Fig. 3 and $\Delta N_r = 450$ and 400 (Fig. 4) for ²³⁵U and ²³⁸U respectively. Approximation of these cumulative sums was performed completely by analogy with [7]. Id est., by singular distribution (k=1) with varied magnitudes of the mean value of neutron amplitude b and its dispersion a. The variant with superposition of four such distributions was used for comparison of the obtained results. The obtained ratios $\chi^2(k=4)/\chi^2(k=1)$ for each interval are shown in Fig. 5, and approximated parameters b and a0 in Fig. 6.

As it is seen from Fig. 4, cumulative sums for 235 U change from interval to interval more strongly than for 238 U. In correspondence with the experimental data [7] and theoretical analysis [12], one can expect, from the one hand, noticeable change of structure of resonances in 235 U just inside of the accessible to the experiment by the time-of-flight method region of neutron energies. On the other hand, one cannot exclude and possibility of resulting influence of omission of s-resonances and increase of portion of the mistakenly identified p-resonances at increase of E_n .

The comparison of the values of ratio $\chi^2(k=4)/\chi^2(k=1)$ for different intervals of neutron energies with the values from [7] allows one to conclude that, with the high probability, the set of the experimental widths corresponds to superposition of several distributions, but it is not the result of random grouping of the widths at some their values. Also, the b and σ parameters undoubtedly change at change of E_n (as a mass of a nucleus), as it follows from theoretical analysis [12] by V.G. Soloviev and L.A. Malov of main principles of fragmentation of the complicated nuclear states. Making more precise reliability this conclusion or its refutation requires the data on some thousands of resonances for many nuclei with different parity of nucleons and from different diapasons of their masses.

In Fig. 7 are compared the best parameters b and σ of distribution of neutron amplitudes of all 157 nuclei in the variant of approximation k=1 with analogous values of the partial distribution, which gives the greatest contribution in approximation of the experimental cumulative sum. Noticeably lesser scattering of the latter is indirect confirmation of conclusion [7] on presence in any nucleus of levels with different structure and above the neutron binding energy.

As it can be seen from comparison of Fig. 7 and the data of Table 1, considerable fluctuations of parameters b and σ point to presence in the tested sets of the reduced neutron widths of noticeable systematical errors, as a minimum. And, as a maximum—on presence of evident deviations of these parameters from assumptions [8]. Therefore, the available data do not allow one to make the final choice between the variants k = 1 and $k \ge 2$.

The results of approximation [3] of the experimental level density below the neutron binding energy, determined from the spectra of intensity of cascade gamma-transitions show that one can expect noticeable change in structure of neutron resonances at change of nucleus excitation energy by $\Delta E_{ex} \equiv 1\text{-}2$ MeV. So, one can expect small enough variations of magnitudes of the parameters b and σ in the interval of neutron energy of about some tens keV or somewhat less. And the best parameters of width distribution in neighboring intervals of neutron energy differ only in limits of errors of approximation. As a result, there is the main basis of quantitative modeling of the approximation process. This was done for two possible variants of the initial model set. It is assumed that such set corresponds [8] to:

(a) the unique (k=1) partial distribution, or to

(b) superposition of several (k=4) partial distributions of neutron amplitudes.

Table 1. The averages of the best values of approximation parameters of variant (a).

| В | b ₁ | b ₂ | b ₃ | b ₄ |
|-----------|--------------------------------------------------------------------------------------|-------------------------------------------------------------------------------------------------------------------------------------------------------------------------------------------------------------------------------------------------------------------------------------------------------|-------------------------------------------------------|-------------------------------------------------------|
| 0 | .=1 11 | - | - 11 2 1 | .= L |
| -0.14(43) | -0.05(19) | 1.60(46) | 1.78(28) | 1.58(52) |
| -0.02(11) | 0.08(8) | 2.07(42) | 1.62(55) | 1.88(46) |
| 0.03(6) | 0.015(86) | 0.73(55) | .2.06(77) | 1.49(60) |
| Σ | σ_1 | σ_2 | σ ₃ | σ ₄ : πουθ |
| 1 | - | - 54 € | • 10 E | - tas han begs |
| 0.90(14) | 0.19(4) | 0.07(8) | 0.05(4) | 0.01(3) |
| 0.88(19) | 0.66(24) | 0.58(34) | 0.82(41) | 0.66(38) |
| 0.90(29) | 0.96(11) | 0.42(23) | 0.64(22) | 0.66(36) |
| С | c _l | c ₂ | C ₃ | C4 5.3 |
| 1 | □ (1) (1) (2) | - ≟ degi uz ud | 411.0 T | |
| 1 | 0.52(9) | 0.26(8) | 0.15(4) | 0.07(2) |
| 1 | 0.90(5) | 0.07(4) | 0.025(19) | 0.004(3) |
| 1 | 0.79(14) | 0.17(14) | 0.03(3) | 0.027(37) |
| | 0 -0.14(43) -0.02(11) 0.03(6) Σ 1 0.90(14) 0.88(19) 0.90(29) | $\begin{array}{cccc} 0 & - & & - & \\ -0.14(43) & -0.05(19) & \\ -0.02(11) & 0.08(8) & \\ 0.03(6) & 0.015(86) & \\ \Sigma & \sigma_1 & \\ 1 & - & \\ 0.90(14) & 0.19(4) & \\ 0.88(19) & 0.66(24) & \\ 0.90(29) & 0.96(11) & \\ C & c_1 & \\ 1 & - & \\ 1 & 0.52(9) & \\ 1 & 0.90(5) & \\ \end{array}$ | $\begin{array}{c ccccccccccccccccccccccccccccccccccc$ | $\begin{array}{c ccccccccccccccccccccccccccccccccccc$ |

Table 2. The averages of the best values of approximation parameters of variant (b).

| parameter | В | b_1 | b_2 | b ₃ | b ₄ |
|---------------------|---------------------|--------------|------------|----------------|----------------|
| model | - | 0 | 1 | 1.4 | 1.7 |
| $N_r = 100$ | -0.4(4) | -0.2(2) | 1.5(3) | 1.7(2) | 2.1(5) |
| $N_r = 500$ | -0.2(1) | -0.2(2) | 1.4(2) | 1.4(2) | 1.8(2) |
| $N_r = 3000$ | -0.3(1) | -0.2(1) | 1.3(1) | 1.5(2) | 1.6(2) |
| parameter | Σ | σ_{l} | σ_2 | σ ₃ | σ ₄ |
| model | - | 0.4 | 0.3 | 0.2 | 0.1 |
| $N_r = 100$ | 0.45(13) | 0.50(1) | 0.28(16) | 0.23(8) | 0.04(4) |
| N _r =500 | 0.31(8) | 0.50(1) | 0.21(5) | 0.24(10) | 0.11(5) |
| $N_r = 3000$ | 0.3(1) | 0.50(1) | 0.31(4) | 0.21(3) | 0.09(2) |
| parameter | C | cı | c_2 | C ₃ | C4 |
| model | ₩ gran to the North | 0.45 | 0.25 | 0.2 | 0.1 |
| $N_r = 100$ | 1 | 0.54(8) | 0.10(11) | 0.17(11) | 0.18(8) |
| $N_r = 500$ | .1 () () | 0.49(10) | 0.20(12) | 0.08(7) | 0.22(12) |
| $N_r = 3000$ | 1 | 0.55(7) | 0.10(9) | 0.06(7) | 0.29(4) |

Accordingly, the quite random approximation parameters in the first variant will be C, b, σ with indexes 1-4, in the second -B and Σ . The analysis was performed for three sets of the random X values which cover the interval of number N_r of the included in analysis resonances.

It should be noted that the mean value $\langle g \Gamma_n^0 \rangle$ in method [7] will be always shifted at presence of superposition of several $(2 \le k \le 4)$ types of the resonance wave functions even at absence of any experimental errors. Therefore, all the parameters of the best approximation will be shifted relatively to the initial values b and σ . The same concerns and parameter Σ of the variant k=1: its significant deviations from unit are always presented in the used normalization to the experimental mean value $\langle \Gamma_n^0 \rangle$.

The random differences between the approximation of the modeled distribution and their initial values are small enough as at determination of B and Σ (Table 1), as for $b_1 - b_4$ and $\sigma_1 - \sigma_4$ (Table 2) even for the set from $N_r = 100$ resonances (random values X).

The dependence of B and Σ on random set number ("mass of nucleus") for variants k=1 and k=4 is shown in Fig. 8. It is possible to estimate from this modeling the number of resonances N_r , which is necessary in order to obtain reliable conclusions on real parameters of neutron amplitudes by quantity of about 3000-4000 and more.

ti en la glade la unidenta de la compania de la co En la compania de la

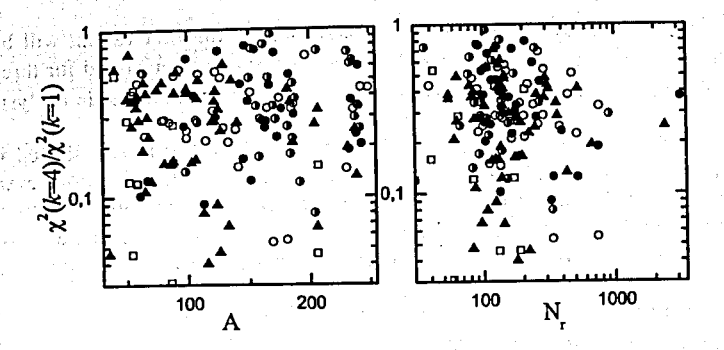


Fig. 1. The ratio of criterions χ^2 for two variants of analysis in function on nuclear mass A or number of resonances N_r . The circles: closed – even-odd, open – odd-even, semi-open – even-even target nuclei. Triangles – p-, squares – d-resonances of any nuclei.

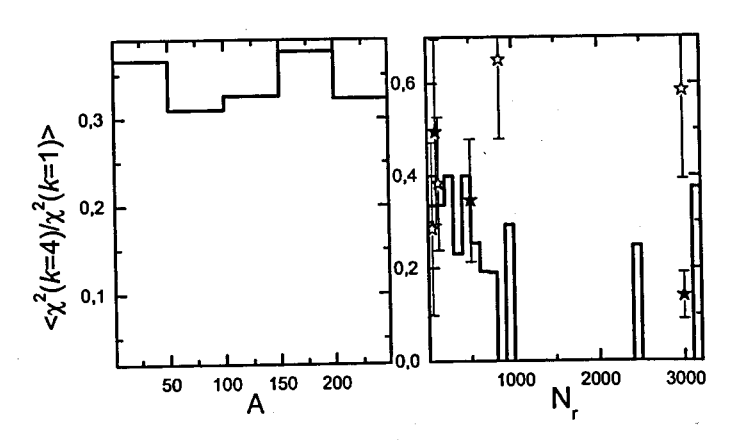
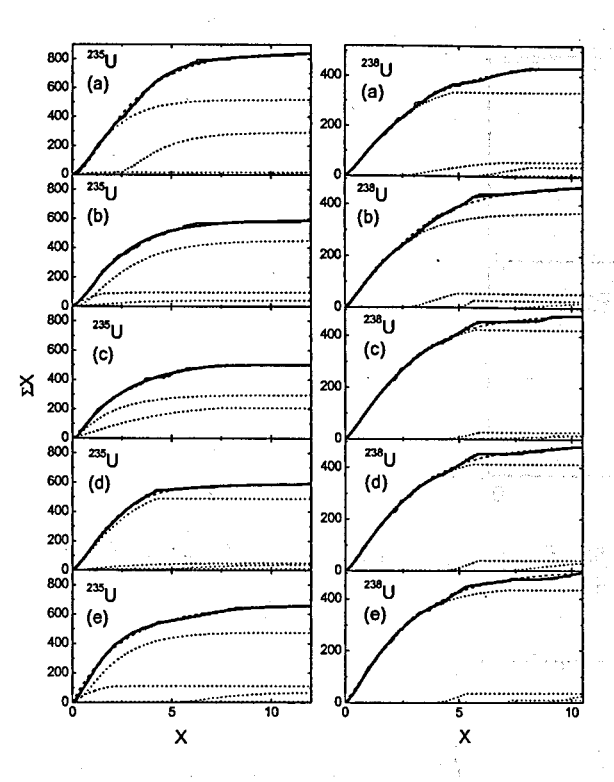


Fig. 2. Histograms are the ratio of average criterions χ^2 for two variants of analysis in function on nuclear mass A or number of resonances N_r . Points with errors – model (expected) value for independent neutron amplitude distributions (closed – the case k=1, open – the case k=4).



1,157

Fig. 3. Approximation of cumulative sums of the relative X values for five intervals of neutron energies of constant width in 235,238 U. Histogram – the experiment, dash line – approximation for k=1, thick line – for k=4, dot lines – the variant of decomposition of the best fit functions over partial functions.

on Stariford and Star in Start and America in the Start and Algeria Starta in Start

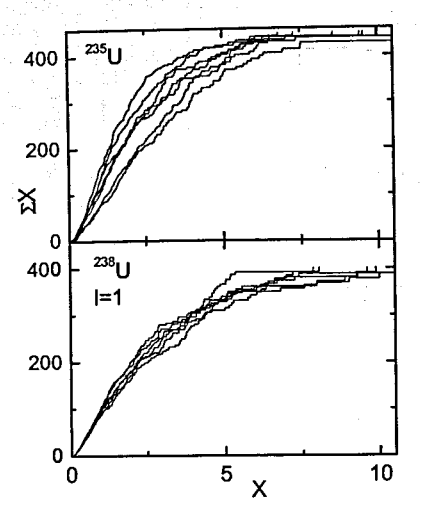


Fig. 4. Cumulative sums of the X values for the same number of resonances in each of 5 intervals of the E_n values of nuclei 235,238 U.

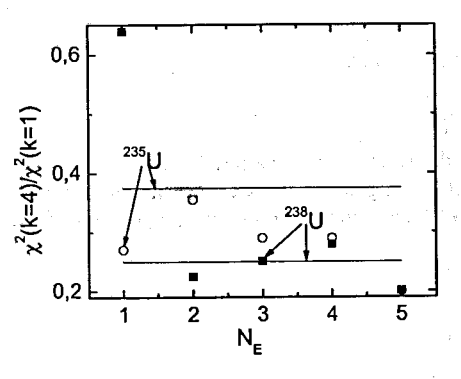


Fig. 5. Points – the ratio of criterions of quality of fitting for interval number N_E for two variants of analysis of the data of Fig. 3. Lines – the value for the total set of resonances [7].

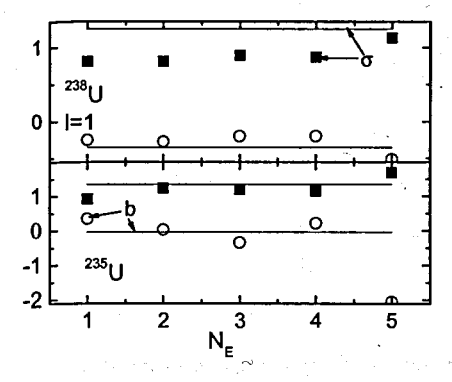


Fig. 6. The values of parameters b and σ for approximation of the data of Fig. 3 (variant k=1). The notations are analogous to Fig. 5.

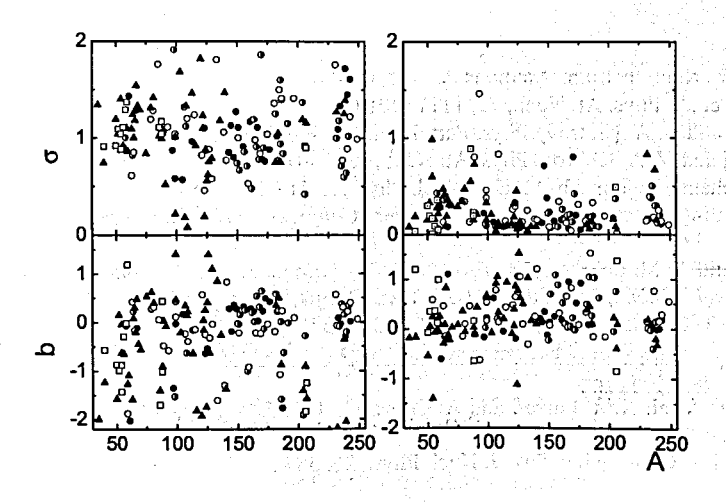


Fig. 7. Left column - the dependence of the best fit [7] values of parameters b and σ on nuclear mass A for variant k=1. Right column - the same but only for partial functions with maximal contribution in the total distribution of variant k=4.

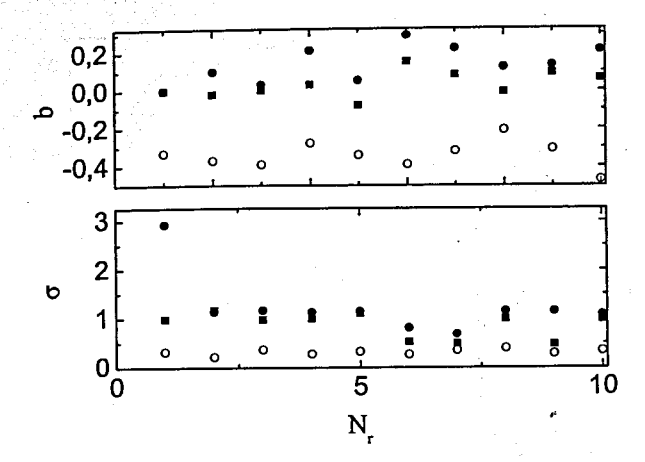


Fig. 8. The same, as in Fig. 7, for the best parameters of approximation of the model data. Closed points – modeling for k=1, b=0 and $\sigma=1$ for the sets $N_r=4000$ (squares) and with omission of 30% – (circles). Open points – the case k=4 for $N_r=3000$ and amplitude corresponding to the greatest contribution in cumulative sum.

References

- 1. A. Schiller et al., Nucl. Instrum. Methods A, 447, (2000) 498.
- 2. B.V. Zhuravlev et al., Phys. At. Nucl., 73, 1111 (2010).
- 3. A.M. Sukhovoj and V. A. Khitrov, Phys. Part. Nucl., 36, 359 (2005).
- 4. A. M. Sukhovoj and V. A. Khitrov, Phys. At. Nucl., 73, 1507 (2010).
- 5. W. Dilg, W. Schantl, H. Vonach, M. Uhl, Nucl. Phys. A, 217, 269 (1973).
- 6. V.M. Strutinsky, in *Proceedings of the International Congress on Nuclear Physics*, (Paris, 1958), p. 617.
- 7. V. A. Khitrov and A. M. Sukhovoj, in *Proc. XIX International Seminar on Interaction of Neutrons with Nuclei, Dubna, May 2011*, E3-2011-xx (Dubna, 2011), p. AMSR1
- 8. C. F. Porter and R. G. Thomas, Phys. Rev. 104, 483 (1956).
- 9. http://www.springermaterials.com/navigation/#1_1_197716.
- 10. http://www-nds.iaea.org.
- 11. H. Derrien, L.C. Leal, N.M. Larson and A. Courcelle, ORNL/TM-2005/241, Oak Rodge National Laboratory, 2005.

and the state of t

and the contraction of the contr

man and a second man coming freel of their section of setting the Wall of the Section of the six in the contribution

12. L.A. Malov and V. G. Soloviev, Sov. J. Nucl. Phys., 26, 384 (1977).

MODIFIED MODEL OF NEUTRON RESONANCES WIDTH DISTRIBUTION. RESULTS OF TOTAL GAMMA-WIDTHS APPROXIMATION

A.M. Sukhovoj, V.A. Khitrov

Joint Institute for Nuclear Research, Dubna, Russia

Abstract discussion of the state of the stat

and the first of the second of

ได้ () และ เกิด () เหตุการพระ จิตยาการจำได้จากให้เกิดเดือน () เพื่องเล่น () การจะ

radionale di la visita del cième de la cième le come de la cième le come de la cième le come de la cième le co

Functional dependences of probability to observe given Γ_n^0 value and algorithms for determination of the most probable magnitudes of the modified model resonance parameters distribution were used for analysis of the experimental data on the total radiative widths of neutron resonances. As in the case of neutron widths, for precise description of the Γ_γ distributions requires a superposition of 3 and more probabilities distributions for squares of the random normally distributed values with the non-zero average and non-unit dispersion.

This result confirms the preliminary conclusion obtained earlier at analysis of Γ_n^0 on presence in all 56 tested sets of resonances several groups noticeably differing by the structure of their wave functions from each other.

1. Introduction

In 1936 N. Bohr suggested the hypothesis [1] on extremely complicated structure of high-lying levels of compound-nucleus. After this, respectively, the properties of neutron resonances are described in frameworks of statistical approach. But, the experience of the science shows that the real picture of the phenomenon under study is usually much more complicated than any hypotheses and notions on it. Most probably, the hypothesis [1] is not a exception, as well.

Estimation of its precision can be performed on the basis of the modern experimental data and theoretical developments of existing nuclear models. So, the realized in FLNP JINR idea of obtaining the direct and reliable experimental information on such nuclear parameters as the level density and radiative strength functions [2], and interpretation of the obtained data [3,4] shows that structure of a nucleus below the neutron binding energy B_n undergoes cyclic change with a step of about $2\Delta_n$. By this, the correlation function of the Cooper pair of nucleons in heated nucleus below B_n insignificantly differs from the analogous value Δ_0 for cold nucleus (although, most probably, decreases at increase of excitation energy). A degree of fragmentation of nuclear structures like n-quasi-particles \otimes m-phonons for these states in region B_n according to theoretical analysis by L.A. Malov and V.G. Soloviev [5], cannot be the same. Id est., one can expect that in the wave functions of neutron resonances at change of their energy can appear available for observation changes.

It is absolutely necessary for their revealing to execute two conditions:

- (a) to use the algorithm of analysis for any experimental data with the lowest possible quantity of model notions and
- (b) to perform quantitative comparison of few variants of approximation of the tested resonance parameter distributions, for example. The more essential is the second condition—just it determines the vector of required changes in the existing notions of nuclear properties in the studied region of excitation. Unfortunately, the variants of analysis of neutron

resonances parameters performed by now did not take into account these circumstances. But, both conditions were to a full degree realized in [6].

2. Conditions of Γ_7 analysis

The intensity of the primary gamma-transitions following decay of neutron resonance depends on the same components of their wave functions. Therefore, in the distributions of partial radiative widths must appear the peculiarities which are analogous to those appearing in distributions of reduced neutron widths. First of all, there is the discrepancy [7] with the Porter-Thomas distribution [8] in any form. The indirect answer on this question can be obtained from the analysis of the distributions of cumulative sums of the relative Γ_{γ} values in maximally wide interval of nuclear mass.

For analysis of form of distribution of the random Γ_{γ} values was used the same algorithm and programs which were prepared for analysis of the reduced neutron widths distribution. The independent variable of analysis $X_{\gamma} = \Gamma_{\gamma} / \langle \Gamma_{\gamma} \rangle$ corresponds to the ratio of total radiative width of given resonance to the mean experimental value of the tested set. Naturally, all events with X=1 (used by determination of Γ_{n}^{0} for some resonances) were excluded from analysis. This selection is really nonessential because corresponding portion of cumulative sum can be with good precision approximated by value $\sigma < 0.01$. The analysis was performed by analogy with the analysis of reduced neutron widths for two hypotheses. The first – the distribution of the total radiative widths of resonances corresponds to distribution of squares of the normally distributed random values with one and the same dispersion and mean value (k=1). The second one's used the same distributions with several set $(k \le 4)$ of different parameters. Practical basis for this variant is obvious asymmetry of cumulative sums of distributions of the experimental X_{γ} values for many nuclei. Unfortunately, the use of relative values of radiative widths inevitably shifts obtained values parameters b and σ .

3. Results of analysis and their interpretation

In Fig. 1 are presented model distributions of squares of the random $X=((\xi+b)/\sigma)^2$ values for parameters b=0.5, 1, 2; $\sigma=0.01$, 0.03, 0.10 for ξ – standard normally distributed random variable. Cumulative sums were normalized, naturally, to the average < X >. In Fig. 2 – approximation of the experimental distributions of Γ_{γ} for ¹⁵¹Eu and ²³⁵U. These target-nuclei essentially differ only by parity of proton number. But difference of he mean spacing D_0 between resonances, neutron binding energy B_n and spin of target I is not changed of principle. In table are presented quantitative results of the relative Γ_{γ} values cumulative sums distributions approximation for some differing by their parameters nuclei with maximal number of their existing experimental values. Also, there is any nonprinciple difference for part of table data, but the part of cumulative sum of two most essential functions of superposition conserves with high precision. There is the sufficient argument in favour of conclusion that the experimental data on neutron resonances parameters correspond to several sets of noticeably differing by their wave functions structure.

In figures 3-8 are presented the results of approximation of the radiative width distributions for 54 sets of the data, although analysis was performed for some larger number of the sets. Practical selection was done by condition that the sets of s-resonances in figures in most cases correspond to not less than 45-50 Γ_7 values. Id est., number of points of the approximating curve for superposition from k=4 approximated "partial" functions exceeds maximal number of parameters of approximation by a factor ≈ 4 and more. The ratios $\chi^2(k=4)/\chi^2(k=1)$ for all 56 data sets are shown in Fig. 9.

The ratio of the criteria χ^2 of the best fit for Γ_{γ} has random nature as for analogous distribution of neutron widths. However, considerable decrease of its value for the case of Γ_{γ} does not allow one to connect the observed picture only with effect of random fluctuations.

Table. The approximated main parameters of nuclei with the largest values of number N_{γ} of experimentally determined values Γ_{γ} . $R = \chi^2(k=4)/\chi^2(k=1)$ — the ratio of the best fit parameters of both variants of analysis; S — the portion of two functions with maximal contribution in cumulative sum; σ and b — dispersion and their most probable mean value.

| Nucleus | N_{γ} | R | $\chi^2(k=4)/N_y$ | S_{I} | σ_{l} | b_I | S_2 | σ_2 | b_2 |
|-----------------------|--------------|-------|-------------------|---------|--------------|-------|-------|------------|-------|
| ⁶⁰ Ni, l=1 | 173 | 0.027 | 0.015 | 0.45 | 0.08 | 0.85 | 0.34 | 0.07 | 0.49 |
| 151Eu | 185 | 0.073 | 0.044 | 0.49 | 0.008 | 1. | 0.36 | 0.02 | 0.95 |
| ¹⁵¹ Sm | 525 | 0.033 | 0.012 | 0.44 | 0.06 | 0.68 | 0.38 | 0.06 | 0.87 |
| ²³⁵ U | 2297 | 0.068 | 0.042 | 0.43 | 0.006 | 0.97 | 0.31 | 0.05 | 0.76 |

It follows from both the data of this figure and form of dependence of cumulative sums of the X_{γ} values for different nuclei that the Γ_{γ} values with high probability depend on structure of the wave function of a neutron resonance, and the set of the experimental values of widths can be divided onto several groups of resonances noticeably differing by structure of wave function of corresponding high-excited nuclear level.

Unfortunately, this conclusion can be mistaken if systematical errors of Γ_{γ} are caused by the strong enough unknown and determinate by experiment condition dependence on resonance energy, its neutron widths and so on, For example, by the larger, as compared with the mean, probability of resonances omission not only with small Γ_n^0 , but and with small Γ_r . Or – in the case if in the experiment was revealed only very small part (for instance, from several to 10-20%) of really existing levels of compound nucleus with fixes spin above B_n . Such possibility follows directly from the attempt [9] approximation of actinides reduced neutron widths experimental distributions and following its extrapolation to the $\Gamma_n^0=0$ value in frameworks of the modified model of neutron widths distribution. (The Porter-Thomas distribution [8] is its particular case).

4. Conclusion

Practically model-free analysis of the neutron resonances total radiative widths distributions confirms the determined specific of the existing experimental data:

(a) the absence of uniformity of the Γ_{ν} distributions for different nuclei,

(b) significantly better correspondence of the experimental data to the hypothesis of superposition in those data the of combination of resonances with noticeably differing structure, than to the assumption on practical (in the frameworks of modern status of science) constancy of their structure.

Probable presence of groups of resonances with the different mean values $<\Gamma_7>$ quite corresponds to the conclusion [10] on difference of the radiative strength functions of the primary transitions which exceed the limits of the expected random fluctuations. This conclusion well explains and difference of the strength functions, measured in the thermal point, with the data for ⁶⁰Ni obtained [11] from re-analysis of the intensities of gamma-cascades following proton capture in several tens of ⁵⁹Co proton resonances [12].

Final conclusion concerning this matter can be obtained after observation corresponding differences in the spectra of the primary transitions in a number of neutron

resonances of the same nucleus. Modern state of nucleus quasi-particle-phonon model development does not exclude [13] possibility of qualitative observation of such dependence.

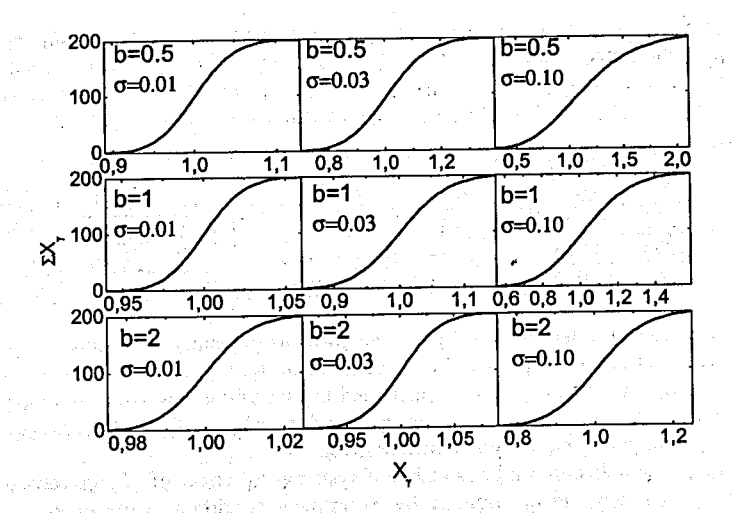


Fig 1. The expected distribution of cumulative sums of relative values Γ_7 of the total radiative widths of resonances. The dispersion σ and mean value b are also given in figure.

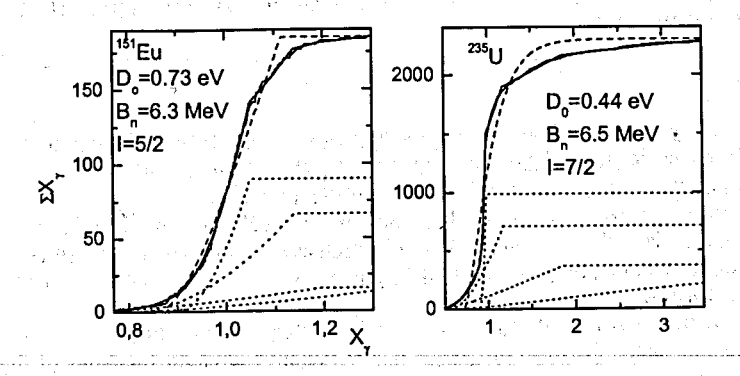


Fig. 2. The result of Γ_7 distribution approximation for ¹⁵¹Eu and ²³⁵U. Histogram – experiment, dashed line – k=1, solid – k=4, dotted lines – variant of decomposition of the last into four "partial" functions.

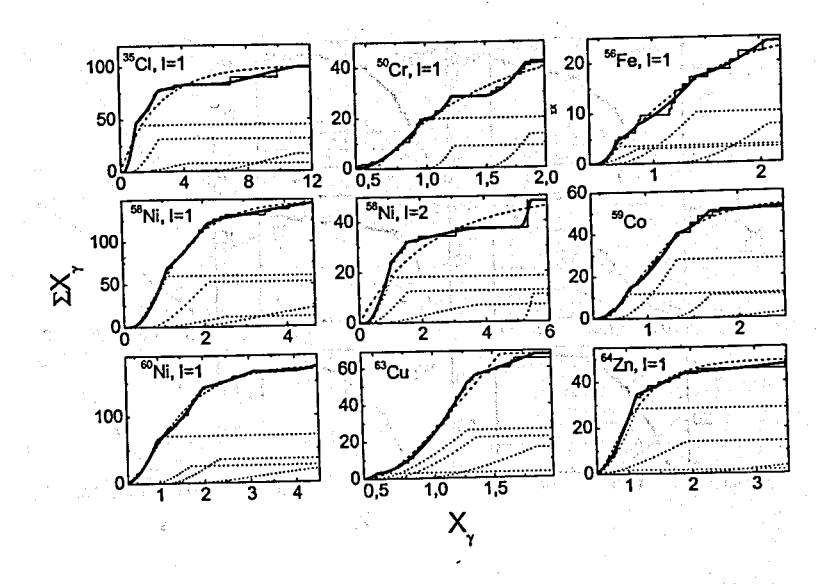


Fig. 3.The same, as in Fig. 2, for ³⁵Cl, ⁵⁰Cr, ⁵⁶Fe, ^{58,60}Ni, ⁵⁹Co, ⁶³Cu and ⁶⁴Zn.

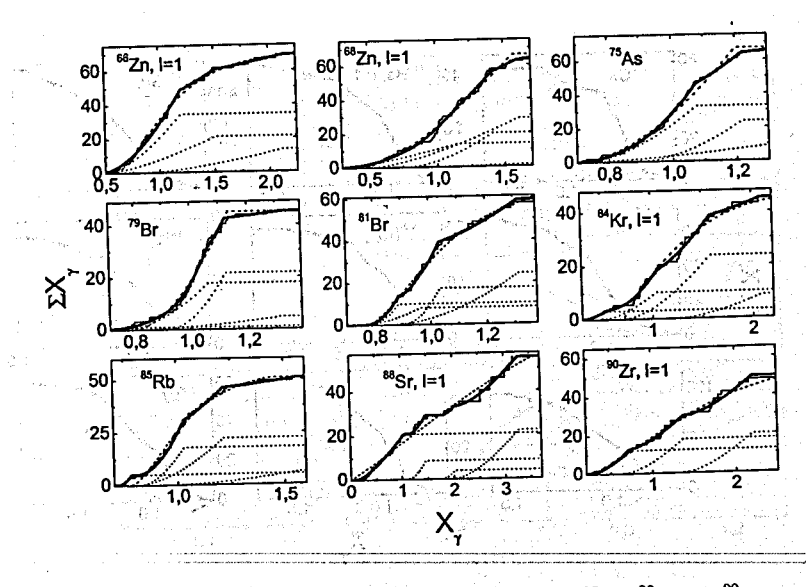


Fig. 4. The same, as in Fig. 2, for ^{66,68}Zn, ⁷⁵As, ^{79,81}Br, ⁸⁴Kr, ⁸⁵Rb, ⁸⁸Sr and ⁹⁰Zr.

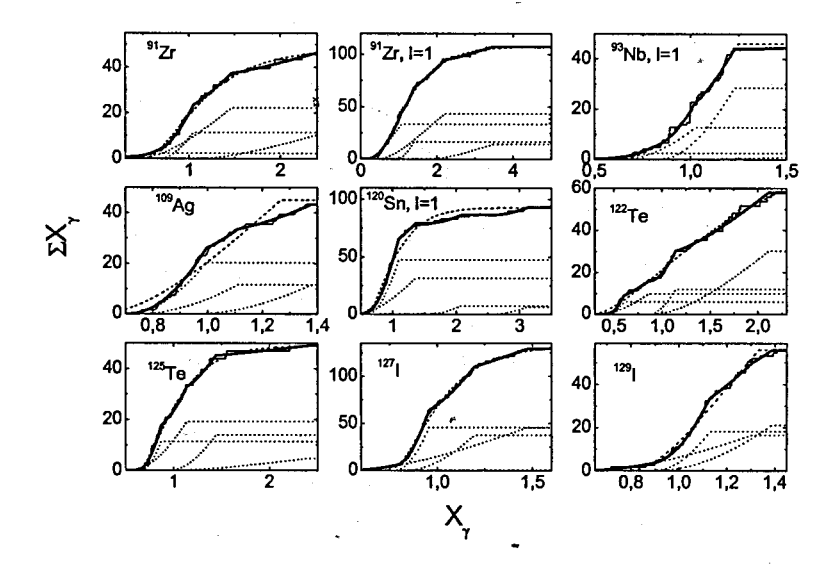


Fig. 5. The same, as in Fig. 2, for 91 Zr, 93 Nb, 109 Ag, 120 Sn, 122,125 Te and 127,129 I.

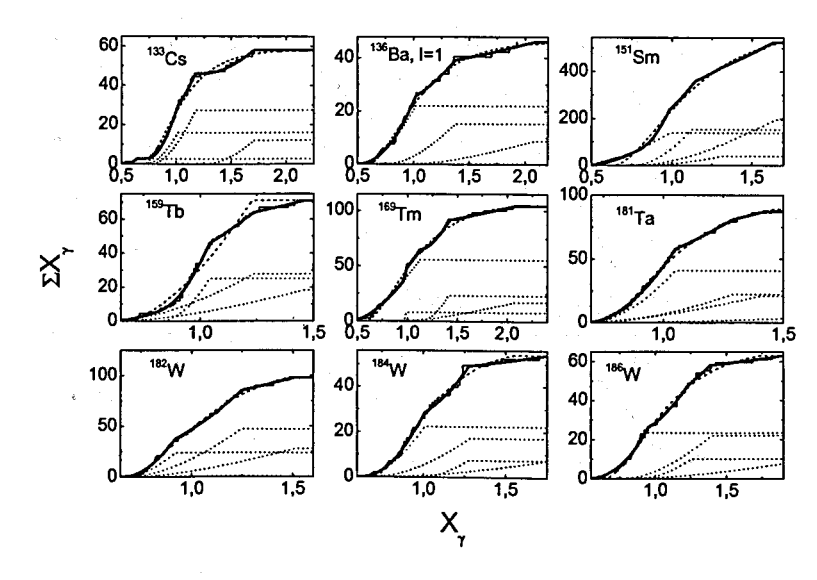


Fig. 6. The same, as in Fig. 2, for 133 Cs, 136 Ba, 151 Sm, 159 Tb, 169 Tm, 181 Ta and 182,184,186 W.

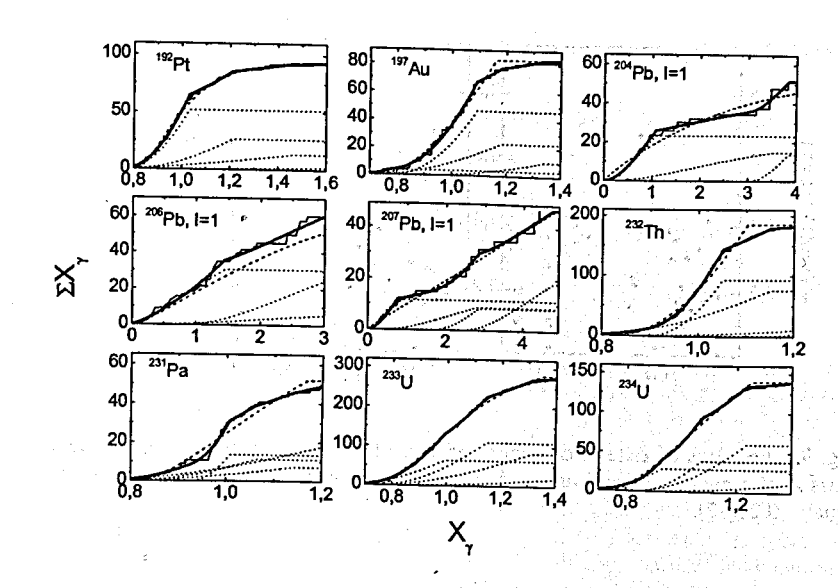


Fig. 7. The same, as in Fig. 2, for 192 Pt, 197 Au, 204,206,207 Pb, 232 Th, 231 Pa and 233,234 U.

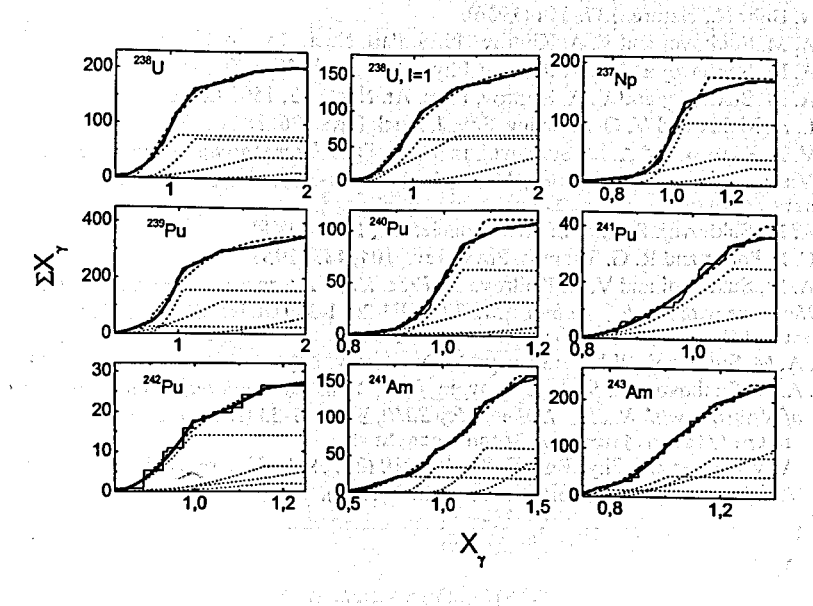


Fig. 8. The same, as in Fig. 2, for ²³⁸U, ²³⁷Np, ^{239,240,241,242}Pu and ^{241,243}Am.

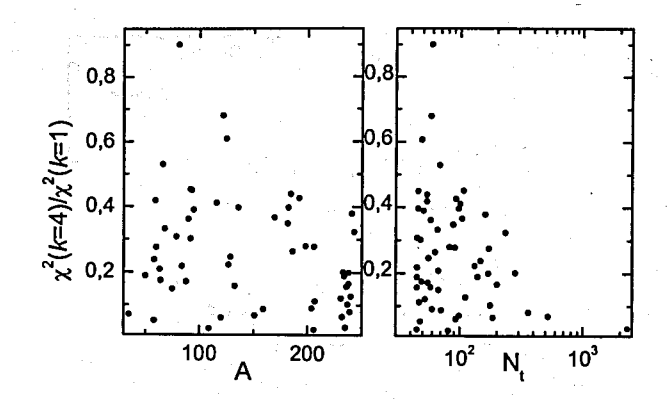


Fig. 9. The ratios of criteria of quality of best fit for two variants of analysis in function of mass A of a nucleus or on number N_i of resonances in the set. The mean value over 56 sets equals 0.26(17).

References

- 1. N. Bohr N., Nature, 137, 344 (1936).
- 2. A. M. Sukhovoj and V. A. Khitrov, Phys. Part. Nucl., 36, 359 (2005).
- 3. A. M. Sukhovoj and V. A. Khitrov, Phys. Part. Nucl., 37, 899 (2006).
- 4. A. M. Sukhovoj and V. A. Khitrov, Phys. At. Nucl., 73, 1507 (2010).
- 5. L. A. Malov and V. G. Soloviev, Sov. J. Nucl. Phys., 26, 384 (1977).
- 6. V. A. Khitrov and A. M. Sukhovoj, in *Proc. XVIII International Seminar on Interaction of Neutrons with Nuclei, Dubna, May 2010*, E3-2011-33 (Dubna, 2011), p. 199; http://isinn.jinr.ru/18/contents.html.
- 7. A. M. Sukhovoj, Physics of atomic nuclei, 71, 1907 (2008).
- 8. C. F. Porter and R. G. Thomas, Phys. Rev. 104, 483 (1956).
- A. M. Sukhovoj and V. A. Khitrov, in Proc. XVIII International Seminar on Interaction of Neutrons with Nuclei, Dubna, May 2010, E3-2011-33 (Dubna, 2011), p. 216; http://isinn.jinr.ru/18/contents.html.
- 10. A. M. Sukhovoj, W.I. Furman and V. A. Khitrov, Phys. At. Nucl., 71, 982 (2008).
- 11. A. M. Sukhovoj and V. A. Khitrov, in *Proc. XVIII International Seminar on Interaction of Neutrons with Nuclei, Dubna, May 2010*, E3-2011-33 (Dubna, 2011), p. 180; http://isinn.jinr.ru/18/contents.html.
- 12. A. Voinov et al., Phys.Rev. C 81, 024319 (2010). A.~Voinov et al., nuc-ex/0907.1819.
- 13. V.G. Soloviev, Sov. J. Part. Nucl., 3, 390 (1972).

MICROPIXEL AVALANCHE PHOTODIODE AS ALPHA PARTICLE DETECTOR

F.Ahmadov^{1,3}, G.Ahmadov^{1,3}, R.Madatov³, Z.Sadygov^{1,2}, S.Tiutiunnikov¹, V.Zhezher¹

¹Joint Institute for Nuclear Research, Dubna, Russia, ²Institute of Physics-ANAS, Baku – Azerbaijan, ³Institute of Radiation Problems-ANAS, Baku – Azerbaijan

ABSTRACT

Public security (explosives and drugs detection) and environment protection (radioactive isotope contamination detection) issues require new methods for detection of ionizing radiation. The most challenging is registration of alpha particles that are absorbed basically at the surface of a detector. The goal of the work is an investigation of detection of alpha particles by silicon micro-pixel photo diodes (MAPD) in combination with lutetium fine silicate (LFS) scintillators.

Challenges of the last decade have made detection of explosives and drugs in baggage and large cargoes an important task. A tagged neutron method was developed to solve the first problem [2]. The method is based on the following principles. The creation of a neutron in the generator as a result of interaction of deuterium beam with a tritium target is accompanied by emission of alpha particle flying in the opposite to the neutron direction. Detection of the alpha particle allows one to determine direction of the neutron and generate a trigger signal. Capture of neutrons within a given nuclei produces a specific for the resulting isotope gamma spectrum. Analysis of the gamma spectrum allows one to determine atomic composition of the substance, and, therefore, identify it. Another issue is a detection of radioactive isotope contamination in various environments. The most challenging task here is registration of alpha particles what do not penetrate deeply within the detector volume.

Design and operation principles of the MAPD were described in [1]. Basic structure of the MAPD is shown in Fig. 1. Investigated photodiode MAPD-3N had 3x3 mm² active area and pixel density 1.5×10⁴ mm². A single pixel gain was of order 10⁴ depending on bias. High pixel density provided for linearity of device's response in wide range of registered energies and sufficient energy resolution.

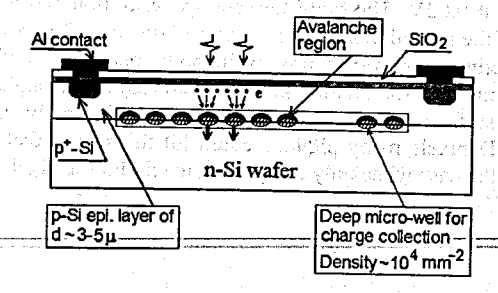


Fig. 1. Basic structure of the MAPD.

A²⁴¹Am isotope (kinetic energy of alpha particles is 5.486 MeV (85 %) and 5.443 MeV (13 %), half life period is 432.7 years) was used as an alpha source. The lutetium fine silicate (LFS) crystal named as "LFS-8" was used as a scintillator. The size of LFS-8 was selected 3x3x0.5 mm³. The decay time of LFS-8 was 19 ns. LFS-8 was coupled to the MAPD-3N with silicone optical grease. The MAPD samples and LFS-8 scintillators were manufactured in collaboration with Zecotek Photonics Singapore Pte. Ltd. [4].

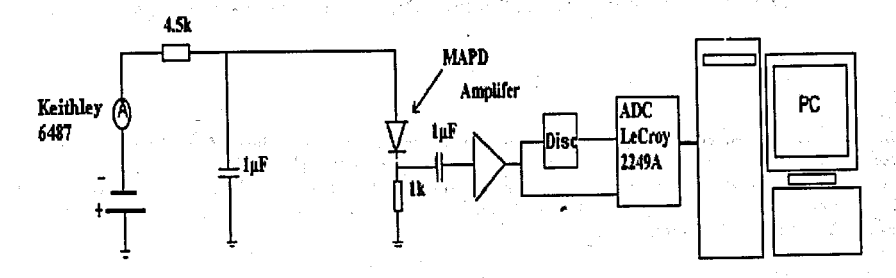


Fig. 2. Block diagram of the experimental setup.

Fig. 2 shows block diagram of the experimental setup. Keithley 6487 voltage source was connected to MAPD through RC-filter. The signals were read out from $1k\Omega$ load resistor through the coupling capacitor and a linear amplifier. Gain of the amplifier was 20 in the case of measurement with LFS scintillator. Delayed signal was fed into LeCroy 2249W ADC. CAEN N-48 shaping discriminator was used to form a gate signal for the ADC. Digitized signal was read out by a personal computer through CAMAC interface. Peak positions and their full width at half maximum (FWHM) were obtained from Gaussian fit. All measurements were carried out at room temperature.

In order to measure alpha spectra with LFS-8 scintillator the later was placed on top of the MAPD under the ²⁴¹Am source. The scintillator crystal was not covered in order to avoid attenuation of alpha particle flux. When an alpha particle hits the scintillator it deposits its entire energy producing light pulse. The scintillation light was detected by MAPD.

Fig. 3 shows the alpha spectrum measured with the LFS-8 scintillator and MAPD at bias voltages in a range of 92.3-93.5V. The measured energy resolution for the 5.5 MeV alpha particles was 14.6% at 93.2V. The quite low energy resolution can be explained by three reasons. First, part of the scintillation light has escaped uncovered LFS-8 scintillator because in our case the reflecting cover would absorb the alpha particles. Second, because of very thin scintillator (0.5 mm) the scintillation photons produced by the alpha particle hit a small part of the detector surface with limited number of pixels. Finally, because of the finite number of the MAPD pixels many photons could hit the same pixel producing the same resulting signal as in the case when only one photon would hit the pixel.

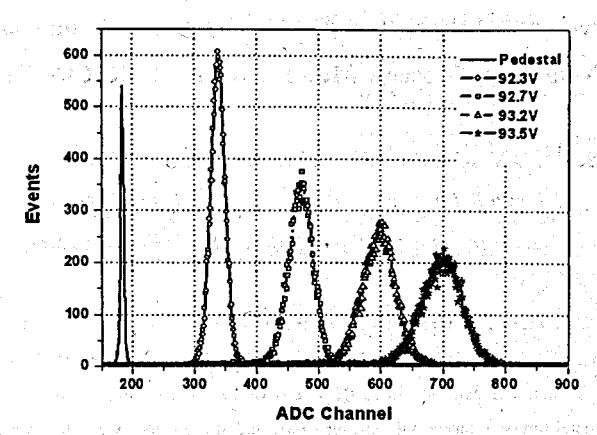


Fig. 3. Spectra of the alpha particle measured with LFS scintillator and MAPD at the different bias voltages (amplifier gain is 20).

The obtained results show that the MAPD could be used to detect and count alpha particles by itself as well as in combination with scintillators.

The measured energy resolution for the 5.5 MeV alpha particles in this case is sufficient to separate signal from background for most practical purposes although additional studies are required to improve energy resolution for alpha particles.

REFERENCES

- [1] Sadygov Z. Ya., Russian Patent № 2316848, priority from 01.06.2006.
- [2] V.M. Bystritski et al., <u>Proceedings of the IV International Symposium on Technology and Mine Problem</u>, Naval Postgraduate School, Monterey, California, March 13-16, 2000.
- [3]. F. Ahmadov, N. Anfimov, Z. Krumshtein, R. Madatov, R. Mechtiyeva, A. Molokanov, A. Nozdrin, A. Olshevski, V. Shvetsov, Z. Sadygov, S. Tyutyunnikov, V. Zhezher et al., Proceedings of International Conference on Perspectives of Peaceful use of Nuclear Energy (ICPPNE), 2010.
- [4] http://www.zecotek.com

Measurements of characteristics of the pulse neutron sources RADEX and IN-06 of the Moscow Meson Factory (INR RAS, Troitsk)

Yu. V. Grigoriev^{1,2}, D.V. Khlustin¹, Zh. V. Mezentseva², I.A. Vasiliev¹, Yu. V. Ryabov¹

I Institute for Nuclear Research RAS, Moscow, Russia

2 Joint Institute for Nuclear Research, Dubna, Russia

Abstract. A source of thermal neutrons IN-06 of the Moscow meson factory (MMF) INR RAS started operation in mid-November 2010. We have carried out time-of-flight measurements on 22.4 m flight path of the first IN-06 neutron channel. The neutron source IN-06 has worked in a starting regime, i.e. a proton beam has been moved on its metal tungsten target only during a day, and at night the proton beam has been shifted on a tungsten target of the RADEX setup. Such a mode of operation allowed to carry out measurements at the IN-06, and on the 50-meter flight path of the RADEX setup with a 8-section liquid (n, γ)-detector (49.5 m) and a neutron cylindrical ³He counter (51.5 m). The registration efficiency of thermal neutrons by the He-3 counter was approximately 100 %. It was used on the 22.4 m flight path of the IN-06 and on the 51.5 m flight path of the RADEX. The usage of the ³He allowed to determine parameters of two neutron sources simultaneously and to carry out comparative analysis of their characteristics. Parameters of a proton beam of the linear accelerator were approximately identical for the IN-06 and for the RADEX.

Time of flight spectra were measured by two systems of the experimental information storage: a slow system with a minimal width of the time channel 4 μ s and a performance < 10^4 n/s [1] and a fast system with a width of the time channel 121.2 ns and a performance < 10^7 n/s. The fluxes of thermal neutrons, measured on the 22.4 m flight path of the IN-06, were determined from the experimental spectra at different frequencies of neutron pulses. At a frequency of 50 Hz the neutron flux was equal to F=821 n/cm²s. A small intensity of the source of thermal neutrons IN-06 is the result of not optimal geometry of a target and moderator, and also of possible losses of the proton beam during its transportation to the tungsten target. The flux of thermal neutrons on the 50 m flight path of the central beam of the pulsed source RADEX was determined F =150 n/cm²s at the following conditions: the frequency of 25 Hz, the pulse duration at half height of 60 μ s, the pulse proton current of 5 mA, the energy of protons of 209 MeV and a diameter of collimator of 2 cm, installed at a distance of 20 m from a moderator.

Earlier in 1998 [2] and 2004 [3] other groups carried out measurements on the pulsed source IN-06, but at that time it was not possible to determine basic characteristics of the neutron source IN-06 because of different reasons. The measurements of time-of-flight spectra at the RADEX setup were realized since its start in 1996 [4, 5, 6], therefore a large amount of the experimental information, including characteristics of the neutron pulsed

source RADEX, was collected. The geometry and other experimental conditions at the IN-06 and at the RADEX differ from each other. A schematic view of experiments at the IN-06 and at the RADEX is presented in Figure I. The moderator's luminous surface at the RADEX was equal to 113 cm². It was caused by internal diameter of a steel neutron guide d = 12 cm.

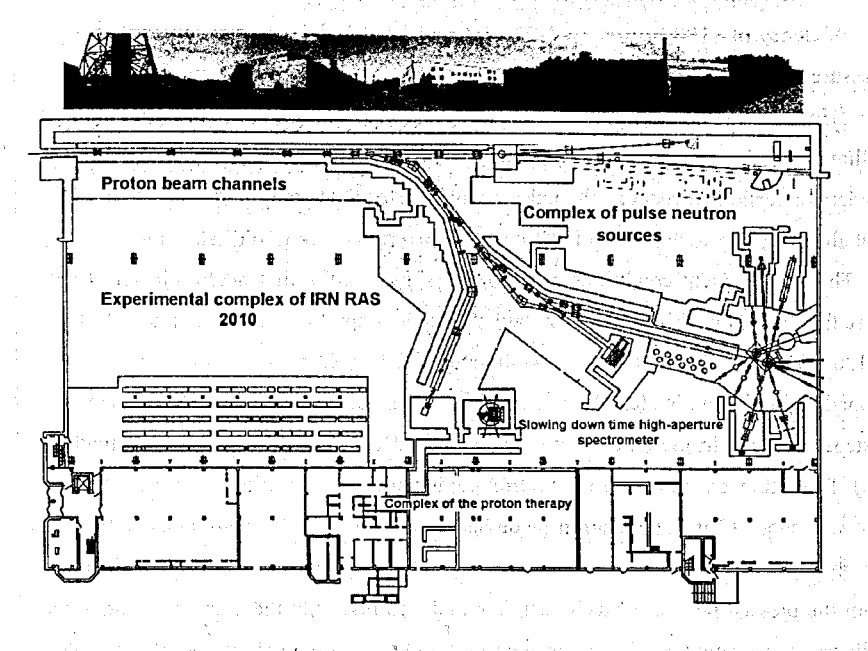


Fig. 1. A general scheme of pulsed neutron sources RADEX and IN-06 placement in experimental complex (building 25) of Institute of Nuclear Researches of the Russian Academy of Sciences.

A collimator 50 cm of a length made of a mixture of paraffin and boron carbide with an aperture of 6 cm in diameter was positioned at a distance of 20 m from moderator in the hole of neutron guide. The resonance filter made of manganese oxide with a thickness of 1 cm and NaCl of the same thickness were installed behind the collimator. Filters allowed to determine positions of a neutron flash and to estimate background at the energy of 336 eV and of 2.4 keV. The width of neutron flashes was approximately 60 μ s, a time delay of 200 μ s. An additional lead collimator was used at a distance of 45 m from moderator. This collimator had an aperture of 6 cm in diameter. The carbon collimator with a length of 1 m with an internal aperture of 6 cm in diameter was located before the iron protection at a distance of 40 m

inside the vacuum neutron guide with a diameter of 17 cm. The powder of Sm₂O₃ packed into the aluminum container was used as a radiator-sample. It was positioned in the center of a liquid (n, γ)-detector.

To determine position of the neutron flashes and their durations, the ³He counter with the efficiency of ~100 % was used. The internal cavity of the counter, filled with ³He at the pressure of 8 atmospheres, has thickness of 3.5 cm and internal diameter of 12 cm. Sometimes this ³He counter was moved to the central neutron channel of the RADEX setup where a collimator with an aperture diameter of 2 cm was installed at a distance of 10 m from the moderator surface. It reduced the pulse count of ³He counter approximately be a factor of 10 that allowed to observe neutron flashes without overloads using "old" slow measuring system.

The measurement conditions of the TOF spectra on the first neutron beam of the IN-06 were the following. Two collimators with rectangular apertures with the area of 17 cm * 8 cm = 136 cm² at the entry of the first collimator and 11.5X6.5 cm = 75 cm² at the exit of the second collimator with a length of 1.7 m and 0.95 m before the mirror neutron guide were at a distance of 0.6 m from vertical water moderator (22X22 cm = 484 cm² area and thickness of 5 cm). The full length of the mirror neutron guide with a cross section of 11.5 cm *6.5 cm = 75 cm² was about 12 m. The neutron guide had a vacuum level of approximately 10⁻² Top. The length of the flight path in measurements was 22.4 m. The core with 2 cm in diameter made from the pressed powder of technical diamond was placed at the end of the flight path. The cylindrical ³He counter [1] was installed in a trap of cadmium sheet and plates made from a mix of paraffin and boron carbide. It was placed on the neutron guide axis and irradiated with neutrons from the moderator surface with the area of 136 sm2. In front of the detector on the neutron guide wall a collimator made of 2 mm thickness cadmium with window area of 10 sm * 3.4 sm = 34 sm² was placed. The diamond sample was used for measurements of a dispersion spectrum at 90° and 180° to the neutron guide axis. Presence of a diamond sample on the neutron beam resulted in reduction of a flux of thermal neutrons by illuminated surface of He³ detector approximately to the value of 15 %.

It is necessary to note, that two independent tungsten targets (top with water cooling used in our measurements and bottom with liquid deuterium moderator) exist in accordance with the technical project IN-06 specialized in the work with thermal and cold neutrons. 12 vacuum neutron guides come to these two targets, some of them for improvement of background conditions look not at the target, but at the peak of neutron flux density in the

moderator. One of those 12 neutron guides has a diameter of 1 m, other three having a standard diameter of 200 mm get out the experimental building and might be lengthened up to 500 meters. The cooling system of the IN-06 was built up for an average current of 1 mA, that at designed protons energy of 600 MeV and pulse-repetition frequency of 100 Hz corresponds to the average target power of 0.6 MW. The name "IN-06" derives from this fact.

Thus, the IN-06 setup has a serious potential of development (by number of operated neutron guides three times more, by density of neutrons flux twice times more), which will be involved in the nearest years. As the IN-06 will come close to the designed parameters, this source approach to other similar installations of our country (the pulsed reactor IBR-2 in JINR, Dubna, and the reactor "PEAK" in Saint Petersburg INP which is currently under construction) by the majority of characteristics and surpass in separate parameters. It could classified among ten best installations of the world.

Two systems of data acquisition were used for storage of the TOF spectra. A slow system on the basis of PC-386 and dialogue program ROM, which simultaneously allowed to measure TOF spectra from the 8-sectional liquid (n, γ) detector and from a He³ cylindrical counter. In parallel with this system the special single-channel high-speed system on the basis of notebook through USB 2.0 port was used. In the first system the width of the time channel was 4 μ s in 4096 time channels. In the second system it was 121.2 ns in 160000 channels, that allowed to observe thermal neutrons spectra in the energy range of thermal neutrons from 0.006 up to 0.2 eV (in time interval $t = 20000 - 3500 \ \mu s = 0.0165 \ s$) at the frequency of neutron fluxes of 50 Hz. The maximum of thermal neutron peak was observed at the energy of 0.06 eV. The following ratio was used to define the flux of thermal neutrons F on the surface of He³ detector (22.4 m):

$$F = \frac{N}{S * T},$$

where N - the total number of registered thermal neutrons during the time T = t*R = 0.0165s*50964 = 841s = 14 minutes at the registration efficiency of 100 %; R - start number of the time analyzer; S - area of the illuminated surface of the detector.

In such measurements a number of registered thermal neutrons was equal to N=22636714 at R=50964. The average flux of pulsed thermal neutrons on the illuminated surface of the He³ detector with the area of $S=34~\rm sm^2$ was determined to be 821 n/s*sm². The maximal peak flux of thermal neutrons at the energy 0.06 eV was $F_{max}=2460n/s*\rm sm^2$.

Below we briefly give a description of the new high-speed system of data acquisition. In Figure 2 and Figure 3 are presented Photo of the system and the general electronic scheme. A prototype of the time - digitizer converter (TDC) has been developed to modernize the data acquisition system made in CAMAC standard for TOF measurements. A start signal and a signal from the detector are connected through the entrance cable header of CP50 type. The device consists of the USB-controller FT245R, the programmed integrated chip (PIC) XC9572XL, the signal shapers on the basis of Schmidt triggers and generator with 66 MHz frequency. In the PIC the 8-digit shift register (SR), registered at the input signal from the detector and also the auxiliary logic containing a counter of time channel number and a final automatic device, formed read and write signals for the USB-controller are realized.

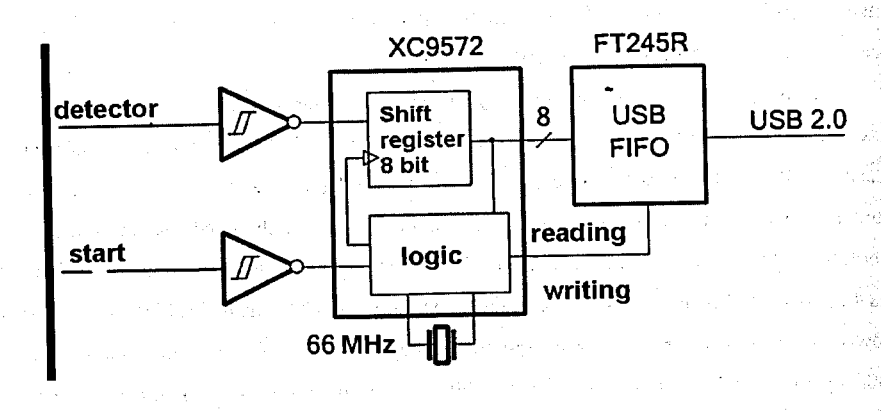


Fig. 2 Functional scheme of the DAQ device

| Maximum number of time channels Maximum number of events in the channel Width of the time channel Minimal period of pulses repetition Minimal duration of pulses registration Level of the entrance signal | 524272 2 ³² -1 121.2 ns 140 ns 1 ns TTL, 5 volt, positive polarity USB 2.0 |
|------------------------------------------------------------------------------------------------------------------------------------------------------------------------------------------------------------|---------------------------------------------------------------------------------------------------------|
| Connection interface with computer | USB 2.0 |

The experimental data come through the bi-directional 8-digit bus to the chip which groups them into the continuity of the protocol USB and transfer them into computer. This chip has buffers FIFO of information reception and transfer with a volume of 256 and 128 bytes respectively for carrying capacity smoothing. The data exchange between TDC and computer is carried out in the following way:

- 1. The command processor transfers into TDC a value specifying a number of time channels;
- 2. TDC passes into sleep mode of a start pulse;
- 3. From the moment of start pulse arrival the shift register starts to work and then the transfer of the information to the computer takes place byte-by-byte;
- 4. After transfer of a required number of time channels the TDC forms a status byte, informing the program about successful or mistaken transfer of data frame at buffer FIFO overflow.

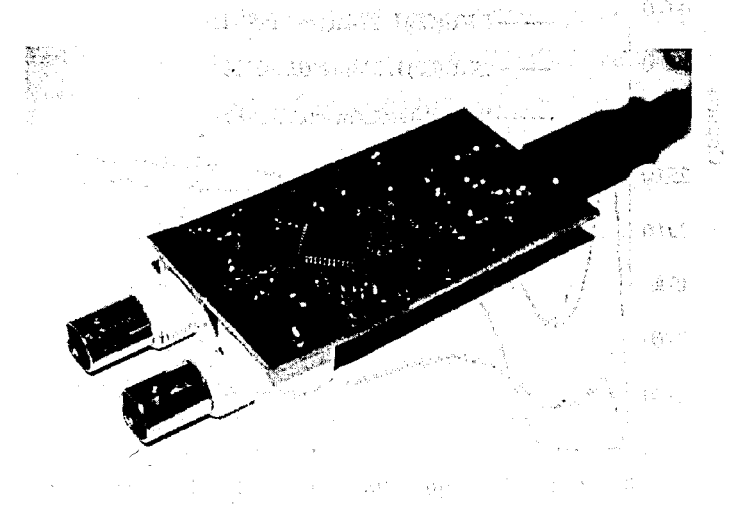


Fig. 3 Photo of the device

A possibility of TDC dumping in initial condition with a command of the command processor is additionally realized. With the exception of storage memory from the TDC structure and load shifting into the computer, the significant simplification of the device was achieved. The maximal data stream, given by the TDC, comes to 8 Mbytes per second. At the same time modern multinucleate processors with a set of vector instructions are available to process at least two orders of magnitude larger data streams. This fact allows construct even faster multichannel TDC, based on the above-mentioned principle, limited only by cash bandwidth of the USB-controllers. The model of TDC was successfully tested with the linear accelerator of protons of the INR of Russian Academy of Science during the beam time at the RADEX and IN-06 setups and also at the isotope complex.

ทริ มาให้เกิดที่ เรียบกรรมเพละครบบาร์ต เหยื หลัง แรก.

For definition of background components the samples of metal cadmium with a thickness of 1mm and indium of 3 mm thickness were installed in the neutron beam before the He³ detector. The measured experimental energy spectra (22.4 m flight path of the first channel of the IN-06) by means of "old" slow system of data acquisition with a time channel width of 4 µs in 4096 channels (t =16384 µs) are presented in Figure 4.

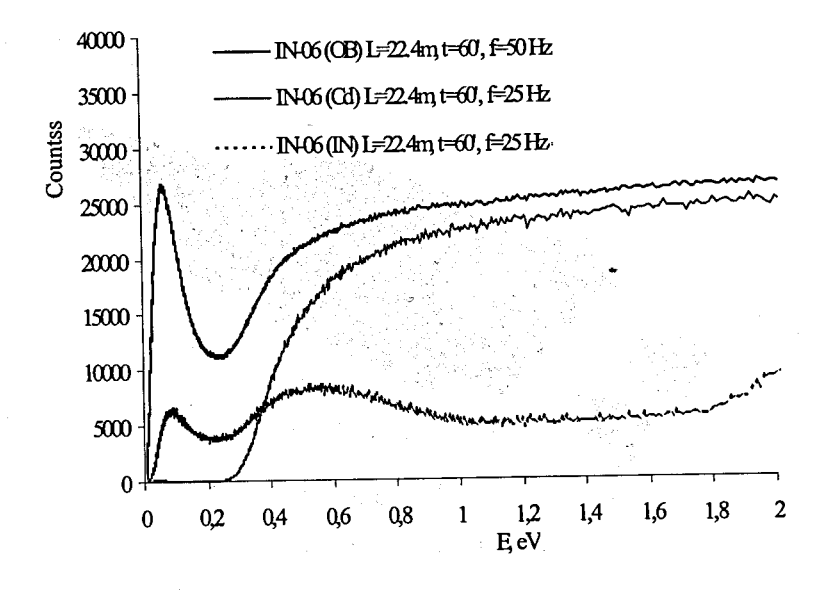


Fig 4. The energy spectra measured at 22.4 m flight path of the first channel of the IN-06 (time channel width 4 μ s in 4096 channels t =16384 μ s)

Spectra with samples of indium and cadmium in the neutron beam are reduced to the common monitor count of the open beam under burst and in the first 100 channels behind neutron burst, where the proximity effect of samples in spectra is very small. As one can see from Figure 4, background components in spectrum of thermal neutrons for the open beam are negligible (about 0.01 %). This is a kind of spallation neutron sources on the basis of proton accelerators and non-multiplying targets from tungsten. For comparison we note that in reactors, even based on the pulsed action such as the IBR-2 (FLNP JINR), presence of delay of neutrons and small subcriticality between bursts results in a level of background components up to 10 %. To the neutron energy region higher than 0.4 eV the background level in this area for the given measurements is about 20 %.

Figure 5 shows the TOF spectra with a sample of cadmium and without it in the neutron beam, measured on the 22.4 meter flight path of the first channel of the IN-06 source by means of fast data acquisition system with a time channel width of 121 ns in 321240 channels (t = 39500 μ s). As well as in case of the parallel measurements carried out with the slow data acquisition system, spectra of the similar form were obtained but with the more pronounced Braggs dip in the thermal part of the energy spectra of diamond sample at the energies of 0.0133 eV (14000 μ s), 0.0049 eV (23000 μ s), 3.7*10⁻³ eV (26000 μ s). As there was no special monitor counter, integral sums under burst and in the first channels after burst were used for reducing to monitor count of the open beam.

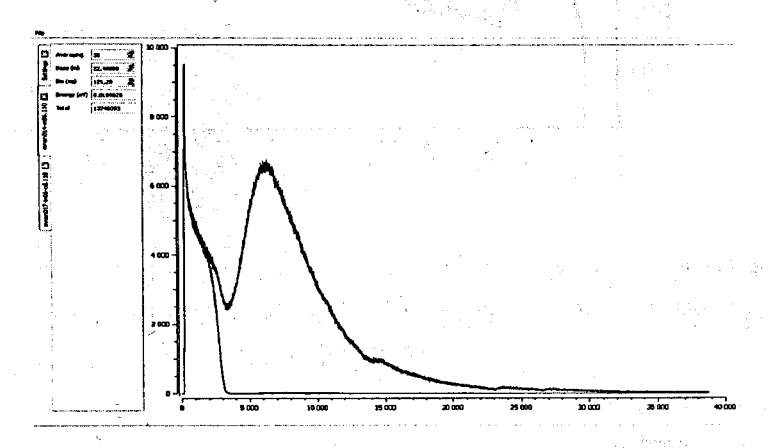


Fig 5. TOF spectra of the open beam and TOF spectra with cadmium sample, measured on the 22.4 m flight path of the first channel of the IN-06 source (time channel width 21 ns in 321240 channels, $t = 39500 \mu s$)

As Figure 5 indicates the main part of neutron spectrum is located within the limits of 20 ms at the 22.4 m flight path. Therefore for the majority of experiments at the IN-06 a frequency of neutron burst with a repetition of 50 Hz is affordable. For special experiments with solid-state subjects and cold neutrons the frequency of 25 Hz or even 10 Hz might be needed due to the presence of recycled neutrons.

The maximum frequency of the accelerator 100 Hz allowing double statistic set speed, could be adjust to the IN-06 only for limited number of tasks on the 11 m flight path. This is one of differences of external environment of the source IN-06 having the thermal and cold neutron spectrum from the neutron source RADEX, where a high frequency of neutron burst

repetition is available due to the resonance neutron spectrum. In some cases at short neutron bursts (about 0,5 ms) and at increase of intensity of neutrons in thermal energy region less than 100 keV, realization of different neutron-nuclear studies is possible at the frequency of 100 Hz.

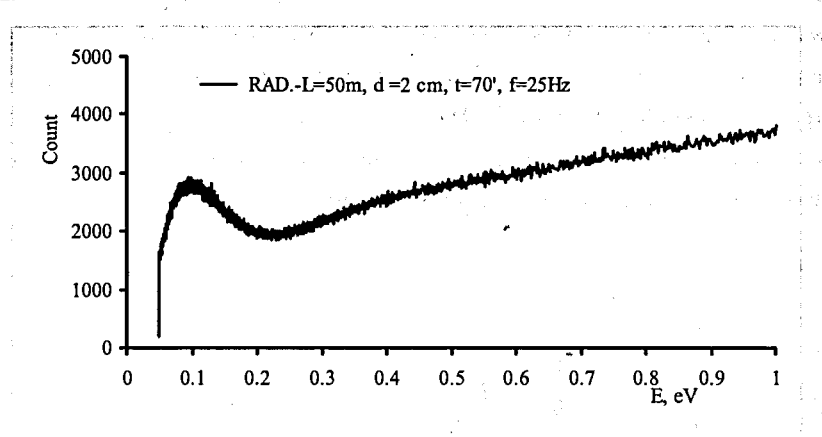


Fig. 6. Energy dependence in the TOF spectrum of the open beam, measured on the 50 m flight path of the central channel of the RADEX setup (time channel width 4 μ s in 4096 channels t = 16384 μ s)

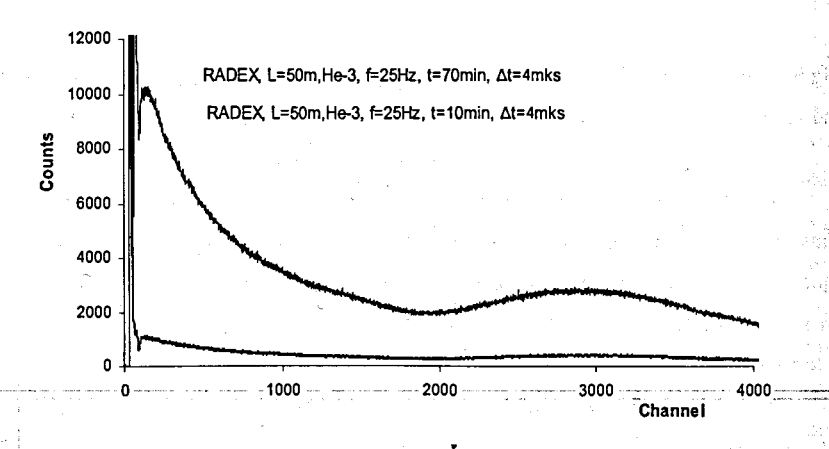


Fig. 7. TOF spectra of the open beam, measured on the 50 meter flight path of the central channel of the RADEX setup (time channel width 4 μ s in 4096 channels $t = 16384 \mu$ s)

Measured time-of-flight spectra at the central flight path of the RADEX setup are presented in Figures 6 - 8. These spectra were used for obtaining flux of thermal neutrons on the 50 m flight path by analogy with the above-mentioned method for the IN-06 source. The flux of thermal neutrons was estimated at the rate of about 150 n/cm²s at the burst frequency of 25 Hz and pulse duration of 60 μ s.

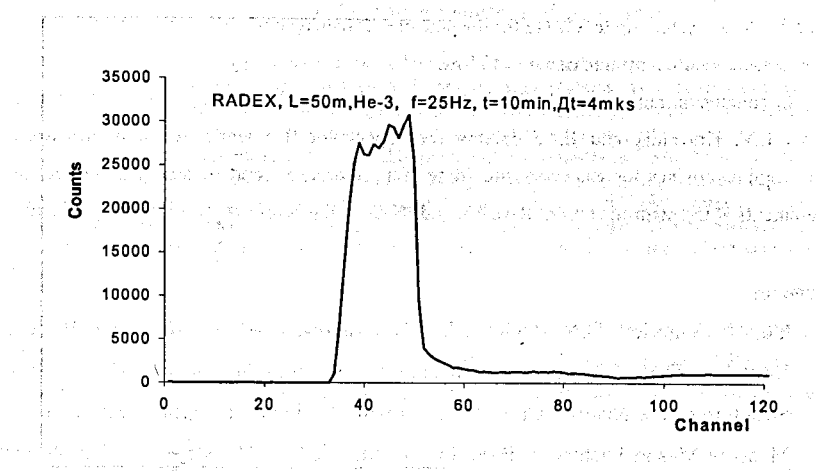


Fig. 8. TOF spectra of the open beam, measured on the 50 meter flight path of the central channel of the RADEX setup (time channel width 4 μ s in 4096 channels t = 16384 μ s)

After recalculation of the RADEX measurement at the same experimental conditions as on the 22.4 m flight path of the IN-06 source we discovered, that the thermal neutron flux at equal characteristics of the proton beam of the RADEX is approximately 20 times larger, than that of the IN-06.

Conclusion

During start measurements at INR of Russian Academy of Science of the pulsed source of thermal neutrons IN-06 measurements of its basic characteristics were carried out, also in parallel measurements of parameters of earlier started neutron source RADEX were realized. Fluxes of thermal neutrons were determined on the 22.4 m flight path of the IN-06 and on the 50 m flight path of the RADEX, at the average proton beam power of 6 kW and available experimental conditions accordingly $F_{in-06} = 821 \text{ n/s*cm}^2$ and $F_{radex} = 150 \text{ n/cm}^2$ s. It turns out, that at the identical proton beam the flux of thermal neutrons at the RADEX is approximately 20 times larger, than at the IN-06. It may be connected with the different orientation of neutron guides of the RADEX and the IN-06 setup (neutron guides of the RADEX look on the neutron production target

whereas neutron guides of the IN-06 look on the water moderator).

During preparation to the around-the-clock running conditions the new high-speed data acquisition system was developed and tested. Comparison with the spectra measured by the old measuring system in standard CAMAC, validate the operation of the new data acquisition system. At the same time maximum statistic set speed has been increased by an order of magnitude from 80 kHz for the "old" system up to 8 MHz for the new one. It managed to reduce the time channel width of the new data acquisition system down to 121 ns.

In conclusion authors would thank director of the INR RAS V.A. Matveev and also deputy-directors L.V. Kravchuk and E.A.Koptelov for support of this work, teams of accelerator and experimental complexes for successful providing of a proton beam and assistance in the realization of measurements at the neutron sources RADEX and IN-06 at the Moscow Meson Factory of INR.

References

- Yu. V. Grigoriev, O.N. Pavlova, B.V. Zhuravlev, A.A. Alekseev, A.I. Berlev, E.A. Koptelov, D.V. Hlustin, Zh.V.Mezentseva. / The Investigation of the Resonance Structure of the Neutron Cross-Sections with the Time-of-Flight Spectrometers at the Moscow Meson Factory. // Proc. Int. Seminar ISINN-16, May 23-24, 2008.-Dubna:-JINR. 2009 P.319-325.
- Yu. Ya. Stavissky/Neutron facilities of Moscow meson and kaon factories. Proc. of International Collaboration on Advanced Neutron Sources ICANS-XI, October 22-26, 1990, KEK, Tsukuba, Japan, p. 87.
- 3. A.P. Zhukov, A.D. Perekrestenko, S.F. Sidorkin, N.M. Sobolevskij./Spectra of neutrons of a pulsed source of neutrons IN-06 INR of the Russian Academy of Sciences. // Moscow: INR RAS. Preprint INR №1140/2005. April, 2005.
- 4. B.A. Benetsky, F.Z. Beketov, M.I. Grachev etc. Preprint INR of the Russian Academy of Sciences № 1058/2001. Moscow: INR of the Russian Academy of Sciences, 2001.
- 5. A.A. Bergman, A.I. Berlev, Yu.V. Grigoriev. Research of resonant structure of neutron sections on TOF spectrometers with pulse neutron sources of Moscow Meson Factory. Preprint INR of the Russian Academy of Science № 1225/2009.-Moscow: INR of the Russian Academy of Science, 2009.

Measurements of Neutron Total and Capture Cross Sections at the TOF spectrometers of the Moscow Meson Factory

Yu.V. Grigoriev^{1,2}, D.V. Khlustin¹, Zh.V. Mezentseva², Yu.V. Ryabov¹

¹Institute for Nuclear Research RAS, Troitsk, Russia ²Joint Institute for Nuclear Research, Dubna, Russia

Abstract. At the 50 meters flight path of the pulsed neutron source RADEX of the Moscow Meson Factory (MMF) INR RAS measurements of neutron total and capture cross sections were carried out. For these measurements a detector system "REPS" consisting of the 8-sectional liquid (n,γ)-detector with a volume of 40 liters (L=49.3 m) and the neutron detector with ³He counters (L=51.5 m) of a high efficiency ε(E_{th.})=95 % was used. Time-of-flight spectra were measured for the thin metal radiator-samples of ⁵⁵Mn, ⁹³Nb, Mo, In, ¹⁴⁸Sm, ¹⁶⁵Ho, ¹⁸¹Ta, W and ²³⁸U with a diameter of 80 mm. The analogous values of the group total and capture cross-sections for above mentioned materials were obtained from the measured time-of-flight spectra at the 18 m (25 m) flight path of a pulsed neutron source with Rb target of the radiochemistry setup MMF by means of ³He, ¹⁰B and NaI (TI) counters. These values were also obtained by GRUCON code on the basis of the estimated data libraries.

To investigate the resonance structure of the neutron cross-sections measurements of time-of-flight spectra have been carried out at the 50 m flight path of the REPS setup (see Fig.1) [1] and at the 18 m flight path of the radiochemical setup (RCS) of the MMF (see Fig. 2).

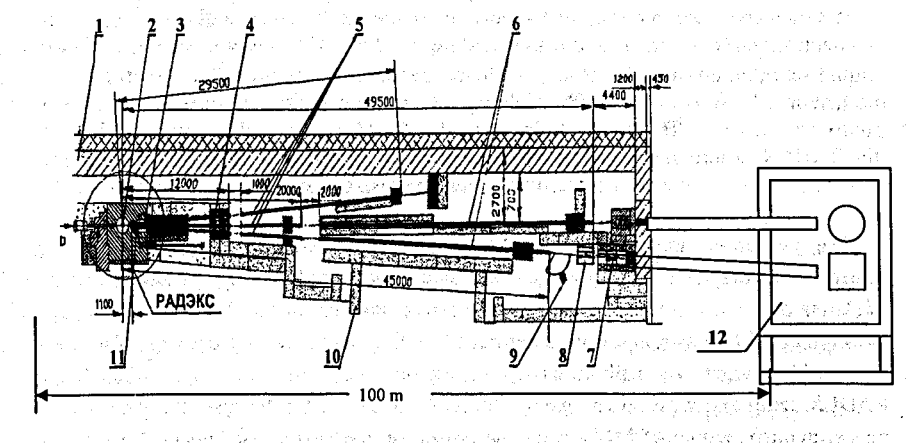
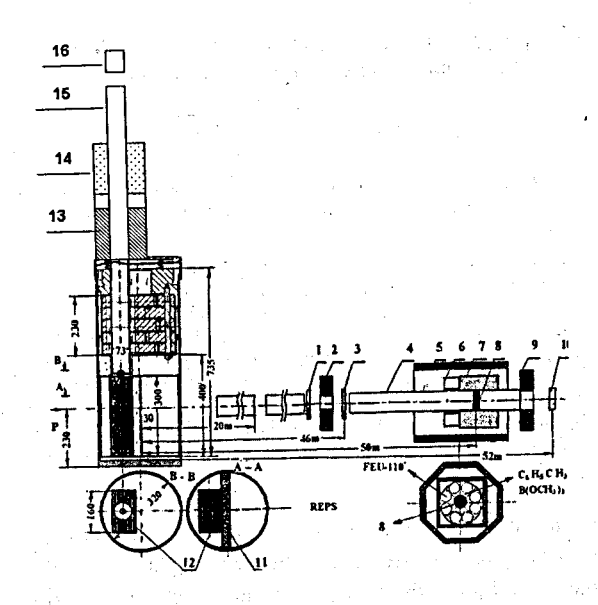


Fig.1 A schematic view of the TOF neutron spectrometer: 1- brick wall, 2-tungsten target with

a water moderator, 3- biological shielding of the neutron source RADEX, 4 - cast-iron shielding from neutrons and gamma-rays, 5 - neutron guide in the from of steel vacuum tube, 7- 3 He neutron detector, 8 - multisectional liquid (n,γ) - detector, 9 - multiangular setup to investigate the neutron scattering, 10 - concrete shielding of the neutron spectrometer, 11- gate of a neutron beam, 12 - experimental building.



100

Fig. 2 The setup REPS at the 50 meter flight path of the pulsed neutron source RADEX with W target and water moderator: 1 - monitor counter, 2, 9 - collimators, 3 - sample-filter, 4 - neutron guide, 5 - boron and lead shielding, 6 - FEU-110 photomultiplier, 7 - 8-sectional liquid scintillation (n,γ)-detector, 8 -radiator- sample, 10 - neutron ³He detector, 11 - water moderator, 12 - W target, 13 - Pb shielding, 14 - neutron multiscattering detector, 15 -neutron guide, 16 - neutron ¹⁰B detector. Indexes 13, 14, 15, 16 correspond to a vertical flying base of the RADEX, where they plan to perform some new experiments, including measurements of the n-n scattering cross section.

The measurements were performed by means of the 8-section liquid (n, γ)-detector and neutron detectors with ³He counters. The metal targets made from a natural tungsten with a thickness of 7 cm were used as the pulse neutron sources (at the RADEX setup) [2]. At the RCS the metal targets made from a natural Rb with a thickness of 6 cm were also served as a source [3]. Targets were illuminated by a proton beam with an energy of 209 MeV at the RADEX setup and with an energy of 160 MeV at the RCS. The operated parameters of the pulsed neutron source of MMF were the pulsed proton current of linear accelerator $I_p = 11$ mA, the proton energy E_p .=209 MeV, the proton pulse repetition rate f = 50 Hz, the proton pulse duration $\tau = 2$ -200 mks.

As the radiator-samples and filter-samples were served metal and oxide disks made from ⁵⁵Mn, ⁹³Nb, Mo, In, ¹⁴⁸Sm, ¹⁶⁵Ho, ¹⁸¹Ta, W and ²³⁸U with a diameter from 50 mm to 80 mm of a different thickness. An intensity level of the neutron beam at the REPS setup was controlled

by a ³He counter (SNM-18) installed at 114 meter flight path before a tungsten target of the RADEX source. At the RCS a ¹⁰B counter (SNM-13) was in use before a Rb target.

The data acquisition was realized by means of measurement modules on the basis of PC with two types of equipment and software: at 1 µs time channel width (author T.G. Petukhova FLNP JINR) and 0.01 µs (developed at INR Troitsk and JINR, [4]). The minimal duration of the time channel is limited to the minimal duration of a proton beam of the accelerator. These two systems in existing measurement conditions were approximately equivalent. The main feature of these measurements is usage of the ion guide as a neutron guide. This allowed perform new experiments requiring much more time measurement and higher energy resolution.

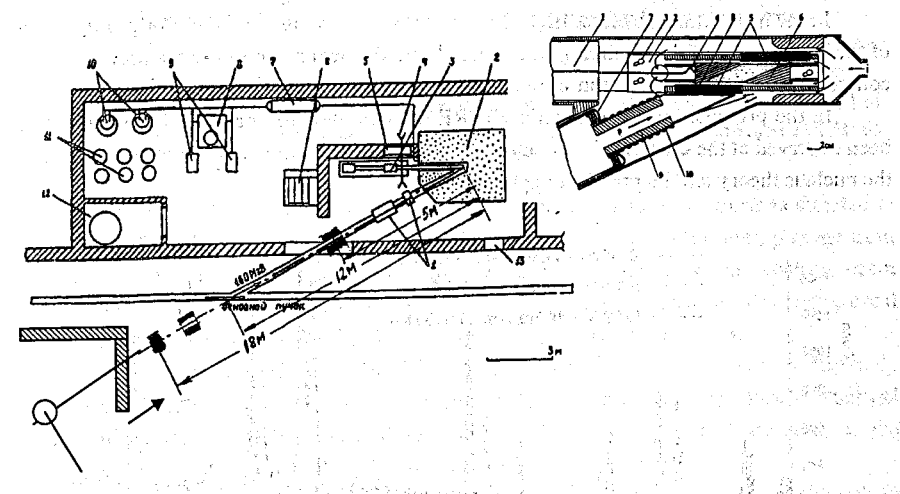


Fig. 3 A schematic view of the neutron setup with a Rb target: 1 – proton ion guide with equipment for a beam control, 2 – cast-iron cube shielding for a target placement, 3-equipment for a target movement, 4..12 – functional elements of the RCC, 13 – entrance into a target hall. A detailed view of the target construction is shown on the right.

In the last 2007-2010s measurements of the time-of-flight spectra of the gamma-rays have been carried out at the radioactive neutron capture by nuclei of 55 Mn, 93 Nb, Mo, In, 148 Sm, 165 Ho, 181 Ta, W and 238 U. For these measurements the 8-section liquid (n, γ)-detector with a total volume of 40 litres and 3 He neutron detector have been installed at the 50 meter flight path of the REPS setup of the Moscow Meson Factory (MMF). A duration of analog pulses was 35 ns and 1 µs from the (n, γ)-detector and from the 3 He neutron counter respectively. The registration efficiency of the (n, γ)-detector was determined using the γ -lines of 60 Co source and was equal to 30 % at the energy resolution of 30 %. The registration efficiency of thermal neutrons of 3 He neutron counter was approximately 95 %. The experimental time-of-flight spectra are shown in Fig. 4 (x-axis corresponds to the energy).

The background components in time-of-flight spectra come out from the gamma-rays and neutrons scattered in the experimental hall. These components were measured by resonance filters having so-called deep "black resonances" like, for example, Al (35 keV), Mn (2.4 keV and 336 eV) and W(20 eV). It should be stressed that protons falling onto the target cause neutrons with a broad energy spectrum in which a 15 % fraction of fast neutrons in the energy range from 14 MeV to 209 MeV after moderation. These neutrons fly out from the target mainly forward where detectors of the REPS setup are located and result in background increase and in overload of spectrometric electronic equipment. At 18 meter and 114 meter flight paths, where proton ion guides were used as neutron guides, the fraction of background neutrons is less because these neutrons fly towards the proton beam.

In the near future 18 meter flight base of an isotope setup will be prolonged by means of the lengthening of the neutron guide channel into the next room through a hole in a concrete wall, that also allows improve background conditions.

In the previous measurements at the REPS setup new resonances of a natural W have been observed at the energy of 7 eV and 18 eV. These results are very interesting in respect to the nucleus theory and its practical applications.

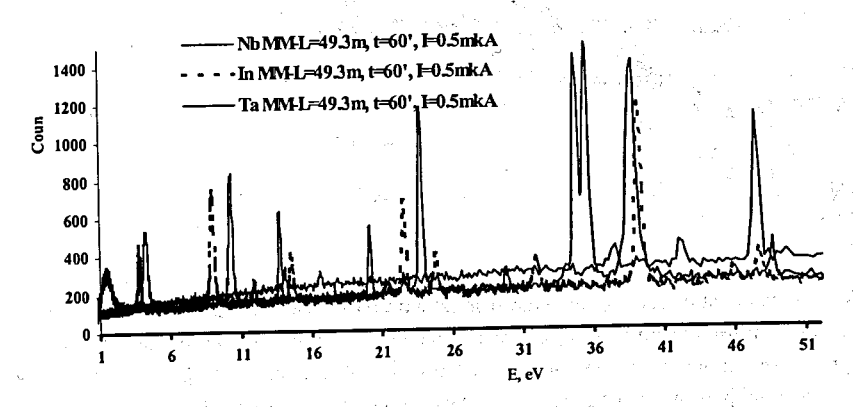


Fig. 4. Time-of-flight spectra of 93 Nb (d=2 mm), In(d=0.5mm), 181 Ta(d=0.2 mm) transmissions, measured by the liquid (n, γ)-detector at 49.3 m flight path. Parameters of proton beam are: E_p=209 MeV, I_p=5 mA, f=50 Hz, Δ t=1.5 μ s, dt_{ch}=1 μ s.

To determine fluxes from thermal neutrons time-of-flight spectra measurements were carried out at the 50 meter flight paths of the neutron source RADEX by means of 3 He counter and at 18 meter flight path of the isotope setup by means of 10 B counter at a neutron burst duration of $\Delta t = 65 \,\mu s$ and 200 μs at a frequency repetition rate of 1 Hz and 50 Hz.

In Fig. 5, 6 time-of-flight spectra, measured at 50 m of the neutron source RADEX and at 18 m flight path of the isotope complex, are presented.

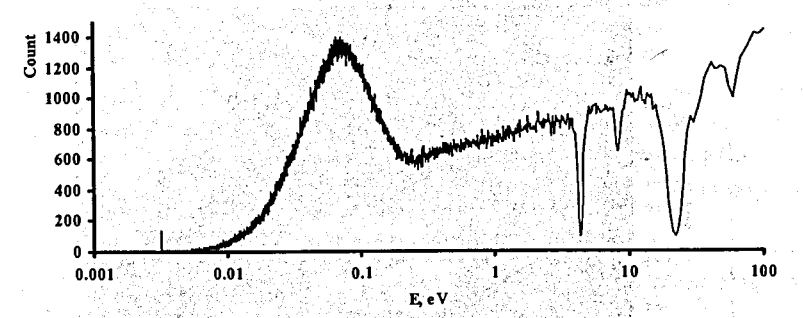


Fig. 5. Time-of-flight spectra of W (d=0.4 mm) transmissions, measured by the 3 He counter at 51 m flight path of the REPS setup. Parameters of proton beam are E_p =209 MeV; I_p =5 mA, f=1 Hz, Δt =65 µs, dt_{ch} =16 µs, t_{mes} = 60 minutes.

As one can see from the Figure 6 a maximum peak of thermal neutrons is situated at the energy of 0.062 eV and a spectrum of thermal neutrons is located in the energy range from 0.0032 to 0.25 eV. It is important that a thin W sample installed in the neutron beam practically did not decrease the neutron beam intensity. It allowed estimate the background components in this energy region using W resonances with a precision of 3 %.

Since the registration efficiency of thermal neutrons by 3 He counter was approximately 95 % and an illuminated detector surface came to 30 cm 2 then averaged flux of thermal neutrons will be $\Phi_{max} = 3000000 \text{ n/(cm}^2*\text{sec)}$ at 51 m flight path of the REPS setup at the proton beam parameters E_p =209 MeV, I_p =10 mA, f=50 Hz, Δt =200 μ s.

The test measurements were performed using the ³He counter at the 18 m flight path of the isotope complex with the Rb target (see Fig.3). The neutron counter was placed by a flank to the neutron flux to achieve the registration efficiency of thermal neutrons of 94 % at a flank surface of 7 cm². Because of copper plates with a thickness of 3 cm located behind the ion guide in the neutron beam the neutron flux decreased by order of magnitude 10. In this case the thermal neutrons flux was 600 n/cm² s. That is why the neutron detector should be well shielded from neutrons and gamma-rays at 27-degree turn of the ion guide and precisely adjusted along the neutron beam rigidly collimated by the ion guide.

If we suppose that thermal neutrons are emitted in ¹⁰He counter direction installed at a distance of 18 m from the target surface of 3 cm², than the thermal neutrons flux at the source surface should be approximately 10¹³ n/cm²s. Evidently the thermal neutrons flux will be 3*10⁶ n/sm²s at a distance of 18 m from the neutron source where the ring monitor detector was placed.

It would be possible to carry out investigations of the (n,n) and (n,p) scattering by the method of incoming beams and overtaking neutrons [6] using of W and U targets to increase the neutron beam intensity.

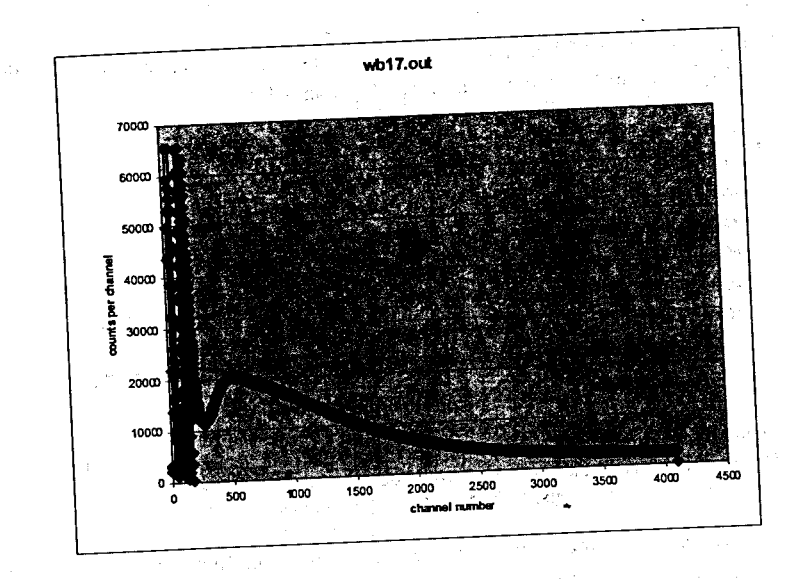


Fig. 6 Time-of-flight spectra, measured by the ^{10}B counter at 18 m flight path of the isotope complex. Parameters of proton beam are E_p =160 MeV, I_p =5 mA, f=50 Hz, Δt =165 μs , dt_{ch} =4 μs , t_{mes} = 10 min.

Conclusion

During last years 2007-2010 several experiments on the resonance structure investigation of neutron cross-sections at time-of-flight spectrometers of the MMF were carried out. Time-of-flight spectra of Mn, Cr, Nb, Mo, In, Ta, W and U metal samples were measured at the REPS setup using the 8-section liquid (n.γ)-detector and ³He counter. The averaged group total transmissions and cross-sections were extracted from the experimental spectra in the energy range from 1 eV to 10 keV.

Two new resonances in the radioactive capture for natural W were revealed at the energies of 4 eV and 17 eV. The new time-of-flight neutron spectrometer was constructed on the basis of 18 m ion guide of the radioisotope setup of the MMF. Test measurements were carried out to determine its characteristics. Similar test measurements were also carried out at the 114 meter ion guide before the neutron source RADEX. These original spectrometers allow increase measurement time of nuclear-physical values in the thermal and resonance neutron energy region.

Also there is in process of creation the vertical neutron guide with high vacuum on installation "RADEX" for original experiments on measurement of n-n scattering and definition of charge radius of a neutron.

References

111

- Berlev A.I., Grigoriev Ju.V., The REPS setup for the investigation of the neutron cross- sections structure and fundamental characteristics of neutron: Preprint INR RAS №1183/2007. – Moscow: INR RAS, 2007.
- 2. Benetsky B.A., Vahetov F.Z., Grachev M.I. e.a., Program of experimental researches on device RADEX: Preprint INR RAS № 1058/2001. Moskow: INR RAS, 2001.
- B.L. Juikov, V.M. Kohanuk, Ju.G. Gabrielants e.a., Device for production of radio nuclei on 160 Mev beam removal of Moskow Meson Factory // Radiochemistry. – 1994. – V.36, Release 6. – P. 499-504.
- 4. Berlev A.I., System for registration, gathering and accumulation of experimental data from nuclear – physical installations by time – of - flight method: Preprint INR RAS № 1189/2007, Moscow: INR RAS, 2007.
- 5. Grigoriev Yu.V., Method for determination cross-sections of neutron neutron interaction: Pat. USSR № 549023. Moscow, 1976.
- 6. E.A. Koptelov, V.A. Fedchenko, O.N. Goncharenko, M.I. Grachev, L.V. Kravchuk, V.A. Matveev, A.D. Perekrestenko, Yu.V. Ryabov and S.F. Sidorkin. Spallation neutrons at INR RAS – a facility status report // ICANS-17, 2005.

version thinks attitude the control of

t foly de la bet find from the latest of accombigion to take the property of the latest of the lates

A MULTI-SECTION FRISCH-GRIDDED IONIZATION CHAMBER FOR STUDIES OF NEUTRON-INDUCED FISSION AT THE GNEIS FACILITY

N.V. Kovalev^{1,2}, I.V. Ryzhov¹, G.A. Tutin¹, O.A. Shcherbakov², A.S. Vorobyev², L.A. Vaishnene²

¹⁾ Khlopin Radium Institute, Saint-Petersburg, Russia ²⁾ Petersburg Nuclear Physics Institute, Gatchina, Russia

Abstract

A multi-section Frisch-gridded ionization chamber adopted for operation at the neutron time-of-flight spectrometer GNEIS is described. The data acquisition system based on a waveform digitizer is discussed as well as the digital signal processing. Results of test measurements carried out in the neutron energy range 1-200 MeV with ²³⁵U and ²³²Th targets are reported.

Introduction

The study of neutron-induced fission has been and still remains one of the most important subjects of nuclear physics and has a great fundamental and practical importance. Nowadays, there is an increasing interest in studying neutron-induced fission of actinides at intermediate energies, i.e., between 20 and 200 MeV. It is motivated by nuclear data needs for feasibility studies of emerging nuclear systems dedicated to the generation of intense radioactive ion beams, incineration of nuclear waste, isotope production, etc.

Successful implementation of such tasks is impossible without a thorough understanding of the physics of the nuclear fission process at intermediate-energy, and can only be based on reliable experimental data. On the other hand, after many years of research the neutron-induced fission of actinides remains an intriguing subject of studies in nuclear physics.

Fragment mass distribution is one of the most important characteristics of the nuclear fission process. At present, a consistent description of mass splitting in fission is far from being achieved. It is believed that the formation of the fission fragment mass distribution is closely connected with the potential energy surface in deformation space (at the stage of saddle-to-scission descent) while dynamical effects (nuclear friction and inertia) have less influence on the shape of the mass spectra. A number of theoretical models have been proposed at different times to quantitatively predict fragment mass yields [1-5]. It should be pointed out that modeling of intermediate-energy neutron-induced fission is severely complicated by the fact that fission, being a relatively slow process, follows pre-equilibrium particle emission and competes with neutron evaporation. As a result, a number of nuclides, each with its own fission characteristics, will contribute to the experimental fission observables. This suggests that a model of fragment formation should be embedded in a proper nuclear reaction code which takes care of pre-fission particle emission (see, e.g., [6, 7]).

Further development of the fission reaction models requires new experimental data at intermediate energies. To date the neutron-induced fission cross sections of many actinides relevant to advanced nuclear applications have been measured at incident energies up to 200 MeV [8-11], but there is a lack of experimental data on fragment mass yields. So far we know only two experiments in which kinetic energy distributions and mass yields of the fission

fragments in the reaction ²³⁸U (n, f) and ²³²Th have been measured as a function of incident neutron energy. The first experiment was performed by Zoller et al. [12] using the neutron source LANSCE at the LANL, but the distribution of the fragments obtained in [12] has a relatively poor statistical support. It is accumulated several thousands of events (per neutron energy interval of 1 MeV) for incident neutron energies from 10 to 100 MeV, which drops to a few hundred events in the region 100-200 MeV. Such a low statistical support complicates the comparison of obtained data with the theoretical predictions. The second experiment was carried out at the neutron beam of the cyclotron facility CYCLONE in Louvain-la-Neuve (LLN). The facility has been described in details in Refs. [13, 14]. It was measured the mass distribution of fragments from ²³⁸U(n,f) and ²³²Th(n,f) reactions at the neutron energies 32.8, 45.3, and 59.9 MeV [15].

In this work we report on the results of test measurements carried out in the neutron energy range 1-200 MeV with ²³⁵U and ²³²Th targets.

Experimental set-up

The experiment was carried out at the neutron time-of-flight spectrometer GNEIS [16] which is based on the 1 GeV proton synchrocyclotron of Petersburg Nuclear Physics Institute (Fig.1). The GNEIS facility is intended for investigations of neutron interaction with atomic nuclei in the energy range from 10⁻²eV up to several hundred MeV.

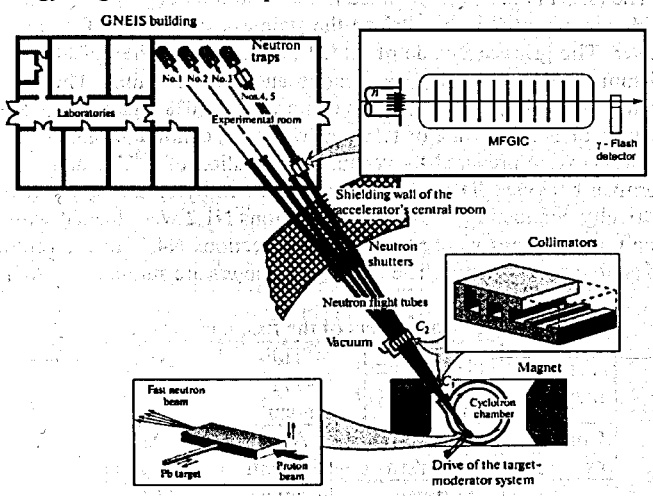
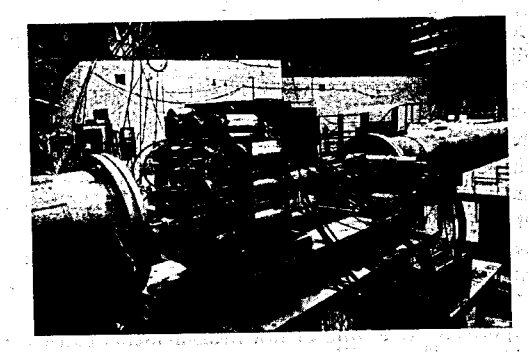


Fig.1. General layout of the measurements at the GNEIS facility.

To detect fission fragments, we used a multisection Frisch-gridded ionization chamber described in details elsewhere [15]. In contrast with our previous measurements, the chamber was slightly modified. In particular, we were forced (due to the background problems) to abandon the scheme with common anodes, so the present detector consists of 5 fully independent twin Frisch-gridded ionization chambers. The ionization chamber was located at a distance of 36.5m from the neutron source in a gap of flight tube of the neutron beam N5 of the GNEIS facility (Fig.2). Close to the chamber (downstream) was located a so-called γ -flash detector – FEU-30 PMT without scintillator which was used to produce a trigger (START) pulse for time-of-flight measurements.



gj.

.140 Aline

Fig.2. Multisection Frisch-gridded ionization chamber at the GNEIS.

The electrode assembly is placed into a thin-walled (1 mm) stainless steel detector housing. All the electrodes are of circular form with a diameter of 110 mm. The anodes are 50 μm thick aluminium foils, sandwiched between two 1 mm thick duralumin rings with inner diameter of 90 mm. The cathodes are stainless steel annular disks of 2 mm thick and 68 mm inner diameter. The target holders are mounted in the central part of each cathode using spring catches. The grids are mounted in parallel on the stainless steel rings of 2 mm thick and 90 mm inner diameter. The grids are made of gilded molybdenum wires of 80 µm in diameter spaced by 1.25 mm. The distance between anode and grid is 8 mm. The cathode to grid distance is 24 mm. The working gas mixture is composed of 90% argon and 10% methane (P-10). The chamber operates at pressure of 1.16 bar (without a continuous gas flow).

The fissile targets were prepared by vacuum evaporation of ²³⁵UF₄ and ²³²ThF₄ onto 30 μg/cm² thick Formvar backings. The backings were covered by 15-20 μg/cm² layer of gold to make them electrically conducting. The chamber sections N1,2 were loaded with the thorium targets, while the uranium ones were placed into the sections N4,5. In the central section, a calibration ²⁵²Cf source was mounted. The targets parameters are summarized in Table.1.

Toble 1 Parameters of the fiscile targets

| Tab | le 1. Paramete: | rs of the fissile | targets. |
|---------------------|--------------------------------------------------------------|---------------------------------------------------------------|-------------------------------------------------------------|
| Fissile material | ²³⁵ UF ₄ ~120 μg/cm ² | ²³² ThF ₄ ~171 μg/cm ² | ²⁵² Cf ~1 f/sec |
| Conduct | Au ~15 μg/cm ² | Au ~15 μg/cm ² | Au ~20 μg/cm² |
| Backing | Formvar ~30 μg/cm ² | Formvar ~30 μg/cm ² | Al ₂ O ₃ \sim 45 µg/cm ² |

Data Acquisition

The data acquisition system (Fig.3) of the experimental set-up is based on two flash ADC waveform digitizers CAEN V1721 which are used for signal processing. The Model V1721 is a VME module with 8 input channels, 8 bit and maximum sampling frequency 500 MS/s. The on-line processing computer software is based on a ROOT package [17].

For the present experiment, the chamber was loaded with 3 fissile targets: 235U, 232Th and ²⁵²Cf. Three signal waveforms (cathode + 2 anode) were recorded for each section, so 10 signal waveforms were recorded for each neutron burst (9 from the chamber and 1 from the γ - flash detector). In total it was accumulated 23 thousands of fission events of ²³⁵U and 15 thousands of fission events of ²³²Th.

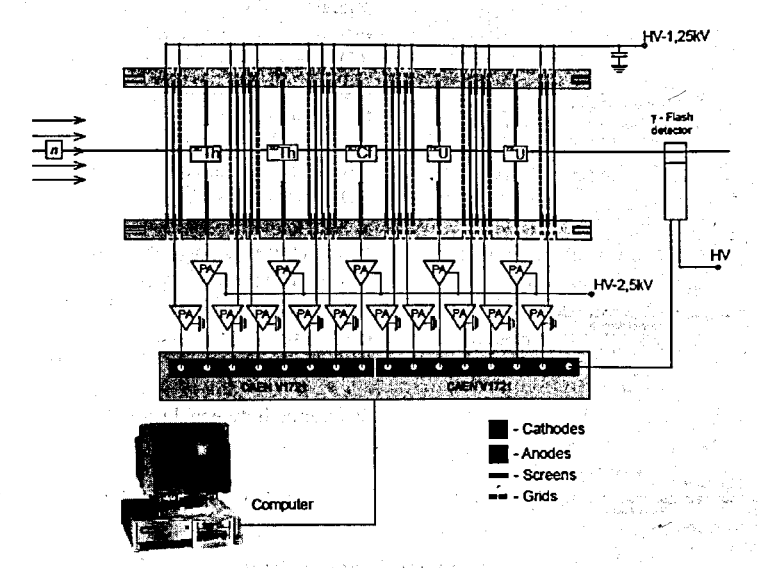


Fig.3. Data acquisition system.

Signal Processing of the plants of the average from other

A specific feature of the TOF spectrometer GNEIS is its relatively high intensity of the neutron and gamma flash. This leads to the fact that each flash results in a noticeable ionization of the working gas in all sections of the chamber. As a result, the shape of background pedestal of a signal is different in different sections. An example of anode signals from each chamber section is shown in Fig.4. To determine the amplitude and time characteristics of the digitized signals, it is necessary to find some characteristic points on a time scale (Fig.5):

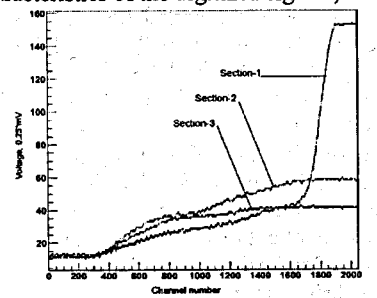
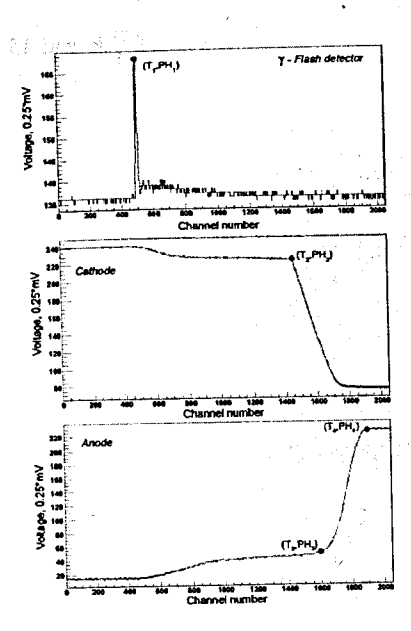


Fig. 4. Anode signals (channel width=2 ns).

- (1) peak of the signal from the y-flash detector - the point in time T₁ when proton bunch impinges the Pb target;
- (2) the beginning of the growth of the cathode signal - the point in time T₂ when ionization of the working gas by fission fragment takes place:
- (3) the end of the growth of the cathode signal - point in time when all electrons pass through the grid:



- (4) the beginning of the growth of the anode signals the point in time T₃ when first electrons pass through the grid;
- (5) the end of the growth of the cathode signal point in time T₄ when all electrons reach the anode.

Calculation of signal characteristics:

- * to determine the incident neutron energy by TOF method it's necessary to calculate the difference between T₂ and T₁;
- * to determine the mass and energy of the fission fragments it's necessary to calculate the difference between pulse- heights PH₄ and PH₄:
- * to determine the emission angle by drifttime technique it's necessary to calculate the difference between T_3 and T_2 .

Fig. 5. Characteristic points of the signals.

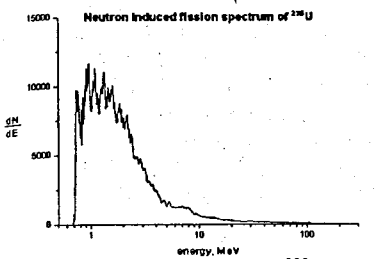
Experimental data analysis

After the calculation of pulse height and time position for each signal from the chamber, the TOF (neutron energy) and pulse height (fragment mass and energy) spectra were obtained. The next step of the data processing procedure consisted in neutron energy and fission fragment energy calibrations for each individual target. The calibration implying transformation of the TOF scale into the neutron energy scale was performed using the relativistic formula and locations of the neutron resonances in the total cross section of lead (material of neutron producing target) observed as resonance dips in TOF spectra (Fig. 6). The vertical arrows indicate position of the resonances while the numbers are resonance energies in MeV.

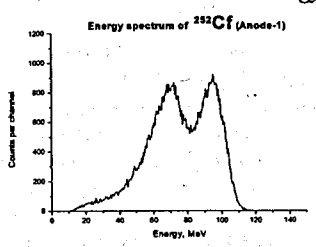


Fig.6. Neutron time-of-flight spectrum measured with the ²³⁵U target

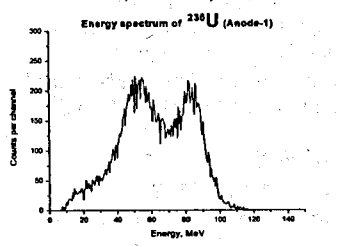
Calibration of the fission fragment energy scale was carried using the well-known alpha-particle lines of ²³⁵U, ²³²Th and ²⁵²Cf. Transformation to the energy scale was carried out using the precision pulse generator. At the present stage of data processing the pulse height defect was not taken into account. Fission fragment kinetic energy distributions obtained in present measurements are given in figures below for all incident neutron energies.



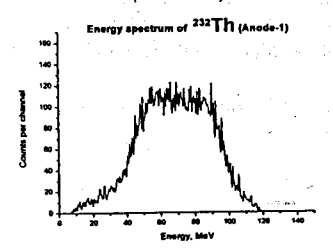
Fission events distribution for ²³⁵U target versus incident neutron energy



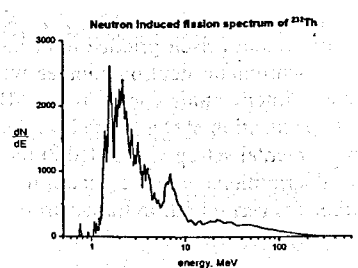
Raw fission fragments spectrum of ²⁵²Cf
(Anode-1)



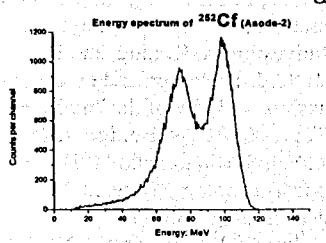
Raw fission fragments spectrum of ²³⁵U (Anode-1)



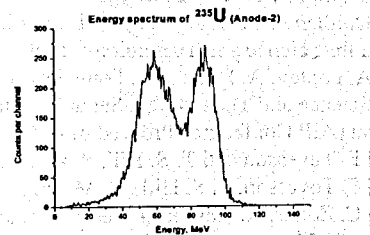
Raw fission fragments spectrum of ²³²Th
(Anode-1)



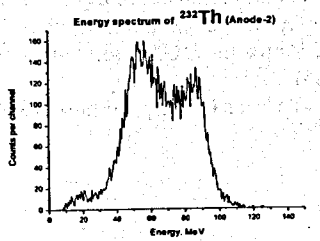
Fission events distribution for ²³²Th target versus incident neutron energy



Raw fission fragments spectrum of ²⁵²C. (Anode-2)



Raw fission fragments spectrum of ²³⁵U
(Anode-2)



Raw fission fragments spectrum of ²³²Th (Anode-2)

Anode-1 - through the backing, downstream; Anode-2 - from the fissile target, upstream.

Conclusion

A multi-section Frisch-gridded ionization chamber formerly used in fission experiments at quasi-monochromatic neutron sources was adopted for measurements on a "white" neutron spectrum in intermediate energy range. Beside a minor modification of the chamber itself, a new data acquisition system based on the flash ADC waveform digitizer was developed. A new experimental set-up was tested in the measurements of fission fragment mass and kinetic energy distributions at the neutron TOF-spectrometer GNEIS. The results of test measurements carried out in the neutron energy range 1-200 MeV with ²³⁵U and ²³²Th targets are reported.

References

- [1] B. Wilkins, E. Steinberg, and R. Chasman, Phys. Rev. C 14, 1832 (1976).
- [2] J. Maruhn and W. Greiner, Phys. Rev. C 13, 2404 (1975).
- [3] M. Duijvestijn, A. Koning, and F.-J. Hambsch, Phys. Rev. C 64, 014607 (2001).
- [4] H. Goutte, J.-F. Berger, and D. Gogny, Intern. J. Mod. Phys. E 15, 292 (2006).
- [5] S. Yavshits, In Proc. of the 2nd Intern. Workshop on Compound Nuclear Reactions and Related Topics CNR*09, Bordeaux, 2009, EPJ Web of Conferences 2, 08004 (2010).
- [6] A. Koning, S. Hilaire, and M. Dujvestijn, in Proc. of the Intern. Conf. on Nuclear Data for Science and Technology, Nice, 2007, ed.: O. Bersillon, F. Gunsing, E. Bauge, and R. Jacqmin (EDP Sciences, 2008) p. 211.
- [7] S. Yavshits, IAEA Report No. NDS-153 (2002); O. Grudzevich and S. Yavshits, in Proc. of the Intern. Conf. on Nuclear Data for Science and Technology, Nice, 2007, Vol. 2, ed.: O. Bersillon, F. Gunsing, E. Bauge, and R. Jacqmin (EDP Sciences, 2008) p. 1213.
- [8] O. Shcherbakov, A. Donets, A. Evdokimov, et al., in Proc. of the Intern. Conf. on Nuclear Data for Science and Technology, Tsukuba, 2001, J. Nucl. Sci. Tech. Suppl. 2, Vol. 1, p. 230.
- [9] A. Laptev, A. Donets, A. Fomichev, et al., in Proc. of the Intern. Conf. on Nuclear Data for Science and Technology, Santa Fe, edited by R. Haight, M. Chadwick, T. Kawano, and P. Talou (AIP Conference Proceedings 769, 2005) p. 865.
- [10] F. Tovesson and T. S. Hill, Phys. Rev. C 75, 034610 (2007).
- [11] F. Tovesson, T. S. Hill, M. Mocko, et al., Phys. Rev. C 79, 014613 (2009).
- [12] C. Zoller, A. Gavron, J. Lestone, et al., IKDA Report No. 95/25 (1995); C. Zoller, Ph.D. thesis, TH Darmstadt (1995).
- [13] A. Bol, P. Leleux, P. Lipnik, et al., Nucl. Instrum. Meth. 214, 169 (1983).
- [14] C. Dupont, P. Leleux, P. Lipnik, et al., Nucl. Instrum. Meth. A 256, 197 (1987).
- [15] I. V. Ryzhov, S. G. Yavshits, G. A. Tutin, et al., Phys. Rev. C83, 054603 (2011).
- [16] N.K. Abrosimov, G.Z. Borukhovich, A.B. Laptev, et al., Nucl. Instrum. and Meth. A242, 121 (1985).
- [17] ROOT User's Guide page http://root.cern.ch/root/doc/RootDoc.html

Status of Pulsed Neutron Facility in Korea

Guinyun Kim^a, Manwoo Lee^a, Kyung Sook Kim^a, Sungchul Yang^a, Eunae Kim^b, Valery Shvetshov^b, Vadim Skoy^b, Moo-Hyun Cho^b, and Won Namkung^c

*Department of Physics, Kyungpook National University, 80 Daehak-ro, Buk-gu, Daegu 702-701, Korea

Division of Advanced Nuclear Engineering, Pohang University of Science and Technology, San 31,

Hyoja-dong, Nam-gu, Pohang 790-784, Korea

Pohang Accelerator Laboratory, Pohang University of Science and Technology, San 31, Hyoja-dong, Nam-gu, Pohang 790-784, Korea

Abstract. We report on activities using a pulsed neutron facility consisting of an electron linear accelerator, a water-cooled Ta target with a water moderator, and a 12 m time-of-flight path. It is possible to measure neutron total cross sections in the neutron energy range from 0.01 eV to a few hundred eV by using the neutron time-of-flight method; photo-neutron cross sections can also measure by using the bremsstrahlung from the electron linac. A 6 LiZnS(Ag) glass scintillator was used as a neutron detector. The neutron flight path from the water-cooled Ta target to the neutron detector was 12.1 m. In this paper, we report total cross sections of Nb and also resonance parameters obtained using the SAMMY fitting program. The present results are compared with the previous experimental results and the evaluated data in ENDF/B-VII. We also report on the mass-yield distribution of fission products in the 2.5-GeV bremsstrahlung-induced fission of nat Pb and 209 Bi measured at the 2.5-GeV electron linac using a recoil catcher and an off-line γ -ray spectrometric technique.

Keywords: Pulsed neutron facility, Time-of-flight method, Neutron total cross-section, Photoneutron cross section, mass-yield distribution.

PACS: 29.87.+g, 25.60.Dz, 28.20.Ka, 29.20.Ej.

INTRODUCTION

Electron linear accelerators (linac) are being used throughout the world in a variety of important applications. The pulsed neutron facility based on an electron linac is effective for measuring energy dependent cross sections with high resolution by the time-of-flight (TOF) technique covering the energy range from thermal neutrons to a few tens of MeV. The measurement of neutron cross sections gives basic information about the internal structure of atomic nuclei and their constituents. Precise measurements of neutron cross sections are of great importance for the safety design of nuclear reactors and for the evaluation of the neutron flux density and the energy spectrum around a reactor.

The pulsed neutron facility based on a 100-MeV electron linac was proposed in 1997 and construction was completed at the Pohang Accelerator Laboratory in 1999 [1]. Its main goal is to provide the infrastructure for nuclear data measurements in Korea.

PULSED NEUTRON FACILITY

The pulsed neutron facility consists of an electron linac, a water-cooled Ta target, and a ~12-m-long TOF path. The characteristics of the facility are described elsewhere [2]. The beam energy of the electron linac is varied from 75 MeV to 50 MeV, and the beam currents at the end of linac are in between 100 mA and 30 mA. The length of electron beam pulse is 1-2 μs, and the pulse repetition rate is 10 Hz. Pulsed neutrons were produced via the ¹⁸¹Ta (γ,xη) reaction by bombarding a metallic Ta-target with the pulsed electron beam. The estimated neutron yield per kW of beam power is 1.9×10¹² n/s for electron energies above 50 MeV at the Ta-target based on the MCNP code [3]. To maximize the thermal neutrons in this facility, we used a cylindrical water moderator contained in an aluminum cylinder with a wall thickness of 0.5 cm, a diameter of 30 cm, and a height of 30 cm. The water level in this experiment was 3 cm above the target surface. The pulsed neutron beam was collimated to 5 cm diameter in the middle position of the collimation system where the sample changer was located. The sample changer consisted of a disc with 4 holes; each hole was 8-cm in diameter, which matched the hole in the collimator in the neutron beam line. The sample changer was controlled remotely by using a CAMAC module.

The neutron guide tubes were constructed of stainless steel with two different diameters, 15 cm and 20 cm, and were placed perpendicularly to the electron beam. The neutron collimation system was mainly composed of H₃BO₃, Pb, and Fe collimators, which were symmetrically tapered from a 10-cm diameter at the beginning to a 5-cm in the middle position where the sample was located, to an 8-cm diameter at the end of guide tube where the neutron detector was placed. There was a 1.8-m-thick concrete wall between the target and the detector room.

NEUTRON TOTAL CROSS SECTION MEASUREMENT

Since the experimental procedure has been published previously [4-6], only a general description is given here. The experimental arrangement for the transmission measurements is shown in Fig. 1.

The neutron detector was located at a distance of 12.1 m from the photo-neutron target. A ⁶Li-ZnS (Ag) scintillator (BC702) with a diameter of 12.5 cm and a thickness of 1.6 cm mounted on an EMI-93090 photomultiplier was used as a neutron detector. During the transmission measurement, the electron linac was operated with a repetition rate of 15 Hz, a pulse width of 1.1 µs, and the electron energy of 65 MeV. The peak current in the beam current monitor located at the end of the second accelerator section was greater than 50 mA, which was almost the same as that in the target. A high purity (99.99%) natural niobium (⁹³Nb 100% abundance in nature) metal plate with a diameter of 80.11±0.01 mm and thickness of 15.04±0.03 mm was used as a transmission sample. The main impurities of this sample were Ta (<0.1%), O (<0.06%), N (<0.04%), and C (<0.02%). A set of notch filters of Co, In, and Cd plates was used for the background measurement and the energy calibration. The configuration of the data acquisition system used in this measurement is also shown in Fig. 1, and details of this are described elsewhere [4].

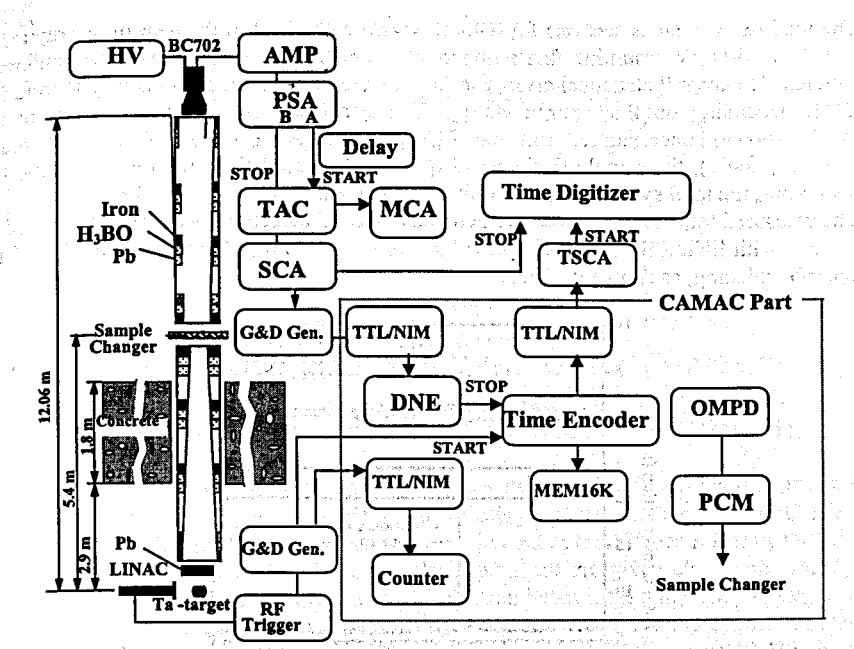


FIGURE 1. Configuration of experimental setup and data acquisition system.

The neutron total cross section is determined by measuring the transmitted neutrons through a known amount of sample and comparing this with the transmitted neutrons without sample. The accumulated neutron TOF spectrum for the open beam operation and for the transmission spectra of the natural Nb sample are shown in Fig. 2, together with the estimated background level, which is indicated by a solid line.

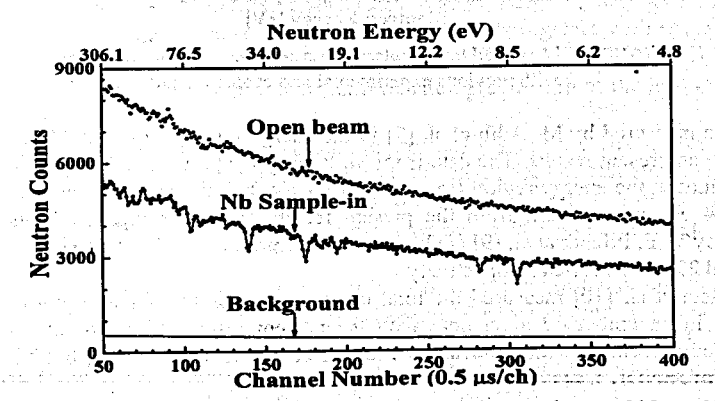


FIGURE 2. Neutron TOF spectra for the sample-in and for the sample out of 15-mm Nb, together with the estimated background level indicated as a solid line.

The total neutron cross sections for natural Nb were obtained in the neutron energy range from 0.05 to 300 eV assuming that numbers of count in each energy group are uniformly distributed. The overall statistical errors for the measured total cross sections ranged from 5% to 25%, depending on the neutron energy. The systematic uncertainties came from the following sources: uncertainties from the flight-path measurements (2.0%), the background estimation (0.04%), the sample thickness (2.6%), and the dead time, the normalization, etc (2.0%). Thus, the total systematic error of the present measurement is about 3.8%.

The measured total cross sections are generally in good agreement with other existing data [7-10] and with ENDF/B-VII.0 [11] and JENDL 3.3 [12] evaluated data assuming 300 K for Doppler broadening, as shown in Fig. 3.

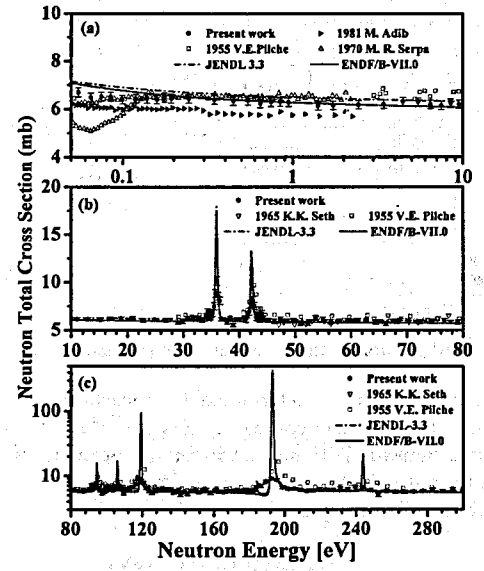


FIGURE 3. Measured total neutron cross sections for nat Nb compared with previous experimental and evaluated data.

O. Tri

The data measured by M. Adib et al. [7] in the energy region from 0.00232 to 2.2461 eV are lower than present results. The data from M. R. Serpa [8] are almost similar to that of the present values in the energy region from 0.14 to 2.1 eV, but his results in the neutron energy below 0.14 eV are different from the present results and other measurements. The data measured by V. E. Pilcher at al. [9] are higher than the present results at energies from 3.03 to 9.47eV and 29.2 to 299.7 eV, respectively.

K. K. Seth et al. [10] measured the total cross sections from 47.1 to 166.9 eV and their results are in general good agreement with the present results. The present results are in general good agreement with the evaluated data from ENDF/B-VII.0 [11] but slightly lower than those of JENDL 3.3 [12].

We fitted the transmission of the natural Nb sample with the SAMMY code [13] to obtain resonance parameters of each resonance peak in the neutron energy region from 10 to 280 eV, as shown in the Fig. 4.

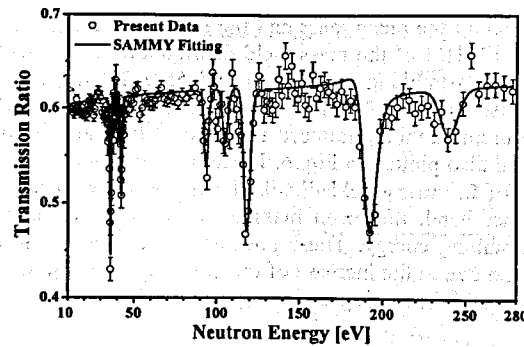


FIGURE 4. Measured transmission of Nb was fitted with the SAMMY code

MASS-YIELD DISTRIBUTION OF FISSION PRODUCTS

The mass-vield distribution of fission products in the 2.5-GeV bremsstrahlung-induced fission of natPb and 209Bi has been measured by using a recoil catcher and an off-line y-ray spectrometric technique. The experiment was carried out at the 10° beam line of the 2.5 GeV electron linac of the PAL. The details on the experiment are given elsewhere [14,15]. The bremsstrahlung was produced when a pulsed electron beam hit a tungsten (W) target with a size of 5 cm × 5 cm and a thickness of 1 mm. The W target was located at 38.5 cm from the electron exit window. The nat Pb metal foil of 0.5 mm thick and 25 cm² area (12.417 g) and the ²⁰⁹Bi metal foil of 3 mm thick and 25 cm² area (74.417 g) were wrapped with 0.025 mm thick aluminum foil with purity more than 99.99%. Each sample was fixed on a stand in air at 24 cm from the W target and positioned at 0° with respect to the direction of the electron beam. Each sample was irradiated for 4-7 hours with the end point energy of 2.5-GeV bremsstrahlung. The irradiated target assembly was cooled for 2 hours. The aluminum catcher and the lead or the bismuth foil were taken out from the irradiated assembly and were mounted separately on two different Perspex (acrylic glass, 1.5 mm thick) plates, The Perspex plate with an Al catcher contains primarily fission products together with reaction products from the Al catcher itself. The other Perspex plate with an irradiated Pb (Bi) metal foil contains fission products and significant (yxn) reaction products from the lead (bismuth) foil with high γ-ray intensity.

The γ -ray activities from fission and reaction products were measured using an energy- and efficiency-calibrated HPGe detector coupled to a PC-based 4K-channel analyzer. The HPGe detector with 20% efficiency was a p-type coaxial CANBERRA detector of 7.62 cm diameter × 7.62 cm length. The γ -ray spectrum was obtained by using a program Gamma Vision 5.0 (EG&G Ortec).

The data analysis was done primarily from the γ -ray spectrum of the fission products of the Al catcher to avoid difficulties of efficiency calibration for low energy γ -rays in the thick lead or bismuth foil. The details on the data analysis are given elsewhere [14,15]. The absolute cumulative yields of the various fission products as a function of the mass number for the 2.5-GeV bremsstrahlung-induced fission of nat Pb and 209Bi are plotted in Fig. 5. We do not consider the charge distribution corrections on the cumulative yields because of the closeness of the fission products to the beta stability line. The yields of fission products are fitted with a

Gaussian curve to obtain the mean mass and the FWHM of the mass-yield distribution. The mean mass and the FWHM of the mass-yield distribution for the photo-fission of nat Pb and 209Bi at 2.5-GeV bremsstrahlung are 94±0.5 and 55.0±2.0 mass units, and 95.0±0.5 and 51.0±2.0 mass units, respectively. The mean mass and the FWHM of the mass-yield distribution in the bremsstrahlung-induced fission of nat Pb and 209Bi at various energies are given in Table 1 and also plotted in Fig. 6. It can be seen from Fig. 6 that for both nat Pb and 209Bi, the FWHM of the mass-yield distribution increases with increasing bremsstrahlung energy. On the other hand, the mean mass of the mass-yield distribution decreases with increasing bremsstrahlung energy. These phenomena are due to the increase of the multinucleon emission and due to the increase of the multi-nucleon emission and the multi-chance of fission probability with increasing excitation energy.

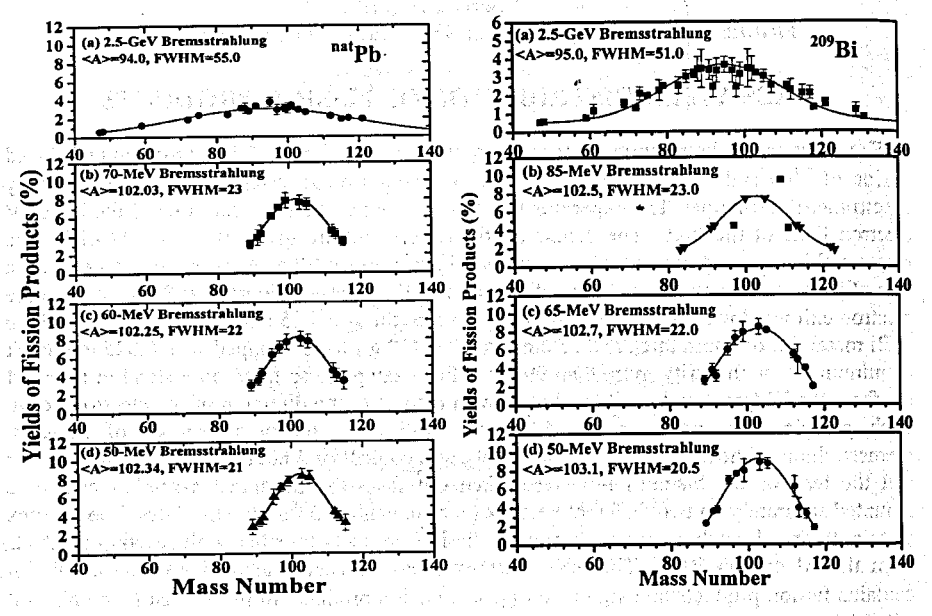


FIGURE 5. Measured yields of fission products (%) from the photo-fission of natPb and 209Bi as a function of the mass number. The line indicates the fitting for the measured data points <A> and FWHM are the mean mass number and the full-width at half-maximum of the mass-yield distribution.

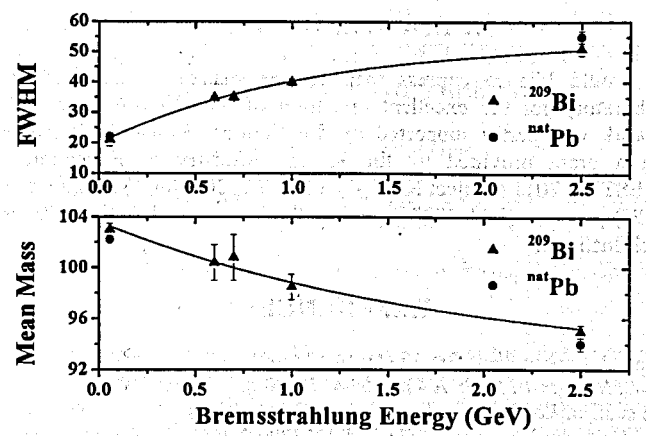


FIGURE 6. The FWHM and the mean mass of the mass-yield distributions for the photo-fission of nat Pb and 209 Bi as a function of the bremsstrahlung energy. The line indicates the polynomial fitting for the data points listed in Table 1.

TABLE 1. Mean mass and FWHM of the mass-yield distribution in the bremsstrahlunginduced fission of patch and 209 Bi

| | | ed lission of Pb and | Dl. | <u> </u> |
|-------------------|-----------------|-----------------------------------------------------------------------------------------------|--------------------------------------------------------------------------------------------------------------------------------------------------------------------------------------------------------------------------------------------------------------------------------------------------------------------------------------------------------------------------------------------------------------------------------------------------------------------------------------------------------------------------------------------------------------------------------------------------------------------------------------------------------------------------------------------------------------------------------------------------------------------------------------------------------------------------------------------------------------------------------------------------------------------------------------------------------------------------------------------------------------------------------------------------------------------------------------------------------------------------------------------------------------------------------------------------------------------------------------------------------------------------------------------------------------------------------------------------------------------------------------------------------------------------------------------------------------------------------------------------------------------------------------------------------------------------------------------------------------------------------------------------------------------------------------------------------------------------------------------------------------------------------------------------------------------------------------------------------------------------------------------------------------------------------------------------------------------------------------------------------------------------------------------------------------------------------------------------------------------------------|------------------------------------------------------------|
| Nuclei | Bremsstrahlung | Mean mass | FWHM | References |
| | energy | (mass units) | (mass units) | e i e ja see jija ka ka Sija sa sa sa sa sa sa sa sa sa |
| | (MeV) | ကြိုင်း လူကိုသို့ လေသည်လို့ လေလေ့သည် ကြို့သို့ သည်။ ကြို့သည် အသည် အတွင်း ကြို့သည် သည် သည်။ | and the first of the control of the second o | Calabatan ka Talahaka Kanadaran |
| nat Pb | 50 - 43 - 4 - 4 | 102.34 | 21 | 3 - 63 Carrier S |
| | 60 | 102.25 | 22 | |
| | 70 | 102.03 | 23 | e Maria jaja in Aray |
| * * | 2500 | 94.0±0.5 | 55.0±2.0 | dosty. Te rachar |
| ²⁰⁹ Bi | 28-40 | 103.5 | 19.0 | [16] |
| | 50 | 103.1 | 20.5 | |
| | 65 | 102.7 | 22.0 | |
| | 85 | 102.5 | 23.0 | [17] |
| | 600 | 100.4±1.4 | 34.8±0.7 | [18] |
| | 700 | 100.4±1.4 | 35.0±1.0 | [19] |
| | | | C (34) | |
| | 1000 | 98.5±1.0 | 40.0±1.0 | [20] |
| | 25000 | 95.0±0.5 | 51.0±2.0 | |

DISCUSSION AND SUMMARY

The Pohang pulsed neutron facility based on an electron linac was constructed for nuclear data measurements in Korea. This paper has presented neutron total cross-sections and resonance parameters for ^{nal}Nb in the neutron energy region from 0.01 eV to 300 eV. These cross sections and resonance parameters are in general consistent with other measured results and the evaluated data. We have also presented the mass-yield distributions of fission products of ^{nal}Pb and ²⁰⁹Bi with bremsstrahlung energies of 50-70 MeV and 2.5 GeV. It was found that the mean mass of the mass yield distribution of the fission products decreases with the increasing bremsstrahlung energy. However, the FWHM of the mass yield distribution increases with the increasing bremsstrahlung energy.

ACKNOWLEDGMENTS

The authors would like to express their sincere thanks to the staff of the Pohang Accelerator Laboratory for the excellent operation of the electron linac and their strong support. This work was partly supported by the National Research Foundation of Korea (NRF) through a grant provided by the Korean Ministry of Education, Science and Technology (MEST) in 2011 (Project No. 2011-0025762, 2011-0006306), by the World Class University (WCU) program (R31-30005), and by the Institutional Activity Program of Korea Atomic Research Institute.

REFERENCES

- 1. G. N. Kim et al., J. Korean Phys. Soc. 38 (1), 14-18 (2001).
- 2. G. N. Kim et al., Nucl. Instr. Meth. A 485, 458-467 (2002).
- 3. V. D. Nguyen et al., J. Korean Phys. Soc. 48 (3), 382-389'(2006)
- 4. V. Skoy et al., J. Korean Phys. Soc. 41 (3), 314-321 (2002).
- 5. A. Meaze et al., J. Korean Phys. Soc. 46 (2), 401-407 (2005).
- 6. T. Wang et al., Nucl. Instr. Meth. B 268 (2), 106-113 (2010).
- 7. M. Adib et al., http://www.nndc.bnl.gov/exfor7/exfor00.htm, EXFOR No. 30591.005 (1981).
- 8. M. R. Serpa, http://www.nndc.bnl.gov/exfor7/exfor00.htm, EXFOR No.10404.006 (1970).
- V. E. Pilcher and R. L. Zimmerman, < http://www.nndc.bnl.gov/exfor7/exfor00.htm>, EXFOR No. 11909.002 (1955).
- 10.K. K. Seth, D. J. Hughes, R. L. Zimmerman, and R. C. Garth, Phys. Rev. 110 (3), 692-700 (1958).
- 11.M. B. Chadwick et al. NuclearData Sheets 107 (12), 2931-3060 (2006).
- 12.K. Shibata et al., J. Nucl. Sci. Technol. 39 (11), 1125-1136 (2002).
- 13.N. M. Larson, ORNL/TM-9179/R5, Oak Ridge National Laboratory (2000).
- 14.H. Naik et al., Eur. Phys. J. A 47(3), 37-46 (2011).
- 15.H. Naik et al., Nucl. Instr. Meth. B 267(11), 1891-1898 (2009).
- 16.R.V. Warnock, R.C. Jensen, J. Inorg. Nucl. Chem. 30 (8), 2011-2016 (1968).
- 17.N. Sugarman, Phys. Rev. 79 (3), 532-533 (1950).
- 18.M. Areskoug, B. Schroder, K. lindgren, Nucl. Phys. A 251 (3), 418-432 (1975).
- 19.B. Schroder, G. Nydahl, B. Forkman, Nucl. Phys. A 143 (3), 449-467 (1970).
- 20.A.P. Komar et al., Sov. J. Nucl. Phys. 10, 30-35 (1970).

COINCIDENCE MODULE FOR SPECTRAL- AND TIME-CORRELATED MULTI-PARTICLE DETECTION WITH FOUR PIXEL DETECTORS TIMEPIX

<u>Vaclav Kraus</u>^{1,2}, and Carlos Granja¹

¹Institute of Experimental and Applied Physics, Czech Technical University in Prague, Czech Republic

²Faculty of Electrical Engineering, University of West Bohemia, Pilsen, Czech Republic

Abstract

An integrated coincidence system for multi-particle detection has been built to validate the coincidence detection and synchronize the readout of several pixel detectors. A system of two and also four detectors was built for measurements of angular correlations of rare fragments in ternary and quaternary fission which are detected in coincidence with the binary fragments. The pixel detectors are operated with the readout interface FITPix which provide power, control and DAQ. FITPix provides in addition signal communication ports and extended operability for the pixel detectors and the Timepix device (such as widely adjustable internal clock, external clock, clock gating, etc.), enables advanced triggering and high frame rate (up to 40 fps). The whole measurement can be triggered by a single event. An integrated analog spectrometer based on the USB 1.1.2 readout interface equipped with devoted module is used to provide a trigger from the common sensor signal of one pixel detector. The coincidence unit then monitors, validates and synchronizes the readout of the digital data. All operation and DAQ are managed by the modular software package Pixelman. The whole system can operate in vacuum and can be configured and extended into more detectors for a wide range of particle coincidence physics experiments.

Introduction

Semiconductor pixel detectors of the Medipix type [1] show great potential for precise studies of fission [2]. These devices provide more complete spectrometric information on different types of particles such as the position of single particles with µm resolution. The Timepix device [3] allows registering in addition the deposited energy and the particle time of interaction per pixel. The physics aim of this program is the detection of rare fission fragments in coincidence with the binary fragments and the measurement of their angular spatial distributions [4].

The pixel detector Timepix

The Timepix detector [3] is composed of a semiconductor integrated chip and a sensor. The chip is divided into a matrix of 65.536 pixels (array of 256×256 pixels of 55 μ m pitch). Sensors can be provided from different semiconductor material (Si, GaAs, CdTe) and also thickness of (300, 700, 1000 μ m). The principle of detection of ionizing radiation is based on the PN junction, which is connected in reverse bias. Under the sensor is placed the ASIC integrated circuit by bump-bonds. The ASIC contains for each pixel an electronic circuit

composed of analog and digital parts. The analog section contains the amplifier and comparator. The comparator threshold can be set by a DAC in each pixel individually. When the energy deposited in the pixel is greater than the preset threshold value, the comparator generates a pulse in the digital part. The digital section includes a processing unit for pulse synchronization with unit clock signal and a 14-bit counter. The digital unit can operate in one of three modes. The first mode is the time over threshold (TOT) mode which measures the energy deposited in the pixel. The second mode is the time of arrival (Timepix) mode which measures the particle time of interaction (arrival time). The third mode is the counting (or Medipix) mode in which the counter counts the number of particles crossing the threshold in the given pixel within a period of time. The counter can also work as a shift register. This mode is used when reading data from the detector. In each column there are shift registers connected to a 3584-bit shift register which is connected to a Fast Shift Register (FSR). FSR is part of the digital interface used to configure the detector, data reading and control. Reading of the data is possible via a serial interface that uses the LVDS voltage standard. The second option is to use 32-bit gate, which uses the CMOS standard. The maximum reading frequency for the whole chipboard is 100MHz.

The FITPix readout interface

FITPix [5] is a new control and DAQ interface for the Medipix type pixel detectors. The interface is based on a FPGA which is located in the digital system. The firmware can be divided into two parts. The first part is responsible for communicating with the PC. The second part devotes to the full operation of pixel detector. The device and the illustration of the architecture are shown in Fig. 1. Currently there are several types of communication standards supported (USB 2.0, Spacewire, RS-232). FITPix reaches up to 90 frames per second which corresponds to a data flow of 90 Mbit/s. The interface can be synchronized via an external port with other devices. This allows coincidence measurements for multi-particle detection.

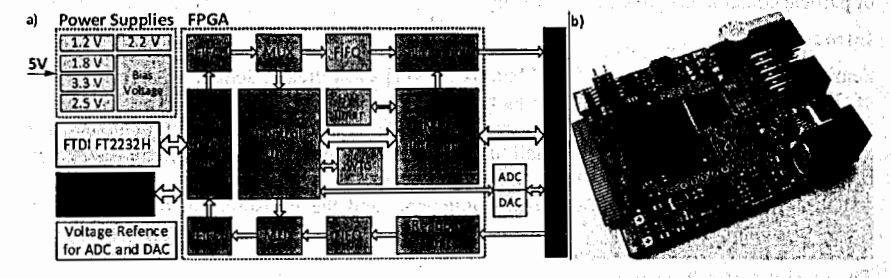


Figure 1: Architecture of FITPix (a) and the assembled interface (b) with dimensions 45 mm × 60 mm. Power consumption is 2.5 W. The interface can operate in vacuum. Figure taken from Ref. [5]

Coincidence module: multi-detector DAQ validation and synchronization

In order to monitor and validate the operation as well as synchronize the data readout of several detectors run in coincidence, an integrated synchronization master unit (coincidence module) was constructed. The layout of the module architecture is shown in Fig. 2.

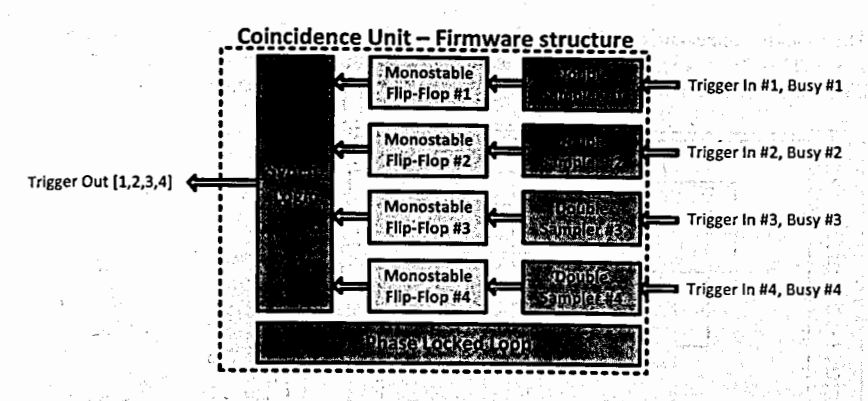


Figure 2: Architecture Iayout and firmware structure of the coincidence module.

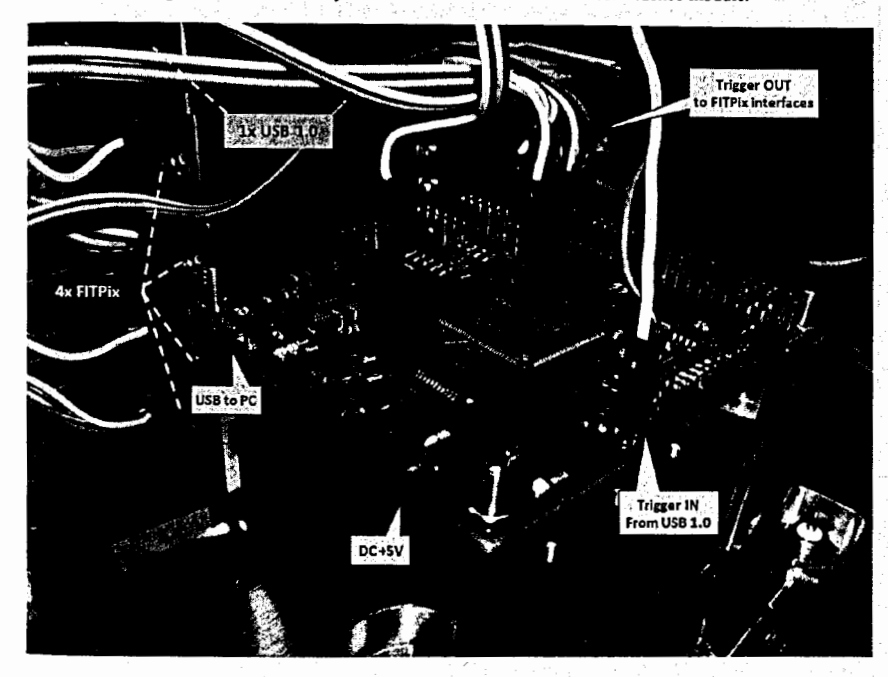


Figure 3: Coincidence module connected to one USB 1.0 interface (provides trigger) and four FITPix interfaces (take trigger). The readout interfaces appear in the background partially hidden.

a construe that the second leaguest this experience of the experience from the sixth excitations

The module connected to one USB 1.0 interface, which produces the trigger in signal, and four FITPix interfaces, which receive the trigger start signal, is shown in Fig. 3. The block diagram of the assembled coincidence system for multi-particle detection is shown in Fig. 4.

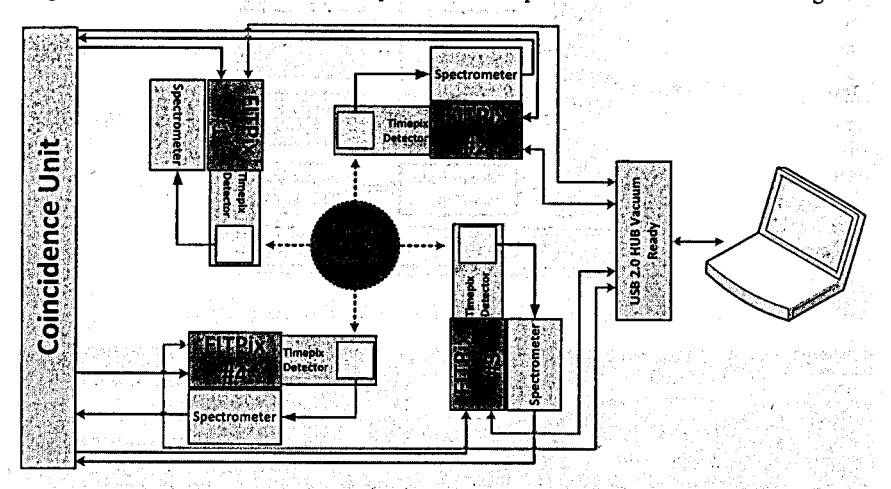


Figure 4: Block diagram of coincidence system for multi-particle detection validated and synchronized by the constructed coincidence module. In the figure all detectors are equipped with devoted analog spectrometric modules.

Each FITPix is assigned with a sync port equipped with several signals: trigger in, busy, out trigger. The coincidence module picks up for example the busy signal from all the interfaces. As long as there remains at least one busy signal classified as active, the coincidence unit ignores the trigger signal from the analog spectrometer (trigger) and the data frames are not readout. The scheme of the signal flow in the coincidence module is shown in Fig. 5.

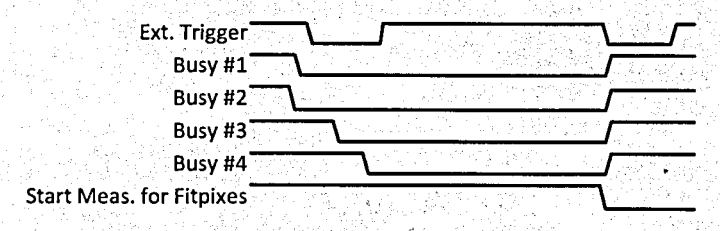


Figure 5: Scheme of signal flow in the coincidence module for the setup in Fig. 4.

Signals from the coincidence unit are linked to the FITPix interfaces via external digital port which is designed to synchronize multiple devices. A busy signal indicates that the given interface is ready and able to handle/receive the external trigger. The unit verifies that all devices are ready in which case passes on any external trigger signal coming and the

measurement can start. A trigger out signal is fed into the interfaces and validates the measurements. The maximum inaccuracy, given by two periods in the dual sampling, is 20 ns (for a 100 MHz frequency is the coincidence unit). Thanks to the structural design of gate array firmware it is easy to add more channels into the coincidence unit and precisely synchronize an arbitrary number of FITPix interfaces (limited only by the number of pins in the FPGA).

Measurement of fission fragments in coincidence

The module was tested on a setup consisting of four pixel detectors, each controlled by separate FITPix interface, and one USB 1.0 interface, housing the analog spectrometric module connected to one sensor for common trigger (setup shown in Fig. 6). The detection of three particles in coincidence is shown in Fig. 7. The setup equipped with the module run continuously for several days providing full synchronization of DAQ readout for all devices.

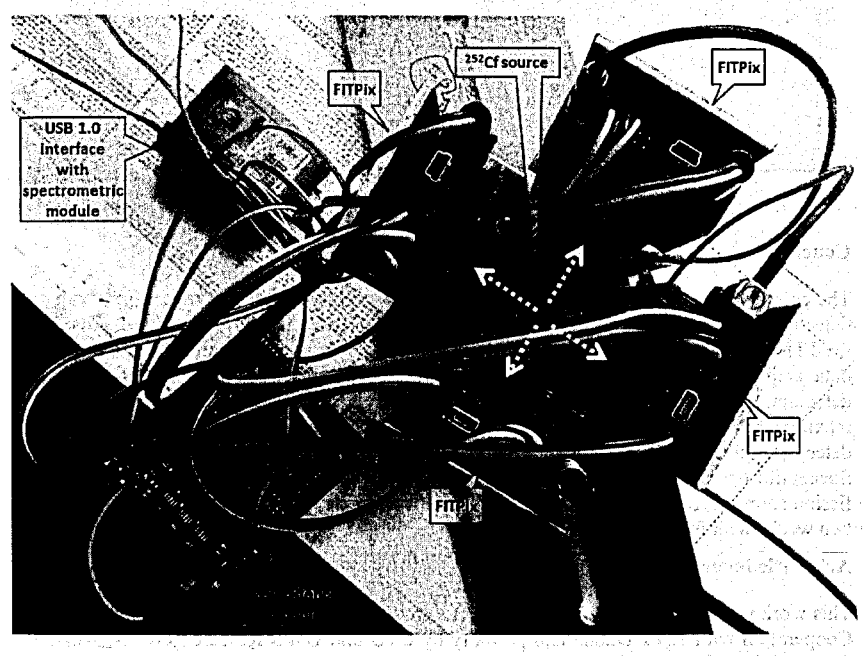


Figure 6: Experimental setup for coincidence detection of fission fragments consisting of four pixel detectors (two Timepix and two Medipix2) devices each controlled by separate FITPix interface. See block layout in Fig. 4.

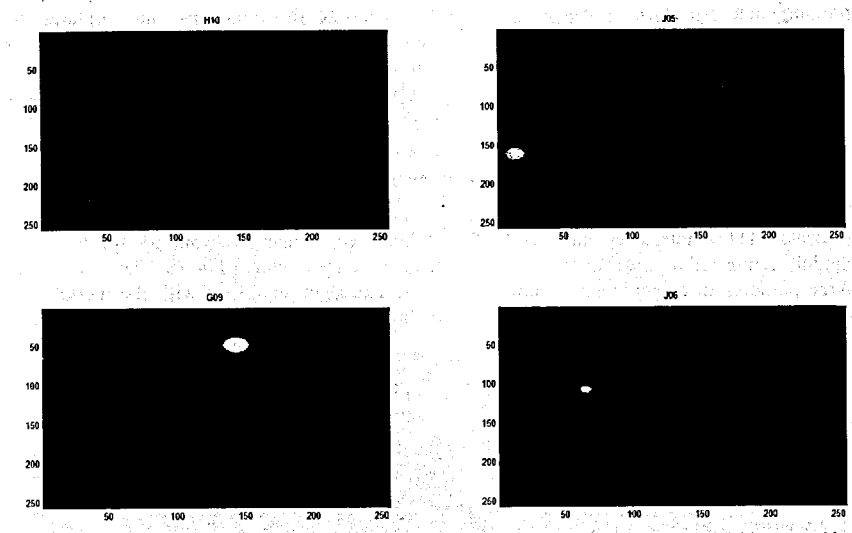


Figure 7: Detection of three particles in coincidence for the setup shown in Fig. 6. Frame acquisition started by trigger (generated by detector TPX J06) and frame exposure time 100 μs.

Conclusions

The coincidence module was developed for precise synchronization of four FITPix-run pixel detectors for the purpose of experiments on correlated detection of fission fragments. While the FITPix interfaces are controlled by the software package Pixelman, which controls the data acquisition, but cannot guarantee a smooth and fully synchronized readout for all detectors. The constructed coincidence module enables accurate synchronization and maximizes the number of data readout rate reaching up to frames per second for four pixel detectors. This gain significantly reduces dead time and eases the offline data evaluation. Successful operation of the module was demonstrated with measurements on a spontaneous fission source. Nearly forty million data frames were readout from up to four detectors during two weeks with full synchronization.

Acknowledments

This work was supported by a Research Grant from the Committee of the Czech Republic for Cooperation with JINR Dubna and partially by CTU and UWB Research Grants SGS-2010-037 a SGS-2010-018. Research performed within the Medipix Collaboration and was carried out in frame of the Research Program MSM6840770029 Fundamental Experiments for the Physics of the Microworld of the Ministry of Education, Health and Sports of the Czech Republic.

References

- [1].X. Llopart, M. Campbell, R. Dinapoli, D. San Segundo, E., Pernigotti, Medipix2—a 64 k pixel readout chip with 55 mm square elements working in single photon counting mode, IEEE Trans. Nucl. Sci. NS-49 (2002) 2279.
- [2] C. Granja, J. Jakůbek, S. Pospíšil, Z. Vykydal, Y. Kopatch, S. Telezhnikov, Positionsensitive spectroscopy of ²³²Cf fission fragments, Nucl. Instr. and Meth. A 574 (2007) 472-478.
- [3].X. Llopart el al, Timepix, A 65 k programmable pixel readout chip for arrival time, energy and/or photon counting measurements, Nucl. Instr. and Meth. A 581 (2007) 485.
- [4].C. Granja, V. Kraus, Y. Kopatch, S.A. Telezhnikov, S. Pospisil, Online correlated detection of rare fission fragments, in these Proceedings.
- [5] V Kraus, M. Holik, J. Jakubek, M. Kroupa, P. Soukup, Z. Vykydal, FITPix Fast Interface for Timepix Pixel Detectors, Journal of Instrumentation 6 (2011) C01079.
- [6] Vykydal, J. Jakubek, M. Platkevic, S. Pospisil, USB Interface for Medipix2 Enabling Energy and Position Detection of Heavy Charged Particles, Nucl. Instr. and Meth. Phys. Res. A 563 (2006) 112-115.

o o no sel ugas lucatora para a o o acellos el lacatora los relaxios

ราการทำ <u>หลังเกิด ผู้ที่ (สมระ</u>สายหน้านใช ซึ่งไป เ

รายเกราะ เอาไม่รู้เกี่ยวให้เกราะหาได้ เก็พ เพลาะคือ

on an included by Pay Contractive Hillian To

างเมืองเออสต์ม อากราช มีสำคัญ เป็นสหรั

a - an Man Hall carles & sealed

o and their till little diffit to him i

ा अध्यानिक अध्यानुष्टिक **मुक्तिमान्यके अ**ध्यान हो तथा

or week terminal the constitution

on the first of the second state of the second

d NAC of Automorae en

a continued the occupied of saff

ON THE POSSIBILITY TO INCREASE A NEUTRON BEAM FLUX OF IREN

L.V.Mitsyna, A.B.Popov, Song Zhaohui¹

Frank Laboratory of Neutron Physics, JINR, 141980, Dubna, Russia

¹Northwest Institute of Nuclear Technology, 710024, Xi'an, China

Abstract

A system of the neutron generating IREN target circled with beryllium cylinder of 11-41 cm thickness is considered. A sizeable (n,2n) cross section for beryllium, which has a value about 0.6 b at 4-10 MeV neutrons energies, can increase a neutron flux of IREN experimental beams, if real neutron spectrum from source has essential part of fast neutrons. Using GEANT and FLUKA codes the neutron yield and time distribution of neutron in W-Be source were estimated.

There is a paradox, which appear on application of the electron accelerator with a neutron-produced target for time-of-flight neutron spectrometry: if the energy of the accelerated electrons reaches or exceeds 30 MeV, the neutron intensity becomes proportional to the electron beam power. In this case it is possible to double the intensity at the facility like IREN due to ones more accelerating section only. And the additional section must duplicate all the parameters of functioning one, what practically demands the funds redoubling. That is why we were interested in the possibility to increase the neutron source intensity for the time-of-flight investigations without using the additional accelerator equipment.

The influence of a beryllium block, which is situated around the tungsten (or uranium-238) bremsstrahlung target, on the neutron source characteristics is considered below. Beryllium has a visible cross section of reaction (n,2n) for fast neutrons and slight scattering cross section at negligible capture.

Using the well-known programs GEANT and FLUKA for different configurations of the target and beryllium block relative position the calculations were made to evaluate a change of neutron yield from the combined source and a flux of resonance neutrons at a required flight path. The cross sections of (n,2n) reaction and of the elastic scattering for Be are presented in Fig.1.

The effect of increasing the number of neutrons after their passing through Be layer with the thickness L can be counted up as:

$$N = N_0 + N_0 \int_0^L [\exp(-n\sigma_t x) n\sigma_t dx] \frac{\sigma_{n,2n}}{\sigma_t} \implies N_0 (1 + \mu),$$

$$\mu = \frac{\sigma_{n,2n}}{\sigma_{i}} [1 - \exp(-n\sigma_{i}L)]$$

In a case of L > 10 cm of Be $\mu \approx \frac{\sigma_{n,2n}}{\sigma_t}$, and for neutron energies more than 4 MeV $\mu \approx 1/2$.

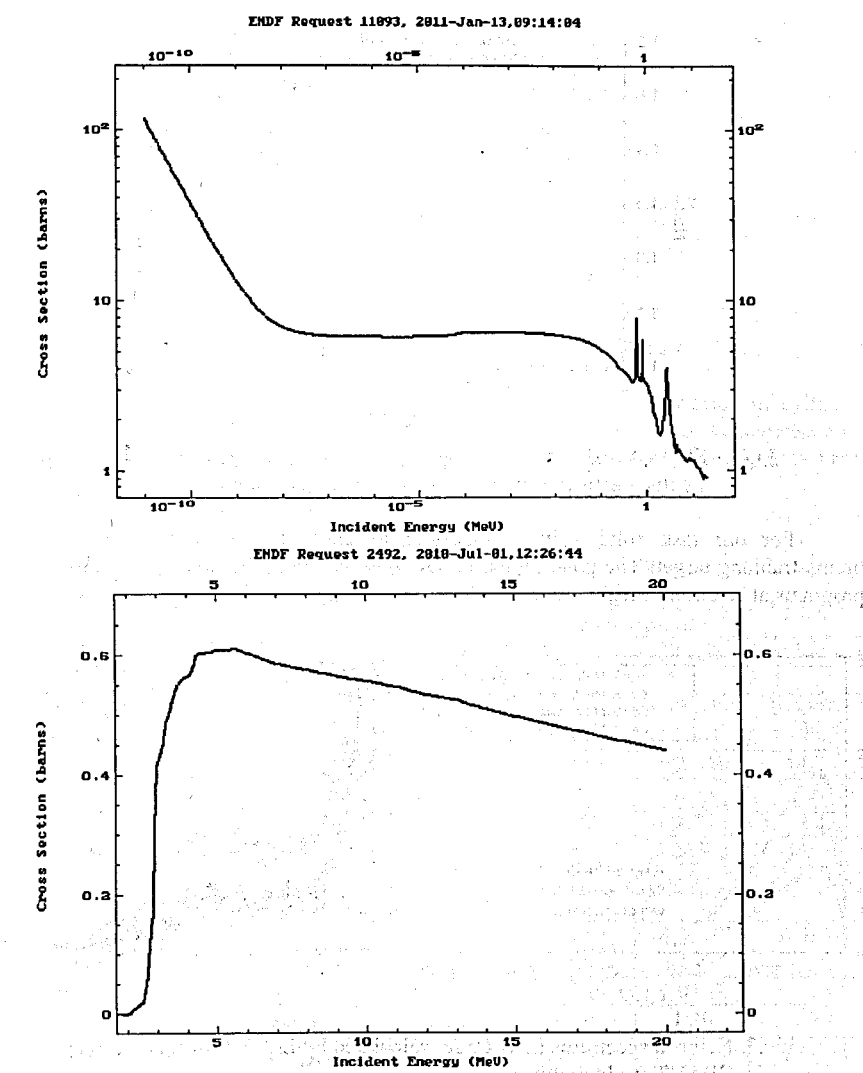


Fig.1. The cross sections of (n,2n) reaction (upper picture) and of the elastic scattering for Be(lower picture).

Thus, one can expect the neutron intensity increase in 1.5 times. The calculations with a Be ball with point neutron source in the center of 5 MeV energy is demonstrated in Fig.2 and

shows that there is the 1.5 multiple neutron intensity increasing if the diameter of Be ball is 20 cm.

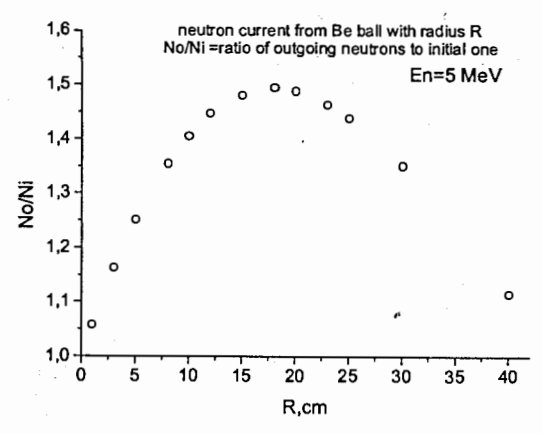


Fig.2. FLUKA calculations of dependency of the neutron yield per incident neutron with energy 5 MeV from the Be ball radius.

For our task solving it is important to know the neutron spectrum from the bremsstrahlung target. The postirradiation neutrons spectra calculated by FLUKA II GEANT programs at electron energies 30 and 50 MeV are presented in Fig. 3.

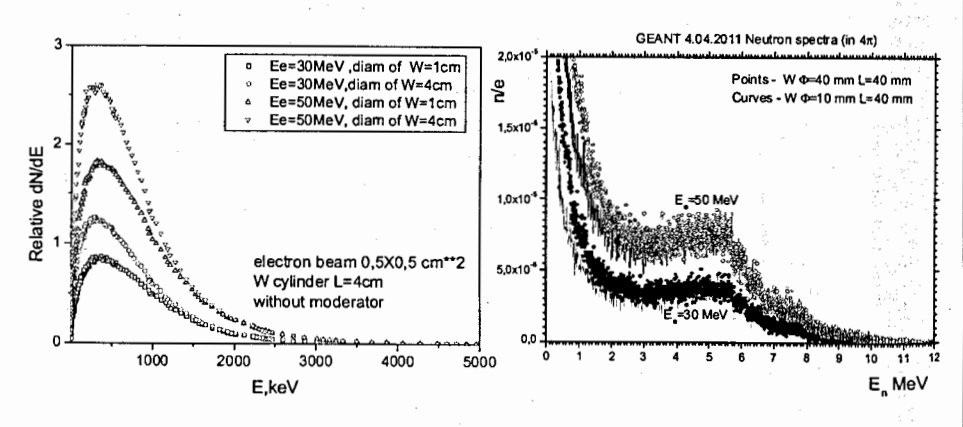


Fig.3. Neutron spectrums in W target calculated by FLUKA (left picture) and GEANT (right picture).

Unfortunately, these two programs bring out not the same spectra, and the results of completed calculations are different. Namely, FLUKA calculations does not give an increase of neutron yield when W target is surrounded by Be, whereas GEANT does it. In Table 1 there are the results of GEANT calculations for the compound W-Be target, which is shown in Fig.4.

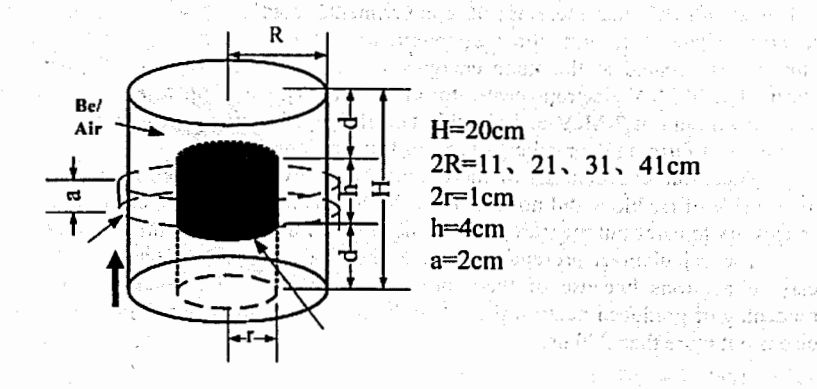


Fig.4. The source construction for demonstrated calculations.

The calculations were carried out using GEANT for tungsten target (in version of cylinder with 1 cm diameter and height L=4cm) inside of beryllium cylinder of different diameters and 20 cm height and for two energies of incident electrons. Two variants of the calculations were carried out: for air-filled cylinder and for beryllium cylinder of the same sizes.

Table 1.

Neutron yields per 1 electron obtained by GEANT.

| | | | | 4 in | |
|--------------------------------------------------------------------------------------------------------------------------------------------------------------------------------------------------------------------------------------------------------------------------------------------------------------------------------------------------------------------------------------------------------------------------------------------------------------------------------------------------------------------------------------------------------------------------------------------------------------------------------------------------------------------------------------------------------------------------------------------------------------------------------------------------------------------------------------------------------------------------------------------------------------------------------------------------------------------------------------------------------------------------------------------------------------------------------------------------------------------------------------------------------------------------------------------------------------------------------------------------------------------------------------------------------------------------------------------------------------------------------------------------------------------------------------------------------------------------------------------------------------------------------------------------------------------------------------------------------------------------------------------------------------------------------------------------------------------------------------------------------------------------------------------------------------------------------------------------------------------------------------------------------------------------------------------------------------------------------------------------------------------------------------------------------------------------------------------------------------------------------|---------------------------|-----------------------------------------------------------------------------------------------------------------|----------------------------------------------------------|-------------------|----------------|
| | | | Cylinder | diameter | |
| | 11 cm | 21 cm | 31 cm | 41 cm | |
| | Electron | energy 30 Me | $\mathbf{e}^{\mathbf{V}_{1,k}}$. The $\mathbf{v}_{1,k}$ | T | are a la Naret |
| | Air | 0.00648 | 0.00642 | 0.00647 | 0.00640 |
| Yield in 4π | | | 0.0064 | 0.0063 | 0.0062 |
| | Be | 0.00728 | 0.00760 | 0.00779 | 0.00767 |
| +la - | Ratio Be/Air | 1.12 | 1.18 | 1.20 | 1.20 |
| Yield from | Air | 0.00575 | 0.00452 | 0.00362 | 0.00289 |
| cylinder side | Be | 0.00662 | 0.00514 | 0.00343 | 0.00200 |
| * 17 - 4 | Ratio Be/Air | 1.15 | 1.14 | 0.95 | 0.69 |
| | Electron | energy 50 Me | e V | Pilone da la | ar of o |
| | Air | 0.0139 | 0.0139 | 0.0139 | 0.0139 |
| Yield in 4π | | 100 mm | 0.0128 | * N * V * * . | |
| · | Be | 0.0159 | 0.0166 | 0.0167 | 0.0167 |
| | Ratio Be/Air | 1.14 | 1.19 | 1.20 | 1.20 |
| Yield from | Air | 0.0123 | 0.00983 | 0.00776 | 0.00631 |
| cylinder side | Be And I | 0.0145 | 0.0112 | 0.00738 | 0.00440 |
| | Ratio Be/Air | 1.18 | 1.14 | 0.95 | 0.70 |
| Table 18 Committee Committ | 5 00 00 10 10 10 10 10 10 | DO NOTE OF A | Carry A. Tilly Co. | The market on the | 11.87 |

^{* -} earmarked values were obtained by FLUKA program

It is significant, that there are little experimental data about photoneutron spectra in the literature. There is information that maximums of photoneutron spectra for wide nuclei diapason are located at the same energies 1-3 MeV. There are also experimental data measured at 30 MeV electron accelerator in Toronto [1], where photoneutron spectrum for Pb have a maximum at 2 MeV and sizeable tail of fast neutrons up to 6 MeV. And there is an experience of forming the medical beams of fast neutrons too [2].

Thus, our expectations of increasing the neutron yield from source by placing the target inside of Be block did not find an undoubted confirmation. To clear up this question it is necessary to carry out measurements at the target of IREN facility putting it into Be block.

The calculations presented in Fig.5 shows that apprehensions about possible time delay of neutrons because of their moving through beryllium (and as a result essential broadening of produced neutron pulse) can be found unfounded, as calculated broadening of pulse is not more than 200 ns.

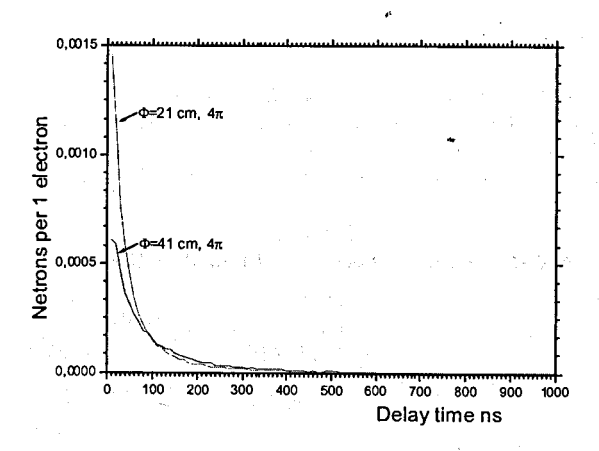


Fig.5. Time delay distribution for neutron moved in beryllium (diameters of Be cylinder are 21 and 41 cm).

In conclusion we wonder to note two important aspects, which follow from our executed calculations: 1) making the W target length longer than 4cm does not increase neutron yield; 2) extension of target cylinder diameter from 1 cm to 4 cm (diameter of incident electron beam is less than 1 cm) augments the neutron yield ~ 1.5 times for electron energies 30 and 50 MeV alike. First result corresponds to conclusion of [3], and the second one contradicts to deductions of this paper.

References.

- 1. K.G.McNeil, J.W.Jury, J.S.Hewitt, Canad.J.Phys., 48, p.950 (1970).
- 2. C.Ongarot et all, Phys. Med. Biol., 45, L55(2000).
- 3. G.G.Bunatian, V.G.Nikolenko, A.B.Popov, JINR Communications, E6-2009-182, Dubna (2009)

MULTIINPUT ENCODER FOR RECORDING SPECTRA OF SCATTERED NEUTRONS USING TIME-OF-FLIGHT METHOD

Shvetsov V.N.¹, Alpatov S.V.², Astahova N.V.³, Gundorin N.A.¹, Enik T.L.¹, Mitsyna L.V.¹, Pikelner L.B.¹, Popov A.B.¹, Salamatin I.M.¹, Salamatin K.M.⁴ Samosvat G.S.¹, Sedyshev P.V.¹, Sirotin A.P.¹

¹FLNP, JINR, Dubna, Russia; ² SIIAA, Dubna, Russia; ³ SII "Atoll", Dubna, Russia; ⁴"Dubna" University, Dubna, Russia

INTRODICTION

#HY

Because of putting into operation of the new neutron source IREN on a base of linear accelerator the conditions of experimentation changed essentially. The short path is used for time-of flight experiments, the new electronics for spectra registration with a narrow channel width and conforming to this software are worked up. In this work the hardware-software system for time-of-flight spectra recording is described, which is intended for investigation of IREN characteristics, of new detectors, and also for execution of the precise experiments in new conditions, specifically, in the experiment for obtaining the n,e-scattering length $b_{\rm ne}$ with the accuracy 2%.

Thereto it is proposed to use the new 8-channel time encoder in the precise experiment for measuring the angular anisotropy of neutrons scattered by noble gases in energy region from a few meV up to 1 eV with use of time-of-flight method. This time encoder connected to the computer USB-2 port will register signals from four neutron detectors and two monitor counters, which control a relative neutron flux in the beam. The program was developed to realize interchange of detectors positions at adjusted parameters, exposition in each of positions and information reservation in 8 spectrums (for each ³Hecounter in two positions). The control of data storage stability relative to monitor reading is provided by this program, and handy visualization of current and collected information is also realized by it.

1. TIME ENCODER DESCRIPTION

The device was made on a base of discrete logic, programmable logical integral circuitry Xilinx of Spartan3E series and microcontroller Cypress of FX2LP series. A functional scheme of the time encoder was shown in Fig.1.

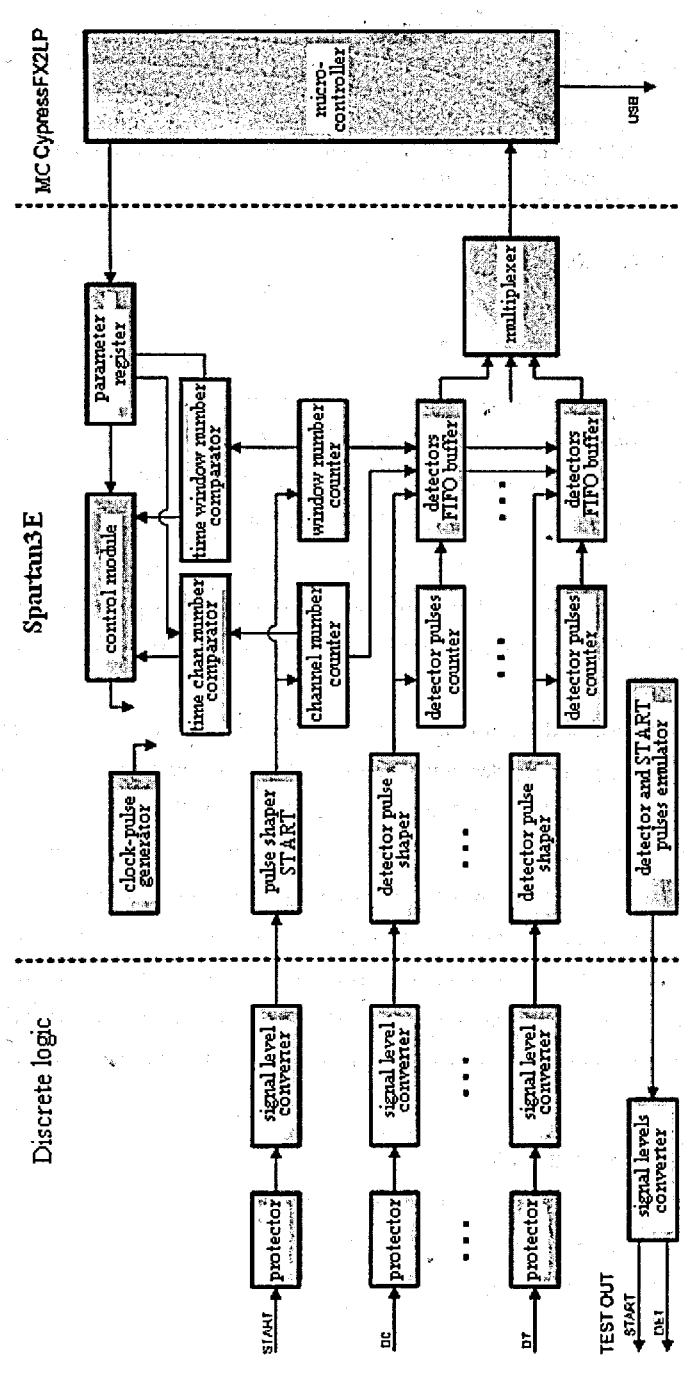


Fig.1. Functional scheme of the time coder

Safeguards were destined to set amplitude limits of voltage and current pulses produced by static electricity discharge and by static of powerful electromagnetic sources. Level of limitation is determined under permissible parameters of scheme elements. The level converters transform an output NIM-CAMAC signal of neutron detectors into LV-TTL standard needed for device operating. A driving generator produces a signal with frequency of 100 MHz, which is used for clocking (synchronization) of all another scheme elements working. Device realizes a detachment of entry pulses fronts (of detector and START pulses) and forms the control signals for a given time moment. The START entry is additionally blocked at a short time (1000 mks) after pulse coming, what guarantee higher stability of device working in conditions of powerful electromagnetic static.

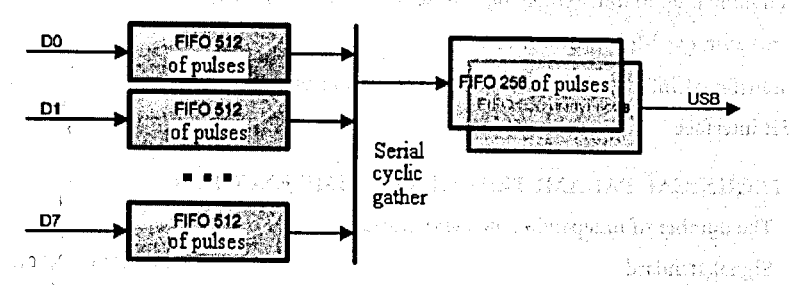


Fig.2. Internal buffers FIFO structure and problems of marries

The time counter cleared and increment of START signal counter is made, when the START pulse come. The value of the time counter is increased every 10 (or 100) ns and "is freezed" on reaching a maximal count. The increment frequency of this counter determines a discontinuity of measurement and maximal time of signal entrance from detector relative to the START one. Each detector pulse produces an increment of corresponding counter of detector pulses, and information about the pulse (current value of time counter and detector number 0....7) is stored to the certain buffer FIFO. If the buffer is overflowed a pulses count is continued without recording of information right up to buffer deallocation (at least partial). A blocking of all detector entry for a given time from the beginning of time window (START pulse appearance) is realized with use of time channel number comparator.

In the parameter registers there is information about parameters of the current measurement run:

recording process status, and the state of detector buffers FIFO;

- desired number of START signals (time windows) for control of recording continuance:
- period of time counter increment (10 or 100 ns);
- duration of blocking the intervals of detector entrances.

A control module coordinates a synchronous work of scheme elements. An emulator of detector and START pulses may be used for calibration and testing. It works irrespective of the rest part of scheme producing pulses of 20 ns duration with periods 10, 485, 760 for detector signals and 10, 485, 740 ns for START pulses. These pulses are converted to physical levels of standard NIM-CAMAC. Microcontroller implements the next functions:

- data moving from the detector buffers FIFO to inside binary buffer FIFO USB;
- data communications through USB;
- alignment up to transferable data volume (divisible by buffers length);
- · receiving and fulfilment of usb-command;
- transfer of information about state of recording process and of detectors buffers FIFO by USB interface.

2. TECHNICAL PARAMETERS OF THE TIME ENCODER

| The number of independent detector entries |
|----------------------------------------------------------------------------------------------------------|
| ■ Signal standard NIM-CAMAC (16 mA) |
| Minimal duration and interval between detector pulses 10 ns |
| Minimal width (discontinuity) of time channel 10 / 100 ns |
| ■ Number of pulse time channel 02 ²¹ -1 |
| ■ Maximal working duration of the time window 20/200 мс |
| ■ Summary number of pulses over each channel 02 ²⁵ -1 |
| Allowable intensity of recorded pulses: |
| o average total count over all detectors 8*10 ⁵ pulse/s |
| o average count at each detector 9*10 ⁵ pulse/s |
| o peak "momentary" total count over all detectors 4096 pulse |
| o peak "momentary" count at each detector 512 pulse |
| Preliminary setting the number of START signals (windows) 12²⁴-1 |
| Parameter of the data volume alignment for transfer 12¹⁶-1 byte |
| Parameter of duration of entry blocking 02²¹-1 chan |
| ■ Interface USB2.0 HS |
| • Overall sizes I40*115*35 mm |

Power supply device

USB (250 mA)

3 SOFTWARE OF TOF SYSTEM

Software of TOF system is operated by Windows and includes:

- programs of driver level;
- a control program;
- program of data sorting control;
- program of data treatment;
- secondary service programs.

CONCLUSION

The time-of-flight spectra obtained at 9-m path of IREN facility is shown in Fig.3. Neutrons were measured by 3 He-counter CHM-17. The spectra consists of three groups of channels with widths 20 ns (in channels up to 1000), 200 ns (in the channel interval 1001 – 5000) and 2000 ns (from 5001 to 8000 channel).

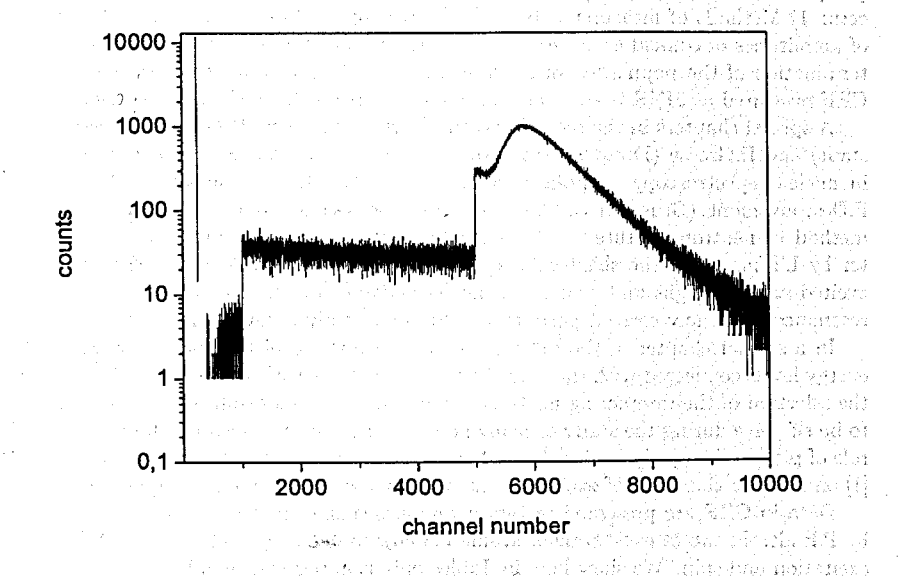


Fig. 3. Neutron spectra obtained at 9 m path of IREN facility

Embodiment of USB-interface provides the system with mobility. It can be used also in out experiments.

Compilation of nuclear excited states CRF

S.I. Sukhoruchkin, Z.N. Soroko, D.S. Sukhoruchkin Petersburg Nuclear Physics Institute, 188300 Gatchina

Abstract

The contents and scientific applications of 5-volumes compilation CRF (Combined Reaction File) of excited states of all nuclei are presented.

1 Introduction

We present here the contents and some scientific applications of 5-volumes compilation CRF (Combined Reaction File) of excited states of all nuclei prepared for vol. LB I/25 Springer (Editor H.Schopper). Volumes A,B,C,D,E contain data for nuclei with Z=1-29, 30-47, 48-60, 61-73 and 74-104. Each volume starts with a chapter in its Introduction written by the invited author to present one of advanced methods of data measurements.

Such a chapter of the first volume is written by A. Sukhovoy and V. Khitrov under the title "Capture γ -ray cascade measurements in JINR (Dubna)". It describes the main advantages of neutron capture gamma-gamma method developed in LNF JINR by the group of scientists headed by Yu. Yazvitsky and Yu. Popov. Parts of this chapter concern: 1) Methods of measurements; 2) Spectroscopic information from the summation of amplitudes of coinciding pulses; 3) Construction of the γ -decay schemes and 4) Determination of the population of levels in cascade. A great number of excited states in CRF measured at JINR is an important step forward in the nuclear spectroscopy.

A special chapters in the second and the fourth volumes written by U.Kneissl (Darmstadt) and E.Grosse (Dresden) are devoted to Nuclear Resonance Fluorescence method in nuclear spectroscopy. Application of nuclear data in astrophysics is described by P.Descouvement (Brussels) in the chapter in the second volume. Description of the method of neutron capture γ -ray coincidence measurements is presented in the chapter by I.Tomandl in the third volume. Compilation CRF contains also data on highly excited states of light and near-magic nuclei derived from charged-particle and neutron resonances. In many cases it permits an additional study of few-nucleon effects.

In a special chapter of the first volume a new method of the correlation analysis of energy levels connected with the study of nuclear tensor forces is considered. It resulted in the selection of the interacting nuclei according to their spin-orbit orientation and seems to be effective during the study of many nonstatistical effects. Such a new outlook on the role of pion-exchange dynamics is based on observations by J.Schiffer et al. and T.Otsuka [1] on a stable character of excitation due to meson-exchange interaction of nucleons.

Data in CRF are presented in tables whose format is analogous to that in the work by P.Endt. In tables each horizontal line belongs to one state. The line starts with the excitation and spin. We show here in Tables only isotopes with number of levels >100.

It was suggested by S.Devons [2] that exactly measured nuclear excitations can show effects connected with the nucleon structure. Nucleon mass splitting $\delta m_N = 1293.3$ keV is definitely one of nucleon low-energy parameters. Presence of excitations equal or rational to the value δm_N [3-6] (called "tuning effect") is considered here.

2 Method of the analysis of spacing distributions

Linear increase of 7/2+ excitations (a slope of 161 keV per neutron pair in Sb-isotopes) abserved by J.Schiffer and T.Otsuka can be considered together with the observed stable character of valence neutron excitations in 101,103Sn (the same Sn core). The excitations which coincide within 1-2 keV are 1/3 of the stable interval D=512 keV in 97,98 Pd (again N=51) and 1/6 of the parameter $\varepsilon_o=1022~{\rm keV}=2m_e$ corresponding to the spin-flip effect in ¹⁰B [5]. Parameter D=161 keV from the linear shift in excitations of $_{123-133}$ Sb is 1/8 of the nucleon mass difference δm_N =1293.3 keV [3-6]. Two parameters D=170 keV= $\varepsilon_o/6$ (E^* in 101,103 Sn) and D=161 keV= $\delta m_N/8$ together with a stable interval 2×161 keV+170 keV=492 keV observed in the independent D-distributions of many nuclei were fixed. These systems were used in the analysis of spacing distributions of other nuclei collected in all five volumes of CRF-compilation. The distribution of observed numbers of isotopes (of elements Z) where stable intervals with values $n \times 161 \text{ keV}$, $n' \times 170 \text{ keV}$ and $n'' \times 492 \text{ keV}$ (n,n',n"=1/2,1,2 etc.) were observed is shown in Fig. 1. Ten regions corresponding to the local maxima in Fig.1 can be noticed: Z=9-11, 19-22, 29-30, 38-39, 45-47, 50-52, 64, 68-69, 76-78, 82. The region Z=50-52 corresponds to discussed by T.Otsuka effects due to pion-exchange dynamics in nuclei around large neutron $\nu 1h_{11/2}$ subshell. The region Z=76-82 corresponds to large proton $\pi 1h_{11/2}$ subshell. Analysis of data is given in [7,8]. Each nucleus where parts of the above mentioned systems of periods where found corresponds to the input $\Delta n=1$ in the distribution in Fig.1.

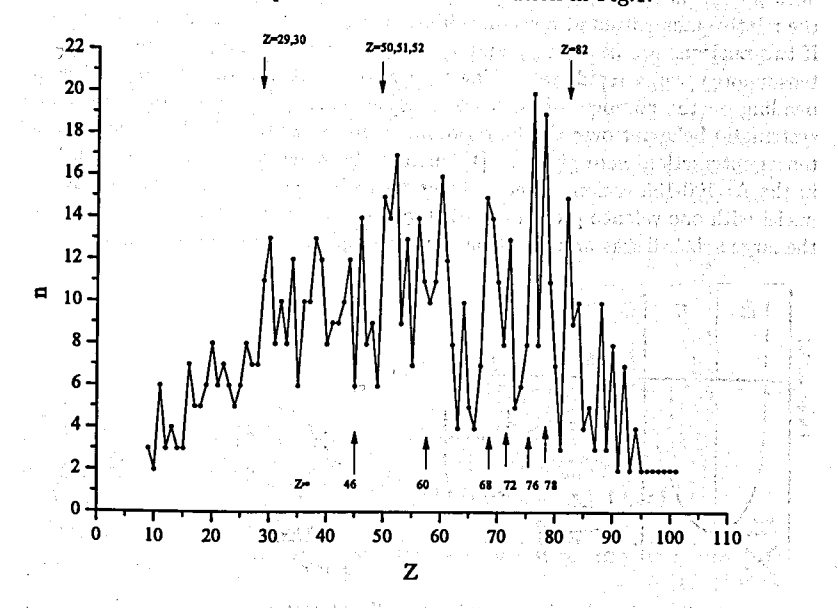


Fig. 1 Distribution of numbers of isotopes where stable intervals with values $n \times 161$ keV, $n' \times 170$ keV and $n'' \times 492$ keV (n,n',n'' = 1/2,1,2 etc.) were found in the analysis of data in CRF.

3 Analysis of data for nuclei with Z=5-47

Strong interactions between nucleons are described in a good approximation by an exchange of mesons – hadrons consisting of a quark and an antiquark. Nucleons themselves are hadrons consisting of three so-called constituent quarks. The pions $(J=0^-)$ and ρ mesons $(J=1^-)$ are the main participants of the interaction. In Fig.2 (left) regions of nucleon interaction are marked: one- and two-pion exchange and the hard core. In the hadronic phase at low temperatures and densities the quarks and gluons (vector fields acting between quarks) are confined in color singlet the composites with almost massless up and down quarks. The progress in the theory is connected with QCD-calculations which include gluon-quark-dressing effect [9,10]. Together with Constituent Quark Model and further development of the Standard Model it forms a solid base for nuclear physics.

T.Otsuka showed [1] that nuclear tensor forces are responsible for the observed systematic shift of energies of states in many nuclei. Fig.2 (right) represents an illustration how the tensor forces work for two interacting nucleons situated on two orbits j and j'. T.Otsuka noticed that "using notations $j_2 = l + 1/2$ and $j_2 = l - 1/2$, where l is the orbital angular momentum, one can see that in the former case the spin and orbital momentum are parallel, whereas in the latter they are opposite. The tensor force is acting only if spins of two nucleons are parallel coupled to the total S=1 (like in the deuteron). Spins can be fixed as being "up", but the orbital motion can be in either way. If two nucleons are in orbits is and is they are moving in opposite directions (marked "a"), the relative momentum at nucleon collision is high, ... the tensor force works attractively. If two nucleons are in orbit $j_{>}$ and $j'_{<}$, they are moving together (marked "b") and the tensor force works repulsively. The tensor force changes the single-particle energy depending on the numbers of nucleons in other orbitals and it becomes evident once the systematic behavior over the long isotope chain is obtained". The clear example of the tensor interaction were given in [1], namely, between states $1g_{7/2}$ ($j_{<}$) and $1h_{11/2}$ ($j_{>}$) in the A=100-130 region. Exact integer ratios between observed excitations in series of nuclei with one valence proton (Z=51 in Sb) and different number of pairs of neutrons in the large subshell was an indication of very simple internucleon dynamics.

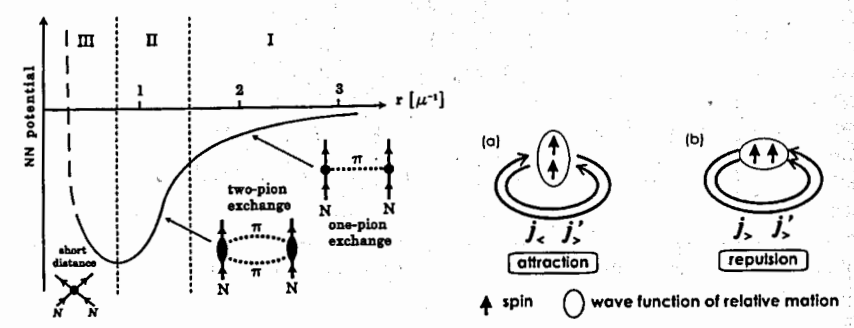


Fig.2 left: Hierarchy of scales governing the NN interaction: the distance r is given in units of the pion Compton wavelength, $\mu^{-1} \simeq 1.4$ fm. right:. Illustration of tensor forces acting between two nucleons on orbits j and j'. Notations <, > mark spin/orbital-momentum orientation [11].

Table 1. Numbers of states in compound nuclei ^AZ with Z≤29 contained in compilation CRF (I/25A). The ratio shows number of states in the book and in the Supplement.

| AZ | N_b/N_s | ^A Z | N_b/N_s | ^{A}Z | N_b/N_s | ^{A}Z | N_b/N_s | ^A Z | N_b/N_s |
|------------------|-----------|-------------------|-----------|--------------------|------------|------------------|-----------|------------------|-----------|
| | | | 1.4 | 40 | in the way | ing s | | | dan Heb |
| 17F | 2/100 | 31S | 104/105 | ⁴³ Ca | 5/243 | 51V | 206/580 | | 115/116 |
| 18F | 433/433 | ^{32}S | 5/322 | ⁴⁴ Ca | 5/161 | ⁵² V | 123/1202 | | 41/842 |
| 19F | 43/238 | 33S | 366/400 | ⁴⁵ Ca | | ⁴⁹ Cr | 189/189 | | 354/354 |
| ²⁰ F | 6/170 | 34S | 38/295 | ⁴⁷ Ca | | 50Cr | 162/162 | ⁵⁹ Co | 6/354 |
| ²⁰ Ne | 250/251 | ^{35}S | 4/139 | ⁴⁸ Ca | 242/251 | ⁵¹ Cr | 270/652 | 60Co | 1/1124 |
| ²¹ Ne | 66/173 | ³⁴ Cl | 36/263 | ⁴¹ Sc | 3/200 | 52Cr | 68/311 | 61Co | 4/120 |
| ²² Ne | 63/152 | 35Cl | 23/328 | ⁴² Sc | 158/159 | ⁵³ Cr | 61/518 | 56Ni | 95/102 |
| ²² Na | 7/214 | 36Cl | 9/397 | ⁴³ Sc | 111/476 | ⁵⁴ Cr | 139/267 | 57Ni | 31/197 |
| ²³ Na | 215/324 | ³⁷ Cl | 63/524 | 44Sc | 31/137 | 55Cr | 54/453 | ⁵⁸ Ni | 518/519 |
| ²⁴ Na | 150/339 | ^{39}Cl | 48/178 | ^{45}Sc | 629/1390 | 51Mn | 57/544 | ⁵⁹ Ni | 630/2316 |
| ²² Mg | 83/116 | ³⁶ Ar | 21/288 | ⁴⁶ Sc | 8/452 | ⁵³ Mn | 357/1127 | ⁶⁰ Ni | 314/314 |
| ²⁴ Mg | 184/331 | ³⁷ Ar | 13/105 | ⁴⁷ Sc | 148/429 | ⁵⁴ Mn | 98/436 | 61Ni | 480/2694 |
| ²⁵ Mg | 129/195 | 38Ar | 777/777 | ⁴⁸ Sc | 20/104 | ⁵⁵ Mn | 55/520 | 62Ni | 8/1837 |
| ²⁶ Mg | 52/343 | ³⁹ Ar | 114/114 | ⁴⁹ Sc | 214/322 | ⁵⁶ Mn | 265/435 | ⁶³ Ni | 8/182 |
| ²⁶ Al | 3/248 | ⁴⁰ Ar | 22/216 | ⁴⁴ Ti | 119/141 | | 91/101 | ⁶⁴ Ni | 110/110 |
| ²⁷ Al | 15/386 | ⁴¹ Ar | 106/438 | ⁴⁶ Ti | 294/448 | ⁵² Fe | 47/101 | ⁶⁵ Ni | 169/169 |
| 28Al | 122/525 | $^{38}\mathrm{K}$ | 103/103 | ⁴⁷ Ti | 214/324 | ⁵³ Fe | 108/108 | ⁵⁸ Cu | 117/117 |
| ²⁷ Si | 62/133 | $^{39}\mathrm{K}$ | 234/235 | ⁴⁸ Ti | 293/405 | ⁵⁴ Fe | 237/237 | ⁵⁹ Cu | 102/583 |
| ²⁸ Si | 17/344 | ⁴⁰ K | 9/305 | $^{49}\mathrm{Ti}$ | 186/201 | ⁵⁵ Fe | 184/1080 | ⁶¹ Cu | 152/859 |
| ²⁹ Si | 5/359 | 41K | 262/460 | | 263/263 | 56 Fe | 311/384 | | 147/147 |
| ³⁰ Si | 170/248 | $^{42}\mathrm{K}$ | 6/453 | 47V | 122/402 | ⁵⁷ Fe | 5/1420 | | 7/589 |
| 30P | 156/156 | | | ^{48}V | 100/207 | ⁵⁸ Fe | 157/311 | ⁶⁴ Cu | 11/762 |
| 31P | 158/530 | ⁴¹ Ca | 1/507 | 49V | 193/1431 | ⁵⁹ Fe | 25/185 | ⁶⁵ Cu | |
| ³² P | 2/496 | ⁴² Ca | 9/590 | $^{50}\mathrm{V}$ | 292/292 | 55 Co | 485/485 | | 124/570 |

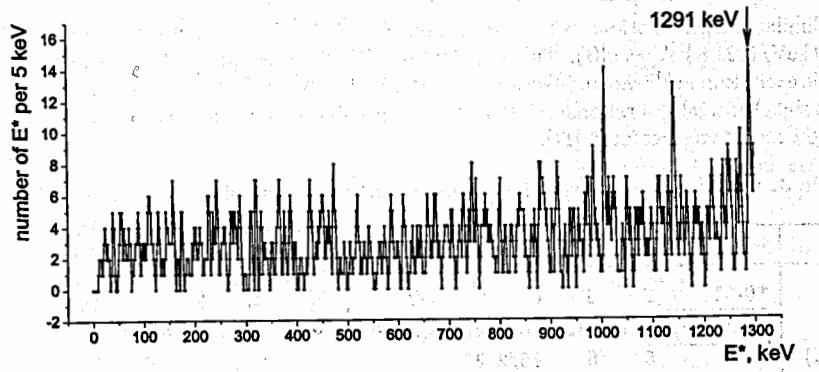


Fig.3 left: Sum E^* -distribution in nuclei with Z=3-29 (ΔE =5 keV). Maximum at E^* =1291 keV close to δm_N corresponds to E^* in ³⁸S (boxed) and many Z-odd nuclei (Table 2).

Exact integer relation 1:2:3 similar to that in Sb-isotopes was noticed in case of valence neutrons N=21,22. Here excitations in three nuclei 41 Ca, 39 Ar and 37 S shown in Table 2 (top left) are proportional to the number of the proton pairs in $1d_{3/2}$ subshell (from 3 in 41 Ca up to 1 in 37 S, ratio 1942.8 keV/646.3 keV=3.006). The excitations in neighbour 37 S- 38 S with one and two valence neutrons (ΔN =1 and ΔN = 2 above N=20 shell) are also exactly rational each other 1292 keV/646.2 keV=1.999. The parameter of this effect coincides with nucleon mass splitting δm_N =1293.3 keV (top right part of Table 2. Appearance of such excitations in Z-odd nuclei with Z=19-29 was noticed earlier (see bottom part of Table 2) and is resulted in maximum at E^* =1291 keV≈ δm_N seen in the total E^* -distribution in all nuclei contained in the first volume of CRF compilation (Z=3-29, Fig 3).

Table 2. Top: Linear trend in E^* (in keV) in levels of N=21 nuclei; the excitations forming the slope 4×161 keV= $D_o/2$ are boxed. Bottom: Stable excitation in nuclei with Z=19-29 with the value 646 keV of $7/2^-$ state ($J^{\pi}=3/2^-$) in ⁶³Co boxed (nucleus with near-magic configuration Z=28-1, N=28-2).

| $\frac{\overline{(Z-14)/2}}{{}^{A}Z}$ | 2 3 ⁴¹ Ca | | 2 ³⁹ Ar | 1 | $(\Delta N=1)$ |) | 0 ³³ Mg | | ³² Si | $\frac{1 (\Delta N = 2)}{^{38}S}$ | <u> </u> |
|---------------------------------------|-------------------------|--------|-----------------------|------------------|------------------|--------|-----------------------|------------------|------------------|-----------------------------------|-------------------------|
| $\frac{E^*}{E}$ | 0.0 | 1942.8 | | 1267 | 0 | 646.2 | 159 | - 484 | 1942 | 1292 | - |
| $2J^{\pi}$ | 7- | 3- | 7- | 3- | 7- | 3- | (7-) | (3^{-}) | 2+ | 2+ | ψş. |
| $n\frac{D_o}{8}$ | 0 | 1941 | . 0 | 1293 | 0 | 646 | 161 | 483 | 1941 | 1293 | |
| n | | 12 | | 8 | | 4 | (1) | 3 | 12 | 8 | |
| ^{A}Z | 41K | 47V | 51 V | ⁵³ Mn | ⁵⁵ Mn | ; | | ⁵⁹ Mn | ⁵³ Co | ⁵⁹ Co | ر داید د <u>د</u> |
| $2J_o^{\pi}$ | 3+ | 3- | 7- | 7- | 5- | | - | 5- | 7- | 7- | <u>;</u> |
| $2J^{\pi}$ | 7- | 11- | 5- | 3- | (11+) | 11- | 1- | 11- | 3- | 3- | |
| E^* | 293.6 | 1294.9 | B20 .1 | 11289.8 | 1289.1 | 1292.1 | 1293.0 | 1300.9 | 646.2 | 1291.6 | i. |
| $n\frac{D_o}{8}$ | 1293 | 1293 | 323 | 1293 | 1293 | 1293 | 1293 | 1293 | 646 | 1293 | 4 |
| n | 8 | 8 | 2_ | 8 | 8 | 8 | 8 | 8 | 4 | 8 | |

Similar integer relations exist in some light nuclei (Table 3, boxed value ε_o , the ratio 5110 keV/1021.8 keV=5.001). The parameter ε_o =2 m_e is three times the above mentioned stable excitation in ^{51,53}Sn and twice the interval D=512 keV in ^{97,38}Pd (N-51,52). In Table 3 (at right) and table 4 rational relation with the parameter ε_o observed in energy intervals of light nuclei are presented [11].

Table 3. Comparison of E^* (keV) in near-magic nuclei with multiples of $^{10}\mathrm{B}$ spin-flip effect.

| | · · · · · · · · · · · · · · · · · · · | | | | | | | | | |
|--------------------|---------------------------------------|------|-----------------|-----------------|--------------------|-----------------|------------------|------------------|-----------------------------------|-----------------------------------|
| $^{A}\mathrm{Z}$ | ¹⁰ B | 10B | ¹⁰ B | ¹² C | ¹² C | ¹⁶ O | ¹⁸ Ne | ¹⁸ Ne | ¹⁸ Ne ¹⁸ Ne | ³⁸ Ar ⁵⁵ Co |
| | +0-+1 | 2- | 3- | 0+ | 0 ⁺ T=2 | 3- | 0+ | 0+ | 2+ | D_{ij} D_{ij} |
| E* | 1021.8(2) | 5110 | 6127 | 7654 | 27595(2) | 6130 | 3576 | 4590 | 5106 6137 | 1021 512 |
| $n(\varepsilon_o)$ | | 5 | | | 27 | | , | • | 5 6 | , |
| | 1022.0 | 5110 | 6132 | 7665 | 27594 | 6132 | 3577 | 4599 | 5110 6132 | 1022 511 |
| | 0.2(2) | 0.3 | 3 | 11 | 1(2) | 2 | 1(2) | 9(8) | 4(8) 5 | 1(2) 1(2) |

Table 4. Comparison of energies in near-magic nuclei (Z=26-29) with integers of $\epsilon_o/12=85$ keV [11].

| | | | | | | | * * * * * * * * * * * * * * * * * * * * | | | | |
|------------------|----------------------------|-------------------------------------------------------------|--------------------------------------------------------------------|------------------------------------------------------------------------------------------------------------------------------|------------------------------------------------------------------------|--------------------------------------------------------------------------------------------------------------------------------------------------------------------------------|----------------------------------------------------------------------------------------------------------------------------------------------------------------------|--------------------------------------------------------------------------------------------------------------------------------------------------------------------------------------------------------------------------------------------|----------------------------------------------------------------------------------------------------------------------------------------------------------------------------------------------------------------------------------------------------------------------------------------------------------------------------------------------------------------------------------------------------------------------------------------------------------------------------------------|---------------------------------------------------------------------------------------------------------------------------------------------------------------------------------------------------------------------------------------------------------------------------------------------------------|-------------------------------------------------------|
| ^{55}Fe | | | ⁵⁵ Co | | $T = \frac{3}{2}$ | ⁵⁷ Ni | 11091 | ⁵⁹ Ni | ⁵⁸ Cu | T=1 | ⁵⁵ Co |
| .0 | 411 | 931 | 4721 | 4748 | 5743 | 0 | 769 111 | 3 0 * 339 | 203 | 1051 1652 | 84 |
| 3- | 1- | 5- | 3- | 3- | 5- | 3- | 5 1- | 3- 5- | 0+ | (1^+) 2 ⁺ | D |
| | | | 1022 | 995 | | | | | | 848 1449 | ۳ |
| | 425 | 935 | 1022 | | | | 765 110 | 7 340 |) | 850 1445 | 85 |
| | 5 | 11 | 12 | ٠. | | | 9 13 | 2 | 1.84 | 10 17 | 1 |
| ⁵⁴ Co | | T=1 | ⁵² Fe | - | | ⁵⁷ Cu | | ⁶⁸ Cu | ⁶⁵ Cu | 14693454 15515-4 | ⁶⁵ Cu |
| Ó | 937 | 1146 | 0 | 849 | 2384 | 0 | 1028 110 | 6 0 84. | 6 0 | 771 1116 | 85 |
| 0+ | 1+ | 2+ | 0+ | 2+ | 4+ | 3- | 5- 1- | 1+ (2+ | <u>)</u> 3- | 5- 1- | D |
| | 935 | 1147 | | 850 | 2384 | | 1022 110 | 7 85 | | 765 1107 | 85 |
| | 11 | 17 | | 10 | 28 | | 12 13 | 1995 H 1994 | | 9 13 | 11 |
| _ | 0 3- 54Co 0 0+ | 0 411 3- 1- 425 5 54Co 0 937 0+ 1+ 935 | 0 411 931 3- 1- 5- 425 935 5 11 64Co T=1 0 937 1146 | 0 411 931 4721 3- 1- 5- 3- 1022 425 935 1022 5 11 12 64Co T=1 52Fe 0 937 1146 0 0+ 1+ 2+ 0+ 935 1147 | 0 411 931 4721 4748 3- 1- 5- 3- 3- 1022 995 425 935 1022 5 11 12 64Co | 0 411 931 4721 4748 5743 3- 1- 5- 3- 3- 5- 1022 995 425 935 1022 5 11 12 64Co T=1 ⁵² Fe 0 937 1146 0 849 2384 0+ 1+ 2+ 0+ 2+ 4+ 935 1147 850 2384 | 0 411 931 4721 4748 5743 0 3 1 5 3 5 3 5 3 5 3 5 3 6 1022 425 935 1022 5 11 12 4Co T=1 52Fe 57Cu 0 937 1146 0 849 2384 0 0 1 + 2 + 0 + 2 + 4 + 3 935 1147 850 2384 | 0 411 931 4721 4748 5743 0 769 111 3- 1- 5- 3- 3- 5- 3- 5- 1- 1022 995 425 935 1022 765 110 5 11 12 9 13 64Co T=1 52Fe 57Cu 0 937 1146 0 849 2384 0 1028 110 0+ 1+ 2+ 0+ 2+ 4+ 3- 5- 1- 935 1147 850 2384 1022 110 | 0 411 931 4721 4748 5743 0 769 1113 0 * 333 3 - 1 - 5 - 3 - 3 - 5 - 3 - 5 - 1 - 3 - 5 - \frac{1022}{5} 995 \\ 425 935 \frac{1022}{5} \text{ 11 12 } \text{ 9 13 } \text{ 2 } \\ \frac{5^4\text{Co}}{5} \text{ T=1 } \frac{5^2\text{Fe}}{5^7\text{Cu}} \text{ \frac{68\text{Cu}}{5} \text{ Cu}} \\ 0 \text{ 937 1146 } 0 \text{ 849 2384 } 0 \text{ 1028 1106 } 0 \text{ 84.} \\ 0 + 1 + 2 + 0 + 2 + 4 + 3 - 5 - 1 - 1 + (2 + 935 1147) \text{ 850 2384 } \text{ 1022 1107} \text{ 855} | 0 411 931 4721 4748 5743 0 769 1113 0 * 339 203 3 - 1 - 5 - 3 - 5 - 3 - 5 - 1 - 3 - 5 - 0 + 1022 995 425 935 1022 765 1107 340 5 11 12 9 13 2 64Co T=1 52Fe 57Cu 68Cu 65Cu 0 937 1146 0 849 2384 0 1028 1106 0 84.6 0 0 + 1 + 2 + 0 + 2 + 4 + 3 - 5 - 1 - 1 + (2 +) 3 - 935 1147 850 2384 1022 1107 85 | $ \begin{array}{cccccccccccccccccccccccccccccccccccc$ |

In Tables 5-6 and Fig.4 results for nuclei with Z=30-47 are presented. Here in the region of $2p_{1/2}$ subshell stable interval close to ε_o appears again (seen as maximum at 1024 keV in total E^* -distribution for the second CRF volume). The close dublet in ⁸⁰Br at this energy (splitting about 1 keV or 10^{-3}) can be compared with nonstatistical effects in neutron resonance data [12] observed by M.Ohkubo. Several special programs for a study of rational relations in nuclear excitations were proposed and can be useful in the analysis of data for nondeformed nuclei.

Table 5. Grouping of excitation E^* at the $\epsilon_o=1022(2)$ keV in nuclei with Z=33-35.

| | | | | | | | ⁸⁰ Br | | |
|----------------|------|-------|-------|-------|-------|------------|--------------------------------------------|------------------|------|
| E*, keV | 1022 | 1023 | 1022 | 1021 | 1024 | 1021.4 | (1 ⁻),2,3 ⁺ | 1024 1023 | 1022 |
| $2J_{o}^{\pi}$ | 2- | 2- | 9+ | 5+ | 1- | 1+ | 1 S. 2 1 1 1 2 1 1 1 1 1 1 1 1 1 1 1 1 1 1 | 3- 5- | 3- |
| $2J^{\pi}$ | ≤ 3+ | 3+,2+ | 1-,3- | 1-,3- | (13+) | (≤ 4) | $(1^{-}),2,3^{+}$ | (5) ⁻ | |
| _ N | 41 | €43 | 39 | 41 | 43 | 45 | 45 | 46 47 | 48 |

Data for nuclei contained in the third volume (Z=48-60) turn to be useful for check of the above discussed effects of the tensor forces in SN-Sb region. Maxima at E^* =161 keV, 483 keV and 644 keV (n=1,3,4 of the period $\delta m_N/8$ =161 keV) support the systematic character of the effect observed by Schiffer and Otsuka as the linear E^* -dependence (the slope 160 keV).

The grouping of excitations at $E^*=1212$ keV (averaging interval 5 keV) corresponds to the well-known effect of stable 2^+ excitations in nuclei around the tin.

Menal standard in the weathern as the ground

Table 6. Numbers of states in compound nuclei AZ with Z=30-47 contained in v. I/25B.

| and the second | | | | | | | • | 4.5 | |
|-----------------------|-----------|--------------------|-------------------------|--------------------|-------------|---------------------|-----------|---------------------|--------------------------------------------------------------------------------------------------------------------------------------------------------------------------------------------------------------------------------------------------------------------------------------------------------------------------------------------------------------------------------------------------------------------------------------------------------------------------------------------------------------------------------------------------------------------------------------------------------------------------------------------------------------------------------------------------------------------------------------------------------------------------------------------------------------------------------------------------------------------------------------------------------------------------------------------------------------------------------------------------------------------------------------------------------------------------------------------------------------------------------------------------------------------------------------------------------------------------------------------------------------------------------------------------------------------------------------------------------------------------------------------------------------------------------------------------------------------------------------------------------------------------------------------------------------------------------------------------------------------------------------------------------------------------------------------------------------------------------------------------------------------------------------------------------------------------------------------------------------------------------------------------------------------------------------------------------------------------------------------------------------------------------------------------------------------------------------------------------------------------------|
| ^A Z | N_b/N_s | $^{A}\mathrm{Z}$ | N_b/N_s | $^{A}\mathrm{Z}$ | N_b/N_s | ^{A}Z | N_b/N_s | $^{A}\mathrm{Z}$ | N_b/N_s |
| 61- | | ~ a . | | | | - | | | M |
| 61 Zn | 131/149 | ⁷⁶ As | 2/156 | 88 Rb | 65/162 | ⁹³ Nb | 15/106 | $^{102}\mathrm{Ru}$ | 137/13 |
| ⁶² Zn | 112/161 | 77 As | 30/1 03 | ⁸⁰ Sr | 125/132 | ⁹⁴ Nb | 32/624 | $^{103}\mathrm{Ru}$ | 131/13 |
| ⁶⁴ Zn* | 230/230 | ⁷⁴ Se | 126/1 2 6 | ⁸¹ Sr | 149/149 | $^{95}{ m Nb}$ | 122/122 | $^{101}\mathrm{Rh}$ | 70/128 |
| ⁶⁵ Zn | 211/594 | ⁷⁵ Se | 60/144 | ⁸³ Sr | 69/114 | ⁹¹ Mo | 87/157 | $^{102}\mathrm{Rh}$ | 125/12 |
| ⁶⁶ Zn | 165/172 | 77 Se | 82/160 | ⁸⁵ Sr | 1/106 | ⁹² Mo | 237/239 | $^{103}\mathrm{Rh}$ | 218/21 |
| ⁶⁷ Zn | 3/528 | ⁷⁸ Se | 185/1 85 | 87Sr | 1/202 | ⁹³ Mo | 55/143 | $^{104}\mathrm{Rh}$ | 204/204 |
| ⁶⁸ Zn | 20/631 | ⁷⁹ Se | 69/1 12 | ⁸⁸ Sr | 362/363 | ⁹⁴ Mo | 184/195 | $^{105}\mathrm{Rh}$ | 104/14 |
| ⁶⁹ Zn | 2/360 | ⁷² Br | 110/110 | ⁸⁹ Sr | 16/581 | ⁹⁵ Mo | 148/166 | $^{97}\mathrm{Pd}$ | 170/170 |
| ⁷¹ Zn | 157/229 | ⁷³ Br | 61/124 | ⁸¹ Y | 114/114 | ⁹⁶ Mo | 120/121 | 98 Pd | 11/199 |
| ⁶⁵ Ga | 331/332 | ⁷⁵ Br | 37/102 | 83Y | 106/106 | ⁹⁷ Mo | 192/192 | ¹⁰² Pd | 111/149 |
| 67 Ga | 39/285 | ⁷⁷ Br | 98/110 | 85Y | 57/117 - | ⁹⁸ Mo | 395/396 | $^{103}\mathrm{Pd}$ | 115/115 |
| $^{69}\mathrm{Ga}$ | 6/112 | ⁷⁹ Br | 106/140 | 87Y | 147/147 | ⁹⁹ Mo | 74/134 | ^{104}Pd | 158/158 |
| ⁷² Ga | 90/110 | ⁸⁰ Br | 149/170 | 89Y | 328/426 | ¹⁰⁰ Mo | 335/335 | ^{105}Pd | 116/116 |
| ⁶⁸ Ge | 129/171 | ⁸¹ Br | 112/112 | 90Y | 20/880 | $^{93}\mathrm{Tc}$ | 117/339 | 106Pd | 135/135 |
| $^{69}{ m Ge}$ | 1/173 | $^{76}{ m Kr}$ | 155/155 | ⁸³ Zr | 98/123 | $^{94}\mathrm{Tc}$ | 111/111 | ¹⁰⁷ Pd | 104/104 |
| $^{70}{ m Ge}$ | 43/191 | ⁷⁸ Kr | 122/122 | $^{86}\mathrm{Zr}$ | 105/113 | $^{95}\mathrm{Tc}$ | 130/141 | 109Pd | 134/134 |
| $^{71}\mathrm{Ge}$ | 2/180 | ⁸¹ Kr | 101/101 | $^{89}\mathrm{Zr}$ | 1/132 | $^{96}\mathrm{Tc}$ | 143/143 | ^{110}Pd | 99/194 |
| ⁷² Ge | 181/181 | ⁸³ Kr | 12/252 | $^{90}{ m Zr}$ | 369/392 | ⁹⁷ Tc | 207/207 | 103 Ag | 122/122 |
| ⁷³ Ge | 8/119 | ⁸⁵ Kr | 5/277 | $^{91}\mathrm{Zr}$ | 54/406 | ⁹⁹ Tc | 63/129 | 105 Ag | 93/203 |
| ⁷⁴ Ge | 38/258 | ⁸⁷ Kr | 143/963 | $^{92}\mathrm{Zr}$ | 236/669 | $^{101}\mathrm{Tc}$ | 106/106 | 106 Ag | 169/169 |
| $^{75}{ m Ge}$ | 57/103 | $^{75}\mathrm{Rb}$ | 119/119 | $^{93}\mathrm{Zr}$ | 17/230 | $^{96}\mathrm{Ru}$ | 114/114 | 10'Ag | 146/146 |
| $^{76}\mathrm{Ge}$ | 14/138 | 81 Rb | 103/1 03 | $^{94}\mathrm{Zr}$ | 17/217 | $^{97}\mathrm{Ru}$ | 134/134 | 108 Ag | 2/168 |
| $^{69}\mathrm{As}$ | 153/162 | $^{83}\mathrm{Rb}$ | 151/151 | $^{95}\mathrm{Zr}$ | 150/355 | $^{98}\mathrm{Ru}$ | 92/102 | 111 Ag | 115/131 |
| ⁷¹ As | 145/145 | $^{85}\mathrm{Rb}$ | 5/117 | $^{96}\mathrm{Zr}$ | 135/135 | 99 Ru | 120/120 | , i | V 5 |
| 73 As | 11/161 | $^{86}\mathrm{Rb}$ | 4/416 | 91Nb | 117/147 | $^{100}\mathrm{Ru}$ | 192/192 | | The second second |
| $^{75}\mathrm{As}$ | 31/122 | $^{87}\mathrm{Rb}$ | 18/117 | ⁹² Nb | 4/165 | $^{101}\mathrm{Ru}$ | 34/150 | | |
| | | | • | | • | | • | | |
| ≥ 1 | | | | | 886 keV | į. | | | |
| umber of E* per 5 keV | | | | | | i | 1024 keV | | A STATE OF THE STA |
| i | | | | 1 | | 1 | | | |
| č. *. 30- | | | 1 | 11 . | | 1 , 1 | 1 1. | ıl 🦾 | gada . |
| ₩] | | i | . 1 1 | l linnal | | | | I h | State of |
| <u> 유</u> 1 | ¥1 . | 1 1.1 | ill . iliki | | | HANNAM. MA | | IH. | William 1 |
| 훹 ²⁰ | , jil., l | 机仙庙 | | | | Alliant, il | | 11 | TAKE 1 |
| 5 ∤ | 1.44 | | 1 1 1 1 1 1 1 1 1 1 1 1 | 14 H. II. | L 11, 1 411 | 11 1 | 1 , 141 | 1 | Salara da da |

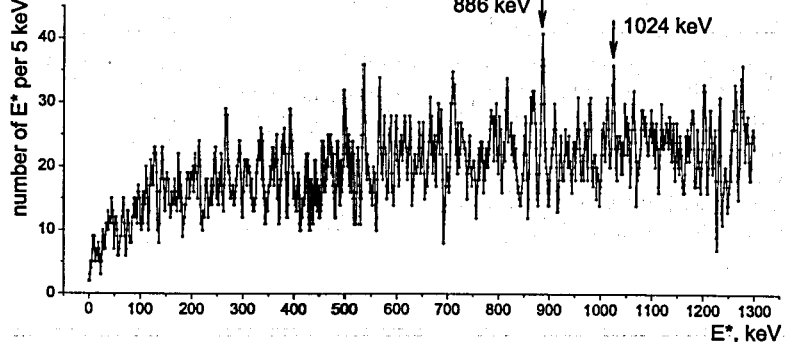


Fig.4 left: Sum E^* -distribution of all nuclei with Z=30-47 (ΔE =5 keV). Maximum at $E^*=1024$ keV corresponds to excitations at $E^*=\varepsilon_0$ in many nuclei with Z=33-37 (Table 5).

Analysis of data for nuclei with Z=48-60 (vol. I/25C)

Table 7. Numbers of bound states in compound nuclei AZ with Z=48-60 contained in v.I/25C. The ratio shows number of states in the book and in the Supplement.

| N _b /N _s | ^A Z | N_b/N_s | ^A Z | N_b/N_s | ^A Z | N_b/N_s | AZ : | NT /NT - W |
|--------------------------------|--------------------------------------------------------------------------------------------------------------------------------------------------------------------------------------|---------------------------------------------------------------------------------------------------------------------------------------------------------------------------------------------------------------------------------------------------------------------------------------------------------------------------------------------------------------------------------------------------------------------------------|--------------------------------------------------------------------------------------------------------------------------------------------------------------------------------------------------------------------------------------------------------------------------------------------------------------------------------------------------------------------------------------------------------------------------------------------------------------------------------------------------------------------------------------------------------------------------------------------------------------------------------------------------------------------------------------------------------------------------------------------------------------------------------------------------------------------------------------------------------------------------------------------------------------------------------------------------------------------------------------------------------------------------------------------------------------------------------------------------------------------------------------------------------------------------------------------------------------------------------------------------------------------------------------------------------------------------------------------------------------------------------------------------------------------------------------------------------------------------------------------------------------------------------------------------------------------------------------------------------------------------------------------------------------------------------------------------------------------------------------------------------------------------------------------------------------------------------------------------------------------------------------------------------------------------------------------------------------------------------------------------------------------------------------------------------------------------------------------------------------------------------------------------------------------------------------------------------------------------------------------------------------------------------------------------------------------------------------------------------------------------------------------------------------------------------------------------------------------------------------------------------------------------------------------------------------------------------------------------------------------------------------------------------------------------------------------------------------------------------------------------------------------------------------------------------------------------------------------------------------------------------------------------------------------------------------------------------------------------------------------------------------------------------------------------------------------------------------------------------------------------------------------------------------------------------------------------------------------------------------------------------------------------------------------------------------------------------------------------------------------------------------------------------------------------------------------------------------------------------------------------------------------------------------------------------------------------------------------------------------------------------------------------------------------------------------------------------------------------------------------------------------------------------------------------------------------------------------------------------------------------------------------------------------------------------------------------------------------------------------------------------------------------------------------------------------------------------------------------------------------------------------------------------------------------------------------------------------------------------------------------------------------------------------------------------------------------------------------------------------------------------------------------------------------------------------------------------------------------------------------------------------------------------------------------------------------------------------------------------------------------------------------------------------------------------------------------------------------------------------------------------------------------------------------------------------------------------------------------------------------------------------------------------------------------------------------------------------------------------------------------------------------------------------------------------------------------------------------------------------------------------------------------------------------------------------------------------------------------------------------------------------------------------------------------------------------------------------------------------------------------------------------------------------------------------------------------------------------------------------------------------------------------------------------------------------------------------------------------------------------------------------------------------------------------------------------------------------------------------------------------------------------------------------------------------------------------------------------------------------------------------------------------------------------------------------------------------------------------------------------------------------------------------------------------------------------------------------------------------------------------------------------------------------------------------------------------------------------------------------------------------------------------------------------------------------------------------------------------------------------------------------------------------------------------------------------------------------------------------------------------------------------------------------------------------------------------------------------------------------------------------------------------------------------------------------------------------------------------------------------------------------------------------------------------------------------------------------------------------------------------------------------------------------------------------------------------------------------------------------------------------------------------------------------------------------------------------------------------------------------------------------------------------------------------------------------------------------------------------------------------------------------------------------------------------------------------------------------------------------------------------------------------------------------------------------------------------------------------------------------------------------------------------------------------------------------------------------------------------------------------------------------------------------------------------------------------------------------------------------------------------------------------------------------------------------|--------------------------------------------------------------------------------------------------------------------------------------------------------------------------------------------------------------------------------------------------------------------------------------------------------------------------------------------------------------------------------------------------------------------------------------------------------------------------------------------------------------------------------------------------------------------------------------------------------------------------------------------------------------------------------------------------------------------------------------------------------------------------------------------------------------------------------------------------------------------------------------------------------------------------------------------------------------------------------------------------------------------------------------------------------------------------------------------------------------------------------|------------------------------------------------------------------------------------------------------------------------------------------------------------------------------------------------------------------------------------------------------------------------------------------------------------------------------------------------------------------------------------------------------------------------------------------------------------------------------------------------------------------------------------------------------------------------------------------------------------------------------------------------------------------------------------------------------------------------------------------------------------------------------------------------------------------------------------------------------------------------------------------------------------------------------------------------------------------------------------------------------------------------------------------------------------------------------------------------------------------------------------------------------------------------------|--------------------------------------------------------------------------------------------------------------------------------------------------------------------------------------------------------------------------------------------------------------------------------------------------------------------------------------------------------------------------------------------------------------------------------------------------------------------------------------------------------------------------------------------------------------------------------------------------------------------------------------------------------------------------------------------------------------------------------------------------------------------------------------------------------------------------------------------------------------------------------------------------------------------------------------------------------------------------------------------------------------------------------------------------------------------------------------------------|--------------------------------------------------------------------------------------------------------------------------------------------------------------------------------------------------------------------------------------------------------------------------------------------------------------------------------------------------------------------------------------------------------------------------------------------------------------------------------------------------------------------------------------------------------------------------------------------------------------------------------------------------------------------------------------------------------------------------------------------------------------------------------------------------------------------------------------------------------------------------------------------------------------------------------------------------------------------------------------------------------------------------------------------------------------------------------------------------------------------------|---------------------------------------------------------------------------------------------------------------------------------------------------------------------------------------------------------------------------------------------------------------------------------------------------------------------------------------------------------------------------------------------------------------------------------------------------------------------------------------------------------------------------------------------------------------------------------------------------------------------------------------------------------------------------------------------------------------------------------------------------------------------------------------------------------------------------------------------------------------------------------------------------------------------------------------------------------------------------------------------------------------------------------------------------------------------------------------------------------------------------------------------------------------------------------------------------------------------------------------------------------------------------------------------------------------------------------------------------------------------------------------------------------------------------------------------------------------------------------------------------------------------------------------------------------------------------------------------------------------------------------------------------------------------------------------------------------------------------------------------------------------------------------------------------------------------------------------------------------------------------------------------------------------------------------------------------------------------------------------------------------------------------------------------------------------------------------------------------------------------------|
| 307/307 | | | | <u> </u> | | 146/148 | 201,33 | N_b/N_s |
| อนกรอนก | _ ¹²² Sn | 102/105 | 117 _I | 120/105 | 12670 | 00/100 | 138.0 | 5 0 /1 4 5 |
| | 123Sn | 103/105 | 119I | 132/185 | ¹²⁶ Ba | 88/133 | ¹³⁸ Ce | 70/117 |
| 116/116 | 124Sn | 88/118 | 121 I | 173/173 | ¹²⁷ Ba | 125/134 | ¹³⁹ Ce | 103/103 |
| 111/111 | | 253/253 | | 171/171 | 128Ba | 153/157 | ¹⁴⁰ Ce | 194/195 |
| | | | | | 131 D | | | 39/120 |
| | | • | 125 T | | | | | 19/118 |
| | | | | | | 197/197 | | 155/167 |
| | | | | | 134D | | 130Pr | 133/152 |
| | | | | | | | 132Pr | 88/144 |
| | | | | | ""Ba | | 133Pr | 214/214 |
| | 110Sb | | | | 130Ba | | 136Pr | 63/105 |
| | 113Sb | | 116Xe | | 138Ba | | ¹³⁷ Pr | 103/103 |
| | 121Sb | 118/191 | · · · · Xe | | 139Ba | | 140Pr | 106/106 |
| .* | | | 118Xe | • | ¹²³ La | | ¹⁴¹ Pr | 188/188 |
| | | | ¹¹⁹ Xe | 152/152 | ¹²⁴ La | 112/112 | ¹⁴² Pr | 13/178 |
| | | | ¹²⁰ Xe | 68/121 | ^{125}La | 101/102 | ¹²⁹ Nd | 124/125 |
| | | | ¹²¹ Xe | 77/124 | ¹²⁷ La | 126/127 | ¹³¹ Nd | 154/154 |
| 67/137 | ¹¹⁰ Te | 155/155 | ¹²² Xe | 125/125 | ^{130}La | 68/107 | | 126/126 |
| 177/177 | ¹¹² Te | 136/136 | ¹²³ Xe | 83/143 | ¹³¹ La | 136/136 | 133Nd | 205/205 |
| 104/125 | | 79/105 | ¹²⁴ Xe | 184/242 | $^{133}\mathrm{La}$ | 143/145 | 134Nd | 124/138 |
| 73/111 | ¹¹⁸ Te | 97/201 | | | ¹³⁴ La | 107/107 | 136Nd | 161/221 |
| 91/108 | ¹¹⁹ Te | | ¹²⁶ Xe | 203/326 | ¹³⁶ La | | 137 Nd | 144/144 |
| 132/143 | ¹²⁰ Te | | ¹²⁷ Xe | 104/107 | ¹³⁹ La | | 138Nd | 64/120 |
| | $^{121}{ m Te}$ | | | | 140La | | 140Nd | 271/271 |
| | ¹²² Te | | ¹³⁰ Xe | 64/116 | ¹²⁵ Ce | 131/131 | 142Nd | 43/247 |
| | ¹²³ Te | | ¹³⁷ Xe | 168/207 | | | 143Nd | 5/252 |
| | ¹²⁴ Te – | | | | | | 144Nd | 23/202 |
| | $^{125}\mathrm{Te}$ | | | | | | 145Nd | 142/142 |
| * | ¹²⁶ Te | | | | | | 146 Nd | 47/291 |
| | | | ¹³¹ Cs | | | | | 139/139 |
| | | | 134Cs | | | | | 31/113 |
| • | | | 142 Cs | | | | | 106/106 |
| | 113 _I | 171/171 | 124Ba | | | | 150Nd | 29/133 |
| | 136/138 147/147 107/301 134/134 273/290 173/173 219/305 235/235 128/180 196/196 56/145 145/146 230/243 67/137 177/177 104/125 73/111 | 136/138 107Sb 147/147 109Sb 147/147 109Sb 107/301 111Sb 134/134 112Sb 273/290 114Sb 173/173 117Sb 219/305 118Sb 225/235 119Sb 128/180 121Sb 196/196 122Sb 56/145 123Sb 145/146 124Sb 230/243 133Sb 67/137 110Te 177/177 112Te 104/125 114Te 73/111 118Te 91/108 119Te 132/143 120Te 134/137 121Te 174/174 122Te 152/271 123Te 190/190 124Te 190/190 124Te 1309/309 125Te 151/151 126Te 166/166 127Te 156/156 129Te 20/137 131Te | 136/138 107Sb 67/67 147/147 109Sb 95/113 107/301 111Sb 114/114 134/134 112Sb 160/160 273/290 114Sb 128/128 173/173 117Sb 55/104 219/305 118Sb 49/146 2235/235 119Sb 143/144 128/180 121Sb 118/191 196/196 122Sb 118/118 56/145 123Sb 24/118 145/146 124Sb 104/104 230/243 133Sb 100/100 67/137 110Te 155/155 177/177 112Te 136/136 104/125 114Te 79/105 73/111 119Te 175/175 132/143 120Te 14/113 84/137 121Te 168/209 174/174 122Te 240/240 190/190 124Te 304/304 309/309 125Te 20/308 151/151 <td>136/138 107Sb 67/67 123I 147/147 109Sb 95/113 124I 107/301 111Sb 114/114 125I 134/134 112Sb 160/160 126I 273/290 114Sb 128/128 127I 173/173 117Sb 55/104 128I 219/305 118Sb 49/146 131I 228/180 121Sb 118/191 117Xe 196/196 122Sb 118/118 118Xe 145/146 123Sb 24/118 119Xe 230/243 133Sb 100/100 121Xe 230/243 133Sb 100/100 121Xe 27/137 110Te 155/155 122Xe 177/177 112Te 136/136 123Xe 104/125 114Te 79/105 124Xe 27/110 118Te 97/201 125Xe 21/108 119Te 175/175 126Xe 21/2143 120Te 14/113 127Xe</td> <td>136/138 107 Sb 67/67 123 I 163/163 147/147 109 Sb 95/113 124 I 107/107 107/301 111 Sb 114/114 125 I 155/156 134/134 112 Sb 160/160 126 I 72/122 273/290 114 Sb 128/128 127 I 117/138 173/173 117 Sb 55/104 128 I 3/232 219/305 118 Sb 49/146 131 I 93/114 235/235 119 Sb 143/144 116 Xe 91/103 128/180 121 Sb 118/191 117 Xe 89/138 196/196 122 Sb 118/118 118 Xe 101/121 26/145 123 Sb 24/118 119 Xe 152/152 145/146 124 Sb 104/104 120 Xe 68/121 230/243 133 Sb 100/100 121 Xe 77/124 57/137 110 Te 155/155 122 Xe 83/143 104/125 14 Te 79/105</td> <td>136/138 107Sb 67/67 123I 163/163 129Ba 147/147 109Sb 95/113 124I 107/107 131Ba 107/301 111Sb 114/114 125I 155/156 132Ba 134/134 112Sb 160/160 126I 72/122 133Ba 134/134 112Sb 128I 3/232 135Ba 273/290 114Sb 128I 3/232 135Ba 173/173 117Sb 55/104 128I 3/232 135Ba 219/305 118Sb 49/146 131I 93/114 136Ba 225/235 119Sb 143/144 116Xe 91/103 138Ba 128/180 121Sb 118/191 117Xe 89/138 139Ba 196/196 122Sb 118/118 118Xe 101/121 123La 26/145 123Sb 24/118 119Xe 152/152 124La 230/243 133Sb 100/100 121Xe 77/124 127La 27/137 110Te 155/155 122Xe 125/125 130La</td> <td>136/138 107Sb 67/67 123I 163/163 129Ba 135/144 147/147 109Sb 95/113 124I 107/107 131Ba 129/129 107/301 111Sb 114/114 125I 155/156 132Ba 197/197 134/134 112Sb 160/160 126I 72/122 133Ba 145/145 273/290 114Sb 128I28 127I 117/138 134Ba 5/125 173/173 117Sb 55/104 128I 3/232 135Ba 134/134 219/305 118Sb 49/146 131I 93/114 136Ba 42/101 228/180 121Sb 118/191 117Xe 89/138 139Ba 10/108 196/196 122Sb 118/118 118Xe 101/121 123La 100/101 116/145 123Sb 24/118 119Xe 152/152 124La 112/112 123O/243 133Sb 100/100 121Xe 77/124 127La 126/127 17/177 112Te 136/136 123Xe 83/143 131La</td> <td> 136/138 107Sb 67/67 123I 163/163 129Ba 135/144 142Ce 147/147 109Sb 95/113 124I 107/107 131Ba 129/129 146Ce 107/301 111Sb 114/114 125I 155/156 132Ba 197/197 128Pr 134/134 112Sb 160/160 126I 72/122 133Ba 145/145 130Pr 1273/290 114Sb 128/128 127I 117/138 134Ba 5/125 132Pr 173/173 117Sb 55/104 128I 3/232 135Ba 134/134 133Pr 129/305 118Sb 49/146 131I 93/114 136Ba 42/101 136Pr 128/180 121Sb 118/191 117Xe 89/138 139Ba 10/108 140Pr 128/180 121Sb 118/191 117Xe 89/138 139Ba 10/108 140Pr 1296/196 122Sb 118/118 118Xe 101/121 123La 100/101 141Pr 145/146 124Sb 104/104 120Xe 68/121 125La 101/102 129Nd 1203/243 133Sb 100/100 121Xe 77/124 127La 126/127 131Nd 130/137 110Te 155/155 122Xe 125/125 130La 68/107 132Nd 137/177 112Te 136/136 123Xe 83/143 131La 136/136 133Nd 130/108 140/108 140/108 140/108 140/108 140/108 140/108 140/108 140/108 140/108 140/108 140/108 140/108 140/108 140/108 140/108 140/108 140/108 140/108 140/108 140/108 140/108 140/108 140/108 140/108 140/108 140/108 140/108 140/108 140/108 140/108 140/108 140/108 140/108 140/108 140/108 140/108 140/108 140/108 140/108 140/108 140/108 140/108 140/108 140/108 140/108 140/108 140/108 140/108 140/108 140/108 140/108 140/108 140/108 140/108 140/108 140/108 140/108 140/108 140/108 140/108 140/108 140/108 140/108 140/108 140/108 140/108 140/108 140/108 140/108 140/108 140/108 140/108 140/108 140/108 140/108 140/108 140/108 140/108 140/108 140/108 140/108 140/108 140/108 140/108 140/108 140/108 140/108 140/108 140/108 140/108 140/108 140/108 140/108 140/108 140/108 140/108 140/108 140/108 140/108 140/108 140/108 140/108 140/108 140/108 140/108 </td> | 136/138 107Sb 67/67 123I 147/147 109Sb 95/113 124I 107/301 111Sb 114/114 125I 134/134 112Sb 160/160 126I 273/290 114Sb 128/128 127I 173/173 117Sb 55/104 128I 219/305 118Sb 49/146 131I 228/180 121Sb 118/191 117Xe 196/196 122Sb 118/118 118Xe 145/146 123Sb 24/118 119Xe 230/243 133Sb 100/100 121Xe 230/243 133Sb 100/100 121Xe 27/137 110Te 155/155 122Xe 177/177 112Te 136/136 123Xe 104/125 114Te 79/105 124Xe 27/110 118Te 97/201 125Xe 21/108 119Te 175/175 126Xe 21/2143 120Te 14/113 127Xe | 136/138 107 Sb 67/67 123 I 163/163 147/147 109 Sb 95/113 124 I 107/107 107/301 111 Sb 114/114 125 I 155/156 134/134 112 Sb 160/160 126 I 72/122 273/290 114 Sb 128/128 127 I 117/138 173/173 117 Sb 55/104 128 I 3/232 219/305 118 Sb 49/146 131 I 93/114 235/235 119 Sb 143/144 116 Xe 91/103 128/180 121 Sb 118/191 117 Xe 89/138 196/196 122 Sb 118/118 118 Xe 101/121 26/145 123 Sb 24/118 119 Xe 152/152 145/146 124 Sb 104/104 120 Xe 68/121 230/243 133 Sb 100/100 121 Xe 77/124 57/137 110 Te 155/155 122 Xe 83/143 104/125 14 Te 79/105 | 136/138 107Sb 67/67 123I 163/163 129Ba 147/147 109Sb 95/113 124I 107/107 131Ba 107/301 111Sb 114/114 125I 155/156 132Ba 134/134 112Sb 160/160 126I 72/122 133Ba 134/134 112Sb 128I 3/232 135Ba 273/290 114Sb 128I 3/232 135Ba 173/173 117Sb 55/104 128I 3/232 135Ba 219/305 118Sb 49/146 131I 93/114 136Ba 225/235 119Sb 143/144 116Xe 91/103 138Ba 128/180 121Sb 118/191 117Xe 89/138 139Ba 196/196 122Sb 118/118 118Xe 101/121 123La 26/145 123Sb 24/118 119Xe 152/152 124La 230/243 133Sb 100/100 121Xe 77/124 127La 27/137 110Te 155/155 122Xe 125/125 130La | 136/138 107Sb 67/67 123I 163/163 129Ba 135/144 147/147 109Sb 95/113 124I 107/107 131Ba 129/129 107/301 111Sb 114/114 125I 155/156 132Ba 197/197 134/134 112Sb 160/160 126I 72/122 133Ba 145/145 273/290 114Sb 128I28 127I 117/138 134Ba 5/125 173/173 117Sb 55/104 128I 3/232 135Ba 134/134 219/305 118Sb 49/146 131I 93/114 136Ba 42/101 228/180 121Sb 118/191 117Xe 89/138 139Ba 10/108 196/196 122Sb 118/118 118Xe 101/121 123La 100/101 116/145 123Sb 24/118 119Xe 152/152 124La 112/112 123O/243 133Sb 100/100 121Xe 77/124 127La 126/127 17/177 112Te 136/136 123Xe 83/143 131La | 136/138 107Sb 67/67 123I 163/163 129Ba 135/144 142Ce 147/147 109Sb 95/113 124I 107/107 131Ba 129/129 146Ce 107/301 111Sb 114/114 125I 155/156 132Ba 197/197 128Pr 134/134 112Sb 160/160 126I 72/122 133Ba 145/145 130Pr 1273/290 114Sb 128/128 127I 117/138 134Ba 5/125 132Pr 173/173 117Sb 55/104 128I 3/232 135Ba 134/134 133Pr 129/305 118Sb 49/146 131I 93/114 136Ba 42/101 136Pr 128/180 121Sb 118/191 117Xe 89/138 139Ba 10/108 140Pr 128/180 121Sb 118/191 117Xe 89/138 139Ba 10/108 140Pr 1296/196 122Sb 118/118 118Xe 101/121 123La 100/101 141Pr 145/146 124Sb 104/104 120Xe 68/121 125La 101/102 129Nd 1203/243 133Sb 100/100 121Xe 77/124 127La 126/127 131Nd 130/137 110Te 155/155 122Xe 125/125 130La 68/107 132Nd 137/177 112Te 136/136 123Xe 83/143 131La 136/136 133Nd 130/108 140/108 140/108 140/108 140/108 140/108 140/108 140/108 140/108 140/108 140/108 140/108 140/108 140/108 140/108 140/108 140/108 140/108 140/108 140/108 140/108 140/108 140/108 140/108 140/108 140/108 140/108 140/108 140/108 140/108 140/108 140/108 140/108 140/108 140/108 140/108 140/108 140/108 140/108 140/108 140/108 140/108 140/108 140/108 140/108 140/108 140/108 140/108 140/108 140/108 140/108 140/108 140/108 140/108 140/108 140/108 140/108 140/108 140/108 140/108 140/108 140/108 140/108 140/108 140/108 140/108 140/108 140/108 140/108 140/108 140/108 140/108 140/108 140/108 140/108 140/108 140/108 140/108 140/108 140/108 140/108 140/108 140/108 140/108 140/108 140/108 140/108 140/108 140/108 140/108 140/108 140/108 140/108 140/108 140/108 140/108 140/108 140/108 140/108 140/108 140/108 140/108 140/108 140/108 140/108 140/108 |

The maximum at $E^*=272$ keV which is close to difference $\delta m_N - \varepsilon_o = 1293$ keV-1022 keV==271 keV is considered in [8]. The additional confirmation of 161 keV/170 keV systems observed in SN-Sb region was obtained with the data for Pd-isotopes where stable intervals D=512 keV, 648 keV and 1293 keV were found [3-5].

5 Analysis of data for nuclei with Z=61-73

Table 8. Numbers of bound states in compound nuclei ^AZ with Z=61-73 contained in v.I/25D. The ratio shows number of states in the book and in the Supplement.

| ^A Z | N _b /N _s | ^A Z | N_b/N_s | $^{A}\mathrm{Z}$ | N_b/N_s | ^{A}Z | N_b/N_s | ^{A}Z | N_b/N_s |
|---------------------|--------------------------------|---------------------|-----------|---------------------|-----------|---------------------|------------|---------------------|-----------|
| | ; 00/10F | | | | 5.07 5.8 | | * '0/ * '8 | | 116/118 |
| | | . 40 | | | | | | | 1,344 |
| ¹³⁶ Pm | 90/105 | ¹⁴⁶ Gd | 10/196 | ¹⁵⁸ Dy | 53/142 | $^{161}\mathrm{Tm}$ | 92/104 | ¹⁷⁵ Lu | 62/138 |
| ¹³⁹ Pm | 96/134 | ¹⁴⁷ Gd | 242/243 | ¹⁵⁹ Dy | 95/124 | $^{162}\mathrm{Tm}$ | 212/212 | $^{176}\mathrm{Lu}$ | 151/195 |
| ¹⁴³ Pm | 101/101 | ¹⁴⁸ Gd | 73/304 | ¹⁶⁰ Dy | 248/249 | $^{163}\mathrm{Tm}$ | 141/141 | ¹⁷⁷ Lu | 141/212 |
| ¹⁴⁷ Pm | 138/138 | ¹⁴⁹ Gd | 82/393 | ¹⁶¹ Dy | 105/183 | $^{164}\mathrm{Tm}$ | 159/175 | ¹⁶⁶ Hf | 187/187 |
| ¹⁵¹ Pm | 133/133 | $^{150}\mathrm{Gd}$ | 23/133 | ¹⁶² Dy | 282/283 | $^{165}\mathrm{Tm}$ | 184/203 | ¹⁶⁸ Hf | 262/262 |
| ¹³⁹ Sm | 62/106 | $^{151}\mathrm{Gd}$ | 225/225 | 163 Dy | 353/354 | $^{166}\mathrm{Tm}$ | 239/239 | ¹⁶⁹ Hf | 159/159 |
| ¹⁴³ Sm | 47/125 | $^{152}\mathrm{Gd}$ | 100/231 | ¹⁶⁴ Dy | 54/171 | $^{167}\mathrm{Tm}$ | 104/164 | ¹⁷⁰ Hf | 231/231 |
| ¹⁴⁴ Sm | 31/184 | $^{153}\mathrm{Gd}$ | 131/220 | ¹⁶⁵ Dy | 25/173 | $^{-168}{ m Tm}$ | 224/226 | $^{171}{ m Hf}$ | 175/175 |
| $^{145}\mathrm{Sm}$ | 171/171 | $^{154}\mathrm{Gd}$ | 248/250 | ¹⁵³ Ho | 116/116 | $^{169}\mathrm{Tm}$ | 152/153 | ¹⁷² Hf | 270/287 |
| ¹⁴⁶ Sm | 11/190 | $^{155}\mathrm{Gd}$ | 119/223 | ¹⁵⁶ Ho | 150/150 | $^{170}\mathrm{Tm}$ | 63/258 | ¹⁷³ Hf | 127/145 |
| ¹⁴⁷ Sm | 102/103 | $^{156}\mathrm{Gd}$ | 125/272 | ¹⁵⁷ Ho | 226/247 | 160Yb | 119/119 | ¹⁷⁴ Hf | 230/255 |
| ¹⁴⁸ Sm | 57/289 | $^{157}\mathrm{Gd}$ | 43/347 | ¹⁵⁸ Ho | 119/120 | 164Yb | 122/134 | ¹⁷⁵ Hf | 146/177 |
| ¹⁴⁹ Sm | 56/193 | $^{158}\mathrm{Gd}$ | 55/217 | ¹⁵⁹ Ho | 125/125 | 166Yb | 132/132 | ¹⁷⁶ Hf | 221/221 |
| ¹⁵⁰ Sm | 191/191 | $^{159}\mathrm{Gd}$ | 44/300 | ¹⁶⁰ Ho | 90/101 | ¹⁶⁷ Yb | 140/176 | ¹⁷⁷ Hf | 125/145 |
| ¹⁵¹ Sm | 239/240 | $^{160}\mathrm{Gd}$ | 105/119 | ¹⁶¹ Ho | 108/154 | ¹⁶⁸ Yb | 197/197 | 179Hf | 249/249 |
| $^{152}\mathrm{Sm}$ | 36/154 | $^{143}\mathrm{Tb}$ | 79/105 | ¹⁶³ Ho | 102/102 | ¹⁶⁹ Yb | 237/237 | ¹⁸⁰ Hf | 139/279 |
| $^{153}\mathrm{Sm}$ | 296/296 | $^{147}\mathrm{Tb}$ | 201/201 | ¹⁶⁵ Ho | 222/278 | ¹⁷⁰ Yb | 124/213 | $^{181}{ m Hf}$ | 47/186 |
| $^{154}\mathrm{Sm}$ | 110/110 | $^{149}\mathrm{Tb}$ | 113/178 | ¹⁶⁶ Ho | 358/358 | ¹⁷¹ Yb | 58/176 | $^{167}\mathrm{Ta}$ | 118/118 |
| $^{155}\mathrm{Sm}$ | 142/142 | $^{150}{ m Tb}$ | 10/115 | $^{156}\mathrm{Er}$ | 122/122 | ¹⁷² Yb | 58/311 | $^{169}\mathrm{Ta}$ | 187/187 |
| ¹⁴² Eu | 54/127 | $^{151}\mathrm{Tb}$ | 308/308 | $^{157}\mathrm{Er}$ | 178/214 | ¹⁷³ Yb | 43/137 | $^{170}\mathrm{Ta}$ | 332/332 |
| ¹⁴³ Eu | 68/202 | $^{152}\mathrm{Tb}$ | 17/142 | 158Er | 129/129 | ¹⁷⁴ Yb | 41/376 | $^{171}\mathrm{Ta}$ | 207/207 |
| ¹⁴⁴ Eu | 7/144 | $^{153}\mathrm{Tb}$ | 139/139 | ¹⁵⁹ Er | 177/197 | ¹⁷⁵ Yb | 47/185 | $^{172}\mathrm{Ta}$ | 171/185 |
| $^{145}\mathrm{Eu}$ | 257/274 | $^{155}\mathrm{Tb}$ | 163/163 | ¹⁶⁰ Er | 200/243 | ¹⁷⁷ Yb | 35/162 | $^{173}\mathrm{Ta}$ | 173/173 |
| ¹⁴⁷ Eu | 203/203 | $^{157}\mathrm{Tb}$ | 96/129 | ¹⁶¹ Er | 112/122 | ¹⁶¹ Lu | 167/167 | ¹⁷⁴ Ta | 127/127 |
| ¹⁴⁸ Eu | 104/104 | $^{159}\mathrm{Tb}$ | 45/118 | $^{162}\mathrm{Er}$ | 128/128 | ¹⁶² Lu | 91/104 | $^{175}\mathrm{Ta}$ | 116/126 |
| ¹⁴⁹ Eu | 130/130 | $^{160}\mathrm{Tb}$ | 63/183 | ¹⁶³ Er | 381/381 | ¹⁶³ Lu | 252/260 | 176 Ta | 127/128 |
| $^{151}\mathrm{Eu}$ | 178/178 | 150 Dv | 61/367 | ¹⁶⁴ Er | 136/204 | ¹⁶⁴ Lu | 117/117 | $^{177}\mathrm{Ta}$ | 196/196 |
| $^{152}\mathrm{Eu}$ | 37/195 | 151 Dv | 175/175 | ¹⁶⁵ Er | 44/105 | ¹⁶⁵ Lu | 309/309 | $^{178}\mathrm{Ta}$ | 159/159 |
| ¹⁵³ Eu | 145/168 | 152 Dy | 77/250 | ¹⁶⁶ Er | 223/233 | ¹⁶⁷ Lu | 188/188 | ¹⁷⁹ Ta | 159/159 |
| ¹⁵⁴ Eu | 159/159 | ¹⁵³ Dy | 143/223 | ¹⁶⁷ Er | 88/200 | ¹⁶⁸ Lu | 118/118 | $^{180}\mathrm{Ta}$ | 166/246 |
| ¹⁴² Gd | 124/124 | 154Dy | 221/221 | ¹⁶⁸ Er | 455/455 | ¹⁶⁹ Lu | 100/101 | $^{181}\mathrm{Ta}$ | 107/139 |
| ¹⁴³ Gd | 60/107 | ¹⁵⁵ Dy | 158/186 | ¹⁶⁹ Er | 157/158 | 170Lu | 203/203 | $^{182}\mathrm{Ta}$ | 178/178 |
| | 98/167 | 156 Dy | 243/314 | 170Er | 113/172 | ¹⁷¹ Lu | 163/202 | | 110/110 |
| ¹⁴⁵ Gd | 151/151 | 157Dy | 205/205 | ¹⁷¹ Er | 56/104 | 174Lu | 58/193 | | |
| 7 41 | | , , | _30,200 | 1 | 55/101 | | 20,100 | | |

In this work we checked a new trend in an interpretation of nonstatistical effects in excitation of a great number of nuclei. The role of the pion-exchange dynamics is seen also for heavy nuclei (see E^* -distributions in Fig. 5-7). Clear nonstatistical effects were observed in D-distributions for 165 Ho and 175 Lu shown in Fig.8. Analysis of neutron resonance data for heavy isotopes could be important.

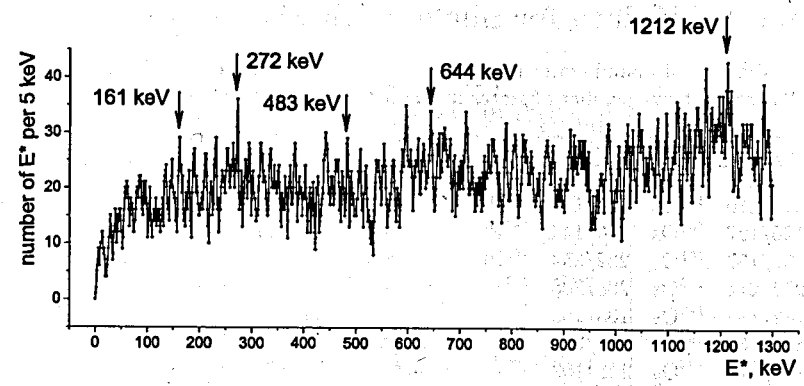


Fig. 5 left: Sum E^* -distribution of all nuclei with Z=48-60 (ΔE =5 keV). Maxima at E^* =161-483-644 keV correspond to excitations in Sb, at E^* = ϵ_o and 1212 keV - to phonons.

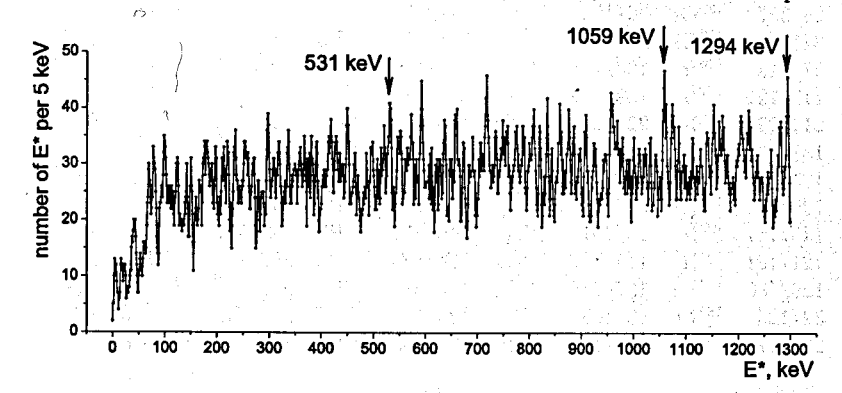


Fig.6 left: Sum E^* -distribution of all nuclei with Z=61-73 (ΔE =5 keV). Maxima at E^* =129? keV correspond to stable excitations E^* close to δm_N =1293.3 keV (see some of them in Table .

Table 9. Excitations (in keV) in even-even heavy nuclei Z=68-76 close to parameters $\delta m_N=1293.3$ keV and $\varepsilon_o=2m_e=1022.0$ keV.

| | | 1 | | | | 1 . | | | | 1 P. 1 1 1 1 1 1 1 1 1 1 1 1 1 1 1 1 1 1 | ing the free free | 1 + 3 d l l l l l |
|---------------|-------------------------|-----------|-------------------------|-------|-------------------|-------------------|------------------------|------------------|------|------------------------------------------|-------------------|-------------------|
| $Z = {}^{A}Z$ | 70 ¹⁶⁰ Yb | 170Yb | 72 ¹⁶² Hf | 172Hf | ¹⁷⁶ Hf | ¹⁷⁸ Hf | 74 ¹⁷² W | ¹⁷⁸ W | 184W | 76 ¹⁷⁶ Os | ¹⁷⁸ Os | ¹⁸⁰ Os |
| | | | | 1.1 | Mary. | | 3.7 | 917 (1) | | | | 11 |
| E^* | 1293 | 1292 | 1293 | 1293 | 1293 | 1291 | 1292 | 1294 | 1295 | 1025.6 | 1023.2 | 1022.9 |
| $2J^{\pi}$ | 2+ | $(4)^{+}$ | | 0+ 1 | 0+ | 3+ | (2,3,4) | 0+ | 5+ | 4+ | 4+ | 3+ |
| N | 90 | 100 | 90 | 100 | | | | | | | 102 | 104 |

6 Analysis of data for nuclei with Z=74-100

Table 10. Numbers of bound states in compound nuclei ^AZ with Z=74-100 contained in v.I/25C. The ratio shows number of states in the book and in the Supplement.

| ^{A}Z | N_b/N_s | ^A Z | N_b/N_s | ^A Z | N_b/N_s | ^A Z | N_b/N_s | $^{A}\mathrm{Z}$ | N_b/N_s |
|---------------------|---------------|---------------------|----------------------------------------------|---------------------|------------|---------------------|---------------|---------------------|-----------|
| 174*** | | 170.0 | | 105- | | 102 | | 010- | 45 |
| 174W | 210/210 | ¹⁷⁹ Os | 134/134 | ¹⁸⁵ Pt | 66/191 | ¹⁹³ Tl | 141/141 | ²¹⁰ Bi | 243/244 |
| 176W | 126/127 | ¹⁸⁰ Os | 140/144 | ¹⁸⁷ Pt | 160/160 | ¹⁹⁴ Tl | 125/125 | ²¹⁰ At | 32/124 |
| 177W | 152/157 | ¹⁸¹ Os | 222/254 | ¹⁹² Pt | 135/181 | ²⁰³ Tl | 15/105 | ²¹¹ At | 26/117 |
| 178W | 274/274 | ¹⁸² Os | 208/208 | $^{194}\mathrm{Pt}$ | 109/150 | $^{204}\mathrm{Tl}$ | 122/258 | ²²⁸ Th | 23/111 |
| ¹⁷⁹ W | 182/185 | ¹⁸³ Os | 103/158 | $^{195}\mathrm{Pt}$ | 19/114 | $^{206}\mathrm{Tl}$ | 95/537 | $^{230}\mathrm{Th}$ | 245/247 |
| 180W | 84/125 | $^{184}\mathrm{Os}$ | 204/204 | ¹⁹⁶ Pt | 142/142 | ¹⁹² Pb | 91/116 | $^{231}\mathrm{Th}$ | 160/160 |
| ¹⁸² W | 178/178 | ¹⁸⁵ Os | 123/192 | ¹⁹⁷ Pt | 1/104 | ¹⁹³ Pb | 238/248 | $^{232}\mathrm{Th}$ | 174/174 |
| ^{183}W | 78/201 | ¹⁸⁶ Os | 108/164 | ¹⁸⁴ Au | 126/126 | ^{Í94} Pb | 327/343 | $^{233}\mathrm{Th}$ | 74/226 |
| ¹⁸⁴ W | 257/257 | ¹⁸⁸ Os | 65/190 | ¹⁸⁷ Au | 312/312 | ¹⁹⁵ Pb | 161/161 | ^{234}U | 152/152 |
| ^{185}W | 28/367 | $^{190}\mathrm{Os}$ | 36/153 | ¹⁸⁹ Au | 74/275 | 196 Pb | 300/300 | $^{235}{ m U}$ | 138/220 |
| ¹⁸⁷ W | 345/346 | $^{192}\mathrm{Os}$ | 22/110 | - ¹⁹⁰ Au | 59/102 | $^{197}\mathrm{Pb}$ | 155/240 | ^{236}U | 122/122 |
| 175 Re | 97/113 | ¹⁷⁶ Ir | 128/128 | ¹⁹¹ Au | 186/186 | $^{198}\mathrm{Pb}$ | ~196/199 | $^{237}{ m U}$ | 226/270 |
| 176 Re | 115/121 | ¹⁷⁷ Ir | 109/122 | ¹⁹⁶ Au | 236/236 | $^{199}\mathrm{Pb}$ | 167/168 | ^{238}U | 118/163 |
| 177 Re | 214/253 | ¹⁷⁸ Ir | 226/226 | ¹⁹⁸ Au | 140/158 | ²⁰¹ Pb | 124/124 | ^{239}U | 61/108 |
| $^{179}\mathrm{Re}$ | 137/137 | ¹⁸¹ Ir | 147/181 | ¹⁹⁰ H∉ | 165/196 | ²⁰⁴ Pb | 180/180 | $^{237}\mathrm{Np}$ | 52/105 |
| 180 Re | 138/138 | ¹⁸⁷ Ir | 202/202 | ¹⁹¹ Hg | 215/217 | ²⁰⁵ Pb | 145/1036 | $^{238}\mathrm{Np}$ | 47/129 |
| $^{181}\mathrm{Re}$ | 130/162 | ¹⁹⁰ Ir | 62/156 | 192Hg | 130/156 | $^{206}\mathrm{Pb}$ | 335/335 | ²³⁹ Pu | 100/125 |
| $^{183}\mathrm{Re}$ | 149/187 | ¹⁹² Ir | 20/231 | $^{193}\mathrm{Hg}$ | 246/252 | $^{207}\mathrm{Pb}$ | 103/961 | ²⁴⁰ Pu | 181/181 |
| 184 Re | 121/121 | ¹⁹⁴ Ir | 118/177 | ¹⁹⁴ Hg | 130/154 | $^{208}\mathrm{Pb}$ | 287/1380 | ²⁴¹ Pu | 57/106 |
| 186 Re | 129/186 | $^{181}\mathrm{Pt}$ | 137/138 | $^{195}\mathrm{He}$ | 135/211 | $^{209}\mathrm{Pb}$ | 9/388 | ²⁴¹ Am | 110/110 |
| ²¹⁰ At | 32/124 | $^{183}\mathrm{Pt}$ | 63/103 | ²⁰⁰ Hg | 133/138 | ²⁰⁸ Bi | 239/246 | ²⁴² Am | 89/165 |
| ²¹¹ At | 26/117 | ¹⁸⁴ Pt | 131/131 | ¹⁸⁹ Tl | 130/130 | ²⁰⁹ Bi | 5/228 | ²⁴⁴ Am | 29/114 |
| | i i | | | | | | • | | |
| ≥ 70 | 44 keV | 4401 | <u>.</u> | | 688 ke | 9V | | | 9.80 |
| \$ 60- | Į į | 146 ke | V | | İ | | | | |
| ē ° | 1 1 | | 1 | _ | 1 1 | | 1 | | 300 |
| £ 50- | | | ıllı, Ma | J | اء ال | . 11 | | i | |
| ber of E* per 5 keV | | ilլե. | MIH MI | w JM IAL | | | | | 11 |
| Ç 40- | | | ****** ****************************** | MANA | | Mile i Mili | | | W. C. |
| ا تھ | 1 1 1 A 1 A 1 | BATHA, ANJ AT F. | Hura Maraili | K WII WE LI | THE TANKER | 441 . ; | Mall int hill | ₹¥`WHTH | 2 |

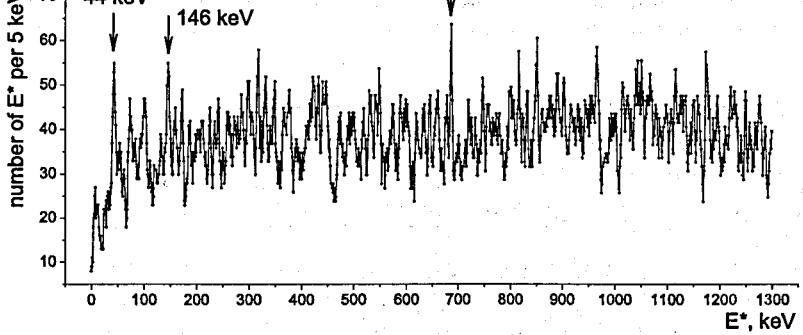


Fig. 7 left: Sum E^* -distribution of all nuclei with Z=74-100 (ΔE =5 keV). Maxima at E^* =44 keV and 146 keV correspond to stable excitations in heavy even-even nuclei (spins 2^+ and 4^+). Stable excitations in the region E^* =683 keV=(2/3) ε_o were considered in [13].

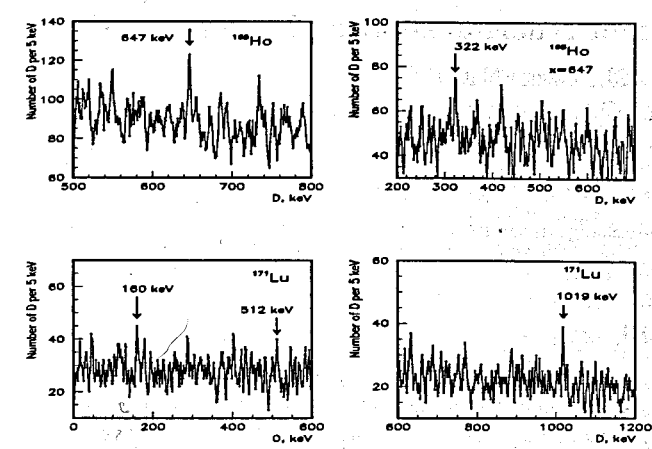


Fig. 8. Top: D-distribution of levels in ¹⁶⁵Ho (n=372) and distribution of intervals adjacent to D=x=647 keV (ratio 2:1). Bottom: D-distribution of levels in ¹⁷⁵Lu (n=139).

7 Conclusions

Tuning effect in nuclear excitations should be considered as confirmation S.Devons suggestion on the presence of fundamental aspects in the analysis of accurately measured nuclear data. The extension of long-range correlations observed in nuclear excitations can be seen in particle masses [3-6]). The specific properties of neutron resonance spectroscopy (high energy resolution, interconnection between excitations and binding energy) could be very useful for a study these fundamental proprieties of nuclear matter.

8 References

- 1. T.Otsuka, T.Suzuku, Y.Utsino, 2008 Nucl. Phys. A 805 127c.
- 2. S.Devons, 1961, Proc. Rutherford Jubileum Conf. Ed. J.Birks, p.611, Heywood.
- 3. S.I.Sukhoruchkin, D.S.Sukhoruchkin, 2011, Int. J. Mod. Phys. E 20 906.
- 4. S.I.Sukhoruchkin, Proc. Hadron 2011 Muenich, 2011, eConf C110613.
- 5. S.I.Sukhoruchkin, Proc. Rutherford Centennial Conf., Manchester, 2011. JPCS, 2012.
- 6. S.I.Sukhoruchkin, http://cgc.physics.miami.edu/Miami2011.html.
- 7. S.I.Sukhoruchkin, D.S.Sukhoruchkin, these Proceedings ISINN-19.
- 8. S.I.Sukhoruchkin, M.S.Sukhoruchkina, these Proceedings ISINN-19.
- 9. M.S.Bhagwal et al., 2007 Phys. Rev. C 76 045203.
- 10. H.L.L. Roberts et al., 2011 Phys. Rev. C 83 065206.
- 11. Landolt-Boerstein New Series Springer vol.I/25A, Editor H. Schopper.
- 12. Landolt-Boerstein New Series Springer vol.I/24A, Editor H. Schopper.
- 13. S.I.Sukhoruchkin, 2008, Int. Rev Phys (IREPHY) 2 No 4, 239.

Compilation of Nuclear Binding Energies MDF

S.I. Sukhoruchkin, D.S. Sukhoruchkin

Petersburg Nuclear Physics Institute, 188300 Gatchina

Abstract

The role of pion-exchange dynamics in tuning effects in nuclear binding energies was studied with data from the compilation MDF (Mass Difference File).

1 Introduction

In this report we describe data analysis from the compilation MDF (Mass Difference File) [1] in connection with A.Arima and A.Bohr remark that nuclear binding energies and nuclear excitations are results of the same nucleon interaction. Hence positions of neutron resonances being the difference between them could provide additional information on properties of nucleon interaction. Correlations in neutron resonance positions were reported by M.Ohkubo, K.Ideno, G.Rohr, F.Belyaev and others (see [2] and the previous previous ISINN). According to Arima-Bohr suggestion the same parameters should be used for the description of few-nucleon effects in both nuclear characteristics E^* and E_B .

It was noticed by C. Detraz: "...the force at work between nucleons is not the genuine strong force but only what spills over from the quark bag. This leads to setting for an effective force ... should not be taken to mean that nuclear science is completely understood ... First, one lesson from a hundred years ago is that a breakthrough is not always foreseen ... The hadronization of quarks ... can best be clarified when quarks are studied within a collective state, i.e. in the nucleus... Concerning point 2 ... it is probably insufficient known that nuclear physics ... has provided illuminating insight into some of the most basic properties of matter. For one of its properties at least, the nucleus exhibits of a pure interaction. It is the weak interaction, as occurs in Fermi transition between two analogous 0+ states" [3]. This remark permits to distinguish in the nuclear spectra the 0^+ state. In the $^{10}{\rm B}$ it is a member of $\pi p_{3/2} \nu p_{3/2}$ multiplet and beside states $0^{+}-1^{+}-2^{+}-3^{+}$ the remaining 1_{1}^{+} state corresponds to the spin-flip effect of 1p nucleons. The corresponding distance $\varepsilon_o = E^*(0^+) - E^*(1_1^+)$ coincides within 10^{-4} with $2m_e$. Presented in Table 1 excitations in light nuclei and standard parameters ε_{2n2p} of the residual interaction of valence nucleons in this region [4] are rational to the ε_o . Relations in any mass/energy data with $2m_e$ and with nucleon and pion mass differences were named "tuning effect".

Table 1. Comparison of E^* and ΔE_B (keV) in near-magic nuclei with multiples of $\varepsilon_o=2m_e$

| ^{A}Z | ¹⁰ B | ¹⁰ B | ¹⁰ B | ¹² C | (T=2) | ¹⁶ O | ¹⁸ Ne | ¹⁸ Ne | ¹⁸ Ne | ¹⁸ Ne | ²⁰ Ne | ⁸ Be |
|--------------------|-----------------|-----------------|-----------------|-----------------|-------|-----------------|------------------|------------------|------------------|------------------|--------------------------------|-----------------|
| J^{π} | +0-+1 | 2- | 3- | 0+ | 0+ | 3- | 0+ | 0_{2}^{+} | 2+ | | $\frac{\varepsilon_{2n2p}}{4}$ | €2n2p |
| | 1021.8(2) | | | | | | | | | | 4076 | 7151 |
| $n(\varepsilon_o)$ | | 5 | 6 | 15/2 | 27 | 6 | 7/2 | 9/2 | 5 | 6 | 4 | 7 |
| | 1022.0 | 5110 | 6132 | 7665 | 27594 | 6132 | 3577 | 4599 | 5110 | 6132 | 4088 | |
| | 0.2(2) | 0.3 | 3 | 11 | 1(2) | 2 | 1(2) | 9(8) | 4(8) | 5 | -12 | -3 |

2 The role of cluster effects

Cluster effect in binding energies is one of the ways for a study of tuning effect. The stability of experimental differences of binding energies ΔE_B in nuclei with N \leq 82 is clearly seen as a sharp maximum in Figure 1 [4] at 46.0 MeV=45 ε_o . It corresponds to the grouping of ΔE_B in nuclei differing with ΔZ =2, ΔN =4 (⁶He cluster, Fig.2 left [5]).

In Tables 2 a long-range correlations in values ΔE_B with the parameter ε_o are seen from their proximity to the integer number of ε_o (small boxed values in the central part of Table 2). Theoretical values ΔE_B from all existing models do not show such effect (large differences at the bottom). Similar correlation was observed in the near-magic light nuclei during the study 4α and 2α clusters (two first columns of Table 3 and Fig 3 top).

| moble 2 | Comps | arison of | ΔE_B , k | eV in nu | clei diffe | fering by $2\Delta Z = \Delta N = 4$ with $45\varepsilon_o = 45990$ | <u>ke</u> V |
|--------------|--------|-----------|------------------|-------------------|-------------|---------------------------------------------------------------------|-------------|
| Nucl. | 133 Cs | /135Cs | 137Cs | ¹³⁵ La | 137 La | 139La 136Ce 138Ce 140Ce 139La | 14.34 |
| Nuci. | 78 | 80 | 82 | 78 | 80 | 82 78 80 82 82 | <u> </u> |
| | 45952 | 45946 | 45970 | 46018 | 45927 | 46024 46087 45997 45996 91975 | . |
| ΔE_B | -38 | -44 | -20 | 28 | -63 | [34] 97 [7] [6] [-5] | 1 3 |
| diff. | | 46353 | 46550 | 45933 | 46203 | 46673 46373 46573 47063 92816 | 5 |
| Theory | 46143 | | | | | 683 383 583 1073 836 | 13% |
| diff | 153 | 363 | 563 | -57 | 213 | 1000 300 300 1010 000 | <u> </u> |

| Table 3. | Compa | rison of | E* an | ΔE_{E} | in ke | V) of : | some ne | ar-magic nuc | lei with | $n \times \varepsilon_o$ |
|--------------------------|--------------|-----------------|------------------|-------------------|--------------|-------------------|-------------------|--------------------------------------------------------------------------------------------------------------------------------------------------------------------------------------------------------------------------------------------------------------------------------------------------------------------------------------------------------------------------------------------------------------------------------------------------------------------------------------------------------------------------------------------------------------------------------------------------------------------------------------------------------------------------------------------------------------------------------------------------------------------------------------------------------------------------------------------------------------------------------------------------------------------------------------------------------------------------------------------------------------------------------------------------------------------------------------------------------------------------------------------------------------------------------------------------------------------------------------------------------------------------------------------------------------------------------------------------------------------------------------------------------------------------------------------------------------------------------------------------------------------------------------------------------------------------------------------------------------------------------------------------------------------------------------------------------------------------------------------------------------------------------------------------------------------------------------------------------------------------------------------------------------------------------------------------------------------------------------------------------------------------------------------------------------------------------------------------------------------------------|--------------|--------------------------|
| ^A Z | 36 K | ³⁹ K | ³⁹ Ca | ¹¹⁹ Sb | 118Sn | ¹⁰¹ Sn | ¹⁰³ Sn | ¹¹⁶ Sn ¹¹⁸ Sn | 118Sn 11 | ¹⁷ Sn |
| N N | 17 | 20 | 19 | 69 | 68 | 51 | 53 | 66 68 | | 67 |
| $2J_o^{\pi}, J_o^{\pi}$ | ΔE_B | ΔE_B | ΔE_B | ΔE_B | ΔE_B | 7+ | 7+ | 0+ 0+ | | 1+ |
| $2J^{\pi},J^{\pi}$ | 4α | 4α | | S_p | S_{p2n} | 5+ | 5+ | 0+ 2+ | man the same | 5+ |
| $E^*, \Delta E_B$ | 147152 | 147160 | 13289 | 5109 | 25547 | 171.7 | 168.0 | and the second of the second o | 2057 | |
| $n(\varepsilon_o)$ | | | 13 | 5. | 25 | 1/6 | 1/6 | 2 2 | ~ ; | - |
| $n \times \varepsilon_o$ | 147168 | 147168 | 13286 | 5110 | 25550 | | 170 | 2044 2044 | | - 24 |
| diff. | 16(10) | -8(2) | 3(5) | -1 | -3(4) | 1 | -1 | 17 -1 | 13 | -2 |

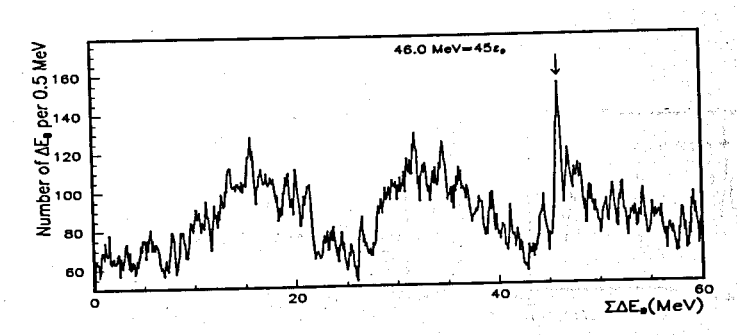
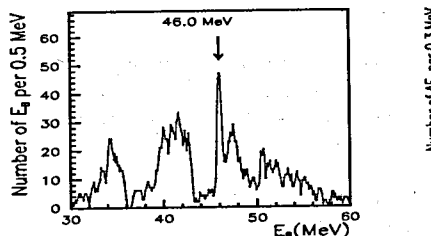


Fig.1. Distribution of differences of binding energies ΔE_B in nuclei with Z \leq 58; the maximum at $45\varepsilon_o$ =46.0 MeV corresponds to the grouping of ΔE_B in nuclei differing with ΔZ =2, ΔN =4.



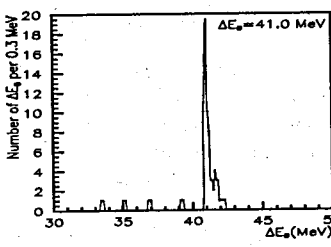


Fig. 2 ΔE_B -distributions connected with ⁶He-clusters in nuclei with N \leq 82 and Z=78,82 [5].

Stability of differences of E_B (values ΔE_B) in light nuclei differing with $\Delta Z = \Delta N = 2$ (accluster) was noticed by F.Everling. It results in maxima in ΔE_B -distributions at 73.6 MeV=9×8 ε_o and 147.3 MeV=18×8 ε_o in nuclei differing with 2 α - and 4 α -clusters ($\Delta Z = \delta N = 4$ and $\Delta Z = \Delta N = 8$, Fig.3 top). Simultaneously the grouping effect in values ΔE_B was found in all even-even nuclei at 409 MeV (close to $50 \times 8\varepsilon_o = 50\delta$, $\delta = 8\varepsilon_o$) and in all odd-odd nuclei at 3×147 MeV=441 MeV (close to $54 \times 8\varepsilon_o = 3 \times 18 = 54\delta$, Fig.2 bottom [5]). Parameter $\delta = 8\varepsilon_o = 16m_e$ is close to the doubled value of the pion β -decay energy ($2\delta m_\pi - 2m_e$) due to the proximity of the pion mass splitting δm_π to $9m_e = \Delta$ [6,7]. In Fig 4 other observed correlations in values E_B with parameters $\Delta = 9m_e$ and $\delta = 16m_e$ are presented [5].

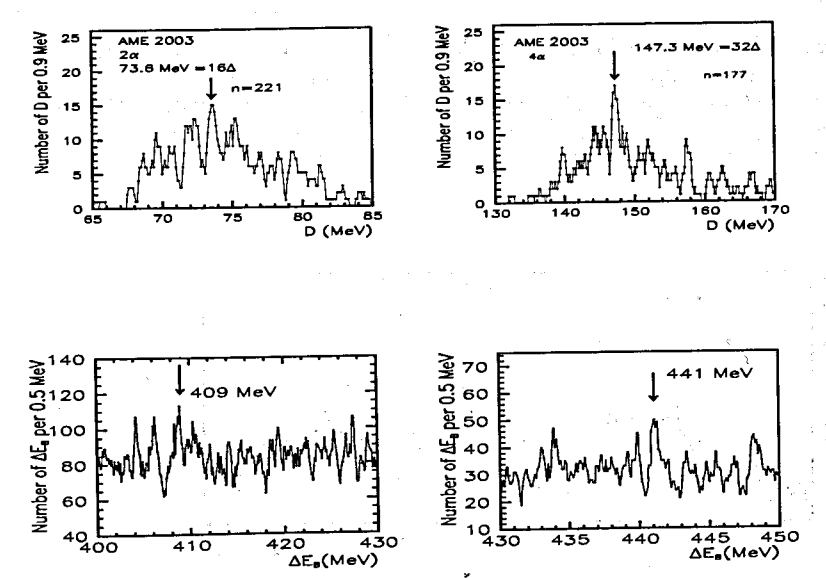


Fig. 3 ΔE_B -distribution of 2α - and 4α -clusters in light nuclei Z \leq 26 (top) [5]. ΔE_B -distribution in all even-even and all odd-odd nuclei separately (bottom).

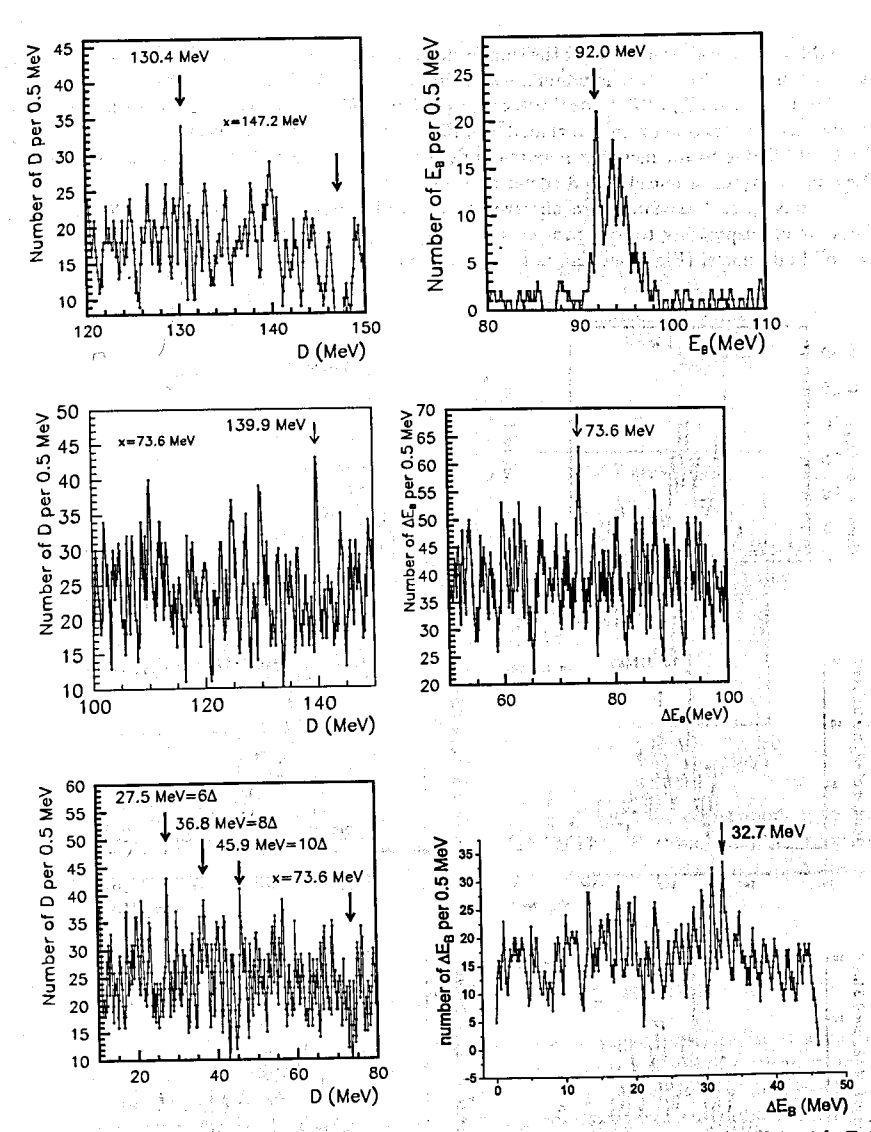


Fig. 4 Top left: Adjacent Interval Method (AIM) analysis of E_B for all nuclei with Z \leq 26 and x=147.2 MeV=18 δ =32 Δ =144 ε_o with the maximum at 130.4 MeV=16 δ . Top right: ΔE_B -distributions for $2\Delta Z = \Delta N$ =8, N even. Center left: AIM analysis of all nuclei with Z \leq 26 and x=73.6 MeV=8 δ , the maximum at 139.9 MeV=17 δ . Center right: AIM analysis of all nuclei Z \leq 26 and x=147.2 MeV=18 δ , the maximum at 73.6 MeV=8 δ . Bottom left: AIM analysis of all nuclei Z \leq 26 and x=73.6 MeV=8 δ =16 Δ . Bottom right: AIM analysis of odd-even nuclei and x=46.0 MeV=45 ε_o with maxima at 31.2 MeV and 32.7 MeV=32 ε_o (data AME2012).

AIM method was used to check the tuning effect in E_B of odd-even nuclei. Using x=46.0 MeV (the maximum in Fig.2) the maximum was found at ΔE_B^{AIM} =32.7 MeV=32 ε_o .

The interval ΔE_B =147.1 MeV=18×8 ε_o was found also in all heavy nuclei differing with Δ Z=8, Δ N=14 (two neutron less than 4⁶He, Fig.7 top). This effect preserves in new data from AME2012 [8]due to the fact that maxima in distributions are located at nearly the same energy ΔE_B for all types of nuclei (Fig.8 center and bottom).

Periods ε_o and $\Delta=9m_e$ were observed in ΔE_B -distributions in N-even and N-odd nuclei Z=50-82 corresponding to four proton separation energies (Fig.6 top) as well as in all N-even and odd-odd nuclei (Fig.6 bottom, data from MDF).

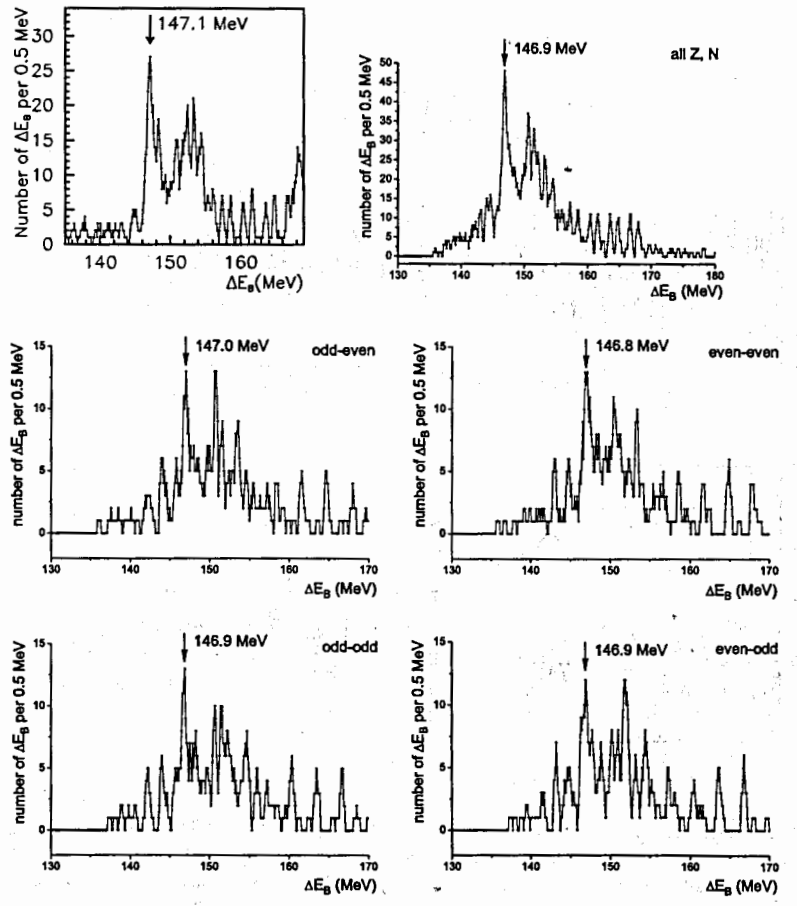


Fig. 5 Top: ΔE_B -distributions in all nuclei with $\Delta Z=8$, $\Delta N=14$ and N=82-126 with data from MDF (left) and from AME2012 [8] (right). Center and bottom: Parts of total ΔE_B -distribution for different types of heavy (N=82-126) nuclei: odd-even, even-even, odd-odd and even-odd nuclei separately (data from AME2012).

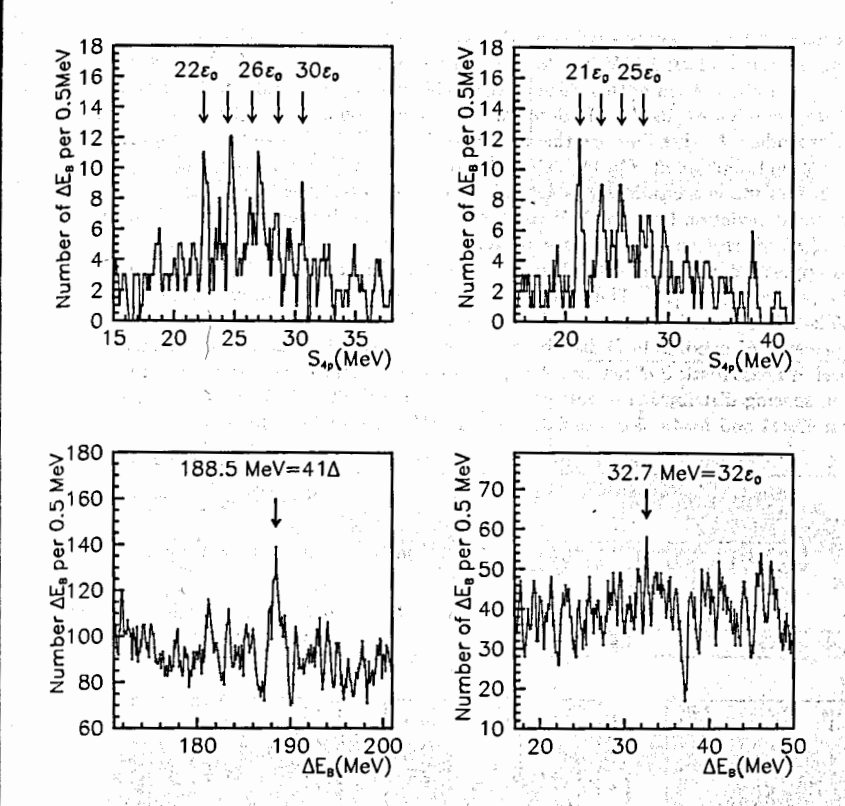


Fig. 6 Top: ΔE_B -distributions in N-even and N-odd nuclei Z=50-82 corresponding to four proton separation energies (period ϵ_o is marked, data from MDF). Bottom: ΔE_B -distributions in all N-even and all odd-odd nuclei, arrows mark integer numbers of periods ϵ_o and $\Delta = 9m_e$.

3 Confirmation of the Devons suggestion

At the 1961 Rutherford Conference Samuel Devons stated a suggestion [9]: "it is a natural temptation to make comparisons between the present stage in the study of nuclear structure with the exploration of atomic structure in Rutherford's time... the study of optical spectra, ... became a fruitful means of examining the refined details of atomic structure after Rutherford's direct approach led to the Bohr theory, and the subsequent development of quantum mechanics. ... there are still to be discovered subtle features of complex nuclei... which may even prove difficult to observe in direct study of the elementary particles themselves ... cases as the study of some elementary-particle ... can be facilitated by observation of phenomena involving complex nuclei, the fullest possible understanding of nuclear structure becomes a prerequisite".

The confirmation of Devons suggestion [10-11] is based on the fact that nucleon mass difference $m_n - m_p = \delta m_N = 1293.3$ keV is a well-known parameter of the nucleon structure. There is a systematical observation of this value as the stable nuclear excitation in Z,N-regions where pion-exchange dominates [10-15]). In data from 5-volumes compilation CRF [14] in three (out of five) independent E^* -distributions there are maxima at 1291-1294 keV ($\approx \delta m_N = 1293$ keV) and a sequence of maxima at $E^* = 161$ keV - 483 keV - 644 keV (Fig,7 bottom) [15].

This effect of stable excitations was noticed initially in Sb-isotopes as a linear trend in E^* for N=72-82 (small deviation from 161 keV×n in Table 4 center). It was explained [12] as a stable character of an interaction between $1g_{7/2}$ proton and pairs of $1h_{11/2}$ neutrons, namely, parallel spins and opposite direction of orbitals of interacting nucleons strongly enhance tensor forces due to the pion-exchange [14]. The observed slope 161 keV manifests itself also as a maximum at D=160 keV in D-distribution of neighbour isotopes 122,124 Sb (Fig. 7 top left).

The presence of maxima in D-distributions due to very stable and simple dynamics could be reflected in nonstatistical effects in spacing of higher excitations seen as neutron resonances. Maxima in spacing distribution of resonances in the same ¹²⁴Sb (Fig.8 top left) correspond to numbers $n=2\times17$ and $n=4\times13$ of the period $\delta''=11$ eV observed by K.Ideno [16].

| Table 4. | Cor | nparison | of <i>E</i> * | in Z | = 51 | nuclei | with n> | (161 | keV=1293 | keV/8). |
|--------------------------------|---------------------|---------------------|---------------------|-------------------|-------------------|-------------------|-------------------|-------------------|-------------------|-------------------|
| $^{A}\mathrm{Z}$ | $^{123}\mathrm{Sb}$ | $^{125}\mathrm{Sb}$ | $^{127}\mathrm{Sb}$ | ¹²⁹ Sb | ¹³¹ Sb | ¹³³ Sb | ¹²⁵ Sb | ¹¹⁹ Sb | ¹¹⁶ Sn | ¹¹⁶ Sn |
| (N-70)/2 | • 1 | 2 | 3 | 4 | 5 | 6 | _ | | | |
| E^* , keV | 160.3 | 332.1 | 491.2 | 645.2 | 798.4 | 962.0 | 644 | 644.0 | 1293.6 | 1292.0 |
| E^* - $\frac{\delta m_N}{8}$ | -1 | -9 | +7 | -1 | -10 | -7 | -2 | -2 | | -1 |
| $n\frac{\delta m_N}{8}$ | 161 | 323 | 484 | 646 | 808 | 969 | 646 | 646 | 1293 | 1293 |
| _E*,Fig.4 | 160 | | 483 | 644 | | | 644 | 644 | | 103/11 |

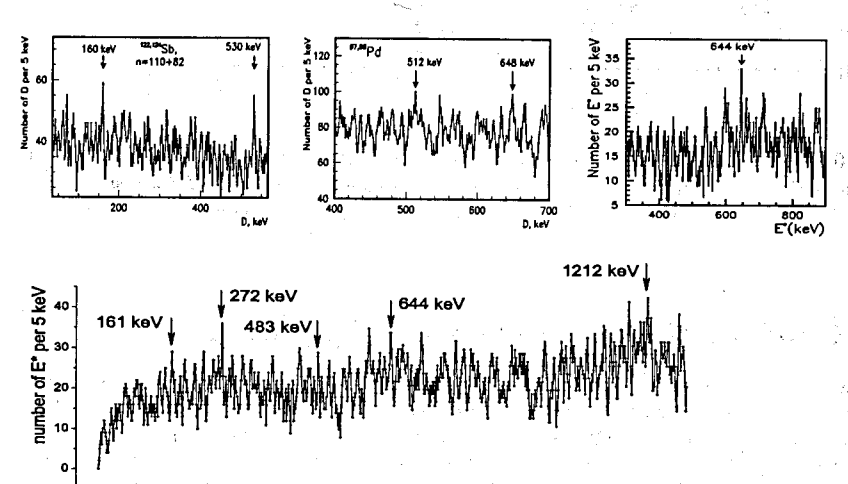


Fig. 7. Top left: Sum D-distribution in 122,124 Sb and the same in 97,98 Pd with maxima at 512 keV= $\varepsilon_o/2$ and 648- $\delta m_N/2$. Top fight: Sum E^* -distribution in Z-odd nuclei Z=47-57. Bottom: Sum E^* -distribution of all nuclei with Z=48-60 (ΔE =5 keV) [14,15], Table 4 bottom line.

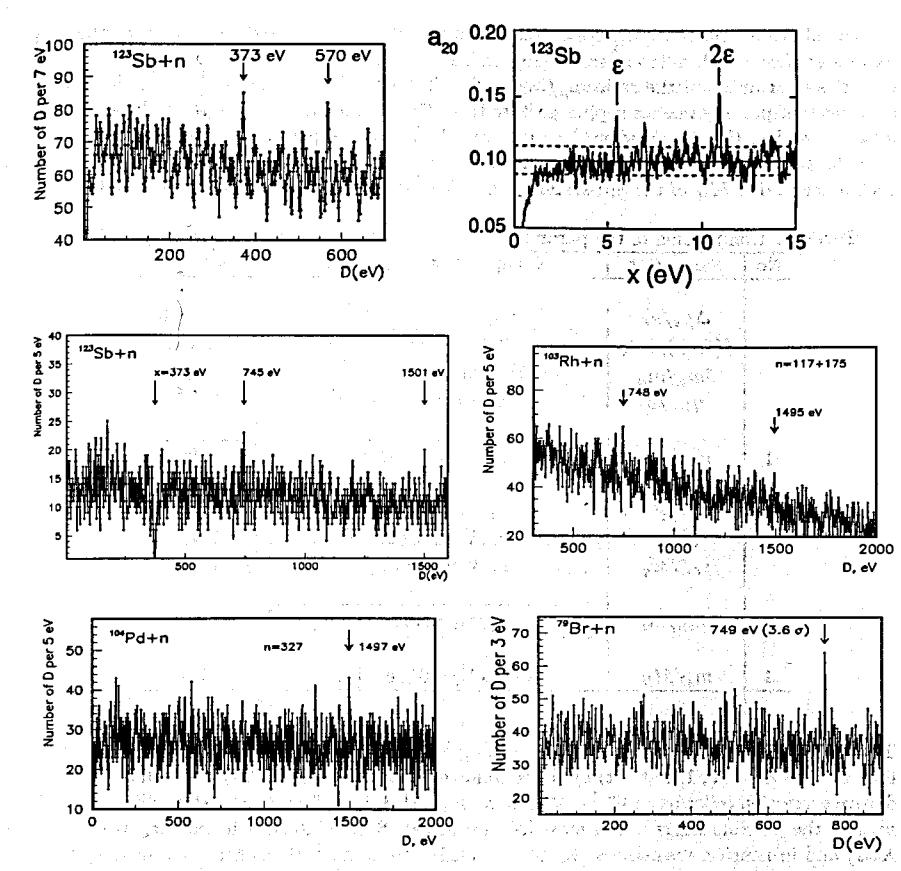


Fig. 8. Top left: Spacing distribution in neutron resonances of ¹²³Sb. Top right: Performed by K.Ideno [16] search for a periodicity in ¹²³Sb resonances: the period $2\varepsilon=11$ eV corresponds to $8\times\varepsilon''=11$ eV introduced in [7].) Center: Spacing distribution of resonances in ¹²³Sb adjacent to x=D=373 eV, the ratio 1:2:4. Bottom: D-distributions in resonances of ¹⁰³Rh, ¹⁰⁴Pd, ⁷⁹Br.

Intervals 373–745–1501 eV (ratio 1:2:4) in ¹²⁴Sb were found by the Adjacent Interval Method [17] (they are forming triplets, Fig.8 center). Such small stable intervals D=750-1500 eV were found also in D-distributions of neutron resonances in ¹⁰⁴Rh, ¹⁰⁵Pd, ⁸⁰Br etc. (Fig.8 bottom). In data for low-lying levels of ^{97,98}Pd observed stable interval D=648=4×161 keV (Fig.4 top center) and D=1293 keV= δm_N [18] correspond to the equidistant excitations in ⁹⁷Pd (N=51) [14].

We come to conclusion that stable character of a part of nucleon interaction which resulted in observed common nonstatistical effects in different nuclei (at low energies and at high excitations as well) could be considered by taking into account the fact that the mass of the charged pion is a natural parameter in pion-exchange processes. The ratios between common intervals $161 \text{ keV} = \delta m_N/8$ and $m_{\pi^{\pm}} = 140 \text{ MeV}$ (1.15·10⁻⁵) and the ratio between D=1500 eV (in resonances) and δm_N are close to the well-known QED radiative correction $\alpha/2\pi = 1.159 \cdot 10^{-5}$.

The above mentioned radiative correction of the type $g/2\pi$ is used frequently for the comparison of effects with different scales [19]. In Table 5 some of such examples are given starting with the coincidence of the ratio m_{μ}/M_Z with $\alpha/2\pi$ used in construction of Table 6 to represent together particle masses (upper part of Table 6), parameters of NRCQM model and stable intervals in E_B , the discussed nuclear intervals of fine and superfine structures and the ratio m_s/M_H between the mass of the current strange quark m_s =147-150 MeV in NRCQM and the preliminary value M_H of the SM-scalar from ATLAS-experiment [20] (bottom line of Table 5)

Table 5. Comparison of the parameter $\alpha/2\pi$ with ratios between mass/energy values.

| No | Parameter | Components of the ratio | Value ×10 ⁵ |
|----|------------------------------|---------------------------------------------------------------|------------------------|
| | | | 1 |
| | $\Delta\mu_e/\mu_e$ | $=\alpha/2\pi$ -0,328 α^2/π^2 | 115.965 |
| | $\delta(\delta m_\pi)/9m_e$ | $[\Delta - 4593,66(48) \text{keV}]/(9m_e = \Delta)$ | 116(10) |
| | $\delta m_\mu/m_\mu$ | $[(23x9m_e-m_{\mu}]/m_{\mu}$ [7] | 112.1 |
| | $\eta_{+-}/2$ | $2.285(19) \times 10^{-3}/2$ [21] | 114(1) |
| 1 | m_{μ}/M_Z | $m_{\mu}/M_Z = 91161(31) \text{ MeV}$ | 115,90(4) |
| 2 | arepsilon''/arepsilon' | 1,35(2) eV/1,16(1) keV [7] | 116(3) |
| | $\varepsilon'/\varepsilon_o$ | $1,16(1) \text{keV}/\varepsilon_o = 1022 \text{ keV}$ [7] | 114(1) |
| | $\epsilon_o/2M_q$ | $\varepsilon_o/3(m_{\Delta}$ - $m_N)$ [7] | 116.02 |
| 3 | $\delta m_n/m_\pi$ | $n = (n \times m_e - m_n)/m_\pi = 161,7(2) \text{ keV}/m_\pi$ | 115.86 |
| 4 | m_s/M_H | 147 keV/126 GeV [20] | 117 |

Table 6. Presentation of parameters of tuning effects in particle masses and nuclear data (in lines marked X=-1, 0, 1, 2 at left) by the common expression $n \cdot 16 m_e (\alpha/2\pi)^X$ M with the QED radiative correction $\alpha/2\pi$ ($\alpha=137^{-1}$). Values m_{π} - m_{e} , $m_{e}/3$, the neutron mass shift $N\delta-m_{n}-m_{e}$ m_s and the possible Higgs boson mass [20] are boxed. Stable intervals in excitations (E*, D_{ij} , X=1) and in neutron resonances (X=2) are considered as indirect confirmation of relations in particle masses (X=-1). The value $\Delta^{\circ} \approx 4$ GeV close to m_b was observed at TEVATRON [23].

| _ X | M | n = 1 | n = 13 | n = 16 | n = 17 | n = 18 | |
|-----|-----|---------------------------------|--------------------|--------------------------|-----------------------------------------------------|------------------------------|-------|
| -1 | 3/2 | 2 | | m _t =171.2 | 1 , | | -150 |
| GeV | 1 | $2\Delta^{\circ}\text{-}2M_{q}$ | $M_{Z} = 91.2$ | $M_{\rm H}{=}115~[22]$ | | $M_{\rm H} = 126$ [20] | |
| . 0 | 1 | _ | $m_\mu=105.7$ | (i) ** . | m_{π} - m_{e} | $m_s = 147 - 150$ | |
| MeV | 1 | 2Δ - $arepsilon_0$ | $106 = \Delta E_B$ | $130 = \Delta E_B$ | $140 = \Delta E_{B}$ | $147.2 = \Delta E_B$ | 77 |
| | 1 | | | | 11. 11. 11. 11. | m_{Δ} - $m_{n}/2=147$ | |
| | 3 | | | $M^{"}_{q} = m_{\rho}/2$ | NRCQM | $M_q = 441 = \Delta E_B$ | 35 |
| 1 | 1. | - | | | $N\delta$ -m _n -m _e =161.6(1) | $170 = m_e/3$ | |
| keV | 1 | 9.5 | 123 | 152 | 161 (¹⁸ F, Sb) | 512 (Co, Pd) | 184 |
| | 4 | | 492 | | 648 (^{97,98} Pd) | 682(Co) | |
| | 8 | | 984 | 1212 | 1293 (Pd), ΣE^* | 1360 (Te) | |
| 2 | 1 | 11 | 143 | 176 | 187, 749 (⁷⁹ Br) | D in neutron | 100 |
| eV | 4 | 44 | 570 (Sb) | | 1500 (Sb,Pd,Rh) | resonances | 175.5 |

Estimation of nucleon structure parameters

In Fig 9 the position of the nucleon mass (N, 940 MeV) among other masses is shown. The nucleon mass in nuclear medium is about 8 MeV below it on line between ω and Ω .

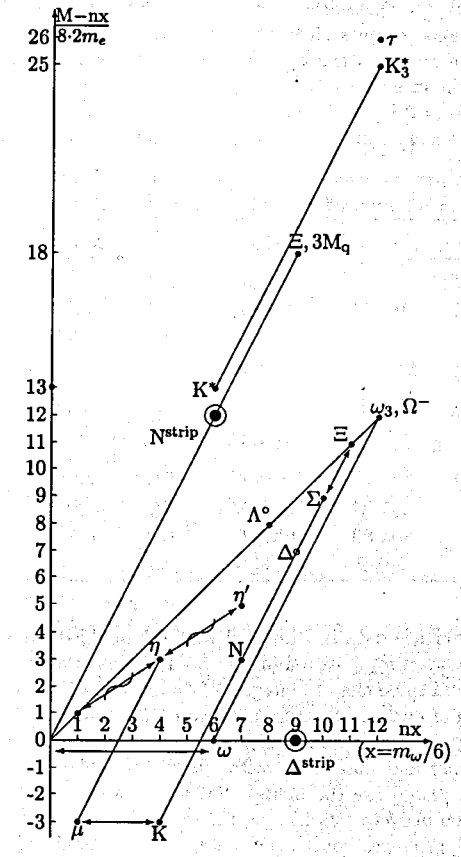


Fig.9. Position of different mass intervals and τ -lepton mass in two-dimensional presentation with the horizontal axis in units $16 \cdot 16m_e$ close to $m_{\omega}/6$. The values $M_i \cdot k \times (16 \cdot 16m_e = \delta)$ are displayed along the vertical axis in $16m_e$ units. τ -lepton is somewhat above the integer number of $M_g = m_{\Xi^-}/3$ (its mass is twice the mass of K*-meson). Two lines with different slopes correspond to the pion mass (140 MeV= $m_{\omega}/6+\delta$) and to the stable intervals $m_{\eta'}-m_{\eta}=m_{\eta'}-m_{\pi}^{\pm}$ (n=50 in units $\delta=16m_e$, crossed arrows). Δ^{strip} and $N^{strip}=880$ MeV are considered in [5]. The proximity of nucleon Δ -excitation $m_{\omega}/6+2\delta=2\times147$ MeV to stable interval between masses of the decuplet baryons (value $m_s=147-150$ MeV) gives the long line from kaon to Ξ . The lines corresponding to 2^+ excitation of both vector mesons $(J^{\pi}=1^--J^{\pi}=3^-)$, from K^* to K_3^* and from ω to ω_3) are parallel with the Sternheimer's interval M_q close to ΔM_{Δ} (these intervals are between η -meson - muon, kaon - nucleon, nucleon - Σ -hyperon).

Additional support for the Devons suggestion was found in the extension of the above discussed long-range correlations in nuclear data with the parameter ε_o , Table 1 for E^* , Tables 2,3 for ΔE_B). Boxed in Tables 5-7 are important relations between the accurately measured masses of the neutron and the electron (from m_p/m_e r ratio and nucleon mass difference). The shift of the neutron mass relative to the integer number of $\delta=16m_e$ (115 $\delta-m_e$) is determined with the accuracy of 0.1 keV and within such uncertainty it accounts $161.6=(1/8)\delta m_N$. The ratio 8-1.0003(2) exists between δm_N and the shift. Such shift was found also in nuclear data.

The confirmation of the value $M_{\rm H}=126$ GeV permits a consideration of additional relations with parameters $m_s=\Delta M_\Delta=\Delta E_B=147$ MeV. Part of them is shown in Fig.9 (and Table 1 in [5]). Possible shift in masses of neutral octet baryons Σ° and Ξ° (Table 7 boxed) zre considered.

Table 7. Comparison of particle masses with periods $3m_e$ and $16m_e$ = δ =8176.0 MeV (N periods), neutron Δ° -excitation is compared with $2\Delta E_B$; asterisk marks values considered elsewhere.

| Particle | m _i , MeV | $m_i/3m_e$ | N∙16m _e | N | $N-16m_e$ | Comments |
|------------------|----------------------|------------|--------------------|-----|------------|----------------------------|
| μ | 105.658367(4) | 68.92* | 106.2878 | 13 | -0.6294 | -0.511-0.118 |
| π^o | 134.9766(6) | 88.05* | 138.9917 | 17 | -4.0174 | - 1 |
| π^{\pm} | 139.5702(4) | 91.04* | | 17 | +0.57624 | +0.511+0.065 |
| p | 938.2720(1) | 612.05* | 940.2380(-1) | 115 | -1.96660 | $-m_e$ - $(9/8)\delta m_N$ |
| \mathbf{n} | 939.5654(1) | 612.89* | ξ. | 115 | -0.6726(1) | $-m_e$ - $(1/8)\delta m_N$ |
| Σ° | 1192.64(2) | 777.98 | 1193.693 | 146 | -1.05(2) | -0.51·2=-1.02 |
| Ξ° | 1314.86(20) | 857.71 | 1316.333 | 161 | -1.47(20) | -0.51·3=-1.53 |
| p , | 775.49(34) | 505.87 | 784.8943 | 96 | -9.40(34) | $-9.20 = -2\Delta$ |
| $\dot{\Delta}^o$ | 1233.8(2) | 804.83 | 1234.57 | 151 | -0.8(2) | |
| Δ°-n | 294.2(2) | 191.9 | 294.3 | 36 | | $2\Delta E_B=294.4$ |

The tuning effect in particle data is connected with the doubled value of the pion β -decay energy $\delta=16m_e$. The pion mass $m_{\pi^{\pm}}$, its parameter $f_{\pi}=131$ MeV, the muon mass and the value $\Delta M_{\Delta}=147$ MeV were found to be close to integers of $\delta=16m_e$ (n=17,16,13,18, Table 7 [10,11]).

Recent understanding of nucleon structure is based on the Standard Model (SM) where the scalar field (Higgs boson with estimated mass M_H) is responsible for fundamental fermion masses (families of quarks/leptons) and masses of vector fields (M_Z, M_W) . Light quarks (together with the electron and neutrino) are the lightest SM-family and the QCD (as a part of SM) describes strong interaction between quarks (and the resulted nucleon interactions). The gluon-quark-dressing effect [24] produces constituent masses out of small initial quark masses (of several MeV). Three constituent masses (M_q) are forming baryon mass and two constituent quark masses (M_q'') are forming masses of vector mesons (m_ω, m_ρ) . The pion and ρ -meson are important for understanding of nucleon structure and their interaction. The pion is a QCD's Goldstone mode [25] and the pion exchange between constituent quarks [26] gives the nucleon Δ -excitation $(m_\rho^0 - m_n = 294 \text{ MeV} = 2\Delta M_\Delta)$ corresponding to the spin-flip of baryon quarks.

The inclusion of the electron mass into comparison with the other energy/mass intervals is based mainly on results obtained with nuclear data. V.Belokurov and D.Shirkov [28] suggested that QED radiative correction $(\alpha/2\pi)$ similar to that in the magnetic moment of the electron μ_e could be assigned to m_e . It should be noticed that there exists the results of the analysis of particle masses performed by R.Frosch who found a period of $3m_e$ [27] in a search for the periodicity in masses. In Table 7 relations between $\delta=16m_e$, $3m_e$ and some particle masses are shown.

There exists the coincidence of the lepton ratio $L=m_{\mu}/m_{e}=206.77$ with the integer L=207=13-16-1 after a small QED correction, namely $m_{\mu}/m_{e}(1-\alpha/2\pi)=207.01$. The same ratio exists between masses of vector bosons $M_{Z}=91.188(2)$ GeV and $M_{W}=80.40(3)$ GeV and two estimates of baryon and meson constituent quark masses $M_{q}=441$ MeV= $(3/2)(m_{\Delta}-m_{N})\approx m_{\Xi}/3=3m_{s}$ and $M_{W}''=m_{\rho}/2=775.5(4)$ MeV/2=387.8(2) MeV. These ratios are $M_{Z}/441$ MeV=206.8 and $M_{W}/(m_{\rho}/2)=207.3$ [10,11]. These empirical relations are in accordance with Y.Nambu suggestion [29] that mass relation can be useful for further development of the Standard Model.

5 Conclusions

Described here study of nonstatistical effects in complex spectra of many nuclei permits the confirmation of the Samuel Devons suggestion about the fundamental aspect in the analysis of accurately measured nuclear data. Recent understanding of strong interaction as a part of the Standard Model and the role of pion-exchange dynamics permitted to distinguish regions of the nuclear chart where observed tuning effect could be explained. Combined analysis of data from three compilations of nuclear data (MDF, CRF, NRF) can provide the material for the development of the fundamental physics.

a leis en es daba baces escentices de Ci

1.5 - Box of www.houhresceninistres.15

6 References

- 1. H.Schopper (Ed.), Landoldt-Boernstein New Series 2009 vol. I/22A. Springer.
- 2. H.Schopper (Ed.), Landoldt-Boernstein New Series 2009 vol. I/24. Springer.
- 3. C.Detraz, Nucl. Phys. A 583 (1995) 3.
- 4. S.I.Sukhoruchkin, D.S.Sukhoruchkin, J. Int. Mod. Phys. E 20 906, 2011.
- 5. S.I.Sukhoruchkin, Int. Rev. Phys. (IREPHY) 2 239, 2008.
- 6. S.I.Sukhoruchkin, Proc. 2nd Conf. Neutr. Cross Section, Washington DC Vol.2 923, 1968.
- 7. S.I.Sukhoruchkin, Stat. Properties of Nuclei ed. Garg G (Plenum Press) 215, 1972.
- 8. J.Audi et al., AME 2012 (to be publ.).
- 9. S.Devons, Proc. Int. Rutherford Jubilee Conf., Manchester (Heywood) 611, 1961.
- 10. S.I.Sukhoruchkin, Proc. Rutherford Centennial Conf., Manchester, 2011. JPCS, IOP, 2012.
- 11. S.I.Sukhoruchkin, http://cgc.physics.miami.edu/Miami2011/Sukhoruchkin.ppt.
- 12. T.Otsuka, T.Suzuku, Y.Utsino, Nucl. Phys. A 805 127c, 2008.
- 13. J.Schiffer, Proc. Rutherford Centennial Conf., Manchester, 2011. JPCS, IOP, 2012.
- 14. H.Schopper (Ed.), Landoldt-Boernstein New Series 2012 vol. I/25A. Springer.
- 15. S.I.Sukhoruchkin, Z.N.Soroko, D.S.Sukhoruchkin, these Proc.
- 16. K.Ideno, Proc. Int. Conf. Neutr. Research, Crete, 1997. SPIE Vol. 2867, p.398.
- 17. S.I.Sukhoruchkin, Proc. ISINN-13, p. 83, 2005. JINR E3-2006-7.
- 18. S.I.Sukhoruchkin, Z.N.Soroko, D.S.Sukhoruchkin, Proc. ISINN-17, p. 209, 2009.
- 19. I.T.Dyatlov, Yad. Phys. 52 152, 1990.
- 20. M.Wielers, http://cgc.physics.miami.edu/Miami2011/Wielers.ppt.
- 21. J.Bernstein, Elem. Particles, Currents. Freeman, 1968.
- 22. P.Igo-Kemenes, J. Phys. G 33 388, 2006.
- 23. V.M.Abazov et al, arXiv: 0905.3381v2[hep-ex] 20 May 2009.
- 24. H.L.L.Roberts et al, Phys. Rev. C 83 065206, 2011.
- 25. L.Glozman, Nucl. Phys. A 629 121c, 1998.
- 26. C.Itoh et al, Phys. Rev. D 40 3660, 1989.
- 27. R.Frosch, Nuovo Cim. 104 913, 1991.
- 28. V.V.Belokurov, D.V.Shirkov, The theory of Particle Interactions. AIP, 1991.
- 29. Y.Nambu, Nucl. Phys. A 629 3c, 1998.

Study of nonstatistical effects due to tensor forces

S.I. Sukhoruchkin, M.S. Sukhoruchkina

Petersburg Nuclear Physics Institute, 188300 Gatchina

Abstract

The effect of the linear trend in excitations E^* of near-magic Sb-isotopes found by J.Schiffer and T.Otsuka was checked with the data for other selected nuclei.

14

1 Introduction

There exists a new outlook on the role of pion-exchange dynamics in nuclear spectroscopy based on the observation by J.Schiffer [1] and T.Otsuka [2] on the interaction of nucleons moving with opposite direction of orbitals ($\nu 1h_{11/2} - \pi 1g_{7/2}$ in case of Sb isotopes). Observed linear trend with the slope 161 keV= $\delta m_N/8$ is shown in Table 1 (boxed values at top are compared with the period $\delta m_N/8$, where $\delta m_N=1293$ keV is nucleon mass splitting). Excitations in N-even Sb isotopes (N=72-82) reflect the stable character of the interaction of the $1g_{7/2}$ proton with numbers (N-70)/2 of neutron pairs in $1h_{11/2}$ subshell. The parameter 161 keV corresponding to such stable interaction manifests itself also as a maximum at 160 keV in D-distribution in neighbour isotopes 122,124 Sb and as a series of maxima at 161 keV, 483 keV and 644 keV in E^* -distribution of all nuclei with Z=48-60 (Fig.5 in [3], Table 1). The similar effect was observed in Pd isotopes (Table 1).

Table 1. Comparison of E^* (in keV) of Z = 50,51 nuclei with $n \times 1293$ keV/8 and $\varepsilon_o = 1022$ keV.

| | | | | | | | | 1 | | taring of i |
|-------------------------|-------------------|-------------------|-------------------|-------------------|-------------------|-------------------|-------|-------------------|-------------------|-----------------------|
| $^{A}\mathrm{Z}$ | ¹³³ Sb | ¹³¹ Sb | ¹²⁹ Sb | ¹²⁷ Sb | ¹²⁵ Sb | ¹²³ Sb | 116Sn | ¹⁰¹ Sn | ¹⁰³ Sn | 117Sn |
| N | 82 | 80 | 78 | 76 | 74 | 72 | 66 | 51 | 53 | 67 |
| (N-70)/2 | 6 | 5 | 4 | 3 | 2 | 1, | | | - | |
| $2J^{\pi},J^{\pi}$ | 5+ | 5+ | 5+ | 5+ | 5+ | 5+ | 2+ | | | 1+,5+ |
| E^* , keV | 962 | 798 | 645 | 491 | 332 | 160.3 | 1293 | 171 | 170 | D=1020 |
| $n\frac{\delta m_N}{8}$ | 969 | 808 | 646 | 484 | 323 | 161 | 1293 | $\varepsilon_o/6$ | $\varepsilon_o/6$ | $arepsilon_o$ |
| E^{\bullet} ,D(Sb,Pd) | | | 644-648 | 483 | | 160-161 | 1293 | | 4 . | $512=\varepsilon_o/2$ |
| D(Sb,Pd) eV | | | 749 | 572 | 375 | | | w | <u> 1900</u> | |

A stable character of excitations in nuclei 101,103 Sn situated over the 100 Sn-core manifests itself in a proximity of E^* =170 keV and E^* =168 keV close to $\varepsilon_o/6$ 101,103 Sn. The parameter ε_o =2 m_e =1022 keV corresponds to the stable phonon in nuclei 116,117,118 Sn (see Table 3 in [4]). Both parameters D=161 keV= δm_N , D=170 keV= $\varepsilon_o/6$ and combined interval 2×161 keV+170 keV=492 keV were used as repères during the analysis of spacing and excitations in all nuclei collected in the recent compilation CRF [5]. Appearance of stable energy intervals related to nucleon mass difference δm_N or m_e was named "tuning effect". The similar effect in particles masses was considered in [6]).

2 Two additional methods of data analysis

Intervals n×161 keV and m×170 keV are seen frequently together (as in Z=50,51 nuclei, Table 1). For example, intervals D=512-682-keV (n=3-4, the period $\varepsilon_o/6$) in the spectrum of 55 Co (Fig.2 left) were studied with a special Adjacent Interval Method (AIM). It consists in the fixation in the spectrum of all pairs of levels (E_i^*, E_j^*) forming a maximum in usual spacing distribution $(D_{ij}=x)$ and plotting D-distributions from the fixed levels to all other levels (E_k^*) in the spectrum $(D_{\uparrow}^{AIM}, D_{\downarrow}^{AIM}$ or $D_{\uparrow\downarrow}^{AIM})$. Arrows indicate the direction (along E^* axis) from the fixed energies. For example, the interval D=1022 keV= ε_o in 55 Co is the distance between the low-lying T=3/2 states. By fixating all intervals $x=\varepsilon_o$, one obtains a distribution with maxima $D_{\uparrow}^{AIM}=511$ keV= $\varepsilon_o/2$ and 324 keV≈ 2 × 161 keV (seen at left in Fig.2, right). These intervals are forming triplets.

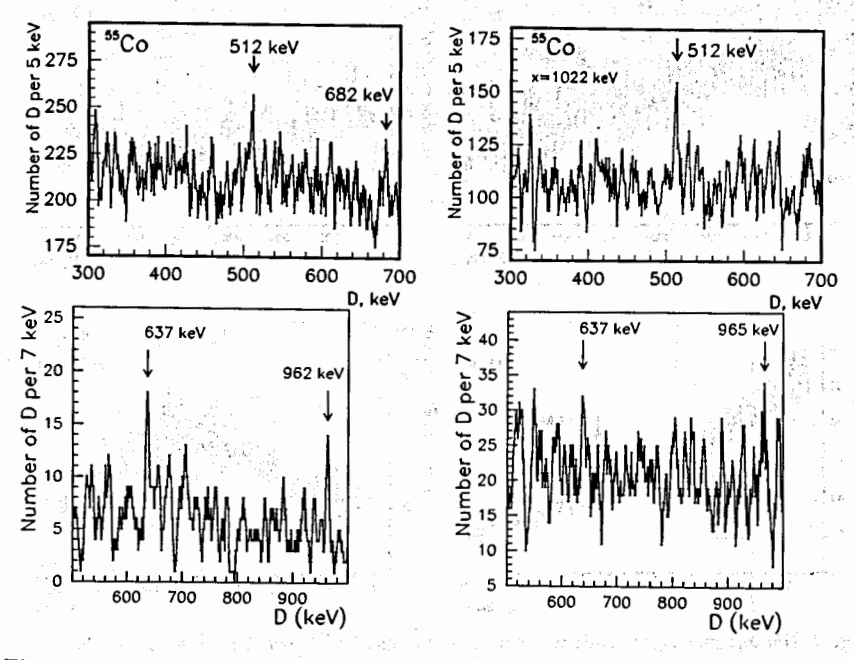


Fig. 1 Top left: D-distribution in ⁵⁵Co. Top right: D_{\uparrow}^{AIM} -distribution for x=1022 keV, ⁵⁵Co. Bottom: D-distributions in ¹⁸F and ²²Na, proximity of D=637 keV and D=962-865 keV.

Stable intervals seen as maxima in D-distributions have frequently proximate values in different neighbour nuclei. Such effect exists in the low-lying levels of $^{18}\mathrm{F}$ ($E^{\star} \leq \! 10$ MeV, number of levels n=80) and in levels of $^{22}\mathrm{Na}$ (Fig.1, bottom). To check this result for $^{18}\mathrm{F}$ the AIM-analysis with x=962 keV was performed. The distribution D_{11}^{AIM} with maxima at 324 keV and 636 keV (1:2:3) corresponds to the period 2×161 keV.

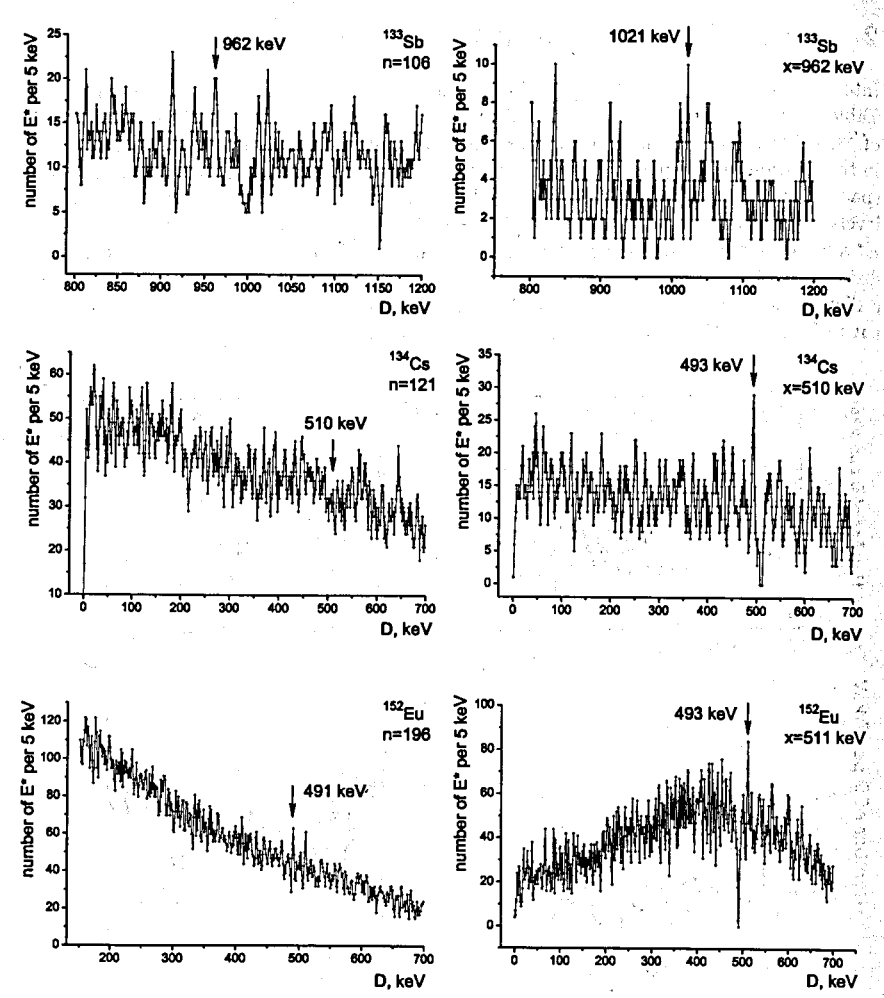


Fig. 2 Top left and right: D-distribution in 133 Sb and D_{\uparrow}^{AIM} -distribution for x=962 keV. Center left and right: D-distribution in 134 Cs and D_{\downarrow}^{AIM} -distribution for x=510 keV. Bottom left and right: D-distribution in 152 Eu and D_{\downarrow}^{AIM} -distribution for x=491 keV.

The second way to check a general character of the pion-exchange dynamics is based on the fact that in highly excited states of the same or neighbour isotopes several close to each other small splitting were observed. For example, intervals D=375-750-1500 eV in $^{124}{\rm Sb}$ and D=750-1500 eV in isotopes of Pd and Rh (Fig.8 in [4]) were considered in [6]. Periodicity in positions of neutron resonances in $^{124}{\rm Sb}$ found by M.Ohkubo [7] is presented in Fig 3. Resonance positions given at the bottom of Fig 3 are expressed as 312 eV+n×88 eV, or as the period 44 eV due to the ratio $131{\rm eV}/(88{\rm eV}/2=44{\rm eV})=2.98$. The ratio 9:13:17 (in units 44 eV) for position/spacing in resonances concerns strong resonances at 572 eV and 750 eV coinciding with D=572 eV and 373 eV-750 eV observed as maxima in the independent spacing distribution in $^{124}{\rm Sb}$ (shown in Fig 8 in [4]).

Two maxima at 44 eV and 572 eV were found independently earlier in sum distribution of resonance positions in all nuclei with 33–56 (Fig.4 top left). A systematic character of intervals of superfine structure (periods 44 eV) corresponds to the discussed structure of the values (including 492 keV and 644 keV=4×161 keV) if one notices that a ratio between such small intervals and intervals in low-lying levels of the same nuclei are close to QED radiative correction ($\alpha/2\pi=1.159\cdot10^{-3}$). Simultaneously a stable interval/period 161 keV is in the same ratio with the mass of charged pion (161.7 keV/(m_{π} =138.6 MeV)=1.167·10⁻³ [6]. This SFERC method (Scaling Factor Equal to Radiative Correction) permits to use the observed nonstatistical effects in neutron resonances as an indirect confirmation of the common and universal nuclear dynamics:

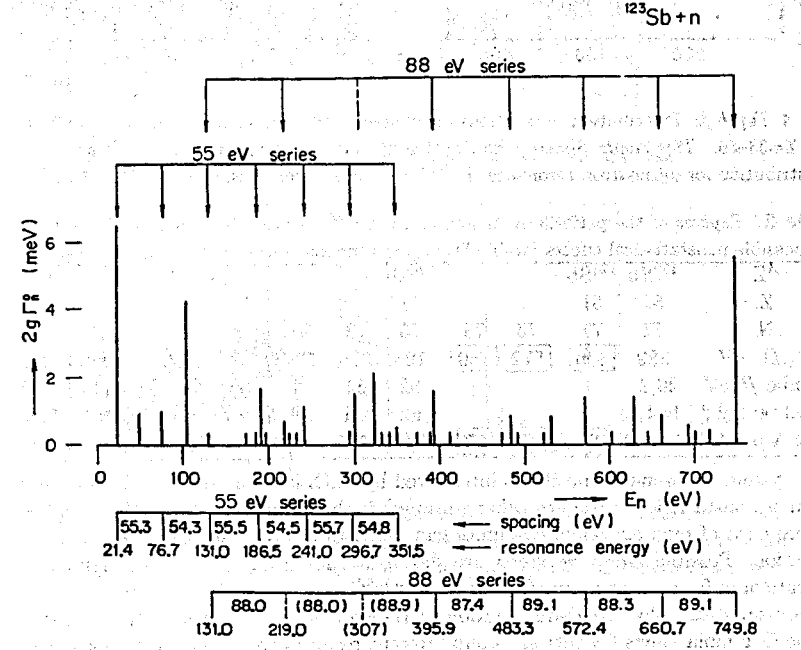


Fig. 3 Positions and neutron widths of resonances in target nucleus ¹²³Sb (by M.Ohkubo [7])

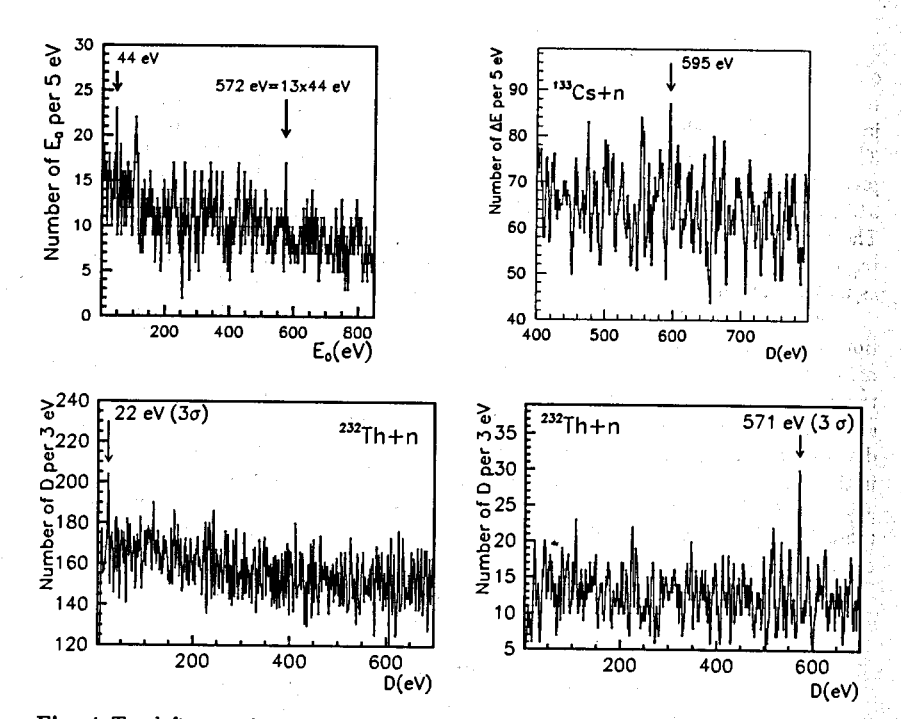


Fig. 4 Top left: Distribution of positions of relatively strong neutron resonances in all nuclei with Z=33-56. Top right: Spacing distribution of all neutron resonances in 134 Cs. Bottom: D-distribution for all neutron resonances in 233 Th and for strong resonances ($g\Gamma_n^o \ge 1 \text{ meV}$).

Table 2. Repères of the periodicity in resonances of ¹²⁴Sb introduced by M.Ohkubo (boxed) and possible nonstatistical effects (stable D) in neutron resonances of the neighbour isotopes.

| | 188 | - O2100 | ob (blac | 10 10) | | CIOII I | SULIAL | ces or | me neigt | ibour isc | nopes. |
|----------------------------|---------------------|-------------------|----------|--------|------------|---------|--------|--------|------------------|-----------|-------------------|
| $^{A}\mathrm{Z}$ | $^{122}\mathrm{Sb}$ | ¹²⁴ Sb | | | ^{124}Sb | | | 128I | 130 _I | | ¹³⁴ Cs |
| ${f z}$ | 51 | 51 | | | 51 | | | 53 | 53 | | 55 |
| N | 71 | _73_ | _73_ | 73 | 73 | 73 | 73 | 75 | 77 | 77 | 79 |
| E_n, D_{ij}, eV | 389 | 396 | 572 | 750 | 198 | 375 | 574 | 88 | 200 | 985 | 396 |
| number/5 eV | 20,25 | | | | 62 | 64 | 61 | 66 | 141,57 | 119 | 24 |
| selection $2g\Gamma_n^o$ | l=1,0 | | | | all | all | all | l=1 | all, l=0 | all | 2meV |
| $n(44eV)=n4\delta''$ | 1meV | 9 | 13 | 17 | 9/2 | 17/2 | 13 | 2 | 9/2 | 5(9/2) | 9 |

A system in resonance positions introduced by M.Ohkubo as repères (fixed intervals) to study nonstatistical effects in other isotopes) is shown in Table 2. In this Z,N region the presence of pion-exchange dynamics can be more clearly manifested even at higher excitation. Possible grouping effects are shown in Table 2 and Fig.4 (top right). More accurate data for resonances in ^{122,124}Sb and ^{133,135}Cs are needed for a definite conclusion.

Nonstatistical effect in D-distribution of resonances in ²³²Th was marked in 60-ties by the Columbia Nevis Cyclotron Group. Recent result is shown in Fig.4 (bottom left). Selection of strong resonances results in a grouping effect at a repère n=13 for 571 eV.

3 Spacing distributions in nuclei with Z=5-29

The first step in the analysis of stable nuclear excitations was obtaining a sum E^* -distribution for all nuclei in the first volume of compilation 1/25A (Z=1-29). The maximum at 1291 keV (Fig.3 top) is due to a grouping of E^* in odd-Z nuclei Z=19-29 (Fig.3 bottom). The maximum at 3936 keV=8×492 keV (Fig.5 center) is discussed later.

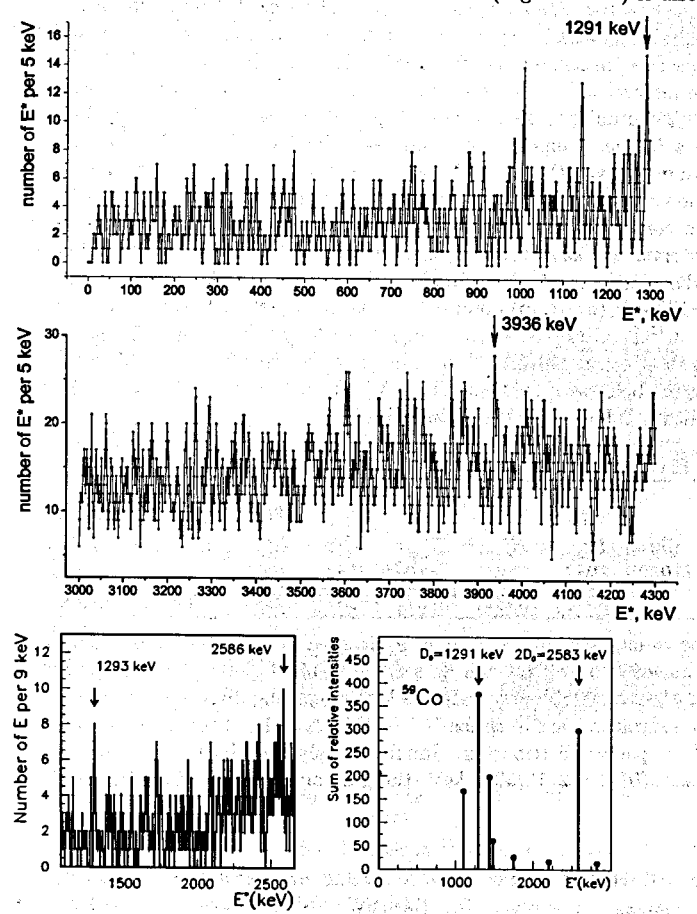


Fig. 5 Top and center: E^* -distribution in nuclei with Z=4-29 for energies E^* =<1300 keV and 3000-4300 keV. Bottom left: E^* -distribution for Z-odd nuclei (Z \leq 29). Bottom right: Strong transitions from proton resonances in ⁵⁹Co to low-lying states at E^* = δm_N and $2\delta m_N$.

In the lightest nuclei only for 18,19,20 F there are a sufficient total numbers of excited states (n=359, 229, 149) to perform the combined correlation analysis. The number of excited states in 18 F used for the analysis could be increased from n=359 to n=431 by inclusion E^* known with uncertainty ≈ 30 keV (this file was not used here).

Stable interval D=1289 keV close to δm_N was found in spacing distribution for all 359 excited states near-magic nucleus ¹⁸F (levels are known with the uncertainty 15 keV or less, distribution is shown in Fig.6 (top). This interval is marked with the arrow, and his clear nonstatistical character was checked by the AIM method. Distribution of D_{+1}^{AIM} (Fig.6 center) has a clear maximum at the exactly doubled value D_{t1}^{AIM} =2577 keV. The distribution of the interval D_1^{AIM} (in downwards direction from the upper levels of pairs forming x=1290 keV) contains a maximum at D_1^{AIM} =1931 keV=(3/2)x (Fig.6 bottom). It corresponds to a frequent appearance of intervals D=642 keV=x/2 below the fixed intervals x. Another interval D=493 keV was observed in total D-distribution for ¹⁸F (Fig. 7 top, deviation about 3σ with smaller energy averaging interval $\Delta E=3$ keV, while ΔE =5 keV is the commonly used parameter). For x=493 keV in D_{11}^{AIM} -distribution there exists the interval 611 keV=(5/4)x. Intervals 614 keV and 490 keV-984 keV were found also in D-distributions of ¹⁹F and ²⁰F. They belong to the system of intervals $n\times(1/4)492$ keV=123 keV (a period) observed also as the above discussed stable intervals 493 keV-611 keV in ¹⁸F. Observed in D-distributions for ¹⁸⁻²⁰F (Fig. 5-7) maxima at D \approx 492 and 984 keV are rational (1:2:8) to the grouping effect at E*=3936 keV. Such excitations appear in nuclei with Z=16-20 (Table 3). In the nucleus ³³S it corresponds to the exactly equidistant $\Delta J=1$ excitation (Table 3 left).

| Table 3 | 3. | Excitat | ions in | light | nuclei | (in ke | V), from | n ³³ S u | p to ³⁹ Ca. |
|-------------------------------------------------------------------------------------|----------------------------------------|---------------|------------------------------------------|----------------------------------------------------------|-------------------------------------------------------------------|------------------------------------|----------|--------------------------------------------|------------------------------------------------------------------------|
| ³³ S, 3 ⁺ 2 <i>J</i> * 5 ⁺ 3 ⁺ | E************************************* | diff. 1968 | 38Cl E _{exp} 1982 3938 | ³⁹ K E_{exp}^{\bullet} 2523 [3939] | ³⁷ Ar E [*] _{exp} 1410 3937 | 38 Ar E* _{exp} 2167 | | D _{ij} (18F) 493 keV 3936/8 | D _{ij} (²⁰ F) 490 keV 984 keV= 3936keV/4 |

Presence of the exact rational relations in excitations of 18 O (the system similar to 18 F, two valence nucleons over 16 O) can be seen in Table 4 (left). Several excitations are rational to the observed stable interval 1778 keV in spacing distribution Three out of four known 0^+ , 4^+ excitations are in ratios "n" (within $\Delta = 5$ keV) to the observed stable interval 1778 keV in spacing distribution. Simultaneously the first 0^+ excitation in 18 O can be expressed as $E(0_1^+)=(12/13)3936$ keV (the groping at 3936 keV see in Fig.5).

Table 4. Rational relation 1:2:3:4 between spacing and excitation energies E^{\bullet} (in keV) in ¹⁸ and relations in spacing D_{ij} (in keV) in light nuclei ¹⁹F and ^{19,20}Ne.

| 18O | | | | | | ¹⁹ Ne | | ¹⁹ F | ²⁰ Ne |
|---------|------|------|-------------|------|------|------------------|--------------------|-----------------|------------------|
| 0+ | 2+ | 4+ | 0+ | 0+ | 4+ | D_{ij} | | D_{ij} | D_{ij} |
| 0.0 | 1982 | 3555 | 3634 | 5336 | 7117 | 77(2) | 908(2) | 339(2) | 339(2) |
| n(1778) | | _2_ | | _3_ | _4_ | 8δ′ | $12\times8\delta'$ | $36\delta'$ | 36δ′ ⋅ |
| n×1778 | | 3556 | (12/13)3936 | 5334 | 7112 | 76 | 909 | 341 | 341 |

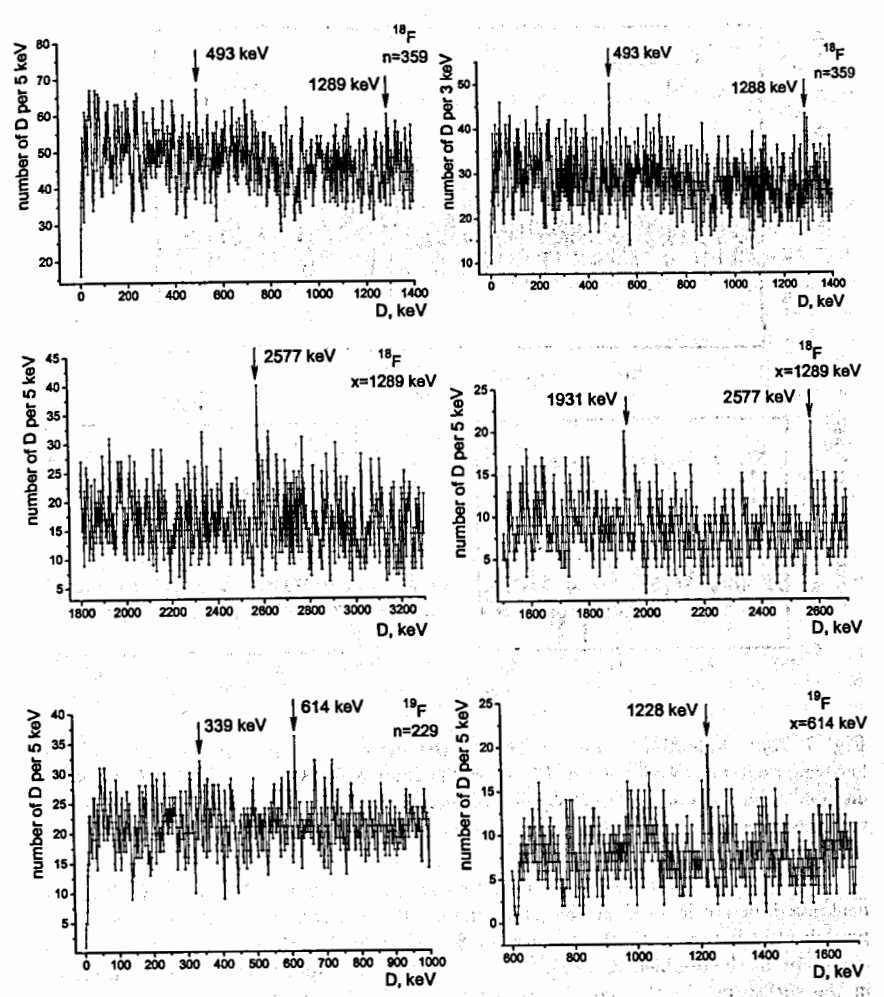


Fig. 6 Top left: D-distribution for all levels in ¹⁸F, maxima at 493 keV and 1289 keV. Top right: D-distribution for all levels in ¹⁸F with averaging interval ΔE =3 keV, maxima are the same as observed with ΔE =5 keV (at left).

Center: D_{\downarrow}^{AIM} -distribution in ¹⁸F x=1289 keV and D_{\downarrow}^{AIM} -distribution in ¹⁸F x=1289 keV which contains additionally interval 1931 keV=(3/2)x.

The transport of the specific of the Admit Admit to

and the contract of the contract of the contract of the con-

Bottom: D-distribution in ¹⁹F and $D_{\rm T}^{AIM}$ -distribution in ¹⁹F x=614 keV.

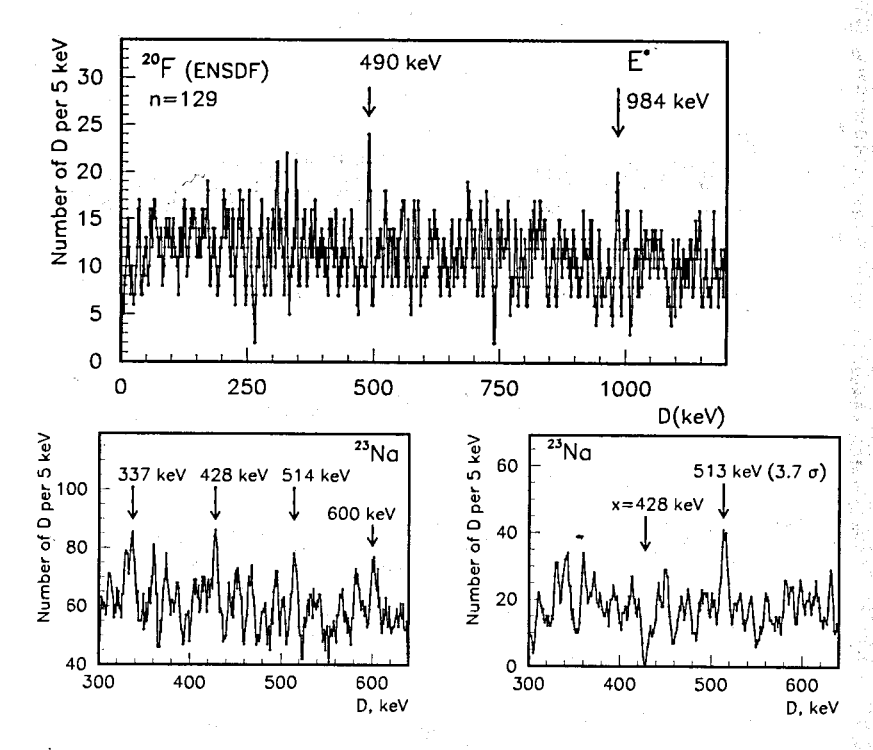


Fig. 7 Top: D-distribution for 20 F levels in the low-energy regions, stable intervals close to low-lying excitations were noticed, E^{\bullet} and stable D are marked with arrows. Bottom: Spacing distribution in levels of 23 Na (n=335) with the maximum at 428 keV and the periodical structure with the parameters of 85 keV checked with the AIM-method (x=428 keV, right).

In spacing distributions of the neighbour N=even isotopes 21 Na and 23 Na the prominent maxima are located at the same energy 428 keV which in 23 Na is a part of the periodical structure with the interval of 85 keV (Fig.7 bottom). The presence of the maximum at the doubled value D_{\uparrow}^{AIM} =2x=857 keV corresponds to pairs of such intervals in the spectrum. In the next N=even isotope 25 Na (number of known levels n=40) a sequence of three stable intervals D=858(2) keV was noticed. The interval D=x=428 keV itself is composed of intervals 203 keV-226 keV. The interval x=428 keV is adjusted with D=514 keV (seen in the spacing distribution in Fig. 7 left) and with D=247 keV equal to 1/2 of the interval 492 keV in spacing distributions of 18,20 F (Table 3, Fig. 6,7.).

The observed rational relations and coincidences in spacing in experimental nuclear spectra of light Z=9-11 nuclei could be used for production of the microscopic nuclear models based on better understanding of nucleon structure.

The tuning effect in particle masses considered in [4,6,8,9] consists in rational relations between the well-know particle masses, namely, masses of muon, pion, neutron, ω -meson, the pion parameter f_{π} , constant splitting between pseudoscalar mesons, the parameter of

residual interaction of constituent quarks (ΔM_{Δ}) and initial constituent quark mass itself $M_q=441~{\rm MeV}=3\Delta M_{\Delta}$. They correspond to n=13,17,115,48,16,50,18,54 with the parameter of the discreteness $\delta=16m_e$ which is very close to double pion β -decay energy. The initial mass of the baryon in NRCQM has a value about 1320 MeV (three quarks about $M_q=436~{\rm MeV}$ [10] or $M_q=440~{\rm MeV}$ from the Ξ -baryon mass [11,12]). Due to the constituent quark interaction this mass becomes the mass of the well-known Δ -baryon (mass 1230 MeV of three quarks with the mass $M_q^{\Delta}=410~{\rm MeV}$ each). The spin dependent residual interaction is well-known from the nucleon Δ -excitation $2\Delta M_{\Delta}=2\times147~{\rm MeV}$ (close to $2\times18\delta$). Difference $m_{\Delta^0}-m_n=1233.4(7)-939.57~{\rm MeV}=293.8(7)~{\rm MeV}=2\times146.9(4)~{\rm MeV}$ coincides with $2\times18\delta$. The mass of nucleons in nuclear medium (m_N^*) is about 8 MeV ($\approx \delta$) less compared with free nucleon mass $m_N=115\delta$ (see Fig.9 in [4]). It means that the difference between $m_N^*\approx114\delta$ and ω -meson mass $(6\times15\delta)$ accounts about 147 MeV=18 δ .

If the preliminary value of scalar field mass M_H =126 GeV [14] will be confirmed, the proximity between ratios in lepton masses $(1/3)m_e/(m_s=\Delta M_\Delta=147~{\rm MeV})/M_H=\alpha/2\pi$ and $m_\mu/M_Z=\alpha/2\pi$ (Table 5) could be connected with the suggestion by V. Belokurov and D. Shirkov that in the electron mass there exists a component proportional to $\alpha/2\pi$ similar to that in the electron magnetic moments (Schwinger term of QED correction). Ratios $(\alpha/2\pi)^{-1}$ in stable nuclear spacing $(\varepsilon_o=2m_e)/(\varepsilon'=9.5~{\rm keV/8}=\delta'/8)/(\varepsilon''=5.5~{\rm eV/4}=\delta''/8)$ were introduced in [15]. The parameter of 5.5 eV of superfine structure in spacing of ¹²⁴Sb was found by K.Ideno and M.Ohkubo [16].

The observed long-range correlations in nuclear data and in nucleon masses themselves are indications on the validity of the common fundamental microscopic approach to the description of results of the nuclear/neutron-resonance spectroscopy.

Table 5 (from [6,8]). Presentation of parameters of tuning effects in particle masses and nuclear data (in lines marked X=-1, 0, 1, 2 at left) by the common expression $n \cdot 16m_e(\alpha/2\pi)^X M$ with the QED radiative correction $\alpha/2\pi$ ($\alpha=137^{-1}$). Values $m_{\pi}-m_e$, $m_e/3$, the neutron mass shift $N\delta - m_n - m_e$, m_s and the possible Higgs boson mass [14] are boxed. Stable intervals in excitations (E*, D_{ij} , X=1) and in neutron resonances (X=2) are considered as confirmation of relations in particle masses (X=-1). The value $\Delta^{\circ} \approx 4 \text{ GeV} \approx m_b$ was observed at TEVATRON.

| X | M | n = 1 | n = 13 | n = 16 | n = 17 | n = 18 |
|-----|-----|------------------------------|-----------------------------------------|------------------------|-----------------------------------------------------|------------------------------|
| -1 | 3/2 | | | m _t =171.2 | 7 Harris 12. | |
| GeV | 1 | $2\Delta^{\circ}$ - $2M_{o}$ | $M_z = 91.2$ | $M_{\rm H} = 115$ | · | $M_{\rm H} = 126$ |
| 0 | 1 | • | $m_{\mu} = 105.7$ | $f_{\pi} = 131$ | m_{π} - m_{e} | $m_s = 147 - 150$ |
| MeV | 1 | 2Δ - $arepsilon_0$ | $106 = \Delta E_{\text{B}}$ | $130 = \Delta E_B$ | $140 = \Delta E_B$ | $147.2 = \Delta E_B$ |
| | 1 | | | | | m_{Δ} - $m_{n}/2=147$ |
| | 3 | | | $M''_{q} = m_{\rho}/2$ | NRCQM | $M_q=441=\Delta E_B$ |
| 1 | 1 | | - 1 - 1 - 1 - 1 - 1 - 1 - 1 - 1 - 1 - 1 | | $N\delta$ -m _n -m _e =161.6(1) | $170=\mathrm{m_e/3}$ |
| keV | 1 | 9.5 | 123 | 152 | 161 (¹⁸ F, Sb) | 512 (Co, Pd) |
| | 4 | | 492 | فالمرابع والمتاريخ | 648 (^{97,98} Pd) | 682(Co) |
| | 8 | | 984 | 1212 | 1293 (Pd), Σ <i>E</i> * | 1360 (Te) |
| 2 | 1 | 11 | 143 | 176 | 187, 749 (⁷⁹ Br) | D in neutron |
| еV | 4 | 44 | 570 (Sb) | | 1500 (Sb,Pd,Rh) | resonances |

4 Discreteness in parameters of nucleon interaction

Dependence of neutron separation energy S_n on the proton number (shown in Fig.8) in case of near-magic nuclei with N=83 and Z=57-61 ($^{140}\text{La}^{-142}\text{Pr}^{-144}\text{Pm}$, $\nu 2f_{7/2}$ and $\pi 2d_{5/2}$ – $\pi 1g_{7/2}$) has exactly linear character with the parameter $\varepsilon_{n,2p}$ =683(1) keV=(2/3) ε_o (boxed values at the bottom of Fig.8. The same $\varepsilon_{n,2p}$ =688(4) keV and $\varepsilon_{n,2n}$ =339(3) keV=(1/3) ε_o correspond to differences in S_n =7493-6806-6467 keV for nuclei $^{124}\text{I}^{-122}\text{Sb}^{-124}\text{Sb}$ (N=71, $\nu 1h_{11/2}$, dark triangle and the box in the middle of Fig.8). In Fig.9 it is seen as maxima in distributions of standard parameters $\varepsilon_{n,2n}$ and $\varepsilon_{n,2p}$. In the isotopes under discussion $^{122,124}\text{Sb}$ these parameters are close to maxima of distributions.

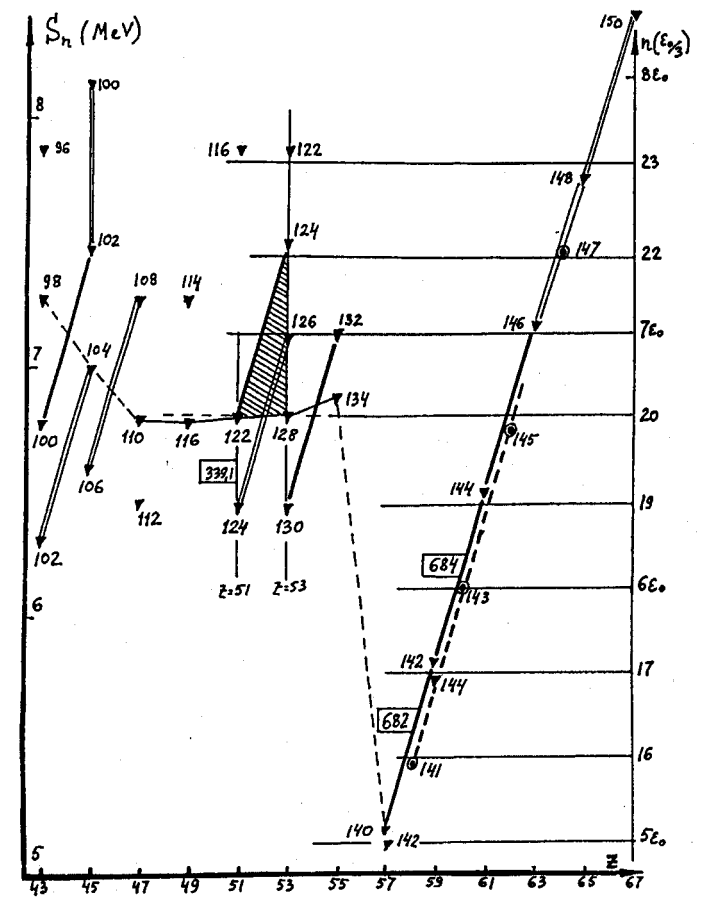


Fig. 8 Dependence of the neutron separation energy S_n on the proton number Z=43-67.

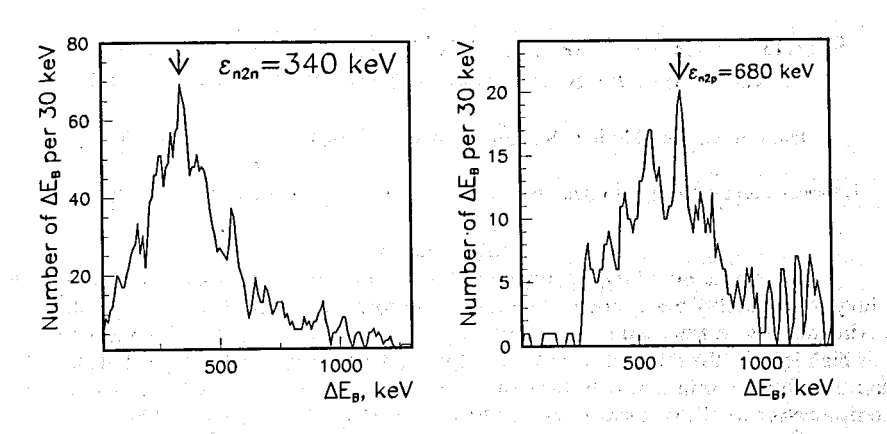


Fig. 9 Left and right: Distributions of residual nucleon interaction parameters ε_{n2n} and ε_{n2p}

5 Conclusions

Presence of stable mass/energy intervals in the regions where the dominance of the pion-exchange dynamics is expected permitted the observation of common tuning effects, the estimation of the common parameters and long-range correlations in nuclear and particle data. Importance of expanding data on highly excited states and the confirmation of the scalar mass SM parameter is outlined.

Authors appreciate the help of D. S. Sukhoruchkin in this work.

6 References

- 1. J.Schiffer, Proc. Rutherford Centennial Conf., Manchester, 2011. JPCS, IOP, 2012.
- 2. T.Otsuka, T.Suzuku, Y.Utsino, Nucl. Phys. A 805 127c, 2008.
- 3. S.I.Sukhoruchkin, Z.N.Soroko, D.S.Sukhoruchkin, these Proc.
- 4. S.I.Sukhoruchkin, D.S.Sukhoruchkin, these Proc.
- 5. H.Schopper (Ed.), Landoldt-Boernstein New Series 2012 vol. I/25A. Springer.
- 6. S.I.Sukhoruchkin, Proc. Rutherford Centennial Conf. Manch. 2011. JPCS, IOP, 2012.
- 7. M.Ohkubo, M.Mizumoto, Y.Nakajima, Report JAERI-M-93-612, 1993.
- 8. S.I.Sukhoruchkin, http://cgc.physics.miami.edu/Miami2011/Sukhoruchkin.ppt.
- 9. R.Frosch, Nuovo Cim. 104 913, 1991.
- 10. C.Itoh et al, Phys. Rev. D 40 3660, 1989.
- 11. L.Glozman, Nucl. Phys. A 629 121c, 1998.
- 12. P.Kropotkin, Field and Matter, (Moscow Univ. 1971) p.106.
- 13. V.V.Belokurov, D.V.Shirkov, The theory of Particle Interactions. AIP, 1991.
- 14. M. Wielers, http://cgc.physics.miami.edu/Miami2011/Wielers.ppt.:
- 15. S.I.Sukhoruchkin, Stat. Properties of Nuclei ed. Garg G (Plenum Press) 215, 1972.
- 16. K.Ideno, M.Ohkubo, J. Phys. Soc. Jpn. 30 (1971), 620.

ा १९८८ च्या १८५५ व्याप्त १५५ प्राप्त १५५ व्याप्त १५५६ व्याप्त १५५६ व्याप्त १५५६ व्याप्त १५५६ व्याप्त १५५६ व्या १९५५ - १९५५ - १९५५ व्याप्त सम्बद्धित व्याप्त १५५६ व्याप्त १५५५ व्याप्त १५५५ व्याप्त १५५५ व्याप्त १५५६ व्याप्त

STUDY OF HEAVY METAL CONTENTS IN SOIL, RIVER WATER, SNOW, NEEDLES AND MOSSES OF IVANOVO REGION

Dunaev A.M., Latukhina K.S., Abdalla A.A., Rumyantsev I.V., Nikiforov A.Yu.

Ivanovo State University of Chemistry and Technology, Russia, Ivanovo, F. Engels prospect, 7

Introduction

An increase of anthropogenic impact causes a degradation of environmental quality, heavy metals (HM) being one of the most dangerous pollutants. They exist in all natural environments and frequently have a tendency of bioaccumulation. Their expressed toxicity and high level of the influence define the urgency of investigation of heavy metals migration and transformation in natural ecosystems. This paper is concerned with the study of HM contamination level in Ivanovo region carried out in this scale for the first time.

Materials and methods

Ivanovo region situated at interfluve of the Volga and Klyaz'ma rivers with an area of 22 000 km² was the object of the investigation. There were 45 squares (Fig. 1) separated within the region with average area of 400 km². Samples of soil, needle of spruce (*Picea Abies*), mosses and snow were taken from each square. Water samples from the main rivers were also sampled.

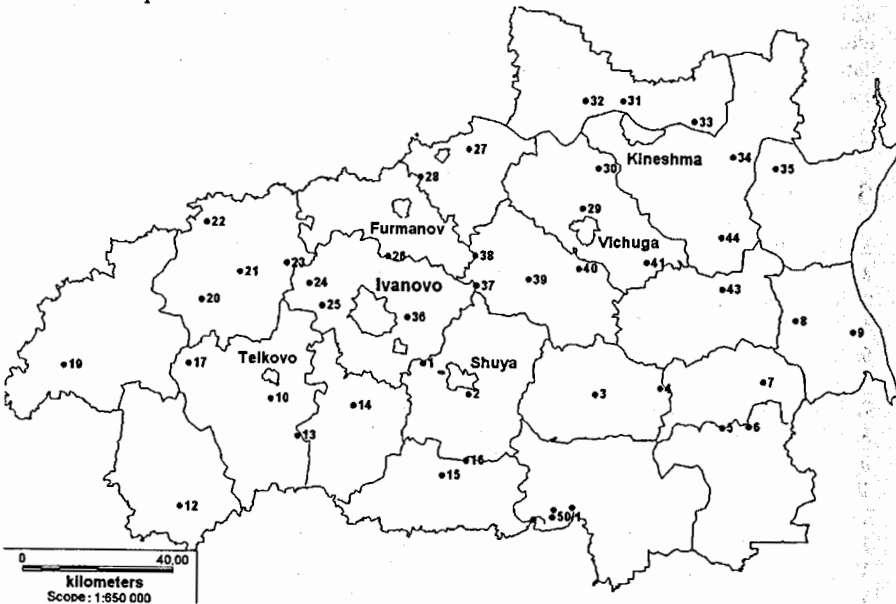


Fig. 1. Sampling map.

Sampling was made according to standard techniques for soil and needles [1], moss [2], snow [3] and water [4]. The analysis of HM content (Pb, Cd, Cr, Cu, Co, Ni, Mn, Fe and Zn) was carried out with the use of flame atomic absorption spectrometry. The concentration

of gross and movable forms of the metals was measured in soil samples, while in others - only gross forms. Determination uncertainties were about 20-30%.

Results and discussion

The data visualization and statistical analysis were employed in results of investigation. Maps of spatial distribution of HM in the examined environments were created with the use of MapInfo software. We applied IDW (Inverse Distance Weighting) interpolation method for the subject maps.

The factor analysis of the given data was done to detect potential origins of the intake and establish the correlation of the HM content in different environments. Processing was carried out by principal component method with the Varimax rotation.

Table 1. HM concentrations in soils and background concentrations (ug/g).

| Metal | min-max | mean | localbg ¹⁾ | sod-podzolic soil [1] | podzolic soil [5] | sod-podzolic soil (Moscow region) ³⁾ [5] | [9] IIos ajlozpod |
|------------------|-------------|------|-----------------------|--------------------------|-------------------|-----------------------------------------------------------|-------------------|
| Cr | <0,01-1,67 | 0,12 | 0,29 | 140 | 180 | 46 | 47 (1,4-530) |
| Mn | <2,5-1880 | 420 | 144 | 650 | 715 | 590 | 270 (7-2000) |
| Fe ²⁾ | 71,4-14400 | 5490 | 2930 | ¥¥,3. | | អ៊ី ស្រែង នេះ កំពុំ ខេត្ត | |
| Со | <0,02-4,58 | 1,3 | 0,88 | | 8,4 | 7,2 | 5,5 (0,1-65) |
| Ni | <0,3-56,4 | 8,67 | 2,43 | 51 | 23,2 | 20 | 13 (1-110) |
| Cu | <0,2-20 | 6,24 | <0,2 | 23 | 15,3 | 27 | 13 (1-70) |
| Zn | 4,17-70 | 19,5 | 11,3 | 49 | 41,3 | 50 | 45 (3,5-220) |
| Cd | <0,002-0,25 | 0,03 | 0,03 | • • | 0,7 | 0,3 | 0,37(0,01-2,7) |
| Pb | <0,02-3,32 | 0,23 | 0,33 | 19 | 11,5 | 25 | 22 (2,3-70) |

^{1) -} local background (average concentration for 10 samples with least concentrations):

Average HM content in the soil samples was within the range of maximum permissible concentration (MPC). However, the increasing HM content in the soil near large industrial centers evidenced of their anthropogenic origin. The most of samples sites had a HM concentration, which was lower than background (Table 1).

Besides, the comparison of HM content in Ivanovo and neighboring regions was made (Table 2). The given data argued about lower level of HM content in Ivanovo region as compared with other regions. The soil of Nizniy Novgorod region was the closest in chemical composition.

 $^{^{2}}$) - in [7] is value 38000 ug/g;

^{3) –} value used for calculations in given work.

Table 2. Data of HM content in soil in Ivanovo and neighboring regions (119/9)

| Metal | Kostroma region, 2010 /8/ | Vladimir region, 2007 /10/ 2010 Vladomir region, 2007 /10/ 2010 | | | | region, |
|-------|---------------------------------|------------------------------------------------------------------|-------|------|-------|---------|
| Form | Gross | Gross | Gross | Mov. | Gross | Mov. |
| Cr | 72,63 | 80 | 11,91 | 0,29 | 0,12 | 0,03 |
| Mn | 645,2 | 692 | | - | 420 | 40,4 |
| Fe | 18398,8 | 27700 | - | - 4. | 5490 | 84 |
| Co - | 15,63 | 6 | - | | 1,3 | - |
| Ni | 23,39 | 29 | 20,46 | 0,78 | 8,67 | 0,99 |
| Cu | 23,23 | | 8,05 | 0,29 | 6,24 | 0,77 |
| Zn | 48,40 | 47 | 25,91 | 0,59 | 19,5 | 3,66 |
| Cd | - | ÷ . | 0,39 | 0,13 | 0,03 | <0,003 |
| Pb | - 1 | 16 | 6,17 | 0,64 | 0,23 | - |

The factor analysis of the given data also confirmed anthropogenic character of areas with higher HM content. Six factors, which explained 76% of the dispersion, were separated. The three most important of them might be interpreted as a result of anthropogenic impact due to activity of different industries and automobile transport.

The analysis of needles showed the absence of Cd, Pb, Cr, Co and particularly Ni. Other elements likely had natural origin.

Table 3. Data of HM content in mosses in Ivanovo and other regions (ug/g).

| | | | Tula (1998-2000) /12/ Udmurtia (2005-2 /13/ | | | | | | 5-2006) |
|----------|---------|----------|---------------------------------------------|-----------|-----------|-----------|-----------|--------|---------|
| | min | max | mean | min | max | mean | min | max | mean |
| Cr | 0,2 | 27 | 1,5 | 0,6 | 28 | 5 | 3 | 48 | 6,2 |
| Mn | 45 | 2200 | 400 | 35 | 820 | 300 | 43 | 700 | 210 |
| Fe | 68 | 3690 | 550 | 350 | 19700 | 2200 | 380 | 3545 | 890 |
| Co | 0,05 | 3,5 | 0,41 | 0,14 | 2,66 | 0,63 | 0,07 | 2,13 | 0,4 |
| Ni | 0,25 | 22 | 2 | 0,7 | 11,7 | 3,7 | 1 | 16 | 4,7 |
| Cu | - 3,2 | 9,2 | 5,1 | . 4 | 36 - | 9 | 3 | 22 | 8,5 |
| Zn | 13 | 85 | 34 | 16 | 105 | 54 | 18 | 115 | 42 |
| Cd | 0,03 | 0,82 | 0,27 | 0,04 | 1,22 | 0,32 | | | |
| Pb | 2,1 | 12,2 | 6 | 3,8 | 18,6 | 8,7 | | | 1161 |
| min, max | and mea | n- minim | al. maxin | al and av | erage cor | centratio | ns respec | tively | Tris |

| | , mile and mount minimus, marine | | | | | | | | | | |
|----|----------------------------------|----------------|-------|---|--|--|--|--|--|--|--|
| | Iva | Ivanovo (2010) | | | | | | | | | |
| | min max mea | | | | | | | | | | |
| Cr | <0,01 | 16,7 | 1,7 | l | | | | | | | |
| Mn | <2,5 | 1250 | 231 | | | | | | | | |
| Fe | 4,17 | 750 | 262 | | | | | | | | |
| Co | <0,02 | <0,02 | <0,02 | l | | | | | | | |
| Ni | <0,3 | 16,6 | 4,3 | ŀ | | | | | | | |
| Cu | <0,2 | 44 | 8,6 | l | | | | | | | |
| Zn | 2,4 | 120 | 31 | | | | | | | | |
| Cd | <0,05 | 1,25 | 0,14 | | | | | | | | |
| Pb | <0,02 | 41,7 | 3,5 | ĺ | | | | | | | |

Heavy metals can migrate from soils into rivers. Thereby, it was also necessitate carrying out the analysis of river water. The content of Fe, Zn and Mn was below maximum permissible concentration for water for all rivers. The excess of this level was marked for Ni compound in two rivers - Matnya and Shacha. The increase of the content in these rivers was probably due to activities of industries of Shuya city and Furmanov city. The excess of copper content above MPC was fixed for seven rivers. The most probable reason of this metal arrival might be erosion from the bedrock and the influence of the river head often situated at swampy area enriched by metal compounds.

The values of the index of water pollution were calculated. The results allowed ranking the water quality in examined rivers. Overwhelming majority (9 of 14) was characterized as first or second class of pollution and was pure. There were three only rivers with class of pollution above 3. It pointed out significant degree of contamination and required the development of measures for changing present situation.

| Table 4. | Factor ana | lysis. | | 10.00 | . 100 vt. v | fastead | r marking Sod |
|----------------------------|-------------------|-----------------------------------------|-----------|------------------|-------------------|-----------------------|--------------------------------------------------------------------------------------------------------------------------------------------------------------------------------------------------------------------------------------------------------------------------------------------------------------------------------------------------------------------------------------------------------------------------------------------------------------------------------------------------------------------------------------------------------------------------------------------------------------------------------------------------------------------------------------------------------------------------------------------------------------------------------------------------------------------------------------------------------------------------------------------------------------------------------------------------------------------------------------------------------------------------------------------------------------------------------------------------------------------------------------------------------------------------------------------------------------------------------------------------------------------------------------------------------------------------------------------------------------------------------------------------------------------------------------------------------------------------------------------------------------------------------------------------------------------------------------------------------------------------------------------------------------------------------------------------------------------------------------------------------------------------------------------------------------------------------------------------------------------------------------------------------------------------------------------------------------------------------------------------------------------------------------------------------------------------------------------------------------------------------|
| - M. 28 | 25 - 63 - | 20 7 | 20 € C | omponen | t i 🤼 🎎 | No. Main | F-FM-44 |
| ا آه آخواهي در اه د اچي | 1 | 2 | 3 | 4 | 5 | 6 | 7 |
| Cd_s_m | 0,957 | | -0,124 | P. A. Gre | Da ta de | -0,105 | affic ? |
| Cr_s_m | 0,957 | i i ymigga | -0,124 | tarist it. | San Strain | -0,105 | चारकाम् म ्दि |
| Cr_m | 0,853 | 100 77 5 | 0,424 | | | | |
| Cu_m | 0,834 | | 0,487 | A STATE OF STATE | a di nationa | | - programme to the contract of |
| Cd_m | . 0,661 as | -0,100 | -0,163 | 0,580 | 10.00 | 11 600 | -0,168 |
| Ni_s_m | 0,637 | 0,394 | -0,296 | | a gala M | -0,102 | NEWWORLD IN |
| Mn_s_m | 200 | 0,932 | 0,227 | 1 1 | | a' | and the state of t |
| Ni_s_g | 10 m | 0,915 | | s Black | 0,154 | S. SEAS | 90507387 |
| Pb_s_g | | 0,768 | 0,352 | KIN HE I | 0,390 | -0,164 | n the part |
| Fe_s_m | -0,184 | 0,756 | 0,150 | -0,131 | -0,250 | Market ag | BERTS TO |
| Fe_s_g | -0,115 | 0,734 | -0,210 | 4-1. F | -0,122 | 0,298 | 48414 |
| Cu_s_g | 0,184 | 0,638 | 古物的 | -0,126 | 0,400 | , 0,135⊴s | a william |
| Pb_m | un solita ja | 24,544, 3 | 0,902 | Para sar | 0,207 | 120 \$ \$100 f | \$2 10 20 |
| Zn_m | | | 0,868 | | Section 1 | , | 0,191 |
| Cd_s_g | Q (20) | 0,370 | 0,636 | 14 1 1 1 1 | 0,589 | -0,127 _{0.5} | ។ នៅវ |
| Fe_n | -0,174 | -0,292 | - Petter? | 0,807 | क्षांत्र सुर्वाद | वया व्यक्ति | 0,167 |
| Zn_n | Complete Salabara | 0,251 | -0,188 | 0,785 | N + #3, 455 . | 0,393 | -0,187 |
| Fe_m | 0,218 | La et si A. E | 0,269 | 0,779 | malla Ros mo | France, refe | 0,197 |
| Cr_s_g | an Pinger | . ************************************ | 0,170 | diregio A | 0,875 | processing | សាល ស្នែងប |
| Co_s_g | 1 d 12 d 14 d | 0,228 | 0,452 | 2027/23/201 | 0,484 | Miller, M. | Paramo, a |
| Cu_n | | 100000000000000000000000000000000000000 | 7 - 5 7 | 0,175 | A Kiye we ter it. | 0,887 | |
| Mn_s_g | -0,150 | 0,135 | emanted i | a kazer | -0,108 | 0,878 | -0,106 |
| Ni_n | 1.44 1800 | D 134 BO EVE | ಲಾವ ಚ≕ರೇ" | र इंडिल्डीहरू | a con oran | wich has | 0,928 |

| Zn_s_g | | 0,122 | 0,345 | | | | 0,795 |
|--------|--------|--------|--------|--------|--------|--------|--------|
| Mn_n | -0,246 | 0,223 | 0,129 | 0,148 | -0,258 | 0,190 | 0,164 |
| Ni_m | 0,465 | | -0,265 | 0,347 | | -0,121 | -0,267 |
| Cu_s_m | -0,221 | -0,132 | | -0,132 | 0,349 | -0,182 | -0,183 |
| Zn_s_m | -0,103 | | -0,147 | | | -0,142 | 1 旗 |
| Mn_m | -0,258 | -0,270 | | | -0,297 | -0,301 | -0,149 |

Extraction Method: Principal Component Analysis.

Rotation Method: Varimax with Kaiser Normalization.

Indexes: s g - soil gross; s m - soil movable; m - moss; n - needles.

Data of 25 moss samples (Hylocomium splendens, Pleurozium schreberi and Polytrichum commune) were processed. All obtained metals were present in samples (Table 3). Values of HM content in moss were compared with the results of the research in Yaroslavl, Tver', Tula region and Udmurtia republic. All these data were measured by NAA method. In fact level of HM content in Ivanovo region was very close with neighbor regions.

Samples of snow were collected on March, 2011. HM content in bulk snow and solid fraction were measured. Composition of snow solid fraction (Zn, Mn, Fe) was an evidence of their soil origin. These metals were most common in soil and under wind transfer they could migrate in snow from roads. In bulk snow Cu, Zn, Mn and Fe were found. The concentrations of copper were the same as those of Nizniy Novgorod region, but zinc content in Ivanovo was less than in Nizniy Novgorod. Intensities of atmospheric deposition, which were calculated from the HM content in snow, were less than urban intensities of HM deposition [5].

Factor analysis of the total array of data of HM content in different environments was made (Table 4). As a result 9 factors, which explained 86% of whole dispersion, were singled out. The first four factors were most important and interesting.

The first factor concerned with movable forms of Cr, Cd and Ni in soil, and Cr, Cd and Cu in moss. Such coincidence might explain the origin of these elements in soil. Moss gets the nutrition elements only from air. Hence Cr and Cd had atmospheric origin.

The second factor combined gross forms of Pb, Ni, Fe and Cu in soil and movable forms of Fe and Mn, probably; being a group of elements migrated into soil from the bedrock. The 4th factor was determined by the content of Fe in needles and moss, and Zn in needles.

The third factor included gross forms of Co and Cd in soil, and Pb and Zn in moss. Origin of this factor probably dealt with the influence of automobile transport.

The samples will be measured by the neutron activation analysis on the basis of the Laboratory of Neutron Physics of Joint Institute of Nuclear Research. It allows extend considerably the number of the observed elements. The results of the research will be included into European Atlas of HM deposition according to the Long Range Transboundary Air Pollution programme. The results of the research will be given in community ecological council for the development of measures of Ivanovo region aimed at the maintenance of favorable quality of environment.

It will be possible to define spatial and temporal trends of HM distribution in natural environments and determine the regularity of their behavior in the environment during next two years.

References

- 1. Procedural instructions for heavy metal determination in soils and plant products. Approved by Deputy of Minister of agriculture 10 March 1992 r.
- 2. Harmens H. et all. Monitoring of atmospheric deposition of heavy metals, nitrogen and POPs in Europe using Bryophytes. Monitoring Manual. Bangor: ICP Vegetation Coordination Centre, 2010. 9 P.
- 3 RD 52.04.186-89. Atmospheric contamination monitoring manual. Moscow, 1991.
- 4. GOST R 51592-2000. «Water. General sampling requirements». Adopted and brought by decree of Standard Committee of RF from 21 april 2000 r. № 117-st.
- 5 Saet Yu.E., Revich B.A., Yanin E.P. etc. M.: Nedra, 1990. 335 P.
- 6. Kabata-Pendias A. Trace elements in soils and plants. 3rd ed.: CRC Press, 2001. 403 P.
- 7. Vinogradov A.P. Geochemistry of rare and dispersed elements in soils. M.: AS USSR,
- 8. Lebedeva O.Yu. Geoecological assessment of distribution of heavy metal gross forms in soils of Kostroma region. Geographical candidate's thesis. St.Peterburg: RSPU of. A.I. Gercen, 2011. 21 P.
- 9. Karpova D.V. Assessment of agricultural status grey forest soils of Vladimir's Opolie. Agricultural doctoral thesis. M.: VladSRICA, 2009. 55 P.
- 10. Kuznetsov V.A. Changing of agroecosystem components in distribution area of dark-grey forest and chernozem soils of Volga-Vyatka region under agricultural usage. Agricultural candidate's thesis. Saransk.: NSAA, 2010. 21 P.
- 11. Ermakova E.V., Frontasyeva M.V., Pavlov S.S., Povtoreiko E.A., Steinnes E. and Cheremisina Ye.N. Air Pollution Studies in Central Russia (Tver and Yaroslavl Regions) Using the Moss Biomonitoring Technique and Neutron Activation Analysis // J. Atm. Chem. 49: 549–561, 2004.
- 12. Ermakova E.V., Frontasyeva M.V., Steinnes E. Air pollution studies in Central Russia (Tula Region) using the moss biomonitoring technique, INAA and AAS // J. Radioanalytical and Nuclear Chem., Vol. 259, No. 1 (2004) 51-58.
- 13. Pankratova Yu.S., Zelnichenko N.I., Frontasieva M.V., Pavlov S.S. Atmospheric contamination on the territory of Udmurtia republic assessment based on analysis of mosses-biomonitors // Problemy regionalnoy ecologii. 2009, № 1 P. 57-63

The second of the second of the second

and the second of the second s

and the confidence of the second section of the

The state of the state of the state of the state of the state of the state of the state of the state of the state of the state of the state of the state of the state of the state of the state of the state of the state of the state of the state of the state of the state of the state of the state of the state of the state of the state of the state of the state of the state of the state of the state of the state of the state of the state of the state of the state of the state of the state of the state of the state of the state of the state of the state of the state of the state of the state of the state of the state of the state of the state of the state of the state of the state of the state of the state of the state of the state of the state of the state of the state of the state of the state of the state of the state of the state of the state of the state of the state of the state of the state of the state of the state of the state of the state of the state of the state of the state of the state of the state of the state of the state of the state of the state of the state of the state of the state of the state of the state of the state of the state of the state of the state of the state of the state of the state of the state of the state of the state of the state of the state of the state of the state of the state of the state of the state of the state of the state of the state of the state of the state of the state of the state of the state of the state of the state of the state of the state of the state of the state of the state of the state of the state of the state of the state of the state of the state of the state of the state of the state of the state of the state of the state of the state of the state of the state of the state of the state of the state of the state of the state of the state of the state of the state of the state of the state of the state of the state of the state of the state of the state of the state of the state of the state of the state of the state of the state of the state of the s

DETERMINATION OF MAGNESIUM, ALUMINUM AND SILICON CONTENT IN WATER SAMPLES BY GAMMA-ACTIVATION AND NEUTRON-ACTIVATION ANALYSES USING THE MT-25 MICROTRON

Maslov O.D., Gustova M.V., Belov A.G. and Drobina T.P.

Joint Institute for Nuclear Research, Dubna, Russia

Abstract. The possibility of determining Mg, Al, and Si content in water samples using nuclear physical methods has been studied. The detections limits of 0.1, 0.03, and 0.1 mg/L for Mg, Al, and Si in water samples have been obtained.

Monitoring of the aluminum and silicon content in water is important because the high concentration of aluminum or the low content of silicon in drinking water may be risk factors for Alzheimer's disease.

INTRODUCTION

Aluminum occupies one of the main places among elements used in the production of industrial materials. Accordingly, there is a necessity of its control and analysis in the nonferrous metallurgy, in an alloy composition of the construction elements, in particular for the space rocket industry, in optical and glass industries. The aluminum content control is important as well in the food-processing industry, agriculture and at drinking water preparation. Aluminum arrives in natural waters from partial dissolution of clay and aluminum silicates, atmospheric precipitation, and waste waters from various manufactures.

Aluminum is rather well known as a metal, soluble forms of which can be poisonous and lead to encephalo- and polyneuropathy with dementia phenomena. Recent research confirms [1,2] that the growth of aluminum content in drinking water increases the risk of Alzheimer's disease. At present in Russia the aluminum maximum admissible concentration (MAC) in process water and public waters is established at a level of 0.2-0.5 mg/L, and in water of reservoirs used for commercial fishing – 0.08 mg/L [3].

According to the data of the American scientists [2], daily consumption of 0.1 mg of aluminum with drinking water increases the risk of dementia 2.26 times and considerably reduces intellectual abilities. However, daily consumption of silicon in drinking water up to 10 mg reduces the risk of a similar disease by 11%. Further research is planned to adjust the

norms of aluminum and silicon content in drinking water. It will be done for the purpose of protection from neurological diseases.

Silicon is a constant component of natural water chemical composition due to wide spread occurrence of silicon compounds in soils and mountain rocks. Significant quantities of silicon arrive into natural waters in the process of ground and water plant bodies dying off, with atmospheric precipitation, and also with industrial waste water of the enterprises producing ceramics, cements, glassware, silicate paint, binding materials, organosilicon rubber, etc. The concentration of silicon in river waters ranges usually from 1 to 20 mg/L. Silicon MAC is equal 10 mg/L [4]. Silicon is a powerful water activator and has important antibacterial properties. The presence of silicon at a concentration more than 2 mg/L detains and inhibits development of blue-green algae [5].

As a rule, chemical analysis methods are used for the determination of Al and Si [6, 7, 8, 9], and this methods are rather labour-consuming. But the urgent character of this problem requires development of new and approbation of the known methods for the elements analysis in environmental media and food.

EXPERIMENTAL

Element analysis of water samples was carried out by gamma-activation and neutron activation analyses using the MT-25 microtron.

Water samples from the Volga river and drinking water samples after standard filter treatment were taken for analysis. Water samples in the volume of 1 L were evaporated, solid residue was packed into packages of 10-micron lavsan film.

Gamma activation and neutron activation analyses. The analysed samples were positioned in the centre of the irradiation unit and irradiated with 22 MeV bremsstrahlung (the average electron current was equal approximately to 15 μ A) or with a thermal neutron flux for 5-15 minutes in a water moderator on the MT-25 microtron. Gamma spectrometric measurement of the irradiated samples for the determination of elements was carried out with the HPGe detector with 1.5 keV resolution on the line of 1.33 MeV (60 Co). Si, Mg, and Al were determined by the following reactions: 29 Si (γ , p) 28 Al ($T_{1/2} = 2.2$ min, $E_{\gamma} = 1779$ keV); 30 Si (γ , p) 29 Al ($T_{1/2} = 6.6$ min, $E_{\gamma} = 1273$ keV); 25 Mg (γ , p) 24 Na ($T_{1/2} = 14.96$ h, $E_{\gamma} = 1369$ keV) and 27 Al (π , γ) 28 Al (π) 28 Al (

on the result of the second control of the second s

RESULTS AND DISCUSSION

The results of some chemical elements determination in water samples are given in Table 1. Fig.1 shows a gamma spectrum of a water sample after activation.

Table 1. Element content in water samples, mg/L

| Elements | MAC, | | Analysis | Detection | | |
|----------|---------|-----------|--------------|---------------------|--------|----------|
| | mg/L | Volga | 1 stage of | 2 stage of water | method | limit, |
| | [4] | | water | purification | | mg/L |
| | - | | purification | (industrial filter) | | 35 (Va.) |
| | | | (coal) | | | |
| Si | 10 | 5.3±0.1 | 1.4±0.1 | 0.8±0.1 | GAA | 0.1 |
| Mg | 20-85 | 17.1±0.4 | 12.5±0.4 | 7.6±0.4 | GAA | 0.1 |
| Al | 0.2-0.5 | 1.02±0.07 | 0.69±0.07 | 0.19±0.07 | NAA | 0.03 |
| C1 | 350 | 2.6±0.3 | 10.7±0.3 | 1.3±0.3 | NAA | 0.1 |
| Na | 200 | 8.7±0.6 | 8.7±0.6 | 8.2±0.6 | NAA | 0.3 |

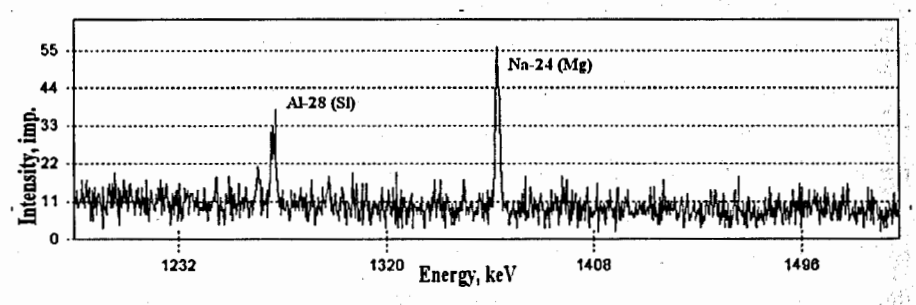


Fig.1 Gamma spectrum of the evaporated sample of water after gamma activation

On the basis of the carried out experiments, the maximum limit detection of Si - 0.1 mg/L, Mg - 0.1 mg/L (GAA), and Al - 0.03 mg/L (NAA) was evaluated. These limits are sufficient for estimation of the given elements at water quality determination.

The content of elements in the Volga water is within the limits of MAC except for aluminum, which exceeds twice the limits. The standard water treatment allows one to lower the Al content to tolerable norms. However, it can be seen from the Tables that water

treatment with coal and industrial filters reduces silicon quantity 10 times in comparison with MAC.

It should be noted as well that the water purification leads hardness salts (Ca, Mg) extraction, as a rule. The low content Ca and Mg is not always favorable for health. A number of ecological and analytic epidimeological studies have found a significant dependence between water hardness and cardiovascular disease [10].

CONCLUSION

- 1. The techniques of the analysis of Si, Mg, and Al with the use of the MT-25 microtron are developed. Si, Mg and Al were determined by the following reactions: 29 Si (γ, p) 28 Al $(T_{1/2}=2.2 \text{ min}, E_{\gamma}=1779 \text{ keV});$ 30 Si (γ, p) 29 Al $(T_{1/2}=6.6 \text{ min}, E_{\gamma}=1273 \text{ keV});$ 25 Mg (γ, p) 24 Na $(T_{1/2}=14.96 \text{ h}, E_{\gamma}=1369 \text{ keV})$ and 27 Al (n, γ) 28 Al $(T_{1/2}=2.2 \text{ min}, E_{\gamma}=1779 \text{ keV}).$
- 2. The detection limits of Si 0.1 mg/L, Mg 0.1 mg/L (GAA) and Al 0.03 mg/L (NAA) are determined. The results obtained are sufficient for estimation of the given elements at water quality determination.
- 3. The content of elements in the Volga water is within the MAC limits except for aluminium, which exceeds twice the limits, but standard water treatment allows one to lower the Al content to tolerable norms. However, the water purification with coal and industrial filters results in a 10-times reduction of silicon quantity in comparison with MAC.

REFERENCES

- Burbaeva G.S., Shevzov P.N. Aluminum as a factor affecting brain microtubule assembly in Alzheimer's disease: Abstr. 8th Sardinian Conf. Neurosci.: Anxiety and Depress.: Neurobiol., Pharmacol. And Clin., Cagliari, 24-28 May, 1995
- Rondeau, J, Commenges, D, Jacqmin-Gadda, H, and Dartigues, J. (2000). Relation between aluminum concentrations in drinking water and Alzheimer's disease: an 8-year follow-up study. // American Journal of Epidemiology, 152 (1), 55-66.
- Christopher N. Martyn, David N. Coggon, Hazel Inskip, Robert F. Lacey and Wendy F. Young Aluminum Concentrations in Drinking Water and Risk of Alzheimer's Disease // Epidemiology Vol. 8, No. 3 (May, 1997), pp. 281-286
- 4. GN 2.1.5.1315-03 Maximum permissible concentration (maximum concentration limit) of chemical substances in water of water objects for economic-drinking and cultural and household water use (in Russian) http://stroyoffis.ru/gn_gigienicesk/gn_2_1_5_1315_03/gn_2_1_5_1315_03.php

- N.I. Hodorovskaya, M.V. Sturova Research influence of concentration of silicon and phosphorus on development Diatoms microflorae basin //News of the Chelyabinsk centre of science, v. 2 (15), 2002 (in Russian) http://www.ebiblioteka.lt/resursai/Uzsienio%20 leidiniai/Celiabinsk/2002 _ 2/2002 _ 2 _ 10 _ 1.pdf
- 6. GOST 26485-85 (USSR State standard specification) Ground. Definition of exchange (mobile) aluminum (in Russian), http://www.gostedu.ru/29263.html
- 7. GOST 12697.6-77 (USSR State standard specification) Aluminum. The method of definition of silicon (in Russian) http://www.gostedu.ru/32897.html
- 8. L.V. Myshlyaeva, V.V. Krasnoschekov Analytical chemistry of silicon M.: Science, 1972, 212 (in Russian).
- 9. Water drinking. Methods of the analysis. M.: State standard specification, 1984. 282 (in Russian).
- World Health Organization (1993a). Guidelines for drinking water quality, 2nd ed. Vol.
 Recommendations. Geneva. 1994. 255

RADIOECOLOGICAL INVESTIGATION AT THE CONSTRUCTION OF «BELENE» NPP

Hr.G. Khristov¹, S. G. Marinova¹, M. V. Gustova², O. D. Maslov²

¹ Plovdiv University "Paisii Khilendarski", Plovdiv, Bulgaria

² JINR, Dubna, Russia

INTRODUCTION

Normally, when nuclear power plants (NPP) are in ordinary mode of operation, the exhausts of the radioactive elements into the environment are insignificant and, in particular, consist of radioactive iodine and cesium. Therefore, it is important to conduct preliminary measurements of soils on the territories with possible radioactive pollution, in order to find out whether there are such radioactive elements as cesium, uranium, thorium and radium. Also it is necessary to define the radioactive background in such areas in order to obtain the database for comparing data after the launching of the NPP.

For this purpose the soil samples taken from the regions of NPP «Belene», the towns of Svishtov and Belene, as well as the villages of Oresh, Dekov, Bulgaria were investigated (Fig. 1)

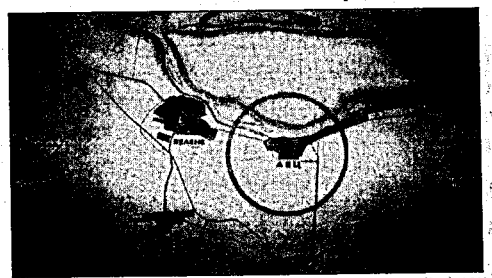


Fig. 1. The Region of NPP "Belene" and place of sampling

EXPERIMENTAL METHODS AND RESULTS

To determine the concentration of natural radioactive elements: U-238, Ra-226, Pb-210, Th-232, K-40 and anthropogenic radionuclide Cs-137 (Table 1), the semiconductor gamma-spectrometer with Ge(Li)-detector with 2,0 keV resolution for 1332 keV gamma-line of ⁶⁰Co was used.

Table 1. The concentration of radioactive elements in soil

| chitation of | Tadioactive | -1 -10 | | 55 TZ: 40 38 | C- 127 | 7.5% |
|--------------|-----------------------------|---------------------------------------------------------|------------------------------------------------------------------------------------|-------------------------------------------------------------------------------------------------------------------|---------------------------------------------------------------------------------------------------------------------------------------------------------------------------------|----------------------------------------------------------------------------------------------------------------------------------------------------------------------------------------|
| U-238 | Ra-226 | Pb-210 | 1 n-232 | K-40 | CS-13/ | , |
| Bq/kg | Bq/kg | Bq/kg | Bq/kg | Bq/kg | Bq/kg | (67) |
| 21±9 | 28±3 | <46 | 28±1 | 439±14 | 3,2±0,2 | - |
| 20±7 | 16±2 | 52±25 | 15±1 | 336±11 | 2,0±0,1 | |
| 48±10 | 45±7 | <62 | 50±1 | 546±18 | 7,9±0,3 | |
| 34±11 | 38±3 | <65 | 40±1 | 539±17 | 1,9±0,1 | 1 |
| | U-238 Bq/kg 21±9 20±7 48±10 | U-238 Ra-226 Bq/kg Bq/kg 21±9 28±3 20±7 16±2 48±10 45±7 | U-238 Ra-226 Pb-210 Bq/kg Bq/kg Bq/kg 21±9 28±3 <46 20±7 16±2 52±25 48±10 45±7 <62 | U-238 Ra-226 Pb-210 Th-232 Bq/kg Bq/kg Bq/kg Bq/kg 21±9 28±3 <46 28±1 20±7 16±2 52±25 15±1 48±10 45±7 <62 50±1 | U-238 Ra-226 Pb-210 Th-232 K-40 Bq/kg Bq/kg Bq/kg Bq/kg Bq/kg 21±9 28±3 <46 | U-238 Ra-226 Pb-210 Th-232 K-40 Cs-137 Bq/kg Bq/kg Bq/kg Bq/kg Bq/kg Bq/kg 21±9 28±3 <46 28±1 439±14 3,2±0,2 20±7 16±2 52±25 15±1 336±11 2,0±0,1 48±10 45±7 <62 50±1 546±18 7,9±0,3 |

In the Table 2 the results of measurement of the natural radiation background in the places of sampling are presented.

Table 2. The natural radiation background in the places of sampling.

| DI C | sound in the places of sampling. |
|-------------------|-------------------------------------|
| Place of sampling | Power of the equivalent dose, μSv/h |
| Svishtov | 0,16 |
| Oresh | 0,13 |
| Dekov | 0,14 |
| Belene | 0,11 |
| Average value | 0,13 |

Another important problem occurring at the NPP construction site is the activation of concrete by the neutron irradiation during reactor operation. One of the important tasks in this area is to choose such a concrete that activates less, so as to decrease the irradiation of the personnel and the pollution of the environment with radioactive wastes on terminating the exploitation of reactors.

The calculation of the concrete activation is complicated because there is insufficient data on the concentration of elements forming long-living nuclides, in particular, Eu, Co, Cs, Fe [1] (Table 3).

Table 3. Nuclear characteristics of the radionuclides

| Element | Reactions with thermal neutrons | Activation cross- section, barn | Radioactive half-life |
|---------|------------------------------------------|------------------------------------|-----------------------|
| Fe | ⁵⁸ Fe(n,g) ⁵⁹ Fe | 1,28 | 44,6 days |
| Со | ⁵⁹ Co(n,g) ⁶⁰ Co | 37,45 | 5,3 years |
| Cs | ¹³³ Cs(n,g) ¹³⁴ Cs | 29,0 | 2,06 years |
| Eu | ¹⁵¹ Eu(n,g) ¹⁵² Eu | 5939 | 13,3 years |
| Eu | ¹⁵³ Eu(n,g) ¹⁵⁴ Eu | 603 | 8,8 years |

The purpose of the present work is to experimentally determine the concentration of these and other elements in concrete samples from NPP «Belene».

Four samples of concrete from different locations of the NPP «Belene» were chosen as an investigation material. These are as follows: sample 1 — reactor building; sample 2 — location near reactor; sample 3 — diesel-generator station; sample 4 — communication channels of special enclosure.

The concentration of elements is determined by means of the RFA-analyzer with the semiconductor Si-detector in the Laboratory of nuclear reactions, JINR, Dubna. The results for 28 elements in concrete samples are presented in Table 4.

Table 4. The concentration of elements in concrete samples.

311

120

| Element | | | samples from conc | |
|---------|-----------|-----------|-------------------|-----------|
| | Sample 1 | Sample 2 | Sample 3 | Sample 4 |
| K ,% | 1.6±0.4 | 1.6±0.4 | 1.6±0.4 | 0.8±0.2 |
| Ca, % | 11±2 | 2.4±0.4 | 14±2 | 5.2±0.5% |
| Ti, % | 0.10±0.05 | 0.12±0.05 | 0.2±0.05 | 0.09±0.05 |
| Mn, % | 0.06±0.01 | 0.06±0.01 | 0.07±0.01 | 0.04±0.01 |
| Fe, % | 1.4±0.2 | 1.2±0.2 | 1.1±0.2 | 0.6±0.2 |
| Co, ppm | ≤10 | ≤10 | ≤10 | ≤11 |
| Ni, ppm | 30.0±3.0 | <24.3 | <23.8 | 40.0±3.0 |
| Cu, ppm | 70±5 | 70±4 | 60±4 | 80±5 |
| Zn, % | 0.20±0.01 | 0.04±0.01 | 0.05±0.01 | 0.19±0.01 |
| As, ppm | <21.0 | <20.3 | <10 | <10 |
| Se, ppm | 2.3±0.6 | <1.2 | 1.7±0.6 | 2.0±0.6 |
| Rb, ppm | 55±6 | 60±6 | 60±6 | 36±6 |
| Sr, ppm | 220±40 | 200±40 | 380±40 | 170±40 |
| Y, ppm | <27.1 | <29.2 | <27.9 | <28.8 |
| Zr, ppm | 600±60 | 1400±60 | 360±60 | 450±60 |
| Nb, ppm | 6±2 | 9±2 | <5.7 | <5.7 |
| Pb, ppm | 110±30 | 40±10 | 40±10 | 80±30 |
| Th, ppm | 17±5 | 21±5 | 17±5 | 17±5 |
| Cd ppm | 3.9±1.0 | 2.1±0.5 | 2.2±0.5 | 5.0±1.0 |
| Sn, ppm | 13±7 | 8±3 | 5±3 | 7±3 |
| Sb, ppm | ≤2.0 | <1.9 | <2.0 | <1.8 |
| Cs, ppm | 10±5 | 9±5 | 20±5 | 9±5 |
| Ba, ppm | 800±50 | 700±50 | 1900±100 | 700±50 |
| La, ppm | 33±5 | 27±5 | 24±5 | 25±5 |
| Ce, ppm | 54±5 | 54±5 | 47±5 | 42±5 |
| Nd, ppm | 40±5 | 30±5 | 40±5 | 40±5 |
| Eu, ppm | ≤0.5 | ≤0.5 | ≤0.5 | 1.0±0.5 |
| Ag, ppm | 1.6±0.5 | 1.4±0.5 | 1.4±0.5 | 1.7±0.5 |

BALL F

In works [2, 3] in portland cements the average concentration of Eu, Co, Cs, Fe is measured to be 2,4 ppm, 6,3 ppm, 1,2 ppm and 1,6 ppm, respectively. The obtained results for the NPP «Belene» concretes show that Eu and Fe values are lower, and Cs values are higher than in portland cements. In order to define the Co value more precisely it is necessary to carry out new investigations applying another method, for example — gamma- and/or neutron-activation analysis.

CONCLUSIONS

The obtained values of the concentration of the natural radionuclides of U-238, Ra-226, Th-232, Pb-210 and K-40 in soil from the NPP «Belene» region appear to be in the frames of average values for Bulgaria, and the value of anthropogenic radionuclide of Cs-137 is lower

than an average for Bulgaria - 25 Bq/kg [4].

The measured level of the radiation background (0,13 µSv/h) is in the frames of average values for Bulgaria [4].

The obtained results indicate the present radiation state and may serve as a basis for future comparisons at estimating the changes of ecological state of the NPP «Belene» region

The novel results were obtained on the element composition of the concretes used at NPP «Belene» construction. These results present a possibility to estimate the induced activation of concretes and the personnel and environment irradiation dose.

The authors acknowledge the financial support of the Fund of the scientific research and mobile projects at the Plovdiv University "Paisii Hilendarski", Bulgaria (Grant FF. 037/2009-2010).

REFERENCES

- 1. Lavdanski P.A., Nazarov V.M. et al. Atomic energy, vol. 64, issue 6, June 1988, pp. 419-
- 2. Lavdanski P.A., Nazarov V.M. et al. Preprint JINR, P14-88-198, Dubna, 1988.
- 3. Hristov Hr.G., Blagoeva E.I., Slaveeva S., Gustova M.V., Maslov O.D., Scientific materials of Bulgarian scientists Union, series B, vol. X, Plovdiv, 2008.
- 4. Bulletin 4, Environmental Ministry, Sofia, 2010.

TEMPORAL VARIATIONS OF 137Cs IN SURFACE AIR IN BRATISLAVA, SLOVAKIA, OVER 33 YEARS and the second of the second second of the second second second second second

Sýkora I., Povinec P., Brestakova L., Florek M., Holý K., Masarik J., Frontasyeva M.V.¹, Steinnes E.²

Dept. of Nuclear Physics and Biophysics, Faculty of Mathematic, Physics and Informatics, Comenius University, Bratislava, Slovak Republic, E-mail: sykora@fmph.uniba.sk

¹FLNP JINR, Dubna, Russian Federation,

²Norwegian University of Science and Technology, NO-7491 Trondheim, Norway The first of the control of the cont

Abstract. The objective of this study is to evaluate the changes in surface atmospheric distribution of 137Cs before and after the Chernobyl accident. Measurements of 137Cs in the air carried out in Bratislava, Slovak Republic, from 1977 until 2010 years show that the main source of 137Cs surface air activity is the residue of the global fallout from the atmospheric nuclear weapon tests. From these measurements it follows that the decrease of 137Cs concentration in air has an exponential dependence with the ecological half-life $\tau = 59.1$ months, except for a significant increase in activity level during the years 1986-1988 due to the Chernobyl accident. At present the level of airborne 137 Cs activity is about $0.3~\mu Bq/m^3$. It appears that the decreasing trend (with ecological half-life) has stopped after the year 2008, and a shift of the 137Cs concentration peak from summer to winter season is observed. This effect may be associated with transfer of radiocaesium from soil to vegetation and subsequent burning of biomass, or with soil resuspension.

Keywords: 137Cs in surface air, Long-term variation, seasonal variation, Chernobyl fallout; nuclear weapons fallout and the state of t

Introduction

The radionuclide ¹³⁷Cs is released to the environment by several types of nuclear activities including testing of nuclear weapons and accidents in nuclear facilities, operation of nuclear power reactors, and reprocessing of spent nuclear fuel. The 137Cs release into atmosphere is a result of nuclear fission, and it can be considered as one of the most hazardous radionuclides in the environment. It has a high fission yield, long physical half-life (30.07 years), high solubility and physico-chemical properties similar to potassium.

The testing of nuclear weapons in the atmosphere involved unrestrained releases of radioactive materials directly to the environment. During atmospheric nuclear bomb testing ¹³⁷Cs was released in the stratosphere. Approximately 10 PBq (1 PBq=10¹⁵ Bq) of ¹³⁷Cs, was injected in the stratosphere (UNSCEAR, 1982) from past tests. A major part of the emissions

The state of the state of the state of the state of the state of the state of the state of the state of the state of the state of the state of the state of the state of the state of the state of the state of the state of the state of the state of the state of the state of the state of the state of the state of the state of the state of the state of the state of the state of the state of the state of the state of the state of the state of the state of the state of the state of the state of the state of the state of the state of the state of the state of the state of the state of the state of the state of the state of the state of the state of the state of the state of the state of the state of the state of the state of the state of the state of the state of the state of the state of the state of the state of the state of the state of the state of the state of the state of the state of the state of the state of the state of the state of the state of the state of the state of the state of the state of the state of the state of the state of the state of the state of the state of the state of the state of the state of the state of the state of the state of the state of the state of the state of the state of the state of the state of the state of the state of the state of the state of the state of the state of the state of the state of the state of the state of the state of the state of the state of the state of the state of the state of the state of the state of the state of the state of the state of the state of the state of the state of the state of the state of the state of the state of the state of the state of the state of the state of the state of the state of the state of the state of the state of the state of the state of the state of the state of the state of the state of the state of the state of the state of the state of the state of the state of the state of the state of the state of the state of the state of the state of the state of the state of the state of the state of the state of the state of the s

(~60%) took place during the period 1961–1962. One may expect that the peak concentration of ¹³⁷Cs in surface air from nuclear bomb tests was observed in 1963 when the radioactive fission products from the explosions began to fall down from the stratospheric reservoir into ground surface atmosphere.

By exchange processes ¹³⁷Cs was transported to the troposphere and further as fallow to the Earth surface. After the end of the atmospheric nuclear weapon tests in 1963 (thermonuclear explosions in the atmosphere were completely terminated in 1980), the content of this radionuclide in the environmental reservoirs gradually decreased. Until the Chernobyl event on 26 April 1986, surface air activity of ¹³⁷Cs occurred mostly as a result of global fallout from atmospheric nuclear weapons tests. The Chernobyl event was restricted in space and time. The radionuclide releases from the damaged reactor occurred mainly over a 10-day period (United Nations, 1994). Totally 77 PBq of 137Cs entered the atmosphere within a few days following the accident. The localized fallout from the event covers large areas of Europe, including Slovakia. According to the assessment of the Russian National Report prepared by the Institute of Nuclear Energy Safety, Moscow, 0.18 PBq of ¹³⁷Cs was deposited to the territory of Slovakia, which is 0.28% of the total deposition in Europe (Shoigu et al., 2008). The distribution of deposition was non-even. Based on measuremenst of ¹³⁷Cs activity over the whole territory of Slovakia from 1990 till 2003 by means of ground gammaspectrometers and atmospheric aerosols sampling equipment it was established (Gluch, 2006) that the generally highest values (> 3000 Bq/m²) were observed in the areas with altitude exceeding 800 m (The HighTatras, The Low Tatras, Štavnica vrchy). The maximum measured values occurred in the vicinity of the towns Banska Štiavnica (18000 Bq.m-2) and Novy Tekov (28700 Bq.m⁻²). In the vicinity of Bratislava the activity was in the range of 1500-1800 Bq/m² (with reference to 1.1.2005).

Systematic monitoring of airborne ¹³⁷Cs activity has been done by the Department of Nuclear Physics and Biophysics of the Comenius University in Slovakia over the periods 1977–1987 and 2002–2010. In the atmosphere the concentrations of ¹³⁷Cs (together with ⁷Be, ⁴⁰K and ²¹⁰Pb, were measured in industrial city of Bratislava. Bratislava (with 0.5 million inhabitants) is situated near borders with Hungary, Austria and Czech Republic and at a distance of 1000 km from the Chernobyl Power Plant, where the 1986 accident occurred.

Material and Methods

Aerosol particles in the atmosphere were collected using aerosol filters SYMPOR 3 (1977-1988) and nitro-cellulose filters (2002-2010), both with a collection efficiency of approximately 100 %. The sampling location was at the Meteorological Station near the Faculty of Mathematics, Physics and Informatics (FMPI), Comenius University, Bratislava (48° 9′ N, 17° 7′ E, 164 m a.s.l.). Using a sampler device with an air-flow rate of 30 m³.h¹ aerosol particles were collected on the nitro-cellulose membrane filters (PRAGOPOR, pore size 0.85 μm, the collection efficiency approximately 100 %). The sampler device is situated at height of 2.85 m above ground at the Meteorological Station near the FMPI. The filters are

changed every week and about 3000 m³ of air is pumped through each sample. In September 2004 the new sampling device was launched and the volume of pumped air increased twofold.

Gamma spectrometry on the air-filter samples was performed in the low-level background counting laboratory of the Department of Nuclear Physics and Biophysics of the Comenius University in Bratislava, Slovakia, using a ORTEC HPGe detector with Be window and Canberra HPGe detector (177 cm³) with a carbon window, placed in a low-level background shield. The measuring time was 24 hours or more. The peaks corresponding to the 46.5 keV, 477 keV, 662 keV and 1461 keV gamma rays of ²¹⁰Pb, ⁷Be, ¹³⁷Cs and ⁴⁰K, respectively, were recorded for activity determination. The uncertainty in the results was mainly due to counting statistics, which was normally 3% or better. The count-rates in the full-energy peaks were corrected for the background of the measurement system and for self-absorption. The detection efficiency for the sample geometry was evaluated from a Monte Carlo model using the GEANT 3 code.

In our department concentration of ¹³⁷Cs was measured from July 01, 1977 (*Povinec et al., 1988*) up to present, regrettably with an interval from August 1, 1988 until January 1, 2002. During the years 1993 - 2000 regular collection of aerosol samples for routine environmental air monitoring was carried out in six measuring points within the Radiation Monitoring Network of Slovak Republik (*Cabanekova, 1998; Cabanekova and Gomola, 2001*).

Result and discussion

dill.

a. Long-term variations

The overall results of the air-particulate monitoring for ¹³⁷Cs is shown in Figure 1 and covers a period from July 01, 1977 (*Povinec et al., 1988*) up to present. In addition to our date we included averaged values from 1993-2000 in the six measuring points used by The Radiation Monitoring Network of Slovak Republic (*Cabanekova, Vladar, 1998, Cabanekova, Gomola, 2001*).

In Bratislava the annual average activity of 137 Cs in surface air decreased regularly from 130 μ Bq/m³ in 1977 down to 0.3 μ Bq/m³ in 2009, except for a significant increase during the years 1986–1987 due to the Chernobyl accident.

From these measurements it appears that the decrease in concentration of 137 Cs in air follows an exponential trend according to the following equation $A = 130 \exp (-0.0169 t)$, if t is expressed in months after 1.01.1977. The apparent ecological mean life-time is 59.1 months (the corresponding half-life time is around 41 months).

Before the Chernobyl accident, the concentration of 137 Cs decreased with approximately the same effective life-time as after 1993 (Fig. 1). In 1983 it varied within the range 20–30 μ Bq/m³. Measurements performed in Sweden (*Kulan*, 2006) gave a value of 28.8 μ Bq/m³ during the period August 1972 - December 1985, close to the present data.

In Slovakia the maximum air concentration of ¹³⁷Cs from the Chernobyl accident at the ground level was registered on May 1, 1986. Monthly averaged concentration for May 1986 was 14500 µBq/m³ (*Povinec et al., 1988*). Then it decreased with an ecological life-time of 2.8 months (half-time 1.93 month). At the end of 1987 it approached again the level determined by the previous recorded decline in global fallout (see inserted picture in Fig. 1).

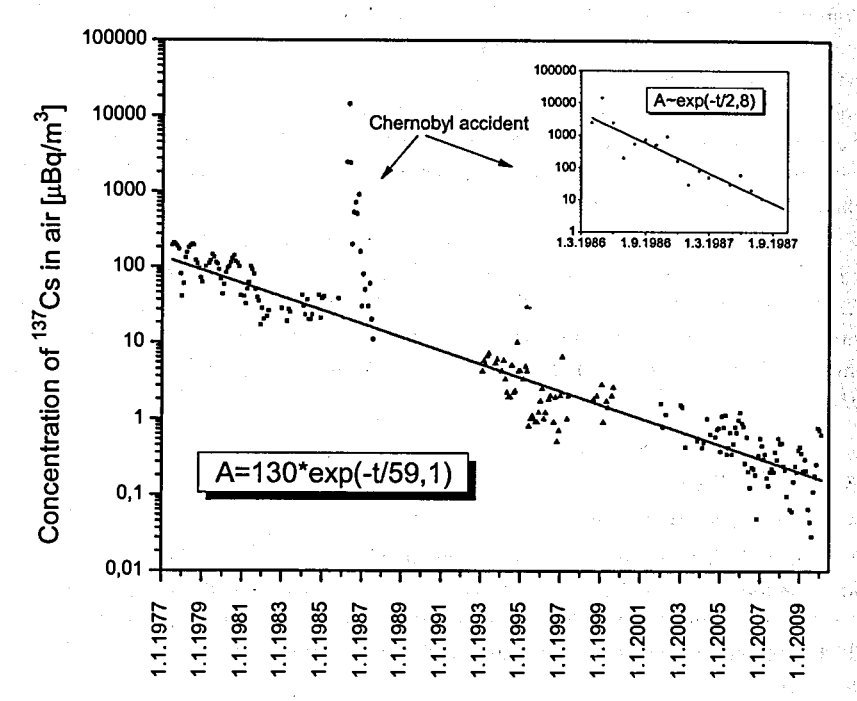


Fig.1. Long-term variation of ¹³⁷Cs in surface air in Bratislava, based on monthly mean values. Inserted picture is monthly average values during 1986–1987. The time t in the formula is in months.

The most active years of testing from the standpoint of the total explosive yields were in 1961–1962. Subsequently, the maximum concentration of 137 Cs in surface air was observed in 1963 (Makhonko, Kim, 2002). They obtained a value of 2450 μ Bq/m³ as a weighted mean over 89 sites used to monitor radioactive aerosols localized in the territory of the former USSR. If to extrapolate our data back to 1963, the concentration of 137 Cs in the vicinity of Bratislava was 2220 μ Bq/m³ at that time.

The trend of decreasing volume activity of ¹³⁷Cs in air appears to cease after the year of 2007 (Fig. 2). This indicates that the current main source of atmospheric ¹³⁷Cs in Slovakia is different from the previous period. As demonstrated by analysis of moss samples

(Aleksiayenak et al., 2011) there is still a considerable residual ¹³⁷Cs activity level in terrestrial surfaces affected by fallout from the Chernobyl accident, and it is conceivable that release of particulate material from these surfaces could be a main source of the current level of ¹³⁷Cs in air in Slovakia.

b. Seasonal variations

In recent years, in contrast to the period 1977–1980, we observe a shift of maximum concentration of ¹³⁷Cs from summer season to winter season (Fig. 2). This is another indication of a change of source distribution of ¹³⁷Cs in air.

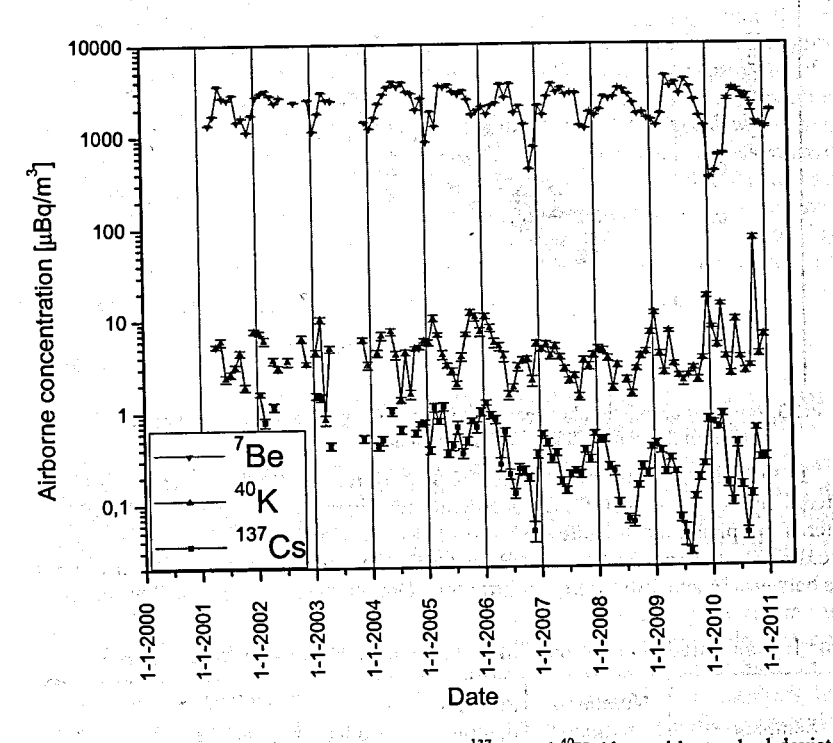


Fig.2. Seasonal variation airborne concentration of ¹³⁷Cs and ⁴⁰K (date with standard deviation) in air in Bratislava over the last years. For comparison the seasonal variations of ⁷Be concentrations are shown.

The seasonal variation of 137 Cs activity concentration in surface air correlates well (R = 0.78) with that of 40 K (Fig. 3). This has been expected as both the source-term (a resuspension from soil) and behavior are similar. We included in this evaluation only the data for the 2007-2010 period, as we assumed that the change in 137 Cs activity concentration in the atmosphere ceased in 2007. The average 40 K and 137 Cs activity concentrations for this period are 4.4 μ Bq m⁻³ and 0.3 μ Bq m⁻³, respectively (the 137 Cs/ 40 K activity ratio is 0.069).

of Slovakia in 2001 and 2002 varied within the range of 0.4–3.5 Bq kg⁻¹ (mean value 1.73 Bq kg⁻¹) and 173–365 Bq kg⁻¹ (mean value 230 Bq/kg), respectively, Table 1. However, ¹³⁷Cs activities in conifer needles were below a detection limit. This would indicate that a root uptake of ¹³⁷Cs by plants could be a dominant process. The concentration of stable K and Cs were determined in Frank Laboratory of Neutron Physics, JINR, at reactor IBR-2 using INAA method.

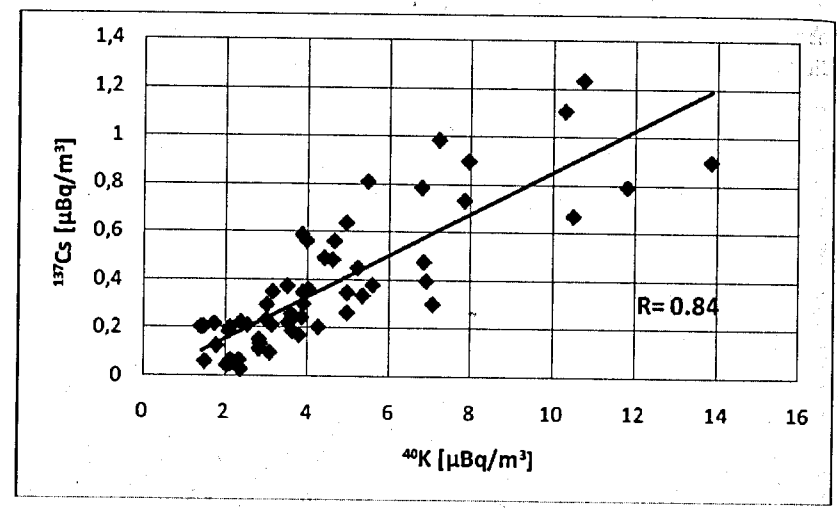


Fig.3. A plot of correlation between activity of ¹³⁷Cs and ⁴⁰K in surface air (Bratislava). Only data from the period 2007-2010 are included.

In the foliage samples the ¹³⁷Cs/⁴⁰K activity ratio is 0.01. Higher ratios (0.064) were registered by Ko et al. (2002) in broadleaf tree litter. Even higher levels of ¹³⁷Cs were registered in piedmont broadleaved forests Malyi Utrish (44⁰44'N, 37⁰26'E) in Russia (approximately the same latitude as Bratislava). Pokarzhevskii et al. (2003) reported ¹³⁷Cs levels between 76 and 140 Bq kg⁻¹ in litter found below oak, hornbeam and beech trees.

Table 1. Concentration of radionuclides in Slovakian samples of foliages, needles and moss.

| | | | - | • | | | |
|----------------------|-------------------|--------------------|---------------------------|---------------------|-----------------------------|--|--|
| Samples | Number of samples | Stable K, mg/kg | ⁴⁰ K, Bq/kg | Stable Cs, mg/kg | ¹³⁷ Cs, Bq/kg | | |
| Foliage (oak, beech) | 25 | 9840 | 230 | 0.044 | 1,77 | | |
| Spruce needles | 2 | 6360 | 120 | 0.22 | <0,2 (DL) | | |
| Moss | 11 | 7080 | 138 | 0.41 | 30 | | |

Possible reasons of increased atmospheric ¹³⁷Cs levels during the autumn-winter season may be due to:

- (i) surface soil resuspension and transport of released ¹³⁷Cs by winds, particularly from open agricultural areas;
- (ii) releases of decomposed plant materials by wind erosion;
- (iii) burning of biomass (Bourcier et al., 2010);
- (iv) specific meteorological conditions during winter with temperature gradient inversions (Povinec et al., 2011).

All these mechanisms could contribute significantly to the observed recent changes in the seasonality of ¹³⁷Cs in Slovakia, where the alternation of annual seasons is regular, and the period of snow cover is insignificant. Bratislava with 0.5 million of inhabitants is also a large industrial zone where specific meteorological conditions during winter prevent dispersion of pollutants from the town, as documented by ¹⁴CO₂ observations in the ground-level air (Povinec et al., 2011). The fact that the ¹³⁷Cs/⁴⁰K ratio observed in aerosols (cf. Fig. 3) exceeds recent values observed in vegetation may indicate that soil resuspension is responsible for at least part of the increased ¹³⁷Cs activity observed during the winter season. The mean ¹³⁷Cs (15 Bq kg⁻¹) and ⁴⁰K (300) levels observed in soil around Bratislava gave for the ¹³⁷Cs/⁴⁰K activity ratio a mean value of 0.05, which is closer to the value for the surface air (0.07) than for the tree leaves (0.01). A few single ¹³⁷Cs peaks observed in one-two months (Fig. 2) may indicate contributions either from biomass burning of highly contaminated areas in the Eastern Europe (Povinec et al., 2011), or from Saharan dust events (Pham et al., 2005).

Conclusions

Sources and variations of ¹³⁷Cs and ⁴⁰K in the ground-level air of Bratislava have been compared and discussed. The main findings of the paper may be summarised as follows:

- The ¹³⁷Cs activity concentration in the surface air between 1977 and 2010 has been decreasing with an ecological half-life of 3.4 years (high values observed during 1986 and 1987 due to the Chernobyl accident were excluded from the evaluation). However, during 2007-2010 the yearly averaged ¹³⁷Cs activity concentrations were almost the same.
- (ii) The increased atmospheric ¹³⁷Cs and ⁴⁰K levels observed during the autumn-winter season may be due to surface soil resuspension and radionuclide transport by winds, particularly from open agricultural areas (also confirmed by high correlation coefficient, R = 0.84, between the ¹³⁷Cs and ⁴⁰K atmospheric levels). Decomposed plant materials, biomass burning and specific meteorological conditions during winter with temperature gradient inversions could also contribute to higher ¹³⁷Cs and ⁴⁰K levels observed during the autumn and winter months.
 - ii) The ¹³⁷Cs/⁴⁰K activity ratio for the surface air (0.07) is closer to the mean value observed in soil (0.05) than to the mean value for the tree leaves (0.01), what would also indicate a predominance of soil resuspension processes on the atmospheric concentrations of these radionuclides during the winter season.

Acknowledgment

This study was supported by Scientific Grant Agency of Ministry of Education of Slovak Republic (VEGA project 1/0678/09), Slovak grant agency APVV (grant number APVV-0420-10), by the Structural Funds of the EU (project OPVaV-2008-26240220004), aw well as by grant of the Plenipotentiary of the Slovak Republic at the Joint Institute for Nuclear Research, Dubna (2011).

References

- Aleksiayenak Yu. V, M.V. Frontasyeva, M. Florek, I. Sykora, K. Holy, J. Masarik, L. Brestakova, M. Jeskovsky, E. Steinnes, A. Faanhof, K. I. Ramatlhape.(2011) Distributions of ¹³⁷Cs and ²¹⁰Pb in moss collected from Belarus and Slovakia. Journal of Radioactivity Environment (in press).
- Bourcier, L., Sellegri, K., O. Masson, R. Zangrando, C. Barbante, A. Gambaro, J.-M. Pichon, J. Boulon and P. Laj, (2010), Experimental evidence of biomass burning as a source of atmospheric ¹³⁷Cs, puy de Dôme (1465 m a.s.l.), France, Atmos. Environ. 44, pp. 2280-2286.
- Cabáneková H., Vladár M., 1998, The monitoring of Air Contamination in the Territory of Slovak Republic. *Journal of Radioecology*, 6 (1998) pp. 3-8.
- Cabaneková H., Gomola I., 2001, Report on radiation situation in the Slovak Republik in 2001, INIS, IAEA, Vienna.
- Environmental Consequences of the Chernobyl Accident and their Remediation: Twenty Years of Experience. Report of the UN Chernobyl Forum Expert Group "Environment" Radiological Assessment Reports, IAEA, Vienna, 2006
- Gluch A., Smolárová H., Čížek P., (2005) Final Report: Reambulácia máp rádioaktivity 137Cs územia Slovenska v mierkach 1: 200 000 a 1: 500 000, Ministry of Environment of The Slovak Republic, State Geological Institute of Dionyz Stur.
- Ko S., T. Aoki, H. Ohnishi, J. Takada, Y. Katayama, Distribution and circulation of radionuclides originating from fallout in a forest. Journal of Radioanalytical and Nuclear Chemistry, Vol. 255, No. 2 (2003) 347-349
- Kulan A., 2006, Seasonal ⁷Be and ¹³⁷Cs activities in surface air before and after the Chemobyl event. *Journal of Environmental Radioactivity* 90 140-150.
- Pham, M.K. La Rosa, J.J., Lee, S.-H., Oregioni, B., Povinec P.P., 2005. Deposition of Saharan dust in Monaco rain 2001-2002: Radionuclides and elemental composition. Physica Scripta 71, 14-17.
- Povinec P., Chudy M., Sýkora I., Szarka J., Pikna M., Holý K., 1988, Aerosol radioactivity monitoring in Bratislava following the Chemobyl accident. J. Radioanal. Nucl. Chem., Letters 126/6/ 467-478.
- Povinec, P.P., Holý, K., Chudý M., Šivo A., Sýkora I., Ješkovský M., Richtáriková M., 2011. Long-term variations of ¹⁴C and ¹³⁷Cs in the Bratislava air implications of different atmospheric transport processes, J. Environmental Radioactivity (in press).

- Pokarzhevskii A. D., Uspenskaya E. Yu., Filimonova Zh. V., Global Radioactive Contamination Background in Terrestrial Ecosystems 13 Years after the Chemobyl Accident Russian Journal of Ecology, Vol. 34, No. 2, 2003, pp. 73–79. (Translated from Ekologiya, No. 2, 2003, pp. 83–89).
- Shoigu S. K. Bolshov L. A., 2008, 20-years of the Chernobyl Accident. The Russian National Report, Institute of Nuclear Energy Safety, Moscow (in Russian). http://www.ibrae.ac.ru/content/view/180/231/
- Makhon'ko K. P., Kim V., 2002 M. Dynamics of Air, Soil, and Water Contamination by Technogenic Radionuclides at the Territory of the USSR and Russia in 1954–2000 Atomic Energy, Vol. 92, No. 5. 2002, p. c. 387-395
- UNSCEAR Report, 1982. Ionizing Radiation: Sources and Biological Effects. United Nations, New York.
- United Nations "Sources and Effects of Ionizing Radiation United Nations Scientific Committee on the Effects of Atomic Radiation", 1994 Report to the General Assembly, with scientific annexes. United Nations sales publication E.94.IX.11. United Nations, New York, 1994.

was the first starting of the best first than the first than the first than the same of the same first

Charge of the Spatiage of the Book Spatial Self Control

্বত্ব হয় বিষয়ে প্ৰত্যুত্ত কৰা কৰা কৰিছিল কৰিছিল কৰা কৰিছিল কৰিছিল কৰিছিল কৰিছিল কৰিছিল কৰিছিল কৰিছিল কৰিছিল

र राज्य के अपने के प्राप्त के अपने के अनुसार के स्वरूप के अधिक के कि इस के किसी है कि है। अपने की अधिक की अधिक इस समामान

ละสังสาราวิทยา (1.10 การวัดเกิดเการ์ (1.50 การสามารถสมารถสิทยาลาริสติตตารสารสารสารสา

ा है। है है अपने क्षेत्र के अपने कार्य कर है। इस के किया किया किया के अपने किया है

ार पहल है है। है के किस के किस में के किस के कि

NEUTRON ACTIVATION ANALYSIS OF Ca, Cl, Mg, Na, AND P CONTENTS IN THE HUMAN OSTEOGENIC SARCOMA

S. Zaichick^{1,2}, V. Zaichick¹

¹ Medical Radiological Research Centre of RAMS, Koroleva str., 4, Obninsk, 249020, Russia, e-mail: <u>vezai@ob</u>ninsk.com

di.

² Current address: Northwestern University, Chicago, IL, 60611, USA

Introduction

Bone tumors are a heterogeneous group of tumors that all arise from bone tissue, which consists of cartilaginous, osteoid and fibrous tissue, and bone marrow elements. Each tissue can give rise to benign or malignant tumors. The differentiation of benign and malignant intraosseous lesions can often be accomplished by means of conventional roentgenology, CT, and MRI. All of these methods of introscopy are very important, particularly for the assessment of tumor location, form, size, and infiltration of the adjacent tissue. However, the radiographic appearance of many lesions is indeterminate, and final diagnosis must be achieved using biopsy and histopathologic evaluation.

It is well known that tissues of human body differ greatly in their contents of chemical elements. Thus, it can be expected that bone tumors of a different origin would have specific elemental composition. In vivo neutron activation analysis (in vivo NAA) allows determination of some chemical element contents (Ca, Cl, and Na) in tumor tissue and has a potential to become a useful tool in oncology diagnostics [1,2].

To our knowledge, no data are available about the chemical element contents of bone tumors with respect to different origin of disease. Therefore, we determined the Ca, Cl, Mg, Na, and P contents in the osteogenic sarcoma and intact bone tissue using instrumental neutron-activation analysis with high resolution spectrometry of short-lived radionuclides (INAA-SLR).

Experimental

Samples of osteogenic sarcoma tissue were obtained from 61 patients (18 females and 43 males from 6 to 71 years old). All patients were hospitalized at the Medical Radiological Research Centre. In all cases the diagnosis has been confirmed by clinical and morphological data. The tumor samples for NAA were received from biopsy and resected specimens. The control group consisted of 27 patients with intact bone (7 females and 20 males from 6 to 50 years old) who died from different deceases. The intact cortical bone samples of femur and tibia were collected at the Department of Pathology, Obninsk City Hospital. All bone samples were freeze dried until constant mass was obtained. Then samples were sealed separately in thin polyethylene films washed with acetone and rectified alcohol. The sealed samples were placed in labeled polyethylene ampoules.

To determine contents of the elements by comparison with a known standard, biological synthetic standards (BSS) prepared from phenol-formaldehyde resins were used [3]. Corrected certified values of BSS element contents were reported by us before [4]. In addition to BSS, aliquots of commercial, chemically pure compounds were also used as standards. Ten certified reference material CRM IAEA H-5 (Animal Bone) and standard reference material SRM NIST 1486 (Bone Meal) sub-samples weighing about 50–100 mg were analyzed in the same conditions as bone samples to estimate the precision and accuracy of results.

The contents of Ca, Cl, Mg, Na, and P were determined by INAA-SLR using a horizontal channel equipped with the pneumatic rabbit system of the WWR-c research nuclear reactor. The neutron flux in the channel was 1.7×10^{13} n cm⁻² s⁻¹. Ampoules with bone samples, BSS, intralaboratory-made standards, CRM and SRM were put into polyethylene rabbits and then irradiated separately for 60 s. Copper foils were used to assess neutron flux. The measurement of each sample was made 1 min after irradiation. The duration of the measurements was 10 min. A coaxial 98 cm³ Ge (Li) detector and a spectrometric unit (NUC 8100), including a PC-coupled multichannel analyzer, were used for measurements. The spectrometric unit provided 2.9 keV resolution at the ⁶⁰Co 1332 keV line. The information of used nuclear reactions, radionuclides, gamma-energies, and other details of the analysis including the quality control of results were reported by us before [5].

A dedicated computer program of NAA mode optimization was used [6]. Using standard programs, the summary of statistics, arithmetic mean, standard deviation, standard error of mean, minimum and maximum values, median, percentiles with 0.025 and 0.975 levels were calculated for different chemical element mass fractions. The reliability of difference in the results between intact bone and osteogenic sarcoma tissue was evaluated by Student's t-test.

Results and discussion

Table 1 represents certain statistical parameters (arithmetic mean, standard deviation, standard error of mean, minimal and maximal values, median, percentiles with 0.025 and 0.975 levels) of the Ca, Cl, Mg, Na, and P mass fractions in intact cortical bone samples and osteogenic sarcoma tissue.

The information of the effect of cancerous transformation on the chemical element contents in bone tissue is presented in Table 2. From Tables 2, it is observed that in osteogenic sarcoma tissue the mass fractions of Cl and Na are higher $(p \le 0.001)$ and the mass fraction of Ca is lower $(p \le 0.001)$ than in normal tissues. Different directions of changes suggest potential of mass fraction ratios of these elements as osteogenic sarcoma markers.

Table 3 depicts our data for some ratios of Ca, Cl, Mg, Na, and P mass fractions in intact cortical bone samples and osteogenic sarcoma tissue. It was shown that higher Cl/Ca and Cl/Na mass fraction ratios as well as lower Ca/P, Ca/Mg, and Ca/Na mass fraction ratios were typical of osteogenic sarcoma tissue compared with intact cortical bone (Table 3).

Fig.1 shows the histograms of Ca/Na, Cl/Ca, and Cl/Na ratios in all samples of intact bone (1) and osteogenic sarcoma tissue (2). Ca/Na, Cl/Ca, and Cl/Na ratios were chosen among others because it is possible to determine these ratios by *in vivo* NAA [1]. Using ratios of chemical elements mass fractions instead of the absolute values of mass fraction is better for making a specific diagnosis because of at least two reasons: 1) relations of elements do not depend on the moisture content (water) in the tissue; 2) defining relations of elements is more convenient for *in vivo* analysis.

Table 1. Some statistical parameters of Ca, Cl, Mg, Na, and P mass fractions in intact cortical bone and osteogenic sarcoma tissue (g·kg⁻¹ dry weight basis)

| Tissue | Element | M | SD | SEM | Min | | 16.1 | - DO 00.5 | |
|------------|---------|------|------|------|-------|------|------|-----------|--------|
| | | | | | | Max | Med | P0.025 | P0.975 |
| Intact | Ca | 222 | 43.6 | 9.3 | 166 | 369 | 212 | 174 | 317 |
| cortical | Cl , | 1.52 | 1.42 | 0.30 | 0.40 | 6.80 | 1.10 | 0.455 | 5.04 |
| bone | Mg | 2.94 | 0.79 | 0.17 | 0.90 | 5.04 | 3.00 | 1.51 | 4.36 |
| n=27 | Na | 6.40 | 1.74 | 0.36 | 3.80 | 11.7 | 6.00 | 4.41 | 10.9 |
| | P | 112 | 29.5 | 6.1 | 66.0 | 174 | 107 | 66.1 | 168 |
| Osteogenic | Ca | 136 | 70 | 10 | 20.4 | 287 | 141 | 22.4 | 279 |
| sarcoma | Cl | 8.68 | 6.81 | 0.99 | 1.60 | 35.4 | 6.60 | 1.73 | 28.8 |
| n=61 | Mg | 2.84 | 1.14 | 0.17 | 0.298 | 5.10 | 2.55 | 1.30 | 4.89 |
| | Na | 8.73 | 3.43 | 0.51 | 2.90 | 15.5 | 8.30 | 3.40 | 15.3 |
| | P | 117 | . 57 | 8.5 | 34 | 306 | 103 | 40.0 | 202 |

M - arithmetic mean; SD - standard deviation; SEM - standard error of mean; Min - minimum value; Max - maximum value; Per. 0.025 - percentile with 0.025 level; Per. 0.975 - percentile with 0.975 level

Table 2. Comparison between mean values (M±SEM) of Ca, Cl, Mg, Na, and P mass fraction in intact cortical bone and osteogenic sarcoma tissue (g·kg⁻¹, dry weight basis)

| | Element | Intact cortical bone (I) | Osteogenic sarcoma (II) | Ratio II to I |
|----------|----------|--------------------------|-------------------------|----------------------|
| | <u> </u> | n=27 | n=61 | p (Student's t-test) |
| Ca | | 222±9 | 137±10 | 0.62° |
| Cl | | 1.52±0.30 | 8.7±1.0 | 5.72° |
| Mg | * | 2.45±0.37 | 2.9±0.2 | 1.18 |
| Na | | 6.40±0.36 | 8.7±0.5 | 1.36° |
| <u>P</u> | | 112±6 | 117±9 | 1.04 |

M - arithmetic mean, SEM - standard error of mean, n - number of samples, $^{c} - p \le 0.001$

Table 3. Comparison between mean values (M±SEM) of Ca/P, Ca/Mg, Ca/Na, Cl/Ca, and Cl/Na mass fraction ratios in intact cortical bone and osteogenic sarcoma tissue

| Element | Intact cortical bone (I) n=27 | Osteogenic sarcoma (II) n=61 | Ratio II to I p (Student's t-test) | | |
|--------------|----------------------------------|---------------------------------|------------------------------------|--|--|
| Ca/P | 2.06±0.07 | 1.31±0.09 | 0.64° | | |
| (Ca/Mg)·0.01 | 0.81±0.07 | 0.49±0.03 | 0.60° | | |
| (Ca/Na) 0.01 | 0.36±0.02 | 0.20±0.02 | 0.56° | | |
| (Cl/Ca)·100 | 0.59±0.10 | 14±4 | 23.7 ^b | | |
| Cl/Na | 0.22±0.03 | 0.84±0.04 | 3.82° | | |

M - arithmetic mean, SEM - standard error of mean, n - number of samples, $^{b}-p \le 0.01, ^{c}-p \le 0.001$

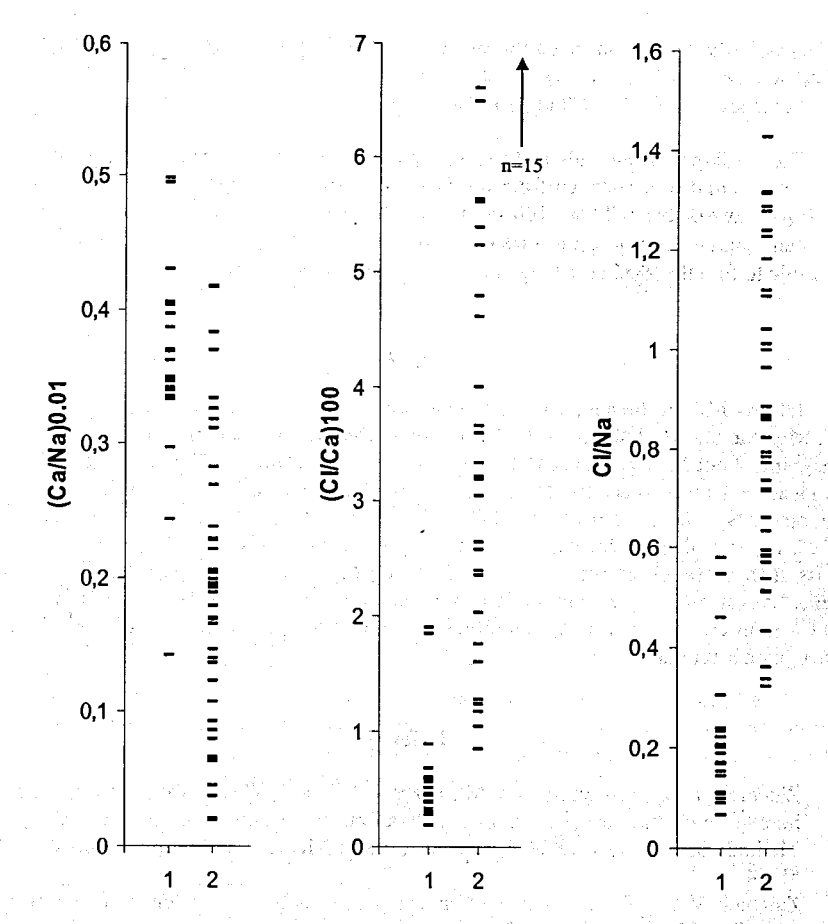


Fig. 1. Histograms of Ca/Na, Cl/Ca, and Cl/Na ratios in all samples of intact bone (1) and osteogenic sarcoma tissue (2)

As evident from the histograms, the Cl/Ca ration is the most information for the differential diagnostics. If (Cl/Ca)×100 ratio level of 1.0 (M±SD) was assumed to be an upper limit of intact bone tissue (Fig.1), the results of estimation "osteogenic sarcoma or intact bone" are the following:

Sensitivity = {correct positive test (CPT)/[CPT + false negative test (FNT)]} \times 100% = 98 \pm 2%;

Specificity = {correct negative test (CNT)/[CNT + false positive test (FPT)]} $\times 100\%$ $= 92\pm 5\%$;

Accuracy = $[(CPT+CNT)/(CPT+FNT+CNT+FPT)] \times 100\% = 96\pm2\%$.

The confidential intervals of these calculations with taking account of the number of the examined samples were taken from the Statistical tables by Genes [7]. In other words, if the analysis showed that (Cl/Ca)×100 ratio does not below 1.0 in tissue of bone examined site, one can diagnose a osteogenic sarcoma with accuracy of 96±2%. Using Cl/Ca -test makes it possible to find the 98±2% osteogenic sarcoma cases (sensitivity).

Conclusions

INAA- SLR is the adequate analytical tools for the non-destructive determination of Ca, Cl, Mg, Na, and P contents in the human bone samples and samples of intraosseous lesions weighing about 50 mg. It needs no more than 15 min (1 min irradiation by neutrons + 1 min exposure + 10 min spectrometric measurement) for analysis. It was found that in osteogenic sarcoma tissue the mass fractions of Cl and Na are significantly higher and the mass fraction of Ca is lower than in normal tissues. Moreover, it was shown that higher Cl/Ca and Cl/Na mass fraction ratios as well as lower Ca/P, Ca/Mg, and Ca/Na mass fraction ratios were typical of osteogenic sarcoma tissue compared with intact cortical bone. Differences between Cl/Ca ratio can be used as an additional test for differential diagnosis of normal bone and osteogenic sarcoma.

References

- Zaichick V.Ye., Kalashnikov V.M., Bizer V.A. The *in vivo* analysis of Ca, Na and Cl in human limb tumours by neutron activation. In: Application of Nuclear Analytical Methods in Biology and Medicine, Institute of Medical Radiology, Obninsk, 1980, pp. 58-74.
- Zaichick V.Ye. The *in vivo* neutron activation analysis of calcium in the skeleton of normal subjects, with hypokinesia and bone diseases. J. Radioanal. Nucl. Chem., Articles, 1993, 169, 307-316.
- 3. Mosulishvili L., Kolomiitsev M., Dundua V., Shonia N., Danilova O. Multi-element standards for instrumental neutron activation analysis of biological materials. J. Radioanal. Chem., 1975, 26, 175-188.
- 4. Zaichick V. Application of synthetic reference materials in the Medical Radiological Research Centre. Fresenius J. Anal. Chem., 1995, 352, 219-223.
- Zaichick V., Dyatlov A., Zaihick S. INAA application in the age dynamics assessment of maijor, minor, and trace elements in the human rib. J. Radioanal. Nucl. Chem., 2000, 244, 189-193.
- Korelo A.M., Zaichick V. (1993) Software to optimize the multielement INAA of medical and environmental samples. In: Activation Analysis in Environment Protection. Join Institute of Nuclear Research, Dubna, pp. 326-332
- Genes V.S. Simple methods for cybernetic data treatment of diagnostic and physiological studies. Nauka. Moscow. 1967.

RELATIONSHIP BETWEEN Ca, Cl, K, Mg, Mn, Na, P, AND Sr CONTENTS IN THE HUMAN RIB BONE INVESTIGATED BY NEUTRON ACTIVATION ANALYSIS

S. Zaichick^{1,2}, V. Zaichick¹

¹ Medical Radiological Research Centre of RAMS; Koroleva str., 4, Obninsk, 249020, Russia, e-mail: <u>vezai@obninsk.com</u>

² Current address: Northwestern University, Chicago, IL, 60611, USA

Introduction and the second of
and the control of th

างการการการการการการและทำว่าการการคลูกกระที่เกิด

og production and the contract of the second behind

The bioaccumulation of chemical elements in human bone is rather a complex process. Factors that influence bioaccumulation include age, gender, genetic inheritance, dietary habits, environmental quality, and so on. Many chemical elements in human organism act antagonistically and/or synergistically. Some elements in the bone can be substituted by other elements and, as a result, change biochemical reactions in humans. Variations in relative content of chemical elements in the bone lead to modulation/dysfunction of bone metabolism.

To use chemical element composition as estimation of bone health in clinical, geographical, environmental and occupational medicine, paleoanthropology, and other directions, it is necessary to know normal levels and age- and gender-related changes of chemical element ratios.

This work had three aims. The first one was to determine the Ca, Cl, K, Mg, Mn, Na, P, and Sr mass fractions in the normal human rib bone by instrumental neutron activation analysis with high resolution spectrometry of short-lived radionuclides (INAA-SLR) and to calculate some statistical parameters of Cl/Ca, K/Ca, Mg/Ca, Mn/Ca, Na/Ca, P/Ca, Sr/Ca, Ca/P, Cl/P, K/P, Mg/P, Mn/P, Na/P, Sr/P, Ca/Mg, Cl/Mg, Mn/Mg, Na/Mg, P/Mg, Sr/Mg, Ca/Cl, K/Cl, Mg/Cl, Mn/Cl, Na/Cl, P/Cl, Sr/Cl, Ca/K, Cl/K, Mg/K, Mn/K, Na/K, P/K, Sr/K, Ca/Na, Cl/Na, K/Na, Mg/Na, Mn/Na, P/Na, and Sr/Na mass fraction ratios. The second aim was to evaluate the effect of age and gender on mean values of ratios of chemical element mass fractions in intact human rib bone. The third aim was to estimate the inter correlations between Ca, Cl, K, Mg, Mn, Na, P, and Sr mass fractions in the normal human rib bone.

All studies were approved by the Medical Radiological Research Center, Obninsk, Ethical Committees.

Experimental

Rib bonc samples were obtained at postmortems from intact cadavers (38 female and 46 male, 15–55 years old) within 24 h of death. The bone samples were immediately frozen at -18 °C until use. All subjects died suddenly due to automobile accident, falls, shootings, stabbing, hanging, acute alcohol poisoning, or hypothermia. The sample sides contacted with surgical instruments were cut off and soft tissue and blood were removed. A titanium tool was used to cut and to scrub samples. Samples were freeze dried until constant mass was obtained. A titanium scalpel was used to cut thin cross sections of the rib weighing about 50–100 mg

and containing cortical and trabecular parts in natural ratio. The rib samples for INAA-SIP were sealed separately in thin polyethylene films washed with acetone and rectified alcohol The sealed samples were placed in labeled polyethylene ampoules.

To determine contents of the elements by comparison with a known standard, biological synthetic standards (BSS) prepared from phenol-formaldehyde resins were used [11 Corrected certified values of BSS element contents were reported by us before [2]. In addition to BSS, aliquots of commercial, chemically pure compounds were also used as standards. Ten CRM IAEA H-5 (Animal Bone) and SRM NIST 1486 (Bone Meal) sub-samples weighing about 50-100 mg were analyzed in the same conditions as bone samples to estimate the precision and accuracy of results.

The contents of Ca, Cl, K, Mg, Mn, Na, P, and Sr were determined by INAA-SLR using a horizontal channel equipped with the pneumatic rabbit system of the WWR-c research nuclear reactor. The neutron flux in the channel was 1.7×10¹³ n cm⁻² s⁻¹. Ampoules with bone samples, BSS, intralaboratory-made standards, and certified reference materials were put into polyethylene rabbits and then irradiated separately for 30 s. Copper foils were used to assess neutron flux. The measurement of each sample was made twice, 1 and 120 min after irradiation. The duration of the first and second measurements was 10 and 20 min respectively. A coaxial 98 cm³ Ge (Li) detector and a spectrometric unit (NUC 8100) including a PC-coupled multichannel analyzer, were used for measurements. The spectrometric unit provided 2.9 keV resolution at the ⁶⁰Co 1332 keV line. The information of used nuclear reactions, radionuclides, gamma-energies, and other details of the analysis including the quality control of results were reported by us before [3].

A dedicated computer program of NAA mode optimization was used [4]. Using standard programs, the summary of statistics, arithmetic mean, standard deviation, standard error of mean, minimum and maximum values, median, percentiles with 0.025 and 0.975 levels were calculated for different ratios of chemical element mass fractions. The reliability of difference in the results between two age groups and between females and males was evaluated by Student's t-test. A correlation analysis was used to identify relationships between elements.

Results and discussion

Tables 1-3 represent certain statistical parameters (arithmetic mean, standard deviation, standard error of mean, minimal and maximal values, median, percentiles with 0.025 and 0.975 levels) of 42 different ratios of Ca, Cl, K, Mg, Mn, Na, P, and Sr mass fractions in the normal rib bone of males and females, and of both females and males, taken together.

The obtained values for Ca/P ratio, as shown in Tables 1-3, agree well with median of means cited by other researchers for the human rib bone [5-7]. No published data referring to ratios of other chemical element mass fractions in human rib bone was found.

To estimate the effect of age on the chemical element ratios in rib bone we examined two age groups: one comprised a younger group with ages from 15 to 35 years and the other comprised older people with ages ranging from 36 to 55 years (Table 4). No changes with age in Ca/P ratio in human rib bone were demonstrated in previously published studies [5-7]. No published data referring to age-related changes of ratios of other chemical element mass fractions in human rib bone were found.

We used the entire data set for both females and males taken separately, seeking to detect the presence of gender-related differences (see Table 5).

Table 1. Some statistical parameters of 42 different ratios of Ca, Cl, K, Mg, Mn, Na, P, and

| | | 1 1 7 1 | |
|--------|--------------------|----------------------|--|
| · a 00 | a fractions in the | normal male rib bone | |
| | | | |

| Sr mass fractions i | n the norm | il male ri | b bone | | <u> </u> | 3.61 | DO 025 | DO 075 |
|--------------------------|------------|------------|-----------|------------|----------|-------------|---------|---------------|
| Ratio | M | SD | SEM | Min | Max | Med | P0.025 | P0.975 |
| (Cl/Ca)×10 ³ | 6.32 | 2.49 | 0.38 | 3.19 | 13.4 | 5.68 | 3.81 | 12.8 |
| $(K/Ca) \times 10^3$ | 5.84 | 2.71 | 0.41 | | 13.1 | 5.85 | 1.64 | 10.8 1.63 |
| $(Mg/Ca) \times 10^2$ | 1.21 | 0.27 | 0.04 | 0.560 | 2.15 | | 0.773 | |
| $(Mn/Ca) \times 10^6$ | 1.56 | 0.91 | 0.14 | 0.303 | | 1.30 | 0.418 | 3.53 |
| (Na/Ca) ×10 ² | 2.61 | 0.53 | 0.08 | 1.28 | 4.56 | 2.55 | 1.92 | 3.75 0.528 |
| P/Ca | 0.433 | 0.061 | 0.009 | 0.319 | 0.634 | | 0.331 | |
| $(Sr/Ca) \times 10^3$ | 1.45 | 0.66 | 0.10 | 0.284 | 2.92 | 1.38 | | 2.62 |
| Ca/P | 2.35 | 0.32 | 0.05 | 1.58 | 3.13 | 2.38 | 1.89 | 3.02 |
| $(Cl/P) \times 10^2$ | 1.47 | 0.55 | 0.08 | 0.635 | 3.11 | 1.34 | 0.733 | 2.59 |
| $(K/P) \times 10^2$ | 1.38 | 0.66 | 0.10 | 0.272 | 3.17 | 1.39 | 0.392 | 2.67 |
| $(Mg/P) \times 10^2$ | 2.82 | | 0.09 | 1.12 | 4.19 | 2.85 | | 3.86 |
| $(Mn/P) \times 10^6$ | 3.59 | 2,23 | 0.35 | 0.724 | 11.9 | | | 9.23 |
| $(Na/P) \times 10^2$ | 6.18 | 1.69 | 0.26 | | 13.6 | 5.93 | | 8.19 |
| $(Sr/P) \times 10^3$ | 3.38 | 1.53 | 0.23 | 0.685 | 7.01 | 3.33 | 0.829 | 6.35 |
| Ca/Mg | 86.9 | 22.1 | 3.3 | 46.6 | 178 | 84.9 | 61.4 | 129 |
| Cl/Mg | 0.537 | 0.207 | 0.031 | 0.237 | 1.16 | | 0.252 | 0.993 |
| K/Mg | 0.493 | 0.236 | | 0.120 | 1.12 | 0.489 | 0.143 | 0.951 |
| $(Mn/Mg) \times 10^4$ | 1.35 | 0.88 | 0.14 | 0.224 | 4.46 | | 0.258 | 3.28 |
| Na/Mg | 2.24 | 0.62 | 0.09 | 1.18 | 4.27 | 2.18 | 1.28 | 3.74 |
| P/Mg | 37.4 | 10.7 | 1.6 | 23.9 | 89.2 | | 25.9 | 53.8 |
| Sr/Mg | 0.125 | 0.066 | 0.010 | | 0.378 | | 0.031 | 0.244 |
| Ca/Cl | 179 | 58.3 | 8.8 | 74.8 | 314 | 176 | 78.2 | 263 |
| K/Cl | 0.963 | 0.441 | | 0.263 | 1.94 | | 0.427 | 1.92 |
| Mg/Cl | 2.15 | 0.84 | | 0.861 | 4.22 | | 1.01 | 3.97 |
| (Mn/Cl) ×10 ⁴ | 2.61 | 1.45 | 0.23 | 0.686 | | | 0.745 | 6.08 |
| Na/Cl | _4.53 | 1.33 | 0.20 | 2.12 | 7.55 | | 2.15 | 7.30 |
| P/Cl | 77.2 | 27.5 | . 4.1 | 32.1 | 157 | | 38.6 | 137 |
| Sr/Cl | 0.248 | 0.133 | | | | | 0.067 | 0.516 |
| Ca/K | 228 | 154 | 23 | 76.4 | 855 | | 92.3 | 610 |
| Cl/K | 1.27 | 0.63 | 0.095 | | | | 0.520 | |
| Mg/K | 2.65 | 1.59 | 0.24 | | | | 1.05 | 7.04 |
| $(Mn/K) \times 10^4$ | 3.11 | 1.92 | 0.30 | | | | 0.676 | |
| Na/K | 5.60 | 3.42 | 0.52 | | | | 2.62 | 14.1 |
| P/K | 99.0 | 68.4 | 10.3 | 31.6 | 367 | | 37.5 | 255 |
| Sr/K | 0.303 | 0.237 | 0.030 | | | | 0.103 | |
| Ca/Na | 39.8 | 8.3 | 1.3 | 21.0 | | | 26.7 | 52.1 |
| Cl/Na | 0.242 | 0.080 | | | | | | |
| K/Na | 0.220 | 0.08 | | | | | | |
| Mg/Na | 0.478 | 0.13 | | | | l8 ∴ 0.458 | | |
| $(Mn/Na) \times 10^4$ | 0.614 | | | | | 0.548 | 0.191 | |
| P/Na | 17.4 | | | 7.37 | 36. | | 12.2 | |
| Sr/Na | 0.559 | 0.27 | 0.04 | 1 0.119 | 1.4 | 1 0.509 | 0.124 | |
| | OD -te- | doed davis | tion: SEM | - standard | error of | mean; Min - | minimum | value; Max |

M - arithmetic mean; SD - standard deviation; SEM - standard error of mean; Min - minimum value: maximum value; Per. 0.025 - percentile with 0.025 level; Per. 0.975 - percentile with 0.975 level

Table 2. Some statistical parameters of 42 different ratios of Ca, Cl, K, Mg, Mn, Na, P, and Sr mass fractions in the normal female rib bone

| Di mass machons m | I tile Hellin | ui ioiiiaic | TIO COIL | | | | | 1 4 4 |
|--------------------------|---------------|-------------|----------|-------|--------|-------|---------------|--------|
| Ratio | M | SD | SEM | Min | Max | Med | P0.025 | P0.975 |
| (Cl/Ca)×10 ³ | 4.26 | 2.68 | 0.44 | 0.699 | 13.6 | 4.18 | 0.749 | 11.0 |
| $(K/Ca) \times 10^3$ | 3.21 | 1.96 | 0.35 | 0.214 | 8.67 | 3.10 | 0.533 | 7.20 |
| $(Mg/Ca) \times 10^2$ | 0.977 | 0.338 | 0.056 | 0.355 | 1.61 | 1.01 | 0.422 | 1.48 |
| $(Mn/Ca) \times 10^6$ | 1.62 | 1.30 | 0.22 | 0.276 | 7.18 | 1.26 | 0.318 | 4.84 |
| (Na/Ca) ×10 ² | 2.41 | 0.58 | 0.096 | 0.860 | 3.88 | 2.38 | 0.885 | 3.38 |
| P/Ca | 0.444 | 0.073 | 0.012 | 0.264 | 0.708 | 0.432 | 0.358 | 0.581 |
| $(Sr/Ca) \times 10^3$ | 1.60 | 1.03 | 0.17 | 0.140 | 5.88 | 1.35 | 0.314 | 3.27 |
| Ca/P | 2.31 | 0.38 | 0.062 | 1.41 | 3.79 | 2.31 | 1.73 | 2.82 |
| $(C1/P) \times 10^2$ | 1.00 | 0.68 | 0.11 | 0.141 | 3.35 | 0.883 | 0.152 | 2.67 |
| $(K/P) \times 10^2$ | 0.763 | 0.483 | 0.085 | 0.052 | 2.11 | 0.724 | 0.114 | 1.64 |
| $(Mg/P) \times 10^2$ | 2.29 | 0.97 | 0.16 | 0.756 | 5.56 | 2.48 | 0.797 | 4.13 |
| $(Mn/P) \times 10^6$ | 3.62 | 2.60 | 0.43 | 0.627 | 12.7 | 2.96 | 0.773 | 11.2 |
| (Na/P) ×10 ² | 5.57 | 1.68 | 0.28 | 1.77 | 11.4 | 5.64 | 2.09 | 8.70 |
| $(Sr/P) \times 10^3$ | 3.71 | 2.54 | 0.42 | 0.352 | 13.3 | 2.88 | 0.749 | 9.60 |
| Ca/Mg | 119 | 53 | 8.7 | 62.2 | 282 | 98.9 | 67.6 | 238 |
| Cl/Mg | 0.423 | 0.178 | 0.029 | 0.124 | .0.911 | 0.401 | 0.171 | 0.851 |
| K/Mg | 0.302 | 0.156 | 0.028 | 0.028 | 0.738 | 0.256 | 0.099 | 0.630 |
| $(Mn/Mg) \times 10^4$ | 2.13 | 2.61 | 0.43 | 0.212 | 12.8 | 1.34 | 0.365 | 10.4 |
| Na/Mg | 2.91 | 1.59 | 0.26 | 0.535 | 7.75 | 2.49 | 1.03 | 6.43 |
| P/Mg | 53.6 | 27.8 | 4.5 | 18.0 | 132 | 40.3 | 24.5 | 126 |
| Sr/Mg | 0.181 | 0.120 | 0.020 | 0.012 | 0.529 | 0.159 | 0.025 | 0.498 |
| Ca/Cl | 357 | 295 | 49 | 73.7 | 1431 | 239 | 91.4 | 1335 |
| K/Cl | 0.733 | 0.302 | 0.053 | 0.051 | 1.36 | 0.704 | 0.270 | 1.33 |
| Mg/Cl | 2.85 | 1.43 | 0.23 | 1.10 | 8.09 | 2.50 | 1.18 | 5.93 |
| $(Mn/Cl) \times 10^4$ | 6.16 | 8.62 | 1.44 | 0.772 | 39.1 | 3.26 | 0.998 | 33.5 |
| Na/Cl | 8.82 | 7.96 | 1.31 | 0.634 | 36.7 | 6.27 | 1.97 | 35.8 |
| P/Cl | 162 | 148 | 24.3 | 29.9 | 710 | 113 | 37.6 | 656 |
| Sr/Cl | 0.536 | 0.634 | 0.104 | 0.063 | 3.78 | 0.376 | 0.064 | 1.84 |
| Ca/K | 598 | 829 | 147 | 115 | 4662 | 322 | 140 | 2288 |
| Cl/K | 2.09 | 3.25 | 0.57 | 0.738 | 19.6 | 1.42 | 0.755 | 6.73 |
| Mg/K | 4.98 | 6.00 | 1.06 | 1.35 | 36.3 | 3.90 | 1.60 | 14.6 |
| $(Mn/K) \times 10^4$ | 6.83 | 7.57 | 1.36 | 0.894 | 39.9 | 4.17 | 1.09 | 24.9 |
| Na/K | 12.2 | 10.8 | 1.9 | 1.55 | 41.8 | 7.54 | 2.92 | 41.5 |
| P/K | 257 | 345 | 61 | 47.5 | 1907 | 138 | 62.0 | 1017 |
| Sr/K | 0.89 | 1.44 | 0.25 | 0.073 | 8.05 | 0.535 | 0.090 | 4.04 |
| Ca/Na | 45.5 | 18.7 | 3.1 | 25.8 | 116 | 42.0 | 29.7 | 113 |
| CI/Na | 0.213 | 0.255 | 0.042 | 0.027 | 1.58 | 0.159 | 0.028 | 0.583 |
| K/Na | 0.147 | 0.117 | 0.042 | 0.027 | 0.643 | 0.133 | 0.028 | 0.378 |
| Mg/Na | 0.456 | 0.300 | 0.049 | 0.129 | 1.87 | 0.133 | 0.024 | 1.01 |
| $(Mn/Na) \times 10^4$ | 0.726 | 0.688 | 0.115 | 0.129 | 3.62 | 0.401 | | |
| P/Na | 20.3 | 9.6 | 1.6 | 8.77 | 56.3 | 17.7 | 0.179 | 0.282 |
| Sr/Na | 0.760 | 0.691 | 0.114 | 0.055 | 3.39 | 0.561 | 11.6 0.131 | 48.0 |
| M - arithmetic mean: S | | | | | | | | 2.93 |

M - arithmetic mean; SD - standard deviation; SEM - standard error of mean; Min - minimum value; Max - maximum value; Per. 0.025 - percentile with 0.025 level; Per. 0.975 - percentile with 0.975 level

Table 3. Some statistical parameters of 42 different ratios of Ca, Cl, K, Mg, Mn, Na, P, and Sr mass fractions in the normal rib bone of both males and females, taken together

| Ratio | M | SD | SEM | Min | Max | Med | P0.025 | P0.975 |
|--------------------------|------------|-------------|-------|-------|-------------|-------------|-----------|-------------|
| (Cl/Ca)×10 ³ | 5.38 | 2.76 | 0.31 | 0.699 | 13.6 | 4.69 | 1.30 | 12.8 |
| $(K/Ca) \times 10^3$ | 4.73 | 2.74 | 0.31 | 0.214 | 13.1 | 4.18 | 0.749 | 10.2 |
| $(Mg/Ca) \times 10^2$ | 1.10 | 0.32 | 0.04 | 0.355 | 2.15 | 1.16 | 0.431 | 1.61 |
| $(Mn/Ca) \times 10^6$ | 1.59 | 1.11 | 0.13 | 0.276 | 7.18 | 1.27 | 0.322 | 4.53 |
| $(Na/Ca) \times 10^2$ | 2.52 | 0.56 | 0.06 | 0.860 | 4.76 | 2.48 | 1.26 | 3.79 |
| P/Ca | 0.438 | 0.066 | 0.007 | 0.264 | 0.708 | 0.426 | 0.331 | 0.567 |
| $(Sr/Ca) \times 10^3$ | 1.52 | 0.85 | 0.10 | 0.140 | 5.88 | 1.38 | 0.331 | 2.92 |
| Ca/P | 2.33 | 0.35 | 0.04 | 1.41 | 3.79 | 2.35 | 1.76 | 3.02 |
| $(CI/P) \times 10^2$ | 1.26 | 0.65 | 0.07 | 0.141 | 3.35 | 1.12 | 0.274 | 2.61 |
| $(K/P) \times 10^2$ | 1.12 | 0.66 | 0.08 | 0.052 | 3.17 | 1.02 | 0.178 | 2.53 |
| $(Mg/P) \times 10^2$ | 2.58 | 0.83 | 0.09 | 0.756 | 5.56 | 2.68 | 0.178 | 3.97 |
| $(Mn/P) \times 10^6$ | 3.61 | 2.40 | 0.28 | 0.627 | 12.7 | 2.98 | 0.785 | 11.1 |
| $(Na/P) \times 10^2$ | 5.90 | 1.70 | 0.19 | 1.77 | 13.6 | 5.79 | 2.17 | 8.40 |
| $(Sr/P) \times 10^3$ | 3.54 | 2.05 | 0.23 | 0.352 | 13.3 | 3.28 | 0.791 | 7.25 |
| Ca/Mg | 102 | 42.4 | 4.7 | 46.6 | 282 | 86.5 | 62.1 | |
| Cl/Mg | 0.485 | 0.202 | 0.022 | 0.124 | 1.16 | 0.449 | 0.184 | 0.915 |
| K/Mg | 0.412 | 0.226 | 0.026 | 0.028 | 1.12 | 0.375 | 0.120 | 0.908 |
| $(Mn/Mg) \times 10^4$ | 1.72 | 1.93 | 0.22 | 0.020 | 12.8 | 1.25 | 0.254 | 6.29 |
| Na/Mg | 2.55 | 1.21 | 0.13 | 0.535 | 7.75 | 2.23 | 1.14 | 6.06 |
| P/Mg | 44.8 | 21.8 | 2.4 | 18.0 | 132 | 37.2 | 25.2 | 110 |
| Sr/Mg | 0.151 | 0.099 | 0.011 | 0.012 | 0.529 | 0.131 | 0.030 | 0.468 |
| Ca/Cl | 260 | 221 | 25 | 73.7 | 1431 | 213 | 77.9 | 770 |
| K/Cl | 0.867 | 0.403 | 0.046 | 0.051 | 1.94 | 0.815 | 0.325 | 1.91 |
| Mg/Cl | 2.47 | 1.19 | 0.13 | 0.860 | 8.09 | 2.23 | 1.09 | 5.45 |
| (Mn/Cl) ×10 ⁴ | 4.29 | 6.24 | 0.72 | 0.686 | 39.1 | 2.64 | 0.769 | 23.7 |
| Na/Cl | 6.49 | 5.84 | 0.65 | 0.634 | 36.7 | 5.05 | 2.12 | 20.1 |
| P/Cl | 116 | 110 | 12 | 29.9 | 710 | 89.7 | 38.4 | 365 |
| Sr/Cl | 0.381 | 0.462 | 0.052 | 0.042 | 3.78 | 0.283 | 0.064 | 1.28 |
| Ca/K | 384 | 576 | 66 | 76.4 | 4662 | 240 | 98.3 | 1342 |
| CI/K | 1.62 | 2.18 | 0.25 | 0.516 | 19.6 | 1.23 | 0.523 | 3.10 |
| Mg/K | 3.63 | 4.21 | 0.48 | 0.892 | 36.3 | 2.67 | 1.10 | 8.31 |
| $(Mn/K) \times 10^4$ | 4.73 | 5.48 | 0.65 | 0.541 | 39.9 | 3.46 | 0.841 | 16.3 |
| Na/K | 8.36 | 8.12 | 0.93 | 1.55 | 41.8 | 5.77 | 2.56 | |
| P/K | 166 | 241 | 28 | 31.6 | 1907 | 97.8 | 39.5 | 568 |
| Sr/K | 0.552 | 0.990 | 0.114 | 0.027 | 8.05 | 0.322 | 0.092 | 2.25 |
| Ca/Na | 42.4 | 14.3 | 1.6 | 21.0 | 116 | 40.4 | 26.4 | 79.6 |
| Cl/Na | 0.229 | 0.181 | 0.020 | 0.027 | 1.58 | 0.198 | 0.050 | 0.471 |
| K/Na | 0.189 | 0.106 | 0.012 | 0.024 | 0.643 | | | 0.391 |
| Mg/Na | 0.468 | 0.223 | 0.025 | 0.129 | 1.87 | 0.448 | 0.165 | 0.877 |
| $(Mn/Na) \times 10^4$ | 0.667 | 0.536 | 0.062 | 0.129 | | 0.547 | 0.179 | 1.91 |
| P/Na | 18.7 | 7.6 | 0.84 | 7.37 | 56.3 | 17.3 | | 46.1 |
| Sr/Na | 0.652 | 0.516 | 0.058 | 0.055 | 3.39 | 0.536 | 0.123 | 1.97 |
| M - arithmetic mean; S | D – standa | rd deviatio | | | rror of mea | ın; Min – ı | minimum v | alue; Max - |

maximum value; Per. 0.025 – percentile with 0.025 level; Per. 0.975 – percentile with 0.975 level

Table 4. Effect of age on mean values (M±SEM) of ratios of chemical element mass fractions in intact human rib bone (Student's t-test)

| Datia | | 7 1 | | | | 200 0000 |
|--------------------------|------------------|----------------|--------------|------------------------|---------------|----------|
| Ratio | 15.05 | Females | | | Males | 13/2015 |
| (01/0-)103 | 15-35 year | 36-55 year | <i>p</i> | 15-35 year | 36-55 year | p |
| $(C1/Ca) \times 10^3$ | 4.73±0.70 | 3.82±0.55 | N.S. | 5.70±0.41 | 6.87±0.60 | N.S. |
| $(K/Ca) \times 10^3$ | 3.33±0.40 | 3.05±0.62 | | 5.19±0.61 | 6.44±0.54 | N.S. |
| $(Mg/Ca) \times 10^2$ | 1.04±0.08 | 0.91±0.08 | N.S. | | 1.19±0.06 | N.S. |
| $(Mn/Ca) \times 10^6$ | 1.48±0.15 | 1.74±0.39 | N.S. | 1.28 ± 0.15 | 1.81±0.23 | N.S. |
| (Na/Ca) ×10 ² | 2.37±0.12 | 2.44±0.15 | N.S. | 2.52 ± 0.09 | 2.69±0.13 | N.S. |
| P/Ca | 0.43±0.01 | 0.46 ± 0.02 | N.S. | 0.43 ± 0.01 | 0.44 ± 0.01 | N.S. |
| $(Sr/Ca) \times 10^3$ | 1.76±0.31 | 1.44±0.15 | N.S. | 1.33±0.15 | 1.56±0.14 | N.S. |
| Ca/P | 2.36±0.05 | 2.26 ± 0.02 | N.S. | 2.36±0.06 | 2.34±0.07 | N.S. |
| $(CI/P) \times 10^2$ | 1.11±0.17 | 0.90±0.15 | N.S. | 1.34±0.09 | 1.59±0.13 | N.S. |
| $(K/P) \times 10^2$ | 0.79 ± 0.10 | 0.73 ± 0.16 | N.S. | 1.23±0.15 | 1.51±0.13 | N.S. |
| $(Mg/P) \times 10^2$ | 2.46±0.18 | 2.12±0.26 | N.S. | 2.92±0.12 | 2.74±0.13 | N.S. |
| $(Mn/P) \times 10^6$ | 3.52±0.39 | 3.71±0.76 | N.S. | 2.97±0.33 | 4.15±0.58 | N.S. |
| $(Na/P) \times 10^2$ | 5.55±0.28 | 5.58±0.48 | N.S. | 5.99±0.30 | 6.36±0.41 | N.S. |
| $(Sr/P) \times 10^3$ | 4.16±0.72 | 3.28±0.44 | N.S. | 3.05±0.31 | 3.70±0.34 | N.S. |
| Ca/Mg | 108±10 | 130±14 | N.S. | 83.4±3.6 | 90.1±5.5 | N.S. |
| Cl/Mg | 0.43 ± 0.04 | 0.41±0.04 | N.S. | 0.47±0.04 | 0.59±0.05 | N.S. |
| K/Mg | 0.31 ± 0.03 | 0.30±0.05 | N.S. | 0.43±0.05 | 0.55±0.04 | N.S. |
| $(Mn/Mg) \times 10^4$ | 1.54±0.21 | 2.66±0.79 | N.S. | 1.04±0.12 | 1.63±0.23 | ≤0.05 |
| Na/Mg | 2.58±0.29 | 3.22±0.43 | N.S. | 2.11±0.12 | 2.37±0.13 | |
| P/Mg | 46.1±4.9 | 60.8±7.4 | N.S. | 35.7±1.7 | 39.0±2.7 | N.S. |
| Sr/Mg | 0.18±0.03 | 0.18±0.03 | N.S. | 0.11±0.01 | 0.14±0.02 | N.S. |
| Ca/Cl | 331±74 | 381±64 | N.S. | 192±12 | 167±12 | N.S. |
| K/Cl | 0.78±0.07 | 0.67±0.08 | N.S. | 0.91±0.09 | | N.S. |
| Mg/Cl | 2.81±0.37 | 2.89±0.30 | N.S. | 2.38±0.18 | 1.01±0.10 | N.S. |
| $(Mn/Cl) \times 10^4$ | 4.56±1.04 | 7.59±0.50 | N.S. | 2.35±0.18 2.35±0.31 | 1.94±0.17 | N.S. |
| Na/Cl | 8.04±1.9 | 9.56±1.8 | N.S. | 4.73±0.31 | 2.84±0.33 | N.S. |
| P/Cl | 143±34 | 181±35 | N.S. | | 4.35±0.28 | N.S. |
| Sr/Cl | 0.56±0.20 | 0.52±0.09 | N.S. | 82.0±5.4 | 72.7±6.1 | N.S. |
| Ca/K | 443±90 | 797±313 | N.S. | 0.25±0.03 | 0.24±0.03 | N.S. |
| Cl/K | 1.48±0.14 | 2.87±313 | | 260±38 | 199±27 | N.S. |
| Mg/K | 3.81±0.40 | 6.50±2.4 | N.S. N.S. | 1.34±0.16 | 1.21±0.11 | N.S. |
| $(Mn/K) \times 10^4$ | 6.10±1.2 | | | 3.07±0.34 | 2.26±0.32 | N.S. |
| Na/K | 10.7±2.3 | 7.72±2.7 | N.S. | 2.86±0.38 | 3.33±0.47 | N.S. |
| P/K | | 14.1±3.2 | N.S. | 6.24±0.87 | 5.02±0.57 | N.S. |
| Sr/K | 192±42 | 342±128 | N.S. | 112±17 | 86.8±12.1 | N.S. |
| | 0.68±0.15 | 1.15±0.55 | N.S. | 0.33±0.06 | 0.28±0.05 | N.S. |
| Ca/Na | 45.6±4.3 | 45.4±4.5 | N.S. | 41.1±2.1 | 38.6±1.5 | N.S. |
| Cl/Na | 0.25±0.08 | 0.18±0.03 | N.S. | 0.23±0.01 | 0.26±0.02 | N.S. |
| K/Na | 0.16±0.03 | 0.13±0.02 | N.S. | 0.20±0.02 | 0.24 ± 0.02 | N.S. |
| Mg/Na | 0.50±0.09 | 0.42±0.05 | N.S. | 0.51±0.03 | 0.45±0.02 | N.S. |
| (Mn/Na) ×10 ⁴ | 0.71±0.14 | 0.74±0.18 | N.S. | 0.51±0.06 | 0.71 ± 0.09 | N.S. |
| P/Na | 19.3±1.7 | 21.3±2.6 | 11.0. | 17.8±1.2 | 17.0±1.0 | N.S. |
| Sr/Na | 0.86±0.21 | 0.67±0.11 | N.S. | 0.54±0.06 | 0.58±0.06 | N.S. |
| M - Arithmetical mea | n, SEM – standar | derror of mean | N.S nor | significant | | 17 |

M - Arithmetical mean, SEM - standard error of mean, N.S. - non significant

Table 5. Effect of gender on mean values (M±SEM) of ratios of chemical element mass fractions in intact human rib bone (Student's t-test)

| nactions in intact | numan no bone (Student | | |
|--------------------------|--------------------------------|--------------------------|-------------------------------------|
| Ratio | Females | | $oldsymbol{p}$. The $oldsymbol{p}$ |
| (Cl/Ca)×10 ³ | 4.26±0.44 | 6.32±0.38 | (i) i ≤0.01 |
| $(K/Ca) \times 10^{3}$ | 3.21±0.35 | 5.84±0.41 | |
| $(Mg/Ca) \times 10^2$ | 0.98±0.06 | 1.21±0.04 | |
| $(Mn/Ca) \times 10^6$ | 1.62±0.22 | 1.56±0.14 | |
| (Na/Ca) ×10 ² | 2.41±0.10 | | san and N.S. Sandah |
| P/Ca | 0.444±0.012 | 0.433±0.009 | N.S. |
| $(Sr/Ca) \times 10^3$ | 1.60±0.17 | 1.45±0.10 | N.S. |
| Ca/P | 2.31±0.06 | 2.35±0.05 | N.S. |
| $(C1/P) \times 10^2$ | 1.00±0.11 | 1.47±0.08 | alaga ≤0.001 |
| $(K/P) \times 10^2$ | 0.76±0.09 | 1.38±0.10 and take | |
| $(Mg/P) \times 10^2$ | 2.29±0.16 | 2.82±0.09 | ≤0.01 |
| $(Mn/P) \times 10^6$ | 3.62±0.43 | 3.59±0.35 | N.S. |
| $(Na/P) \times 10^2$ | 5.57±0.28 | 6.18±0.26 | N.S. |
| $(Sr/P) \times 10^3$ | 3.71±0.42 | 3.38±0.23 | N.S. |
| Ca/Mg | 119±9 | 86.9±3.3 | ≤0.01 |
| Cl/Mg | 0.423±0.029 | 0.537±0.031 | ≤0.01 |
| K/Mg | 0.302±0.028 | 0.493±0.036 | ≤0.001 |
| $(Mn/Mg) \times 10^4$ | 2.13±0.43 | 1.35±0.14 | N.S. |
| Na/Mg | 2.91±0.26 | 2.24±0.09 | ≤0.05 |
| P/Mg | 53.6±4.5 | 37.4±1.6 | ≤0.01 |
| Sr/Mg | 0.181±0.020 | 0.125±0.010 | ≤0.05 |
| Ca/Cl | 357±49 | 179±9 | ≤0.001 |
| K/Cl | 0.733±0.053 | 0.963±0.067 | ≤0.01 |
| Mg/Cl | 2.85±0.23 | 2.15±0.13 | ≤0.01 |
| (Mn/Cl) ×10 ⁴ | 6.16±1.44 | 2.61±0.23 | ≤0.05 |
| Na/Cl | 8.82±1.32 | 4.53±0.20 | ≤0.01 |
| P/Cl | 162±24 | 77.2±4.1 | . ≤0.01 |
| Sr/Cl | 0.536±0.104 | 0.248±0.020 | ≤0.01 |
| Ca/K | 598±147 | 228±23 | ≤0.05 |
| Cl/K | 2.09±0.57 | 1.27±0.10 | N.S. |
| Mg/K | 4.98±1.06 | 2.65±0.24 | ≤0.05 |
| $(Mn/K) \times 10^4$ | 6.83±1.36 | 3.11±0.30 | ≤0.01 |
| Na/K | 12.2±1.9 | 5.60±0.52 | ≤0.01 |
| P/K | 257±61 | 99.0±10.3 | ≤0.05 |
| Sr/K | 0.888±0.250 | 0.303±0.036 | ≤0.05 |
| Ca/Na | 45.5±3.1 | 39.8±1.3 | N.S. |
| Cl/Na | 0.213±0.042 | 0.242±0.012 | N.S. |
| K/Na | 0.147±0.021 | 0.220±0.013 | ≤0.01 |
| Mg/Na | 0.456±0.049 | 0.478±0.020 | N.S. |
| (Mn/Na) ×10 ⁴ | 0.726±0.115 | 0.614±0.055 | N.S. |
| P/Na | 20.3±1.6 | 17.4±0.8 | N.S. |
| Sr/Na | 0.760±0.114 | 0.559±0.041 | N.S. |
| M - Arithmetical me | ean, SEM - standard error of m | ean, N.S non significant | |

M - Arithmetical mean, SEM - standard error of mean, N.S. - non significant

A statistically significant tendency of gender-related differences was detected for Cl/Ca, K/Ca, Mg/Ca, Cl/P, K/P, Mg/P, Ca/Mg, Cl/Mg, K/Mg, Na/Mg, P/Mg, Sr/Mg, Ca/Cl, K/Cl, Mg/Cl, Mn/Cl, Na/Cl, P/Cl, Sr/Cl, Ca/K, Mg/K, Mn/K, Na/K, P/K, Sr/K, and K/Na mass fractions ratios. No gender-related dependence in Ca/P ratio in human rib bone was found in previously published studies [5-7]. Any published data referring to gender dependence of ratios of other chemical element mass fractions in human rib bone was not found.

Table 6 depicts the inter-correlation calculations including all chemical elements identified by us. The positive inter-correlations of Ca mass fractions with Mg (p<0.001), Mn (p<0.001), Na (p<0.001), P (p<0.001), and Sr (p<0.05) mass fractions were found in normal human rib-bone tissue.

Table 6. Inter-correlations (r – coefficient of correlation) of Ca, Cl, K, Mg, Mn, Na, P, and S_r mass fractions in the normal human rib bone

| mass fractions in the normal number no bone | | | | | | | | | |
|---------------------------------------------|----------------------------------------------------------------------------------------------------------------------|--------------------------------------------------------------------------------------------------------------------------------------------------------------------------------------------------------------------------------------|---------------------------------------------------------------------------------------------------------------------------------------------------------------------------------------------------------------------------------------------------------------------------------------------------------------------------------------------------------|-----------------------------------------------------------------------------------------------------------------------------------------------------------------------------------------------------------------------------------------------------------------------------------------------------------------------------------------------------------------------------------------------------------------------------------------------------------------------|-----------------------------------------------------------------------------------------------------------------------------------------------------------------------------------------------------------------------------------------------------------------------------------------------------------------------------------------------------------------------------------------------------------------------------------------------------------------------------------------------------------------------------------------------------------------------------------------|--------------------------------------------------------|--------------------------------------------------------|--|--|
| Ca | Cl | K | Mg | Mn | Na | P | Sr | | |
| 1.00 | 0.144 | 0.047 | 0.562° | 0.305 ^b | 0.648° | 0.813 ^c | 0.264ª | | |
| 0.144 | 1.00 | 0.525^{c} | 0.470^{c} | 0.348^{b} | 0.038 | 0.067 | 0.251^{a} | | |
| 0.047 | 0.525^{c} | 1.00 | 0.332^{b} | 0.352^{b} | 0.312 ^b | -0.038 | 0.106 | | |
| 0.562° | 0.470^{c} | 0.332^{b} | 1.00 | 0.084 | 0.308^{b} | 0.487^{c} | 0.261^{a} | | |
| 0.305^{b} | 0.348^{b} | 0.352^{b} | 0.084 | 1.00 | 0.297^{b} | 0.274^{a} | 0.102 | | |
| 0.648^{c} | 0.038 | 0.312^{b} | 0.308^{b} | 0.297^{b} | 1.00 | 0.418° | 0.123 | | |
| 0.813° | 0.067 | -0.038 | 0.487^{c} | 0.274^{a} | 0.418^{c} | 1.00 | 0.250^{a} | | |
| 0.264 ^a | 0.251 ^a | 0.106 | 0.261 ^a | 0.102 | 0.123 | 0.250 ^a | 1.00 | | |
| | Ca 1.00 0.144 0.047 0.562 ^c 0.305 ^b 0.648 ^c 0.813 ^c | Ca Cl 1.00 0.144 0.144 1.00 0.047 0.525° 0.562° 0.470° 0.305° 0.348° 0.648° 0.038 0.813° 0.067 | Ca Cl K 1.00 0.144 0.047 0.144 1.00 0.525° 0.047 0.525° 1.00 0.562° 0.470° 0.332b° 0.305b 0.348b 0.352b° 0.648° 0.038 0.312b° 0.813° 0.067 -0.038 | Ca Cl K Mg 1.00 0.144 0.047 0.562° 0.144 1.00 0.525° 0.470° 0.047 0.525° 1.00 0.332° 0.562° 0.470° 0.332° 1.00 0.305° 0.348° 0.352° 0.084 0.648° 0.038 0.312° 0.308° 0.813° 0.067 -0.038 0.487° | Ca Cl K Mg Mn 1.00 0.144 0.047 0.562° 0.305° 0.144 1.00 0.525° 0.470° 0.348° 0.047 0.525° 1.00 0.332° 0.352° 0.562° 0.470° 0.332° 1.00 0.084 0.305° 0.348° 0.352° 0.084 1.00° 0.648° 0.038 0.312° 0.308° 0.297° 0.813° 0.067 -0.038 0.487° 0.274° | $ \begin{array}{c ccccccccccccccccccccccccccccccccccc$ | $ \begin{array}{c ccccccccccccccccccccccccccccccccccc$ | | |

Statistically significant difference: $a - p \le 0.05$, $b - p \le 0.01$, $c - p \le 0.001$.

Conclusions

All the deceased were citizens of Obninsk, a small city of non-industrial region 105 km south-west from Moscow. None of those who died a sudden death had suffered from any systematic or chronic disorders before. Thus, our data for Cl/Ca, K/Ca, Mg/Ca, Mn/Ca, Na/Ca, P/Ca, Sr/Ca, Ca/P, Cl/P, K/P, Mg/P, Mn/P, Na/P, Sr/P, Ca/Mg, Cl/Mg, Mn/Mg, Na/Mg, P/Mg, Sr/Mg, Ca/Cl, K/Cl, Mg/Cl, Mn/Cl, Na/Cl, P/Cl, Sr/Cl, Ca/K, Cl/K, Mg/K, Mn/K, Na/K, P/K, Sr/K, Ca/Na, Cl/Na, K/Na, Mg/Na, Mn/Na, P/Na, and Sr/Na mass fraction ratios in the intact rib bone may serve as indicative normal values for residents of the Central European region of Russia.

References

- 1. Mosulishvili L. et al. J. Radioanal. Chem., 1975, 26, 175-188.
- 2. Zaichick V. Fresenius J. Anal. Chem., 1995, 352, 219-223.
- 3. Zaichick V., Dyatlov A., Zaichick S. J. Radioanal. Nucl. Chem., 2000, 244, 189-193.
- 4. Korelo A., Zaichick V. In: Activation analysis in environment protection. Dubna: JINR, 1993, pp. 326–332.
- Zaichick V., Tzaphlidou M. In: Proceedings of 3rd International Symposium on Trace Elements in Humans: New Perspectives. Athens. Greece, 2001, pp. 1090-1099.
- 6. Tzaphlidou M., Zaichick V. Appl. Rad. Isotop., 2002, 57, 779-783.
- 7. Tzaphlidou M., Zaichick V. Journal of Biological Trace Element Research, 2003, 93, 63-74.

THE EFFECT OF AGE ON THE ZINC CONTENT IN PROSTATE OF HEALTHY MEN INVESTIGATED BY INAA AND ICP-MS

S. Zaichick^{1,3}, V. Zaichick¹, V. Karandashev², C. Nosenko²

¹ Medical Radiological Research Centre of the Russian Ministry of Health and Social Development, Koroleva str., 4, Obninsk, 249020, Russia, e-mail: vezai@obninsk.com

² Institute of Microelectronics Technology and High Purity Materials, Chernogolovka 142432, Russia

³ Current address: Northwestern University, Chicago, IL, 60611, USA

Introduction

Globally, prostate cancer is the sixth most common cancer, and the third most common cancer in males in Western industrialized countries [1,2]. In North America, it is the most common cancer in males and, except for lung cancer, is the leading cause of death from cancer [3-5]. Although the etiology of prostate cancer is unknown, several risk factors including age and diet (calcium, zinc and some other nutrients) have been well identified [6,7]. It is also reported that the risk of having prostate cancer drastically increase with age, being three orders of magnitude higher for the age group 40–79 years than in those younger than 39 years [7,8].

It is well known that zinc levels in the peripheral zone of dorsal and lateral lobes of the prostate are almost 10 times higher than in other soft tissues [9]. The high content of zinc in the prostate suggests that zinc may play a role in prostate health. Therefore, in investigating the effect of diet on prostate cancer risk, much attention has been paid to dietary and supplemental zinc [10-19], as well as consumption of red meat [20-25], as it is a major source of zinc from food for the residents of the continental countries [26]. It should also be noted that zinc is more bioavailable in red meat and less bioavailable in vegetables [27]. Estimates of per capita zinc intake in many countries showed a positive correlation with mortality from prostatic cancer [10, 11, 18]. A positive association with risk of prostate cancer was also observed in a population-based case-control study in the island of Oahu, Hawaii [12]. Leitzmann et al. [19] examined the association between supplemental zinc intake and prostate cancer risk among 46,974 U.S. men participating in the Health Professionals Follow-Up Study. It was shown that men who consumed more than 100mg/day did have a relative risk of advanced prostate cancer of 2.29-2.37 greater than nonusers. Consumption of red meat has been proposed as a possible risk factor for prostate cancer [21]. Many epidemiological studies that have presented results on this subject showed statistically significant increased risk with increasing meat consumption [20-25]. On the contrary, modest to moderate inverse associations were observed in two case-control studies for dietary zinc [15] and zinc supplement use [17]. Some case-control studies have not observed a cancer protective association for dietary or combined dietary and supplemental zinc intake [13,14,16]. The possibility that zinc adversely affects prostate cancer opposes its possible beneficial effect on the health of elderly individuals [28-32]. It is, therefore, important clarify the role of dietary zinc and supplemental zinc on prostate cancer risk among older men.

At present there are two diametrically opposite points of view on this issue. Proponents of the position that high zinc intakes and, consequently, high intraprostatic zinc concentrations may be positively associated with prostate cancer risk use multiple arguments to support their theory [18,19,33]. For example, zinc enhances the activity of telomerase [34], an enzyme thought to be responsible for unlimited proliferation tumor cells, the activity of which is increased in prostate cancer [35]. Zinc has also been found to antagonize the potential inhibitory effect of bisphosphonates on prostate tumor cell invasion [36]. Excessive intake of zinc has undesirable metabolic effects, such as immune dysfunction [37] and impaired antioxidant defense [38] that are potentially related to prostate cancer. In humans, zinc intake is positively correlated with circulating levels of insulinlike growth factor-I [39] and testosterone [40] that are directly related to prostate carcinogenesis. Much data have been accumulated on both direct and indirect effect of zinc on the DNA, and to its vital role for prostatic cell division [41-43]. All these facts allow it to be assumed that excessive intracellular concentrations of zinc are probably one of the main factors acting at both initiation and promotion stages of prostate carcinogenesis. Thus, zinc supplementation could promote the development of prostate cancer.

Much of the interest in zinc as an agent for prostate cancer treatment and prevention [44-46] is due to studies that have shown a marked reduction in prostate tissue zinc levels in prostate cancer cells versus normal prostate cells [9]. Proponents of this theory think that high cellular zinc accumulation is detrimental to the malignant activities of prostate cancer cells. Due to lifestyle, eating and dietary habits, and physiological effects of aging, the elderly male population is normally predisposed to conditions of zinc deficiency [28-31,47], which can increase their susceptibility to prostate cancer. According to their hypothesis in the absence of zinc supplement cellular zinc uptake will be depressed and zinc levels in prostate normal cells will be reduced [44,46].

There are few studies regarding the effect of age on Zn content in prostate, using chemical techniques and instrumental methods [48-51]. However, majority of these data are based on non-intact tissue. In many studies tissue samples are ashed. In other cases, prostate samples are treated with solvents (distilled water, ethanol, etc.) and then are dried at high temperature for many hours. There is evidence that by these methods some amount of chemical elements is lost upon treatment [52]. Moreover, only one study used a quality control using certified reference material for Zn content [51].

This work had three aims. The first one was to assess the Zn content in intact prostate of healthy men using instrumental neutron activation analysis (INAA) and inductively coupled plasma mass spectrometry (ICP-MS). The second aim was to evaluate the quality of obtained results. The third aim was to compare the contents of Zn in different age groups.

All studies were approved by the Institute of Forensic Medicine, Moscow, and the Medical Radiological Research Center, Obninsk, Ethical Committees.

Experimental

Prostates were removed at necropsy from 64 men (mean age 36.5 years, range 13-60) who had died suddenly. The majority of deaths were due to traumas. Some of deaths were due

to alcohol poisoning and acute illness (cardiac insufficiency, stroke, embolism of pulmonary artery) but without inpatient treatment. Information about chronic alcoholism or other diseases was not available from the medical reports of subjects. All cadavers had undergone routine autopsy at the Institute of Forensic Medicine, Moscow. Tissue samples were collected from the peripheral zone of prostate dorsal and lateral lobes within 2 days of death and then divided into two portions. One of them was used for morphological study while another was intended for chemical element analysis. A histological examination was used to control the age norm conformity as well as the absence of microadenomatosis and latent cancer. After the samples intended for chemical element analysis were weighed, they were transferred to – 20 °C and stored until the day of transportation in the Medical Radiological Research Center (MRRC), Obninsk. In the MRRC all samples were freeze-dried and homogenized. The pounded samples weighing about 50 mg were used for Zn measurement by INAA and ICP-MS. A tool made of titanium and plastic was used for sampling and sample preparation.

A vertical channel of nuclear reactor was applied to determine the Zn content by instrumental neutron activation analysis with high resolution spectrometry of long-lived radionuclides (INAA-LLR). The quartz ampoule with prostate samples, standards, and certified reference materials was soldered, positioned in a transport aluminum container and exposed to a 24-h neutron irradiation in a vertical channel with a neutron flux of 1.3×10^{13} n cm⁻² s⁻¹. Ten days after irradiation samples were reweighed and repacked. The samples were measured for period from 10 to 30 days after irradiation. The duration of measurements was from 20 min to 10 h subject to pulse counting rate. The gamma spectrometer included the 100 cm3 Ge(Li) detector and on-line computer-based MCA system. The spectrometer provided a resolution of 1.9 keV on the 60Co 1332 keV line. Details of nuclear reactions, radionuclides, gamma energies, methods of analysis and the results of quality control were presented in our earlier publications concerning the chemical elements of intact human prostate [53].

For ICP-MS analysis 1.5 mL of concentrated HNO₃ (Nitric acid 65%, max. 0.0000005% Hg, GR, ISO, Merck) and 0.3 mL of H₂O₂ (pure for analysis) were added to tissue samples, placed in one-chamber autoclaves (Ancon-AT2, Ltd., Russia) and then heated for 3 h at 160–200 °C to decompose. After autoclaves were cooled to room temperature solutions from the decomposed samples were diluted with deionized water (up to 20 mL) and transferred to plastic measuring bottles. Simultaneously, the same procedure was performed in autoclaves without tissue samples (only HNO₃ + H₂O₂ + deionized water), and the resultant solutions were used as control samples. Sample aliquots were used to determine the content of Zn by ICP-MS using an ICP-MS Thermo-Fisher "X-7" (Thermo Electron, USA). The measurements were made with the spectrometer parameters: RF generator power – 1250 W, nebulizer – PolyCon, spray chamber – cooling 3°C, plasma gas flow rate – 12 L/min, auxiliary flow rate –0.9 L/min, nebuliser flow rate – 0.9 L/min, sample update – 0.8 mL/min, resolution – 0.8M.

The main parameters of mass-spectrum measurements were: detector mode – double (pulse counting and analogous) and scanning mode – Survey Scan and Peak Jumping. The setting for the Survey Scan was: the number of runs – 10, dwell time – 0.6 ms, channels per mass – 10, acquisition duration – 13.2 s. The setting for the Peak Jumping was: sweeps – 25, dwell time – 10 ms, channels per mass – 1, acquisition duration – 34 s.

The Zn contents in aqueous solutions were determined by the quantitative method using calibration solutions (*High Purity Standards, USA*) with 5, 10, and 100 µkg/L. Indium was used as an internal standard in all measurements.

tern gereitster verbeiter i Franzische

The detection limit (DL) was calculated as: $DL = C_{Zn} + 3 \cdot SD$, where C_{Zn} is a mean value of the Zn concentration for measurements in control samples and SD is a standard deviation of C_{Zn} determination in control samples.

Uncertainties of Zn determination in prostate samples by ICP-MS expressed as mean relative standard deviation (±RSD) in repeatability study did not exceed 10%.

Ten certified reference material (CRM) IAEA H-4 Animal muscle [54] and IAEA HH-1 Human hair [55] sub-samples and three certified reference material INCT-SBF-4 Soya bean flour of the Institute of Nuclear Chemistry and Technology (Poland) sub-samples weighing about 50–100 mg were treated and analyzed in the same conditions as that of the prostate samples to estimate the precision and accuracy of results. The CRM IAEA H-4 Animal muscle and IAEA HH-1 Human hair sub-samples were analyzed by INAA-LLR. The CRM INCT-SBF-4 Soya bean flour sub-samples were analyzed by ICP-MS.

All prostate samples were prepared in duplicate and mean value of Zn content was used in final calculation. Using standard programs, the summary of statistics, arithmetic mean, standard deviation, standard error of mean, minimum and maximum values, median, and percentiles with 0.025 and 0.975 levels were calculated for Zn content. The reliability of difference in the results between three age groups was evaluated by Student's t-test.

Results and discussion

Table 1 depicts our data for Zn mass fractions in sub-samples of certified reference material and the certified values of these materials. Good agreement with the certified data of certified reference materials indicate an acceptable accuracy of the results obtained in the study of Zn mass fraction in the prostate tissue.

Table 1. INAA-LLR and ICP-MS data of Zn content (M±SD) in Certified Reference Materials compared to certified values (mg/kg on dry weight basis)

| Certified | IN | AA-LLR | | CP-MS |
|--------------------|------------------------|------------------|-------------|------------------|
| Reference Material | Certificate | This work result | Certificate | This work result |
| IAEA H-4 | | | | TIMS WORK TOSUIT |
| Animal muscle | 86.3±11.5 ^a | 91±2 | | |
| IAEA HH-1 | | 7122 | | |
| Human hair | 174±9ª | 173±17 | _ | 1940 |
| INCT-SBF-4 | | 175117 | | |
| Soya bean flour | · <u>-</u> | · . | 52.3° ±1.3 | 54.8±6.6 |
| Mean orithmetical | - CD | | <u> </u> | 34.6±0.0 |

Mean – arithmetical mean, SD – standard deviation, a – certified values

Fig. 1 shows the individual data for Zn mass fraction obtained by INAA (A) and ICP-MS (B) in all samples of prostate tissue, and exponential lines of trend with age.

Table 2 represents certain statistical parameters (arithmetic mean, standard deviation, standard error of mean, minimal and maximal values, median, percentiles with 0.025 and 0.975 levels) of the Zn content in intact prostate of apparently healthy men obtained by INAA-LLR, ICP-MS, and INAA-LLR + ICP-MS (together). The coefficient of correlation between INAA-LLR and ICP-MS data was r = 0.993.

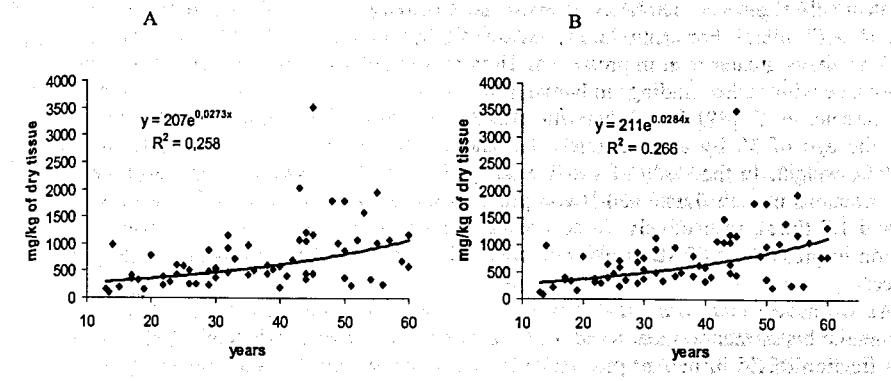


Fig. 1. Individual data for Zn mass fraction obtained by INAA (A) and ICP-MS (B) in all samples of prostate tissue, and exponential lines of trend with age.

Table 2. Some statistical parameters of Zn content (mg/kg on dry weight basis) in the prostate tissue of healthy men obtained by INAA-LLR, ICP-MS, and INAA-LLR + ICP-MS (together)

| dissue of ficultity files | 1 Obtaine | u by min | M-LLIX, I | CI -WIS, and INA | V-PPIC. | icr-ivis (lugelliei |
|---------------------------|-----------|----------|-----------|------------------|---------|---------------------|
| Method | M | SD | SEM | Min Max | Med | P0.025 P0.975 |
| INAA-LLR | 722 | 576 | 72 | 90.0 3513 | 533 | 152 1987 |
| ICP-MS | 746 | 556 | 69 | 71.6 3510 | 619 | 145 1865 |
| INAA + ICP-MS | 734 | 562 | 50 | 80,8 3512 | 568 | 148 1865 |
| | | | | | | |

M - arithmetic mean; SD - standard deviation; SEM - standard error of mean; Min - minimum value; Max - maximum value; Per. 0.025 - percentile with 0.025 level; Per. 0.975 - percentile with 0.975 level

To estimate the effect of age on Zn content in prostate (Table 3) we examined three age groups: the first comprised a younger group with ages from 13 to 20 years (mean age 16.3 years, n=9), the second comprised men with ages ranging from 21 to 40 years (mean age 30.4 years, n=28) and the last one comprised older persons with ages ranging from41 to 60 years (mean age 49.6 years, n=27). The values of Zn content obtained by INAA-LLR, ICP-MS, and INAA-LLR + ICP-MS (together) were used in calculation.

Table 3. Effect of age on mean values (M±SEM) of Zn contents (mg·kg⁻¹, dry weight basis)

| Method | | Age groups | | Ratios, p | (Student's t-test) |
|----------|---------------------------------------------------------------------------------------------------------------------------------------------------------------------------------------------------------------------------------|--------------------|--------------------|-----------------------------|-------------------------------------|
| | Group 1 | Group 2 | Group 3 | 2 to 1 | 3 to 1 3 to 2 |
| _ | 13-20 year n=9 | 21-40 year n=28 | 41-60 year n=27 | a dide | Andrews |
| INAA-LLR | 384±102 | 521±44 | 1045±140 | 1.36 | 2.72 ^b 2.01 ^b |
| ICP-MS | 382±103 | 557±44 | 1150±203 | 1.46 | 3.01 ^a 2.06 ^a |
| INAA+ | n de la companya de La companya de la co | 520120 | 1007.100 | in named or in spage sil | 2.86 ^b 2.04 ^b |
| _ICP-MS | 383±73 | 539±30 | 1097±120 | 1.41 | 2.86 2.04 |

M - arithmetic mean, SEM - standard error of mean, $^a-p \le 0.01$, $^b-p \le 0.001$

A statistically significant tendency of age-related increase in Zn mass fraction was observed in prostate (Table 3). For example, in prostate of 50 years old men the mean Zn mass fraction was 2.86 times greater than in prostate of 16 years old persons, respectively. This result is in accordance with earlier findings in human prostate [48-51]. For example, Heinzsch et al. [48] and Leissner et al. [49] found that zinc content in whole adult normal prostate was higher after the age of 30 by approximately 1.9 and 1.5 times, respectively, in spite of similar prostatic weight. In the study of Tisell et al. [50], men 50-69 years of age had higher zinc mass fractions in their dorsal and lateral prostatic lobes than had men 20-29 years of age by 1.6 and 1.7 times, respectively. In accordance with Oldereid et al. [51], the mean Zn mass fraction in prostate of 60 years old men was 3 times greater than in prostate of 20 year old subjects.

As we have found, the age-dependent increases of the Zn mass fractions followed an exponential better than a linear trend (Fig. 1). The finding, that age-dependent changes in the mass fraction of Zn in human prostate best fit exponential curve, was previously published [51].

The obtained values of Zn mass fraction, as shown in Table 4, agree well with median of means cited by other researchers for the human prostate, including samples received from persons who died from different diseases. A number of values for chemical element mass fractions were not expressed on a dry weight basis by the authors of the cited references. However, we calculated these values using published data for water—80% [56] and ash—1% on wet weight basis [57] contents in prostate of adult men.

Table 4. Median, minimum and maximum value of means of Zn contents (mg/kg on dry weight basis) in intact prostate of adult males according to data from the literature in comparison with our results

| | Published data [Refer | encel | This work resu | 1. |
|------------------------|---------------------------|--------------------------|----------------|------|
| Median | Minimum | Maximum | M±SD | |
| of means, (n)* | of means, (n)** | of means, (n)** | n=64 | 4781 |
| 482 (48) | 111 (-) [58] | 2735 (10) [59] | 7241560 | |
| 141 - arruntifette mea | n: SD – standard deviatio | n. (n) * number of all C | | |

All the deceased were citizens of Moscow. None of those who died a sudden death had suffered from any systematic or chronic disorders before. The normal state of prostates was confirmed by morphological study. Thus, our data for Zn mass fractions in intact human prostate may serve as indicative normal values for urban population of the Russian Central European region.

Conclusions

INAA-LLR and ICP-MS are the adequate analytical tools for the non-destructive determination of Zn content in the tissue samples of human prostate. From the time of puberty and up to 60 years the mass fraction of Zn in prostate tissue exponentially increases almost 3

times. Thus, the data do not support the hypothesis of age-related deficiency of zinc in prostate tissue and the need for zinc supplementation for the correction of this deficit.

Acknowledgments

We are grateful to Prof. A.A. Zhavoronkov, Institute of Human Morphology, Russian Academy of Medical Sciences, Moscow, for supplying prostate samples.

References

- 1. Kumar, R.J., Barqawi, A.B., Crawford, E.D. US Oncology Review, 2004, pp. 1-6.
- 2. Pischon, T. et al. Cancer Epidemiol. Biomarkers Prev., 2008, 17, 3252-3261.
- 3. Cohen, L.A. Ann. NY Acad. Sci., 2002, 963, 148-155.
- 4. Jones, B.A. et al. Cancer Epidemiol. Biomarkers Prev., 2008, 17, 2825-2834.
- 5. Van Patten, C.L., De Boer, J.G., Tomlinson Guns, E.S. J. Urol., 2008, 180, 2314-2322.
- 6. Yamada, K. et al. Int. J. Cancer, 2000, 89, 259-264.
- 7. Rebbeck, T.R. Cancer Epidemiol. Biomarkers Prev., 2006, 15, 1569-1571.
- 8. Jemal, A. et al. CA Cancer J. Clin., 2003, 53, 5-26.
- 9. Zaichick, V., Sviridova, T., Zaichick, S. Int. Urol. Nephrol., 1997, 29, 565-574.
- 10. Schrauzer, G.N., White, D.A., Schneider, C.J. Bioinorg. Chem., 1977, 7, 35-56.
- 11. Whelan, P., Walker, B.E., Kelleher, J. Br. J. Urol., 1983, 55, 525-528.
- 12. Kolonel, L.N., Yoshizawa, C.N., Hankin, J.H. Am. J. Epidemiol., 1988, 127, 999-1012.
- 13. West, D.W. et al. Cancer Causes Control, 1991, 2, 85-94.
- 14. Andersson, S.O. et al. Int. J. Cancer, 1996, 68, 716-722.
- 15. Key, T.J.A. et al. Br. J. Cancer, 1997, 76, 678-687.
- 16. Vlajinac, H.D. et al. Eur. J. Cancer, 1997, 33, 101-107.
- 17. Kristal, A.R. et al. Cancer Epidemiol. Biomarkers Prev., 1999, 8, 887-892.
- 18. Zaichick, V., Zaichick, S. In: Mengen und Spurenelemente. 19. Arbeitstagung. Friedrich-Schiller-Universitat, Jena, 1999, pp.104-115.
- 19. Leitzmann, M.F. et al. J. Natl. Cancer Inst., 2003, 95, 1004-1007.
- 20. Whittemore, A.S. et al. J. Nat. Cancer Inst., 1995, 87, 652-661.
- 21. Food, nutrition and the prevention of cancer: a global perspective. Vol. 1, first ed. American Institute for Cancer Research, Washington, District of Columbia, 1997.
- 22. Hayes, R.B. et al. Cancer Epidemiol. Biomarkers Prev., 1999, 8, 25-34.
- 23. Kolonel, L.N. Epidemiol. Rev., 2001, 23, 72-81.
- 24. Michaud, D.S. et al. Cancer Causes Control, 2001, 12, 557-567.
- 25. Cross, A.J. et al. Red meat intake and prostate cancer risk in the PLCO Cancer Screening Trial. B86. Frontiers in cancer prevention. AACR, Seattle, Washington, 2004.
- 26. Platz, E.A., Helzlsouer, K.J. Epidemiol. Rev., 2001, 23, 93-101.
- Groff, J.L., Gropper, S.S. Advanced nutrition and human metabolism. Wadsworth, Belmont, CA, 2000.
- 28. Mocchegiani, E., Muaaioli, M., Giacconi, R. Biogeront., 2000, 1, 133-143.
- 29. Ekmekcioglu, C. Nahrung, 2001, 45, 309-316.
- 30. High, K.P. Clin. Infect. Dis., 2001, 33, 1892-1900.
- 31. Padro, L. et al. J. Nutrit. Health Aging, 2002, 6, 31-33.

- 32. Miyata, S. Nippon Ronen Igakkai Zasshi, 2007, 44, 677-689.
- 33. Zaichick, V. J. Radioanal. Nucl. Chem., 2004a, 262, 229-234.
- 34. Nemoto, K. et al. Biochem. Pharmacol., 2000, 59, 401-405.
- 35. Sommerfeld, H.J. et al. Cancer Research, 1996, 56, 218-226.
- 36. Boissier, S. et al. Cancer Research, 2000, 60, 2949-2954.
- 37. Chandra, R.K. JAMA, 1984, 252, 1443-1446.
- 38. Samman, S., Roberts, D.C. Atherosclerosis, 1988, 70, 247-252.
- 39. Holmes, M.D. et al. Cancer Epidemiol. Biomarkers Prev., 2002, 11, 852-861.
- 40. Prasad, A.S. et al. Nutrition, 1996, 12, 344-348.
- 41. Schwartz, M.K. Cancer Res., 1975, 35, 3481-3487.
- 42. Matusik, R.J. et al. Biochem. Cell. Biol., 1986, 64, 601-607.
- 43. Blok, L.J. et al. Mol. Endocrinol., 1995, 9, 1610-1620.
- 44. Costello, L.C. et al. Journal of the National Cancer Institute, 2004, 96, 239-240.
- 45. Costello, L.C. et al. Cancer Causes Control, 2005, 16, 901-915.
- 46. Costello, L.C., Franklin, R.B. Molecular Cancer, 2006, 5, 17-30.
- 47. Vaquero, M.P. J. Nutrit. Health Aging, 2002, 6, 147-153.
- 48. Hienzsch, E., Schneider, H.-J., Anke, M. Zeitschrift für Urologie und Nephrologie, 1970, 63, 543-546.
- 49. Leissner, K.M., Fielkegard, B., Tisell, L.E. Invest. Urol., 1980, 18, 32-35.
- 50. Tisell, L.E., Fielkegard, B., Leissner, K.M. J. Urol., 1982, 128, 403-405.
- 51. Oldereid, N.B. et al. J. Reprod. Fertil., 1993, 99, 421-425.
- 52. Zaichick, V. Trace Elements in Medicine, 2004b, 5(3), 17-22.
- 53. Zaichick, S., Zaichick, V. Applied Radiation and Isotopes, 2011, 69, 827-833.
- 54. Parr, R. 1980. Inter-comparison of minor and trace elements in IAEA animal muscle (H-4). Report No 2. IAEA, Vienna.
- 55. M'Baku, S.B., Parr, R.M. 1982. Interlaboratory study of trace and other elements in the 1AEA powdered human hair reference material, HH-1. J. Radioanal. Chem. 69, 171-180.
- 56. Györkey, F. et al. Cancer Res., 1967, 27, 1349-1353.
- 57. Saltzman, B.E. et al. Environmental Research, 1990, 52, 126-145.
- 58. Anspaugh, L.R. et al. Compilation of Published Information on Elemental Concentrations in human Organs in Both Normal and Diseased States. No. UCRL-51013Pt., 1971-1973, pp. 1-4.
- 59. Jafa, A. et al. Indian J. Cancer, 1980, 17, 34-37.

TIME DIFFERENTIAL PERTURBED ANGULAR CORRELATION STUDY OF VEGETABLE OILS

C. Oprea, A. Velichkov, I.A. Oprea, D.V. Filosofov, P. J. Szalanski

Joint Institute for Nuclear Research (JINR), Dubna 141980, Russian Federation

Abstract

We present a series of measurements of the time- and reactant-dependent interactions in the angular correlation of **IIIn** in vegetable oils. In our studies we employ Time Differential Perturbed Angular Correlation (TDPAC) of the **IIIn** In Cd **\mathcal{T}\mathcal{T}\mathcal{C}\text{ ascade from } *IIIn** probe nucleus to investigate aspects related to physicochemical structure of vegetable oil (as for example, Oleum embryonum triticu). The above experiments are carried out using a homemade TDPAC spectrometer which consisting of a four detector fast-slow coincidence system using *NaI(TI)* scintillators with a time resolution of 2.5 ns.

Keywords: TDPAC, 111 In, vegetable oil, Electric Field Gradient, physicochemical organization

Introduction

After the first paper of D. R. Hamilton (1940) on the theory of the directional correlation of γ - γ cascade, it took seven years before Brady and Deutsch (1947) realized the experimental adequate conditions to measure such a correlation. Then the perturbed angular correlation started as a nuclear physics technique used in measuring spins and parities.

Following the technological development of the experimental PAC installations, the perturbed angular correlation spectroscopy (PAC) has been widespread applied in a large variety of condense matter studies from the atomic scale to elementary defect itself and nowadays one uses the vacancy clusters as the object of investigation. The most common application of PAC is the time differential perturbed angular correlation (TDPAC) which measures the angular correlation between pairs of gamma rays emitted by radioactive nuclei, as fraction of the time the nucleus spends in the intermediate state.

During the present researches, the ^{III}In TDPAC measurements were conducted to explore the physicochemical structure and TDPAC dynamics of vegetable oil (as for example, Oleum embryonum triticu that was previously tested biologically). ^{III}In is frequently used in biomedical and pharmaceutical researches and it is readily available.

Theoretical background of TDPAC

This section reflects the nuclear physical origins of the quadrupole interaction and describes the magnetic interaction in hyperfine interactions (HFIs) that can be used in condense matter applications. The interaction of the magnetic moment and quadrupole moment of the probe nucleus with the extra nuclear magnetic field and electric field gradients respectively (HFIs) result in the perturbation of the angular correlation of γ - rays.

The basis of perturbed angular correlation consists in producing a radioactive nuclei (in excited state with nuclear spin $|I_i, m_i\rangle$) that decays over a $\gamma\gamma$ -cascade by emission of γ to the intermediate state I, followed by decay (to the ground state $|I_f, m_f\rangle$ of the daughter nucleus I_f

by emission of a second y-quant γ . The angular correlation function $W(\gamma, \gamma, t)$ is a measure of the probability that γ is detected in direction $\rightarrow k$, and γ is detected in direction $\rightarrow k$. Utilizing the density matrix formalism [4,5] it can be written as

$$W(\gamma_1, \gamma_2, t) = \sum_{mm'} \langle m | \rho(\gamma_2, 0) | m' \rangle \langle m' | \rho(\gamma_1, 0) | m \rangle, \tag{1}$$

where m, m' define the inhomogeneous population of the m-states of the intermediate state: the matrix elements $\langle m|\rho(\gamma_i,0|m)\rangle$ are the probabilities of finding the system in an eigenstate m immediately after the i_{i} transition. Performing the mm-sum the relative probability $W(\theta)d\Omega$ of detecting γ_2 in the solid angle $d\Omega$ with the angle θ in respect to γ_1 is obtained as Legendre polynomials

$$W(\theta) = \sum_{k=even}^{k_{max}} A_{kk} P_k(\cos \theta)$$
 (2)

where $A_{kk} \equiv A_k (\gamma_1) A_k (\gamma_2)$ are the angular correlation coefficients and are depending of the angular momenta of the state and the multipolarities of the transitions; the sum is only over even k because the odd A_{kk} disappear as a consequence of parity conservation and $0 \le k \le min(2I_s, l_i + l'_i)$ (Note: the polarization of the γ photons is not measured).

The summation is finite due to conservation of angular momentum. For the frequently used I =5/2 the summation index limit is $k_{max} = 4$, thus

$$W(\theta) = 1 + A_{22}P_2(\cos\theta) + A_{44}P_4(\cos\theta)$$
(3)

Through the perturbation of the probe nucleus during the finite lifetime of the intermediate state from the hyperfine interaction of magnetic or electric extra field gradients of measured sample material the angular correlation function depends only on the angle between γ detections, θ , and time between detections, t as

$$W(\theta, t) = \sum_{k=0}^{k_{max}} A_{kk} G_{kk}(t) P_k(\cos \theta), \tag{4}$$

where $G_{kk}(t)$ is the perturbation factor containing the information about the interaction.

The interaction can occur between the nuclear magnetic dipole moment μ of the intermediate state Is and the extranuclear magnetic field B or between the nuclear electric quadrupole moment Q and the extranuclear electric field gradient $V = \nabla^2 \phi$.

Magnetic hyperfine interactions

The magnetic hyperfine interaction is measured by the Larmor-frequency

$$\omega_L = \frac{|g\mu_N B|}{\hbar} \qquad \text{if the proposed of $

where g is the dimensionless g-factor (Land é-factor) of the intermediate state; μ_N is the nuclear magneton ($\mu_N = 5.05 \cdot 10^{-27} \text{ J/T}$); B is the magnitude of the magnetic field at the probe, (i.e. the hyperfine magnetic field).

The magnetic hyperfine interaction splits the intermediate state into |2I+I| equidistant sublevels with ΔE

$$\Delta E = \hbar \omega_t = -g \mu_N B \tag{6}$$

Electric hyperfine interactions

The electric hyperfine interaction between the charge distribution of the nucleus and the extranuclear static electric field occurs only for electric field gradients (EFG) that are strong enough to be measured.

The energy of the sublevels for axially symmetric EFGs is

$$E_{Q} = \frac{eQV_{\pi}}{4I(2I-1)} \cdot (3m^{2} - I(I+1)) \tag{7}$$

where Q is the quadrupole moment; V_{zz} is the the principal component of EFG with largest magnitude; e is the fundamental unit of charge; I is the total spin of the intermediate nuclear state.

The energy difference between two sublevels m and m' is given by

$$\Delta E_Q = \hbar \omega_0 \cdot 3 \left| m^2 - m^{12} \right| \tag{8}$$

where ω_0 is the quadrupole frequency.

It can be deduced from (8) that the splitting of the sublevels of electric quadrupole hyperfine interaction is non-equidistant since it depends on the angular moment I of the sublevel. Practically is used the quadrupole coupling frequency vo which measures the strength of the electric hyperfine interaction in time and is independent from the nuclear spin I_{FO}

$$v_{Q} = \left| \frac{eQV_{\pi}}{h} \right|$$
 (9)

Experimental methodology

TDPAC sources

The PAC probe nucleus should to acts as a foreign agent that scopes out its environment and emits/decays by correlated γ - ray cascades. TDPAC method measures the angular correlation as fraction of the time the nucleus spends in the intermediate state. For this the intermediate state needs to meet the following expectations:

- it must have a reasonably long lifetime so that the probe has time to "feel" the extranuclear fields and to interact with them:
- the γ ray energies should to be sufficiently different so that γ_1 and γ_2 can be distinguished;
- the nuclear moments of the intermediate state, as well as the anisotropy of the angular correlation between γ rays have to be large enough to allow the measurement of the perturbation function;

the parent nucleus must be available, and it must have a long enough lifetime to be practical to work with.

The sensitive ¹¹¹In/¹¹¹Cd-PAC probe nucleus has been diffused into the oil material under study for experimental EFGs determination. ¹¹¹Cd is the decay product of electron-capture-decay of ¹¹¹In with a half-life of 2.83 days. The properties of the PAC pair parent-daughter probe nuclei relevant for TDPAC measurements are presented in Table 1.

Table 1: Relevant properties of PAC probe nuclei

| Parent to probe decay | A ₂ | T _{1/2} | γ ₁ [keV] | γ ₂ [keV] | I | t _{1/2} [ns] | g-factor | Quadrupole Moment |
|--------------------------------------|----------------|------------------|-------------------------|-------------------------|-----|-----------------------|----------|----------------------|
| ¹¹¹ In→ ¹¹¹ Cd | -0.18 | 2.83 d | 171 | 245 | 5/2 | 85 | -0.306 | +0.83(13) |

Note. $T_{1/2}$ is the half-life of parent nucleus; I and $t_{1/2}$ are nuclear spin and half-life, respectively, of the intermediate level in the $\gamma_1 - \gamma_2$ cascade; g-factors and quadrupole moments are of the intermediate state.

Although all the experiments were based on the measurement of the electric field gradient (EFG) at the probe sites, they have been performed with different biochemical reactivants concerning vegetable oil properties. In order to study the physicochemical structure of vegetable oil, the biochemical reactivants as ether, heptanol [CH₃(CH₂)₈CH₃], and Dekan [CH₃(CH₂)₅CH₂OH], were employed in experimental measurements. They were used in different chemical complex solutions, as ¹¹¹In in ether + 14% HDPD, ¹¹¹In in 500ml CH₃(CH₂)₈CH₃ +13% HDPD, and ¹¹¹In in 21% HDPD + CH₃(CH₂)₅CH₂OH.

TDPAC spectrometry

The above experiments are carried out using a home-made TDPAC spectrometer (Brudanin, NIMA 2005), which consisting of a 4-detector fast-slow coincidence system using NaI(Tl) scintillators (40 x 40 mm) arranged in the plane at 90° intervals. The fast timing signal is fed into the time-to-amplitude converter which allows to measuring the time the nucleus spent in the intermediate state of the cascade. The delayed coincidence counts $W(\theta, t)$ within a resolution time of 2.5 ns between the 90° and 180° detector pairs were recorded and stored as histograms.

Starting from the equation 2 the number of coincidences measured by the apparatus can be calculated as

$$N(\theta, t) = N_0 e^{-\lambda t} \cdot W(\theta) = N_0 e^{-\lambda t} \cdot (1 + A_{22} P_2(\cos \theta) + A_{44} P_4(\cos \theta)$$
 (10)

where N_0 is the total counting rate; λ the decay constant; the rest term describes the anisotropic emission probability; usually the coefficient A_{44} is much smaller than A_{22} ($A_{44} \ll A_{22}$). Then $A_2G_2(t)$ is defined as the ratio

$$A_2G_2(t) = 2 \left| \frac{N(180^{\circ}, t) - N(90^{\circ}, t)}{N(180^{\circ}, t) + 2N(90^{\circ}, t)} \right|, \tag{11}$$

The least-squares fitting from the angular correlation perturbation models for (EFG) narameter determination was used:

$$A_2G_2(t) = a_0 + a_1 \exp(-\lambda_2 t) \text{ (dynamic)}$$

$$A_2G_2(t) = a_0 + a_1 \cos(\omega_0 t) \exp(-\Lambda t) \text{ (static)},$$
(12)

where $G_2(t)$ is perturbation function extracted from the time spectra; λ_2 is relaxation parameter; Λ is width of the quadrupole frequency distribution relative to mean value of ω_0 .

Results

By the use of biochemical solutions the formation of homogeneous phases with similar local structures previously observed in the liquid state occurs (Figs 1-5). The spectra from the Figs 1-3 displays a superposition of signals corresponding at least to two different environments of the probes due to a degree of disorder around the radionuclide-probes. As it can be seen in figures, the error bars increase with time between γ - ray emissions.

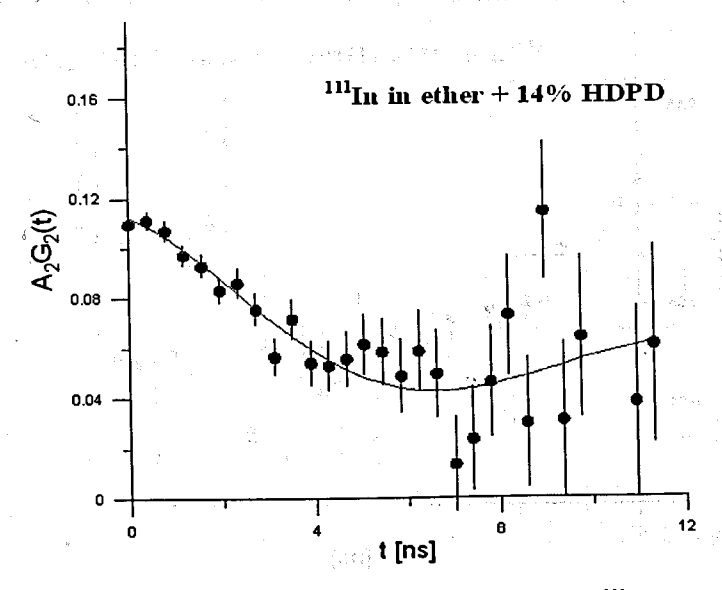


Fig. 1. TDPAC perturbation spectra of $^{111}In/^{111}Cd$ γ - γ cascade using ^{111}In in ether + 14% HDPD solution; v_Q =137(12) MHz quadrupole frequency for axial symmetric EFG (η =0)

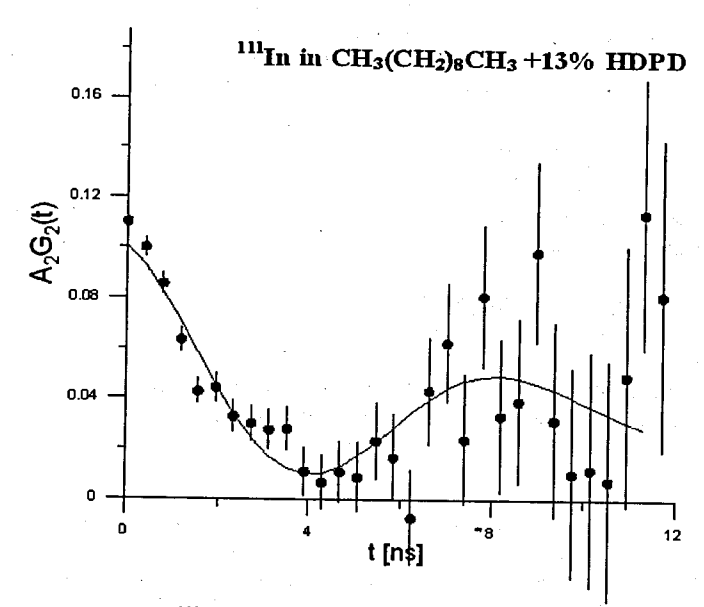


Fig. 2. TDPAC spectra of $^{111}In/^{111}Cd$ γ - γ cascade using ^{111}In in 500ml CH₃(CH₂)₈CH₃ +13% HDPD solution; v_Q =218(10) MHz quadrupole frequency for axial symmetric EFG (η =0)

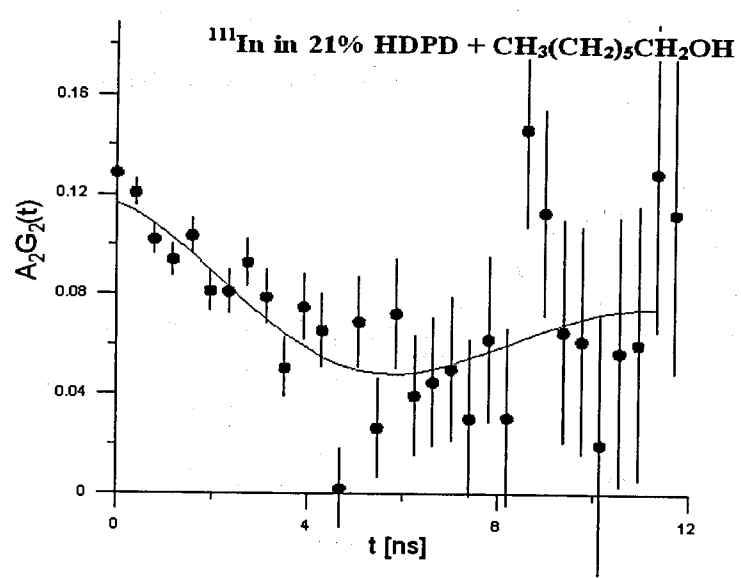


Fig. 3. TDDPAC spectra of $^{111}In/^{111}Cd\gamma - \gamma$ cascade using ^{111}In in 21% HDPD + $CH_3(CH_2)_3CH_2OH$ solution; v_Q =156(16) MHz quadrupole frequency for EFG (η =0)

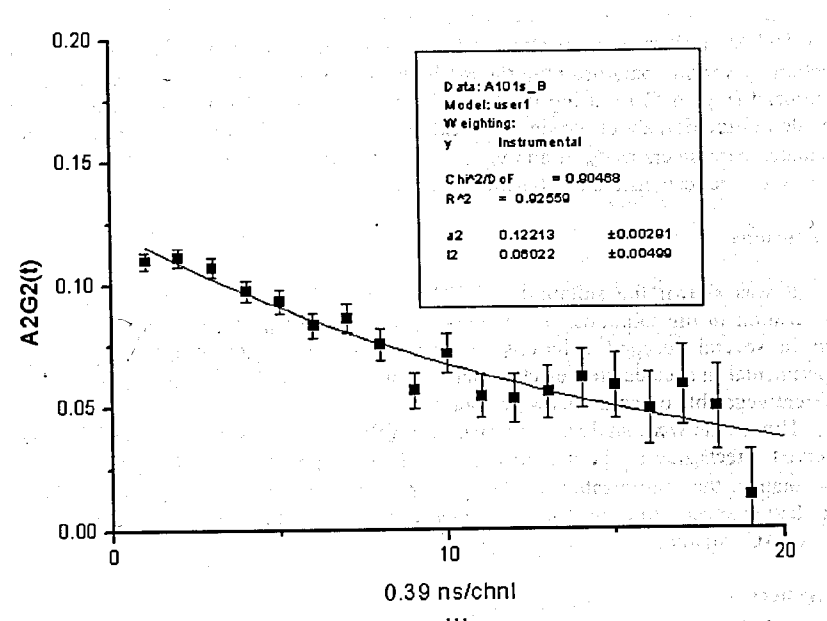


Fig. 4. Fitting χ^2 of the TDPAC spectra for ¹¹¹In in ether + 14% HDPD solution (Fourier transform display)

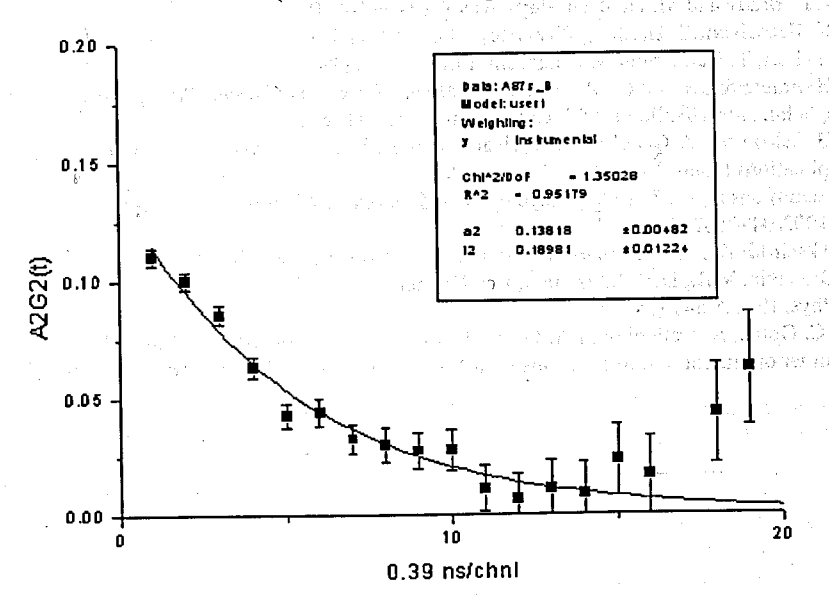


Fig. 5. Fitting χ^2 of the TDPAC spectra for ¹¹¹In in $CH_3(CH_2)_8CH_3 + 13\%$ HDPD solution (Fourier transform display)

TDPAC perturbation spectra are fitted to a theoretical expression of the perturbation function by varying parameters in the model function until a χ^2 goodness of fit parameter is minimized (Figs 4-5) by using the DEPAC software. Best-fit values obtained from fits can provide information about physicochemical organization of the vegetable oil. From the fitting calculated parameters as a_0 , a_1 and v_0 , it results that these processes of diffusion of the PAC probe in oil are responsible for dynamic character of the perturbation of angular correlation.

Conclusions

It was shown the suitability of TDPAC method to analyzing the physicochemical organization in oil solutions. It was developed an experimental methodology by diffusing III in several reactant solutions of preparation the vegetable oil analytical samples. Experimental and calculated electric field gradients (EFG) on III in probe atom diffused in different vegetable oil solutions were obtained.

The results were analyzed in terms of a diffusion process approach which explains the observed effects due to the dynamic character of the perturbation of angular correlation. It was obtained the minimization of the χ^2 fit parameter up to best-fit values for the TDPAC perturbation spectra to a full-line theoretical expression of the perturbation function by using the DEPAC software.

References

- 1. D.R. Hamilton, Phys. Rev. 58 (1940) 122
- 2. E.L. Brady and M. Deutsch, Phys. Rev. 72 (1947) 870
- 3. K. Krusch and J. Gardner, Phys. Rev. B 24 (1981) 4587
- 4. A. Lerf, T. Butz: Angew. Chem. Int. Ed. Engl. 26 (1987) 110
- 5. H. Frauenfelder and R. M. Steffen, in: Alpha-, Beta- and Gamma-Ray Spectroscopy, Ed. K. Siegbahn, North-Holland Publ. Comp. Amsterdam (1965)
- 6. G. Schatz and A. Weidinger: Nuclear Condensed Matter Physics: Nuclear Methods and Applications (John Wiley, New York, 1996)
- 7. Hemmingsen, L., T. Butz. Encyclopedia of Inorganic Chemistry (2008) DOI: 10.1002/0470862106.ia322.
- 8. Akselrod, Z.Z., D.V. Filossofov, et al. Z. Naturforsch. 55a (2000) 151
- 9. Brudanin, V.B., D.V. Filossofov, O.I. Kochetov, N.A. Korolev, et al. Nucl. Instrum. Meth. in Phys. Res. A 547 (2005) 389
- 10. C. Oprea, A. Velichkov, I.A. Oprea, D.V. Filosofov. Proceedings of the XVIIth Int. Seminar on Interaction of Neutrons with Nuclei (ISINN-17), Dubna, RF (2010) 399

Evaluation of parity violation effects for thermal neutrons scattering on 204Pb nucleus

 A. Oprea, C. Oprea, Yu. M. Gledenov, P.V. Sedyshev
 141980 Dubna, Moscow Region, Russian Federation Joint Institute for Nuclear Research (JINR)
 Frank Laboratory for Neutron Physics (FLNP)

Abstract. Isotopes of Lead are suitable for studies of parity violation effects in nuclear reactions. We have estimated the energetic dependences of some of these effects in the elastic scattering of thermal and resonance neutrons on ^{204}Pb . For this nucleus experimentally was found a great value than expected of the neutron spin rotation. The spin rotation of the transversal polarized neutron beam passing trough the matter was explained by the presence of the weak interaction but in the case of ^{204}Pb the measured unexpected value may indicate also, the presence of an unknown negative resonance of the compound nucleus ^{205}Pb .

Introduction

The presence of the weak interaction between nucleons in compound nucleus leads to the asymmetry effects in nuclear reactions. In the elastic scattering of neutrons some of these effects which can be measured in the experiment are [1]: the asymmetry of the emitted neutrons, the spin rotation of the transversal polarized neutrons beam and the longitudinal polarization of an initial unpolarized neutrons beam.

We used the approach very well described in [1] and applied the obtained formulas in the case of ^{204}Pb . First we used for our estimation of the mentioned parity violation effects the resonance parameters from [2] and after that the parameters for unknown negative P resonance proposed in [3] in order to explain the big unexpected value for spin rotation.

The natural Lead is a mixing of four isotopes with following masses and abundances 204 (1.43%), 206 (24.15%), 207 (22.4%) and 208 (52.4%). The isotope 208 Pb is double magic and therefore all Lead isotopes have low levels densitie [3]. The analysis effectuated in [3] suggested that the main contribution to the spin rotation comes mainly from 204 Pb isotope. The experimental value for the spin rotation is of order of a few units of 10^{-6} [4, 5]. This value is of three order higher than the theoretical estimation [3].

In this work we evaluate the energetic dependence of the three mentioned effects in the two levels approximation for elastic scattering of neutrons on ^{204}Pb nucleus, first using the resonance parameters from [2]. After we compare the results with the values obtained with parameters for negative resonance from [3]. According with [2] the S and P resonance parameters for ^{204}Pb nucleus with widths parametric expressions from [2] and [6] are:

$$E_S = -2980 \text{ eV} \text{ and } E_P = 480 \text{ eV}$$
 (1)

The negative P resonance parameters proposed in [3] extracted from the comparison between experimental [4, 5] and theoretical values [3] are:

$$E_P = -16 \, eV \text{ and } \Gamma_P = 3 \times 10^{-3} \, eV$$
 (2)

Main formulas

Now it is the time to define the parity violation effects. Let suppose that we have a transversal polarized neutrons beam interacting with a target nucleus. Due to the presence of weak interaction, in the process of scattering in the outgoing channel appears an asymmetry of scattered neutrons and by definition this effect has the following form:

$$\alpha = \frac{\frac{d\sigma(\uparrow)}{d\Omega} - \frac{d\sigma(\downarrow)}{d\Omega}}{\frac{d\sigma(\uparrow)}{d\Omega} + \frac{d\sigma(\downarrow)}{d\Omega}}$$
(3)

 $\frac{d\sigma(\uparrow)}{d\Omega}$, $\frac{d\sigma(\downarrow)}{d\Omega}$ = differential cross section of scattered neutrons with spin up (\uparrow) and down

(1) related to the initial neutrons spin direction.

For the rotation angle of initial neutron spin on length unit we have:

$$\frac{d\Phi}{dz} = -N\lambda \operatorname{Re}(f_+ - f_-) \tag{4}$$

With simple transformations the neutron rotation angle can be written as:

$$\Phi = \frac{1}{N\sigma_{tot}} \cdot \frac{d\Phi}{dz} = \frac{\text{Re}(f_- - f_+)}{\text{Im}(f_- + f_+)}$$
(5)

The terms in relations (4), (5) are: N = number of target nucleus on volume unit, $\lambda =$ neutron wave length, f_{t} , f_{z} = scattering amplitude on zero degree direction with positive (+) and negative (-) neutron spirality, σ_{tot} = the total cross section.

The last effect is the longitudinal polarization of an incident not polarized neutron defined by the relation:

$$P = \frac{\sigma_{-} - \sigma_{+}}{\sigma_{-} + \sigma_{-}} \tag{6}$$

 σ_{-} , σ_{+} = total cross section with negative (-) and positive (+) spirality.

The physical quantities defined in relations (3), (4) and (6) correspond to the following correlations between main vectors (as neutron spins and neutron initial and outgoing directions):

$$\alpha \rightarrow \left(\vec{\sigma_i} \cdot \vec{n_f}\right), \ \Phi \rightarrow \left(\vec{\sigma_i} \times \vec{\sigma_f}\right) \cdot \vec{n_f}, \ P \rightarrow \left(\vec{\sigma_f} \cdot \vec{n_f}\right)$$
 (7)

 $\sigma_i, \sigma_i, n_i, n_i$ = initial (i) and final (f) unit vectors of neutron spin and impulse

directions. Using the relations of definition (3), (4), (6) and the approach described in [1] we have obtained the following expressions for the asymmetry of emitted neutrons (a), rotation angle of outgoing neutron spin (Φ) and longitudinal polarization (P) in the two levels approximation in the case elastic scattered neutrons on ²⁰⁴Pb nucleus:

$$\alpha = 2W_{SP}\sqrt{\Gamma_S^n \Gamma_P^n} \frac{\Gamma_S^n (E - E_P) - \Gamma_P^n (E - E_S) + 2kR(E - E_S)(E - E_P)}{(\Gamma_P^n)^2 [P] + (\Gamma_P^n)^2 [S] + 4(kR)^2 [S][P]}$$
(8)

$$\Phi = \frac{4W_{SP}\sqrt{\Gamma_{S}^{n}\Gamma_{P}^{n}}}{[S][P]} \cdot \frac{(E - E_{S})(E - E_{P}) - \frac{\Gamma_{S}^{n}\Gamma_{P}^{n}}{4}}{\frac{\Gamma_{S}^{n}\Gamma_{S}^{n}}{[S]} + \frac{\Gamma_{P}\Gamma_{P}^{n}}{[P]} + 4(kR)^{2}}$$

$$P = -2W_{SP}\sqrt{\Gamma_{S}^{n}\Gamma_{P}^{n}} \cdot \frac{(E - E_{S})\Gamma_{P} + (E - E_{P})\Gamma_{S}}{\Gamma_{S}\Gamma_{S}^{n}[P] + \Gamma_{P}\Gamma_{P}^{n}[S] + 4(kR)^{2}[S][P]}$$
(10)

$$P = -2W_{SP}\sqrt{\Gamma_S^n \Gamma_P^n} \frac{(E - E_S)\Gamma_P + (E - E_P)\Gamma_S}{\Gamma_S \Gamma_S^n [P] + \Gamma_P \Gamma_P^n [S] + 4(kR)^2 [S][P]}$$
(10)

The factors of $(kR)^2$ present in (8-10) are due to the potential scattering included in calculations. The elements of (8-10) are: Γ_S , Γ_P = total S, P widths, Γ_S^n , Γ_P^n = neutron S, P widths, E_S , E_P = S, P resonance energy, k = neutron wave number, R = nucleus radius, $W_{SP} =$ weak matrix element;

$$[S] = (E - E_S)^2 + \frac{\Gamma_S^2}{4}, [P] = (E - E_P)^2 + \frac{\Gamma_P^2}{4}.$$

Results

Experimental results for the spin rotation around the impulse direction of polarized transversal neutrons are [3-5]:

$$\Phi = (2.24 \pm 0.33) \cdot 10^{-6} \text{ and } \Phi = (3.53 \pm 0.79) \cdot 10^{-6} \text{ rad}$$
 (11)

Using the resonance parameters from [2] and considering for the weak matrix element a value of order of $W_{SP} = 2 \cdot 10^4 \text{ eV}$ (fair value for heavy elements [1], [3]) the theoretical estimation gives for spin rotation for thermal neutrons the result:

$$\Phi = -6.28 \cdot 10^{-8} \text{ rad}$$
 (12)

With P resonance parameters suggested in [3] $(E_P = -16 \text{ eV})$ and S resonance parameters from [2] we have for spin rotation a value in a very good agreement with experimental data (11):

$$\Phi = 1.88 \cdot 10^{-6} \text{ rad}$$
 (13)

The asymmetry (α) and longitudinal polarization (P) for incident thermal neutrons are of order of 10^{13} and 10^{11} respectively with parameters from [2] and higher with resonance parameters from [3] (10^{14} and 10^{8} order magnitude) but still very difficult to measure in the experiment and therefore we did not insisted in the analysis of them.

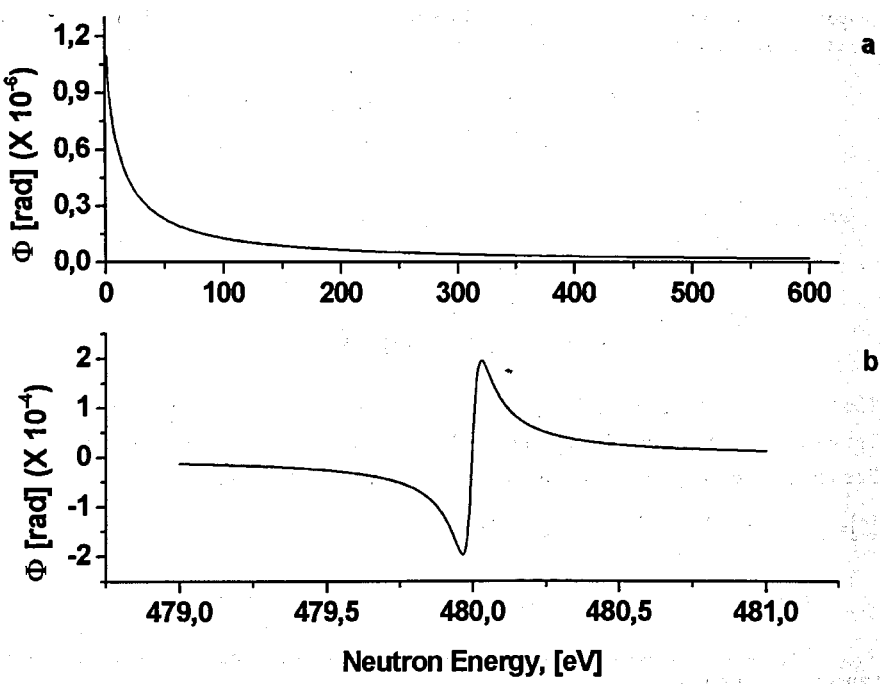


Figure 1. Spin rotation for neutrons scattering on ²⁰⁴Pb in the two levels approximations using a) parameters from [3] supposing the existence of negative P resonance, $E_P = -16 \text{ eV}$ b) parameters from [2] around the S resonance with $E_S = 480 \text{ eV}$ energy

In Figure 1 we have illustrated two interesting cases of spin rotation angle using different resonance parameters. In the case a) due to the fact that in the estimation we used two negative resonances (one S and one P) the spin rotation angle is decreasing with the energy. In the second b) case with one S negative resonance ($E_S = -2.98 \text{ keV}$) and one P resonance ($E_P = 0.48 \text{ keV}$) we obtained the well known expected shape of asymmetry effects in the two levels approximation estimated by authors for (n,p) reaction for ^{35}Cl and ^{14}N [7] nuclei.

We have obtained the energetic dependences in the scattering of neutrons on 204Pb nucleus for other parity violation effects i.e. asymmetry of emitted neutrons (a) and longitudinal polarization (P) but there are not presented here because they are some order of magnitude lower than the spin rotation (D) and therefore very difficult to be experimentally measured but their shape are similar to those from Figure 1 a) and b).

Discussion

We have evaluated the asymmetry effects due to the presence of weak interaction in the two levels approximation using two sets of resonance parameters [2], [3]. The parameters from [2] are universal accepted but the evaluated effects for thermal incident neutrons energy (E_{th} = 0.0253 eV) have very low values that are very difficult to measure experimentally. As we mentioned before the coefficients α and P in the thermal point are lower than 10^{-10} and the spin rotation Φ is of order of 10^{-8} .

The situation is changing in better with resonance parameters from [3] where the main idea is that the author had obtained from experimental data and theoretical evaluation in the two levels approximation for thermal energy the existence of an negative P resonance with energy E_P = -16 eV. The α and P effects increase with two or three order of magnitude and the spin rotation Φ is of order $10^{-5} - 10^{-6}$ in a very good agreement with the experiment (see relations (11-13)). This fact makes sense to effectuate an experiment for measurement of spin rotation angle of neutrons scattered on 204Pb in thermal region.

In Figure 1 a) and b) we have the energetic dependence of spin angle rotation for the two sets of resonance parameters. From Figure 1 b) (resonance parameters from [2]) results that around the P resonance $E_P = 480 \text{ eV}$ the spin rotation reaches the values 10^{-4} , change it sign in a very short energy interval (about 2 eV) and is zero in the resonance. In the experiment it is more easier to evaluate a 10⁻⁴ effect but here it is very difficult to find source that can give us the necessary intensity for incident transversal polarized neutrons with energy around 480 eV.

Finally it is of interest to evaluate the effect of other resonances in spite of the fact that in many papers their influence is neglected due to the very low value of the cross section.

The work was supported partially by the Program of Collaboration between JINR and Romanian Research Institutes on 2010 and 2011 years under the coordination of Romanian Plenipotentiary Representative to JINR. The before as a fire form the education in the second of the con-

References

[1] V.E. Bunakov, V. P. Gudkov, Materials of XVIth Winter School of Leningrad Institute for Nuclear Physics, p. 32-52, UDK 539.172, Leningrad, USSR, 1981 (in Russian)

William to the State of the section the state of the the

- [2] Mughabghab S.F., Divadeenam M., Holden N.E. Neutron Cross Sections. NY, Academic Press, 1981. v.2
- [3] G. A. Lobov, Yadernaya Fizika v. 63, № 8, p. 1465-1468, 2000 (in Russian)
- [4] G. A. Lobov, Preprint of Institute for Theoretical and Experimental Physics (ITEF), ITEF-20, Moscow, 1982 (in Russian)
- [5] Heckel B.R. et all., Phys.Lett. v. B119, p.209, 1982
- [6] Radiatsionyi zahvat neytronov Compendium, EnergoAtomIzdat, Moskva, 1986 (in Russian)
- [7] A. I, Oprea, C. Oprea, Yu. M. Gledenov, P.V. Sedyshev, C. Pirvutoiu, D. Vladoiu, Romanian Reports in Physics, v.63, № 2, p357-375, 2011

TRACE HEAVY METAL UPTAKE BY CROP ROOTS

C. Oprea, M.V. Gustova, I.A. Oprea

Joint Institute for Nuclear Research (JINR), Dubna 141980, Russian Federation

Abstract

Cabbage, potato and celeriac, grown in industrially polluted region, were included in the present research. We investigated the level of pollution and the way heavy metals enter the crop root, by surveying soil and plant samples. The contents of heavy metals in chosen samples were determined by analytical measurements with photon neutron activation spectrometry method (IPNAA). In particular, cabbage is suitable for growing in industrially polluted regions as it removes considerable quantities of heavy metals from the soil by the own root system and can be used as potential crop for remediate soil from heavy metals.

Keywords: crop root, IPNAA, heavy metals, bio-accumulation, uptake

Introduction

The behavior of heavy metals released by industrial activities is reflected in agriculture lands and that has been the center of much attention during the last decades. Previous experiments established that a clearly distinguished species characteristic exists in the accumulation of heavy metals in the vegetative parts of several agricrops. As a developed continuation of the earlier researches of the paper's authors, *The Project: Trace Heavy Metal Uptake by Crop Roots (2011-2012)* was started.

Toxic heavy metals such as As, Co, Cr, Fe, Ni and Zn, are constantly released into the environment. In particular, heavy metal pollution of soil is a significant environmental problem with a negative potential impact on human health and agriculture. The crop root, as an important interface of soil and plants, plays a significant role in transmission of contaminated soil by heavy metals through the food chain. This project develops a

methodology to evaluate transport of the main contaminating trace heavy metals from root soil and its uptake by crop roots.

The aim of this study was the continuation of the previous researches of the heavy metal bioaccumulation in the several agricrops. Determination of heavy metals in agricultural crops is frequently required in health-related environmental studies, because of severe toxicity of trace amounts of such elements for human organism.

For the assay of essential and trace heavy metals content in the aimed samples the photon neutron activation spectrometry method was already been tested and it is employed during the present researches.

การการเราะได้ เมื่อตาสพัสดาสมัย

Materials and methods

Sampling

The environmental samples were collected from the agricultural area surrounding a ferrous work near Ploiesti. The experimental plots were situated at different distances (0.5 and 15 km) from the source of pollution—the Ferrous-Metal Work. The same types of samples were recorded from a rural area chosen as a clean spot, situated at 20 km remoteness.

Sample preparation

Prior to analysis the crop samples were rinsed with distilled water to remove the adhering particles from soil and/or atmospheric deposition. For each type of crop, an average sample was prepared by mixing the samples collected from a site (three pieces). Then the samples were air dried for about one month and later by 48 hours at 40°C in the thermostat until constant weight. Aliquots of about 2 g of each sample were used for IPNAA. The fresh/dry mass ratio determined for crops were 7.62, 5.24 and 8.36 for cabbage root, potato root and celeriac root, respectively.

For the heavy metal assay, the photon neutron activation analysis at the Microtron MT-25 was used. The analytical methodology of IPNAA at MT-25 was largely described in our previous papers (see list of references).

The method provides detection limits of about 10 % for the elemental concentrations in investigated crops. On the crop samples were done four types of measurements, in order to account the elemental concentrations based on the activity of very short-, short-, medium- and long lived isotopes which exhibit times of disintegration of about few minutes, few hours, 1-3 days and, respectively, more than 4 days.

Results and discussion

Contents of toxic heavy metals such as As, Co, Cr, Fe, Ni and Zn, were determined by IPNAA in the studied crop roots, respectively cabbage, potato and celeriac (Table 1). As it is observed, the crop species showed remarkable difference in metal bio-accumulation and uptake from the root soil.

Table 1. Heavy metal concentrations (mg/kg) in crop root at 1 km from the ferrous complex as x±SD; x -average value (mg/kg) from five repetitions; SD: mean standard deviation

| HM / Crop | Cabbage root | Potato root | Celeriac root |
|-----------|-----------------|-----------------|---------------------------------------|
| type | • | | e e e e e e e e e e e e e e e e e e e |
| Cr | 17.5 ± 0.7 | 4.7 ± 0.3 | 7.2 ± 0.4 |
| Fe | 5370 ± 110 | 518 ± 26 | 632 ± 35 |
| Co | 5.08 ± 0.11 | 0.71 ± 0.04 | 0.95 ± 0.05 |
| Ni | 8.32 ± 0.25 | 1.30 ± 0.21 | 0.85 ± 0.17 |
| Zn | 61 ± 2.0 | 24 ± 1.5 | 28 ± 1.6 |
| As | 0.73 ± 0.09 | 0.22 ± 0.05 | 0.30 ± 0.07 |

The content of the same inorganic constituents for the concerned root soil are reported (Table 2). The distribution in the bio-accumulation of heavy metals from soil to plant for the studied crops seems to be selective, following the decreasing order: soil>root>pulp>leaf. Cabbage is the crop that most strongly absorbs and accumulates heavy metals from the soil. (as shown in Tables 1 and 2). With some exceptions, the levels of the heavy metals recorded in plants are in agreement with the normative allowable levels established in Romania.

A strongly exhibited tendency towards diminution of the contents of heavy metals in the soils and crop roots is observed with the increase of the distance from the ferrous smelter complex. The results concerning this aspect will constitute the subject of another report.

But taken Docker's and Indicate that

Table 2. Heavy metal concentrations (mg/kg) in host soil of the crop root at 1 km from the ferrous complex as x±SD; x -average value (mg/kg) from five repetitions;

SD: mean standard deviation

| HM / Crop | Soil of | | Soil of |
|-----------|----------------|----------------|---------------|
| type | cabbage root | | celeriac root |
| Cr | 64.7 ± 3.0 | 75.3 ± 4.2 | 64.1 ± 3.0 |
| Fe | 31650 ± 450 | 38150 ± 650 | 30840 ± 450 |
| Со | 18.3 ± 0.5 | 21.6 ± 0.5 | 18.1 ± 0.5 |
| Ni | 41 ± 9 | 48 ± 12 | 40±9 |
| Zn | 95 ± 15 | 115 ± 20 | 92 ± 13 |
| As | 14.1 ± 1.5 | 18.3 ± 2.5 | 13.8 ± 1.4 |

Conclusion

It was established from the present findings that cabbage root is a hyper-accumulator of most of the trace heavy metals such as Fe, Zn and As. This peculiarity could be used for selection of this vegetable crop for cultivation on metal contaminated soils.

The three vegetable crop species also showed notable differences in respect of heavy metal uptake and their bio-accumulation. Then our results may be useful for selecting suitable crop species for different metal contaminated soils.

References

- [1] Allison DW, Dzialo C (1981). Plant Soil 62: 81
- [2] Barman SC, LAL MM (1994). J Environ Biol 15:107
- [3] Barman SC, Saku RK, Bhargava SK, Chaterjee C (2000).

Bull Environ. Contam. Toxicol. 64:489

- [4] Khairiah J, Zalifah MK, Yin YK, Aminah A (2004). J Biol Sci 7:1438
- [5] MCKenna IM, Chaney RL, Williams FM (1993). Environ Res 8(3-4):679
- [6] Oprea C, Maslov OD, Gustova MV, Belov AG, Szalanski PJ, Oprea IA (2009). Vacuum 83 1:S162
- [7] Oprea CD, Mihul A (2003). Romanian Rep in Phys 55 32:91
- [8] Oprea C, Gustova MV, Oprea IA, Maslov OD, Belov AG, Ciofu R (2011). Proceedings of ISINN-18:322
- [9] Oprea C, Maslov OD, Gustova, MV, Belov AG, Oprea IA, Ciofu R, Mihul A (2010). Proceedings of ISINN-17:91
- [10] Sanders JR, Mc Grath SP, Adams T (1987). Environ Pollut 44:193
- [11] Tlustos P, Balik J, Pavlikova D, Szakova J (1997). Rostlinna Vyroba 43(10):487

Air Filters Components Activity Measurements with HpGe Gamma Spectrometer

Valery Shvetsov^{1,2}, J.H.Bang², Y.C. Byun³, Moo-Hyun Cho², Manwoo Lee⁴, and E.A. Kim²

Frank Laboratory of Neutron Physics, Joint Institute for Nuclear Research, 141980, Joliot-Curie-6, Dubna, Russia

²Division of Advanced Nuclear Engineering, Pohang University of Science and Technology, Pohang 790-784, Korea

³ Research Institute of Science and Technology, San 32 Hyoja-dong, Nam-gu Pohang 790-600, Korea ⁴ Department of Physics, Kyungpook National University, Daegu 702-701, Korea

Abstract

Authors present the results of radioactive nuclides identification in the air filter materials, collected at the territory of Pohang city (Republic of Korea) one month after the Fukusima nuclear power plant accident.

Introduction

Experiment on air filters activity measurements have been conducted at POSTECH University located at Pohang city on the east side of the Republic of Korea one month after the devastating earthquake and tsunami demolished many small cities and villages at Japan as well as severely damaged several blocks of the Fukusima nuclear power plant. Air filters were collected approximately one month after the earthquake at a distance of about 1000 km to the South-West from Fukusima.

There are several kinds of detectors that detect the gamma rays emitted from radioactive samples, but High-Purity Germanium detector (HPGe) is widely used because of the high resolution and efficiency.

We used the HPGe detector (ORTEC, GEM-30180) with 20% efficiency for our measurements. The detector is p-type, which can measure the energy spectrum range of 100 keV to 10 MeV, and the energy resolution (FWHM) is 1.63 keV with 1.33 MeV ⁶⁰Co gamma line. To accumulate pulse height spectra we used the computer based DAQ system with Gamma-Vision 32^[1] software from ORTEC. The detector location is the first floor of Neutron laboratory at Pohang accelerator laboratory. Detector shielding consists of about 20 cm thick lead and 5 cm copper. Detector and shielding are shown at Fig.1.



Fig.1. Detector and shielding box view

Samples collection and preparation

To collect necessary amount of the sample, we need a filtering system because an amount of the radioactive nuclides of interest is too small in the air to be directly detected. The filtering system collects the dust assumed that the radioactive nuclides are included in atmosphere. The system was set up on the open roof of RIST building located at Pohang city (Republic of Korea) around 18 meters above the ground (Fig.2).

The collector consists of two parts, namely: pump and filter. The pump sucks the air into the filter. The pumping rate is about 1 Nm³/min at constant rate.

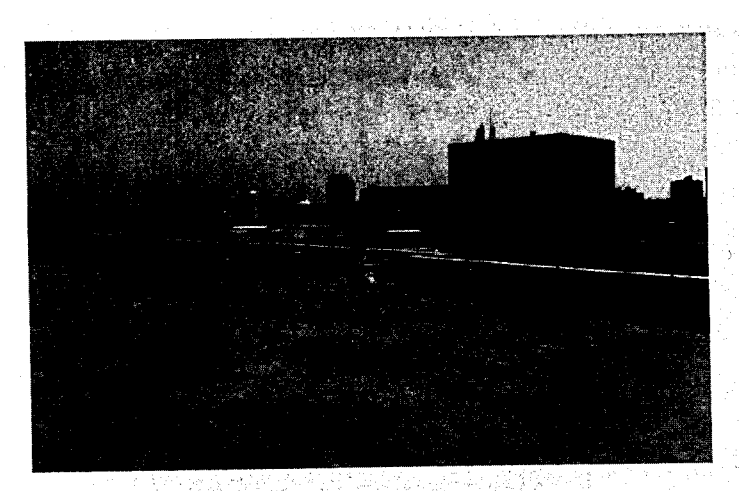


Fig.2. Air filtering system location at the roof of the RIST building

We collected two different filter samples using same pumping equipment. It took one day per sample to be sufficiently collected for this research. First filter sample in paper form was made by QMA (Quartz Microfiber Filters, Cat No. 1851-865, particle retention (0.3 μ m): minimum 99.95%) and had the following sampling time: 13.04.2011, 14:00 \sim 14.04.2011, 14:00 (around 24 hours). As the result of sampling, the weight of collected particulates was 0.161 g and the total flow was 1440.1 Nm³/day. The average concentration of particulates representing the amount of the dust in air is 111 μ g/Nm³ (Fig.3).

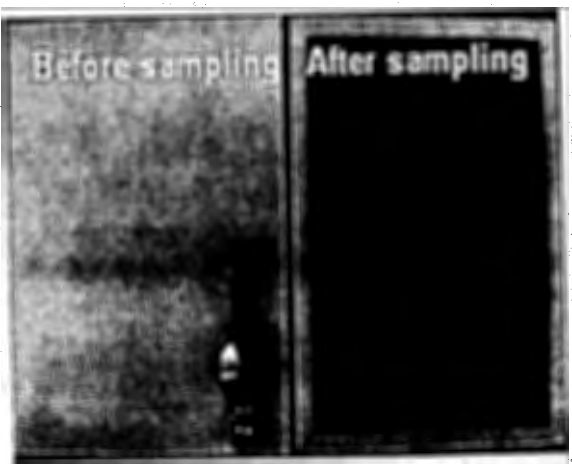


Fig.3. QMA paper before and after sampling

Second sample was different from QMA filter in many ways. In case of second, it is comprised of 3 layers of foam rubber, AC (Absorbent Coal) and foam rubber in order (Fig.4). The AC filter was also collected below the same condition of QMA filter.

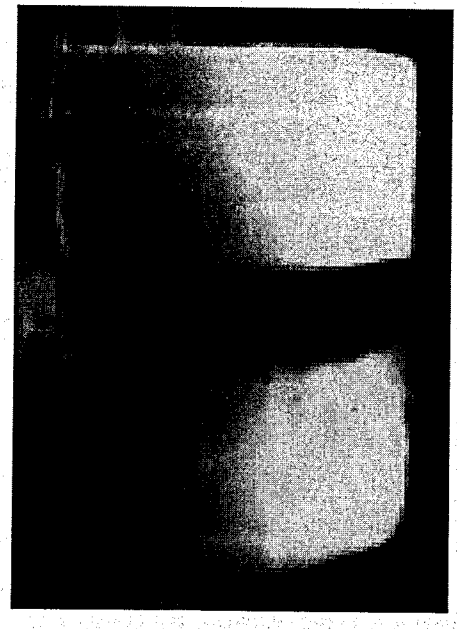


Fig.4. Second sample: foam rubber (top and bottom) and AC layer in the middle

Measurements

Sample measurements were performed three times according to the type of filter sample material. The first was of AC filter a couple of days later after filter collection. After conducting the pretests, energy calibration, peak identifications and background measurements, it was carried out in the Pb-Cu shielding structure by HpGe detector for 100300sec. The beaker of AC was parallel to the axial of the detector and was put close by the end of the detector head as possible so that the activity calculation of the nuclides of interest can be more convenient. Secondly, two paper filters, which were respectively collected on the different days, March 14 and April 13, were measured after the AC filter measurement. Since they are very thin and wide compare to the AC sample, it is difficult to achieve the detector count rate, which should be large to identify the signal of interest in

given time. Therefore, we have to compress the paper filters by folding it in four layers and then the folded paper filters were put on the surface of the detector head. Measurement time duration was 156139 sec for April's sample and 170060 sec for March's sample respectively. The next measurement was conducted with the foam rubbers. They were collected at the same time with AC filter. Since each of foam rubber was inserted at the top and bottom of the collecting rod with AC filter as the center, the position of two foam rubbers make difference. As the result, we just measured the bottom rubber. We supposed that the accumulated amount of the dust on top rubber is a negligible quantity because the top rubber plays the role as the inlet of airflow and the bottom rubber play the role as the outlet.

Results

Before sample measurements, the detector background was carefully investigated. First, we measured experimentally the efficiency of our passive background shielding.

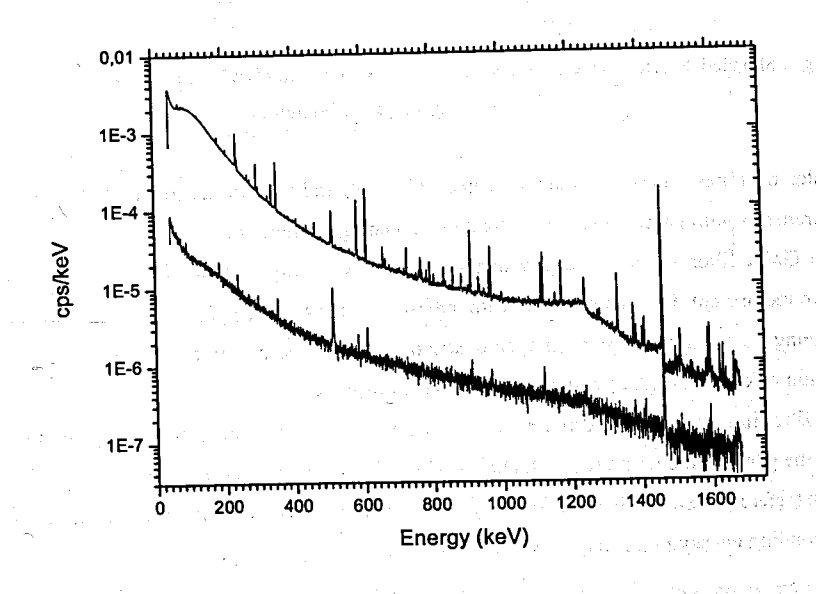


Fig. 5. Detector background without shielding (upper spectra) and inside the shielding box (lower spectra)

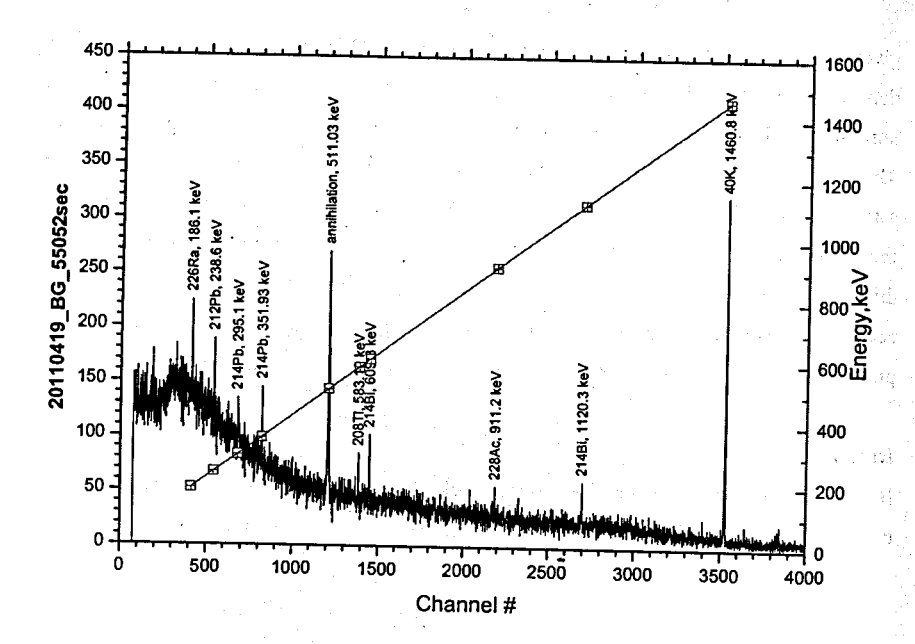


Fig. 6. Shielded detector background spectra accumulated during 55052 seconds with nuclides identification and energy calibration

Fig.6 demonstrates one of the shielded detector background spectra accumulated during our measurements with gamma lines identification and energy calibration.

The QMA filter samples measurements did not reveal any nuclides different from the background except for gamma line with measured energy 477.662(9) keV that we are identifying as the line from cosmogenic origin nuclide ⁷Be, produced by GCR particles spallation reaction at oxygen and nitrogen in the atmosphere.

AC filter in its turn also did not reveal any gamma lines different from background ones except the gamma line with identified energy 364.4 (1) keV which potentially could be the ¹³¹I line (reference energy 364.489 keV). AC filter material spectrum with background one in corresponding energy range are shown at Fig.8.

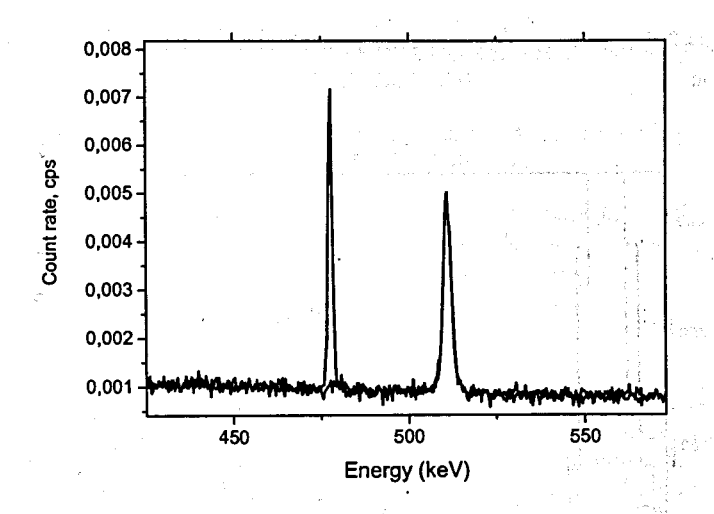


Fig.7. ⁷Be gamma line 477.6 keV (left) registered from QMA filter

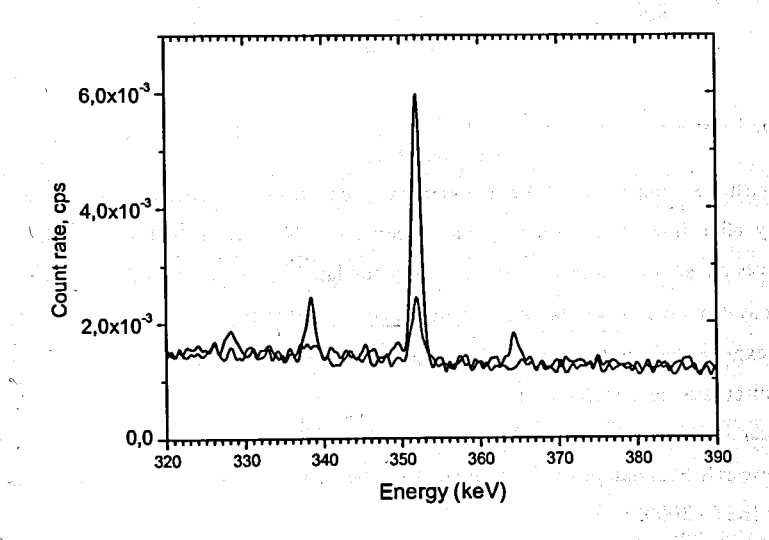


Fig.8. AC filter material spectra compared to the background spectra

To clarify the nuclide identification in the latter case we repeat the measurements with AC filter material approximately one month after the sample collection. Having in mind the ¹³¹I

lifetime that is 8 days, we supposed that corresponding peak would disappear one month after collection.

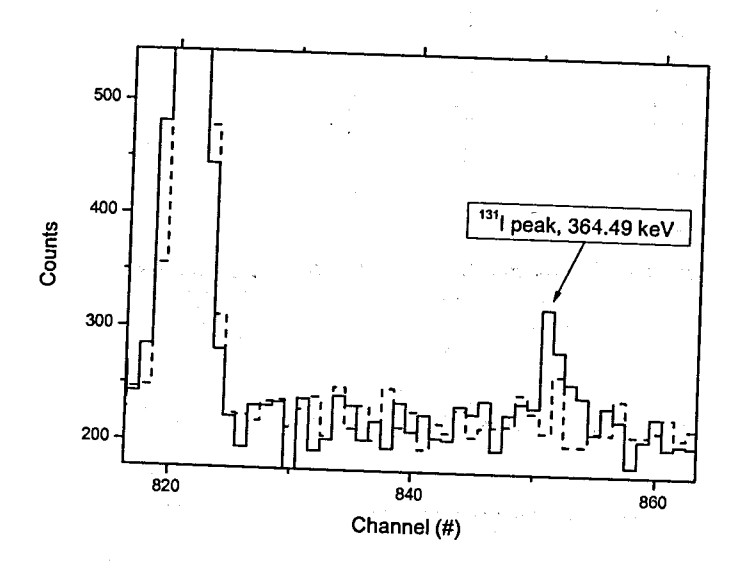


Fig. 9. ¹³¹I peak disappear 1 month after sample collection. Solid line – "fresh" sample, dashed line – one month later.

Fig.9 demonstrates comparison of the two gamma spectra from AC filter material collected immediately after filter collection and one month later. Numerical analysis of the data obtained gives an activity estimates for the ¹³¹I accumulated in AC material during 1 day of the air filter system operation (1440 Nm³ of air) equal to 0.6±0.1 Bq.

Authors express their gratitude to the Leading Engineer of the FLNP JINR Sergey Pavlov for fruitful discussion and advice.

This research was supported by WCU (World Class University) program through the National Research Foundation of Korea funded by the Ministry of Education, Science and Technology (R31 - 30005)

References:

MEASUREMENT OF THE P-ODD EFFECT IN RADIATIVE CROSS SECTION ON NATURAL LEAD

Vesna V. A.¹, Gledenov Yu. M.², Lazebnik I. M.¹, Nesvizhevsky V. V.³, Sedyshev P. V.², Shulgina E. V.¹

¹ Petersburg Nuclear Physics Institute RAS, Gatchina, Russia ² Joint Institute for Nuclear Research, Dubna, Russia ³ Institut Laue-Langevin, Grenoble, France

Abstract

The measurements of the P-odd asymmetry in radiative cross section on natural lead have been performed at the PF1B instrument of the ILL reactor (Grenoble, France). The integral flux of cold (mean wave length is 4.7 Å) neutrons was $\sim 10^{10}$ l/c. The neutron polarization was not worse than 92 %. Polarization was been switching by an adiabatic flipper. The sample was placed into a box of lithium rubber opened from a side of beam entrance. Two crystals of NaI (Tl) served as the detectors. The integral method of P-odd effect measurement was applied. Measurements, including the "0"-experiment, lasted 17 days. Taking into account the result of "0-test", an effect of asymmetry is a_3 (nat Pb) = $(2.3 \pm 3.5) \cdot 10^{-7}$ or $a_7 \le 8.1 \cdot 10^{-7}$ at 90% c. 1.

Introduction

Natural lead is a mixture of four isotopes: 204(1.43%), 206(24.15%), 207(22.4%), and 208(52.4%). None of the isotopes contains any suitable pairs of s- and p-resonances that may be responsible for P-odd effects in reactions with neutrons.

Nevertheless, in two measurements of the spin rotation angle for neutrons polarised transversely to their momentum vector in a sample of natural lead there was obtained the rotation angle $\Delta\phi=(2.24\pm0.33)\cdot10^{-6}$ rad/cm [1] and $\Delta\phi=(3.53\pm0.79)\cdot10^{-6}$ rad/cm [2]. Moreover, the measurement of the effect in a sample enriched with the isotope ²⁰⁷Pb to 87% gave the spin rotation angle $\Delta\phi<4.3\cdot10^{-6}$ at 90% c. l. [2]. This establishes the grounds for making the conclusion that the isotope ²⁰⁴Pb is a source of the effect.

The mechanism responsible for the observed spin rotation angle of neutrons traversing a lead sample is mixing of the compound-nucleus states of the spin having opposite parities. Paper [3] suggests the existence of a "negative" p- wave resonance in 204 Pb to explain the P-odd effect in the spin rotation angle. Another measurement of $\Delta \phi$ was done with a Pb sample enriched with 204 Pb to 36.6 %. [4]. The obtained result for the neutron spin rotation angle in the lead sample is $\Delta \phi = (8 \pm 2) \cdot 10^{-5}$ rad/cm for the lead with 100% content of 204 Pb. It is shown [5] that the traditionally being measured effect includes two components, namely truly spin rotation when transmitting through the sample and some addition explained by instrumental error of the method. Recently, a search for the p-resonance in the measurement of the radiative neutron capture cross section at resonance energy was undertaken in Dubna [6]. The group used a sample of natural Pb and a sample enriched with 204 Pb to 36.6 %. The

http://pdf.directindustry.com/pdf/ortec/a66-b32-gammavision-32-gamma-spectrum-analysis-software/50423-143328.html

conclusion of paper [6] is that the isotope 207 Pb has a strong "negative" p- resonance, which may explain the parity-violation effect in natural lead. Therefore, in comparison with the conclusion of papers [1,2,4] and [6] there appears some contradiction concerning 204 Pb.

From our point of view there are the possibilities to obtain additional information which may help to solve this problem. According to the optical theorem the P-odd effect in neutron spin rotation must be accompanied with P-odd effects in the total cross section

$$a_n = \frac{\sigma_{tot}^+ - \sigma_{tot}^-}{\sigma_{tot}^+ + \sigma_{tot}^-} = \frac{\Delta \sigma_{tot}}{2\sigma_{tot}}$$
 (1)

and in the radiative capture cross section

$$a_{\gamma} = \frac{\sigma_{\gamma}^{+} - \sigma_{\gamma}^{-}}{\sigma_{\gamma}^{+} + \sigma_{\gamma}^{-}} = \frac{\Delta \sigma_{\gamma}}{2\sigma_{\gamma}}$$
 (2)

for longitudinally polarized neutrons. Here, σ^+_{lot} , σ_{lot} and σ^+_{R} , σ^-_{r} are the total cross sections and radiative capture cross sections for the neutrons having opposite polarizations with respect to the momentum. Although these effects are much weaker than that in the $\Delta \phi$ measurement, the realization of these experiments is much easier methodologically. As it was shown by numerous experiments $\Delta \sigma_{lot} \cong \Delta \sigma_r$ for slow neutrons. As far as the radiative neutron capture cross section for natural lead at thermal energy (0.17 b) is much less than the total cross section (11 b), we decided to carry out an experiment on the measurement of parity violation effect namely in radiative cross section.

Experiment

The measurements were performed on the PF1B beam of polarized cold neutrons [7] at the Institut Laue-Langevin (ILL) in Grenoble, France. The average neutron wavelength at the PF1B was $\langle \lambda_n \rangle = 4.7$ Å. The neutron beam at the sample position was 80 mm by 50 mm. The total neutron flux at the sample was equal to $\sim 10^{10}$ c⁻¹. The neutron polarization was not worse than 92 %. A scheme of experiment is shown in Fig. 1. The guiding magnetic field was produced by Helmholtz coils (not shown in figure); it was reversed periodically during measurements. The strength of guiding magnetic field was equal to several Oersteds. The neutron polarization was reversed via switching high-frequency flipper. A sample was placed between two detectors. The sample represented 2 cylinders of natural lead (99.95% purity) in diameter of 80 mm and height 100 mm located one after another on the neutron beam axe. Necessary condition of measurement of P-odd asymmetry in γ -quanta is full absorption of the neutrons scattered by the sample. Therefore the target was located in a box of lithium rubber (⁶LiF) with the thickness of ~1.9 mm opened from an neutron entrace side.

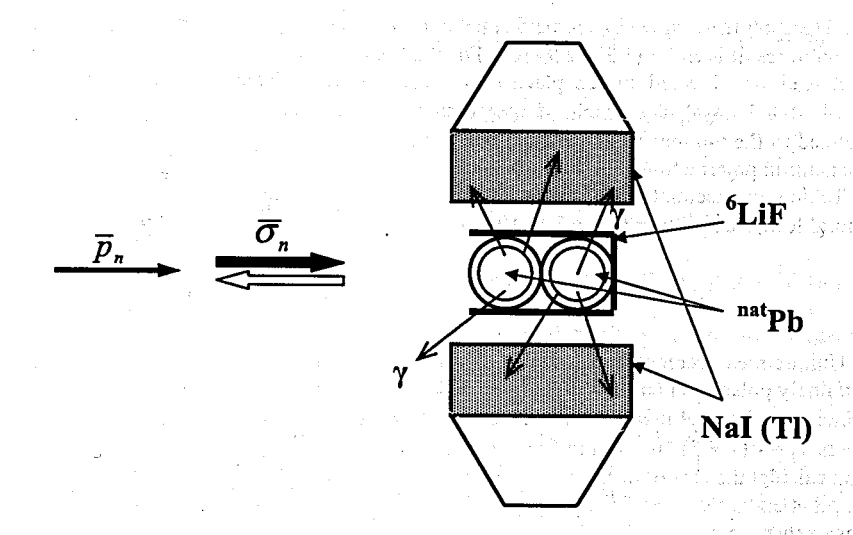


Fig. 1. A scheme of experiment.

Each γ -quanta detector consists of an NaI (TI) crystal with a diameter of 200 mm and a thickness of 100 mm. "Hamamatsu" S3204-03 photodiodes with a size of 18×18 mm² were used to detect scintillation photons. The photodiodes are connected to the NaI(TI) crystals via Plexiglas light-guides. The detectors were inserted into aluminium-alloy cases. A current method for the event detection was used (for more details see, for example, [8, 9]). The current preamplifiers used in our experiment converted the detector current into the output voltage. The output signal was digitized by a digital signal processor [10]. In experiment a quantity was measured:

$$\delta_{\gamma} = \frac{l_{\gamma}^+ - l_{\gamma}^-}{l_{\gamma}^+ + l_{\gamma}^-} \tag{3},$$

where I_r^+ , I_r^- are the intensities of detected γ -quanta corresponding to the different neutron helicities. This quantity is connected with the asimmetry in radiative capture cross section as $a_r \approx -\delta/P_n$, where P_n is polarization of neutron beam. For reducing influence of the reactor power fluctuations, the frequency of neutron polarization switching was higher than main frequencies of reactor noise spectrum [10]. Frequency of switching of polarization in experiment was equal to 8.3 Hz. To compensate false asymmetries the direction of the guiding magnetic field was reversed every series (every 4 min). For the averaged values we took into account the direction reverse of actual P-odd effect due to reverse of the guiding magnetic field. The P-odd effects are added in this case, because they have opposite signs.

Before main experiment the working ability of the setup was tested in the measurement of the radiative capture asymmetry for natural Br. We used a 30 g sample of the KBr powder. For 4 hours of measurement we obtained P-odd effect in radiative cross section $a_1(Br) = (11.0 \pm 1.3) \cdot 10^{-6}$, that coincides with the earlier result of Ref. [11] $a_1(Br) = (10.5 \pm 1.4) \cdot 10^{-6}$.

Measurements on lead were performed during ~ 10 days. The corrected for the neutron polarization result is $a_{\gamma}^{m} = (3.3 \pm 2.9) \cdot 10^{-7}$. For the "zero" experiment a box of lithium rubber without lead was located to the place of a target between detectors. Measurement time cotsisted of 6.5 days. The result of measurement is $a_{0} = (1.0 \pm 2.0) \cdot 10^{-7}$. The value is normalized to the γ -intensity in measurement with lead (see, for example, [8]) and corrected for the neutron polarization.

Taking into account "zero" experiment the asymmetry of radiative capture cross section on natural lead is a_{χ} (^{nat}Pb) = $(2.3 \pm 3.5) \cdot 10^{-7}$ or $a_{\gamma} \le 8.1 \cdot 10^{-7}$ at 90% c. l.

Discussion

Unique measurement of the P-odd asymmetry in total cross section at passage of the longitudinally polarized neutrons trough natural lead has been performed in [12]. Result of this experiment (an integral neutron flux was $2 \cdot 10^7$ c⁻¹, polarization was 85 %) at thermal neutron energy is $a_n = -(7 \pm 8) \cdot 10^{-7}$. Using Exp. (1) and (2) and taking in to account that $\Delta \sigma_{tot} \cong \Delta \sigma_p$ one can calculat the size of a_p from a_n for thermal neutrons ($\lambda = 1.8 \text{ Å}$): $a_p = (3.1 \pm 3.5) \cdot 10^{-6}$. It is seen, that an experimental accuracy received by us is 100 times better the accuracy of the previous experiment.

In Ref [3] G. Lobov performed the calculation of the P-odd asymmetry in total cross section for natural lead under assumption of existence of negative p-wave resonance in ²⁰⁴Pb with $E_p = -16$ eV. He used the typical parameters for p-wave resonances: a neutron width is $\Gamma^n_P = 3 \cdot 10^{-3}$ eV, a radiation width is $\Gamma^n_P = 0.1$ eV. For s-wave resonances he took experimentally known resonances with $E_S = -2.98$ keV, $\Gamma^n_S = 72$ eV [13]. Using experimental values for the neutron spin rotation [1, 2] and relation between $\Delta \phi$ and a_n

$$\Delta \varphi = n \, \Delta \sigma \frac{E - E_P}{\Gamma_P} \tag{4}$$

$$\Delta \sigma = 2 \, a_n(E) \, \sigma \tag{5}$$

the author has calculated size of P-odd effect in total cross section for ^{nat}Pb at neutron energies corresponding to the wave lengths of $\lambda = 6.8$ Å and $\lambda = 1.8$ Å: $a_n^{calc} = 2 \cdot 10^{-7}$ and $a_n^{calc} = 1 \cdot 10^{-9}$ respectively. As the total cross section in (4) and (5) he used the values of σ (6.8 Å) = 2.25 b and σ (1.8 Å) = 0.65 b. However, as one can see from [13], this size corresponds to the radiative cross section with the 1/v behavior. Thus, from our point of view, he actually calculated P-odd effect in radiative cross section, instead of total cross section where it is necessary to consider potential scattering. Therefore, if we are right, his calculation can be compared directly with our experimental result.

According to the same work [3], $a_n \sim 1/\sqrt{E_n}$, where E_n is the energy of neutrons. Then, for neutron energy in our experiment ($\lambda = 4.7\text{Å}$), the Lobov's estimation gives $a_{\gamma}^{calc} = 1.4 \cdot 10^{-7}$.

As one can see, the accuracy reached in our experiment is insufficient for certain conclusions about presence or absence a negative p-wave resonances. It is necessary to increase for increasing, at least, in 3-4 times. There is a possibility to reduce significantly the background coming from the interaction of neutrons with air and construction materials of installation [10] and to increase the measurement time. According our estimation the accuracy

of experiment can be increased in factor of 2-5, that can be sufficient for unequivocal conclusions.

This work is supported by the Russian Foundation for Basic Research, Grant No. 10-02-00174-a.

References

- B. Heckel, N. F. Ramsey, R. Gahler, O. Schaerpf, W. Dress, P. D. Miller, R. Golub, J. Byrne, J. M. Pendlebury. Phys. Lett. B 119 (1982) 298.
- V. P. Bolotsky, O. N. Ermakov, R. Golub, I. L. Karpikhin, P. A. Krupchitsky, S. Lamoreaux, Yad. Fiz. 59 (1996) 1873.
- 3. G. A. Lobov. Phys. At. Nucl. 63 (2000) 1387.
- R. Golub, I. L. Karpikhin, P. A. Krupchitsky, S. Lamoreaux, V. V. Vasiliev. Phys. At. Nucl. 65 (2002) 795
- 5. V. V. Vasiliev. Phys. At. Nucl. 65(7) (2002) 1228.
- J. Andrzejewski, N. A. Gundorin, I. L. Karpikhin, L. Lason, G. A. Lobov, D. V. Matveev, L. B. Pikelner. Phys. At. Nucl. 67 (2004) 1257.
- 7. H. Abele et al. NIM A 562 (2006) 407.
- V. A. Vesna, Yu. M. Gledenov, V. V. Nesvizhevsky, A. K. Petoukhov, P. V. Sedyshev, T. Soldner, O. Zimmer, E. V. Shulgina. Phys. Rev. C77 (2008) 03550.
- 9. V. A. Vesna, Yu. M. Gledenov, V. V. Nesvizhevsky, P. V. Sedyshev, E. V. Shulgina. European Phys. J. A Hadrons and Nuclei 47 (2011) 43-51
- V. A. Vesna, Yu. M. Gledenov, P. V. Sedyshev, E. V. Shulgina. Exp. Instr. Tech. 55 (No11) 2010, 1687.
- V. A. Vesna, E. A, Kolomenskij, V. M. Lobashev, A. N. Pirozhkov, L. M. Smotritskij, N. A. Titov. JETPh Let. 35 (1982) 433 (351 in Russian).
- 12. Yu. G. Abov, O. N. Ermakov, I. L. Karpikhin, P. A. Krupchitski, Yu. E. Kuznetsov, V. F. Perepelitsa, V. I. Petrushin. Yad. Fiz. 40 (1984). 1585.
- 13. S. Mughabghab et. al. Neutron Cross Sections. N. Y. Acad. Press. 1 (1984)

But a latin negati (14) olojih

NUCLEAR ANALYTICAL METHODS AS INTERFACE OF ENVIRONMENTAL AND TRACEABILITY EVALUATIONS

C. Oprea, M.V. Gustova, O.D. Maslov, A.G. Belov, I.A. Oprea, A. Mihul*

Joint Institute for Nuclear Research (JINR), Dubna 141980, Russian Federation

*Bucharest University, Faculty of Physics, Bucharest, Romania

Abstract

Nuclear Analytical Methods (NAM) could provide the basic tools for certifying environmental natural-matrix and for verifying environmental and radioanalytical test samples for the traceability evaluation. The effects of environmental pollution on soil-plant-water system are under observation of worldwide scientists reunited in different national and international scientific organizations and analytical laboratories. An example of the use of radioanalytical methods to probe key questions about the environmental media evaluation in view of the element patterns of the main pollutants was been tested and further described.

Keywords: Nuclear Analytical Methods, traceability, elements, environment assessment

Introduction

Natural-matrix of environmental samples provides the basis for the assessment of the cleanliness of the natural ecosystems, the air quality and consequently the human health environmental conditions.

In the present project, some environmental pollution indicators, such as some known biomonitors, soil and others, all from a natural ecosystem greatly affected by natural and anthropogenic causes, should to be characterized by several spectrometric methods of activation analysis at the microtron MT-25 and XRF analysis. The space and time integrated sampling of surface area over transects should to reveal pollution sources, the physical and biological status of the region.

NAM traceability

The main objectives of the NAM include measurements on the composition and nature of matter in space and time, in order to gain quantitative and qualitative information on their uncertainties, validation and traceability to known standards.

Traceability is defined as the property of a result of a value measurement whereby it can be compared with an appropriate standard, through an unbroken chain of comparisons, all having stated uncertainties. Usually such a testing method is applied considering generally international or national accepted standards. The test samples from nature should be similar to those routinely tested by participating laboratory in the comparison exercise.

Generally applied, there are two ways to establish traceability of the element levels in the biological material:

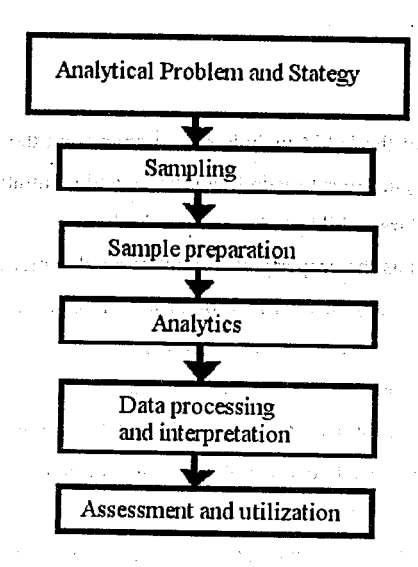
- 1. To use an absolute method as activation analysis by direct measurements;
- 2. To use an etalon e.g. to relate the found values to the level in a certified reference material of similar composition and element concentration; the etalon should to be measured together with the unknown sample.

Biological matrices can vary substantially from each other. Most, however, contain various amounts of interfering elements, making them potentially problematic to analyze.

Samples with too different concentration levels of the analyte pose another type of problem. For example, if the element concentration is too high to be analyzed by the direct measurement, the sample suffers a radiochemical pretreatment. If this preparation is too larger, the matrix can be changed to a level where it no longer will have the same influence on the analyte, thus becoming an entirely different analysis.

Any NAM procedure consists of sampling and sample preparation, measurement of the test sample, evaluation of the measurement (data reduction), and reporting measurement results in terms of an estimate of the measurand amount and its uncertainty. The detectable analyte depends on the selectivity of the analytical procedure (Figure 1). In a sequence presentation, it is a step by step procedure of information quantification-localization interpretation.

News problems on Establish of



William a MAR

Figure 1. Procedure of analytical method

Reference materials

Reference Materials (SRM OR CRM) are materials of whose chemical composition is sufficiently homogeneous and well established to be used for calibration and/or assessment of analytical method and also for etalonate the measured values to material. In many analytical determinations, the reliability of measurements is based on the reference materials. The certification of references materials should include the primary methods (i.e. methods of a highest metrological quality) to make property values traceable to SI-unit (Figure 2).

CRMs have the form of pellets, globules, shot, wires and bars, intended to be used as amount of substance standard. They can be constituted from pure elements, blends or synthetic mixtures, or even spiked or unspiked real-life standards. The pure elements can be used as:

- the amount of substance standard, if all impurities are known as determined in stated uncertainty limits;
- the chemical composition standards, if the high quality content of the all metallic traces are at ultra trace level certified.

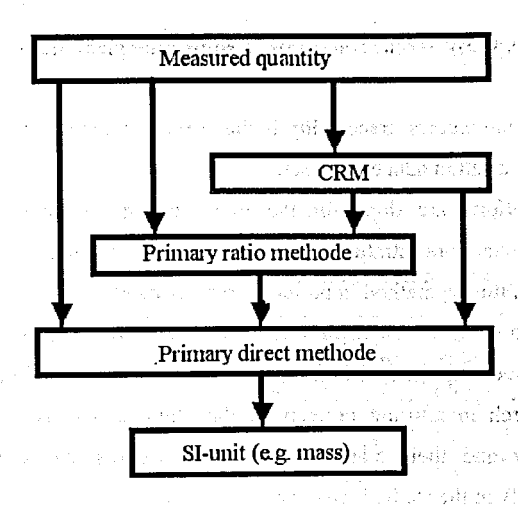


Figure 2. Traceability of a measurement result

In the routine analytical evaluation of biological materials, a matrix-matched reference material of a similar composition as the measurand better to be used as a control sample.

Measurement assurance

The measurement assurance approach is generally understood as the measurement quality control for the high-level calibration analytical procedures (NIST, NBS). For the most applications, measurements with insufficient accuracy can result in erroneous consequences. Then it has to be established a monitoring of the state of routine statistical quality control of the experiments in order to assure a quantified measurement uncertainty. Without a valid uncertainty statement and evidence that that the measurement process remains in an assured state of statistical control, no one can determine whether a given measurement is adequate for the intended scope. Since the uncertainty of a calibration process may change with time, the traceability of the measurement is foreseen in measurement assurance. In general, the sources of standard uncertainty in NAM procedure should be grouped according to the step by step analysis into four categories: i) preparation of the sample and comparator; ii) irradiation; iii) γ -ray spectrometry measurement; iv) radiochemical separation, if performed.

Application: Traceability of trace elements in some biological materials

In environmental studies, traceability is the proof of trueness of a peculiarity observed in the element concentration data overall set.

Continuous efforts are done for the improvement of analytical measurement of environmental pollutant concentrations, including trace heavy metals. Vegetation is often of primary interest monitoring method in polluted areas to stabilize soil with respect to wind and water erosion and to minimize downward translocation of contaminants. Field and analytical evaluations are needed to quantify the effects of vegetation on the leaching of metals.

Several research monitoring projects of the main author (see list of references) is currently underway and their main features is the assessment and improving of the environmental quality in the studied territory.

Impact of mobility of pollutants on vegetation was monitored by the two types of biomonitors used to indicate the level of regional pollution, namely mosses and agricrops. They were sampled according to transect of 55 km from the frontier RO-HU up to Western Carpathians, accounting for 880 km² network. The *Pleurozium schreberi* mosses were chosen for this monitoring study as they are widely spread in the investigated area. As crop monitoring results, the concentration values of maize constituents were used in presentation.

AA and XRF analytical measurements were performed to determinate concentrations of heavy metals in vegetation samples. The CRMS wheat RJI, moss DK-1 and chernozem CII-3 were used for precision, quality assurance and control (QA/QC) for element measurements. The precision of analytical procedures was expressed as StDev which ranged from 5-10 %. The recovery rates of measured elements ranged as 68-92 %.

The concentrations of the most significant elements for the survey done are shown in Table 1 as overall mean values charactering the low altitude (plain) area.

The values along transect are expressed as biological concentration factor (BCF) and translocation factor (TF). BCF is done by the ratio between element concentration in plant root and that in own soil:

$$BCF = \frac{c_{element_{rool}}}{c_{element_{rool}}} \tag{1}$$

TF is the ratio between element concentration in plant shoot to that in plant root:

$$TF = \frac{c_{element_{shoot}}}{c_{element_{root}}} \tag{2}$$

Table 1. Mean values in mosses and crops (mg/kg)

| | Mosses | | Crop 1 | root | Crop shoots | | Soil | |
|-------------|--------|--------------|--------|--------------|-------------|--------------|------|--------------|
| Metal | Mean | StDev (%) | Mean | StDev (%) | Mean | StDev (%) | Mean | StDev (%) |
| As | 0.58 | 21 | 0.26 | 15 | 0.22 | 8 | 1.7 | 12 |
| Cd | 0.35 | 15 | 0.23 | 21 | 0.15 | 11 | 1.4 | 3 |
| Cr | 8.5 | 13 | 16.2 | 10 | 14 | 23 | 35.7 | 16 |
| Cu | 48.2 | 25 | 38.6 | 15 | 26 | 15 | 38.5 | 5 |
| Ni | 10.7 | 27 | 15.7 | 19 | 12 | 12 | 32 | 13 |
| Pb | 44.9 | 17 | 21.8 | 14 - | 18.2 | 25 | 28.5 | 18 |
| Sb | 0.21 | 9 | 0.16 | 23 | 0.13 | 12 | 0.31 | 9 |
| V | 11.4 | 20 | 17 | 11 | 10.3 | 13 12 1 | 85.3 | 12 |
| Zn | 38.8 | 16 | 58 | 24 | 54 | 9 | 64 | 10 |

Accumulation of selected metals varied greatly among plants species due to differences in the mechanism of element uptake. The crop species monitored was efficient to absorb and translocate more than one metal from roots to shoots. The results indicated that none of the plants were recognized as hyperaccumulator because they accumulated heavy metals less than 1000 mg/kg.

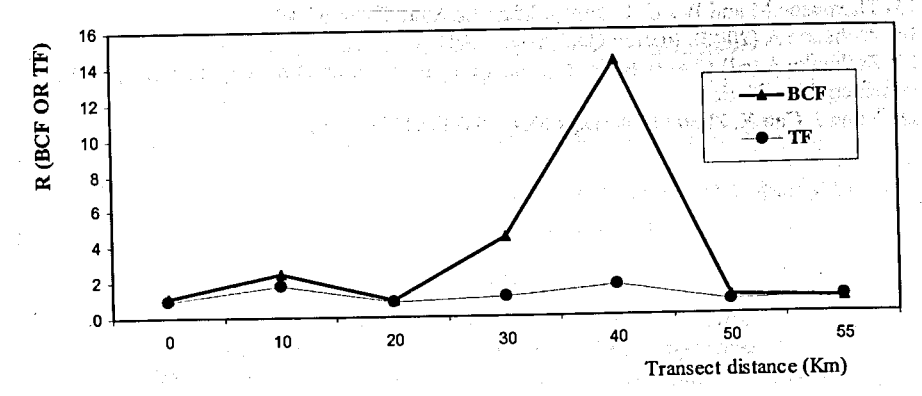


Figure 1. BCF and TF for lead concentration in crops

Note: A part of the experimental material (measured spectra) is still under processing. When the work will be ready, several aspects as demonstration of traceability for environmental radionuclide measurements, and the basis for measurement comparison over time comparing with data from literature are foreseen. There is expected more information on the metal accumulation and mechanisms of plant growing on contaminated soil to survive.

References

- [1] Cameron JM (1977). Measurement assurance, NBS Report:77-1240
- [2] Croarkin C (1983). Measurement assurance programs Part II: Development and implementation. NBS Special Publication: 676-II
- [3] Currie, LA (1995). J Pure & Appl Chem 67:1699
- [4] Ehrlich CD, Rasberry SD (1998). J Res NIST 103:93
- [5] EURACHEM (1995). Quantifying uncertainty in analytical measurement. 1st Ed.
- [6] ISO/IEC Guide 43-1 (1997). Internat. Org. for Standardization, Genève, Switzerland
- [7] Liu H, Probst A, Liao B (2005). STOTEN 339:153
- [8] MO 147 (1998). Romanian Law of Metrology
- [9] C. Oprea, S. Filip, A. Baluta, P. Pater, M. Fener, G. Istvan, A. Teusdea, M. Costea (2005). Environment & Progress 3:273
- [10] Oprea C, Maslov OD, Gustova MV, Belov AG, Szalanski PJ, Oprea IA, (2009). Vacuum 83 1:S162
- [11] Oprea CD, Mihul A, (2003). Romanian Rep in Phys 55 32:91
- [12] Oprea C, Gustova MV, Oprea IA, Maslov OD, Belov AG, Ciofu R, (2011). Proceedings of ISINN-18, 322
- [13] Oprea C, Maslov OD, Gustova, MV, Belov AG, Oprea IA, Ciofu R, Mihul A (2010). Proceedings of ISINN-17, 91
- [14] Parkany M (ed) (1993). Quality assurance for Analytical Laboratories, Royal Society of Chemistry, London, UK
- [15] Thompson M and Wood R (1995). J Pure & Appl Chem 67:49
- [16] Zschunke A (2000). Accred Qual Assur 5:441
- [17] Zschunke A (ed) (2000). Reference materials in analytical chemistry. Springer, Berlin Heidelberg New York
- [18] Yoon J, Cao X, Zhou Q, Ma LQ (2006). STOTEN 368:456

Научное издание

NEUTRON SPECTROSCOPY, NUCLEAR STRUCTURE, RELATED TOPICS

XIX International Seminar on Interaction of Neutrons with Nuclei Proceedings of the Seminar

НЕЙТРОННАЯ СПЕКТРОСКОПИЯ, СТРУКТУРА ЯДРА И СВЯЗАННЫЕ ВОПРОСЫ

XIX Международный семинар по взаимодействию нейтронов с ядрами Труды семинара

Ответственная за подготовку сборника к печати Л. В. Мицына.

Сборник отпечатан методом прямого репродуцирования с оригиналов, предоставленных оргкомитетом.

E3-2012-30

Получено 14.03.2011. Подписано в печать 11.04.2012. Формат 60×90/16. Бумага офсетная. Печать офсетная. Усл. печ. л. 25,13. Уч.-изд. л. 43,93. Тираж 170 экз. Заказ № 57599.

Издательский отдел Объединенного института ядерных исследований 141980, г. Дубна, Московская обл., ул. Жолио-Кюри, б. E-mail: publish@jinr.ru www.iinr.ru/publish/